Plio-Pleistocene Reconstruction of East African and Arabian Sea Palaeoclimate

Thesis submitted for the degree of Doctor of Philosophy,

Department of Geography, UCL

Katy Elisabeth Wilson

I, Katy Elisabeth Wilson, confirm that the work presented in this thesis is my own. Where information has been derived from other sources, I confirm that this has been indicated in the thesis.

…… June 2011

Abstract

Superimposed upon a long-term trend of aridification, the climate history of Africa was punctuated by episodes of extreme climate variability, characterised by the precessionally-forced appearance and disappearance of large lake systems within the East African Rift Valley. In order to investigate the nature of low-latitude climate variability during the Late Pliocene and Early Pleistocene, this thesis combines high-resolution analyses from one of the lake phases in the Central Kenyan Rift with the reconstruction of long-term changes in the transport of wind-borne terrigenous dust to the Arabian Sea. Climate in both regions is strongly influenced by relative changes in the strength of the Indian Ocean monsoons, which determine rainfall distribution in equatorial East Africa and generate the low-level winds which transport dust offshore from the Arabian Peninsula. In the Baringo-Bogoria basin in the Central Kenyan Rift, a well-dated package of fluvio-lacustrine sediments and diatomite units documents a major humid phase between 2.7 and 2.55 million years ago (Ma), coincident with the intensification of glaciation in the Northern Hemisphere. Stable oxygen isotope measurements of diatom silica, combined with the XRF analysis of whole-sample geochemistry, reveal that the deep lake phase was characterised by wet-dry cycles lasting, on average, 1,400 years. Over longer timescales, variations in the aeolian delivery of lithogenic matter to the Arabian Sea, reflected in normalised flux of titanium, show that monsoonal circulation prior to 2.6 Ma was highly variable and primarily driven by orbitally-forced changes in tropical summer insolation, modulated by the 400,000 year cycle of orbital eccentricity. Millennial-scale fluctuations in the dust record also support the evidence of abrupt wet-dry cycles in East Africa. Such high-resolution cycles are rarely found in older records, thus giving a valuable insight to the nature of short-term fluctuations in Plio-Pleistocene climate.

Acknowledgements

There are a great many people to whom I owe thanks and gratitude for their support throughout the completion of this Ph.D. thesis. First and foremost, I am immensely grateful to my supervisor, Prof. Mark Maslin, for his unstinting belief, encouragement and guidance, and for always having 'a minute' when I knock on the door. I am also greatly indebted to my second supervisor, Dr. Anson Mackay, who has been an invaluable source of help and advice on a huge range of subjects.

This project would not have been possible were it not for the ongoing work of the Baringo Paleontological Research Program (led by Dr. Andrew Hill of Yale University), who have been working in the Tugen Hills for more than forty years. Very special thanks must go to my mentor, Dr. John Kingston, for his boundless enthusiasm, inspiring discussions about diatomite sequences and for leading the bush-whacking adventures which resulted in my legs being ripped to pieces by acacia for three years in a row. I am also grateful to Dr. Alan Deino for all his work to provide dates for the Barsemoi sequence; to Dr. Robert Edgar for counting endless numbers of diatom slides and to Boniface Kimeu, Julius, Brown, Bryce Carlson and Suzy Cote for their assistance in the field. I would also like to thank Emily Goble and Chris Gilbert for making the constant vehicle breakdowns bearable with never-ending hilarity and bouts of rock-throwing.

I would also like to thank Professor Melanie Leng for her continuing guidance through the highs and lows of diatom stable isotope analysis, to Dr. George Swann for all his advice and for acting as a sounding board for some of my contamination theories, to Professor Jonathan Holmes for his isotope expertise and finally, to Dr. Gavin Simpson who has helped me enormously with the development of numerical models. I would also like to thank Professor Martin Trauth of Universität Potsdam for his invaluable MATLAB® expertise and for providing so much help with complicated lines of code whenever I couldn't understand them. I am also extremely grateful to Martin for inviting me to participate in the Suguta Valley 2010 expedition and for giving me the chance to explore a different section of the Kenyan Rift Valley with his team.

I am extremely grateful to Janet Hope for both personal and technical support over the last few years and to Ian Patmore and Tula Maxted for assistance in the lab. I would also like to thank Jim Davy for his help with SEM/EDX, Professor Juergen Thurow for training on the use of the XRF scanner and Hilary Sloane for assistance at the NERC Isotope Geosciences

Laboratory (NIGL), and particularly for taking two days to introduce me to the joys of the fluorination line. A large part of this project would not have been possible were it not for the help and support of Dr. Lallan Gupta of the Integrated Ocean Drilling Program (IODP) repository in Kochi, Japan. By taking the unprecedented step of allowing the release of archive core material to an external institution, Dr. Gupta ensured that I was able to complete the analysis for this project on time. On a related note, I would also like to extend my thanks to all the users of the basement cold store who tolerated the presence of the 'coffin' for 8 months!

There are a great many (past and present) Ph.D. students at UCL to whom I owe considerable thanks for providing endless advice, entertainment and cups of tea and coffee. In no particular order, these are: Alex Dickson, Ginnie Panizzo, George Swann, Jon Tyler, Adam Young, Matt Owen, Charlie Hall, Emma Wiik, Jorge Salgado and Luca Marazzi – thank you all for being great friends, conference partners and sources of constant amusement and distraction.

On a more personal note I am hugely grateful to my family for their continued support and encouragement but particularly to my parents who have always shown an interest in my research, to Jo for being the best sister I could ever ask for, and to my brother Ed for being a saint and managing to put up with me for the last five months. Finally, I would like to thank Iain, for knowing what I wanted to do before I did and for giving me the courage and conviction to follow my dreams. I couldn't have done it without you.

This research was funded by a NERC Ph.D. studentship (NE/F008635/1) with support for isotope analysis through NIGL facility grants (IP/1082/1108 and IP/1104/0509). Additional funding was also received from the Quaternary Research Association Bill Bishop Award, a UCL research bursary and the UCL Graduate School Conference Fund.

This thesis is dedicated to my niece Georgia, and to the memory of my late uncle Nick.

Table of Contents

Title page 1
Abstract 3
Acknowledgements 4
Contents 6
List of figures 10
List of tables 12

Chapter 1: Introduction and Palaeoclimate History 13

1.1 Introduction 13
1.2 Aims and Objectives 14
1.3 Thesis Structure 16
1.4 The Intensification of Northern Hemisphere Glaciation 17
1.4.1 The Mid-Pliocene Warm Period 19
1.4.2 The transition to cooler climates (iNHG) 21
1.4.3 Potential causal mechanisms for the iNHG 21
1.4.4 Summary 26
1.5 Evidence for Sub-Orbital Scale Climate Change during the Pliocene 26
1.6 Low-Latitude Climate Change during the Plio-Pleistocene 28
1.6.1 The long-term aridification of Africa 30
1.6.2 Possible causes of aridification 33
1.6.3 Evidence for precessionally-forced climate change in the tropics 34
1.6.4 Episodes of extreme climate variability 35
1.7 Tropical Monsoonal Circulation 39
1.7.1 Geological evolution of monsoonal circulation 40
1.7.2 Precessional forcing of monsoonal variations 41
1.7.3 Monsoon circulation and glaciation 43
1.8 Summary 44

Chapter 2: Theoretical Background - Stable Isotope Geochemistry 45

2.1 Introduction 45
2.2 Introduction to Stable Isotope Geochemistry 45
2.2.1 Equilibrium isotope exchange 46
2.2.2 Kinetic isotope effects 46
2.2.3 Disequilibrium effects 47
2.3 The Application of Stable Isotopes as a Palaeoenvironmental Tool 49
2.4 Oxygen Isotope Systematics 50
2.4.1 Isotopes in precipitation 51
2.4.2 Oxygen isotopes in lacustrine environments 54
2.4.3 Oxygen isotopes in marine environments 58
2.5 Carbon Isotope Systematics 62
2.5.1 Factors affecting the $\delta^{13}C$ of DIC in seawater 63
2.5.2 Factors affecting the $\delta^{13}C$ of foraminifera 64
2.5.3 Factors affecting the $\delta^{13}C$ of bulk organic matter 65
2.6 Summary 66

Chapter 3: The Baringo-Bogoria Basin 67
3.1 Introduction 67
3.2 Lake Baringo 67
3.3 Geomorphlogy of the Baringo-Bogoria basin 69
3.4 Modern Climatic Setting 71
3.4.1 Atmospheric circulation 72
3.4.2 Rainfall Variability 74
3.4.3 Factors influencing East African climate 79
3.5 Regional Geological Setting 82
3.5.1 The Muruyur Formation: 15.5 - 15 Ma 83
3.5.2 The Ngorora Formation: 13 - 8.5 Ma 84
3.5.3 Mpesida Beds: 7 - 6.2 Ma 85
3.5.4 Lukeino Formation: 6.2 - 5.6 Ma 85
3.5.5 Chemeron Formation: 5.3 - 1.6 Ma 86
3.5.6 Kapthurin Formation: 0.7 - 0.2 Ma 86
3.6 The Barsemoi Diatomites: 2.68-2.55 Ma 87
3.6.1 Site description 88
3.6.2 Chronology of the Barsemoi diatomites 92
3.7 Summary 93

Chapter 4: Barsemoi Diatomites - Methodologies 94
4.1 Introduction 94
4.2 Characterisation of diatomite units 94
4.2.1 Sediment stratigraphy 94
4.2.2 Variations in diatom assemblage 94
4.3 Oxygen isotopes in biogenic silica 96
4.3.1 Laboratory analysis techniques for $\delta^{18}O_{diatom}$ 96
4.3.2 Comparison of analytical techniques 101
4.3.3 Sample cleaning and preparation 102
4.3.4 Isotope vital effects 106
4.4 Geochemistry: Contamination of the $\delta^{18}O_{diatom}$ signal 108
4.4.1 SEM/EDS microprobe analysis 109
4.4.2 Infrared spectroscopy 109
4.4.3 Whole-sample geochemistry by X-ray fluorescence spectrometry 110
4.5 Statistical and multivariate analyses 111
4.5.1 Ordination techniques 111
4.5.2 Mass-balance calculations 112
4.6 Summary 114

Chapter 5: The Palaeoenvironmental Reconstruction of Climate Variability and Lake Evolution at Palaeo-lake Baringo 116
5.1 Diatomite characterisation 116
5.1.1 Meso-scale sedimentological stratigraphy 116
5.1.2 Variations in diatom assemblage 118
5.2 Assessing contamination with the $\delta^{18}O_{diatom}$ record 123
5.2.1 Oxygen isotope analysis of biogenic silica 123
5.2.2 Qualitative assessment of contamination 125
5.2.3 Quantitative assessment of contamination 127

5.2.4 Modelling of oxygen isotope signal ... 131
5.3 Evaluation of $\delta^{18}O$ changes recorded in the Barsemoi diatomite sequence ... 142
5.4 Evolution of palaeo-lake Baringo ... 147
5.5 Millennial-scale cyclicity in the Barsemoi diatomite sequence ... 151
5.5.1 The manifestation of millennial-scale cyclicity in African palaeoclimate records . 153
5.5.2 Mechanisms for millennial-scale cyclicity ... 156
5.5.3 Millennial-scale cyclicity during the Pliocene ... 158
5.6 Summary ... 161

Chapter 6: The Arabian Sea ... 163
6.1 Introduction ... 163
6.2 The Owen Ridge – ODP Sites 721 and 722 ... 164
6.3 Modern Climatic Setting ... 167
6.3.1 Indian Ocean monsoonal circulation ... 168
6.3.2 The aeolian dust flux ... 170
6.4 Oceanographic Setting ... 172
6.4.1 Indian Ocean circulation ... 172
6.4.2 Interannual variability ... 174
6.4.3 Arabian Sea circulation ... 176
6.5 Summary ... 178

Chapter 7: Arabian Sea Project Methodologies ... 180
7.1 Introduction ... 180
7.2 Core Sampling ... 180
7.3 Foraminiferal Stable Isotopes ... 181
7.3.1 Sample preparation and analysis ... 182
7.4 Bulk Organics ... 183
7.4.1 Sample preparation ... 183
7.5 X-Ray Fluorescence Elemental Analysis ... 184
7.5.1 Background information ... 184
7.5.2 Core preparation and measurement ... 186
7.5.3 Calibration of XRF data ... 187
7.6 Core Chronology ... 187
7.6.1 Composite depth model ... 187
7.6.2 Orbital dating ... 190
7.7 Data Analysis ... 190
7.7.1 Generalised additive and linear modelling ... 191
7.7.2 Spectral analysis ... 192
7.8 Summary ... 193

Chapter 8: A 600-kyr Record of Dust Transport to the Arabian Sea ... 194
8.1 Outline ... 194
8.2 Revised Chronology for ODP site 721/722 ... 194
8.2.1 Benthic foraminiferal isotopes ... 196
8.2.2 Correlation to the LR04 global benthic stack ... 196
8.2.3 Sedimentation rates ... 197
8.2.4 Comparison to other age models ... 199
8.2.5 Summary ... 199

8.3 Elemental Indicators of Terrigenous Dust Flux 201
8.3.1 Calibration and normalisation of XRF data 201
8.3.2 The interpretation of geochemical trends as records of aeolian dust flux 204
8.3.3 XRF elemental ratios 206
8.3.4 Summary 210
8.4 Time-Series Analysis of Ti/Al data 211
8.4.1 Generalised additive models (GAM) 212
8.4.2 Spectral analysis 213
8.4.3 Summary 221
8.5 Low-latitude Monsoonal Variability during the Pliocene 222
8.5.1 Sea surface temperatures 222
8.5.2 Tropical records of aeolian dust supply 226
8.5.3 Orbital changes in insolation 236
8.5.4 Correlation to the Barsemoi Diatomites 239
8.6 Summary 242

Chapter 9: Project Synthesis 245
9.1 Summary of Results 245
9.1.1 Tropical climate fluctuations: A comparison to Barsemoi Diatomite #4 246
9.1.2 The impact of high-latitude changes upon tropical climate 249
9.1.3 Linking African palaeoclimate changes with early human evolution 250
9.1.4 Summary of findings 251
9.2 Directions for Future Research 252

Chapter 10: References 256

List of Figures

Chapter 1.

Figure 1.1: Map showing locations of study sites 14
Figure 1.2: Plio-Pleistocene evolution of high-latitude climate.. 18
Figure 1.3: Comparison of major transitions in Plio-Pleistocene climate. 29
Figure 1.4: Lacustrine and tectonic history of East Africa. 36

Chapter 2.

Figure 2.1: Global distribution of annual weighted $\delta^{18}O$ values of precipitation 52
Figure 2.2: Controls of the $\delta^{18}O$ composition of lacustrine diatom silica..... 56
Figure 2.3: Distribution of surface ocean $\delta^{13}C$ values. 62
Figure 2.4: Controls on the $\delta^{13}C$ composition of foraminifera. 64

Chapter 3.

Figure 3.1: Satellite view of the Central Kenyan Rift Valley 68
Figure 3.2: Geomorphology of the Kenyan Rift Valley and the Baringo region 70
Figure 3.3: Seasonal changes in atmospheric circulation over Africa.. 73
Figure 3.4: Mean position of the mid-level African Easterly Jet. 74
Figure 3.5: Mean annual precipitation distribution over Africa. 75
Figure 3.6: Schematic monthly transect of East African rainfall 77
Figure 3.7: Monthy precipitation $\delta^{18}O$ values for Tanzania and Ethiopia.. 79
Figure 3.8: Site map of the Tugen Hills detailing exposures of the Chemeron formation. 83
Figure 3.9: Stratigraphic framework of the Tugen Hills geological sequence. 84
Figure 3.10: Photographic plates depicting type section of the Barsemoi Diatomites 89
Figure 3.11: General stratigraphic correlations between Barsemoi Diatomite exposures.. 91
Figure 3.12: Interpolated 40Ar/39Ar ages for the Barsemoi Diatomites. 92

Chapter 4.

Figure 4.1: Variations in diatom assemblage throughout the Barsemoi Diatomites 95
Figure 4.2: Schematic illustration of method used for cleaning of diatom samples.. 103
Figure 4.3: Illustration of SPLITT separation. 106

Chapter 5.

Figure 5.1: Sediment stratigraphic section of Barsemoi Diatomite type section 117
Figure 5.2: Variations in diatom assemblage for diatomite unit #4. 118
Figure 5.3: Scanning electron microscope images of *Aulacoseira* and *Stephanodiscus*. 119
Figure 5.4: Raw $\delta^{18}O$ isotope and XRF data from diatomite samples 124
Figure 5.5: Scanning electron microscope images to assess diatom purity.. 126
Figure 5.6: Results of IR spectroscopy 127
Figure 5.7: Results from contamination models tested to correct $\delta^{18}O_{diatom}$ values 134
Figure 5.8: Ordination biplot showing results of PCA performed on XRF results 136
Figure 5.9: Attribute plots for elements indicative of tephra contamination. 137
Figure 5.10: Attribute plots for elements indicative of clay contamination 138
Figure 5.11: Conceptual model for three end-member contamination models. 139
Figure 5.12: Ternary plot showing modelled distribution of $\delta^{18}O$ values. 140
Figure 5.13: PCA axis 1 scores against modelled clay contamination proportions. 142
Figure 5.14: Compilation of $\delta^{18}O_{modelled}$ values, contamination and assemblage changes 143
Figure 5.15: Mesoscale wind circulation changes in East Africa.. 145
Figure 5.16: Setting of Barsemoi Diatomites against changes in insolation. 148
Figure 5.17: Conceptual models for development of Rift Valley lakes 150

Chapter 6.

Figure 6.1: Map showing study sites with satellite image of Arabian dust plume 164
Figure 6.2: Regional bathymetry of the Arabian Sea and setting of the Owen Ridge.. 165
Figure 6.3: Schematic profile of the Owen Ridge. 166
Figure 6.4: Seasonal monsoon wind stress fields over the Indian Ocean. 168
Figure 6.5: Indian Ocean surface water circulation during summer 171
Figure 6.6: Indian Ocean surface water circulation during winter.. 172
Figure 6.7: Variations in Indian Ocean temperature, salinity and nutrient concentration. 173
Figure 6.8: Arabian Sea upper water profiles of nutrient upwelling. 176

Chapter 7.

Figure 7.1: Photographic compilation of archive core halves from ODP Site 721/722..... 181
Figure 7.2: Illustration and scanning electron microscope image of *Uvigerina peregrina*.. ... 182
Figure 7.3: Schematic illustration of XRF scanner..... 185
Figure 7.4: Spliced composite depth model for ODP Sites 722 and 721..... 188

Chapter 8.

Figure 8.1: Raw $\delta^{18}O$, inorganic $\delta^{13}C$ and organic $\delta^{13}C$ data against composite depth 195
Figure 8.2: Alignment of $\delta^{18}O$ data to LR04 benthic stack.. 197
Figure 8.3: Comparison of published age-depth models for ODP Site 721/722. 198
Figure 8.4: Detailed comparison of chronology to age model of Clemens et al. (1996).. 200
Figure 8.5: Gaussian distribution of modelled XRF fluorescence spectra 201
Figure 8.6: Raw elemental count data from XRF analysis 202
Figure 8.7: Illustration of the effect of hiatus in core data 204
Figure 8.8: Time-series data for aeolian dust flux parameters Ti/Al, Fe/Al and K/Al 207
Figure 8.9 Glacial-interglacial changes in Ti/Al and grain size. 208
Figure 8.10: Trend and derivatives of gamma GLM applied to the Ti/Al time-series 211
Figure 8.11: Lomb-Scargle power spectrum of filtered Ti/Al data series.. 214
Figure 8.12: Illustration of long-term correlation between Ti/Al and eccentricity..... 215
Figure 8.13: Compiled results of wavelet analysis and gamma GLM modelled trend..... 217
Figure 8.14: Power spectrum for analysis of LR04 benthic stack between 3-2 Ma 220
Figure 8.15: Compiled dust and oceanic parameters measured on ODP Site 721/722..... 223
Figure 8.16: Compilation of regional Plio-Pleistocene dust records. 224
Figure 8.17: Map showing locations of regional dust records..... 226
Figure 8.18: Comparison of previous measurements of terrigenous dust flux at 721/722.. 227
Figure 8.19: Spectral comparison of records from ODP 721/722 and ODP 967..... 235
Figure 8.20: Correlation of changes in Arabian Sea dust flux to Barsemoi Diatomites 240

Chapter 9.

Figure 9.1: Compiled changes in low-latitude climate during diatomite unit #4..... 247
Figure 9.2: Power spectrum for Ti/Al data between 2.625 Ma and 2.600 Ma..... 248

List of Tables

Table 5.1: Results of XRF analysis of purified diatomite samples 128
Table 5.2: Summary of the development of contamination models to correct $\delta^{18}O$ values.. . 132
Table 5.3: Summary of Pliocene-aged records of millennial-scale climate oscillations 159
Table 7.1: Composite depth model for ODP Sites 721 and 722..... 189

Chapter 1: Introduction and Palaeoclimate History

1.1 Introduction

The transition from the warm, stable conditions of the Middle Pliocene to the high-amplitude glacial cycles which characterised much of the Pleistocene was marked by a prolonged period of cooling which culminated in the intensification of Northern Hemisphere glaciation (iNHG) between 2.7 and 2.5 million years ago (Ma). Whilst the progressive expansion of ice sheets in the high northern latitudes is well documented, the precise mechanisms responsible for the iNHG and its impact on low-latitude climate processes remain somewhat uncertain. This study focuses on reconstructing environmental change in equatorial East Africa and the Arabian Sea in order to understand the nature of low-latitude climate change during the Plio-Pleistocene in relation to the relative intensity of regional monsoon circulation. At present, the Indian Ocean and Asian monsoonal systems form significant components of tropical and sub-tropical climate variability throughout Asia and Africa. The seasonal reversal of atmospheric circulation and precipitation distribution that gives rise to the monsoons generates major rainy periods in central East Africa and drives the seasonal upwelling of cold, nutrient-rich water in the Arabian Sea.

The lacustrine history of the East African Rift Valley is characterised by a number of periods of extreme wet-dry climate variability which are coincident with major transitions in global climate. One such period occurs between 2.7 and 2.5 Ma, coincident with the iNHG, and was characterised by enhanced humidity which led to the episodic development of a large freshwater lake system within the Baringo-Bogoria basin. This is marked by a series of diatomite deposits (the Barsemoi Diatomites) exposed in the Tugen Hills near the present-day Lake Baringo in the Central Kenyan Rift (figure 1.1). Radiometric dating demonstrates that the timing of diatomite deposition closely approximates maxima in the 30 °N (June) insolation curve, implying that regional moisture availability during the Late Pliocene was controlled by precessionally-forced monsoonal circulation (Deino et al., 2006; Kingston et al., 2007). The first element of this research project focuses on the high-resolution analysis of one of these diatomite units in order to investigate the cyclical lake development and sub-orbital scale climate changes which occur during periods of extreme wet-dry variability.

The second element of this study involves the wider investigation of changes in the geochemical composition of ocean sediment material which record long-term fluctuations in

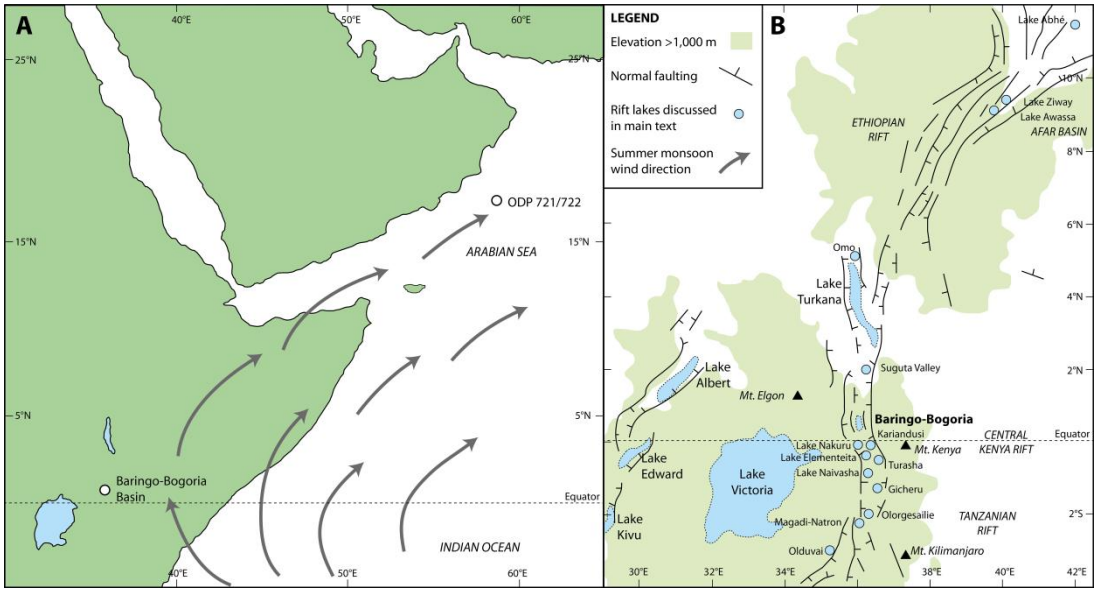

Figure 1.1 Map (A) illustrating the relative locations of the sites studied in this project: the Baringo-Bogoria Basin in the East African Rift Valley (EARS) and Ocean Drilling Program (ODP) Sites 721 and 722 situated on the Owen Ridge in the Arabian Sea. Arrows indicate the wind direction of the Indian Ocean summer monsoon circulation, a major component of the regional climate system. Map (B) shows the relative position of the Baringo-Bogoria Basin within the EARS and the locations of the other Rift Valley lakes discussed in the text.

the flux of terrigenous dust delivered to the Arabian Sea (figure 1.1) from the nearby continents. The aeolian transport of dust to the Arabian Sea is controlled by the intensity of the Indian Ocean monsoon which affects source area climate conditions and local wind regimes, the strength of which drive offshore upwelling of cold, nutrient-rich water. Ocean Drilling Program (ODP) Sites 721 and 722, located on the Owen Ridge in the Arabian Sea, are ideally situated to record past changes in the dynamics of the Indian Ocean monsoon. Through the combination of the high-resolution analysis of terrestrial palaeoclimate archives and oceanic sediment records, it is possible to contextualise short-term lake level fluctuations in East Africa with the Late Pliocene – Early Pleistocene (hereafter referred to as Plio-Pleistocene) evolution of the Indian Ocean monsoonal system.

1.2 Aims and Objectives

The aim of this research project is to explore and critically assess the nature of long-term and short-term variability of low-latitude monsoonal circulation during the Plio-Pleistocene (between 2.9 and 2.3 Ma) through the analysis of both terrestrial and oceanic palaeoclimate archives. Through the detailed analysis of one of the Barsemoi diatomite units, coupled with the assessment of long-term changes in the Indian Ocean monsoon recorded in Arabian Sea sediments from ODP Sites 721 and 722, this study has the following aims:

1. Understand the links between precessional forcing, monsoonal circulation and moisture availability in East Africa in order to investigate lake level changes during Plio-Pleistocene wet phases.
2. Investigate the origin of palaeolakes within the East African Rift Valley (EARS)
3. Establish the extent to which oxygen isotope records from biogenic silica in diatomite deposits can be used as a reliable proxy for palaeoclimate change.
4. Correlate terrestrial and oceanic palaeoclimate records of monsoon variability in order to better understand the dynamics of monsoonal circulation during the Plio-Pleistocene.

Furthermore, the objectives of this project are to:

a. Provide a high-resolution reconstruction of changes in oxygen isotope composition throughout one of the Barsemoi diatomite units exposed in the Central Kenyan Rift Valley in order to investigate short-term, sub-orbital scale variations in climate change during the Pliocene. These results will be assessed alongside changes in diatom assemblage.
b. Develop a method to assess levels of contamination remaining within purified diatomite samples prior to analysis. Small quantities of non-diatom material such as clay and/or tephra can significantly bias oxygen isotope data, thus creating spurious results. In order to accurately model oxygen isotope values to obtain a 'true' climate signal, it is important to correctly assess the proportion and geochemical signature of any contaminant material.
c. Develop a revised chronology for ODP Sites 721/722 in the Arabian Sea for the period between 2.9 and 2.3 Ma, based on benthic foraminiferal oxygen isotopes tied to the LR04 global benthic stack (Lisiecki and Raymo, 2005) using the position of the Gauss/Matuyama boundary (2.608 Ma) as an independent tie-point. Due to differences in the previously published age-depth models for these sites, it is important to re-assess the chronology in order to compare data with other palaeoclimate archives from the region.
d. Provide a high-resolution reconstruction of changes in the flux of lithogenic material to the Arabian Sea between 2.9 and 2.3 Ma in order to assess long-term variations in the intensity of the Indian Ocean monsoon system during the Plio-Pleistocene and to investigate the context of episodic lake development in the East African Rift Valley.

e. Conduct time-series analyses to assess and compare aeolian dust flux data from ODP Sites 721/722 with other Plio-Pleistocene records from around Africa in order to investigate trends and transitions in the record.

1.3 Thesis Structure

Chapters in this Ph.D. thesis are grouped together and sequenced in order to address the different sites and methods employed in this research project. Chapters 1 and 2 review the literature and theoretical background to this study. Chapter 1 reviews the current scientific understanding of Plio-Pleistocene climate change and the transition from the warm stable conditions of the Mid-Pliocene to the intensification of glaciation in the Northern Hemisphere. This is followed by an outline of dominant low-latitude environmental changes during the Pliocene, with particular emphasis on records from East Africa, and an introduction to the dynamics and forcing of monsoonal circulation in the tropics. Chapter 2 reviews the use of stable isotope geochemistry, particularly oxygen isotopes from biogenic silica and calcium carbonate, as proxies for investigating palaeoclimatic change in both lacustrine and marine environments.

Chapters 3, 4 and 5 cover the investigation into the precessionally-forced rhythmic development of a series of freshwater lakes in the Baringo-Bogoria basin which coincide with the intensification of Northern Hemisphere glaciation. Specifically, Chapter 3 introduces the Baringo-Bogoria study area and reviews the climatic and geological settings of the region. This is followed by a discussion of the Barsemoi Diatomites which includes a discussion of the established chronology for the section. Chapter 4 outlines the methods undertaken to investigate palaeoenvironmental change recorded during one lake cycle represented by one of the Barsemoi Diatomite units. This includes the stable isotope analysis of diatomite material and outlines the development of a method to assess the geochemical signature of remnant contamination within cleaned samples. Chapter 5 outlines the results from the investigation of the Barsemoi Diatomites. This begins with a characterisation of the diatomite units using sedimentary stratigraphy and variations in diatom assemblage, with emphasis on diatomite unit #4. This is followed by qualitative and quantitative assessments of contamination remaining within the purified diatomite material and the use of different techniques to correctly model diatom oxygen isotope values. The chapter ends with a discussion of the variability revealed within the modelled oxygen isotope data and the record is compared with other data in order to discuss the context of Pliocene environmental changes on sub-orbital timescales.

Chapters 6, 7 and 8 deal with the investigation of variations in the long-term evolution of the Indian Ocean monsoon during the Late Pliocene (between 2.9 and 2.3 million years ago) as documented by changes in the aeolian dust flux to the Arabian Sea, using core material from Ocean Drilling Program (ODP) Sites 721 and 722. Chapter 6 introduces the ODP core sites on the Owen Ridge and outlines the modern climatic and oceanographic settings of the Arabian Sea, with particular emphasis on the Indian Ocean monsoonal circulation. Chapter 7 outlines the methods used to analyse core material from ODP Sites 721 and 722. Information is given concerning the development of a new chronology for sections analysed using benthic foraminiferal oxygen isotopes. The use of XRF core scanners as a tool for investigating high-resolution geochemical changes is also discussed in order to establish an elemental indicator for changes in aeolian dust flux. Chapter 8 covers the results of these analyses. The chapter begins with the construction of an oxygen isotope chronology and a comparison to published age models from ODP Sites 721 and 722. This is followed by discussion of the results from the XRF scanning of core material and the selection of elemental proxies to represent changes in aeolian dust flux. Of these, the ratio of titanium to aluminium is further investigated using time-series analysis techniques to explore long- and short-term trends and variations within the data set. The record is then compared with sea surface temperature and aeolian flux data from the Arabian Sea and other long-term Plio-Pleistocene dust records from around Africa to assess the synchroneity of changes in regional monsoon circulation.

Chapter 9 provides a synthesis of the findings of this research project and correlates the results from the Baringo-Bogoria basin with the longer-term dust record from the Arabian Sea in order to assess the extent to which environmental fluctuations in the East African Rift Valley are related to forcing of the Indian Ocean monsoonal system.

1.4 The Intensification of Northern Hemisphere Glaciation

During the Late Pliocene, the Earth's climate underwent a global transition from the warm, stable conditions of the Mid-Pliocene Warm Period (MPWP), between 5 and 3 million years ago (Ma), to a period of prolonged cooling which was characterised by the significant build-up of ice in the Northern Hemisphere. The intensification of Northern Hemisphere glaciation (iNHG) began in the Late Pliocene and was marked by the large-scale expansion of ice sheets in Southern Greenland, followed by the progressive onset of glaciation in Northern Greenland, the Eurasian Arctic, Northeast Asia and the North American continent

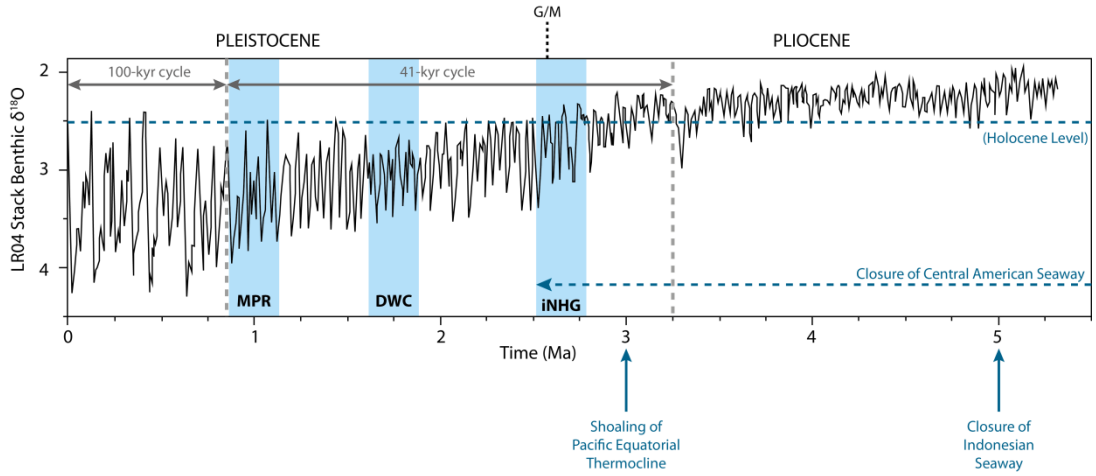

Figure 1.2 Plio-Pleistocene evolution of high-latitude climate. Benthic foraminiferal oxygen isotope data from the LR04 global stack (Lisiecki and Raymo, 2005), showing the timing of the intensification of Northern Hemisphere glaciation (iNHG) and onset of modest 41-kyr obliquity cycles following the warm Middle Pliocene. Relative timings for some of the events thought to have triggered the iNHG are also shown. DWC = Development of Walker Circulation; MPR = Mid-Pleistocene Revolution; G/M = position of the Gauss/Matuyama palaeomagnetic reversal, marking the transition between the Pliocene and the Pleistocene. Adapted from Raymo (1994).

between 2.7–2.5 Ma (Maslin et al., 1995a, 1998; Kleiven et al., 2002; Thierens et al., 2011). Concomitant with a global ice volume increase at ~2.7 Ma, an increase in the input of ice-rafted debris (IRD) indicates that there was a marked glacial expansion in the circum-Arctic regions of the Barents Sea and northern Greenland and Canada (Knies et al., 2009). Much of the current understanding of the transition from the MPWP to the iNHG was initially derived from the measurement of oxygen isotope ratios of foraminifera preserved within the

marine sediment record (e.g. Shackleton and Opdyke, 1977; Shackleton et al., 1984). By combining oxygen isotope ($\delta^{18}O$) data from the Deep Sea Drilling Project (DSDP) Site 552 in the North Atlantic Ocean with evidence for the influx of IRD, Shackleton et al. (1984) demonstrated that positive excursions in the $\delta^{18}O$ record represent periods of significant ice build-up on the nearby continents. Gradually increasing $\delta^{18}O$ values during the Late Pliocene (figure 1.2) are accompanied by a gradual increase in the volume of IRD transported into the Norwegian Sea and North Pacific and Atlantic Oceans (Raymo, 1994). As long-term components of the climate system, ice sheets play an important role in modulating climate variability by transmitting and amplifying changes that correspond to variations in insolation (Imbrie et al., 1992; 1993; Clark et al., 1999).

Milankovitch forcing can be defined as periodic variations in the amount of insolation received at the Earth's surface, driven by changes in the orbital parameters of eccentricity, obliquity and precession (Milankovitch, 1949). Whilst the causes behind the pacing of

individual glacial and interglacial cycles after approximately 2.6 Ma are tied to variations in the dominant orbital periodicities of 96 kyr (eccentricity), 41 kyr (obliquity) and 23 kyr (precession) (Imbrie et al., 1992), changes in insolation cannot solely account for the long-term global cooling trend during the Late Cenozoic which culminated in the iNHG. Since the iNHG approximately 2.7 million years ago, the Earth's climate has been particularly sensitive to modulations in orbital forcing. Glacial cycles have been orbitally forced, rather than being self-sustained or paced by orbital changes, and have a characteristic "saw-tooth" asymmetry during the last 1.0 million years, whilst the relative duration of interglacial periods has gradually decreased (Lisiecki and Raymo, 2007). Plio-Pleistocene cooling occurred in a stepwise fashion commencing with the onset of modest obliquity-driven 41-kyr glacial cycles at approximately 2.7 Ma, followed by a shift towards more pronounced, higher amplitude 41-kyr cycles after 1.8-1.6 Ma before this is progressively superceded by the onset of 100-kyr cycles after 1.1-0.9 Ma, known as the Mid-Pleistocene Revolution (MPR) (figure 1.2) (Imbrie et al., 1992, 1993; Shackleton et al., 1984, 1990). These 100-kyr cycles are traditionally thought to be dominated by the influence of eccentricity however Maslin and Ridgwell (2005) suggest that they are more closely linked to multiples of the precessional cycle which are paced, but not driven, by the eccentricity cycle. The ability of Milankovitch theory to solely explain the strong correlation between the Earth's orbital eccentricity and the 100 kyr glacial cycles of the Late Pleistocene remains controversial (Raymo and Ruddiman, 1992; Raymo, 1998; Ruggieri et al., 2009). The contribution of eccentricity to changes in radiation is too small to have a direct impact on climate change, but instead affects insolation through modulation of the precession cycle (Imbrie et al., 1993; Clemens and Tiedemann, 1997). Examination of the Plio-Pleistocene palaeoclimatic record reveals three relatively abrupt transitions at approximately 2.7-2.5 Ma (iNHG), at 1.9-1.7 Ma coincident with the development of Walker Circulation and at the MPR between 1.1 and 0.9 Ma. These transitional periods are marked by episodes of intense climatic variability which resulted in the reorganisation of the global climate system (Maslin and Christensen, 2007).

1.4.1 The Mid-Pliocene Warm Period

The Mid-Pliocene warm period (MPWP) between 5 and 3 million years ago is believed to have been the last episode when global average temperatures were significantly warmer than at present, and has been described as an extended interglacial characterised by relative climatic stability, similar to the Holocene or Marine Isotope Stage 11 (MIS 11) (Draut et al., 2003). It is postulated that air temperatures in high-latitude regions were up to 10°C warmer

than today (Budyko and Izrael, 1987) whilst mid-latitude sea surface temperatures (SST) were up to 3-4°C warmer than present (Dowsett et al., 1996; Wara et al., 2005; Lawrence et al., 2006). This was accompanied by a substantial reduction in the volume of Arctic Ocean sea-ice (Cronin et al., 1993), high eustatic sea levels (Dowsett and Cronin, 1989; Kennett and Hodell, 1993) and strong North Atlantic Deep Water (NADW) formation (Raymo, 1994; Kim and Crowley, 2000).

Numerous hypotheses have been proposed to explain the persistent global warming during the MPWP. The first explanation invokes higher atmospheric ρCO_2 levels (~35% greater than pre-anthropogenic levels), inferred from the counting of stomatal leaf densities (Van der Burgh et al., 1993), the analysis of the $\delta^{13}C$ ratios of marine organic carbon (Raymo et al., 1996) and general circulation modelling (GCM) studies (Haywood et al., 2005). A second hypothesis, sometimes invoked in combination with increased ρCO_2 levels (e.g. Crowley, 1996), suggests that enhanced thermohaline circulation caused greater heat advection from equatorial to high-latitude regions (Dowsett et al., 1992; Haywood et al., 2000a). An additional explanation proposes that increased regional wind stress and deep ocean ventilation in the Atlantic and Pacific Oceans resulted from enhanced subtropical atmospheric and oceanic gyral circulation (Ravelo and Andreasen, 2000; Haywood et al., 2000b). Furthermore, Seki et al. (2010) find that a marked and relatively rapid decline in Pliocene pCO_2 levels (from ~400 ppm to ~280 ppm) was closely linked to ice growth in the Northern Hemisphere as part of the intensification of glaciation.

More recently, studies of ocean material from the equatorial Pacific have indicated that conditions during the MPWP were similar to a continual 'El Niño-like' state whereby a deepening of the thermocline and reduction in the west-east SST gradient in the Pacific Ocean were related to the possible existence of weaker state of zonal atmospheric Walker circulation (Molnar and Cane, 2002; Ravelo and Wara, 2004; Ravelo et al., 2004; Wara et al., 2005; Fedorov et al., 2006; Ravelo et al., 2006; Scroxton et al., 2011; Shukla et al., 2011). However, permanent El Niño conditions are not supported by evidence from coral deposits in the Philippines, which suggest that climate variability during the MPWP was similar in character to present day ENSO events (Haywood et al., 2007; Watanabe et al., 2011).

1.4.2 The transition to cooler climates (iNHG)

The period from 3.1 Ma until 2.95 Ma during saw a gradual 'cooling' shift in climate oscillations from a time when global average temperatures were approximately 3°C warmer than present. It was not until after 2.95 Ma that 'cold' intervals became cooler than present while warm episodes still remained significantly warmer than the Holocene (Raymo, 1994). From the analysis of palaeoclimate data, it is evident that the amplitude of 10^4-10^6 year climate oscillations increased as the climate progressively cooled during the Plio-Pleistocene (Ravelo et al., 2004). Oceanic sediment records suggest that the long-term cooling culminated in the progressive glaciation of the Eurasian Arctic and Northeast Asia regions at ~ 2.74 Ma, followed by the glaciation of Alaska at 2.70 Ma and the significant glaciation of Northeast America at 2.54 Ma (Maslin et al., 1995a, 1998). This large-scale build-up of ice in the Northern Hemisphere was preceded by smaller-scale increases in ice-volume, notably in Iceland (McDougall and Wensink, 1966), the Sierra Nevada, California (Curry, 1966) and in the Barents Sea (Knies et al., 2009). Generally, the transition from the end of the MPWP to the iNHG was gradual rather than abrupt, although in some locations such as the North Pacific Ocean, the onset of significant Northern Hemisphere glaciation seems to have occurred specifically at 2.7 Ma (± 50 kyr) once certain regional climate thresholds were reached (Haug et al., 1999, 2005).

1.4.3 Potential causal mechanisms for the iNHG

Haug et al. (2001) argue that three factors are required in order to trigger and maintain ice-sheet growth in the Northern Hemisphere:

1. Long-term global cooling should have reached a critical threshold at 65 °N ensuring that precipitation falls as snow rather than rain thus enhancing seasonality;
2. Moisture needs to be introduced to the high northern latitudes;
3. Astronomically forced insolation levels should be low enough to prevent the ablation of winter snowfall.

Whilst there is a great deal of evidence for the expansion of Northern Hemisphere ice sheets, the precise mechanisms responsible for the initiation of the iNHG remain unclear and have been the subject of much debate. A number of these alternatives are discussed in the following sections:

1.4.3.1 Closure of the Central American Seaway

The final closure of the Central American Seaway has been proposed by a number of authors as a tectonically-driven mechanism capable of intensifying glaciation via the modification of ocean heat transport (Keigwin, 1982; Driscoll and Haug, 1998; Haug and Tiedemann, 1998; Bartoli et al., 2005). Marine carbon isotope ($\delta^{13}C$) records from Atlantic and Pacific deep-sea sediments indicate parallel variability until approximately 14 to 11 Ma when a shoaling of the Panamanian Isthmus is believed to have begun (Schmittner et al., 2004). A study by Duque-Caro (1990) of sediments from the Aratro Basin near Colombia suggests that between 12.9 and 11.8 Ma, major uplift of the Panama sill created an effective biogeographic circulation barrier restricting deep-water flow between the Pacific and Atlantic Oceans. A divergence in the Pacific and Atlantic $\delta^{13}C$ records of benthic foraminifera (Keigwin, 1982; Collins et al., 1996; Wright and Miller, 1996) and records of bottom water temperatures derived from the Mg/Ca ratios of benthic foraminifera (Lear et al., 2003) implies a further shoaling of the seaway between 6-8 Ma. A comparison of planktonic foraminifera $\delta^{18}O$ records from the Eastern Equatorial Pacific and the Caribbean Sea (Lear et al., 2003) shows a divergence in values between 4.7 and 4.2 Ma, demonstrating a shoaling of the seaway to less than 100m depth and the establishment of the modern Pacific-Caribbean salinity contrast and the development of the Western Atlantic Warm Pool. By correlating mollusc records from the Pacific and Caribbean coasts using a biostratigraphic framework, Coates et al. (1992) concluded that evolutionary divergence had occurred by 3.5 Ma. Final closure, allowing the widespread migration of land mammals, is believed to have been achieved by 2.7 Ma (Marshall, 1988; Webb, 1997). The closure of the Panama Gateway culminated with a marked increase in sea surface temperatures and a decrease in salinity in the Caribbean Sea between 2.95 and 2.82 Ma (Bartoli et al., 2005). This resulted in a strengthening of the Atlantic Gulf Stream and thus, through a series of ocean-atmosphere feedbacks, prompted an increase in moisture supply towards the Eurasian continental landmasses.

A number of modelling studies have attempted to simulate the impact of the closure of the Panama Gateway (e.g. Murdock et al., 1997; Prange and Schulz, 2004; Klocker et al., 2005; Schneider and Schmittner, 2006; Steph et al., 2006; Lunt et al., 2008), however these often use idealised boundary conditions and simplified representations of the ocean or atmosphere. The majority of these studies indicate that, following the restriction of surface water flow through the Panama seaway, a reorganisation of ocean circulation results in an increase in North Atlantic thermohaline circulation and formation of the North Atlantic Deep Water (NADW) (e.g. Schneider and Schmittner, 2006). More recently, Lunt et al.

(2008) tested the climatic response to the closure of the gateway using a fully-coupled dynamic ocean-atmosphere general circulation model (GCM) developed using boundary conditions derived from the Pliocene PRISM2 dataset (see Dowsett et al., 1999) and a high resolution dynamic ice-sheet model. By simulating "open" and "closed" modes of the Panama seaway, Lunt et al. (2008) find that the formation of the Panama Isthmus results in enhanced thermohaline circulation and increased precipitation over Greenland and North America. However the difference between the two modes is small and they conclude that whilst the closure of the Panama seaway enhanced the iNHG, it was probably not a major driving mechanism. Additionally, results from the modelling study by Klocker et al. (2005) suggest that closure of the seaway could have hindered ice sheet growth through decreased perennial snow cover and enhanced poleward heat transport.

1.4.3.2 Restriction of Indonesian throughflow

Alternatively, Cane and Molnar (2001) suggest that the closure of the Indonesian seaway could have been responsible for many of the climatic changes which are associated with the iNHG, such as the aridification of Africa. Based on the outcome of a modelling study, Cane and Molnar (2001) propose that the northward displacement of New Guinea and Australia approximately 5 million years ago (Srinivasan and Sinha, 1998) caused a switch in the source waters for the Indonesian seaway. Prior to 5 Ma, warm water from the South Pacific passed into the Indian Ocean, thus generating warm sea surface temperatures and greater levels of convective precipitation in East Africa. Modern observational studies demonstrate a clear linkage between warmer Indian Ocean SSTs and increased East African rainfall through the intensification of the Indian Ocean summer monsoon (Goddard and Graham, 1999). Cane and Molnar (2001) suggest that as New Guinea moved north, warm source waters were replaced by colder North Pacific water resulting in a decrease in SSTs throughout the Indian Ocean. The resulting atmospheric response would have caused a reduction in rainfall levels over East Africa resulting in the long-term aridification of Africa. Jochum et al. (2009) attempted to evaluate this hypothesis using a fully-coupled GCM. They found that widening the Indonesian seaway has the effect of increasing the inflow of South Pacific waters to the Indian Ocean but also of increasing the eastward equatorial transport of Pacific surface waters. The resulting expansion of the western Pacific warm pool causes a weaker, more irregular ENSO component and an equatorward shift in the position of the ITCZ (Jochum et al., 2009). Whilst this is broadly supportive of Cane and Molnar's hypothesis, it does not explain the 3-4°C warming of the Pacific proposed for the Middle Pliocene (Dowsett et al., 1996; Wara et al., 2005; Lawrence et al., 2006).

1.4.3.3 The uplift of the Tibetan Plateau

A number of studies support a mechanism whereby the progressive uplift of the Tibetan-Himalayan and Sierran-Coloradan regions altered atmospheric circulation patterns (Ruddiman et al., 1988; Ruddiman and Kutzbach, 1990; Qiang et al., 2001; Boos and Kuang, 2010). The subsequent diversion of cold polar air masses over North America and Europe led to decreased summer ablation causing a gradual amplification of glaciation in the Northern Hemisphere. However this theory is complicated by other studies, which suggest that the Tibetan Plateau had already reached its maximum elevation by the late Miocene (Copeland et al., 1987; Molnar and England, 1990, Harrison et al., 1992). Indeed, Molnar et al., (1993) suggest that an apparently rapid and marked strengthening of monsoonal circulation approximately 8 million years ago may have been linked to the abrupt uplift of the Tibetan Plateau. Raymo and Ruddiman (1992) expand on this and suggest that the tectonically-driven increase in chemical weathering associated with strengthened monsoonal circulation would have caused a drawdown of atmospheric CO_2 thus leading to global cooling. This is supported by results from an atmospheric GCM study by Boos and Kuang (2010) who find that the presence of the Himalayas strengthens monsoonal circulation through the orographic insulation of warm, moist air over the Indian sub-continent. However, the authors also suggest that the removal of the Tibetan Plateau (but not the Himalayan mountain ranges) from their models does not have a significant impact on the large-scale monsoon system, implying that direct heating of the Plateau is less important than previously thought (Boos and Kuang, 2010).

1.4.3.4 Decrease in atmospheric CO_2 levels coupled with positive feedbacks

Following on from section 1.4.3.3, it has also been suggested that the onset of significant ice build-up in Antarctica was the result of climatic cooling caused by a decrease in atmospheric carbon dioxide levels (DeConto and Pollard, 2003). It has also been proposed that Milankovitch forcing and tectonically-induced changes in carbon dioxide were the principal external factors driving the shift towards colder climates during the iNHG (Saltzman and Verbitsky, 1993; Ravelo and Wara, 2004). The strengthening of CO_2 and albedo feedbacks by enhanced sea level regression or aridification, coupled with ongoing global cooling could have resulted in the build-up of ice in the Northern Hemisphere (Raymo et al., 2006). Raymo and co-workers (Raymo et al., 1988; Raymo and Ruddiman, 1992) also recognise that variations in greenhouse gases such as CO_2 or H_2O can have a significant effect on the thermal radiative balance of the atmosphere. They propose that global chemical weathering rates have increased over the last 5 million years and that this

led to a "reverse greenhouse effect" resulting in the long-term cooling trend observed since the late Miocene.

1.4.3.5 The influence of orbital forcing

It is widely believed that variations in orbital parameters alone are not sufficient to be solely responsible for imposing the preconditions required for the iNHG. However Maslin et al. (1995a, 1998) suggest that whilst other tectonically driven mechanisms may have contributed to a decrease in atmospheric CO_2 levels and the resultant cooling of the Northern Hemisphere, the iNHG was largely triggered by orbital changes. Orbital obliquity has a significant effect on seasonality in the Northern Hemisphere (Ruddiman and MacIntyre, 1981). Therefore, as the amplitude of obliquity modulation increased after 3 Ma, seasonality would also have increased. Coupled with a progressively cooling climate, this would promote snow and ice build-up once a critical threshold was reached whereby conditions during summer are not sufficient to melt the winter snowfall (Maslin et al., 1995a).

1.4.3.6 Ocean heat transport and changes in circulation

Philander and Fedorov (2003) argue that changes in oceanic circulation were a critical factor responsible for driving many of the various climatic changes associated with the iNHG. These changes can be described by alterations to deep ocean thermohaline circulation (through variations in the formation of the NADW) and shallow, wind-driven circulation of the ventilated thermocline in the tropics and sub-tropics (ENSO). Philander and Fedorov (2003) propose that ongoing global cooling during the Cenozoic led to a gradual shoaling of the thermocline. By ~3 Ma, the thermocline was sufficiently shallow to allow the wind-driven upwelling of cold waters which had a strong influence on low-latitide SST patterns. This introduced certain ocean-atmosphere feedback mechanisms by which oceanic surface conditions in high-latitude areas could affect the depth of the tropical thermocline. They suggest that this can also account for the amplification in the Earth's response to orbital obliquity at the time of the iNHG. Brierley and Fedorov (2010) further investigate this hypothesis by modelling changes in zonal and meridional SST gradients throughout the Plio-Pleistocene glacial cycles. They find that an increase in the meridional SST gradient has the effect of reducing global air temperatures by 3.2 °C and increasing snowfall over North America, creating conditions favourable for the growth of Northern Hemisphere ice sheets. The establishment of modern zonal temperature gradients induces an additional 0.6

°C of cooling which is thought to produce sufficient total global cooling to account for ice sheet inception (Brierley and Fedorov, 2010). The changes in zonal and meridional temperature gradients also have important regional consequences, driving processes such as the long-term aridification of Africa and the strengthening of monsoon circulation over India.

1.4.4 Summary

Whilst many authors favour a hypothesis whereby the gradual closing of the Central American Seaway acts as a trigger for the iNHG, there is still great deal of ambiguity surrounding the actual mechanisms responsible for this major transition in global climate. It is probable that there is not one individual mechanism that can solely account for the complex changes in ice volume, ocean thermal structure and atmospheric circulation around the iNHG. More likely is a scenario involving the interplay of a number of the previously described theories whereby increased tectonic activity, changes in ocean circulation and decreasing greenhouses gases, coupled with changes in orbital parameters all interact through a network of positive feedbacks to alter global climate patterns.

1.5 Evidence for Sub-Orbital Scale Climate Change during the Pliocene

The relative scarcity of older, high-resolution palaeoclimate archives has thus far limited scientific understanding of sub-Milankovitch variability during periods prior to approximately 100 kyr BP. The nature of short-term climate variability during the Late Pliocene and Early Pleistocene is particularly poorly understood. Where evidence has been found for millennial-scale climate oscillations during the Pliocene (e.g. Draut et al., 2003; Steenbrink et al., 2003; Carter and Gammon, 2004; Becker et al., 2005, 2006; Niemitz and Billups, 2005; Bartoli et al., 2006; Kloosterboer-van Hoeve et al., 2006; Bolton et al., 2010; Weber et al., 2010), it has normally come from North Atlantic Ocean marine sediment cores, which offer the best opportunity for studying long-term climate variability at high resolution.

Analysis of Mid Pliocene (3.3-3.1 Ma) benthic and planktonic foraminiferal $\delta^{18}O$ and $\delta^{13}C$ records from ODP Site 981 on the southeast side of the Rockall Plateau in the North Atlantic indicate that millennial-scale (~ 1-2 kyr) variability existed during the Mid Pliocene Warm Period and that the oscillations occur with lower amplitude than observed during the Late Quaternary glacial stages (Draut et al., 2003). Thus it appears that sub-Milankovitch variations occurred prior to the iNHG, however the limitations of the age model used do not

allow confident dating of this interval. In order to compare the nature of sub-Milankovitch climate variability before and after the iNHG, Bartoli et al. (2006) conducted a high-resolution study of ODP Site 984 on the Reykjanes Ridge in the North Atlantic. They find that during glacial stages prior to the iNHG (which they place at 2.9-2.8 Ma), short-term climate variability was dominated by characteristic solar cycles (at 500±100 and 900±100 yrs) (Bond et al., 1999), whereas during glacial stages after the iNHG, there is evidence for 'Dansgaard-Oeschger (D-O) type' variability at a periodicity of 1,470 yr (and its multiples of 2,900 and 4,400 yr), albeit with lower amplitude than D-O cycles recorded in the Late Quaternary. Bartoli et al. (2006) suggest that synglacial D-O cycles, and thus climate variability on these timescales, during the Late Pliocene was driven by Northern Hemisphere ice sheet instabilities. This is supported by Bolton et al. (2010) who note that the amplitude of Late Quaternary millennial-scale oscillations was larger during glacial stages and that the emergence of millennial-scale cyclicity may be linked to the iNHG. Their record from Integrated Ocean Drilling Program (IODP) Site U1313 in the subpolar North Atlantic spans MIS 103-95 (~ 2.6 - 2.4 Ma) and reveals low amplitude variability (~ 1.8 - 6.2 kyr) that persists throughout both glacial and interglacial stages during the Late Pliocene, implying that the threshold responsible for the amplification of this signal to Late Quaternary levels had not been crossed at this time (Bolton et al., 2010).

A high-resolution 3.9 million-year record of gamma ray measurements from ODP Site 1119 near New Zealand is interpreted to represent fluctuations in clay content, indicative of variations in the supply of glacially-derived rock flour from the South Island ice cap (Carter and Gammon, 2004). The record documents long-term cooling since the Mid-Pliocene and has been closely linked, where possible, to the deuterium isotope record from the Vostok ice core in Antarctica and correlated to oxygen isotope data from ODP Site 1143 (Western tropical Pacific Ocean), Site 659 (Eastern tropical Atlantic Ocean) and Site 758 (Central tropical Indian Ocean). Carter and Gammon (2004) find that a closely coupled relationship exists between the Southern Hemisphere atmospheric climate signal (as determined from variations in the waxing and waning of the South Island ice cap) and the global oceanic climate record at a resolution of ~ 1-2 kyr for much of their record.

Currently, the only Pliocene-aged, terrestrial-based records of millennial-scale climate variability are from a series of lacustrine sediments preserved within the Ptolemais Basin in Northwest Greece (Steenbrink et al., 2003; Kloosterboer-van Hoeve et al., 2006). The Early Pliocene section of the sequence spans ~ 115 ka and is composed of m-scale cycles of black lignites and grey or beige marls which were deposited in a marginal shallow lake

environment. Colour reflectance (Steenbrink et al., 2003) and pollen (Kloosterboer-van Hoeve et al., 2006) analysis of these sediments reveals distinct basin-wide within-cycle environmental variability at periods of ~ 11-10 kyr, ~ 5.5 kyr and ~ 2.5-1.5 kyr corresponding to harmonics of the precessional cycle. Elsewhere in the Mediterranean, evidence for millennial-scale variability during the Late Pliocene is preserved in series of rhythmically bedded marine sediments exposed at Monte San Nicola in southern Sicily (Becker et al., 2005). Isotopic and foraminiferal data from the sequence reflect rapid climate oscillations between 2.56 and 2.50 Ma (MIS 100) on timescales of ~ 1.5-4.5 kyr. Becker et al. (2005) speculate that during stadial events, winter surface cooling and deep convection in the Mediterranean were more intense as a consequence of the influence of cold winds from Europe or the Atlantic Ocean. This pattern is not observed at Site 967 in the eastern Mediterranean where climate variability occurs on timescales of ~ 3-5 kyr.

1.6 Low-Latitude Climate Change during the Plio-Pleistocene

The role of the low-latitudes in driving or contributing toward climatic change is considered by many to be a passive one. As a result of the global cooling prior to the iNHG, it is thought the ITCZ shifted southwards to its present northernmost position of 12 °N between 4.4 and 4.3 Ma (Rea 1994; Billups et al., 1999). A more northerly position of the ITCZ in the early Pliocene would have profoundly altered rainfall distribution and atmospheric circulation in the low-latitudes. In the tropics and sub-tropics, there is widespread evidence for more extreme climatic variability after 2.7 Ma, probably related to the iNHG (Broccoli et al., 2006). One of the most pronounced features of low-latitude climate is the seasonal change brought about by monsoonal circulation over the African and Asian continents, particularly where monsoon systems are associated with the Tibetan Plateau region. Differential land-ocean sensible heating during boreal summer results in the seasonal formation of atmospheric low (land) and high (ocean) pressure cells. This drives the transport of moisture-laden air from the ocean to the continent, generating monsoonal rainfall, the production of which is enhanced by the orographic barrier posed by the Himalayas (Boos and Kuang, 2010). Much of the current understanding of low-latitude environmental change during the late Cenozoic comes from Africa, particularly East Africa which has been intensively studied due to its rich fossiliferous strata including numerous hominid-bearing localities. Records of Pliocene climate change from low-latitude terrestrial sites outside of Africa are relatively few but largely focus on understanding changes in the East Asian and Indian Ocean monsoonal systems (e.g. An, 2000; deMenocal, 2004; Sun et al., 2006b).

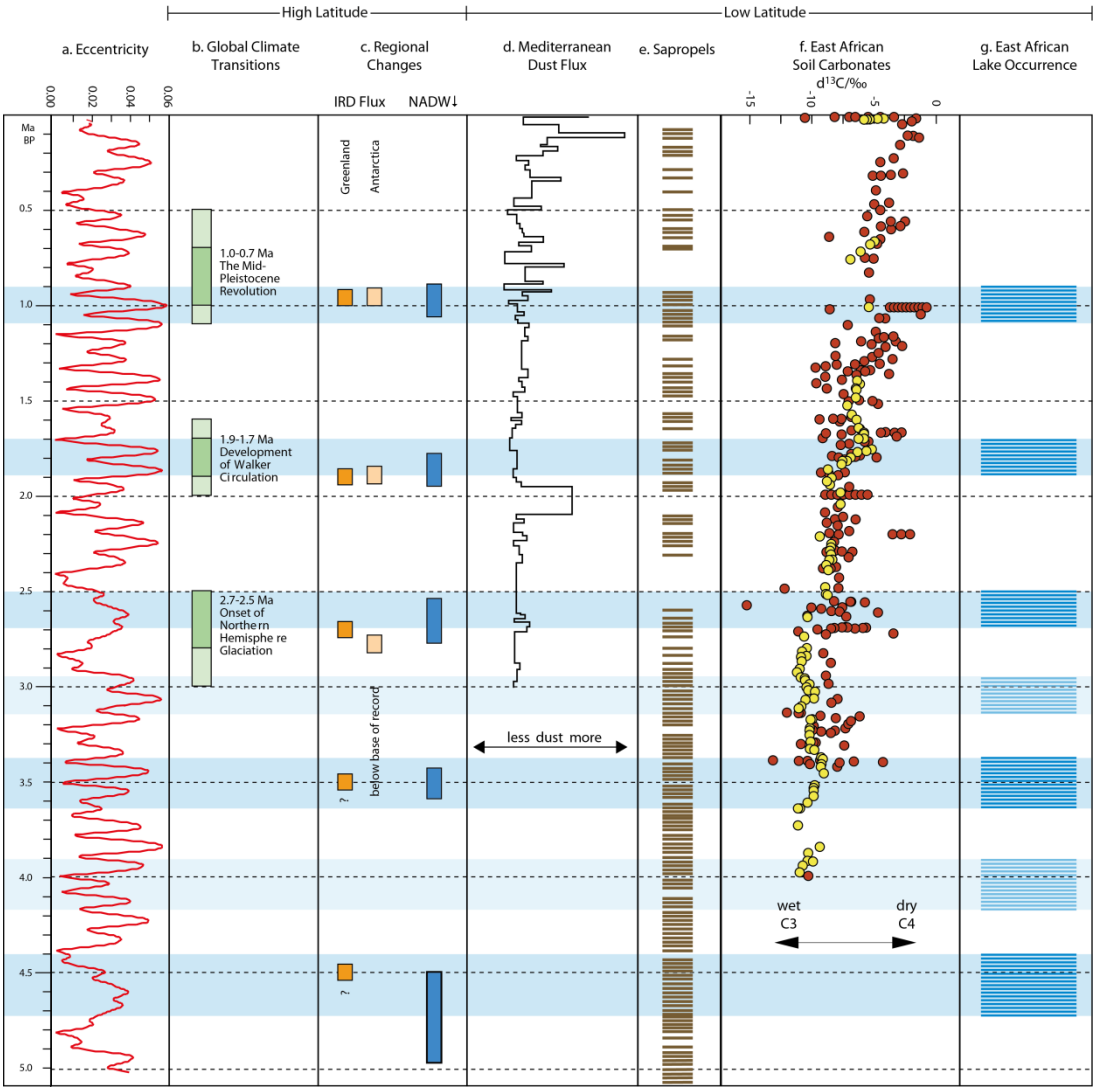

Figure 1.3 Comparison of Plio-Pleistocene variations in eccentricity with the timings of major transitions in global climate, changes in the Mediterranean dust flux (ODP Site 967; Larrasoaña et al., 2003) and timings of sapropel formation in the Mediterranean Sea (Lourens et al., 2004). Also shown is the long-term trend towards the emergence of C_4 plants as illustrated by East African soil carbonate $\delta^{13}C$ data from Levin et al. (2004) (yellow dots) and Wynn et al. (2004) (red dots). East African lake phases (compiled from Trauth et al., 2005, 2007) are coincident with global climate transitions. Modified from Maslin and Trauth (2009).

A review of the lacustrine history of the East Africa Rift Valley by Trauth et al. (2005, 2007) demonstrates that, superimposed upon a long-term trend towards aridification in Africa, there were three major humid phases characterised by extreme climate variability during the last 3 million years. These periods are coincident with major global climate transitions at 2.7-2.5 Ma (the iNHG), 1.9-1.7 Ma (the development of Walker circulation) and between 1.1 and 0.9 Ma (the Mid-Pleistocene Revolution) (figure 1.3). A number of long-term records of African palaeoclimate demonstrate increased climate variability and

step-like shifts in the amplitude and period of aeolian variability during the Late Pliocene and Early Pleistocene, around the time of the iNHG and during the aforementioned periods of major global climate change (Tiedemann et al., 1994; deMenocal, 1995, 2004; Clemens et al., 1996; Gasse, 2006). Clay mineral assemblage data and pollen spectra from ocean sediment records from the Arabian Sea and West African margin appear to indicate an increase in the concentration of aeolian dust coming from the Sahara and Arabian Peninsula at around 2.8 Ma, indicating a transition to a more variable, arid climate (deMenocal, 1995, 2004). Re-analysis of this sequence has recently questioned the timing of these transitions (Trauth et al., 2009). The long-term aridification of Africa between 5 and 3 million years ago that led to a gradual spreading of grassland vegetation throughout Tropical Africa (Bonnefille et al., 2004; Bobe and Behrensmeyer, 2004) has been attributed to a variety of factors, including the suppression of strong monsoonal circulation caused by the global cooling which culminated in the iNHG (deMenocal, 2004), a decrease in SST in the Indian Ocean (Cane and Molnar, 2001) and tectonic activity which resulted in the uplift of Southeast and East Africa, particularly the Kenyan and Ethiopian Highlands (Tyson and Preston-White, 2000; Sepulchre et al., 2006).

1.6.1 The long-term aridification of Africa

Palaeovegetation records derived from fossil fauna and flora suggest that during the Late Miocene and Early Pliocene, Africa was warmer and more humid than at present (e.g. Kingston et al., 1994; Cerling et al., 1997; Griffin, 1999; Ségalen et al., 2007). A transition from a warmer, wetter climate to cooler, drier and more seasonally variable conditions is supported by evidence from studies across the African continent (e.g. Griffin, 1999; Wolde Gabriel et al., 2001; deMenocal, 2004). Analysis of the proportions of C_3 and C_4 plants shows that there was a widespread increase in the amount of C_4 biomass over the last 6 million years (figure 1.3) (Kingston et al., 1994; Morgan et al., 1994). Cerling et al. (1997) suggest that this change is related to a decrease in levels of atmospheric CO_2 and that the change in C_3:C_4 ratio occurred earlier at lower latitudes, as the threshold favouring C_3-photosynthesising plants is higher at warmer temperatures. In addition, C_4 photosynthesis is more efficient in arid conditions. The emergence of the C_4 grass biome during the Late Miocene in Africa is characterised by shrinking forests and the appearance of more open grassland areas. Pedogenic $\delta^{13}C$ data (figure 1.3) suggest that, by the early Pleistocene, open landscapes dominated by C_4 plants had become a major environmental component in East Africa (Ségalen et al., 2007, and references therein).

In Central Ethiopia, the presence of woodland at 4.4 Ma (Wolde Gabriel et al., 1994) and even rainforest habitats/environments until ~3.4 Ma (Bonnefille, 1995) indicates warmer, wetter and more stable climatic conditions that are thought to characterise the Middle Pliocene in Africa. Similarly in the Omo region of Southern Ethiopia (Wesselman, 1995) and in Eastern Central Ethiopia (Bonnefille, 1983), a marked shift in palynological records at 2.4-2.5 Ma indicates that mesic riverine and forest taxa were replaced by xeric grassland and open savannah species as part of a general increase in the prominence of grassland taxa between 5 Ma and 3 Ma, implying increasing aridity (Bonnefille et al., 2004; Bobe and Behrensmeyer, 2004). A comprehensive examination of fossil material from the Omo basin documents a decrease in woodland and forest species alongside an increase in grassland species between 3.6 and 2.4 Ma (Bobe and Behrensmeyer, 2004) whilst in Northern Ethiopia evidence has been found for montane forests and evergreen bushland between 3.3 Ma and 2.9 Ma (Bonnefille, 1983). The analysis of high-resolution pollen data from the Hadar formation in the Middle Awash Valley in the Southern Afar region of Ethiopia suggests that a transitional period between 3.4 and 2.9 million years ago was characterised by extreme environmental variability (Bonnefille et al., 1983).

Further south, in the Central Kenyan Rift, isotopic analysis of pedogenic carbonates in the Turkana and Olduvai Basins implies a gradual stepwise replacement of woodland by open savannah grasslands between 3 Ma and 1 Ma (Cerling and Hay, 1988; Cerling, 1992). Morgan et al. (1994) compared isotopic evidence for the emergence of C_4-dominated biomes in the Central Kenyan Rift with data from the Potwar Plateau in Pakistan. Using tooth enamel apatite $\delta^{13}C$ values, they demonstrate that C_4 grasses are first recorded as a dietary component in Pakistan at 9.4 Ma and increase in abundance over the next few million years, whilst in Kenya they are not recorded as a primary herbivore dietary resource until 7 Ma. Whilst the trajectory of C_4 biomass expansion appears different in East Africa (Kingston et al., 1994) and in the Siwaliks in Pakistan (Quade and Cerling, 1995), C_4 plants dominate landscapes by the early Pleistocene (Ségalen et al., 2007). Morgan et al. (1994) propose that C_4 grasses evolved gradually in favourable ecosystems in response to a number of environmental and physiological factors affecting photosynthesis rather than in response to changing atmospheric conditions. Analysis of biome diversity suggests that the overall transition from a montane forest environment towards grassland and open savannah indicative of a cooler and drier climate, was punctuated by wet episodes lasting a few thousand years. Within one heavy-sampled interval between ~3.37 and 3.35 Ma, a major cooling shift of up to 5°C is associated with a 200-300 mm/yr increase in precipitation and a humidity index indicative of forest vegetation (Bonnefille et al., 2004).

A trend of increasing aridity is observed in other palynological (Bonnefille, 1983), terrestrial isotopic (Abell, 1982; Cerling et al., 1997; Levin et al., 2004; Wynn et al., 2004; Feakins et al., 2005) and macrofaunal (Vrba, 1985a; Wesselman, 1985; Grine, 1986) studies in Northeast Africa. Furthermore, analysis of oceanic sediment records from the equatorial Atlantic Ocean shows an intensification in terrigenous dust flux at ~2.4 Ma, implying weaker southwesterly monsoonal flow over Northern Africa during boreal summers therefore increasing Sahelian aridity (deMenocal, 1995, 2004). A strengthening of Northern Hemisphere winter trade winds, coupled with a more southerly average position of the ITCZ over Africa is also thought to enhance the equatorial dust flux. Additionally, a 60-70% increase in opal flux at approximately 2.5 Ma implies a stronger zonal component of the Southern Hemisphere trade winds during austral winter (Ruddiman and Janecek, 1989). Brown (1995) correlated changes in the Arabian Sea dust flux derived from magnetic susceptibility measurements from Ocean Drilling Program (ODP) Sites 721/722 with moisture-indicator lithofacies such as ostracods and molluscs from the Turkana Basin during the Early Pleistocene. Brown (1995) showed that a number peaks in dust flux between 2.11 and 1.89 Ma were coincident with low stands in the lake basin marked by mollusc beds and abundant fossil wood deposits suggesting that regional climate in East Africa is closely linked with conditions in Arabia.

Off the Namibian coast of Southwest Africa, the Benguela Current facilitates the redistribution of oceanic heat from the Southern to Northern Hemisphere and creates one of the world's major upwelling systems. Intensified upwelling of the Benguela Current and an associated decrease in SSTs after 3.2 Ma is proposed to have triggered a transition from warm, wet conditions towards a cooler drier climate in Southern Africa with the development of a strong cross-continental temperature gradient (Marlow et al., 2000). Prior to approximately 4 Ma, habitat reconstructions from sites throughout South Africa based on mammalian fossil assemblages indicate wooded, humid environments. This was followed by a gradual transition to more open habitat conditions, that was complete by 2 Ma (Reed, 1997). A millennial-resolution pollen record of Late Pliocene climate change from ODP Site 1082 records vegetation development in southwest Africa and suggests that rapid desiccation at approximately 2.2 Ma (Dupont et al., 2005) is associated with the proposed increase in upwelling and decrease in SSTs along the Namibian coast. The impact of the iNHG upon continental vegetation in southern Africa between 2.56 Ma and 2.51 Ma during Marine Isotope Stage 100 (MIS 100) is assessed by Denison et al. (2005) who investigate changes in $\delta^{13}C$ and n-alkane abundances and find that the variations closely track the

precessionally-forced orbital cycle and are primarily driven by changes in monsoon strength. The development of a strong continental temperature gradient resulting from increased Benguela Current upwelling is believed to have initiated arid conditions in Southwest Africa (Tyson and Partridge, 2000). This is thought to have been enhanced by the subsequent uplift of the East Africa and Zimbabwe regions during the Late Pliocene, thus creating rain shadows to the west which intensify the trend towards aridification (Tyson and Preston-White, 2000). Increasing aridity during the Late Pliocene is also consistent with results documented from the analysis of carbon isotopes in fossilised tooth enamel which indicate a general increase and domination of arid conditions by the end of the Pliocene (Lee-Thorpe et al., 2007). However, these results do not suggest a major shift in climate at the time of the iNHG.

Evidence of increasing aridity at this time is not restricted to Africa and the surrounding regions. During the Early Pleistocene there was also an expansion in areas of loess distribution across the Chinese Loess Plateau. Whilst the cause of this expansion is not known, it has been linked to the neotectonic uplift of the Tibetan Plateau, Himalayan Mountains and Tian Shan Mountains during the Pliocene, which would have increased aridification through the isolation of regional climate regimes (Dodonov and Zhou, 2008). Strengthening glacial cycles during the Pleistocene further enhanced this climatic desiccation.

1.6.2 Possible causes of aridification

deMenocal (2004) attributes the cause of aridification in Africa to the amplification of glacial cycles in the Northern Hemisphere (iNHG). The relationship between African climate sensitivity and changes in high-latitude glacial boundary conditions has been examined using a number of general circulation models (GCM) (Clark et al., 1999; deMenocal and Rind, 1996). These demonstrate a link between the timing of cool, arid conditions in Africa and maximum glacial conditions. Alternatively, modelling work by Sepulchre et al. (2006) demonstrates that the tectonic uplift of East Africa had a marked influence on rainfall distribution through the re-organisation of atmospheric circulation. As uplift increased, wind patterns became less zonal and a rain shadow effect occurs, reducing levels of available moisture, and producing the strong aridification seen in palaeoenvironmental records (Sepulchre et al., 2006). A further cause is suggested by Cane and Molnar (2001) who attribute the increase in African aridity to a change in sea surface temperatures in the Indian Ocean. They propose that the restriction in the flow of warm

South Pacific water through the Indonesian seaway, caused by the northward displacement of New Guinea, channelled cooler North Pacific waters to the Indian Ocean leading to a decrease in SSTs. They suggest that this would have resulted in a reduction in the amount of rainfall over East Africa and even that associated changes in equatorial Pacific oceanic circulation would have acted as a feedback mechanism to further enhance global cooling and stimulate ice sheet growth.

1.6.3 Evidence for precessionally-forced climate change in the tropics

Orbital forcing has a clear and marked influence on high-latitude climate as is evident in the timing of modest 41-kyr and ~ 100-kyr glacial cycles during the Pleistocene. It also influences major transitions in global climate during the Late Cenozoic and, through precessional forcing, plays an important role in driving patterns of seasonality and rainfall in the tropics. Abundant evidence from the palaeoclimatic record demonstrates the precessional forcing of moisture availability in and around Africa during the Pliocene (deMenocal 1995, 2004; Dennison et al., 2005; Deino et al., 2006; Hopley et al., 2007; Kingston et al., 2007) and Pleistocene (Brown and Feibel, 1991; Tiedemann et al., 1994; Brown, 1995; Reichart et al., 1998; Clemens and Prell, 2003, 2007; Trauth et al., 2003; Hopley et al., 2007; Lepre et al., 2007; Maslin and Christensen, 2007; Tierney et al., 2008; Verschuren et al., 2009; Ziegler et al., 2010). There is also widespread evidence for precessionally-forced climate change elsewhere in the tropics and sub-tropics during the Plio-Pleistocene, such as in the timing of sapropel formation in the Mediterranean Sea and loess sequences on the Chinese Loess Plateau (e.g. Rossignol-Strick, 1983; Bush et al., 2002; Larrasoaña et al., 2003; Lourens et al., 2004; Wang et al., 2001, 2004, Sun et al., 2006b; Wang, 2009). In addition, climate modelling (Clement et al., 2004) has also demonstrated a clear relationship between precession and tropical moisture availability, illustrating that a 180° shift in precession has the effect of causing a shift in seasonality and altering annual precipitation levels in the tropics by at least 180 mm/year.

Whilst there is much evidence for the direct influence of precession on low-latitude environments and tropical monsoon strength, the impact of orbital forcing on African climate is not straightforward. For example, the impact of orbital forcing on high-latitude glacial cycles has an indirect influence on other factors such as SST, atmospheric circulation patterns, the strength of meridional temperature gradients and concentrations of atmospheric greenhouse gases such as CO_2, CH_4 and water vapour. These indirect effects occur alongside the direct precessional-forcing of African climate through changes in seasonality

and the strength of the monsoon systems, and thus understanding the nature of the individual driving mechanisms is highly complex. African palaeoclimate records may therefore exhibit more complex variance, controlled by precessional and obliquity cycles (e.g. Hopley et al., 2007). These issues are further complicated by the presence of precessional harmonics which create seasonality cycles of ~ 11.5 kyr and ~ 5 kyr in duration according to the magnitude and timing of insolation maxima and minima (Berger et al., 2006). Theoretically, this means that African climate could be responding to orbital and sub-orbital seasonality cycles of ~23-kyr, ~ 11.5-kyr and ~ 5-kyr. The presence of half-precessional cycles has been demonstrated in sediment records from Lake Challa in Tanzania (Verschuren et al., 2009). Detailed examination of further high-resolution palaeoclimate archives is required in order to fully understand this phenomenon and the relationship between tropical moisture availability and seasonality, and to identify the role of glacial-interglacial, orbital and sub-orbital cycles in influencing African climate.

1.6.4 Episodes of extreme climate variability

Tropical environmental stability in East Africa and surrounding regions is determined by a number of direct and indirect forcing factors, which operate on timescales ranging from 10^8 to 10^6 years (volcano-tectonic uplift of the East African Rift System (EARS) and Tibetan Plateau), to 10^5 – 10^4 years (orbitally-forced changes in insolation, glacial-interglacial cycles), to shorter periods of 10^3 to 10^0 years (variations in solar irradiance, ENSO cycles, changes in Indian Ocean Dipole). The greater amplitude of longer-term mechanisms, such as the development of the East African plateau, means that these factors have a greater potential for driving dramatic shifts in vegetation and evolutionary change.

During the Late Cenozoic, there were a number of transitions in global climate. In addition to the iNHG, the development of Walker circulation (1.9 – 1.7 Ma) and the Mid-Pleistocene Revolution (MPR) (1.1 – 0.9 Ma) during the Plio-Pleistocene, two other transitions during the Miocene have been identified (Maslin and Christensen, 2007). The first of these is gradual emergence and expansion of C_4 grasses which was accompanied by a major change in floral composition and an evolutionary shift in faunal communities, commonly referred to as the Savannah Hypothesis (e.g. Dart, 1925, 1953; deMenocal, 1995; Potts, 1998a). The second is the Messinian Salinity Crisis which was caused by the closure of the Gibraltar Strait and resulted in the transient isolation of the Mediterranean Basin causing it to dessicate several times between 5.96 Ma and 5.33 Ma when normal marine conditions were established following the Terminal Messinian Flood (Krijgsman et al., 1999). A compilation of records of moisture history from East Africa by Trauth et al. (2005, 2007) (figure 1.4)

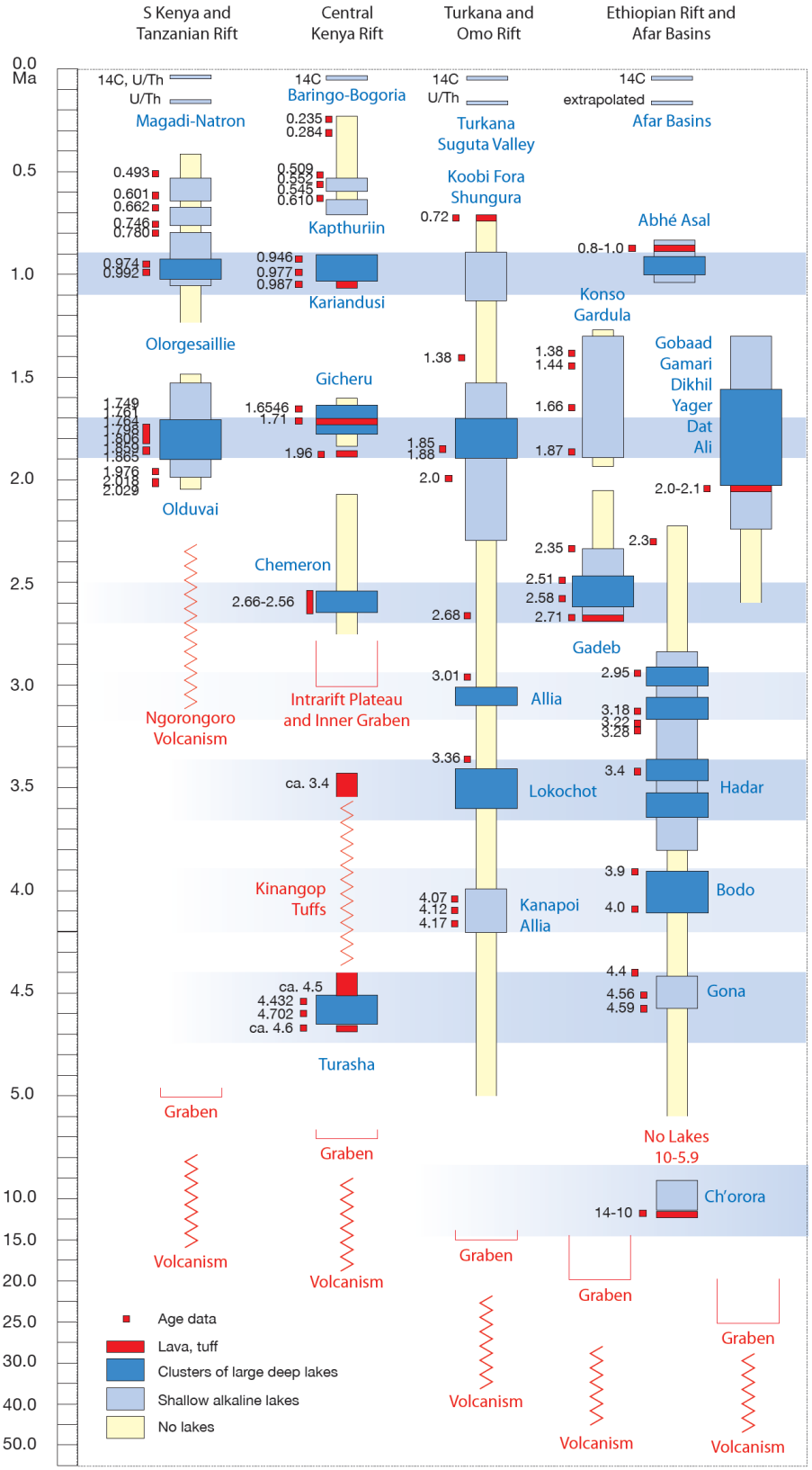

Figure 1.4 Compilation of lacustrine records and episodes of tectonism from the sites in the East African Rift Valley (EARS). Trauth et al. (2005) propose three periods of extreme lake level variability which coincide with major global climate transitions. Areas within the EARS are shown moving from South (Tanzanian Rift) to the North (Ethiopian Rift). From Maslin and Trauth (2009).

demonstrates that the transitions in global climate during the Late Pliocene and Pleistocene were characterised by wet-dry lake phases when the EARS was periodically occupied by deep freshwater lakes. Figure 1.4 shows that the occurrence of these lakes begins in the Ethiopian Rift and Afar Basins and spreads gradually southwards through the Turkana and Omo Rifts to the Central Kenyan Rift to the South Kenyan and Tanzanian Rifts.

Between 2.7 Ma and 2.5 Ma (coincident with the iNHG), diatomite exposures in the Ethiopian Gadeb Plain and Tugen Hills in the Central Kenyan Rift indicate that deep lakes occupied the Afar and Baringo-Bogoria basins, respectively (Williams et al., 1979; Kingston et al., 2007). The timing and nature of the diatomite exposures in the Baringo basin is discussed in further detail in chapter 3. Diatomite exposures at Gadeb have been dated to between 2.7 Ma and 2.35 Ma, and consist of extremely pure diatomite at the base which grades upwards into a series of diatomaceous clays and silts (Williams et al., 1979). Lake Gadeb is thought to have been moderately deep (at least 40 m) and aerially extensive (~ 155 km^2). Within the Baringo-Bogoria basin, the Barsemoi diatomites are exposed in the Tugen Hills, a complex tilted fault block containing a sedimentary sequence spanning the last 16 Ma. The Barsemoi diatomites are interbedded with fluvial and alluvial deposits and indicate the presence of a deep (up to 150 m) freshwater lake which periodically occupied the axial portion of the Central Kenyan Rift between 2.68 Ma and 2.55 Ma. Calibrated $^{40}Ar/^{39}Ar$ dates constrain the age of each diatomite unit and demonstrate that the associated wet/dry cycles were paced by precessionally-forced climate variations.

In addition to lake phases coincident with the iNHG, the development of Walker circulation and the MPR, there is also evidence for lake phases prior to 2.7 Ma, between ~ 2.95 and ~ 3.2 Ma, between ~ 3.3 and ~3.4 Ma and between ~3.9 and ~ 4.0 Ma (Trauth et al., 2007). In the southern Afar Basin, the Bodo and Hadar palaeolakes (ca. 4.0 - 2.95 Ma) deposited thick sedimentary sequences of alternating clays, sands and diatomites respresenting swamp, shallow saline and freshwater lake environments, respectively (Williams et al., 1979; Bonnefille, 1983; Gasse, 1990; Wolde-Gabriel et al., 2000). Sedimentary bedding cycles both here and in the Baringo-Bogoria basin are approximately 20-25 kyr in duration indicating that environmental fluctuations were paced by the precessional orbital cycle (deMenocal, 2004; Deino et al., 2006; Kingston et al., 2007). Elsewhere in the Middle Awash Valley, examination of vertebrate fossil specimens from a hominid-bearing faunal assemblage suggests that at ~ 2.45 Ma, the area was characterised by a shallow freshwater lake environment (deHeinzelin et al., 1999).

During the later Pleistocene there is evidence for a lake phase between 1.9 Ma and 1.7 Ma, concomitant with the development of Walker circulation which caused a cooling shift in SSTs and the establishment of a strong E-W gradient in the Pacific Ocean (Ravelo et al., 2004). Large deep lakes existed in most parts of the EARS (figure 1.4) at this time as evidenced in exposures from Olduvai Gorge (Ashley and Hay, 2002), Gicheru Basin (Baker et al., 1988), the Koobi Fora formation (McDougall and Watkins, 1988; Brown and Feibel, 1991; Leakey et al., 1995, 1998) and in the Afar Basin (Gasse, 1990). A later lake phase, between 1.1 Ma and 0.9 Ma (figure 1.4), coincides with the Mid-Pleistocene Revolution which marks a significant shift in the pacing of Northern Hemisphere ice ages towards large-amplitude 100-kyr glacial cycles. Evidence for Rift Valley lakes during this time comes from the Olorgesaillie sequence (Potts, 1998a), the Kariandusi Formation in the Nakuru-Elementeita Basin (Deino et al., 2004) and in the Lake Abhé and Asal Basins (Gasse, 1990) – see figures 1.1 and 1.4.

There is also widespread evidence in the EARS of dramatic lake level fluctuations during the African Humid Period (AHP). Following the end of the Last Glacial Maximum when African climate was generally characterised by enhanced aridity, the AHP (from 14.8 kyr BP to 5.5 kyr BP) is thought to have been linked to an intensification of monsoonal circulation over Africa and the Indian Ocean which climate models suggest yielded an increase in precipitation of 35-45 % (Prell and Kutzbach, 1987). More recent hydrological models have revised this figure to 15-30 % and suggest that this increase would have been sufficient to support lakes as deep as 150 m (Bergner et al., 2003). During the AHP, the presently arid Suguta Valley in Northern Kenya was occupied by a large (2,500 km^2), deep (300 m) lake that underwent rapid short-term fluctuations in lake level of between 30-100 m and dried out completely by 5.0 kyr BP (Garcin et al., 2009; Junginger et al., 2010) Elsewhere, evidence from Lake Baringo (Renault and Owen, 1980; Renault et al., 2000), Lake Turkana (Owen et al., 1982) and Lake Ziway-Shalla (Gillespie et al., 1983) indicates that other EARS lakes also responded rapidly to changes in tropical moisture availability during the AHP.

1.6.4.1 The role of amplifier lakes

The term ‘amplifier lake’ was originally defined by Street (1980) and refers to closed basin lakes typical of arid and semi-arid regions which respond rapidly and dramatically to variations in precipitation and fluctuations in climate. Recent sensitivity studies of a number of the EARS lakes have lead Trauth and co-workers (Olaka et al., 2010; Trauth et al., 2010)

to identify lakes such as palaeo-lake Suguta and others (e.g. Lake Naivasha, Lake Nakuru, Lake Elementeita, Lake Ziway; figure 1.1) as amplifier lakes. Trauth et al. (2010) develop this idea further and find that amplifier lakes respond to orbitally-forced climate changes, often experiencing large-amplitude rises and falls in lake level over centennial to millennial timescales. They are characterised by typical half-graben basin morphologies with elevated catchments that attract increased precipitation which is offset by the high evaporative potential of the Rift Valley floor. Whether a particular lake amplifies or not is believed to be largely determined by the ratio between the lake, the water balance and the size of the catchment area. Street (1980) describes three factors that can explain different degrees of lake sensitivity: 1) hydrological balance; 2) nature of basin relief and; 3) shifts in water balance through time. Olaka et al. (2010) expand on this and use changes in the aridity index (AI) and hypsometric integral (HI) to classify different types of lakes within the EARS. The authors use AI to describe the effective moisture within the catchment areas and HI to describe the geomorphic characteristics and elevation distribution across the lake catchment using data from digital elevation models (DEMs).

Larger systems such as Lake Victoria or Lake Chad were found to respond more slowly to environmental forcing and are therefore classed as "non-amplifier lakes" (Street, 1980). Amplifier lakes became important during key phases of extreme climate variability when precessional forcing of climate conditions in the EARS resulted in the abrupt appearance and disappearance of large lake systems, such as palaeo-lake Baringo. Trauth et al. (2010) also propose that amplifier lakes played a key role in driving speciation and natural selection in hominin evolution during the Plio-Pleistocene by forming important barriers to population migration and mixing.

1.7 Tropical Monsoonal Circulation

Within the tropics and sub-tropics, climatic variability is dominated by monsoonal circulation within both the Northern and Southern Hemispheres. The monsoons are major dynamic components of the modern climate system and as such play an extremely important role in influencing the agricultural and socio-economic development of some of the most densely populated regions on Earth. The seasonal changes in atmospheric circulation drive the formation of extensive zones of convective precipitation, which generate the rainy seasons that are so vital for the livelihood and well-being of people in countries in tropical regions. These seasonal shifts also impact upon the equatorial oceans, resulting in changes in sea-surface temperature, salinity, current strength and direction. In regions such as the

Northwest Arabian Sea, the dynamic changes in wind stress forcing also lead to the seasonal upwelling of cool, nutrient-rich waters, which generate high levels of primary productivity.

Recent developments in the study of the monsoon systems around the world have led to the notion that monsoons are not regional or localised phenomena, but can be thought of as a 'global monsoon' system that is an integral component of the Intertropical Convergence Zone (ITCZ) (Chao and Chen, 2001; Gadgil, 2003; Wang, 2009). The ITCZ is a circum-global phenomenon, sometimes referred to as the 'climatic equator', which is characterised by a zone of increased cloudiness and precipitation that experiences a seasonal northward and southward migration that lags the insolation maxima by approximately one month (Nicholson, 1996). In the Atlantic and eastern Pacific Oceans, the ITCZ is situated to the north of the equator and exhibits relatively minor seasonal shifts accompanied by limited generation of convective moisture. However in the western Pacific and Indian Ocean, the seasonal excursions of the ITCZ into each hemisphere are more extensive and the resultant meeting of hemispheric trade winds generates intensive tropical typhoons, forming the atmospheric region of low pressure known as the 'monsoon trough' (Chao, 2000). Wang (2009) argues that the 'global monsoon' should be considered, alongside high-latitude ice sheet forcing, as one of the two major factors responsible for driving the evolution of the climate system.

1.7.1 Geological evolution of monsoonal circulation

Examination of the geological record suggests that the global monsoon existed throughout much of the Phanerozoic eon (~545 Ma until present) (Gordon, 1975; Kutzbach and Gallimore, 1989; Parrish, 1993). The historical evolution of monsoon circulation and the nature of monsoon forcing over several timescales can be described as follows (Wang, 2009):

The Wilson Cycle — Over timescales of 10^6 to 10^8 years, the global monsoon is controlled by tectonic forcing. The Wilson cycle consists of alternating periods of sea-floor spreading and continental collision which generate corresponding variations in monsoonal cycles (Webster, 1981). Periodic aggregations of landmasses into 'mega-continents' such as Pangaea are thought to have been accompanied by the generation of 'mega-monsoons'.

Orbital Cycles — On timescales of 10^4 to 10^5 years, monsoon circulation responds to changes in the orbital cycles of precession (23 kyr) and eccentricity (~100 and ~400 kyr). These complex variations have become the focus of late Cenozoic palaeoclimate studies of monsoon evolution. This is further discussed in the following sections.

Solar Cycles — On sub-orbital timescales ($\leq 10^3$ years), fluctuations in the global monsoon occur in response to variations in solar activity such as the 200-year Suess cycle (Beer and van Geel, 2008). The response is further complicated by the response of the monsoon system to high-latitude climate changes, such as Dansgaard-Oeschger (D-O) events, which occur with a periodicity of approximately 1,400 years and are believed to originate in the North Atlantic during glacial stages.

Understanding the evolution of monsoonal systems in response to orbital and solar cycles is of great importance for evaluating and predicting how the Earth's climate might change in the future. In order to understand the long-term variability of the monsoonal circulation it is necessary to compliment the observational data and modelling experiments that primarily drive modern climate science with the examination of palaeoclimate proxies from geological archives. However, of the proxies used to reconstruct past variations in monsoon circulation (e.g. chemical composition of stalagmites, methane concentration in ice cores, aeolian dust flux, isotopic signatures of foraminiferal shells), none are direct indicators of monsoon strength and almost all are affected by multiple factors which complicate their interpretation.

1.7.2 Precessional forcing of monsoonal variations

As the Earth moves around the Sun, its orbital eccentricity (the ellipticity of the orbit) and obliquity (the degree of axial tilt) vary through time. In addition, the Earth also wobbles on its axis (precession). The resultant impact on the seasonal and spatial distribution of incoming solar radiation varies according to the influence of the different orbital parameters and associated periodicities. Over longer timescales there is abundant evidence that monsoonal variations occur in response to the eccentricity cycles of 96 kyr and 400 kyr (e.g. Tiedemann et al., 1994; deMenocal, 1995; Wehausen and Brumsack, 2002), however the most dominant forcing occurs over the 23-kyr and 19-kyr precessional cycles, with most variance occurring over the 23-kyr cycle. There is currently an ongoing, unresolved debate

concerning the orbital forcing of the monsoon system regarding differences which arise from the analysis of proxy records from marine and terrestrial environments. Put simply, the controversy concerns the degree to which precessional cycles directly influence monsoonal strength and the length of the measured phase of the summer monsoon (i.e. the lag of maximum monsoon intensity behind insolation maxima).

In the early 1980s, John Kutzbach used a simple climate model to propose that changes in orbital configuration during the early Holocene led to increased Northern Hemisphere summer insolation and an intensification in the strength of the Asian monsoon (Kutzbach, 1981; Kutzbach and Otto-Bliesner, 1982). Subsequent studies of the timing of sapropel layers in the Mediterranean (Rossignol-Strick, 1983) and the repeated appearance and disappearance of lake systems in Africa (Kutzbach and Street-Perrott, 1985; Pokras and Mix, 1987) found evidence for a strong precessional pacing of monsoon intensity. Evidence for precessional 23-kyr cyclicity is also found in records of productivity from the Arabian Sea (Reichart et al., 1998), in precisely dated $\delta^{18}O$ sequences from speleothems in Southern China (et al., 2001, 2005, 2008a), in records of $\delta^{18}O_{air}$ (Bender et al., 1994) and atmospheric methane (CH_4) concentration obtained from the Vostok ice core in Antarctica (Petit et al., 1999) and the atmospheric CH_4 record from the GISP2 ice core in Greenland (Brook et al., 1996). Changes in atmospheric CH_4 are thought to be heavily influenced by the insolation forcing of monsoonal wetland regions (Brook et al., 1996), while variations in $\delta^{18}O_{air}$ are believed to partly reflect changes in global biomass, driven mainly by tropical monsoon circulation (Shackleton, 2000).

Kutzbach's theory that the intensity of low-latitude monsoon systems responds primarily to the 23-kyr precessional cycle is in contrast with the findings of Steve Clemens, Warren Prell and co-workers who propose a more complicated view of monsoonal forcing based on findings from the Arabian Sea (Clemens and Prell, 1990, 1991, 2003; Clemens et al., 1991, 1996, 2008). Clemens and Prell (2003) constructed a 350-kyr "summer monsoon stack" from five summer monsoon proxies obtained from three sites in the Arabian Sea. The resulting "summer monsoon factor" is found to be sensitive to both precession and obliquity forcing. Peaks in monsoon intensity were found to lag Northern Hemisphere insolation maxima by approximately 8,000 years implying that latent heat export from the southern Indian Ocean, which is greatest during obliquity maxima, and sensible heating of the Asian plateau are two important driving mechanisms for monsoon variability within the obliquity band. The importance of obliquity as a driving mechanism for the tropical monsoons is

supported by the findings of Sun et al. (2006a) who studied the timing of stacked loess sequences from the Chinese Loess Plateau.

Ruddiman (2006) questioned Clemens and Prell's view as being at odds with Kutzbach's original theory and emerging ice core (Petit et al., 1999; Ruddiman and Raymo, 2003) and stalagmite $\delta^{18}O$ data (Wang et al., 2005) which support a dominant precessional control on monsoon intensity with almost no phase lag. Ruddiman (2006) argues that the obliquity-dominated proxies examined by Clemens and Prell (2003) in the Arabian Sea are more likely to be associated with processes related to the winter monsoon. The crux of the debate lies in the proposed differences in phase lag suggested by different studies. Whilst Ruddiman (2006) and Kutzbach et al. (2007) suggest a minimal or 'zero-phase' lag and Clemens and Prell (2003, 2007) suggest a phase lag of approximately 8,000 years, evidence from the Mediterranean basin suggests that maximum intensity of the African monsoon lags Northern Hemisphere summer insolation maxima by approximately 3,000 years (Hilgen et al., 1993; Lourens et al., 1996; Tuenter et al., 2005; Ziegler et al., 2010). Differences arise between estimates based on marine and terrestrial proxies and questions remain as to the extent to which obliquity forcing exerts any influence on the tropical monsoonal systems through the control of high-latitude processes. Variations in orbital obliquity control the northward transport of heat between 20 °N and 60 °N and the influence of obliquity increases the higher the latitude (Maslin and Ridgwell, 2005). Through its affect on latitudinal heat flux, it has a considerable influence on climate in the mid-latitudes of the Northern Hemisphere but also affects the strength of regional monsoonal circulation (Lisiecki and Raymo, 2007). In addition to this, key questions remain unanswered concerning the validity of some proxies as being truly representative of summer monsoon intensity, since monsoon variability itself is a complex combination of both global and regional components (Wang, 2009).

1.7.3 Monsoon circulation and glaciation

The linkages between monsoonal circulation and glacial-interglacial cycles are less clear than the connection between monsoon strength and precessional forcing. However, the presence of continental ice sheets in the Northern Hemisphere has been shown to suppress monsoonal circulation e.g. during the Last Glacial Maximum (Prell and Van Campo, 1986). This may be due to differences in SST, atmospheric CO_2, albedo and/or seasonal snow cover (Prell and Kutzbach, 1992). Broadly speaking, during periods of ice sheet expansion, the latitudinal thermal gradient is increased resulting in compression of the northward and

southward migrations of the ITCZ which impacts upon the strength of the summer and winter monsoons. Loess-palaeosol records from China appear to demonstrate a close relationship with the occurrence of Northern Hemisphere glacial cycles; loess accumulation during glacial stages suggests an enhancement in the volume of dust transport by the winter monsoon while palaeosol formation during interglacials implies increased moisture transport from the summer monsoon (Sun et al., 2006b). However Wang (2009) cautions against adopting a simplistic relationship between monsoon strength and glaciations without using phase comparisons and suggests that monsoon variability should be considered in the broader context of tropical and sub-tropical variability involving ocean-atmosphere-terrestrial interactions through factors such as SST and moisture availability.

1.8 Summary

Plio-Pleistocene climate fluctuations and environmental shifts in equatorial Africa, and elsewhere in the tropics, have been closely linked to precessionally-forced changes in insolation which, through the modification of monsoon systems, caused alternating periods of extreme aridity and wetness. Palaeoclimate records suggest that a long-term trend of aridification in Africa, coincident with ongoing global cooling, was punctuated by a series of these wet-dry cycles coincident with key transitions in global climate history. Climate variability between 2.7 Ma and 2.5 Ma, coeval with a stepwise shift towards modest 41-kyr glacial cycles and the intensification of glaciation in the Northern Hemisphere, is characterised by enhanced precipitation in East Africa which resulted in the development and rhythmic cycling of a major lake system in the Baringo-Bogoria basin.

The paucity of high-resolution palaeoclimate archives from terrestrial environments, particularly in the tropics and sub-tropics means that it can be difficult to reconstruct patterns of climate variability in regions such as East Africa. The relative lack of climate change records becomes even more pronounced when addressing environmental changes during older periods such as the Pliocene and Miocene, such that scientific understanding of climate variability during these times is often largely constrained to the analysis of oceanic sediments. The package of lacustrine diatomites preserved within the Baringo-Bogoria basin in the Central Kenya Rift therefore presents a rare opportunity to study high-resolution terrestrial climate changes during an important lake phase coincident with a major transition in global climate.

Chapter 2: Theoretical Background - Stable Isotope Geochemistry

2.1 Introduction

In order to contextualise the changes recorded in the Baringo-Bogoria basin with longer-term variations in regional climate, this work is paired with the investigation of changes in the flux of lithogenic material to the Arabian Sea which acts as an indicator of source region aridity, linked to low-latitude monsoonal circulation. The oxygen isotope analysis of benthic foraminifera is adopted in order to establish a chronological framework for this longer-term record. This was complemented by the analysis of the stable carbon isotope composition of both inorganic (foraminifera) and organic (bulk sediment) matter as part of a wider study (not included as part of this thesis) to analyse changes in palaeoceanographic parameters such as productivity and deep water circulation. The analysis and interpretation of the stable isotopic composition of lacustrine diatoms (oxygen) and marine foraminifera (oxygen and carbon) therefore forms a key component of this project and the following chapter aims to review the theoretical background and application of oxygen, and to lesser extent, carbon stable isotope geochemistry in Palaeoclimatology.

2.2 Introduction to Stable Isotope Geochemistry

Stable isotopes of any given element are defined by differences in the number of neutrons within the nuclei, while each containing the same number of protons. Whilst changes in the number of neutrons do not affect the major chemical properties of the element, the consequent variations in atomic mass cause minor differences in the chemical and physical properties of individual isotopes. With the exception of 21 monoisotopic elements (including fluorine, sodium, aluminium & phosphorus), most elements have at least two naturally occurring isotopes that are either stable or radioactive. Classical stable isotope geochemistry is primarily concerned with the stable isotope ratios of only six elements (H, C, N, O, S & Cl), however recent advancements in the application of stable isotope ratios in palaeoclimatological studies has seen the increasing use of other isotopes such as Si, Ca, Fe and others (e.g. Revel et al., 1996; De La Rocha et al., 1998).

By the means of chemical, physical and/or biological processes, isotopic fractionations create distinctive isotopic signatures within compounds and as such, can provide information on palaeoenvironmental conditions or processes, providing the fractionation

processes are clearly understood. The isotopic ratio of any given sample reflects the conditions of its formation and is measured in terms of parts per mil (‰) and by using δ notation, such that:

$$\delta = \frac{R_{sample} - R_{standard}}{R_{standard}} \text{ x } 1000\ (‰) \quad \text{or} \quad \delta = \frac{R_{sample}}{R_{standard}} - 1 \text{ x } 10^3\ (‰) \qquad \textit{(Equation 1)}$$

where R_{sample} is the isotopic ratio of the compound being analysed and $R_{standard}$ is the isotopic ratio of the standard being used in analysis. Isotope fractionation occurs through a variety of processes, the most important of which are summarised below. Detailed background and historical information regarding stable isotopes and their application in palaeoclimatological studies can be found within Criss (1999), Sharp (2007) and Hoefs (2009).

2.2.1 Equilibrium isotope exchange

Equilibrium isotope exchange occurs where there is no net reaction during isotopic fractionation between two compounds. When an isotopically light atom is substituted by a heavier isotope, nuclear charge and electron distribution remain unchanged, however there are slight differences in the internal energies which result from variations in atomic mass. Consequently this leads to a subtle preference for heavy isotopes to fractionate into compounds with a higher oxidation state (Sharp, 2007). Within the majority of materials, fractionation varies as a function of $1/T^2$ (where T = temperature) and therefore, within equilibrium isotope exchange, an equilibrium constant 'K' is primarily dependent on temperature with any pressure dependency usually below analytical detection limits (Clayton et al., 1975). As such, the measured fractionation of two phases (e.g. water and the precipitating substance) can be used to estimate the temperature of formation. This temperature dependence of isotopic fractionation led to the widespread application of a palaeotemperature scale (Urey et al., 1948, 1951; Epstein et al., 1951).

2.2.2 Kinetic isotope effects

The kinetic isotope effect is a dependence of the rate of a chemical reaction on the isotopic composition of any reactant material. Overall net reactions which result in kinetic isotope effects are normally associated with fast, incomplete or unidirectional processes such as evaporation and diffusion as well as dissociation reactions and almost all biological reactions. The theory of kinetic energy gives different velocities depending on the isotopic

composition of molecular compounds which can lead to isotopic fractionations in a number of ways. The magnitude of any isotopic fractionation is governed by factors such as the amount of kinetic energy involved in forming and separating bonds, isotopic abundances within the reactant material, environmental conditions and the nature of the reactive pathways. An isotopic substitution will greatly alter the reaction rate (Sharp, 2007). When this substitution occurs at a site where a chemical bond is broken or formed, it is termed a primary isotope effect. A smaller rate change, or secondary isotope effect, is observed when the substitution is not involved in bond breakage or formation. Chemical bonds between isotopes of a lower atomic mass are more easily broken and reacted than those between heavier isotopes and as such, newly formed compounds will be preferentially enriched in the lighter isotope whilst the reactant will gradually become preferentially enriched in the heavier isotope.

The fractionation of isotopes between two substances can be defined by a fractionation factor α or a separation factor ε, such that:

$$\varepsilon_{P-R} = (\alpha_{P-R} - 1).1000 \qquad \textit{(Equation 2)}$$

and where:

$$\alpha_{P-R} = \frac{R_P}{R_R} \qquad \textit{(Equation 3)}$$

where R_P and R_R are the ratios of the isotope in the product and reactant respectively. ε expresses α in terms of the ‰ difference between the two phases.

2.2.3 Disequilibrium effects

Disequilibrium can occur where certain biological organisms consistently precipitate their shells out of isotopic equilibrium with the surrounding environment, although it is not solely restricted to organisms (Wefer and Berger, 1991; Holmes and Chivas, 2002; Swann et al., 2007). For example, foraminifera may deposit their shells out of oxygen isotope equilibrium with ambient water. This phenomenon has been explained by a combination of kinetic and metabolic effects associated with changes in precipitation rates, local environmental conditions or biological life cycles. Where a given organism exhibits a systematic disequilibrium effect, the deviation from equilibrium is usually constant and therefore, can be corrected for and does not hinder the use of stable isotope geochemistry as a

palaeoenvironmental tool. In the case of biogenic carbonates, which have more traditionally been used to explore the application of carbon and oxygen stable isotope analysis, carbonates are rarely deposited in carbon isotopic equilibrium with dissolved carbon in the surrounding water. Metabolic processes, involving the removal of isotopically depleted CO_2 (i.e. $^{12}C^{16}O_2$) from the carbon pool during photosynthesis and the addition of light CO_2 to the pool through respiration, can have a significant impact on the carbon isotopic ratios of dissolved inorganic carbon (DIC) in the carbon pool utilised for calcification. Kinetic processes that affect vital effects concern the diffusion and chemical reaction rates of different isotopically substituted molecules, where isotopically lighter molecules diffuse faster and react faster with other substances than heavier molecules.

In addition to disequilibrium effects related to metabolic and kinetic processes, isotopic fractionation may also be controlled by chemical speciation. However, the extent to which speciation differences affect fractionation is poorly understood. Spero et al. (1997) demonstrated, through laboratory culturing experiments on planktonic foraminifera, that pH-dependent variations in seawater can have a significant impact on the oxygen and carbon isotope ratios of the secreted calcite of certain organisms. They found that with increasing pH and an associated linear increase in $[CO_3^{2-}]$, both oxygen ($\delta^{18}O$) and carbon ($\delta^{13}C$) isotope values decrease below those values predicted by the equilibrium relationship. Zeebe (1999) proposed a simple fractionation mechanism to explain this empirical observation and suggested that the amount of oxygen present in both dissolved bicarbonate and carbonate species in the water at the time of formation equals the resulting oxygen isotope composition of the precipitated carbonate. The suggestion that glacial oceans were more alkaline than at present (Rickaby et al., 2008), makes this especially important when reconstructing palaeotemperature data from the oxygen isotope analysis of foraminifera. In the case of silicate organisms such as diatoms, Swann et al. (2007, 2008) found that large negative isotopic offsets of up to 3.5‰ exist between different size fractions of cleaned diatoms from Ocean Drilling Program (ODP) site 882 in the North Pacific. Whilst the mechanisms governing these offsets are not fully understood, Swann et al., (2008) suggest that this could possibly relate to an inter/intra speciation effect controlled by a number of possible processes including environmental factors, such as changes in nutrient availability or local climatic conditions, or biological factors such as variations in growth rate, life cycle stage and silica maturation.

2.3 The Application of Stable Isotopes as a Palaeoenvironmental Tool

The first use of stable isotope geochemistry as a tool to better understand palaeoclimatic variability was proposed by Harold Urey (1947, 1948) who developed the basic principle of the carbonate palaeothermometer which is based on the temperature-dependence of the fractionation between calcite and water. Epstein et al. (1951) then conducted a series of laboratory culturing experiments in order to develop referencing conditions using a simple empirical calibration. This work was further expanded upon by other authors who used this relationship to reconstruct the timing of glacial/interglacial cycles and the mechanisms governing these shifts in climate (Emiliani, 1955, 1966, 1971; Shackleton, 1967, 1974). The subsequent continued development of the technique led to the establishment of a series of palaeotemperature equations (e.g. O'Neil et al., 1969; Shackleton, 1974; Hays and Grossman, 1991; Kim and O'Neil, 1997). These are discussed in greater detail in section 2.4.4.2.

Within marine environments, the analysis of isotope ratios allows the reconstruction of a number of environmental parameters such as palaeoproductivity (e.g. Ruhlemann et al., 1999; Schneider et al., 1994), palaeosalinity (e.g. Duplessy et al., 1991, 1992; Maslin et al., 1995b; Rohling 2000), vertical water column stratification (e.g. Niebler et al., 1999), surface and bottom water palaeotemperatures (e.g. Zachos et al., 2001), the degree of upwelling, nutrient availability and utilisation (e.g. Wefer et al., 1999), pCO_2 (e.g. Pagani et al., 1999), deep ocean circulation (e.g. Duplessy et al., 1988; Sarnthein et al., 1994), thermocline depth (e.g. Mulitza et al., 1997) and changes in terrestrial vegetation (e.g. Hughen et al., 2004). Stable isotopes from carbonates, silicates and organic matter have also been widely used to investigate palaeoclimate change in lacustrine settings. Typically, the application of stable isotope measurements to fossil material has been used to obtain information regarding a number of factors such as palaeotemperature (e.g. Brandriss et al., 1998), air mass source area (e.g. Shemesh et al., 2001a,b), precipitation/evaporation ratio (e.g. Wolfe et al., 2000, 2003), variations in catchment vegetation (Lamb et al., 2004) and internal lake processes, such as stratification and nutrient limitation, in both hydrologically open and closed lake systems (Chivas et al., 1993; Leng and Marshall, 2004; Leng et al., 2005). The application of stable isotopes to palaeoenvironmental studies has been extended to include studies of changing isotopic ratios in water, tree rings, speleothems and fossilised bones and teeth, in response to changing climate patterns (see reviews in Leng, 2005).

Historically, the application of stable isotope geochemistry in palaeoclimatic reconstructions has generally been based on biogenic and authigenic carbonates. However the global

distribution of carbonates is not consistent and many lakes and parts of the oceans, particularly in high-latitude regions, are devoid of any significant carbonate deposition. High-latitude regions are widely believed to have played a key role in driving periods of major long-term global climate change (e.g. deMenocal 1995; deMenocal and Rind, 1996; Shackleton 2000; Trauth et al., 2005). It has thus become increasingly important to generate palaeoclimate reconstructions from these regions and as such, the development of stable isotope palaeolimnological (e.g. Barker et al., 2001, 2007; Jones et al., 2004; Swann et al., 2010) and palaeoceanographic (e.g. Swann et al., 2008; Swann and Leng, 2009) records from biogenic silica has become more common. These records complement the existing carbonate-based climate data derived from mid- and low-latitude areas and help to generate a more complete picture of global climate variability with particular emphasis on inter-hemispheric teleconnections and feedback mechanisms.

The following section aims to review the existing work and current understanding of the use of oxygen isotopes in both carbonates and silicates. Due to the greater use of stable oxygen isotope geochemistry as a proxy for reconstructing climatic variability as part of this study, focus is given to the understanding of oxygen isotope systematics. A brief review of carbon isotope systematics in the marine environment is given in section 2.5. Since the lake records developed here are based on silica, carbon is not relevant and is only discussed in the context of marine settings.

2.4 Oxygen Isotope Systematics

Oxygen isotopes have been fundamental in the development of stable isotope geochemistry as a tool for reconstructing different palaeoenvironmental parameters such as temperature, ocean circulation and global ice volume, as well as being a tool for establishing chronological control e.g. SPECMAP (Imbrie et al., 1984) and LR04 stack (Lisiecki and Raymo, 2005). There are three naturally occurring stable isotopes of oxygen: ^{16}O (99.763% abundance), ^{17}O (0.0375% abundance) and ^{18}O (0.1995% abundance) (Garlick, 1974). The relative abundance of these isotopes is preferentially enriched or depleted by processes including thermodynamic and kinetic fractionation. Ratios of oxygen isotopes ($\delta^{18}O$ per mil) are measured as a relative deviation from a laboratory standard, as expressed in equation 1. The laboratory isotopic standard depends on the type of material being analysed: for carbonates this is the Vienna Pee Dee Belemnite (V-PDB), for water, ice, snow and silicates Standard Mean Ocean Water (SMOW) is used. These have been adapted from historical

standards to comply with the guidelines outlined by the International Atomic Energy Agency of Vienna (Coplen, 1996).

2.4.1 Isotopes in precipitation

The global water cycle is generally regarded as a closed system meaning that the volume of water vapour lost from the oceans during evaporation is equal to the amount of water returned to the oceans through precipitation and continental runoff, including fluvial inputs (Gat, 2000). The region between the latitudes of 30°N and 30°S contributes 65% of the global oceanic evaporation flux and consequentially is a major source for global precipitation (Peixoto and Oort, 1983). The oceanic reservoir has a notably uniform isotopic compostion for oxygen and hydrogen ($^{2}H/^{1}H$ or δD) where $\delta^{18}O = 0 \pm 1$ and $\delta D = 0 \pm 5$ per mil relative to SMOW; any values outside of this range tend to be confined to surface waters with variable salinities (Craig and Gordon, 1965). The linear relationship between the proportions of $\delta^{18}O$ and δD in precipitation is defined as the Global Meteoric Water Line (GMWL) and can be modelled by the following empirical relationship (Craig, 1961):

$$\delta D = 8 * \delta^{18}O + 10 \qquad \textit{(Equation 4)}$$

where the y-intercept (+10) is defined as the deuterium excess (Dansgaard, 1964).

The deuterium excess is an important parameter resulting from the kinetic effects which accompany the evaporation of seawater. It is strongly related to other factors such as seasonality, temperature, relative humidity, recycling of water droplets in the air and wind velocity, particularly at the point of vapour source, and can be used to characterise the temporal evolution and interactions between different airmasses (Merlivat and Jouzel, 1979; Fröhlich et al., 2008). Local precipitation values very often deviate from the GMWL and exhibit variations in the deuterium excess giving rise to Local Meteoric Water Lines (LMWL) that exhibit different gradients and intercepts for specific regions. Deuterium excess values are also subject to temporal variations over timescales ranging from annual to orbital and provide a useful means of assessing past climate variability (e.g. Niedermeyer et al., 2010). With the exception of palaeoclimatological archives within ice core records, deuterium excess values from palaeo-precipitation are rarely reconstructed.

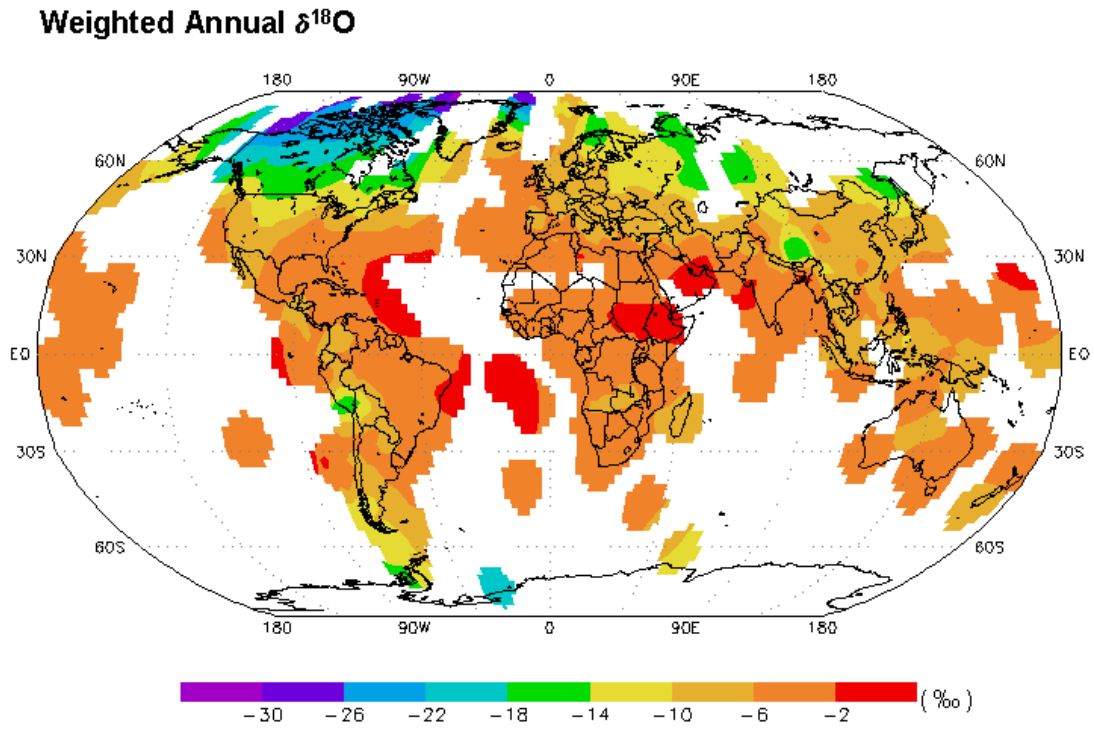

Figure 2.1 Spatial distribution of the weighted annual mean for the oxygen isotope composition of precipitation (δ_P). From IAEA/WMO (2006).

The oxygen isotopic composition of precipitation (δ_P, where $\delta_P = \delta^{18}O$) varies globally (figure 2.1) and is governed by the $\delta^{18}O$ value and sea surface temperature of the moisture source, the condensation temperature at time of precipitation formation, relative atmospheric humidity levels, air mass circulation and the efficiency of water vapour transport (Darling et al., 2005). According to the Rayleigh model of precipitation, heavy isotopologues are preferentially condensed resulting in the enrichment of heavier isotopes in precipitation and a relative depletion in the heavy isotope content of the remnant water vapour.

As precipitation falls, isotopic exchange continues to occur between the falling raindrops and warm ascending air masses. As a consequence, the raindrops become less enriched in heavy isotopes (Gat, 2000). This continuing fractionation with rising ambient air is only applicable in the case of rainfall and does not occur in the formation of precipitation in the solid state. Therefore, the isotopic composition of snow and hail is judged to be reflective of within-cloud processes and is naturally more enriched in heavy isotopes (Rozanski et al., 1993).

There are a number of other factors which may affect the isotopic composition of precipitation (δ_P):

Continentality — As clouds move further inland, meteoric waters become increasingly depleted in heavy isotopes due to progressive moisture loss through rainfall with increasing distance from the moisture source (Dansgaard 1964; Darling et al., 2005). The recycling of transpired moisture as clouds move further inland also compounds the effect of continentality.

Altitude & Latitude — Increases in latitude and altitude have the effect of decreasing temperature which induces condensation and precipitation leading to a further decrease in δ_P. This also results in evaporative effects due to the uplift of the air mass and the loss of vapour during rainout. The effect of altitude on ^{18}O in mid-latitudes generally leads to a decrease of between 0.15-0.30 ‰ per 100m of altitude gained (Dansgaard 1964; Siegenthaler and Oeschger, 1980; Clark and Fritz, 1997).

Amount Effect — The 'amount effect' is manifested as an apparent correlation between the heavy isotope composition and rainfall quantity and is also related to rainfall intensity. Dansgaard (1964) observed that, during drier months, the partial evaporative enrichment of raindrops below the cloud base may be important due to low relative humidity. This effect is commonly observed in oceanic islands and in coastal areas in the tropics where the seasonal temperature variations are minimal, however the offsets resulting from the amount effect can effectively be overridden by other isotopic processes.

Seasonality — The same factors which cause long-term variations in δ_P also operate in seasonal cycles, resulting in the isotopic depletion of winter precipitation, particularly in the mid-high latitudes (Rozanski et al., 1993). This is influenced by marked seasonal temperature differences in these regions and seasonal variability in other factors such as the degree of rainout, the evapotranspiration flux from land, changing airmass source areas and circulation patterns and changes in the type of rainfall e.g. frontal or convective (Darling and Talbot, 2003).

2.4.2 Oxygen isotopes in lacustrine environments

Once meteoric water reaches the ground it is often modified. Within lacustrine environments, the isotopic signature of inorganic materials such as carbonates and silicates is thought to be reflective of changes in both temperature and precipitation of the source area as well as the local precipitation/evaporation (P/E) regime.

For mineral precipitation in equilibrium, the isotopic composition of the substance is predictable by thermodynamics (Leng et al., 2005). In lacustrine environments, this process is controlled principally by the temperature and the isotopic composition of the lake water. In theory, if there is no change in the lake water composition, then palaeotemperatures can be estimated using fractionation equations. However, in practise this is complicated as both temperature and lake water composition may be affected by different variables and changes in climate processes. The isotopic balance of a lake system can be expressed in the following mass-balance equation (Leng and Barker, 2006):

$$\frac{\partial(\delta_{\text{lakewater}} V)}{\partial t} = P\delta_P + R\delta_R + G_i\delta_{GI} - G_o\delta_{\text{lakewater}} - E\delta_E - S_o\delta_{\text{lakewater}} \qquad \textit{(Equation 5)}$$

where P is the amount of direct precipitation at the lake surface, R represents surface inflow into the lake, G_i is the amount of groundwater inflow, G_o is the groundwater outflow, E is the amount of evaporation from the lake surface and S_o is the degree of surface outflow from the lake. δ_P, δ_R, δ_{Gi}, δ_E and $\delta_{\text{lakewater}}$ represent the isotopic compositions of precipitation, surface inflow, groundwater inflow, evaporated moisture and lakewater, respectively. As equation 5 shows, δ_P is only one component of a highly complex system, all facets of which should be considered.

Outside of the tropics, where the isotopic composition of precipitation entering lake systems (δ_P) is strongly influenced by the amount effect, δ_P covaries linearly with temperature. The relationship between δ_P and temperature change (d*T*) is defined by the Dansgaard equation (Dansgaard 1964):

$$\frac{d\delta_P}{dT} \sim +0.2‰/\,°C \text{ to } +0.7‰/\,°C \qquad \textit{(Equation 6)}$$

Lakes can be classified into one of two types: open or closed. Hydrologically 'open' lakes have an active outflow. The dominant factor controlling $\delta^{18}O_{lakewater}$ in open lakes, subject to minimal evaporation, is variations in the isotopic composition of precipitation and groundwater inflow entering the lake (Clark and Fritz, 1997). In closed lake systems, especially in arid environments and where groundwater outflow is insignificant, the roles of δ_P and temperature are minimal relative to the importance of the ratio between precipitation and evaporation (P/E budget). In areas where the change in δ_P is potentially large, variations in δ_P may be more important than previously thought (e.g. Henderson et al., 2010). Closed lakes become enriched in ^{18}O depending on variations in local evaporation rates, the magnitude of which are affected by changes in temperature, wind velocity and relative humidity. When assessing $\delta^{18}O$ records from either open or closed lake systems, it is important to consider the lake's hydrological setting including factors such as the water turnover time, catchment size, catchment processes and seasonal variations in $\delta^{18}O_{lakewater}$.

2.4.2.1 Oxygen isotopes in lacustrine silicates

Diatoms are one of the principal sources of biogenic silica used for lake-based palaeoclimatic reconstructions. They are unicellular, photosynthetic, eukaryotic algae which generate siliceous cell walls that form distinctive rigid frustules (Round et al., 1990). Diatom silica is precipitated in isotopic equilibrium with the surrounding ambient water and are later preserved within the sediment record (Leng and Barker, 2006). Biogenic silica is abundant in areas devoid of carbonate sedimentation, such as in soft-water lakes and the high-latitude oceans, and thus provide reliable isotope records to complement the existing palaeoclimate records derived from carbonates. Diatoms are ubiquitous in most lacustrine environments where levels of key nutrients such as silicon, nitrogen and phosphorus are sufficient to sustain diatom productivity. Diatom species differ from each other in their ability to successfully utilise varying nutrient levels and to withstand changes in different physical conditions, such as light availability and mixing within the water column. Diatom productivity within lacustrine environments is largely controlled by seasonal climate patterns which influence lake habitat conditions such as the depth of vertical mixing and nutrient availability. In large monomictic tropical lakes, increased mixing, and thus productivity, tends to occur during the dry season (Bootsma, 1993), whilst in dimictic temperate lakes, mixing occurs twice each year, during spring and autumn when similarities between the temperature and density of the hypolimnion and epilimnion create a strong mixing regime whereby diatom productivity takes place through the exploitation of

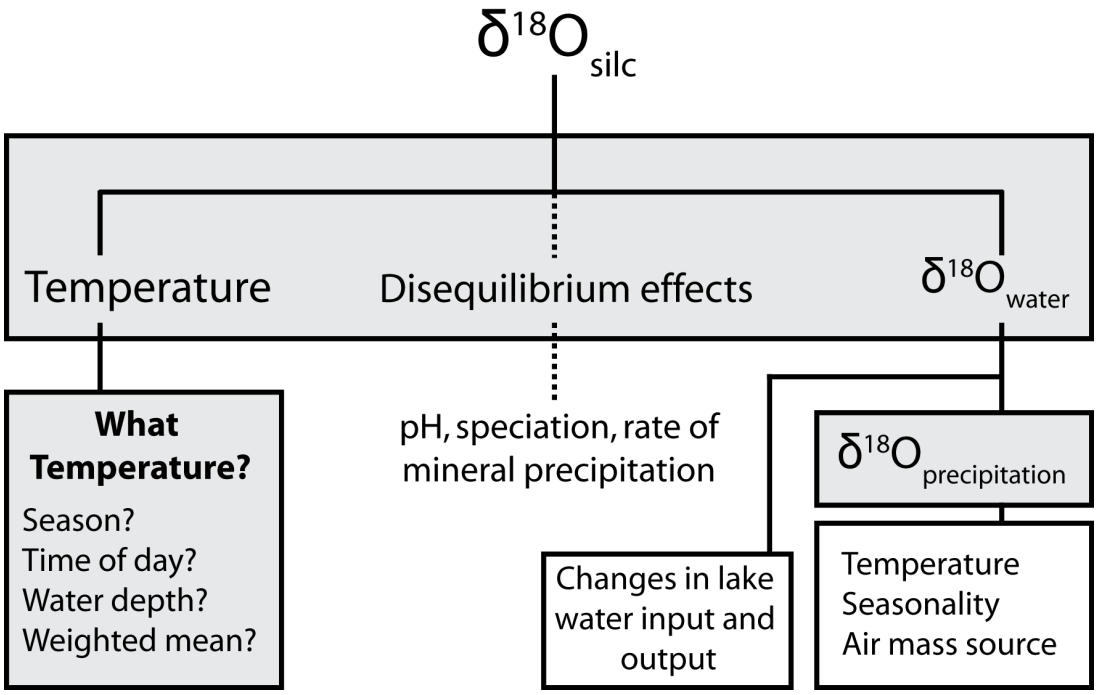

Figure 2.2 Schematic diagram illustrating controls on the oxygen isotope composition of lacustrine diatom silica. The importance of temperature varies depending on location and becomes more relevant for high-latitude and high-altitude sites. In low-latitude regions, the oxygen isotopic signal of precipitation and thus the lakewater in which the diatom silica precipitates becomes more important. Modified from Leng and Barker (2006).

nutrient-rich waters (Leng and Barker, 2006). The isotopic signature of diatom silica ($\delta^{18}O_{diatom}$) is largely acquired during these growth periods which generally coincide with the dry season, and thus the seasonal productivity cycles and climatic conditions, specific to each individual lake, are an important consideration in the interpretation of records of $\delta^{18}O_{diatom}$.

Within lacustrine environments, $\delta^{18}O_{diatom}$ varies as a function of temperature and/or the isotopic composition of ambient lake water (figure 2.2) which in turn is heavily influenced by the balance between precipitation and evaporation. In all lakes, a possible additional control is exerted by depth constraints within the water column. These constraints, such as vertical stratification, limit diatom productivity to the upper parts of the water column and can result in a $\delta^{18}O_{diatom}$ value that is reflective of a localised $\delta^{18}O_{water}$ signal (Raubitschek et al., 1999).

A number of calibration studies have attempted to define an empirical relationship between $\delta^{18}O_{diatom}$ and temperature (Labeyrie, 1974; Juillet-Leclerc and Labeyrie, 1987; Matheney and Knauth, 1989; Shemesh et al., 1992; Brandriss et al., 1998). Based on bulk diatom

samples, the estimated average temperature dependence ranges from -0.2‰/°C to -0.5‰/°C. More recently, diatom culturing experiments using individual marine diatom species (Brandriss et al., 1998) and the study of planktonic diatoms from sediment traps in a small maar lake (Lake Holzmaar) in Germany (Moschen et al., 2005) and in Lake Annecy in France (Crespin et al., 2010), have estimated the diatom-temperature coefficient to be approximately -0.2‰/°C. However, Schmidt et al. (1997) found no regular correlation between $\delta^{18}O_{diatom}$ and temperature, which has led to the suggestion that the temperature-dependent oxygen isotope fractionation of some biogenic silica may have occurred during early diagenesis rather than during later growth stages (Leng and Barker, 2006).

In tropical regions, where there is little or no variation in seasonal temperatures, the effect of changes in δ_P and therefore variations in the isotopic composition of ambient lakewater ($\delta^{18}O_{lakewater}$) become more important in determining values of $\delta^{18}O_{diatom}$. The phase change associated with evaporation results in depleted ^{16}O isotopologues being preferentially evaporated leaving lakewater relatively enriched in the heavier ^{18}O isotope. The degree to which evaporation increases $\delta^{18}O_{lakewater}$ is dependent on factors such as humidity or the residence time of a lake, which can vary according to changes in basin hydrology or groundwater flux. A number of studies have investigated the degree to which the influence of evaporation and variations in the amount of precipitation are important for driving changes in the $\delta^{18}O_{diatom}$ record, particularly in tropical regions (e.g. Rietti-Shati et al., 1998; Cole et al., 1999; Lamb et al., 2000, 2005; Barker et al., 2001, 2007; Shemesh et al., 2001a,b; Polissar et al., 2006). In addition, changes in $\delta^{18}O_{lakewater}$ may also occur through changes in, or at, the precipitation source area. For example, Rosqvist et al. (2004) showed that changes in the $\delta^{18}O_{diatom}$ record from a lake in Northern Sweden over the past 5000 years reveal a lowering trend with stepwise spikes illustrating a 1000-yr cyclicity. Coupled with evidence for glacial advance they suggest that persistent changes in atmospheric circulation patterns and dominant air mass source could have caused the ensuing isotopic depletion. Changes in the predominance of cold polar air masses have also been invoked as the cause for variations in the $\delta^{18}O_{diatom}$ record from Lake Chuna on the Kola Peninsula in Northwest Russia (Jones et al., 2004). Furthermore, changes in the $\delta^{18}O_{diatom}$ record from Lake Baikal are thought to reflect differences in the composition of river inflow between northern and southern catchment areas where the variability of δ_P is determined by latitudinal differences (Mackay et al., 2011). A detailed and extensive review of the use of oxygen isotopes in lacustrine biogenic silica as a proxy for palaeoclimatic change can be found in Leng and Barker (2006).

Providing robust and thorough cleaning procedures (see section 4.3.3) are followed to ensure purity, $\delta^{18}O_{diatom}$ offers an important palaeoclimatic proxy that provides additional information to complement our current understanding of past climatic change. Although a relatively new tool, the study of the oxygen isotope signature of diatoms preserved in the sediment record has been increasingly used in both marine and lacustrine environments (Swann and Leng, 2009). Recently however, the validity of $\delta^{18}O_{diatom}$ records has been shown to be compromised by contamination remaining within purified samples, even after cleaning (Brewer et al., 2008). This is explored further in chapters 4 and 5.

2.4.3 Oxygen isotopes in marine environments

In marine environments, there are a number of factors that may influence the oxygen isotope composition of seawater ($\delta^{18}O_w$) which is, in turn, reflected in the isotopic composition of foraminiferal calcite ($\delta^{18}O_c$) assuming that thermodynamic isotopic equilibrium exists between seawater and calcite. The first factor is the water temperature at which the mineral is precipitated at (δ_T) whereby the $\delta^{18}O$ signal incorporated into the precipitate decreases with increasing temperature; the second is the $\delta^{18}O$ composition of the water itself, in which the minerals are precipitated ($\delta^{18}O_w$). In turn, $\delta^{18}O_w$ is controlled by global factors, such as the volume of ^{18}O-depleted freshwater water trapped in ice sheets ($\Delta\delta_{GIV}$), and local influences ($\Delta\delta_{local}$), such as the regional freshwater input to the oceans through riverine flux, local precipitation and iceberg discharge. In addition to this, vital effects such as the species-specific incorporation of oxygen into the precipitated calcite, also have an effect on the oxygen isotope signal (Maslin and Swann, 2005; Ravelo and Hillaire-Marcel, 2007). This can be displayed as:

$$\Delta\delta^{18}O_M = \Delta\delta^{18}O_w + \Delta\delta_T = \Delta\delta_{GIV} + \Delta\delta_{local} + \Delta\delta_T + \text{vital effects} \qquad \textit{(Equation 7)}$$

where $\Delta\delta^{18}O_M$ refers to the oxygen isotope signal of the precipitated mineral. In the case of foraminifera, the offset between the $\delta^{18}O$ of foraminifera and the $\delta^{18}O$ of seawater is dependent upon temperature, whereby the $\delta^{18}O$ of calcite is enriched by ~30-35 ‰ in comparison with ambient water (Ravelo and Hillaire-Marcel, 2007). Using this information, the $\delta^{18}O$ value of these different parameters can be reconstructed over long timescales of up to 50 million years and beyond (e.g. Zachos et al., 2001).

2.4.3.1 Factors affecting the $\delta^{18}O$ of seawater

Shackleton (1967) demonstrated that a significant component of the $\delta^{18}O_c$ signal is attributable to the proportion of water stored within continental ice masses and that fluctuations in global ice volume are reflected in the $\delta^{18}O$ values of benthic foraminifera preserved within deep-sea sediments. Ice sheets act as reservoirs of low-$\delta^{18}O$ water, with values in the range of -30 to -50 ‰ (IAEA 2000). The growth and decay of continental ice sheets restricts the input of low-$\delta^{18}O$ precipitation to the oceans, causing an increase in mean ocean $\delta^{18}O_w$ over millennial-scale, ocean mixing timescales as well as resulting in a lowering of global eustatic sea levels (Shackleton, 1967, 1987; Chappell and Shackleton, 1986; Waelbroeck et al., 2002). Fairbanks (1989) provided the first calibration for global ice volume changes by reconstructing relative sea level (RSL) change from submerged corals off Barbados and equated that a drop in sea level of 120 m is approximately equivalent to a change in $\delta^{18}O$ of 1.3 ‰. Since then, there has been some degree of debate regarding the precise change in RSL and consequently the proportion of the glacial-interglacial variation in benthic foraminiferal $\delta^{18}O$ values that can be attributed to changes in global ice volume. This is believed to be 1 ‰ ± 0.1 ‰ (Duplessy et al., 2002; Schrag et al., 2002; Waelbroeck et al., 2002), however estimates range from 0.8 ‰ (Schrag et al., 1996; Burns and Maslin, 1999) to 1.7 ‰ (Broecker and Denton, 1989). The idea that marine $\delta^{18}O$ records are an accurate reflection of global ice volume is based on the assumptions that the oxygen isotope composition of glacial ice is constant and that benthic temperatures remain constant. However, the sequestration of ^{18}O-depleted precipitation in continental ice sheets is nonlinear as the $\delta^{18}O$ value of ice in near-coastal locations or at lower altitudes will be higher (see section 2.4.1) (Mix and Ruddiman, 1984).

Foraminiferal $\delta^{18}O$ records are also affected by local processes, which influence the $\delta^{18}O$ of seawater. These include regional fluctuations in the precipitation/evaporation balance, which causes variations in local sea-surface salinity. Enhanced evaporation results in an increase in $\delta^{18}O_w$ values and salinity whilst increased precipitation leads to a decrease in $\delta^{18}O_w$ through the greater input of freshwater to the system. Whilst $\delta^{18}O$ values from planktonic foraminifera are not directly related to sea-surface salinity, they are both affected by the same variations in precipitation and evaporation and thus there is a linear relationship between the two. Providing that the temperature, ice-volume and carbonate ion concentration components can be accounted for, it is possible to calcuate local salinity changes from $\delta^{18}O$ records (Duplessy et al., 1991; Maslin et al., 1995b; Schmidt et al., 2004) using the following equation:

$$S_{local} = (\delta_{fresh} - \Delta\delta_{local})(S_{ocean}/ \delta_{fresh} - \delta_{ocean}) \quad \textit{(Equation 8)}$$

where S_{local} represents mean local salinity, δ_{fresh} represents the end-member $\delta^{18}O$ value of freshwater whilst the definition for $\Delta\delta_{local}$ is the same as for equation 7. S_{ocean} is mean ocean salinity calculated due to the concentration effect resulting from the global decrease in sea-level that occurs during periods when continental ice mass growth is enhanced:

$$S_{ocean} = 34.74 \text{ x RSL} / (3900\text{-RSL}) \quad \textit{(Equation 9)}$$

where RSL is measured in metres. However as discussed previously, there are uncertainties concerning the precise change in RSL, which in turn impacts upon the accuracy of estimates of S_{ocean}. δ_{ocean} is the end-member $\delta^{18}O$ value of saline water, calculated using estimates of sea-level coupled with $\delta^{18}O$-sea-level scaling, dependent on the time period being investigated (Schrag et al., 1996):

$$\delta_{ocean} = \text{modern } \delta_{ocean} + (0.012 \text{ x RSL}) \quad \textit{(Equation 10)}$$

Accounting for geographical variations in salinity and therefore $\delta^{18}O_w$, the global distribution of surface water salinity and $\delta^{18}O_w$ is approximately 0.5 ‰/1.0 psu. Other processes linked to the growth and shrinking of sea-ice, as well as advection and upwelling of seawater, can also impact local surface water $\delta^{18}O$ values, particularly in high latitude regions (Rohling and Bigg, 1998). In addition to the factors described above, values of $\delta^{18}O_w$ can also be affected by changes in pH, which alter the relative abundance of dissolved carbonate species and which, in turn, can account for a small portion of the variability observed in foraminiferal $\delta^{18}O$ values (Zeebe, 1999).

2.4.3.2 Factors affecting the $\delta^{18}O$ of foraminifera

The interpretation of foraminiferal stable oxygen isotope ($\delta^{18}O_c$) data must take account of all processes described above which affect the $\delta^{18}O$ of seawater and thus impact the calcification of the foraminiferal shells. Laboratory culture experiments have shown that the temperature of the seawater directly affects the rate of exchange of oxygen between water and inorganic calcite (McCrea, 1950; Craig, 1965; O'Neil et al., 1969). As the ocean temperature increases, there is a corresponding decrease in $\delta^{18}O_c$ such that a 4 °C change in temperature causes a change in $\delta^{18}O_c$ of approximately 1 ‰, assuming that there is no change in global ice volume or local influences (Maslin and Swann, 2005). A number of palaeotemperature equations have been proposed to combine changes in water temperature with changes in the calcite-water fractionation of $\delta^{18}O$. The two most commonly used

equations are based on the work of O'Neil et al. (1969) who investigated equilibrium fractionation factors between water and divalent metal carbonates. Following on from this, and on the basis of empirical calibrations to core-top data, Shackleton (1974) proposed that:

$$T = 16.9 - 4.38\,(\delta_c - \delta_w) + 0.1\,(\delta_c - \delta_w)^2 \qquad \textit{(Equation 11)}$$

which was later reassessed by Hays and Grossman (1991) as:

$$T = 15.7 - 4.36\,(\delta_c - \delta_w) + 0.12\,(\delta_c - \delta_w)^2 \qquad \textit{(Equation 12)}$$

where T is the isotopic temperature estimate, δ_c is the $\delta^{18}O$ value of foraminiferal calcite and δ_w is the $\delta^{18}O$ of surface water. Consequently, the higher the calcification temperature, the lower the resulting $\delta^{18}O_c$ value. Kim and O'Neil (1997) express the temperature-dependence of inorganic calcite, assumed to have precipitated at isotopic equilibrium between 0-500 degrees Kelvin (K), as:

$$1000\ln\alpha\,(\delta_c - \delta_w) = 2.76\,(10^6 T^{-2}) - 3.96 \qquad \textit{(Equation 13)}$$

Where α is the fractionation factor and the temperature T is expressed in Kelvin. Leng and Marshall (2004) have rearranged this equation in the more convenient form:

$$T = 13.8 - 4.58\,(\delta_c - \delta_w) + 0.08\,(\delta_c - \delta_w)^2 \qquad \textit{(Equation 14)}$$

This quadratic calibration is similar to those proposed by Shackleton (1974) and Hays and Grossman (1991) and all suggest a $\delta^{18}O$/temperature gradient exhibited in foraminifera of ~0.25‰/°C (Waelbroeck et al., 2005).

For the early Cenozoic, prior to the formation of major global ice masses, $\delta^{18}O$ records of marine carbonates are a highly effective palaeothermometer, providing local influences on $\delta^{18}O$ can be accounted for (e.g. Zachos et al., 2001). For more recent studies, it is possible to reconstruct variations in sea surface temperature (SST) using a variety of palaeothermometry techniques including assemblage counts, algal biomarkers and Mg/Ca ratios to calculate the calcification temperatures of planktonic foraminifera (Barker et al., 2005).

Carbonate ion concentrations and biological and ontogenic 'vital effects' such as the species-specific incorporation of oxygen into biogenic calcite can also affect biomineralisation and resulting values of $\delta^{18}O_c$. Spero et al. (1997) speculate that higher pH and alkalinity values in oceans during glacial periods may alter carbonate ion concentrations. Increasing carbonate ion concentrations [CO_3^{2-}] may cause a decrease in the

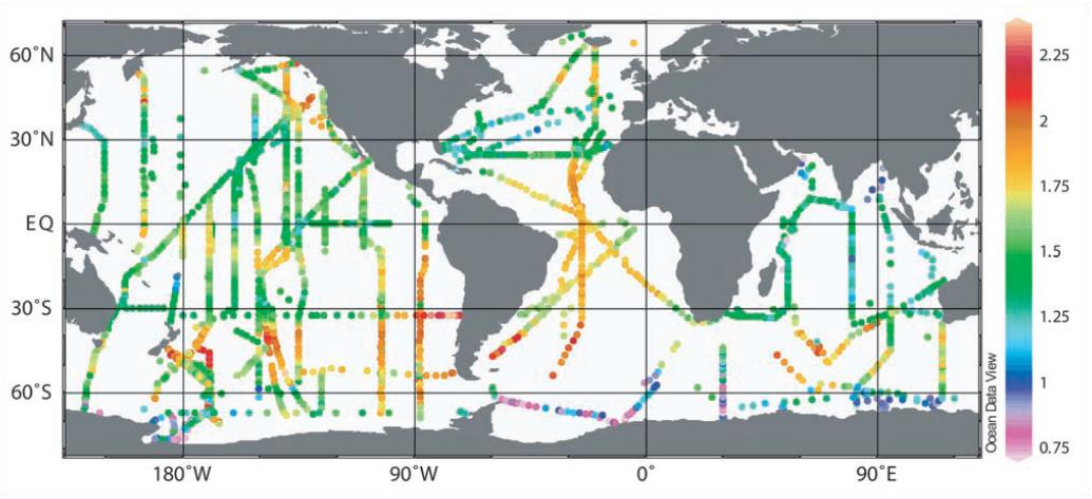

Figure 2.3 Distribution of surface ocean $\delta^{13}C$. Data was measured as part of the World Ocean Circulation Experiment (WOCE) in 1995. From Quay et al. (2003).

$\delta^{18}O$ of calcite through an influence on calcification rates, which induces kinetic fractionation effects. However, the exact role that pH and carbonate ion concentrations play on the isotopic composition of foraminiferal calcite remains unclear and requires further investigation (Zeebe, 2005). Biological 'vital effects' have been found to exist between different sizes and species of foraminifera which result in differences in $\delta^{18}O_c$. These vital effects are related to changes in depth habitat and in the intensity of photosynthetic activity that occur throughout the foraminiferal life cycle (Williams et al., 1979; Ravelo and Fairbanks, 1995). For a detailed and comprehensive review of the stable isotope geochemistry of foraminiferal calcite, see Rohling and Cooke (2003).

2.5 Carbon Isotope Systematics

There are three naturally occurring isotopes of carbon, ^{12}C (98.93% abundance) and ^{13}C (1.07% abundance) which are both stable, and ^{14}C (0.0000000001% abundance) which is radioactive. Carbon isotope values ($\delta^{13}C$) are routinely measured on foraminiferal shells and are expressed as a ratio of the heavier ^{13}C isotope to ^{12}C. The carbon isotopic signature ($\delta^{13}C$) of marine carbonates such as foraminifera is reflective of the carbon isotope composition of dissolved inorganic carbon (DIC) in the seawater from which the foraminiferal shell was precipitated. Due to the relatively rapid speed of biogenic calcification, which results in kinetic isotope fractionation and the presence of strong biological vital effects, calcification does not occur in isotopic equilibrium with seawater. The distribution of $\delta^{13}C$ of DIC ($\delta^{13}C_{DIC}$) is neither spatially nor temporally uniform

throughout the global ocean (figure 2.3). This, coupled with the greater number of parameters which influence values of foraminiferal $\delta^{13}C$, means that the interpretation of carbon isotope data is more complicated than that of oxygen isotope records.

2.5.1 Factors affecting the $\delta^{13}C$ of DIC in seawater

Changes in average values of global oceanic $\delta^{13}C_{DIC}$ can be the result of variations in the amount of carbon stored on land and alterations in the source/sink of carbon from geological reservoirs, while changes in local $\delta^{13}C_{DIC}$ also reflect the relative mixing of different water masses and the balance between photosynthesis and respiration (Ravelo and Hillaire-Marcel, 2007). Values of $\delta^{13}C_{DIC}$ in the ocean reflect ocean-atmosphere-biosphere interactions and perturbations in the global carbon cycle. The terrestrial biosphere acts as a reservoir of ^{13}C-depleted carbon due to the preferential use of ^{12}C during photosynthesis. During growth of this biosphere reservoir, ^{12}C is sequestered which leads to an increase in oceanic $\delta^{13}C_{DIC}$. The average values of $\delta^{13}C$ in the ocean and atmosphere can be affected by changes in other carbon sinks or sources through geological processes such as volcanic outgassing and release of methane clathrates (Ravelo and Hillaire-Marcel, 2007). Temperature-dependent equilibration between surface ocean DIC and atmospheric CO_2 is an important control over variations in the $\delta^{13}C$ of atmospheric CO_2 but has a diminished influence on the $\delta^{13}C$ of DIC in surface water, and a negligible effect on whole-ocean $\delta^{13}C_{DIC}$ due to the increased levels of inorganic carbon contained within the oceans. Therefore changes in the terrestrial biosphere become the primary forcing mechanism behind changes in $\delta^{13}C_{DIC}$ values for the global ocean.

The local balance between photosynthesis and respiration and other mechanisms such as volcanic outgassing and seafloor spreading can have a profound effect on values of $\delta^{13}C_{DIC}$ over both shorter (10^2-10^3 years) and longer (> 10^4 years) timescales. In surface waters, levels of photosynthesis exceed those of respiration whereas in the deep ocean, respiration of organic particulate matter dominates. This results in differences in the levels of DIC, and thus $\delta^{13}C_{DIC}$, at different depths within the water column, such that in surface waters DIC is low and values of $\delta^{13}C_{DIC}$ are high, and vice versa. The processes of photosynthesis and respiration also affect the oceanic distribution of nutrients, such that the concentrations of nitrates and phosphates are inversely related to $\delta^{13}C_{DIC}$ (Ortiz et al., 2000). Glacial-interglacial variations in $\delta^{13}C$ are thus often thought to reflect changes in palaeoproductivity (Zahn et al., 1986; Sarnthein et al., 1988).

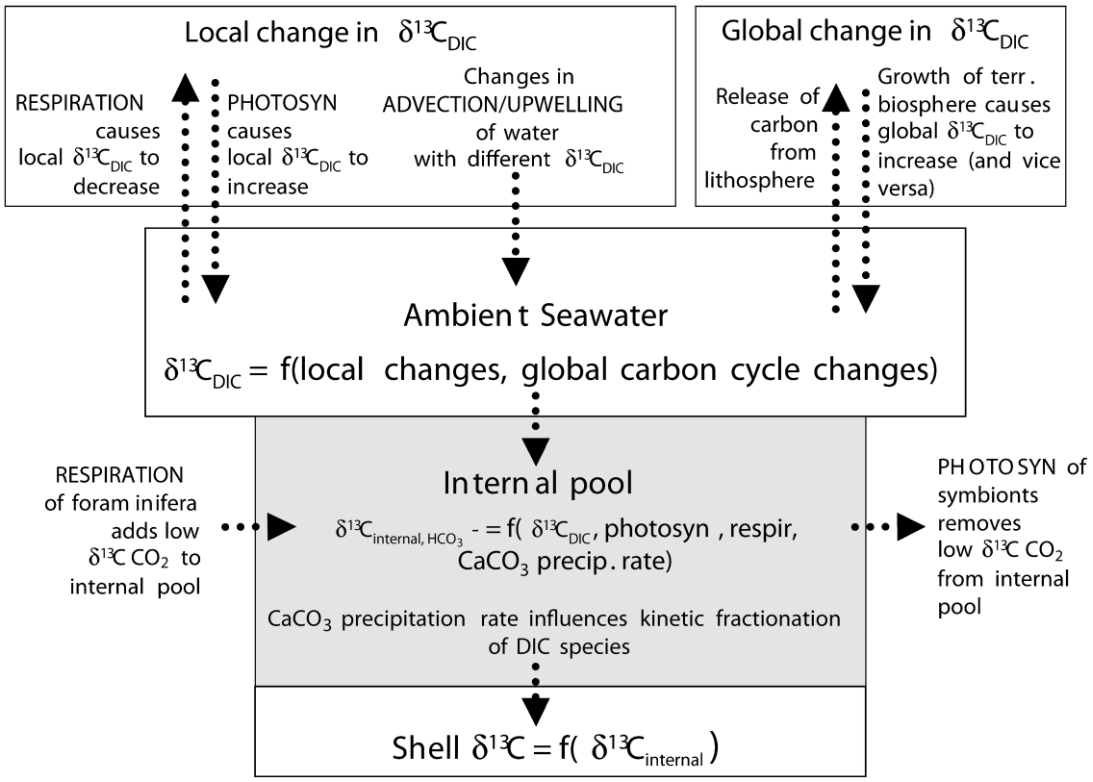

Figure 2.4 Summary of factors influencing the carbon isotope composition ($\delta^{13}C$) of foraminiferal shells (PHOTOSYN = photosynthesis). From Ravelo and Hillaire-Marcel (2007).

However there are other possible causes for local changes in the $\delta^{13}C_{DIC}$ of seawater at any particular location, namely the formation, circulation and relative mixture of water masses. The cooling and sinking of deep water masses imprints a $\delta^{13}C_{DIC}$ signature reflective of the surface-water at the site of formation. This may differ from place to place. For example, North Atlantic Deep Water (NADW) has relatively high $\delta^{13}C_{DIC}$ values whereas the Antarctic Bottom Water (AABW) has relatively low $\delta^{13}C_{DIC}$ values (figure 2.3). The $\delta^{13}C_{DIC}$ of surface water is also influenced by local changes in the relative mixing ratios of different water masses through processes such as the vertical upwelling of cold, nutrient-rich, low $\delta^{13}C_{DIC}$ waters in areas such as off the southwest coast of Africa, the Californian coast and the Arabian Sea (Kroopnick, 1985).

2.5.2 Factors affecting the $\delta^{13}C$ of foraminifera

The $\delta^{13}C$ signature of foraminiferal calcite is readily affected by changes in microhabitat conditions and may not be in isotopic equilibrium with DIC. Abiotic kinetic fractionation results in an enrichment of 1.0 ± 0.2 ‰ of the $\delta^{13}C$ of foraminiferal calcite with respect to $\delta^{13}C_{DIC}$, however this offset can vary widely depending on ontogeny and specific vital

effects in both planktonic and benthic foraminifera (Ravelo and Fairbanks, 1995; Grossman, 1987).

Through changes to the internal carbon pool and microenvironmental conditions such as pH and DIC concentration (figure 2.4), $\delta^{13}C$ values of calcite are affected by algal photosynthesis and respiration. Since the $\delta^{13}C$ of calcite precipitated by foraminifera is drawn from this internal pool, the carbon isotopic composition of foraminifera can reflect increases in photosynthesis (enriched in ^{13}C) or respiration (depleted in ^{13}C) as well as changes in the rate of isotopic equilibration during CO_2 hydroxylation and hydration which has an impact on the chemical properties of the carbon pool (e.g. pH, $[CO_3^{2-}]$) (Spero et al., 1997).

Substantial differences between the carbon isotopic composition of juvenile and adult foraminifera can depend on a number of factors, including changes in habitat during life cycles, seasonal shifts in environmental conditions, deposition of secondary calcite within large shells, differential dissolution during early diagenetic processes, metabolic rate and specific vital effects (Lohmann, 2006). Large differences in habitat and ecological preferences (temperature, light and nutrient requirements) between various planktonic foraminifera species are reflected in the $\delta^{13}C_{DIC}$ of ambient seawater at different depths in the water column where their calcite shells are precipitated. Similarly, epifaunal and infaunal benthic foraminifera species live and calcify at different depths within the sediment and have differing oxygen and nutrient requirements. Changes in porewater gradients and $\delta^{13}C_{DIC}$ values are therefore reflected in the isotopic composition of different species (Mackensen et al., 2000). A detailed review of the factors affecting the stable isotope composition of foraminifera is given by Rohling and Cooke (2003).

2.5.3 Factors affecting the $\delta^{13}C$ of bulk organic matter

The abundance of total organic carbon (TOC), and more specifically the flux of TOC to the ocean floor, can be used as a measure of the export of organic matter from the euphotic zone to the deep ocean. TOC in ocean sediments is composed of both land-sourced organic matter and that derived from marine sources. The terrestrial component of TOC is influenced by climate, erosion and the transport of terrigenous material to the oceans while the marine component reflects primary productivity (Leventhal, 2004). The ratio of carbon to nitrogen (C/N) is used to determine the relative proportions of land- and marine-sourced organic matter. The concentrations of TOC and the carbon isotope composition of bulk

organic material ($\delta^{13}C_{org}$) can be used to define the source and depositional environment of organic matter since marine organic carbon is typically enriched in ^{13}C relative to terrestrial organic carbon from C_3 vascular plants (Stein, 1991). In general, values of marine-derived $\delta^{13}C_{org}$ range from -18 ‰ to -22 ‰ (Druffel et al., 1992) whilst land-sourced organic matter has typical values of -24 ‰ to -30 ‰ (Opsahl and Zepp, 2001). $\delta^{13}C_{org}$ values therefore reflect a combination of ocean productivity, surface water CO_2 concentrations, the input of terrestrial material to the site and diagenetic effects. However complications to the $\delta^{13}C_{org}$ signal can arise due to the mixed input of C_3 and C_4 plant carbon and from variations in the $\delta^{13}C_{org}$ values recorded for end-member marine organic carbon (Maslin and Swann, 2005).

2.6 Summary

This thesis requires the use of a number of different techniques involving isotope analysis of both marine (benthic foraminifera and bulk sediment) and lacustrine (diatom frustules) material. In order to understand the context of these changes in response to variations in climate, it is important to understand the fundamental processes governing isotope fractionation and incorporation of the isotopic signal into the precipitated mineral. These are different in oceanic and continental environments but isotope geochemistry is a useful tool for investigating changes in both realms.

Chapter 3: The Baringo-Bogoria Basin

3.1 Introduction

Reviews of the evidence for lacustrine history and climate variability in the East African Rift Valley (EARS) by Trauth et al. (2005, 2007) have suggested that a long-term trend of aridification was punctuated by a series of three major humid periods (2.7 - 2.5 Ma, 1.9 - 1.7 Ma & 1.1 - 0.9 Ma) coincident with global climate transitions. The period between 2.7 Ma and 2.5 Ma is coeval with the intensification of ice sheet growth and cooling in the Northern Hemisphere. Well-dated diatomite units (the Barsemoi Diatomites) exposed within the Chemeron Formation near Lake Baringo in the Central Kenyan Rift record the rhythmic cycling of a major freshwater lake system between 2.68 and 2.55 Ma. The timing of diatomite formation during wet periods closely approximates maxima in the 30°N (June) insolation curve implying that regional precipitation at this time was controlled by precessionally-forced monsoonal circulation (Deino et al., 2006; Kingston et al., 2007). Orbitally-induced changes in insolation have been implicated as a driving mechanism for climatic change and have been specifically linked to environmental change in the EARS, particularly to tropical African rainfall variability through fluctuations in the strength of monsoonal circulation. In particular, a precessional control on tropical moisture availability has been widely invoked in other studies (e.g. deMenocal, 1995, 2004; Larrasoaña et al., 2003; Lourens et al., 2004; Denison et al., 2005; Schefuss et al., 2005; Berger et al., 2006; Maslin and Trauth, 2009; Trauth et al., 2009, 2010; Scholz et al., 2011). Equatorial climate is not only affected by low-latitude changes in insolation; changes to eccentricity and obliquity amplitudes in mid- to high- latitudes may also have an indirect, yet significant effect, by driving changes to systems such as the Indian Ocean and East Asian monsoons and Atlantic Ocean SSTs (Deino et al., 2006).

3.2 Lake Baringo

Modern day Lake Baringo is situated in the Central Kenyan Rift (figure 3.1), part of the EARS (0° 20’ to 1° N, 36° 5’ E). The extent of the lake varies greatly from year to year depending on the strength and duration of the rainy season. As such, the surface area of the lake varies between 108 and 160 km^2 and drains a catchment encompassing a total area of 6200km^2 (Odada et al., 2006; Tarits et al., 2006). The lake lies in the axial graben of the Central Kenyan Rift at an altitude of 970 m.a.s.l. and is, on average, 21 km long by 13 km wide. Records indicate that between 1969 and 1972 the average depth of the lake was 8 m

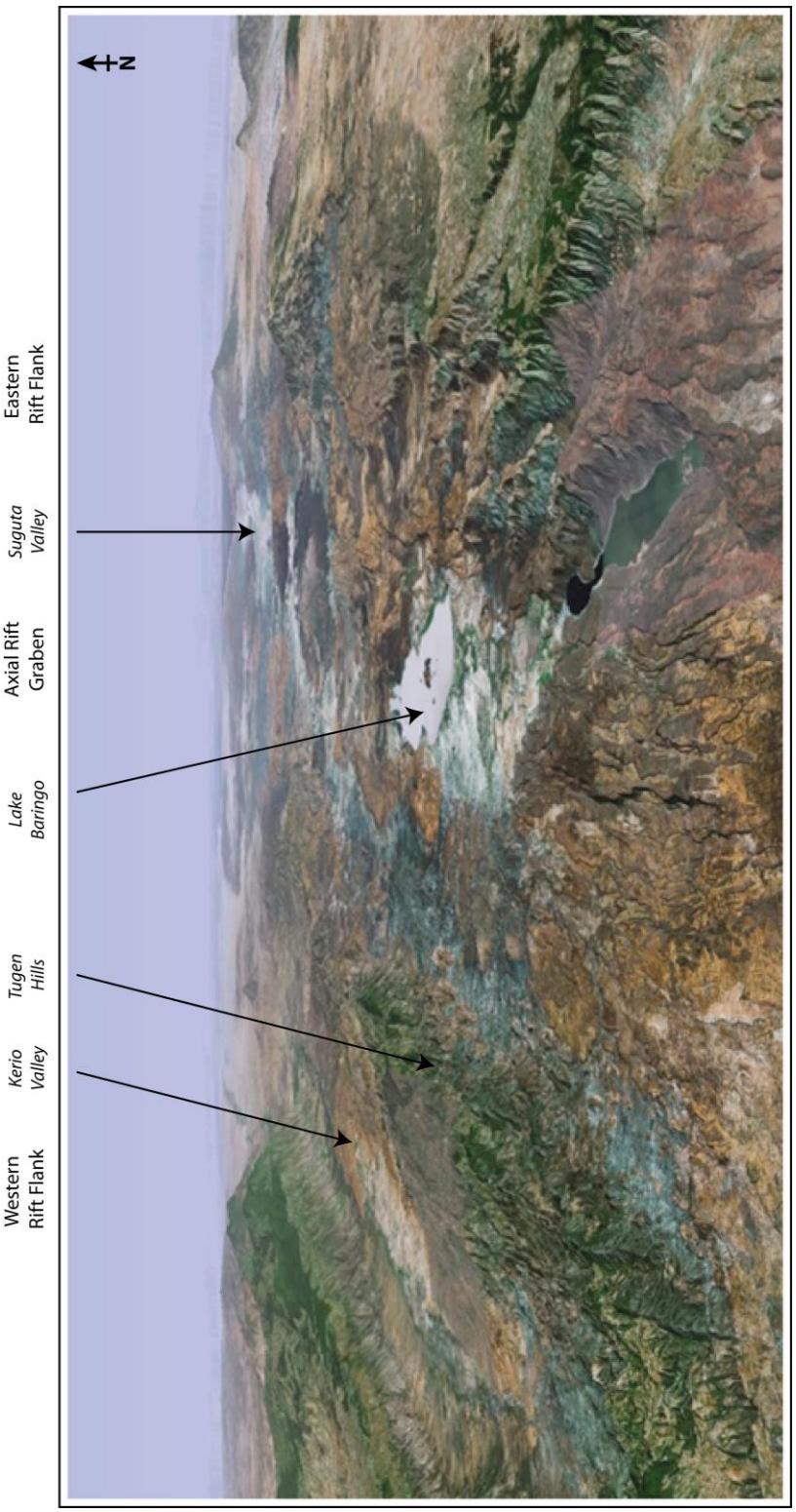

Figure 3.1 Satellite view of the Central Kenya Rift Valley, looking north along the rift axis. Modern day Lake Baringo is shown in the centre of the image with the Tugen Hills situated to the west where the main exposures of the Chemeron Formation are located. Image from Google Earth

(Odada et al., 2006), however this has decreased in recent years and the current depth of the lake is less than 4 m. The region around Lake Baringo is semi-arid, with mean annual rainfall rates that range from 600 – 900 mm on the valley floor to > 1000 mm in the adjacent highlands, including the Tugen Hills. Potential evaporation in the area is in excess of 2600 mm per year, so the survival of the modern day lake is reliant on the inflow from rivers in the drainage basin. The mean annual water temperature of the lake is +23 – +26 °C with a pH range of 8.0 to 9.1 and conductivity of approximately 1.5 mS/cm. Lake Baringo is largely fed by inflow from two perennial rivers, the Molo and the Perkerra and a number of ephemeral stream/river systems only active during the rainy seasons. Despite having no surface outflow and the high evaporation rates of the rift valley floor, Lake Baringo remains fresh and the overall salinity of the lake is largely the same as suggested by the earliest analyses conducted in 1929-1930 (salinity of 0.5-0.7 ‰) (Ballot et al., 2003). Tarits et al. (2006) suggest that this is the result of subsurface groundwater seepage through faulted lavas and permeable sediments.

The character of the modern Lake Baringo bears very little resemblance to the much larger lake system which periodically occupied this portion of the rift during the Miocene, Pliocene and Pleistocene. Referred to as Lake Kapthurin by Renault et al. (1999, 2000), palaeo-lake Baringo (described here) is believed to have become highly alkaline and saline during different low-level stages in its history, as marked by the presence of authigenic zeolites formed from $NaCO_3$-rich lake and pore waters (Renault et al., 1999), and that the palaeo-lake varied from being an extensive freshwater lake (Kingston et al., 2007) to a shallow alkaline, saline playa-lake.

3.3 Geomorphology of the Baringo-Bogoria Basin

The Baringo-Bogoria basin is separated from the Nakuru basin to the south by the Menengai Caldera, where activity started at approximately 0.18 Ma and continued until the early Holocene (Grove, 1986). To the north, the basin is separated from the Suguta Valley by the Silali, Paka and Korosi volcanic complexes. The Laikipia Border Fault and the Elgeyo Border Fault mark the eastern and western boundaries of the rift valley, respectively while the Saimo Fault separates the Kerio Valley from the main rift basin (figure 3.2). Figure 3.2 shows the present topography and tectonic structure of the Kenyan section of the East African Rift System and illustrates complex network of normal faults and transverse zones which characterise the tectonic structure of the basin.

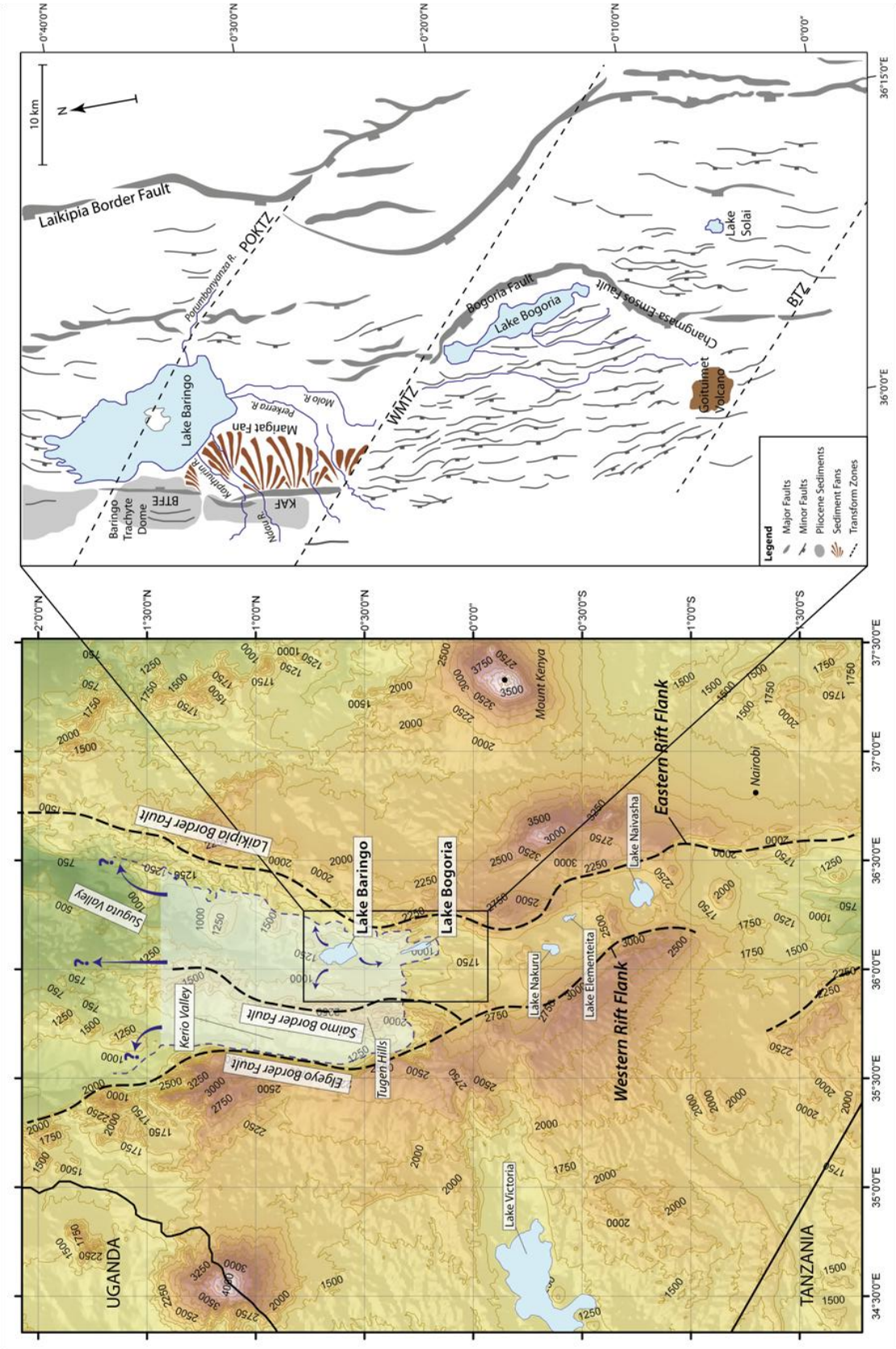

Figure 3.2 Topography and tectonic structure of the EARS in Kenya. Detailed caption overleaf

During the Quaternary there has been extensive volcanic and tectonic activity in this section of the rift, notably uplift along the Saimo Fault which resulted in the formation of the Tugen Hills (figure 3.2) (Williams and Chapman, 1986). The modern day setting of the basin means that if a large freshwater lake were to develop, it would be bound to the west by the Tugen Hills and the Saimo Fault and by the Bogoria Fault, north of the Menangai Caldera to the south. However, given the Quaternary-aged changes in the tectonics and geomorphology of the region that followed the deposition of the sediments studied here, there is very little certainty regarding what the dimensions of any ancient lakes may have been since the volcanic complexes to the north and south, and Tugen Hills to the west are all the result of relatively recent geologic activity. Figure 3.2 shows the potential overflow directions and possible extent of the palaeolakes, based on the topographic barriers formed by the rift flanks and by the Bogoria Fault to the south; the potential boundaries to the north are less clearly defined.

3.4 Modern Climatic Setting

Climate in the EARS is determined by the influence of regional factors, such as rift topography, coastal currents and oceanic SST fluctuations, on large-scale atmospheric circulation creating a complex and locally variable climate regime. Diurnal fluctuations in temperature and wind circulation at local to meso-scales also dominate climate patterns often leaving a greater imprint than interannual and multi-annual fluctuations which are more important in higher latitudes (Odada et al., 2003).

Plio-Pleistocene climate fluctuations and environmental change in equatorial Africa have been linked to orbitally-induced changes in insolation, particularly those modulated by precessional cycles (Kingston et al., 2007). However, the exact mechanisms by which these changes are translated into a climatic response are poorly understood. In order to investigate variations in East African climate during the Pliocene, it is first necessary to gain an understanding of the meteorological systems and climate dynamics which currently govern regional and extra-regional weather patterns.

Figure 3.2 From previous page. Topographic map of the East African rift valley in southern and central Kenya. The primary faults and rift flanks are marked (dashed lines) in addition to the potential extent (pale blue shading) and overflow directions (blue arrows) for palaeolake Baringo. Enlarged map shows tectonic structure of the Baringo-Bogoria basin which is split by the Porumbonyanza-Ol Kokwe (POKTZ), Wasages-Marmanet (WMTZ) and the Bahati (BTZ) Transverse Zones. The Baringo Trachyte Fault Escarpment (BTFE) and Kapthurin Fault (KAF) which lie between modern day Lake Baringo and the Tugen Hills are also shown. The dimensions for an ancient lake system are restricted by the Laikipia and Elgeyo Border Faults to the east and west, respectively, and by the Bogoria Fault to the south.

3.4.1 Atmospheric circulation

In the tropics, a very slight pressure difference is capable of inducing considerable convergent or divergent horizontal air flows which become the quasi-permanent circulation features that characterise African climate. Two major interacting modes of atmospheric circulation are prevalent over Africa. Mean meridional climate in the tropics and subtropics is dominated by Hadley circulation which may be described as vertical helical cells that ascend in the Intertropical Convergence Zone (ITCZ) near the equator and subside in subtropical anticyclonic cells. A second atmospheric circulation mode, the Rossby type, is represented by a zone of extratropical surface westerlies associated with travelling mid-latitude cyclones that occur as a continuous chain of wave-like meandering distortions (Nicholson and Flohn, 1980).

3.4.1.1 Hadley cell circulation

A seasonal displacement of the ITCZ affects the relative strength of the Hadley cell circulation, such that during boreal summer when the ITCZ is situated north of the equator, the northern hemisphere Hadley cell is weak and confined to a narrow latitudinal range whilst the southern hemisphere cell is comparatively strong and latitudinally extensive. This situation is reversed during austral summer (Nicholson and Flohn, 1980; Nicholson, 2000). Convergent air, rising from within the equatorial trough, subsides at the tops of both the northern and southern hemisphere Hadley cells creating subtropical, semi-permanent anticyclones over the North Pacific and North Atlantic Oceans in the northern hemisphere, and over the South Pacific, South Atlantic and Indian Oceans in the southern hemisphere (Hastenrath, 1991).

Divergent airflows at the surface of the subtropical anticyclones form the NE and SE (Indian Ocean) monsoons or trade winds which, as the lower branch of Hadley circulation, converge and ascend at the equatorial trough (Buckle, 1996). The movement of the trade winds, from the edges of the subtropical high pressure cells towards the ITCZ, results in the accumulation of sensible heat and water vapour which is consequently released in the equatorial trough resulting in an intensification of tropical Hadley cell circulation. The ITCZ and equatorial trough are hence often characterised by abundant cloud cover and precipitation (Nicholson, 1986; Hastenrath, 1991).

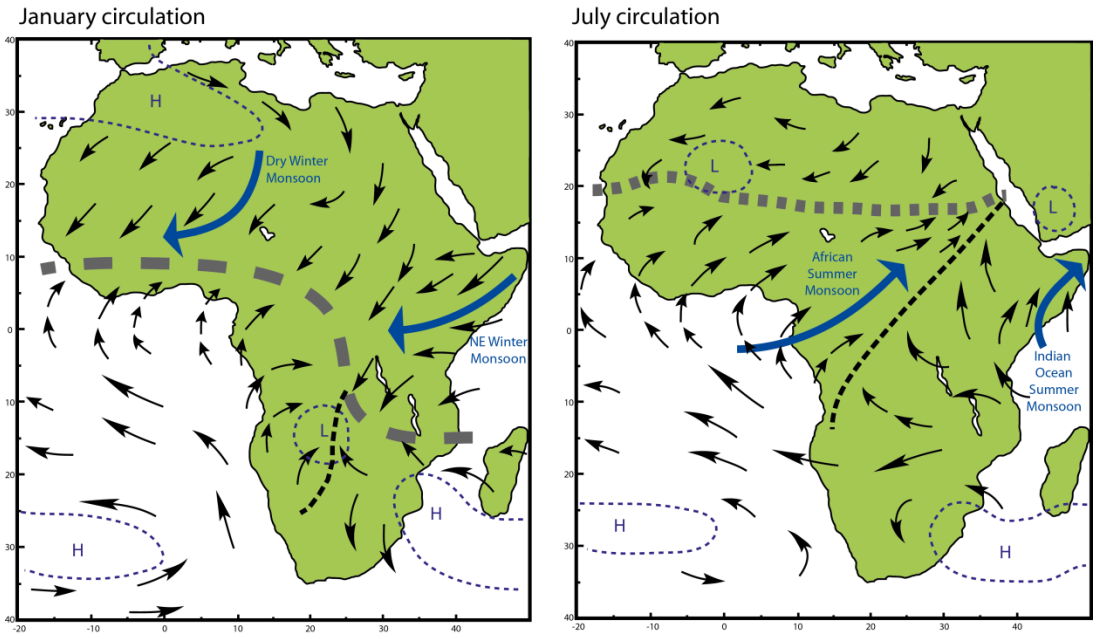

Figure 3.3 Schematic illustration of atmospheric circulation over Africa indicating major air mass convergence zones. Thick grey dashed line marks the seasonal position of the Intertropical Convergence Zone and the thin black dashed line represents the location of the Congo Air Boundary (CAB). Black arrows indicate prevailing wind direction whilst thick blue arrows illustrate dominant monsoonal systems. Red star indicates location of Lake Baringo. Modified from Nicholson (2000).

3.4.1.2 Atmospheric circulation in East Africa

Complex interactions between a number of major airstreams and convergence zones, superimposed upon regional factors exert a vital control over climate in the EARS (Nicholson, 2000). Seasonal shifts in the positions of subtropical high pressure cells govern the movement and strength of these airstreams, namely the Congo air stream and the NE and SE (Indian Ocean) monsoons (Kiage and Liu, 2006). The Congo air stream, with westerly and southwesterly flow, originates in the South Atlantic and is a humid, convergent air-mass which is thermally unstable and generates rainfall in the northwestern part of the region. The NE monsoon originates in the Arabian Desert and forms a dry wind whilst the SE (Indian Ocean) monsoon originates in the Indian Ocean, forming a moist air-mass (see section 3.3.3.1). The three air-masses are separated by two surface convergence zones; the ITCZ which separates the two monsoons and the Congo Air Boundary separating the easterlies and westerlies (figure 3.3) (Trauth et al. 2003; Kiage and Liu, 2006). The Congo Air Boundary is a north-south trending convergence zone which separates unstable moist westerly air from the Atlantic Ocean and drier air from the Indian Ocean (Nicholson, 1996).

In addition to shifts in the position of the convergence zones and subtropical anticyclonic cells, there is also a seasonal migration in upper-level air flow dynamics. Over equatorial

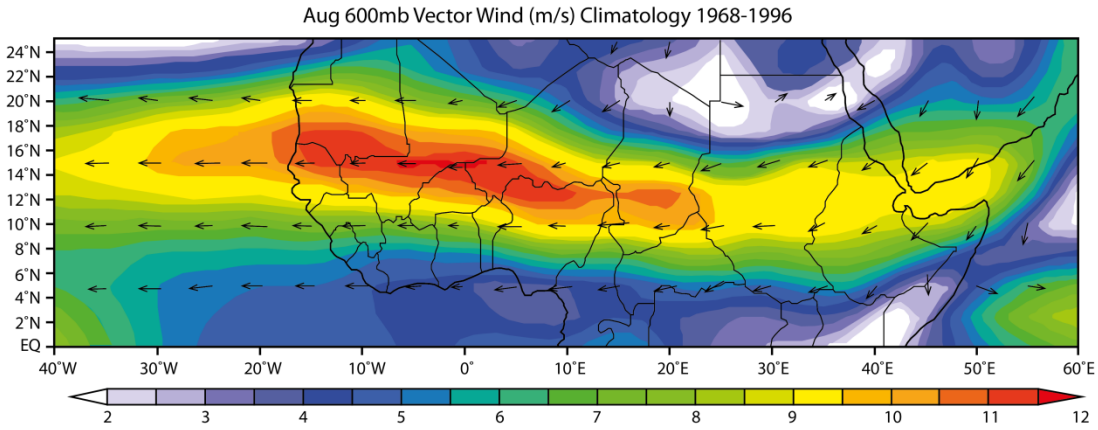

Figure 3.4 Illustration showing the mean position of the mid-level African Easterly Jet (AEJ) during August. Colours correspond to wind velocity in m/s shown in legend. Data from NOAA-CIRES Climate Diagnostics Centre.

cells, there is also a seasonal migration in upper-level air flow dynamics. Over equatorial Africa an upper-level easterly flow is comprised of three jet streams; the Tropical Easterly Jet (TEJ), the African Easterly Jet (AEJ) and the East African Low-Level Jet, which are important for the development of boreal summer rainfall over areas of equatorial and Northern Africa (figure 3.4) (Nicholson, 2000). The TEJ is a band of strong easterlies which extend from SE Asia across the Indian Ocean to Africa and the Atlantic Ocean during boreal summer. It is associated with the upper tropospheric pressure gradient which develops as a result of a reversal in the N-S temperature gradient (Hastenrath, 1991; Buckle, 1996). The AEJ (figure 3.4) is active in the lower-middle troposphere over West Africa and provides energy for the development and maintenance of the West African monsoonal system and for the oceanward transport of the West African dust plume during boreal summer (deMenocal, 1995; Nicholson, 2000). The East African Low-Level Jet is active in the lower troposphere between May and September over the western Indian Ocean and shows similar characteristics to the large-scale features of surface circulation. Strongly influenced and deflected by the landmass of the Kenyan-Ethiopian-Somali Highlands, it sweeps in a wide arc across East Africa from Madagascar before retroflecting towards the Indian subcontinent forming an integral part of the Indian Ocean monsoonal circulation (Hastenrath, 1991). The interplay of these different modes of atmospheric circulation plays an important role in controlling the dynamics of modern climate in the EARS.

3.4.2 Rainfall Variability

Most of Africa is subhumid to semi-arid and experiences one or more prolonged dry seasons throughout the year, interspersed with periods of seasonal rainfall which intensify in

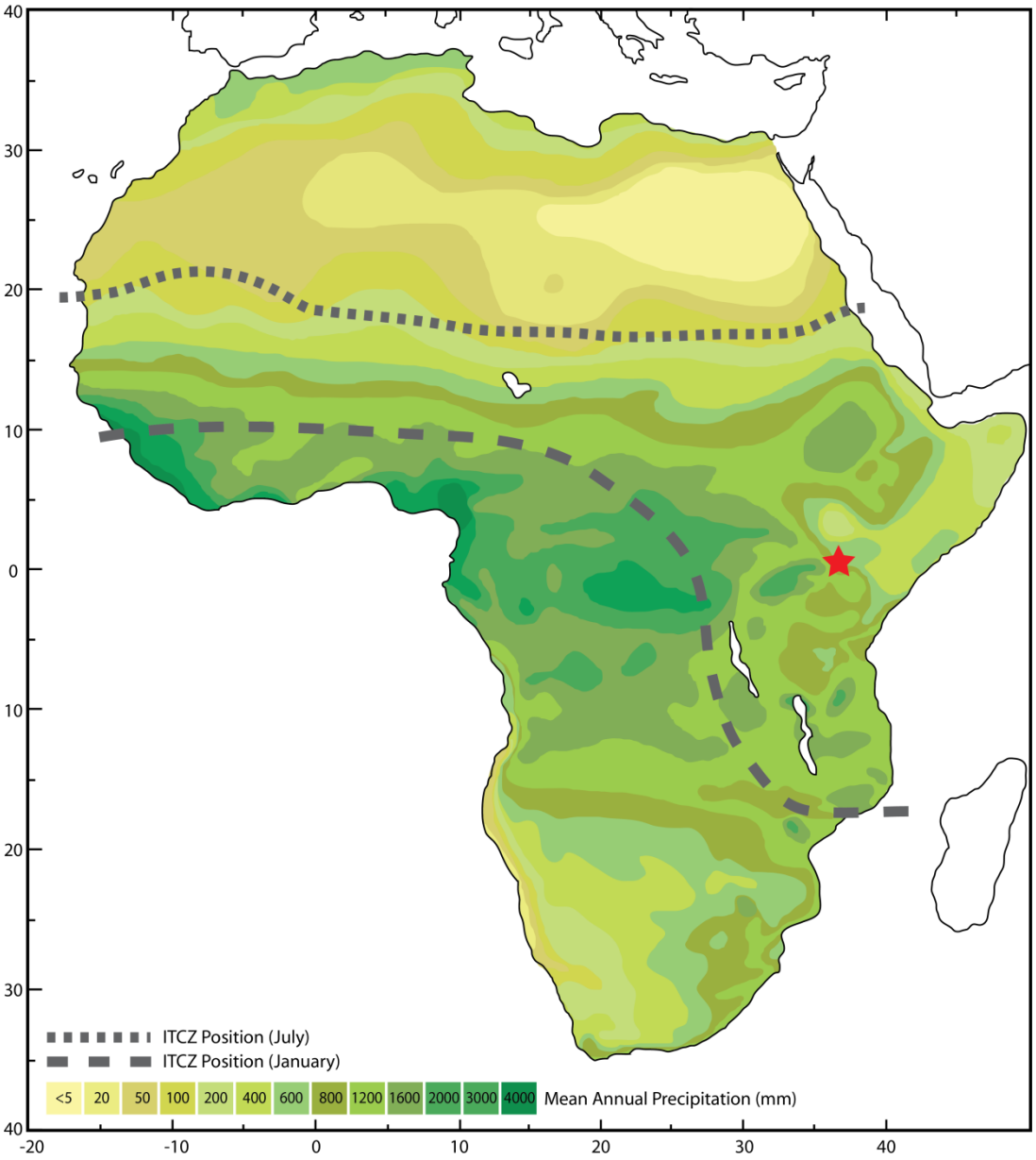

Figure 3.5 Map showing mean annual rainfall distribution over the African continent. Seasonal positions of the ITCZ are shown by dashed grey (January) and dotted grey (July) lines. Modified from Nicholson (2000).

quantity and duration towards the equator where the northward and southward passages of the ITCZ induce two rainy seasons each year (figures 3.5 and 3.6). The majority of continental Africa lies in tropical or subtropical latitudes with only the poleward extremes of the continent experiencing a true cold season as part of a Mediterranean-type climate (Hastenrath, 1991). Although many areas of the continent are arid or semi-arid, rainfall regimes are highly variable and locally complex, creating areas of desertification within regions that are ordinarily subhumid (Nicholson, 2001). Anthropogenic activity has further intensified the impact of such extreme climatic conditions (Balling, 2005).

Environmental change in Africa is most directly related to rainfall and the variability that arises in the intensity and duration of the rainy seasons (Goddard and Graham, 1999). In contrast to the high latitudes, where temperature is the dominant climatic variable, low latitudes exhibit extreme variations in precipitation associated with the seasonal migration of the ITCZ and monsoonal circulation (figure 3.5) (deMenocal and Bloemendal, 1995; Nicholson, 2001). Rainfall regimes over Africa are particularly complex and are controlled by a number of dynamic factors such as the interactions of different air-masses, sea-surface temperatures (SSTs), monsoonal circulation and El Niño Southern Oscillation (ENSO) (Nicholson, 2001). It is important to distinguish that the factors which exert a control over mean climate in Africa, which is regionally diverse and highly variable, are different to the large-scale atmospheric and oceanic aspects of circulation which control the temporal variability of precipitation (Nicholson, 2000).

3.4.2.1 Continental rainfall variability

Climate in northern Africa is characterised by a wet-and-dry season regime (Buckle, 1996). Following a three-month dry period during boreal summer, the onset of the rainy season is controlled by the West African monsoon which results in the land to the north of the Sahara becoming progressively drier as precipitation is inhibited by a layer of dry air which sits above moist air at lower levels (Nicholson and Flohn, 1980; Nicholson, 1986).

In West Africa dry stable Saharan air dominates during boreal winter imposing a dry season, whilst an increased influence of humid, maritime air from the Atlantic Ocean between April and October creates a rainy season with monsoonal conditions that are most intense during July and August (Buckle, 1996).

In Central Africa, rainfall is highly seasonal with one primary wet season lasting throughout the boreal winter with the majority of precipitation falling during November, December and January. Precipitation in this region is largely associated with the migration of the ITCZ such that during some years when the ITCZ does not advance any further than 12 °S, countries such as Zimbabwe and southern Zambia receive very little moisture (Buckle, 1996; Nicholson, 1993).

Rainfall variability in southern Africa is controlled by subtropical anticyclones which induce seasonal drought in the region from April to September as a result of the subsidence of dry air. Between October and March, a weakened continental high is temporarily

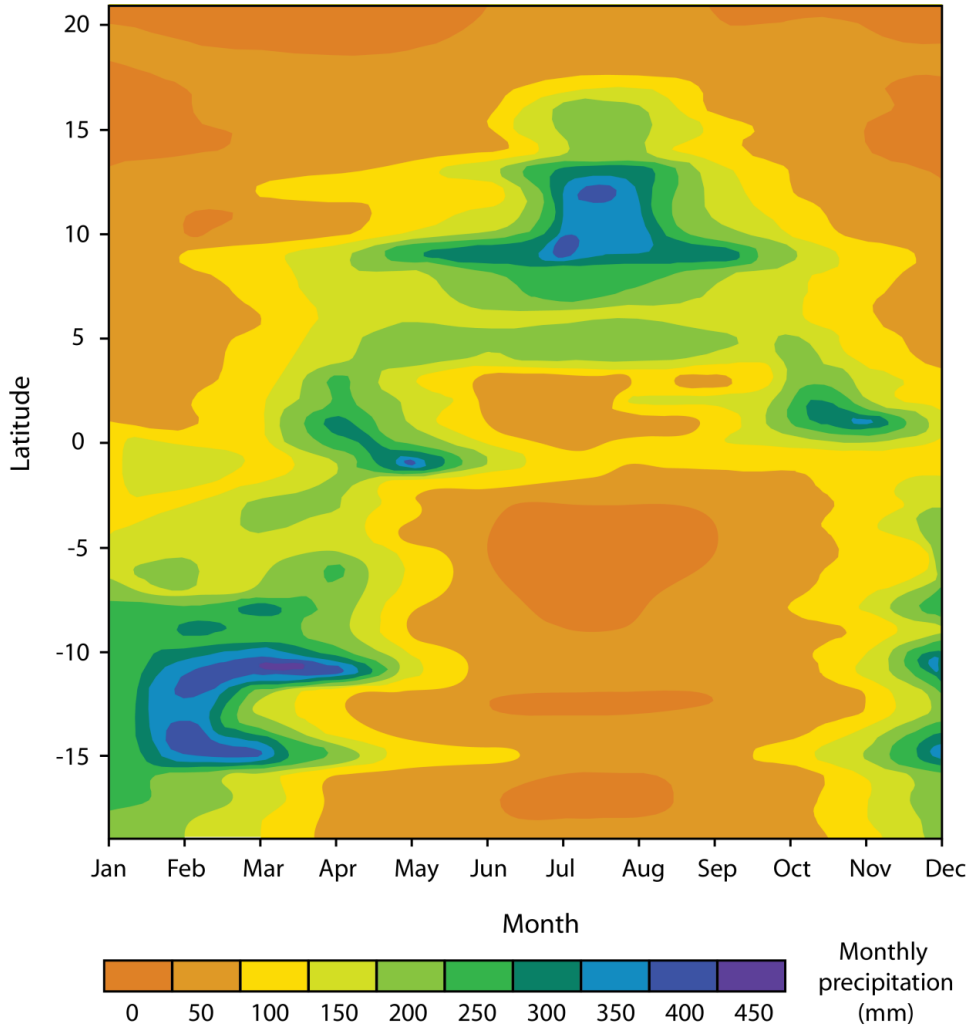

Figure 3.6 Gridded representation of mean monthly rainfall values for meteorological stations along a North-South gradient in East Africa. The sites transect ranges between longitudes of 28°65' E (Ndola, Zambia) and 39°20' E (Dar Es Salaam, Tanzania). Resulting data illustrates the bimodal nature of rainfall in equatorial regions coincident with the north- and south-ward passages of the ITCZ. Data compiled from GNIP database and interpolated using data meshing tool (IAEA/WMO, 2006).

replaced by a shallow surface low pressure cell which draws in moist maritime air permitting summer rainfall (Buckle, 1996).

Nicholson (1986, 2000) investigated modes of spatial and temporal rainfall variability over Africa and found that large-scale climatic fluctuations occur across most of the continent. The interrelationship between spatial rainfall variability in tropical and extratropical regions is indicative of the strong inter-hemispheric teleconnections, which are apparent in African climate.

3.4.2.2 Regional rainfall variability in East Africa

Annual rainfall variability in equatorial East Africa follows a bimodal distribution with maximum precipitation occurring during the months of April to June ('long rains') and October to November ('short rains'), reflecting the passage of the sun, and the ITCZ, back and forth across the equator (figure 3.6) (Nicholson, 2000; Odada et al., 2003). The 'short rains' are coincident with a relatively rapid southward migration of the ITCZ creating a short yet intense period of rainfall. Contrastingly, the 'long rains' occur as the ITCZ moves northwards at a slower rate, thus inducing a longer period of rainfall (Goddard and Graham, 1999; Black et al., 2003). In addition to the strong linkages with the ITCZ, an element of North East African rainfall is also related to the westerly airstream of the African monsoon which is governed by the relative stability of the NE and SE monsoons. However, its effects are highly variable as a result of rift-related topography, and local rainfall distribution is highly regionally complex (deMenocal, 1995). Despite the complexity and variability of the local climatic regimes, interannual variations in rainfall are coherent and show strong teleconnections to the rest of the continent (Odada et al., 2003).

Recent investigations into the isotopic composition of water samples from Eastern and North-eastern Africa (Levin et al., 2009, 2010; Williams, 2010) have demonstrated that there is a significant isotopic enrichment of surface and subsurface waters in Ethiopia compared to waters from regions at similar altitudes elsewhere in tropical Africa. This reflects a regional difference in moisture source in Ethiopia during the 'Kiremt' rains (June-September) when precipitation is associated with westerly winds driven by the African monsoon which result in the precipitation of continentally transpired rainfall to the north of the Congo Air Boundary (Nicholson, 1996). The isotopic composition of water samples from Kenya mirrors that of those from Dar Es Salaam and is consistent with an Indian Ocean moisture source (Levin et al., 2009). This difference creates a regional divide which is reflected in the difference in isotopic composition of waters from Kenya and Ethiopia implying that the Kenyan section of the EARS is not subject to significant continental rainfall associated with the African monsoon (figure 3.7).

Tropical African rainfall variability is closely related to SST fluctuations in the Indian and Atlantic Oceans, and tends to be enhanced by ENSO-induced changes which primarily affect the 'short rains' (Clemens et al., 1991; Odada et al., 2003). Spatial variability in precipitation is closely related to regional topography with the exposed eastern shoulder of the rift valley generating orographic rainfall from the movement of the easterly trade winds. Consequently, this region of the EARS receives large amounts of precipitation whereas the

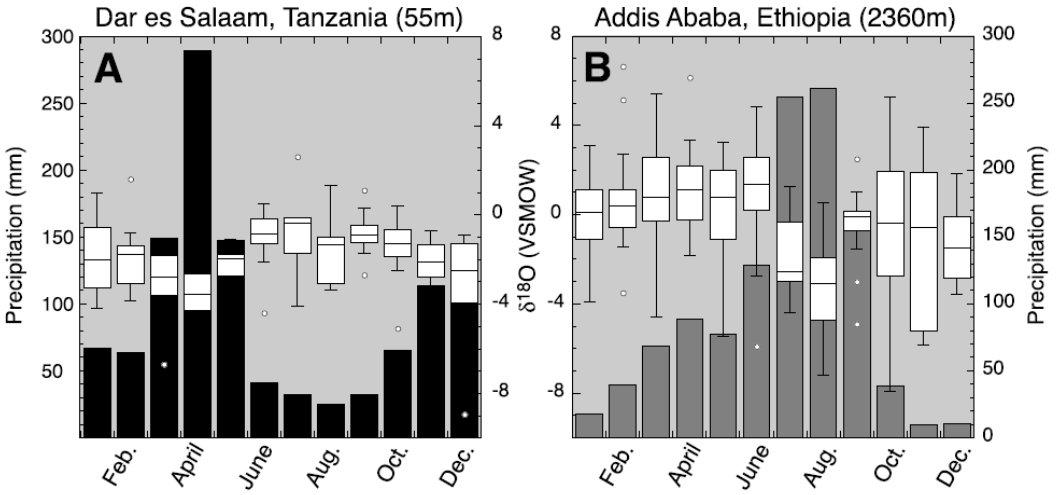

Figure 3.7 Box and whisker plots of GNIP monthly precipitation $\delta^{18}O$ values (shown by white boxes with mean and range, expressed in per mil ‰ units) for Dar Es Salaam, Tanzania (plot A) and Addis Ababa, Ethiopia (plot B) underlain by histogram showing monthly rainfall values for both sites. Figure from Levin et al. (2009), data from IAEA/WMO (2006).

valley floor receives less rainfall generated by convectional storms associated with the ITCZ. Large inland lakes such as Lake Turkana or Lake Tanganyika may also modify monsoonal flow and affect the influence of the Indian monsoon thus exerting a secondary control over spatial rainfall variability (Hastenrath, 1991).

3.4.3 Factors influencing East African climate

A number of driving mechanisms, including the ITCZ, exert an influence over climatic conditions in East Africa. These are discussed below in further detail.

3.4.3.1 Monsoonal Circulation

Annual rainfall cycles in equatorial Africa are affected by the strength of African-Asian monsoonal circulation which influences rainfall intensity in the region. Synoptically, the climate in East Africa is affected by the interplay between the NE monsoon in January when the ITCZ is in the southern hemisphere and the SE or Indian Ocean summer monsoon in July when the ITCZ has migrated to the north; this leads to a strengthening of Hadley cell circulation in the opposite hemisphere (Kiage and Liu, 2006). The timing of maximum monthly rainfall lags the migration of the sun by approximately one month (Black et al., 2003). This interaction allows moist, onshore easterly winds to dominate the lower tropospheric airflow creating greater levels of rainfall in coastal areas (>1200 mm) (Buckle,

1996). Prevailing precipitation patterns are a direct consequence of these circulation patterns and the frontal systems generated within the convergence zones of the ITCZ and the Congo Air Boundary (figure 3.3) (Nicholson, 2000).

Monsoonal circulation over the Indian Ocean during boreal summer results from differential (land-ocean) sensible heating and latent heating in the troposphere. Cross-equatorial airflow moves from an area of high pressure in the southern Indian Ocean towards a low pressure cell situated over the Himalayas via eastern Africa and Arabia. This results in movement of moist humid air over East Africa creating the 'long rains' and induces upwelling of cold, nutrient-rich waters in the Arabian Sea (Clemens et al., 1991; Hastenrath, 1995).

3.4.3.2 Intertropical Convergence Zone (ITCZ)

The intertropical convergence zone is a broad zone within the equatorial trough where the airstreams from both hemispheres converge on one another producing an area of increased cloudiness and precipitation as a result of convection induced by convergence (Buckle, 1996). The seasonal development of the tropical rain belt over Africa is driven by several features of atmospheric circulation, which in turn, control the location and character of the ITCZ (Nicholson, 2001). The ITCZ advances gradually northward to the Saharan margin (~20°N) during boreal summer when the sun is directly overhead and migrates more rapidly southwards towards the northern boundary of the Kalahari Desert (~20°S) during austral summer generating distinct wet and dry seasons across tropical Africa (Nicholson, 1986). The ITCZ does not migrate as far south of the equator as it does to the north due to the smaller land area and larger meridional temperature gradient of the southern hemisphere. An asymmetry in SSTs and irregular local coastal geometries such as the bulge of the African continent to the north of the Gulf of Guinea also contribute to this phenomenon (Philander et al. 1996). It is thought that the off-equatorial average position of the ITCZ is dependent on a positive feedback between atmospheric heating associated with moist deep convection and boundary-layer convergence which feeds and is intensified by the resulting convection (Charney, 1971; Waliser and Somerville, 1994).

The seasonal behaviour of the ITCZ and the associated changes in atmospheric circulation have a direct influence over monsoonal activity in sub-Saharan and equatorial Africa by acting to separate two convergent thermally stable airstreams, the NE and SE monsoons or trade winds (Hastenrath, 1991; Kiage and Liu, 2006). During boreal winter, the equatorial trough remains close to the equator, confining precipitation to the south whilst the annual

migration of the system in boreal summer towards the north enables cross-equatorial moist, cool monsoon air to penetrate deeper into the continent bringing rainfall to sub-Saharan Africa (Hastenrath, 1991). The diverse and dynamic nature of factors influencing rainfall and climate variability over the African continent means that it is virtually impossible to identify a common causal mechanism such as fluctuations in the position of the ITCZ which is solely responsible for producing monsoonal conditions which are locally, highly complex.

3.4.3.3 ENSO Cycles

El Niño Southern Oscillation (ENSO) cycles are characterised by a mean southward shift in the position of ITCZ over the Pacific Ocean which causes an interannual perturbation in atmospheric circulation (Haug et al., 2001). Occurring every 3-7 years, ENSO events are characterised by enhanced Walker circulation and consist of a high phase (La Niña) and a low phase (El Niño) (Bigg, 1996; Obasi, 2005).

During the El Niño phase, a periodic build-up of warm water in the eastern and central equatorial Pacific Ocean leads to intensified drought over Africa as a whole and warm SST anomalies in the Atlantic and Indian Oceans (Barry and Chorley, 1995; Nicholson and Kim, 1997). Conversely during the La Niña phase, rising air over continental Africa produces high levels of convective precipitation whilst cool SST anomalies occur in the Atlantic and Indian Oceans (Nicholson and Selato, 2000).

In Africa, ENSO cycles are known to create significant spatial and temporal perturbations in regional climate and additionally vary with the evolution pattern of the different phases (Obasi 2005). Throughout eastern and southern Africa there is a strong seasonally-specific ENSO signal in rainfall variability which is initially manifested through SST changes in the Atlantic and Indian Oceans, suggesting that SST variability rather than the ENSO itself is a factor of primary importance in its influence over African climate (Nicholson, 2000, 2001; Nicholson and Selato, 2000). The onset of the ENSO signal commences in southern Africa and propagates latitudinally northwards causing equatorial regions to exhibit an out-of-phase relationship with the rest of the continent (Nicholson and Kim, 1997).

The ‘short rains’ in East Africa exhibit a strong inverse relationship to the Southern Oscillation through a combination of different mechanisms. During the high ENSO phase (La Niña), equatorial westerly winds are accelerated due to an anomalous eastward pressure gradient during October and November. These westerlies drive the eastward equatorial jet

which further affects the zonal pressure gradient by creating a feedback with SSTs which are cooled as a result of local upwelling (Hastenrath, 1995). During La Niña, pronounced cold water anomalies in the Indian Ocean suppress convection. Combined with a strong monsoonal wind, this results in a decrease in continental precipitation over East Africa during the 'short rains' season creating strong negative rainfall anomalies (Nicholson and Selato, 2000). During El Niño events, a positive feedback effect is strongest between July and November allowing an amplification of SST anomalies whereas between January and April this positive feedback is weakened. This means that, in an El Niño year, during the 'short rains' in East Africa, there is above-average precipitation and that during the 'long rains' of the following year there is below-average precipitation (Nicholson and Kim, 1997). It is thought that this relationship is linked to above-average SSTs in the western equatorial Indian Ocean which increase convergence and convection over East Africa (Goddard and Graham, 1999; Nicholson and Selato, 2000).

3.5 Regional Geological Setting

The East African Rift System (EARS) extends for more than 5,000 km between the Gulf of Aden and Mozambique. It forms the least developed arm of the more extensive Afro-Arabian Rift System which encompasses the embryonic ocean basin of the Red Sea and links up with the West and Central African Rift Systems (Fairhead, 1986; Reading, 1986). The Tugen Hills form part of the Central Kenyan Rift, a half graben heavily faulted on its eastern margin, which stretches south from Lake Turkana towards the equator (figures 3.1, 3.8) (Williams and Chapman, 1986).

The Barsemoi diatomites make up part of the Chemeron Formation which is exposed within the Tugen Hills (figure 3.9). The Tugen Hills is a complex, westward tilting fault block which extends for 75 km between the Kerio Valley and the Baringo-Suguta axial trough and is uplifted along the N-S trending synthetic Saimo fault. The fault block represents a 3,000 m thick sedimentary succession spanning the period between 14 - 1 Ma that was deposited in a down-warped half-graben that has served as a depositional basin since the initiation of rift activity in the region approximately 16 million years ago (Chapman et al., 1978; Morley et al., 1992).

The sedimentary sequence (figure 3.9) has undergone extensive erosion, uplift and structural deformation and is now primarily exposed in the eastern foothills and fault scarps of the

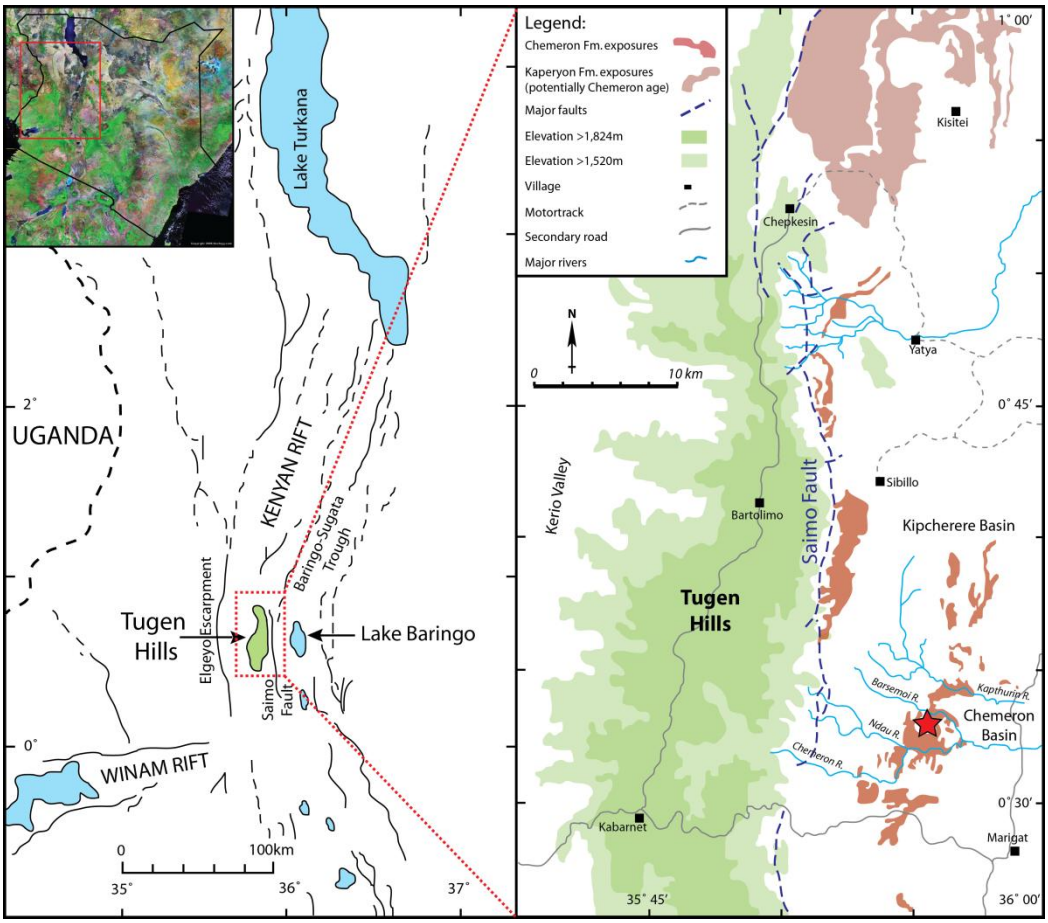

Figure 3.8 Site map showing the location of the Tugen Hills within the Kemya (inset satellite image) and the Central Kenyan Rift Valley and their relation to the western flank of the main rift (Elgeyo Escarpment). Known outcrops of sediments belonging to the Chemeron Formation (including the Barsemoi Diatomites) are shown in brown. Extensive N-S normal faulting means that there is little lateral continuity between exposures. Red star marks the location of section A-A' and sampling locality for sequences RE8 and RE26. After Kingston et al. (2007).

Tugen Hills (Hill et al., 1986; Kingston et al., 2007). The sequence rests on top of a metamorphic basement and has been subdivided into five major formations largely defined and separated from each other by volcanic lavas. These are described in the following sections.

3.5.1 The Muruyur Formation: 15.5 - 15 Ma

The Muruyur beds are up to 275 m thick and consist primarily of tuffaceous and lacustrine sediments with occasional palaeosols and are defined as lying between the flows of the Sidekh and Tiim Phonolites (Chapman, 1971; Hill et al., 1986). The Muruyur Formation contains an extensive bone bed (up to 20 cm thick) covering an area of at least 2,500 m^2. It exhibits a diverse faunal vertebrate assemblage similar in composition to other early Miocene sites in Africa (Hill, 1995, 1999).

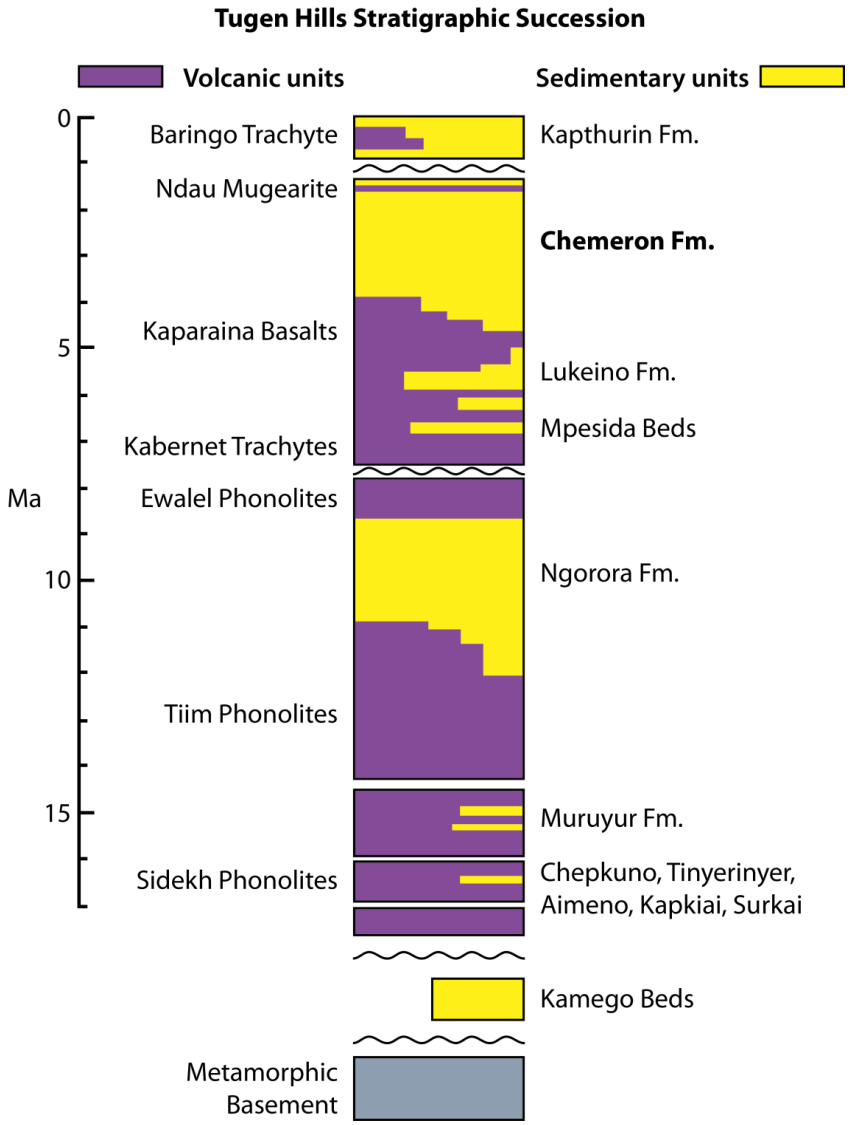

Figure 3.9 Generalised stratigraphic framework for the sedimentary units within the Tugen Hills geological sequence. Units are juxtaposed against corresponding volcanic deposits shown in purple. Redrawn from Kingston et al. (2007).

3.5.2 The Ngorora Formation: 13 - 8.5 Ma

The Ngorora Formation is spatially and temporally extensive, consisting of up to 400 m of sediments ranging from agglomerates to finely laminated lacustrine shales including a series of volcanics and both primary and reworked tuffs (Bishop and Chapman, 1970; Hill et al., 1985, 1986). It is bounded above by the Ewalel Phonolites and below by the Tiim Phonolites. A re-analysis of the palaeomagnetic stratigraphy and lithostratigraphy of the Ngorora Formation (Deino and Potts, 1990) in conjunction with age determinations on tuffs throughout the section has provided greater chronological constraint on the sedimentation of the Ngorora Formation. Outcrops of Ngorora sediments occur in distinct fault-bounded

basins separated by up to 50 km. The separation of these sediment packages by fault activity creates difficulty with correlation as there can be abrupt changes in facies across fault boundaries (Hill, 1995). Fauna from most Ngorora sites closely resembles faunal assemblages from other early Miocene sites. Faunal assemblages from later Ngorora sites contain more modern or advanced elements, including the oldest know colobine monkeys and some of the oldest known equids in sub-saharan Africa (Hill, 1999; Gilbert et al., 2010).

3.5.3 Mpesida Beds: 7 - 6.2 Ma

Above the Ewalel Phonolites and bracketed by the flows of the overlying Kabarnet Trachytes, are the Mpesida Beds. Less extensive than the Ngorora Formation, the Mpesida Beds consist of approximately 30 m of silts, sandstones, feldspathic tuffs, pumice-rich tuffs and conglomeratic lenses (Hill et al., 1986). The presence of a major angular unconformity between the phonolites and the trachytes and the formation of a weathering horizon on the phonolites is suggestive of a considerable hiatus in the sequence. There is relatively little chronological control within the unit itself; age constraints are restricted to the bounding units which are well dated (Hill, 1999).

Palaeoenvironmental information is provided by numerous fossilised fragments of trees, leaves and branches embedded within ash flow deposits. The Mpesida Beds mark the first appearance in Africa of entire families such as Elephantidae and the first Leporids and represent an important transition in the African faunal record from the typical middle-Miocene assemblages of the Ngorora Formation towards the characteristics of contemporary faunal communities (Hill, 1995; Kingston et al., 2002).

3.5.4 Lukeino Formation: 6.2 - 5.6 Ma

Overlying the Kabernet Trachytes is the Lukeino Formation, which in turn is overlain by the Kaparaina Basalts. This unit consists of a variety of lacustrine, epiclastic and pyroclastic sediments. The lacustrine facies occur in the form of diatomite beds which are separated by a series of tuffs and ash layers, some of which contain large K-feldspar phenocrysts and can be used for radiometric age determinations. In places, there has been extensive post-depositional alteration of the diatomites causing ferrigenous red staining which highlights laminations present within the sediments.

The fauna from the Lukeino Formation is more diverse than that from the Mpesida Beds but this is thought to reflect a greater quantity of fossil material rather than an actual change in faunal diversity (Hill et al., 1986). Despite this, the Lukeino Formation does contain a number of newer modern elements such as pigs (Hill, 1999).

3.5.5 Chemeron Formation: 5.3 - 1.6 Ma

Above the Kaparaina Basalts lies the Chemeron Formation which is discontinuously exposed in the eastern foothills of the Tugen Hills, primarily within two depositional basins. The type section is exposed within the Chemeron basin and is dissected by the Kapthurin, Barsemoi, Ndau and Chemeron rivers which flow east from the Tugen Hills towards Lake Baringo (figure 3.8). Sediments are also exposed in the Kipcherere basin 10km to the northwest. Sediments in the Chemeron basin range from 3.2 – 1.6 Ma whilst the Kipcherere succession is older, typically dating from approximately 5 Ma.

The Chemeron Formation was formally described by McCall et al. (1967) and is believed to be the only sequence in Africa that encompasses the whole of the Pliocene. It was previously believed that the Chemeron Formation could be separated into distinct upper and lower units, however recent work (e.g. Hill, 1999) has revealed stratigraphic continuity throughout the unit. Disruption of the sediments by extensive N-S normal faulting makes establishing correlation between different sites problematic. The Chemeron Formation consists of a series of sub-aerial and lacustrine sediments such as finely stratified silts, mudstones, sandstones and diatomites (including the Barsemoi Diatomites) which are intersected by a number of ash-fall tuffs, some of which display characteristics that enable some degree of lateral correlation between isolated exposures (Kingston et al., 2007). Work has also been attempted to trace tuffs within this section to those found elsewhere, such as in the Turkana Basin and the Hadar and Middle Awash areas of Ethiopia (Namwamba, 1993; Brown, 1994). Chemeron strata spanning 3.7 myr are separated from the overlying Kapthurin Formation by an angular unconformity. The uppermost Chemeron sediments (top 3-5 m) overlie the volcanic Ndau Trachymugearite mafic flow dated at 1.57 Ma (Chapman and Brook, 1978).

3.5.6 Kapthurin Formation: 0.7 - 0.2 Ma

The middle-Pleistocene Kapthurin Formation is the most recent of the extensive fossiliferous units that comprise the Tugen Hills sequence. Ranging in age from 0.7 – 0.2

Ma, the Kapthurin Formation unconformably overlies the Chemeron Formation and also oversteps the Kaparaina basalts in places (Hill et al., 1986). The unit consists of sediments of fluvial, volcanic and lacustrine origin with an estimated thickness of >125 m and covering an area in excess of 150 km^2 (McBrearty, 1999). Throughout most of the Tugen Hills area, the Kapthurin Formation caps the depositional sequence, however in the East, towards the central axis of the rift, the sediments are overlain by the Loboi silts of Holocene age (McBrearty, 1999). Sediments within the Kapthurin Formation were subdivided into 5 informal units (K1 – K5) by Martyn (1969) and vary in composition from lacustrine or fluvial silts and gravels (K1, K3, K5) to pumaceous or bedded tuffs (K2, K4). Fossils and artefacts have been found throughout the Kapthurin Formation, particularly within horizons in the K3 sub-unit, including a number of hominid remains which can be ascribed to either *Homo erectus* or to *Homo rhodesiensis* (McBrearty et al., 1996, Wood, 1999) and the first fossil chimpanzee specimen (McBrearty and Jablonski, 2005).

3.6 The Barsemoi Diatomites: 2.68-2.55 Ma

Diatomaceous deposits are widespread in the Miocene, Pliocene and Pleistocene-aged sedimentary units of the East African rift system. Historically, confusion concerning the classification of these sediments has resulted in many diatomaceous units, of varying grades and conditions, being termed 'diatomites'. In general, pure diatomites are grey to white in colour, appearing very similar in appearance to chalk. They are very fine-grained with a low specific gravity and are highly porous, owing to the siliceous framework of the diatom frustules (Owen, 2002). They also have a very low density and will float on water until saturated, providing a useful means of distinguishing between diatomite material and the pale-coloured volcanic tuffaceous deposits commonly found in the same sediment sequences in the Tugen Hills. A detailed review of the classification of diatomaceous deposits by Owen (2002) attempts to address the sometimes overly simplistic terminology and re-classifies different diatomaceous sediments according to their physical, geochemical and depositional properties, including descriptive terms for the degrees of fragmentation, dissolution and homogeneity (see Owen, 2002 for further details). In the most basic form of Owen's classification, diatomite is defined as being almost entirely composed (> 90% by volume) of diatom frustules. As the diatom content decreases, sediments are defined as siliciclastic or tuffaceous diatomite (70-90% diatom content), sub diatomite (50-70% diatoms), diatomitic (10-50% diatoms) and diatom-poor (< 10% diatoms).

Within the younger sediments of the Chemeron formation are a number of diatomites interbedded with fluvial and alluvial deposits. These are also intercalated with several siliceous, air-fall ash layers, or tuffs. In addition to one known diatomite, thought to be approximately 3.2 million years old (Deino et al., 2006), and a series of currently undated diatomites exposed along a major tributary to the Ndau river, there is a lithologic package of five diatomites (figure 3.10, **A**) which vary in thickness between 3-8 m and are intermittently exposed for ~6 km N-S along strike in the Barsemoi, Ndau and Kapthurin river drainage systems. Known as the Barsemoi Diatomites, these diatomites are composed almost exclusively of intact and fragmented freshwater diatom frustules (~95% by volume). According to the classification scheme of Owen (2002), the Barsemoi Diatomites range from laminated, intact diatomites to laminated and homogenous fragmented siliciclastic diatomites.

Calibrated $^{40}Ar/^{39}Ar$ ages obtained for sediments within the sequence constrain the chronology of the diatomite units to 2.68–2.55 Ma (Deino et al., 2006). The diatomites are representative of a precessionally-driven, major freshwater lake system which occupied the Baringo Basin during this time. The occurrence of these units is coincident with a 400-kyr eccentricity maximum and the timing of the palaeolakes closely approximates maxima in the 30°N (June) insolation curve. The diatomites and the associated wet/dry cycles recur at intervals of 23.2 kyr which closely resemble the 22.5-kyr periodicity of the insolation signal and implies a precessional control on tropical East African climate during the Late Pliocene (Deino et al., 2006; Kingston et al., 2007).

3.6.1 Site description

The type section for the Barsemoi Diatomites (section A-A') (figure 3.9) is exposed along a gully which forms part of a tributary to the Barsemoi river drainage system. At this locality all five diatomite units are well exposed in a continuous sequence from a faulted shear zone below the base of diatomite unit #1 at the head of the gully to a series of interbedded sandstone and tuff horizons which overlie diatomite unit #5 further downstream. Whilst the sequence is traceable in other areas of the eastern Tugen Hills, extensive N-S faulting means that the units are not laterally continuous and that exposure of the complete sequence is rare. Section A-A' offers the best stratigraphic representation of this sequence and the best location for further study. Both the diatomite sequences from unit #4 mentioned in this study (RE8 and RE26) were sampled from type section A-A'; the sample locality for RE8 is within the main base of the gully whilst RE26 was sampled from a more northerly point of

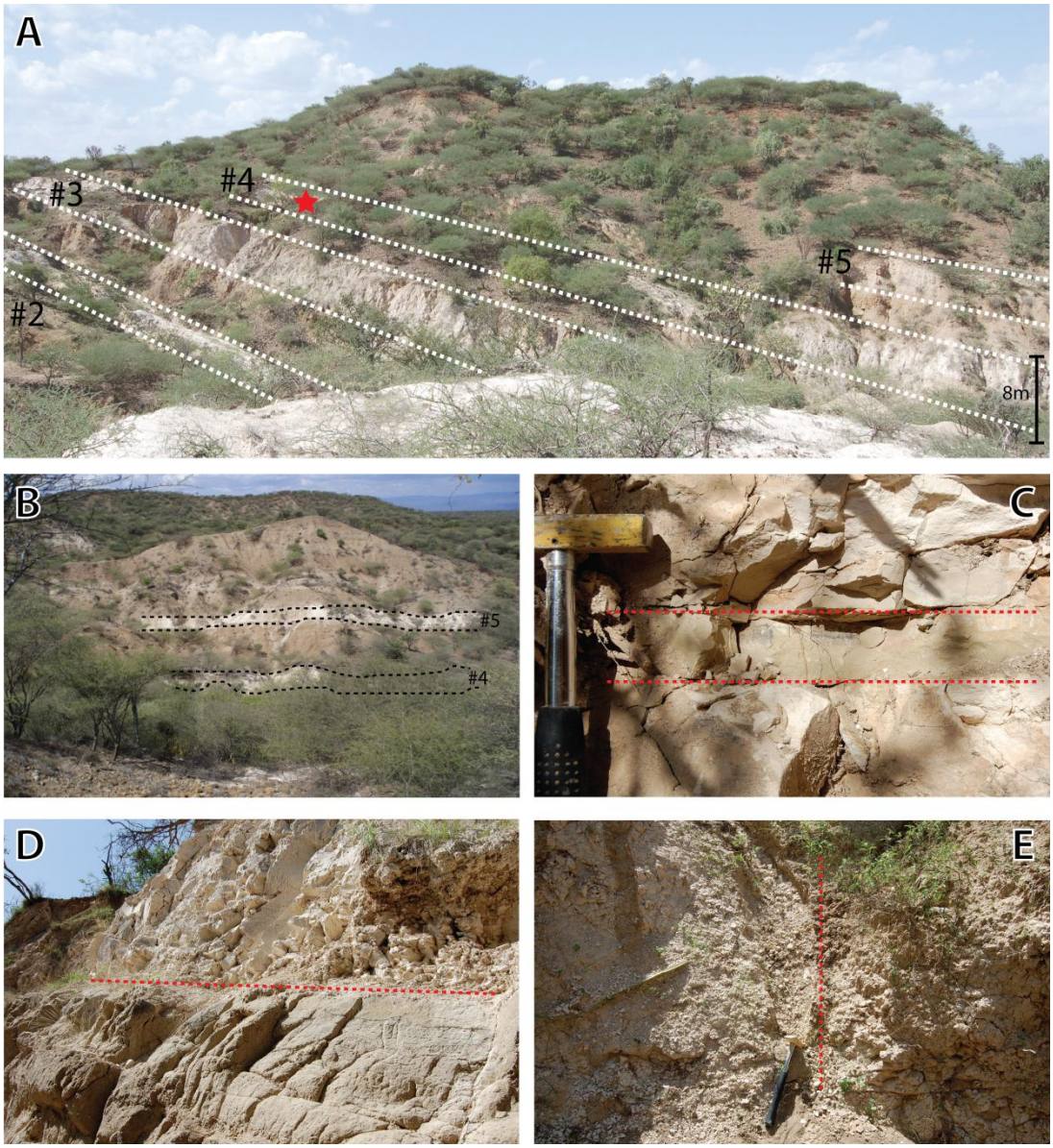

Figure 3.10 Photographs depicting detail of Barsemoi Diatomite exposures. Photograph **A** illustrates a cross-section view of the type section of the Barsemoi Diatomites (stratigraphic section A-A'), looking northwards. Diatomite units 2 - 5 are captured as labelled; diatomite unit #1 is just out of sight to the lower left corner of the image. The sampling point for the sequence analysed in this study (RE26) is depicted by the red star. Scale bar marks the thickness of diatomite unit #4. Photograph **B** depicts the upper 3 diatomite units (#3, #4, #5) exposed within a tributary to the Ndau river, to the south of the Barsemoi river. The positions of units #4 and #5 are shown as labelled; unit #3 is underfoot and can be seen in the foreground. Photo **C** shows the grey-green air-fall tephra layer (7cm thick) present within diatomite unit #4 which acts as a marker bed and has been dated to 2.590 ± 0.003 Ma (normalised on orbital timescales to 2.612 Ma) (Deino et al., 2006)**.** Photograph **D** shows the base of diatomite unit #4. The base of the unit has a sharp contact with the underlying silt-rich conglomeratic sediments. Photograph **E** shows the upper boundary of diatomite unit #4, which is marked by a gradational contact with the overlying clay unit. The dashed red line marks the approximate position of the boundary between the two units. Photographs **C**, **D**, and **E** depict Barsemoi section A-A' and show the sampling points of sequence RE8, described in the text. Geological hammer is shown for scale in photos **C** and **E**.

the section (figure 3.10, **A**).

For the purpose of this project, samples from diatomite unit #4 were selected for detailed analysis in order to gain an insight into the palaeoclimate variability governing the freshwater lake cycles represented by the five diatomite units. The rationale behind the selection of diatomite unit #4 was as follows:

- Of all the diatomite beds, unit #4 has the best chronological constraint; the Gauss/Matuyama palaeomagnetic reversal in polarity (2.610 Ma) is situated with the upper part of the unit whilst a green-grey tuff layer (~7 cm thick) (UCH574, Deino et al., 2006) is located within the diatomite (figure 3.10), approximately 1.65 m above the base of unit #4. This tuff has been dated to 2.590 ± 0.003 Ma and normalised to 2.612 Ma on orbital time scales (Deino et al., 2006). A tuff unit underlying the diatomite has also been dated meaning that the timing of the diatomite is well understood.

  The presence of the green-grey interbedded tuff layer within diatomite #4 provides an excellent marker horizon (figures 3.10, **C**; 3.9) for investigating lateral continuity of the sequence in an area heavily disrupted by faulting associated with the uplift of the Tugen Hills.
- The unit is well exposed in a number of localities within the tributary and gully walls, thus providing numerous opportunities for sampling
- Initial investigation in the diatom assemblage variations (Kingston et al., 2007) show that changes in diatom flora throughout unit #4 were typical of a general pattern documenting the interplay between different diatom genera during each lake phase (see chapter 5.1.2).

The material analysed during this project was obtained from sequence RE26, first sampled in July 1994 and re-sampled at higher resolution during June 2008. The sampling point for sequence RE26 (figure 3.10, **A**) is situated along a goat path cut through the section towards the northern limits of the exposures of section A-A'. Material from RE8, analysed in a previous study (Kingston et al., 2007) is also described in this thesis. The sampling locality for sequence RE8 was within the main exposure of diatomite unit #4 in section A-A', which are primarily exposed along a dry stream bed which forms a tributary to the main Barsemoi river channel.

The work described herewith was conducted using material sampled by the Baringo Paleontological Research Project (BPRP), in collaboration with the National Museums of

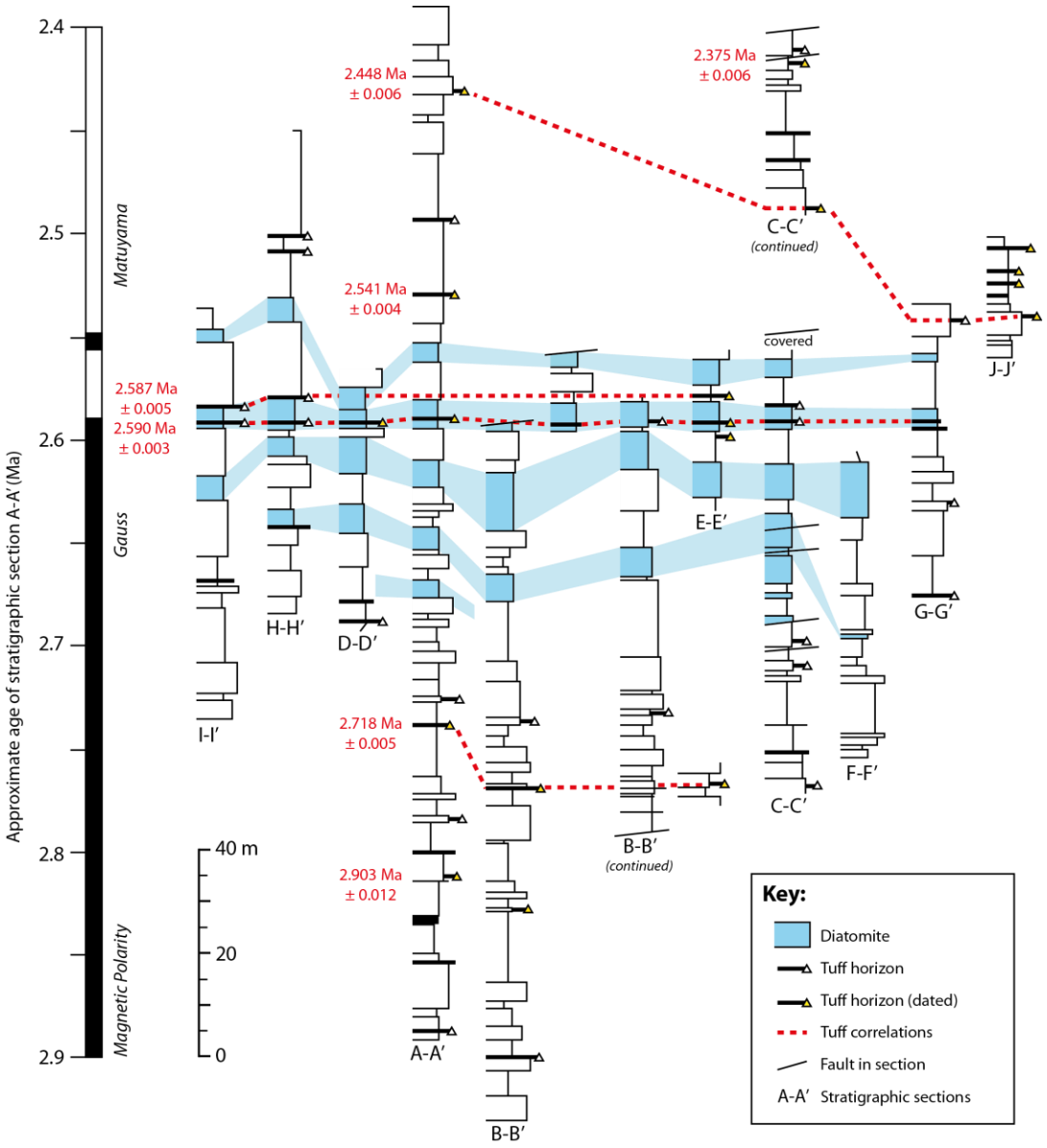

Figure 3.11 Illustrated model of stratigraphic sections spanning the Chemeron Formation sediments, with particular emphasis on the Barsemoi Diatomites (units shown in blue). Correlations between diatomite units are shown in addition to dated tephra horizons. Diatomite unit #4 and the intercalated tephra marker unit are shown (second youngest diatomite), coincident with the Gauss/Matuyama palaeomagnetic reversal. Redrawn and modified from Kingston et al. (2007).

Kenya during July 1994, June 2008 and June 2009. The sampling program was conducted under a research permit (OP/13/001/C 1391) from the Government of the Republic of Kenya and an export license from the Ministry of Mines and Geology of the Republic of Kenya granted to Andrew Hill of the BPRP.

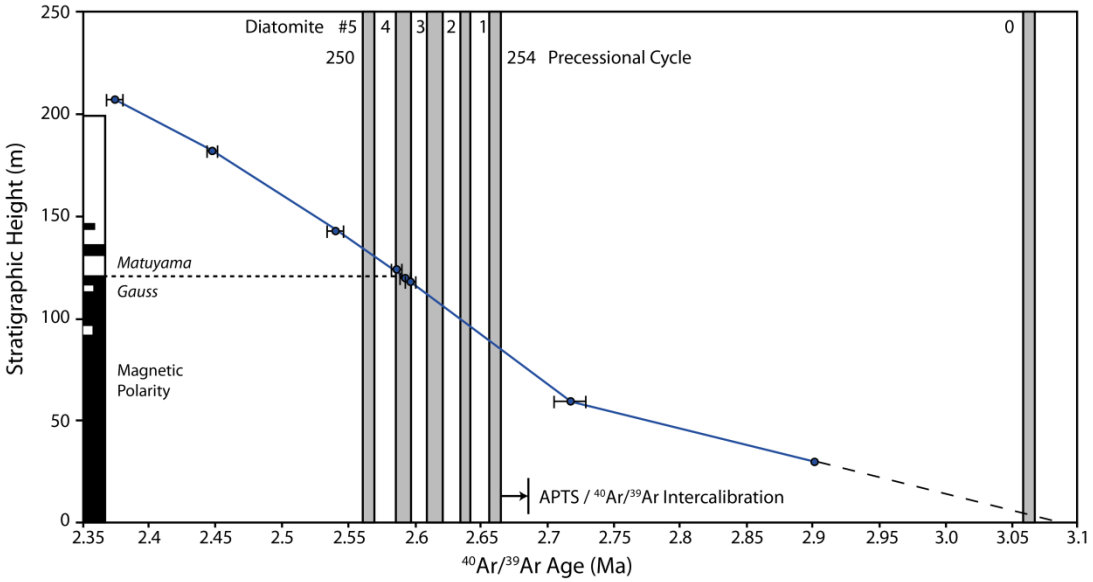

Figure 3.12 Interpolated $^{40}Ar/^{39}Ar$ ages versus stratigraphic height for section A-A'. Positions of diatomite units #1 to #5 shown along with position of an additional diatomite unit dated to approximately 3 Myr BP. The APTS arrow shows the correlation necessary to normalise the $^{40}Ar/^{39}Ar$ ages to orbital timescales. From Deino et al. (2006).

3.6.2 Chronology of the Barsemoi diatomites

The fluvio-lacustrine package of sediments that characterises the upper part of the Chemeron Formation and contains the Barsemoi Diatomites spans the period between 3.10 and 2.35 Ma. The timing of the Barsemoi Diatomites reveals that the occurrence of the diatomites is centred on a 400-kyr eccentricity maximum and recur at an orbital precessional interval of every 23-kyr (Deino et al., 2006). The establishment of high-resolution chronological control for this succession is based on palaeomagnetic reversal stratigraphy and calibrated radiometric age determinations using $^{40}Ar/^{39}Ar$ single-crystal laser-fusion dating methods.

Within the Barsemoi sequence, diatomites are interbedded with silts, sands and conglomeratic units in addition to a number of tuff horizons. Eight of these anorthoclase-bearing tephra units were deemed suitable for radioisotopic dating and were measured in replicate from parallel sections using $^{40}Ar/^{39}Ar$ age determinations. Analyses were conducted at the Berkeley Geochronology Centre using the single-crystal, laser-fusion method. A summary of the relevant analytical results is described in Deino et al. (2006), and the positions of the dated units within the stratigraphic type section are shown in figure 3.11. Based on the $^{40}Ar/^{39}Ar$ ages of the intercalated tuff units, Deino et al. (2006) estimate a uniform sedimentation rate of 16cm/kyr. This was then used to interpolate approximate

dates for the upper and lower diatomite contacts (figure 3.12). The processes employed and subsequent results are fully described in Deino et al. (2006).

The palaeomagnetic Gauss/Matuyama reversal boundary was identified within the upper part of diatomite unit #4 (see figures 3.11 and 3.12 for correlations between units and relation to G/M reversal). Based on the weighted mean of $^{40}Ar/^{39}Ar$ dates established for bounding tuff units, the date of the reversal boundary is taken as 2.589 ± 0.003 Ma (Deino et al., 2006). When calibrated and normalised to orbital timescales, the date of the G/M boundary in this sequence is revised to 2.610 Ma, which is in close agreement with the age of 2.608 Ma assigned to the LR04 stack based on orbitally-tuned benthic foraminifera $\delta^{18}O$ records from marine cores (Lisiecki & Raymo 2005). Uncertainties in the diatomite ages once adjusted to the astronomical polarity timescale (APTS) are on the order of ±0.3% (± 8 kyr); this was deemed sufficiently precise to tune the Barsemoi sequence uniquely to the APTS (Deino et al., 2006; Kingston et al., 2007).

The overall timing of the five diatomite units (figure 3.12) correlates with maxima in the 30 °N (June) insolation curve, which is the dominant driving mechanism for the generation for the SE or Indian Ocean summer monsoon. The average duration of each lake cycle is 23.2 kyr implying that that moisture availability at this time was closely controlled by orbital precession.

3.7 Summary

Precipitation distribution within the East African Rift Valley is dominated by the northward and southward migrations of the ITCZ in conjunction with regional monsoonal circulation. It is hypothesised that periodic enhancement or reduction in the intensity of the monsoon system lead to periods of extreme wet-dry climate variability in the East African Rift Valley, which coincided with major transitions in global climate. A sedimentary sequence exposed within the Tugen Hills, to the west of Lake Baringo contains five diatomite units which document the appearance and disappearance of an extensive, freshwater lake system in the Baringo-Bogoria basin between 2.68 and 2.55 Ma, coincident with the intensification of glaciation in the Northern Hemisphere. Radiometric $^{40}Ar/^{39}Ar$ dating of intercalated tuffaceous deposits within this sequence demonstrates that each lake cycle has an average duration of 23.2 kyr, implying that regional moisture availability at this time was controlled by precession. This study aims to conduct high-resolution analyses of one of these lake cycles in order to better understand the extreme climate variability which generated such dramatic lake level fluctuations within the Baringo-Bogoria basin.

Chapter 4: Barsemoi Diatomites - Methodologies

4.1 Introduction

The following chapter outlines the range of methods used to investigate changes recorded within the Barsemoi Diatomites. Section 4.2 describes the methods undertaken to characterise the nature of inter- and intra-variability within the diatomites and associated sediments of the Chemeron Formation using stratigraphic logging of the sedimentary sequences and analysis of changes in diatom flora. Section 4.3 concerns the stable oxygen isotope analysis of samples of biogenic silica from diatomite #4, whilst section 4.4 details the methods adopted to characterise the nature and geochemical composition of contamination remaining within diatomite samples following cleaning. Section 4.5 describes the multivariate statistics and mass-balance calculations used to model stable oxygen isotope values to account for any remaining contamination.

4.2 Characterisation of diatomite units

4.2.1 Sediment stratigraphy

Sediments of the Chemeron Formation were logged and described by John Kingston of Emory University during 1994 (figure 3.11). The type section for the Barsemoi Diatomites (section A-A') was re-described in detail as part of this study in 2009, close to the sampling locations for sequences RE8 and RE26 (see sections 3.5.1 and 4.2.2). Approximately 90 m of sediments were logged on a m-scale using a Brunton geological compass and topographic abney level in order to assess large-scale variations in litho-facies.

4.2.2 Variations in diatom assemblage

Previous quantitative examination of the diatom assemblage variability within the Barsemoi diatomite units indicates that more than 90% of the diatom frustules preserved within the sediments belong to either the *Aulacoseira* (e.g. *Aulacoseira granulata* (Ehr.) Simonsen) or *Stephanodiscus* (e.g. *Stephanodiscus astraea* var. *intermedians* (Ehr.) Grun) genera (Kingston et al., 2007). There is a significant amount of variation both within and between the five diatomite units (figure 4.1). The relative abundances of *Aulacoseira* and *Stephanodiscus* vary temporally between 0-100% throughout the sequence; these variations are thought to reflect nutrient and light availability in the lake and the differing resource

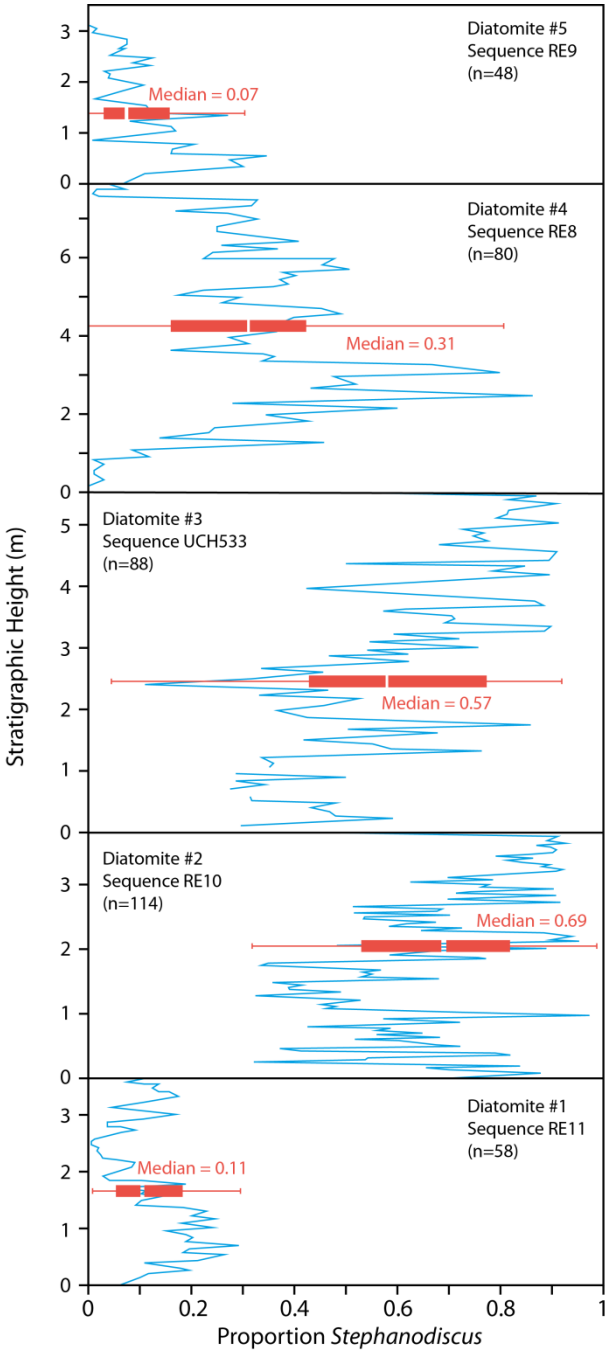

Figure 4.1 Temporal variability in diatom species assemblage throughout the five diatomite units, based on the proportion of *Stephanodiscus* versus *Aulacoseira* species using the relationship 'Proportion S = S/(A+S)'. Data are plotted from sequences originally analysed in 1994 by Dr R. Edgar of Harvard University. Red bars show Box and Whisker plots based on collective data from each of the diatomites and indicate the median, interquartile range and overall range of the data. Modified from Kingston et al. (2007).

requirements of the two genera (Kilham, 1971, 1990; Kilham et al., 1986, Gasse et al., 1983).

As part of the work previously conducted by the Baringo Paleontological Research Project (BPRP), diatomite samples from diatomite unit #4 (sequence RE8) have already been investigated and described by Dr. Robert Edgar of Harvard University (Kingston et al., 2007). For the purposes of this project, aliquots of diatomite material sampled at 10 cm intervals from sequence RE26 were cleaned for oxygen isotope analysis following the methods outlined below and examined in order to establish changes in diatom species assemblage throughout the stratigraphic section, specifically variations in the proportional relationship between *Aulacoseira* and *Stephanodiscus* species. All diatom counts described here were conducted by Dr. Edgar.

4.3 Oxygen isotopes in biogenic silica

As discussed in Chapter 2, the use of oxygen isotope ratios in calcium carbonates is well established in palaeoclimate studies as a means of investigating changes in temperature and hydrology over time (e.g. Emiliani, 1955, 1966; Shackleton, 1967, 1974; Duplessy et al., 1991). However in areas where conditions do not favour the preservation of authigenic and biogenic carbonates, such as in non-alkaline or dilute oligotrophic lakes and in the Southern Ocean, the isotopic analysis of biogenic silica has offered considerable potential for expanding our understanding of changing climates. Biogenic silica exists in numerous forms: as sponge spicules from both marine and freshwater sponges, as phytolithic remains from terrestrial plants, as radiolarian and, mostly commonly, in the form of diatoms. The analysis of diatom oxygen was first developed in the 1970s (Mopper and Garlick, 1971; Labeyrie, 1974) and has since been widely applied in both marine and lacustrine studies. Matheney and Knauth (1989), Brandriss et al. (1998) and Leng and Barker (2006) all offer comprehensive reviews of previous work concerning the use of oxygen isotope ratios from biogenic silica in palaeoclimate research (also see chapter 2.3.3).

4.3.1 Laboratory analysis techniques for $\delta^{18}O_{diatom}$

Silicates are composed of silica tetrahedrons (SiO_4^{--}) which form covalent bonds (-Si-O-Si) through the condensation of two Si-OH groups to create $(SiO_2)_n$:

$$\text{-Si-OH + -Si-OH} \rightarrow \text{-Si-O-Si + } H_2O \qquad \textit{(Equation 15)}$$

Diatom frustules are commonly believed to consist of an inner tetrahedrally bonded silica skeleton (Si-O-Si) surrounded by an outer hydrous layer composed of multiple layers of

water molecules adsorbed by hydroxyl radicals, where hydrogen is bound to oxygen atoms at unbridged Si-O terminations (Hurd et al., 1979; Labeyrie and Juillet, 1982). Juillet (1980a,b) was able to demonstrate, through gradual dissolution of the superficial layers of the frustule, that the dense internal silica skeleton is isotopically homogenous whilst the outer hydrous layer is freely exchangeable with any surrounding water which comes into contact with the diatom silica. The complex layered distribution of the components is related to the mode of diatom frustule formation and its differential porosity (Leng and Barker, 2006). The porosity of biogenic silica is relatively high, in the range of 30-130 m^2/g (Lewin, 1961), and as such water or atmospheric moisture can easily diffuse into or out of the diatom frustule resulting in isotopic exchange during hydroxylation and dehydroxylation (Labeyrie, 1979).

When this 'free' pore water is taken into consideration in addition to the hydrated silica, amorphous biogenic silica may contain as much as 7-12% weight water, compared to 1% weight for quartz (Knauth, 1973; Labeyrie and Juillet, 1982). The presence of the weakly bonded, less dense, outer hydrous layer represents a considerable problem for analysing the isotopic composition of diatom silica ($\delta^{18}O_{diatom}$) as it is estimated that 20-30% of the diatom oxygen needs to be removed before stable $\delta^{18}O_{diatom}$ values are reached (Leng et al., 2001). To date, there are a number of methods which have been developed in order to remove the outer hydrous layer from biogenic silica and to disassociate the stronger internal Si-O bonds. These techniques are explored in the following sections.

4.3.1.1 Vacuum Dehydration

Early experiments using vacuum dehydration were first described by Degens and Epstein (1962) and Mopper and Garlick (1971), and subsequently expanded upon by the work of L.D. Labeyrie (1972, 1974, 1979). Labeyrie observed that the physical structure of biogenic silica is altered over time whereby silica progressively becomes increasingly crystalline as water is lost from its original highly hydrated state. Vacuum dehydration involves the acceleration of this process using heat such that trapped pore waters are volatilised by heating above 100°C in a vacuum. The remaining hydrous component, in the form of hydroxyl molecules partly chemically bound to silicon atoms, is disassociated by heating above 1000°C under vacuum conditions (Labeyrie, 1974). Labeyrie demonstrated that, since there is only weak isotopic fractionation during oxygen exchange between silica and water at high temperatures, the removal of this hydrous component leaves behind the original formation silica (Labeyrie, 1974).

Using this method, Labeyrie (1974) analysed recent and living samples of diatom silica and marine sponge spicules and, having established sufficiently replicable results, was able to develop the first temperature dependent silica-water fractionation factor for biogenic silica. The calibration conforms to an extrapolation to lower temperatures of an experimentally-derived silica-water temperature fractionation factor derived by Clayton et al. (1972) for quartz formation. Labeyrie's preparation method and fractionation factor were later applied to studies of marine sediments from the eastern Pacific Ocean (Mikkelsen et al., 1978), the Gulf of California (Wang and Yeh, 1985) and to the modern culture experiments of Brandriss et al. (1998) who showed that further isotope exchange by atomic diffusion is possible at higher temperatures.

4.3.1.2 Controlled Isotope Exchange (CIE)

Whilst attempts to remove the outer hydrous silica layer using vacuum dehydration improved analytical reproducibility, it was found that the $\delta^{18}O_{diatom}$ signal was contaminated by partial isotopic exchanges with water used during sample preparation (Labeyrie and Juillet, 1982). Initial $\delta^{18}O$ measurements performed on biogenic silica (e.g. Mopper and Garlick, 1971; Labeyrie, 1974; Mikkelsen et al., 1978) were compromised by the presence of this surficial hydrous silica layer which is reactive under lower energy conditions than the more stable inner skeletal silica which is not subject to isotope exchange during sample preparation. Using this principle, Labeyrie and Juillet (1982) hypothesised that it should be possible to correct for this problem by allowing the exchange of the hydrous oxygen with oxygen atoms of known isotopic composition, thus giving rise to the Controlled Isotope Exchange (CIE) method. Under CIE, the outer hydrous layer of diatom silica is labelled at 200°C for six hours with a water of known $\delta^{18}O$ ratio, before being heated under vacuum to 1000°C (Labeyrie and Juillet, 1982; Juillet-Leclerc and Labeyrie, 1987). Once measurements of $\delta^{18}O_{diatom}$ are obtained, mass-balance calculations are applied to determine the isotopic composition of the non-exchangeable silica within the diatom:

$$\delta^{18}O_{measured} = x\delta^{18}O_{water} + (1-x)\delta^{18}O_{non-exch} \qquad \textit{(Equation 16)}$$

where $\delta^{18}O_{measured}$ is the $\delta^{18}O_{diatom}$ after vacuum heating, $\delta^{18}O_{non\text{-}exch}$ is the $\delta^{18}O$ of the non-exchangeable silica within the diatom, $\delta^{18}O_{water}$ is the $\delta^{18}O$ of the laboratory water used during CIE and x is the level of oxygen exchangeability within the diatom. Juillet-Leclerc and Labeyrie (1987) applied CIE to studies of diatom silica from marine and lacustrine

surface sediments in order to further improve the silica-water temperature fractionation factor developed by Labeyrie (1974). Since its development, the use of CIE has been pioneered by Aldo Shemesh and colleagues from the Weitzman Institute of Science, Israel who have applied the method to contemporary and palaeoenvironmental studies of both marine and lacustrine sediments (e.g. Shemesh et al., 1988, 1992, 1994, 1995, 2001a,b; Shemesh 1992; Rietti-Shati et al., 1998; Rioual et al., 2001; Hu and Shemesh, 2003).

4.3.1.3 IR-Laser Fluorination

A relatively recent development in the stable oxygen isotope analysis of samples of biogenic silica is the application of an IR-laser extraction step, pioneered by Julien Crespin and Anne Alexandre at CEREGE, Aix en Provence and by Bernhard Chapligin at AWI, Potsdam. The laser fluorination technique can be performed on microscopic samples, permits a visual control on the success of the fluorination step and is considerably faster than conventional fluorination methods (Crespin et al., 2008; Chapligin et al., 2010a). Following the removal of the outer hydrous layer by CIE (Crespin et al., 2008, 2010) or by helium flow dehydration (HFD) or a vacuum bead melting (VBM) technique (Chapligin et al., 2010a), molecular oxygen is extracted from biogenic silica in an IR-laser extraction line in a nickel sample holder which has been prefluorinated with BrF_5. Samples are preheated with a 2000 μm laser beam and the liberated oxygen is measured for isotopic composition using a dual-inlet mass spectrometer (for full details of method, see Crespin et al., 2008 and Chapligin et al., 2010a). Initial results for this method (e.g. Alexandre et al., 2006; Crespin et al., 2010; Dodd and Sharp, 2010) have been encouraging and long-term reproducibility is ± 0.26 ‰ for phytoliths and ± 0.17 ‰ for diatoms (Crespin et al., 2008).

4.3.1.4 Inductive High Temperature carbon Reduction (iHTR)

An additional technique for analysing $\delta^{18}O_{diatom}$ which avoids the need for a fluorine-based reagent and produces high levels of reproducibility was described by Lücke et al. (2005). The Inductive High Temperature carbon Reduction (iHTR) technique involves the reduction of silica with graphite at high temperatures (1550°C) under vacuum to produce carbon monoxide for isotope analysis. Weakly bonded oxygen atoms within the outer hydroxyl layer and any remaining organic components are first removed by stepwise heating at 850°C and 1050°C (believed to be below the threshold for reduction and isotope exchange with the structural silica). The technique has the potential to be a much faster, relatively simple way of analysing $\delta^{18}O_{diatom}$ without requiring the use of extremely volatile reagents such as ClF_3

and BrF_5. Moschen et al. (2005) used the iHTR technique to analyse phytoplankton samples from Lake Holzmaar, Germany and were able to demonstrate that the $\delta^{18}O$ values of biogenic silica reflect conditions (temperature and $\delta^{18}O_{water}$) of the formation water. However further application of the method to sediment archive material is needed to assess the long-term viability of the technique (Leng & Barker 2006).

4.3.1.5 Stepwise Fluorination

As an alternative to the CIE method, a technique involving the progressive reaction of the silica with a fluorine compound was adapted from the early fluorination methods established by Taylor and Epstein (1962) and Epstein and Taylor (1971). It was noted that the first oxygen fractions released from the hydrous silica layer were depleted in ^{18}O compared to oxygen recovered in subsequent reactions leading to values which eventually stabilise at a 'plateau' $\delta^{18}O$ value (Haimson and Knauth, 1983; Thorliefson 1984; Thorliefson and Knauth, 1984; Matheney and Knauth, 1989). Based on these observations, Matheney and Knauth (1989) argued that the hydrous component of the biogenic silica preferentially reacts with first leaving the anhydrous non-exchangeable silica to react last. The Stepwise Fluorination (SWF) method involves the use of a fluorine-based reagent such as ClF_3 or BrF_5 to extract oxygen from different layers of the diatom silica in three separate stages (Leng & Barker 2006):

Outgassing: Stage one involves outgassing to remove surficial and loosely bound water in nickel reaction tubes at room temperature.

Prefluorination: Stage two is a prefluorination step involving a stoichiometric deficiency of the reagent (either ClF_3 or BrF_5) at low temperatures.

Full Reaction: Stage three involves a full reaction at high temperature with an excess of reagent over an extended period. This second fluorination step liberates oxygen from inner Si-O-Si layer which is converted to carbon dioxide by exposure to graphite as described by Clayton and Mayeda (1963). The carbon dioxide is collected and isotopic ratios analysed by standard mass spectrometry techniques.

Since its development, the SWF method has been widely applied to analyse $\delta^{18}O_{diatom}$ from both lake and marine sediment records (e.g. Barker et al., 2001; Leng et al., 2001; Jones et al., 2004; Morley et al., 2004; Haug et al., 2005; Lamb et al., 2005; Leng et al., 2005; Swann

et al., 2007, 2008, 2010; Tyler et al., 2008; Swann and Leng, 2009; Leng and Swann, 2010; Hernandez et al., 2011; Swann and Patwardhan, 2011).

For this project, following sample purification, cleaned diatom material was analysed for $\delta^{18}O_{diatom}$ at the NERC Isotope Geosciences Laboratory, Keyworth, UK (NIGL) using the SWF technique described by Leng and Barker (2006) and Leng and Sloane (2008).

4.3.2 Comparison of analytical techniques

The two main analytical techniques, CIE and SWF, have different advantages and limitations, however comparisons of both the techniques and laboratories currently in operation are scarce (cf. Schmidt et al., 1997). Both methods require fluorination to disassociate the silicon and oxygen however CIE has the advantage of only requiring one analysis step whilst SWF needs at least two fluorination stages. SWF will act to remove a proportion of the non-diatom contamination remaining in samples such as fine fraction clays, thus ensuring more reliable results (Matheney & Knauth 1989); however it is unclear what structural types of oxygen are being removed at each stage (Brandriss et al., 1998). Under CIE the level of exchangeable oxygen can vary significantly between samples of different ages, thereby allowing for the possibility that not all exchangeable oxygen reacts completely (Juillet 1980a,b; Schmidt et al., 1997; Brandriss et al., 1998). A direct comparison of the CIE and SWF techniques (Schmidt et al., 1997) found that both produced similar, reliable results but that with the CIE method the exchangeability of the silica was variable due to uncertainty in the size of the hydroxyl layer in different diatom taxa. With the CIE method remaining dependent on the isotopic composition of labelled water, calibration of the CIE technique against fluorination results is advised (Schmidt et al., 1997).

More recently, an ongoing inter-laboratory comparison study has formed part of the doctoral research of Bernhard Chapligin at the Alfred Wenger Institute, Potsdam. This study has involved the participation of all the main laboratories across the world and the comparison of the variety of analytical techniques adopted for the measurement of oxygen isotope composition in biogenic silica. All the different methods described above (with the exception of vacuum dehydration) are included in this work and all labs performed an initial calibration to the NBS-28 standard. A range of samples comprising different diatom and phytolith standards were measured at each laboratory; purity for each standard was found to be greater than 96% (Chapligin et al., 2010b). Initial results suggest within lab

reproducibility is between 0.2 and 0.5 ‰ and that with the exception of two laboratories, there is excellent coherency between the different methods (Chapligin et al., 2010b).

4.3.3 Sample cleaning, preparation

The extraction of oxygen isotopes from diatom silica ($\delta^{18}O_{diatom}$) requires that samples are first purified and are free from contamination since the methods used for isotope analysis will liberate oxygen from all components within the sample (e.g. clay, tephra, carbonates and organic matter) (Juillet-Leclerc 1986). Preliminary studies of uncleaned sediment of Eemian to early Holocene age from Lake Baikal show a similarity between diatom concentration and the $\delta^{18}O$ of the bulk material (previously assumed to be purest diatomite) and clearly demonstrate the effect that contaminant materials, which have lower $\delta^{18}O$ values (~ + 10‰) compared to $\delta^{18}O_{diatom}$, can have on the bulk $\delta^{18}O$ curve (Morley et al., 2004).

Early methods for sample preparation involved different stages of chemical attack, sieving and differential settling depending on the type of contaminant being removed. Labeyrie (1979) described the use of a potassium permanganate and nitric acid mixture to remove organic material from samples. However Juillet-Leclerc (1986) found this to be inefficient and further developed the technique to include the use of an equimolar mixture of concentrated perchloric and nitric acids. He also found that this also had the effect of causing dissolution and etching of the surficial silica layer and acted to disassociate any adsorbed clay particles which had adhered to the surface of the diatom frustule (van Bennekom & van der Gaast 1976; Juillet-Leclerc 1986). Clay particles are subsequently removed by sieving at 5 or 10 μm whereas coarser silt grains are removed by differential settling in water and extraction using a pipette (e.g. Juillet-Leclerc & Labeyrie 1987; Shemesh et al., 1988). Shemesh et al. (1995) modified the above methodology with the addition of a heavy liquid separation stage using sodium polytungstate to separate diatom frustules from any remaining clastic material.

Morley et al. (2004) described a structured cleaning process for the purification of diatom silica prior to isotope analysis which aimed to provide a semi-quantitative assessment of diatom and contamination content at each stage of cleaning. They were subsequently able to show that even after undertaking intensive physical and chemical cleaning, it was not possible to obtain 100% pure diatom samples (diatom concentrations ranged from 33% to 99%) when contaminant particles are of a similar size to the diatom frustules (Morley et al., 2005). Problems caused by contamination are further explored in section 5.3. The procedure

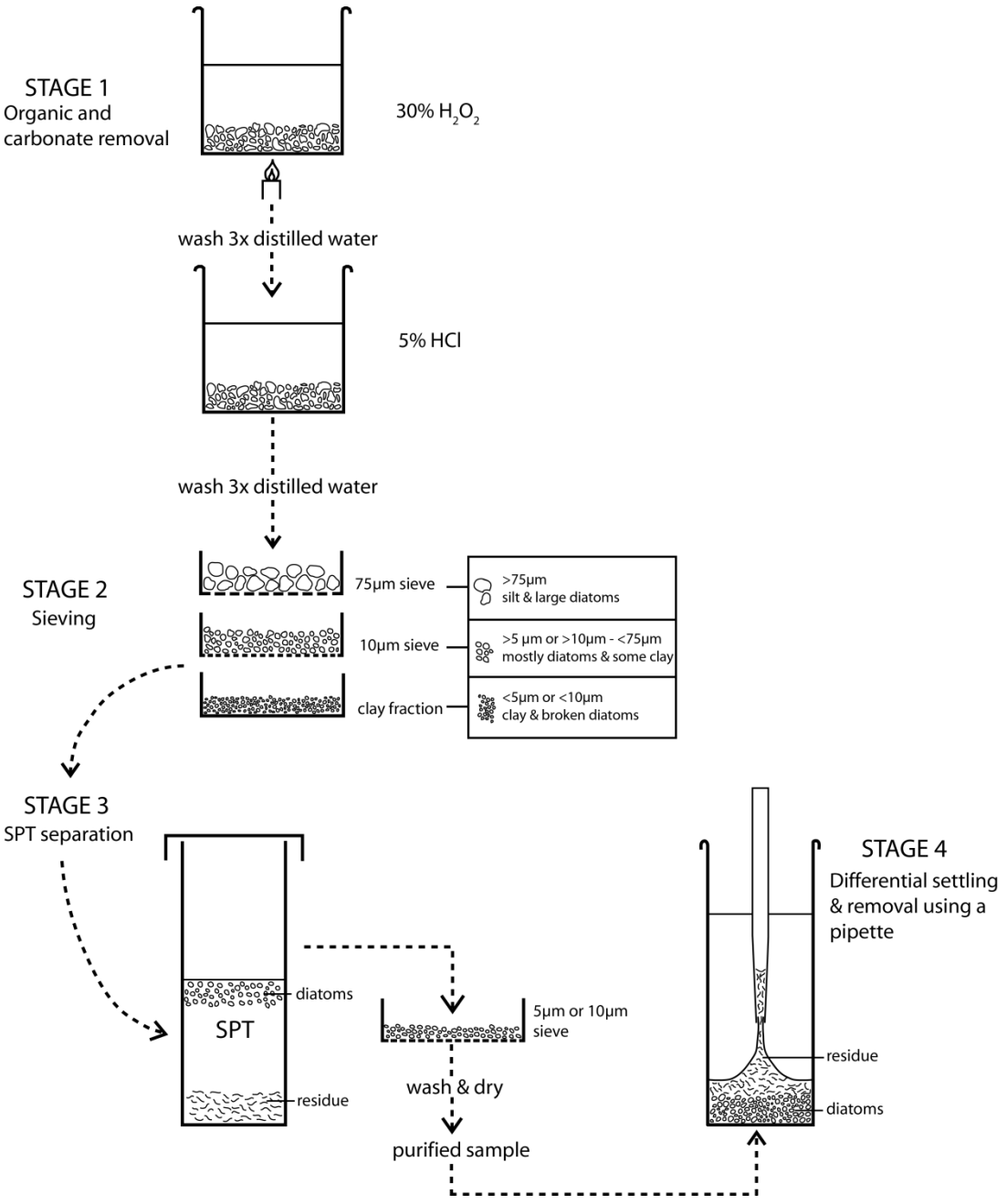

Figure 4.2 Schematic drawing of purification procedure for cleaning of diatom material in preparation for oxygen isotope analysis. The method for this study was modified as shown above to include an experimental sieving stage at 5 µm using cellulose nitrate membranes. The differential settling stage of the process was conducted after heavy liquid separation using sodium polytungstate (SPT). Modified from Morley et al. (2004) according to procedure adopted as part of this study.

adopted for this study is a modified version of that outlined by Morley et al. (2004) and consists of four stages described below (figure 4.2):

Stage 1: Organic and Carbonate Removal

Due to the consolidated nature of the samples, a few grams of diatomaceous/diatomite material were first soaked in deionised water and freeze-dried in order to assist sample disaggregation. It was noted at this stage that, upon drying, the diatomite samples became flaky in nature and developed a 'layered' appearance. In order to remove any organic material, the samples were then heated in 30% H_2O_2 at 90°C for 3 hours (or until any reaction had ended), then washed three times with deionised water in a centrifuge (1200 rpm for 4 minutes). In order to remove any carbonate material, samples were then treated with 5% HCl for 12 hours, then again washed three times with deionised water in a centrifuge.

Stage 2: Sieving

Samples were first wet-sieved with 1 ltr of deionised water at 75 μm to remove all larger diatom valves and detrital mineral grains. Further sieving is normally undertaken to obtain a single diatom size fraction between 10 and 75 μm, however the Barsemoi diatomites contain a significant proportion of *Stephanodiscus* species with valve diameters ranging from 7-30 μm (average ~12 μm; R. Edgar, personal communication). Therefore, in order to avoid creating a bias towards larger (predominantly *Aulacoseira*) species, samples were then sieved under vacuum using 5 μm cellulose nitrate membranes in order to remove small clay particles and broken diatom fragments. Further experimental sieving at 10 μm was found to help to maximise the removal of mineral and clay particles from the samples.

Stage 3: Heavy Liquid Separation

Sodium polytungstate ($3Na_2WO_4 9WO_3 \cdot H_2O$) or SPT is a heavy liquid commonly used to separate materials of different densities where the density of the SPT can be varied by dilution with deionised water or by concentration with evaporation (Munsterman & Kerstholt 1996). In this instance, 15 ml of SPT (specific gravity of 2.1) was added to centrifuge tubes containing the sieved fractions obtained in stage 2. Samples were mixed using a vortex mixer then continuously centrifuged at 2500 rpm for 20 minutes. Following centrifugation, diatom-rich material (< 2.1 sg) forms a float on top of the liquid while heavier detrital grains (> 2.1 sg) sink to the bottom of the tube. The diatom 'float' is extracted by pipette into a second centrifuge tube which is then topped up with deionised water and centrifuged at 1200 rpm for 4 minutes. SPT is removed from the diatoms using a combination of repeated centrifuge washing with deionised water and a final sieving stage at 10 and 5 μm. Morley et al. (2004) found that, without including

this final sieving stage, values of $\delta^{18}O$ were 6.5‰ lower than expected, an effect which they attribute to insufficient removal of SPT from the diatom samples. Experiments using different specific gravities of 2.2 and 2.05 did not result in any improvement in diatom extraction.

Stage 4: Differential Settling

In contrast to the method outlined by Morley et al. (2004), the addition of a differential settling stage at the end of the cleaning process was found to be more beneficial for the removal of any remaining clay particles. Cleaned material was centrifuged with deionised water for 1200 rpm for 4 minutes and, in opposition to what was expected, resulted in the sinking of diatom-rich material to the bottom of the sample. Fine, slower settling clay particles then form a thin visibly darker band on top of the diatoms and this is carefully removed by pipette. The process is repeated in stages until the majority of the visible clay particles have been removed. The purified diatom material is then dried at 40°C for 48 hours prior to further analysis.

An alternative approach to heavy liquid separation for cleaning diatom samples is to use gravitational split-flow lateral-transport thin fractionation (SPLITT). Developed by J.C. Giddings (Giddings, 1985) and first applied to diatoms at the University of Jülich (Schleser et al., 2001; Rings et al., 2004), SPLITT uses controlled laminar flow to gradually separate particles in suspension with different sinking velocities. A homogenous suspension of the sample (A´) is introduced to a carrier fluid (deionised water) (B´) in a thin channel 371 μm high. Peristaltic pumps control the velocities of the A´ (10 ml/min) and B´ (15 ml/min) streams such that when the two flows merge, a laminar current is developed. Inner and outer splitter plates cause particles to migrate through this current according to their size and density: the upper A sample collected contains finer, less dense, more hydrodynamic particles whilst the lower B sample contains denser, coarser particles (figure 4.3) (Rings et al., 2004). Outputs A and B can then be examined and re-processed through SPLITT enabling greater discrimination between diatoms and mineral grains. The main advantages of SPLITT are a high throughput and small losses and that it avoids the requirement for a heavy liquid phase which introduces products other than deionised water into the samples and is difficult to remove. However since no two samples are identical, there is a need for repetition. In addition to negating the need for a heavy liquid stage, SPLITT also has the potential ability to isolate specific taxa where they might be of different size, density or shape.

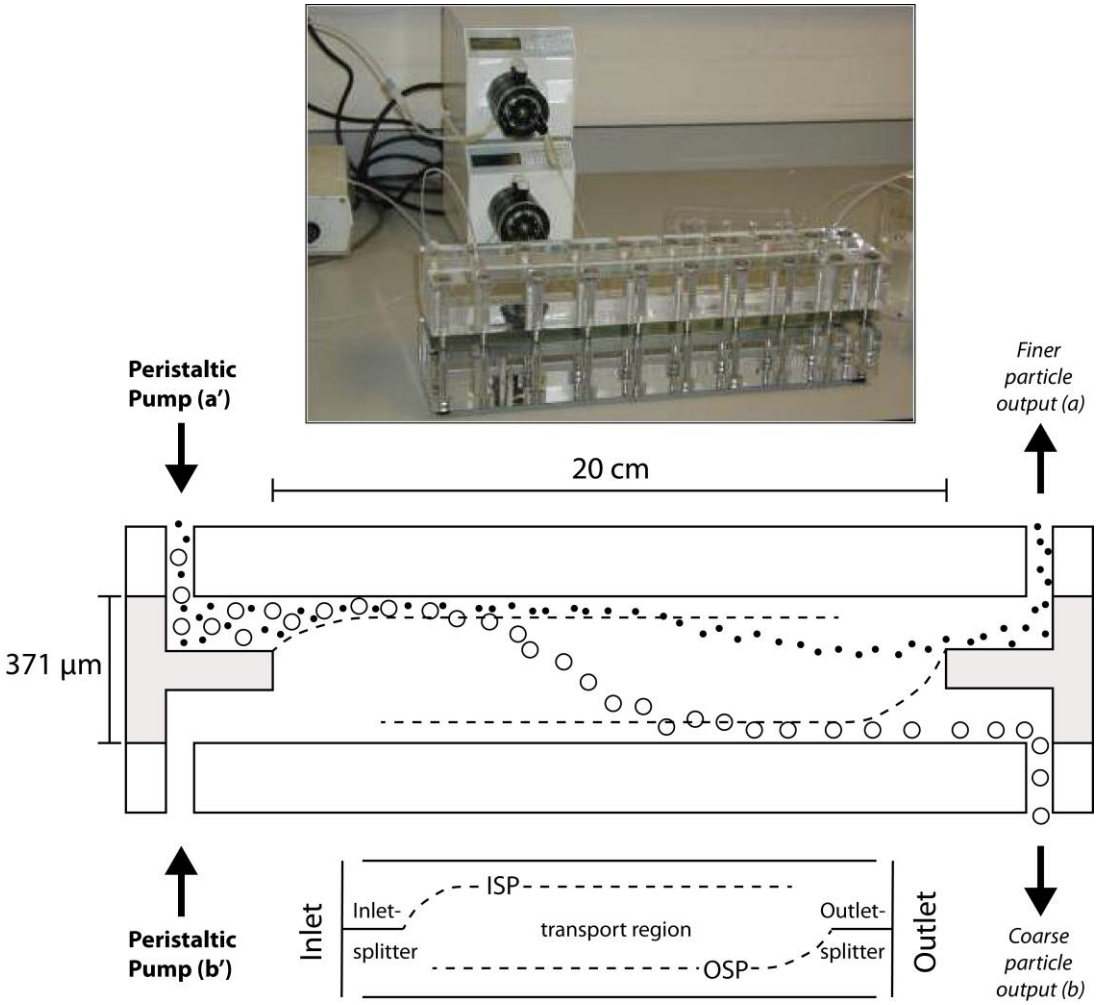

Figure 4.3 Schematic illustration of gravitational split-cell lateral-transport thin fractionation (SPLITT). Inflow of sample and point a' and water at point b' are controlled by peristaltic pumps and a bubble trap. Convergent laminar flow is split via inner and outer splitter plates (ISP and OSP) which act to divide the flow into coarse (b) and fine (a) outputs. Redrawn from Rings et al. (2004).

Following sample cleaning and preparation using the methods outlined above, the oxygen isotope composition of material analysed for this project was sent to the NERC Isotope Geosciences Laboratory (NIGL) in Nottinghamshire for analysis using the stepwise fluorination method described above (section 4.1.3.4).

4.3.4 Isotope vital effects

It is assumed that diatoms precipitate in isotopic equilibrium with the water in which they are formed. However potential species effects in $\delta^{18}O_{diatom}$ may arise from isotope exchange during sediment burial or early diagenesis or from differences between or within diatom species, resulting in deviations from isotopic equilibrium. To date, a number of published studies using culture experiments (Binz, 1987; Brandriss et al., 1998; Schmidt et al., 2001),

sediment trap data (Moschen et al., 2005) and down-core analyses (Juillet-Leclerc and Labeyrie, 1987; Shemesh et al., 1995; Schiff et al., 2009) have found little or no evidence for the existence of vital or species effects within diatoms.

Due to the problems associated with purification and separation of individual taxa, oxygen isotope measurements of diatom silica are commonly made on samples of mixed species assemblage. Despite the numerous advancements made in the use of $\delta^{18}O_{diatom}$ as a tool for palaeoclimatic reconstruction, very little is understood about the limitations posed by potential interspecies and intraspecies offsets in $\delta^{18}O_{diatom}$. It has been shown that other organisms sometimes exhibit significant deviations from isotopic equilibrium. For example, freshwater ostracods display offsets of between 0.3‰ and 2.5‰ (Xia et al., 1997; von Grafenstein et al., 1999; Holmes and Chivas, 2002) whilst in marine foraminifera, species offsets of up to 6‰ have been reported (Duplessy et al., 1970; Wefer and Berger, 1991; Spero and Lea, 1993; Bemis et al., 1998). However studies of biogenic carbonates such as ostracods and foraminifera can easily overcome such interspecies offsets or vital effects by isolating single species for analysis, a process which is extremely difficult in the analysis of diatom silica due to their smaller size.

Early studies of interspecific offsets in $\delta^{18}O_{diatom}$ found little evidence to indicate that such significant differences might exist between diatom species. Brandriss et al. (1998) found an offset of 0.6 ‰ between two cultured diatom taxa while data from a study by Shemesh et al. (1995) display an offset of 0.2 ‰ between two different diatom size fractions. Differences of this magnitude are generally within the range of analytical reproducibility for the analysis of $\delta^{18}O_{diatom}$ (1σ = 0.15‰ – 0.3‰) (Leng and Barker, 2006) and thus offsets have, to date, been regarded as negligible. Recent work by Swann et al. (2007, 2008) has demonstrated large isotope offsets of up to 3.5‰ between different diatom size fractions. The mechanisms controlling these offsets are not understood. However Swann et al. (2007, 2008) hypothesise that they may arise from a number of possible processes such as changes in nutrient availability, growth rate, life cycle stage or variations in silica maturation state and environmental conditions.

Experimental work using SPLITT at Lancaster University was conducted during the course of this project on cleaned diatom material in an attempt to separate *Aulacoseira* and *Stephanodiscus* species based on their respective size and density characteristics, with the aim of addressing potential interspecific differences in $\delta^{18}O_{diatom}$. However these experiments proved inconclusive and whilst it was possible to largely isolate *Aulacoseira*

species, it was not possible to obtain samples consisting of *Stephanodiscus* or to extract enough material for isotope analysis. Further work is required to pursue this in greater detail.

4.4 Geochemistry: Contamination of the $\delta^{18}O_{diatom}$ signal

As described above, the analysis of $\delta^{18}O_{diatom}$ has become an increasingly popular proxy for palaeoclimatic change particularly where carbonates are rare or absent from the sediment record. Until recently, purification using the chemical and physical cleaning steps described above was thought to be sufficient to remove non-diatom material from samples. However it has become apparent that the precision of $\delta^{18}O_{diatom}$ data can be compromised by the presence of tephras, clays and carbonates which remain within the purified diatom samples analysed for $\delta^{18}O$ (Brewer et al., 2008). Because oxygen is liberated from all components of the sample during the analytical procedure, even small proportions of contamination can cause significant negative excursions and high-frequency noise in the $\delta^{18}O_{diatom}$ record, masking any true climate signal (Morley et al., 2005; Lamb et al., 2007; Brewer et al., 2008). Morley et al. (2005) found the average $\delta^{18}O$ value of silt remaining within purified diatom samples from Lake Baikal to be +12.3‰ whilst Lamb et al., (2005) found tephra (average $\delta^{18}O$ value of +11.6 ‰) and carbonate to be the primary contaminants affecting the $\delta^{18}O_{diatom}$ signal.

In order to first establish the relative purity of the diatomites within the Barsemoi sequence, a pilot study was conducted using eight samples from diatomite unit #4. Samples were chosen for this study on the basis that they represented points of change in the diatom assemblage record and appeared representative of places in the palaeoclimatic record documented by diatomite unit #4 where potentially important shifts in climate might have occurred. The cleaned samples were analysed for $\delta^{18}O_{diatom}$ and major element geochemistry by X-ray fluorescence spectrometry. Based on the results of this early work, the study was expanded to further investigate the palaeoclimate record as documented by the $\delta^{18}O_{diatom}$ signal, whilst also making a full assessment of the geochemical signature of each sample in order to make accurate corrections to $\delta^{18}O_{diatom}$ values where necessary. The qualitative and quantitative techniques employed to explore contamination within cleaned samples are discussed below.

4.4.1 SEM/EDS microprobe analysis

Samples were examined using electron optical imagery by scanning electron microscopy (SEM) and energy dispersive system (EDS) microprobe spot analysis in order to ascertain the type and composition of contamination which might be present within the Barsemoi diatomite samples. Bulk, uncleaned diatomite samples and samples of purified diatom material cleaned using the methods outlined above were analysed. Analysis of the diatomite (both cleaned and uncleaned) was focussed towards identifying contaminant particles present within the samples and obtaining geochemical profiles to help quantify differences in the different components.

Prior to analysis, uncleaned fragments of bulk diatomite material were glued to aluminium sample stubs using a conductive epoxy resin before being coated with a thin layer of conductive silver paint followed by an ultrathin layer of carbon powder. The coating of the sample with a conductive substance prevents the build up of static electricity on the sample surface during electron irradiation. Aliquots of cleaned diatom material were pipetted on to cover slips and dried overnight prior to being glued to sample stubs and coated with carbon powder. Analyses were conducted using a Jeol JSM-6480 LV Variable Pressure Analytical Scanning Electron Microscope within the UCL Department of Earth Sciences.

4.4.2 Infrared spectroscopy

As part of a series of experiments conducted by Dr. George Swann at the NERC Isotope Geosciences Laboratory, infrared (IR) spectroscopy was used to analyse a number of samples (n=4) of purified diatom silica from the Barsemoi diatomite sequence. Samples were analysed using single-bounce Attenuated Total Reflection Fourier Transform-IR (ATR_FTIR) which avoids the compression of samples into pellets. FTIR spectra of pure silica samples typically consist of two distinct peaks centred at wavenumbers of < 1300 cm^{-1} and > 2500 cm^{-1} which correspond to different silica modes and hydroxyl molecules (-OH) respectively (Swann and Patwardhan, 2011). The conversion of the results obtained here into quantifiable estimates of contamination levels was performed according to the FTIR mass-balancing technique described by Swann and Patwardhan (2011) to reflect the weighted balance of oxygen molecules contained within pure diatom and end-member contaminant samples using the following equation:

(*Equation 17)*

$$\%\,\text{Contamination} = \left[\frac{\%\,\text{IR} \times (\%\,\text{contamination}_{O}/100)}{(\%\,\text{IR} \times (\%\,\text{contamination}_{O}/100)) + ((100 - \%\,\text{IR}) \times 0.5326)} \right] \times 100$$

where %IR is the IR output expressed as a percentage of oxygen contamination which assumes that diatoms are composed entirely of SiO_2 (consisting of 53.26% oxygen) and that non-diatom material consists solely of the end-member contaminant material analysed, here assumed to be Al_2O_3 (composed of 47.13% oxygen); % contamination is thus 47.13, reflecting the composition of the contaminant sample. Results are expressed as a percentage of total contamination and compared to results from analysis by X-ray fluorescence spectrometry (XRF) based on levels of aluminium oxide (Al_2O_3).

Analyses were conducted in the Department of Chemistry, Nottingham Trent University. This approach has since been further developed and successfully applied to material from Lake Baikal (for full details and discussion of the silica spectrum, see Swann and Patwardhan, 2011).

4.4.3 Whole-sample geochemistry by X-ray fluorescence spectrometry

The application of whole-sample geochemistry to analyse contamination remaining within purified diatom samples was first described by Lamb et al. (2007) and later expanded by Brewer et al. (2008), Swann and Leng (2009) and Mackay et al. (2011). By adopting a chemical-based technique to investigate contamination, they hoped to find a means of quantifying the type and volume of contaminant material affecting cleaned diatom samples, and thus develop a way of removing its effect on the $\delta^{18}O_{diatom}$ curve using mass-balance calculations. The ongoing development of techniques used to assess biogenic silica purity has largely (with the exception of the FTIR method (Swann and Patwardhan, 2011)) been based around the use of XRF spectrometry to quantify variations in geochemical composition. In relatively simple systems, such as those where only one contaminant is present, it is easier to accurately quantify changes in the nature and amount of contamination present. However within the Barsemoi Diatomites, the sediment was deposited in a system known to experience high sediment (clay and silt) influx from the catchment (Tarits et al., 2006) and to contain several substantial air-fall ash deposits from volcanic activity in the EARS (Deino et al., 2006). In addition to this the diatomite units are extremely old and have been compacted, lithified and subaerially exposed over millions of years.

Aliquots (0.1-0.3 g) of diatom silica, prepared for oxygen isotope analysis at the NERC Isotope Geosciences Laboratory, Keyworth and purified following the method described in section 4.3.3 were also analysed for whole-sample geochemistry by X-ray fluorescence

(XRF) spectrometry using glass fusion beads. A sample of the green-grey tuff layer (UCH534) used for dating by $^{40}Ar/^{39}Ar$ single-crystal laser-fusion was also analysed to provide a geochemical signature of an 'end-member' contaminant. Hereafter, this sample is referred to as #TUFF. Analyses were conducted at the Department of Geology, University of Leicester and at the British Geological Survey, Keyworth. Fused glass beads were prepared from approximately 0.1 g of ignited diatom silica powder which had been dried overnight at 105°C to remove moisture prior to ignition. Sample powders were mixed with a flux consisting of 80% Li-metaborate and 20% Li-tetraborate at a sample to flux ratio of 1:5 in Pt-Au crucibles which were heated and homogenised at ~1050°C on an oxygen/gas burner system. The resulting melt was cast in a Pt-Au dish to form the fusion beads before cooling. Trace elements were analysed from 32 mm diameter pressed powder briquettes prepared from 10 g of fine ground powder mixed with ~ 20-25 drops of 7% PVA solution and pressed at 10 tons per square inch (N. Marsh, personal communication). Samples were analysed using PANalytical Axios Advanced XRF spectrometers at the University of Leicester (major and trace elements) and the British Geological Survey (major element data only). This method has the advantage of having high flux-to-rock ratios which produce linear calibration curves enabling the precise and accurate determination of major and trace element geochemistry using relatively small sample weights (Brewer et al., 2008).

4.5 Statistical and multivariate analyses

Inspection of the cleaned diatomite samples using light microscopy and SEM analysis showed the presence of two different types of contaminant, likely to be clay and tephra particles. In order to better understand the geochemical differences between these two substances and to assess the quantity of each present within the purified samples, statistical techniques were adopted.

4.5.1 Ordination techniques

Exploratory statistical analysis of the major and trace element geochemical data produced during analysis by XRF spectrometry was conducted using Principal Components Analysis (PCA) in order to explore variation in the chemical composition of the purified samples and to thus establish relationships between different elemental components present within different types of contamination. PCA was focussed on inter-species correlations and species data were centred and standardised in order to calculate a correlation matrix for the data. Based on the outcome of this analysis and on complications with the analytical

procedure for running XRF spectrometry at the University of Leicester (N. Marsh, pers. comm.), sample 4099 (stratigraphic height = 460 cm) was identified as an outlier and removed from the data set prior to further analysis. Sample 4074 was also identified and removed as an outlier as its low sample weight (<0.1 g) proved to be below the limits of analytical detection. Statistical analyses were conducted using Canoco ver. 4.5 for Windows and ordination biplots were produced using the associated program CanoDraw (ter Braak and Šmilauer, 2002).

4.5.2 Mass-balance calculations

Based on the analysis of the geochemical data using indirect ordination techniques described above, it was possible to isolate groups of samples with common geochemical characteristics in terms of the composition of any contamination remaining within the samples. On the basis of this analysis, in conjunction with the information gained from SEM imagery, light microscopy and IR spectroscopy, two principal contaminant groups were identified; tephra and clay. In order to estimate the proportions of each contaminant remaining within the purified samples and to thus establish a means of accurately correcting for the effects of contamination on the $\delta^{18}O_{diatom}$ curve, the following procedures were adopted.

4.5.2.1 Contamination by clay

Following the work of Morley et al. (2005) and Brewer et al. (2008), initial estimates of clay or silt contamination are based on the percentage of aluminium oxide (Al_2O_3) present within each sample. Al content is believed to be a good indicator of general contamination present within a sample and was judged to be a good starting point for examining the relative purity of the cleaned material. The Al_2O_3 content is converted to %contamination by comparison to modern physico-chemical data from Lake Baringo (Tarits et al., 2006) where sediments exhibit an average of 23.05% Al oxide, such that:

$$\%\,\text{contamination} = \left[\frac{\text{Sample}_{Al} - \text{Clean}_{Al}}{\text{Modern}_{Al}}\right] \times 100 \qquad \textit{(Equation 18)}$$

where $Clean_{Al}$ reflects the Al_2O_3 component present within a pure diatomite end-member, in this case the BFC diatomite standard, and where $Modern_{Al}$ is equal to 23.05 % (Tarits et al., 2006). The technique for using Al_2O_3 as an indicator for contamination has been further

developed by Mackay et al. (2011) who employ a two-stage mass-balance process to differentiate the proportions of diatom and silt within samples with respect to oxygen.

Identification of clay as a principal contaminant was more complicated than that of the tephra as no end-member sample of pure clay was available. However SEM imagery and light microscopy strongly suggested that clay accounted for a significant proportion of the remaining contamination within the purfied diatom samples. Clay particles have been observed to adhere to diatom frustules by electrostatic charge (Morley et al., 2005) and can often become trapped within the diatom structure, particularly within cylindrical diatom valves such as *Aulacoseira granulata*. The results of the PCA described above suggest that clay contamination within the sequence is indicated by enrichment in MgO, Al_2O_3, Fe_2O_3 and TiO_2 relative to the cleanest samples and uncontaminated BFC standard. As such, estimates of the proportion of clay contamination present with each sample were calculated based on the elemental oxide concentrations of MgO, Al_2O_3, Fe_2O_3 and TiO_2 (%):

$$\%\,\text{oxide} = \left[\frac{\text{Sample}_{ox} - \text{Clean}_{ox}}{\text{Clay}_{ox}}\right] \times 100 \qquad \textit{(Equation 19)}$$

where Sample_{ox} is the measured oxide content (%) of an individual sample, Clean_{ox} is the elemental oxide abundance of the least contaminated sample. As above, initial values for Clay_{ox} were taken from measurements of the chemical composition of modern suspended sediments within Lake Baringo (Tarits et al., 2006). However this was subsequently revised following additional analyses of clay particles within cleaned samples using SEM and EDS microprobe. For the assessment of % Clay, each oxide component was calculated independently (using equation 19), and then used in the development of different models to assess contamination levels (see chapter 5.2.4).

4.5.2.2 Contamination by tephra

Initial estimates of tephra contamination were based on the work of Lamb et al. (2005, 2007) and Brewer et al. (2008) who attempt to characterise tephra present within cleaned diatom samples from Lake Tilo, Ethiopia. Geochemical analysis of the tephra samples from the Barsemoi Diatomites indicates distinct differences between the geochemical composition of uncontaminated diatom material and that of the tephra samples. With respect to the uncontaminated laboratory diatomite standard (BFC) and the cleanest samples within the dataset, the tephra is strongly enriched in key major elemental oxides such as CaO,

Na_2O, K_2O and MnO. As such, the proportion of tephra within the samples was calculated following the method described above (using equation 19) by assessing overall sample oxide contamination and combining these values depending on the requirements of the model tested (see chapter 5.2.4). For the assessment of tephra 'indicator' oxides, samples #4134, #TUFF and #TUFF 2 were used as end-member values for pure tephra material.

4.5.2.3 Corrections to $\delta^{18}O_{diatom}$

In order to model the isotopic data and remove the effect of contamination from the $\delta^{18}O_{diatom}$ curve, the following mass-balance equation was used, after Swann and Leng (2009):

$$\delta^{18}O_{model} = \frac{\left(\delta^{18}O_{sample} - \%contamination/100\right) \times \delta^{18}O_{contaminant}}{\%purity/100} \qquad \textit{(Equation 20)}$$

where $\delta^{18}O_{sample}$ is the original measured $\delta^{18}O$ value of the sample and % contamination is the level of contamination derived from the elemental oxide abundances deemed to be indicative of clay or tephra enrichment. $\delta^{18}O_{contaminant}$ is the oxygen isotope composition of end-member contaminant, which varies depending on the model tested for the correction of isotope values (see chapter 5.2.4 and table 5.2). In later models, which assume that contamination within the Barsemoi Diatomites arises from two different sources, equation 20 is modified as follows:

(Equation 21)

$$\delta^{18}O_{model} = \frac{\delta^{18}O_{sample} - \left[\left(\%\,contaminant1/100 \times \delta^{18}O_{contaminant\,1}\right) + \left(\%\,contaminant2/100 \times \delta^{18}O_{contaminant\,2}\right)\right]}{\%\,purity/100}$$

where contaminant 1 (tephra) and contaminant 2 (clay) are treated separately. Values for $\delta^{18}O_{contaminant1}$ and $\delta^{18}O_{contaminant2}$ used in different models are outlined in table 5.2. Modelled oxygen isotope values are expressed as per mil (‰) relative to Standard Mean Ocean Water (SMOW).

4.6 Summary

The Barsemoi Diatomites were investigated using a number of different techniques to assess the cyclical development of a large freshwater lake system between 2.68 and 2.55 Ma. Meso-scale sedimentological stratigraphy and analysis of diatom assemblage changes are used in conjunction with the oxygen isotope analysis of one diatomite unit (unit #4). Samples of diatomite material were cleaned using chemical and physical methods adapted

from those described by Morley et al. (2004). Purified samples were analysed for oxygen isotope composition and a number of methods, including XRF were used to investigate the geochemical composition of the samples in order to assess contamination remaining within the samples. Results were then used to develop a model for the correction of oxygen isotope data to establish a 'true' climate signal.

Chapter 5: The Palaeoenvironmental Reconstruction of Climate Variability and Lake Evolution at Palaeo-lake Baringo

5.1 Diatomite characterisation

The following section concerns the qualitative assessment of the Barsemoi diatomite sequence on both large and small scales. Section 5.1.1 outlines the sedimentological and stratigraphic setting of the five Barsemoi diatomite units, within the framework of the Chemeron Formation, in order to understand large-scale changes in depositional environment as inferred from lithofacies changes. Section 5.1.2 deals with changes in diatom assemblage throughout diatomite unit #4 and how variations in species composition can be reflective of changes in lake hydrology and water chemistry.

5.1.1 Meso-scale sedimentological stratigraphy

The stratigraphic section for sediments from the Barsemoi type section (A-A') is displayed in figure 5.1. Sections were logged on a m-scale by John Kingston of Emory University in 1994 and myself in 2009 in order to distinguish large-scale changes in lithofacies and shifts in depositional environments. The section spans almost 90 m and is exposed along the flowpath of a tributary to the main Barsemoi River (figure 3.8). Transitions from sands and gravels to silts, clays and diatomites are indicative of shifts from fluvial towards alluvial and lacustrine depositional environments, and can be used to gain an overview of climatic fluctuations associated with the deposition of the entire upper Chemeron Formation, including the period of diatomite deposition during the Late Pliocene. The timing and nature of the sequence has previously been described in detail by Deino et al. (2006) and Kingston et al. (2007) who have shown that the cyclical nature of the sediments in the Barsemoi sections is closely linked to precessionally-forced climate change.

Figure 5.1 shows how changes in lithology are indicative of large-scale meso-cycles marked by an upwards coarsening of sediments associated with each of the five diatomite units, and overlying silts and sands indicating a shallowing of the lake, following periods of diatomite deposition. The nature of the sediments is such that the base of each diatomite unit is marked by a sharp contact with the underlying sediments, whereas the upper part of the units are characterised by a more gradational transition typified by a shift towards clayey

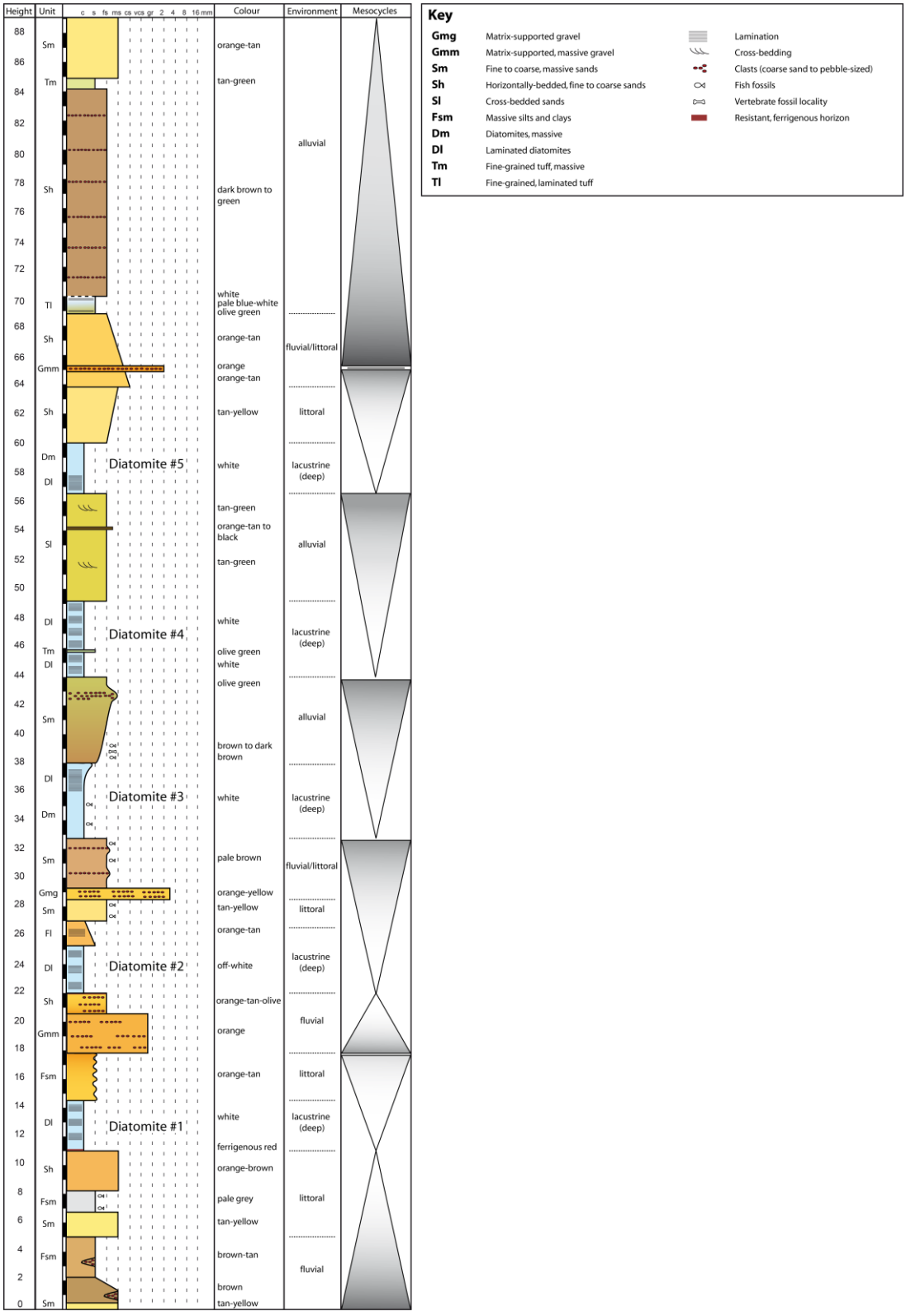

Figure 5.1 Stratigraphic representation of sedimentary sequence exposed in the type section for the Barsemoi Diatomites (section A-A'), spanning the period between 2.5 and 2.8 million years ago. Meso-cycles illustrate the patterns of sediment cycling associated with precessionally-forced wet-dry climate fluctuations.

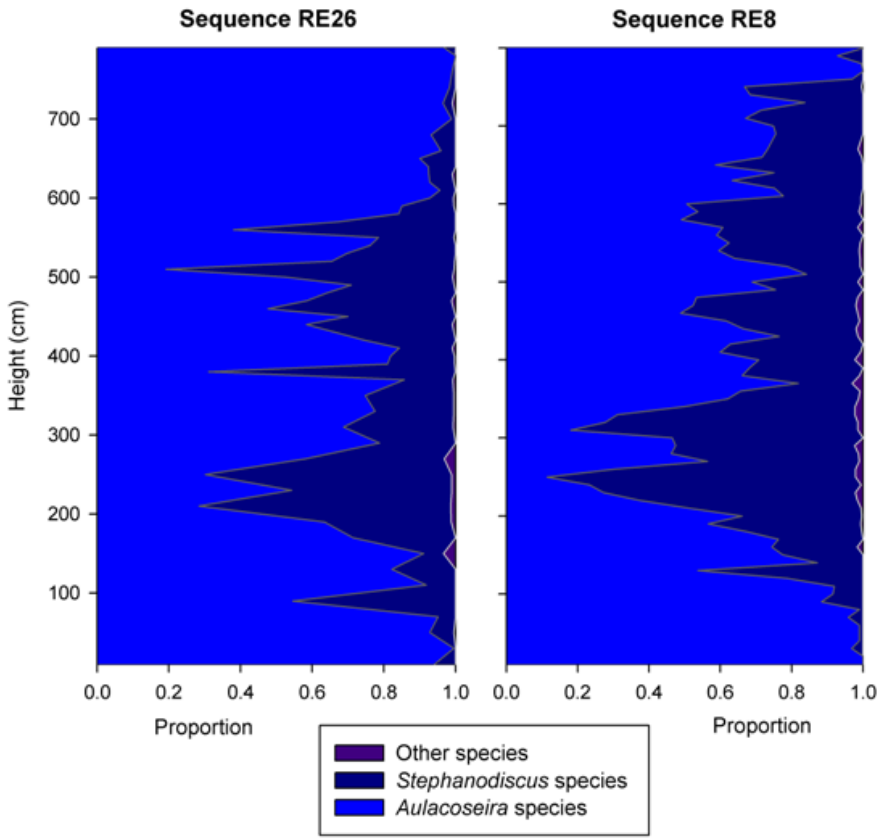

Figure 5.2 Diatom species variability for sequences RE26 (this study) and RE8 (Kingston et al., 2007) sampled from diatomite unit #4 at different locations along the exposures of Barsemoi A-A' type section. Sequence RE8 data provided by R. Edgar, Harvard University.

diatomites and clays. This is suggestive of an abrupt onset of deep water conditions conducive to diatomite deposition, followed by a more gradual termination of these conditions and shift towards a more shallow water environment. This is also implied in the inferred meso-cycles outlined in figure 5.1 that have been shown to cover rhythmic precessionally-driven cycles averaging 23.2 kyr in length (Deino et al., 2006).

5.1.2 Variations in diatom assemblage

Diatom species assemblage counts indicate significant variation throughout the diatomite #4 sequence (figure 5.2). The record is dominated by variations between the *Aulacoseira* (*A. agassizii*, *A. granulata* var. *granulata*, *A. granulata* var. *valida* and *A. nyassensis*) and *Stephanodiscus* genera (figure 5.3), which account for ≥ 97% of the diatom abundance. The relative abundance of *Aulacoseira* species ranges from ~ 20% to 100% whereas *Stephanodiscus* species account for 0% to ~ 80%. Other species constitute a maximum of 3% of the assemblage throughout the record (figure 5.2) and thus do not account for any significant variation in species abundance. The variations in assemblage may, therefore, be

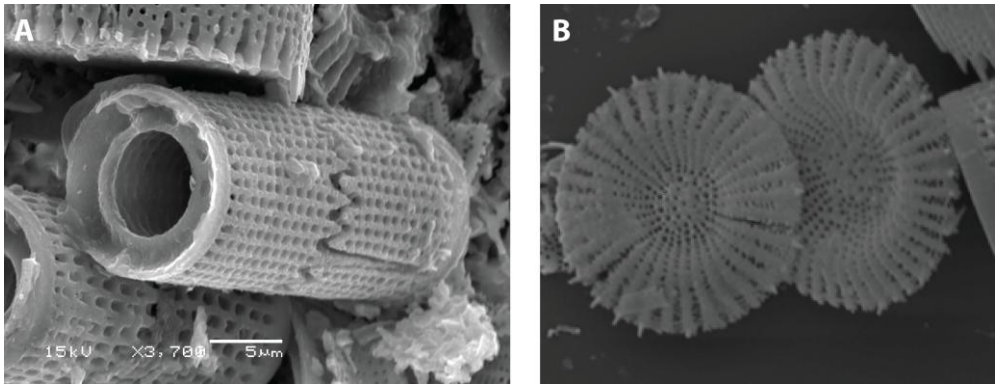

Figure 5.3 Scanning electron microscope (SEM) images of *Aulacoseira granulata* (image A) and *Stephanodiscus* species (image B).

taken as a record of the relative balance between the *Aulacoseira* and *Stephanodiscus* genera. It is relatively common for fossil diatom records from African lakes to be dominated by only a few diatom species e.g. Lake Albert (Harvey 1976); Lake Naivasha (Bergner *et al.*, 2009); Lake Challa (E. Hurrell, pers. comm.); Lake Malawi (Barker *et al.*, 2007) and the Nakuru-Elmenteita lake basin (Gasse 2006). Moreover, it is also common for older, more established lakes to exhibit low plankton diversity and a number of hypotheses have been put forward to explain this phenomenon including competitive exclusion (Hutchinson 1961), habitat isolation and lengthened lake turnover (Bradbury & Krebs 1982) and a stable diversity model based on resource availability gradients and competition theory (Edlund 2006).

Through the analysis of the dominant diatom species (*Aulacoseira* and *Stephanodiscus*) prevalent in the sequence, and in conjunction with modern water chemistry data, it is possible to gain an insight in the hydrological setting of palaeo-lake Baringo at the time of diatomite deposition. The European Diatom Database (EDDI) (Battarbee et al., 2001) contains an East African training set consisting of 187 samples from 98 sites throughout Ethiopia, Kenya, Uganda, Tanzania and Malawi and which includes a number of contemporary water and plankton samples from Lake Baringo. Some of these samples consist of up to 97.5% of *Aulacoseira* species (predominantly *Aulacoseira granulata* var. *angustissima* and var. *angustissima* fo. *curvata*), which is reflective of the composition of some of the RE26 samples. In addition to the collated information for the relevant *Aulacoseira* and *Stephanodiscus* species, the water chemistry data associated with these samples suggest that optimal conditions for pH, conductivity and total phosphorus, which favour the production of *Aulacoseira* and *Stephanodiscus*, are as follows:

pH range	7.5 – 8.5
Conductivity	30 – 1,800 μS/cm
Total Phosphorus	24 – 32 μg/l

Whilst this may give a broad indication of the water chemistry of the lake, it is far from precise and does not explain the almost exclusive production of *Aulacoseira* and *Stephanodiscus* species or why these two genera should dominate not only throughout diatomite #4, but also through the five lake cycles represented by the Barsemoi diatomites (figure 4.1) (Kingston et al., 2007).

Whilst the *Aulacoseira* species found in the diatomite #4 samples are also commonly found in modern samples, it was not possible to accurately identify the predominant *Stephanodiscus* species present within diatomite #4. Due to distinct morphological differences between the *Stephanodiscus* specimens found in the RE26 samples and the documented morphotypes of *Stephanodiscus* species, it was not possible to assign a taxonomically correct name to the species. Instead, it is referred to as (R. Edgar, pers. comm.):

> "the informally named *Stephanodiscus* 'spRE26', which agrees with the description of *S. astraea* var. *intermedia* Fricke (*sensu* Gasse (1980), illegitimate name, and *sensu* Gasse et al. (2002), as *S.* aff. *Medius* Håkansson), except that it at least bears a greater number of valve face costae and fewer areolae spanning the base of a triangular fascicle than expected for a given size"

Discriminant analysis of the *Stephanodiscus* 'spRE26' diatom valves suggests that there is a large amount of character variability between the samples. In samples moving up section, the number of costae per valve decreases while the costae and fascicle widths increase, the interspine distances increase and the areolae in radial striae become larger and further apart (R.Edgar, pers. comm.).

At the base of the RE26 sequence (figure 5.2), *Aulacoseira* species are dominant and account for almost 95% of the diatom abundance. There is also a notable dominance of *Aulacoseira* species at points in the diatom record which coincide with tuff layers, namely at approximately 150-160 cm and at the top of the sequence (between 780-790 cm). *Stephanodiscus* species only dominate over *Aulacoseira* species (>50 %) during five short intervals throughout the entire sequence (210-270 cm, ~380 cm, ~460 cm, 505-515 cm, 555-565 cm). Within the upper third of the section, the abundance of *Stephanodiscus* species declines rapidly and once more the sequence becomes strongly dominated by *Aulacoseira*.

The marked fluctuations between the relative abundance of *Aulacoseira* and *Stephanodiscus* are likely to be indicative of shifts in the hydrological setting of the lake.

When the diatom assemblage data from sequence RE26 are compared to that of RE8 (Kingston *et al.*, 2007), it becomes clear that there is considerable spatial as well as temporal variation in the relative abundances of *Aulacoseira* and *Stephanodiscus* species (figure 5.2). The sampling localities are separated by an approximate distance of 200 m along a continuous stratigraphic exposure in section A-A'. Whilst there are parts of the records that show similar variations in species assemblage, there are a number of places where an apparent dominance of *Stephanodiscus* species in the RE8 sequence (figure 5.2) is not reflected in the RE26 sequence. However there are a number of potential caveats to consider with respect to the direct comparison of these records. Most importantly, the two sequences were sampled at different times and were pre-treated for analysis in different ways (RE26 samples underwent extensive physical and chemical cleaning prior to isotope analysis). This may have introduced a potential bias towards the preservation of *Aulacoseira* within the record due to breakages incurred as a result of sieving as *Stephanodiscus* valves which were observed to be generally smaller and more subject to dissolution than *Aulacoseira* species. In addition to this, a number of other factors should also be considered:

1. Due to the age and discontinuous nature of the Chemeron Formation exposures, very little is known about variations in lake bathymetry, palaeoshorelines or the hydrological setting of the palaeolake. Despite only being separated by a short distance, the two sampling points may represent two different depositional environments within the lake.
2. The bases of the stratigraphic sections may vary depending on the localised nature of the exposures.
3. Due to the time period elapsed, it is possible that extensive N-S faulting within the rift valley, during the uplift of the Tugen Hills, could have resulted in localised compression of the sequence.

It is thus important to be careful when making direct comparisons between the sequences based solely on stratigraphic height. However, in broad terms the sequences are both dominated by *Aulacoseira* species at the base or during the early phases of the lake cycle and indicate a fairly rapid increase in the proportion of *Stephanodiscus* species through time. Whilst *Aulacoseira* species remain largely dominant throughout the sequences, *Stephanodiscus* species remain a successful competitor and are present, to varying degrees,

throughout most of the lake cycle. However in the upper third of the section, *Aulacoseira* species account for between 80 and 100% of the diatom assemblage implying that hydrological and therefore also environmental conditions at this time favoured the dominance of *Aulacoseira* species.

Differences in the habitat conditions (light, vertical mixing) and resource requirements of nutrients such as silicon and phosphorus (expressed as a ratio Si:P) of the two genera can provide an indication of changes in palaeoenvironment throughout the evolution of a lake cycle (Kilham 1971; Kilham *et al.*,1986). *Stephanodiscus* species are typically euplanktonic (i.e. truely planktonic in character) and require high concentrations of phosphorus in order to become dominant. They are successful competitors when both light and silica levels are low and, provided that P supply is not limited, also grow well when light and Si levels are higher (Kilham et al., 1986). Kilham (1971) notes that *Stephanodiscus astraea* only dominates in large African lakes when Si concentrations are low. In contrast, *Aulacoseira* species are meroplanktonic (i.e. only part of the life cycle is planktonic) and flourish when Si supply to the epilimnion is enhanced. This occurs during periods of wind-induced deep mixing in lakes which increases the depth of the epilimnion and silica supply. Meroplanktonic diatoms typically have dense silica frustules that are less susceptible to dissolution, and high nutrient requirements and need significant water column turbulence in order to maintain high growth rates (Kilham 1990). *Aulacoseira* species are well adapted to low light conditions and require relatively high Si:P ratios. Compared to *Stephanodiscus* species, *Aulacoseira* are more likely to dominate in waters of higher Si concentrations, while variations between different *Aulacoseira* species (e.g. *Aulacoseira granulata*, *Aulacoseira agassizii*, *Aulacoseira nyassensis*) may be ranked along a light: P gradient (Kilham *et al.,* 1986).

Nutrient availability and light distribution within a lake are primarily a function of lake hydrodynamics and thus ultimately, climate (Talling 1986; Habeyran & Hecky 1987; Lehman *et al*., 1998; Owen 2002; Stone et al., in press). The mixing regime of the lake is also an important driving force for the factors which favour the dominance of *Aulacoseira* and *Stephanodiscus*. When lakes are well mixed at depth *Aulacoseira* predominates, whereas *Stephanodiscus* is more likely to dominate in the euphotic zone when lakes are thermally stratified and the mixing depth is restricted. Mixing regimes are a function of upwelling intensity and lake turnover, thermal stratification gradients and wind duration, fetch and intensity (Lehman *et al.,* 1998). Gasse *et al.* (2002) describe variation between *Aulacoseira* and *Stephanodiscus* as a function of atmospheric temperature and windiness:

Aulacoseira predominates under cool, windy conditions; *Stephanodiscus* is more dominant in warmer, less windy climates. Thus the variations displayed in figure 5.2 may perhaps be regarded as a broad indicator of changes in mixing regime driven by wind intensity. Periods of enhanced windiness in the East African Rift Valley are closely linked to monsoonal activity and the seasonal north- and south-ward migrations of the ITCZ (Nicholson, 1996), as described in chapter 3.3.

5.2 Assessing contamination within the $\delta^{18}O_{diatom}$ record

The following section concerns the refinement of the oxygen isotope analysis of diatom material and the development of a method to account for the presence of contamination within cleaned diatomite samples, through qualitative, quantitative and statistical analyses. All raw data is presented in figure 5.4.

5.2.1 Oxygen isotope analysis of biogenic silica

As described in chapter 4.3.3, aliquots of cleaned diatomite material from Barsemoi diatomite #4 were analysed for oxygen isotope composition at the NERC Isotope Geoscience Laboratory in Keyworth. Samples were analysed in two batches comprised of an initial pilot study (n=8) followed by an expanded study (n=41) of the whole section. Values of $\delta^{18}O_{diatom}$ vary between 16 and 37 ‰ with an overall decrease in values towards the top of the section (figure 5.4). Within run reproducibility of the diatomite samples were 0.2 ‰ and 0.5 ‰ for the pilot and extended studies, respectively, whilst between run reproducibility of the BFC diatomite standard was 0.22 ‰. As outlined in chapter 4.4, it is necessary to investigate the nature of any possible contamination remaining within the cleaned diatom material, in order to accurately assess the amount of variability within the $\delta^{18}O_{diatom}$ that results from changes in the oxygen isotope composition of the lake water determined by climate-driven changes in the isotopic composition of precipitation.

In addition to the impurities caused by catchment-derived components such as tephra, clays or carbonates, there is also the possibility of secondary isotopic exchange between amorphous diatom silica and sedimentary pore water which could theoretically occur during settling or sedimentation (Schmidt et al., 2001). This could potentially limit the applicability of $\delta^{18}O_{diatom}$ measurements as a palaeoclimatic proxy if the diatom frustules are subject to secondary diagenesis. The issue of successive isotopic reactions remains unresolved (Swann

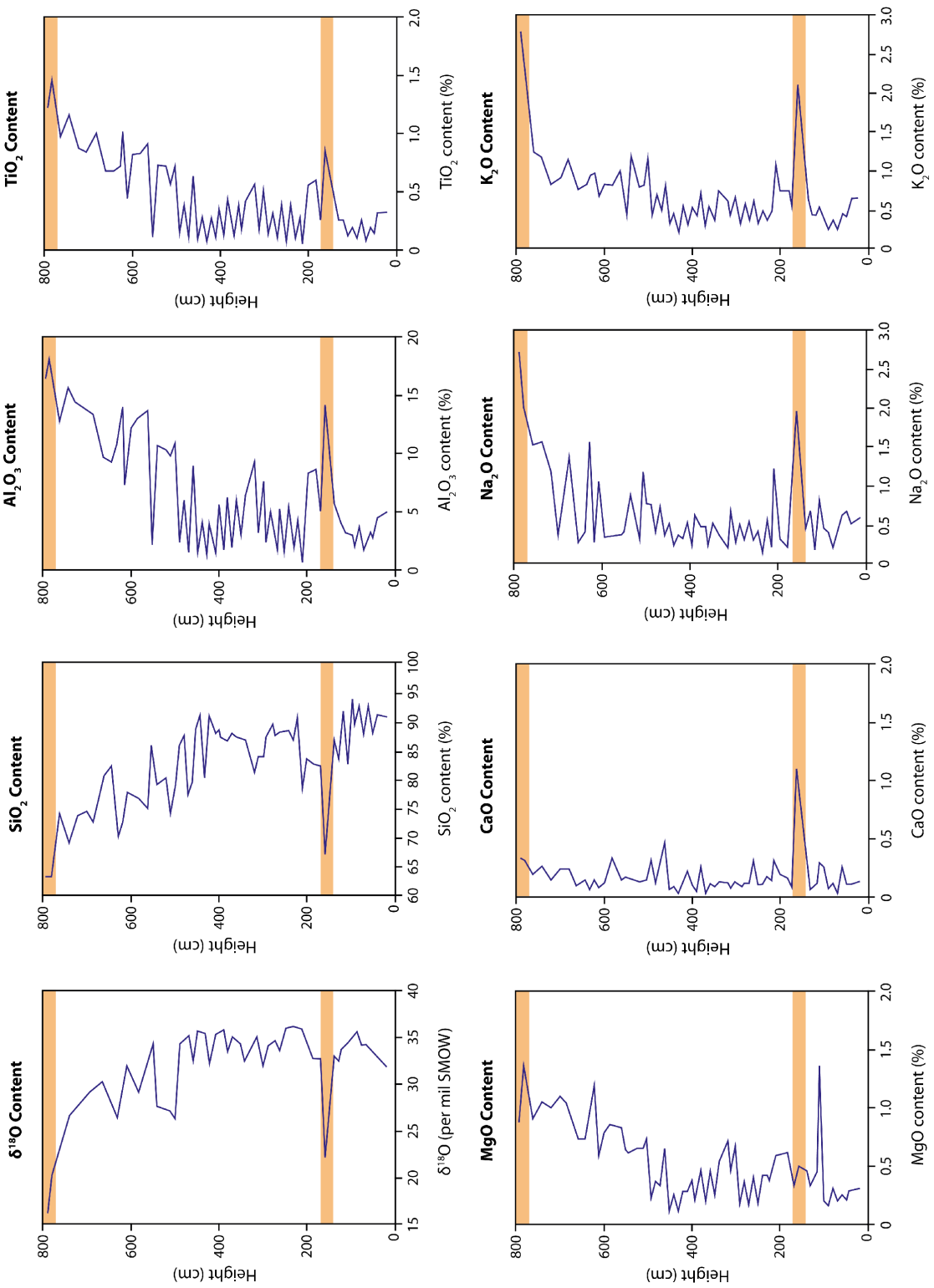

Figure 5.4 Original raw data for samples of cleaned diatomite material from diatomite unit #4. Graphs show variations in oxygen isotope composition ($\delta^{18}O$) and variations in different elemental oxides, measured using XRF analysis.

et al., 2006). However it is assumed, for the purposes of this study, that any secondary isotope exchange only affects the outer hydrous silica layer of the diatom frustule. The removal of this layer during the stepwise fluorination procedure ensures that only the inner, more stable diatom silica is measured for $\delta^{18}O_{diatom}$ and that values of $\delta^{18}O_{diatom}$ can be reliably used for palaeoclimatic reconstruction.

5.2.2 Qualitative assessment of contamination

Scanning electron microscopy (SEM) images of diatomite material (both before and after cleaning) are displayed in figure 5.5. It is clear from the images that whilst the purification steps undertaken to clean the samples prior to isotope analysis are able to remove a significant amount of non-diatom material, there are still small amounts of contamination remaining within the samples. The SEM images indicate that, in places, a considerable amount of clay can remain within the diatomite samples after cleaning and demonstrate how small platy clay fragments adhere to diatom frustules by electrostatic charge or become stuck inside cylindrical diatom frustules (figure 5.5, image **C**).

Tephra shards also constitute a significant contamination component within the analysed samples (figure 5.5, images **H**, **I**), although this was less obvious under analysis by SEM. The presence of a 7 cm-thick air-fall tuff layer within the sequence and another, less distinctive tephra layer towards the top of the stratigraphic sequence (not laterally continuous) imply that contamination by tephra may occur throughout the sequence due to the reworking of particles throughout the section (Deino et al., 2006; Kingston et al., 2007; Lamb et al., 2007; Brewer et al., 2008). It is thus important to make an individual quantitative assessment of the major and trace element geochemistry of each sample in order to better understand how much of the variation in the $\delta^{18}O_{diatom}$ data is reflective of a true climate signal and to develop an appropriate model for correcting $\delta^{18}O_{diatom}$ values for the effects of contamination.

As outlined in chapter 4.4.2, a small number of samples from sequence RE26 were analysed by Dr. George Swann of Nottingham University using infrared (IR) spectroscopy to assess contamination levels in purified samples in relation to samples of tephra (sample #TUFF) and the laboratory standard BFC diatomite. Results are shown in figure 5.6. The differences in IR spectra arise from the different wavelength peaks that represent different compounds. For example, peaks at 1075 correspond to the number of Si-O-Si bonds in a sample, whilst wavelengths of 1120 and 800 correspond to Si-OH bonds (Swann and Patwardhan, 2011). It

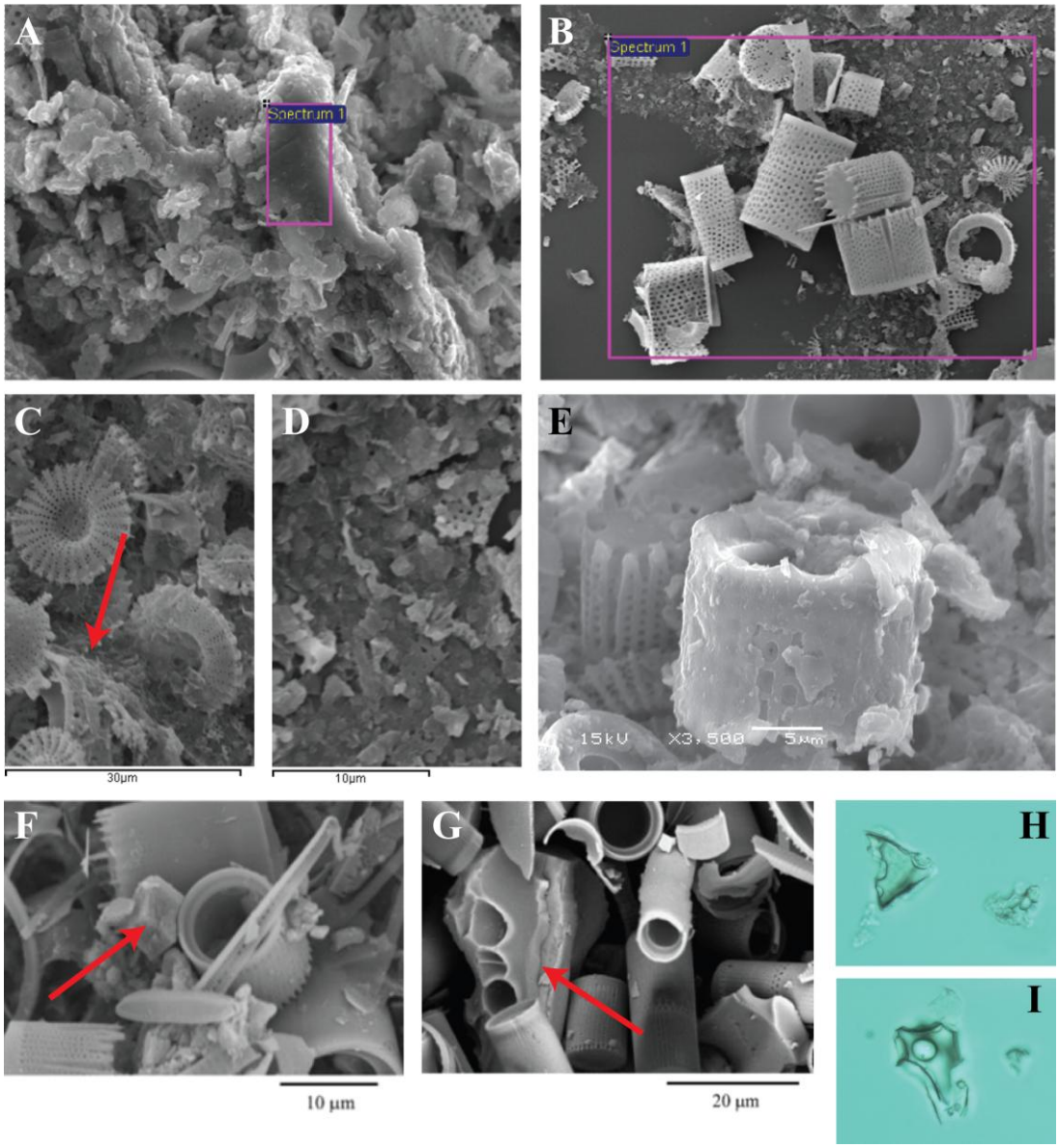

Figure 5.5 Collection of images taken using scanning electron microscopy (SEM) and light microscopy to assess contamination and purity levels in samples. Images **A** and **B** show diatomite material before and after purification respectively, demonstrating that it is possible to remove a significant portion of non-diatom material via rigorous chemical and physical cleaning techniques. Images **C** and **D** show fragments of platy clays which remain in the samples after purification, necessitating the need for further geochemical assessment using x-ray fluorescence (XRF) spectrometry. Image **E** illustrates the degree to which secondary clays and precipitates can form and adhere to diatom frustules. Images **F** and **G** are taken from Brewer et al. (2008) and show contamination by carbonate and tephra (indicated by red arrows), respectively, within samples from Lake Tilo in Ethiopia. Images **H** and **I** are optical light microscopy (magnification x 1000) pictures of tephra shards from within sample #4069 in diatomite unit #4, coincident with the grey-green air-fall tuff layer.

is clear from the results that there is a marked difference in the IR spectra of the samples. The spectra for samples #4055 and #4061 are broadly similar to the black line representing the BFC laboratory standard, implying that these samples are relatively clean as they follow

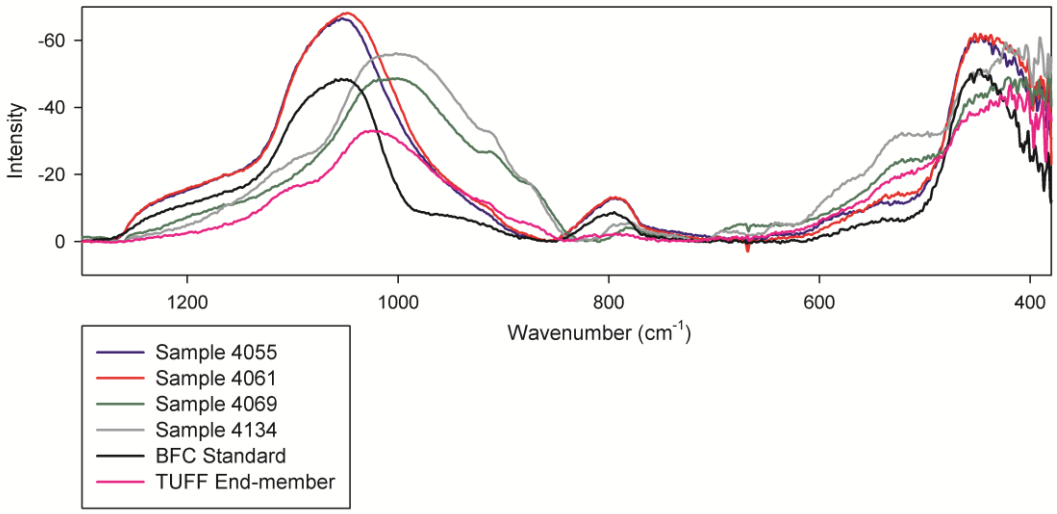

Figure 5.6 Results of experimental use of IR spectroscopy to assess sample purity. The x-axis (wavenumber) represents changes in the electromagnetic spectrum whereby each wavelength corresponds to a different compound. Data produced by Dr. G. Swann, Nottingham University.

the BFC curve at most wavelengths. However the curves for samples #4069 and #4134 closely mirror the pink curve (sample #TUFF) indicating that they contain a considerable amount of tephra contamination within them. This work is currently ongoing and is included here purely as a new way of assessing diatom contamination in a qualitative manner.

5.2.3 Quantitative assessment of contamination

Aliquots of all samples sent for oxygen isotope analysis ($\delta^{18}O_{diatom}$) were also analysed by X-ray fluorescence (XRF) spectrometry in order to assess major and trace element geochemistry and to quantify the effect of the remaining contamination on the $\delta^{18}O_{diatom}$ signal. Whole-sample chemical compositions for samples from diatomite #4 are displayed in table 5.1 as percentages of major element oxides. Trace element concentrations were also determined for those samples analysed at the University of Leicester and were initially used for determining contamination levels in some models.

The geochemical composition of the BFC laboratory standard diatomite was taken from Brewer *et al*., (2008) and is included as an indication of the chemical composition of what is considered to be pure diatomite material. The marked differences in the chemistry of the end-member tephra and clay contaminants and the cleanest diatom samples provide a means of determining the level and type of contamination present within samples. At this stage, samples #4074 (200 cm) and #4099 (460 cm) were removed from further analysis of the

Table 5.1 Compiled XRF results for major oxide compositions of Barsemoi diatomite samples from sequence RE26.

Sample	Height	Lab	SiO_2	TiO_2	Al_2O_3	Fe_2O_3	MnO	MgO	CaO	Na_2O	K_2O	P_2O_5	Total
4055	20	Leics	89.50	0.32	4.75	2.28	0.02	0.31	0.12	0.59	0.62	<0.01	98.52
4057	40	Leics	89.73	0.31	4.31	2.21	0.02	0.28	0.10	0.50	0.61	<0.01	98.07
4058	50	BGS	88.02	0.14	2.67	1.61	0.06	0.22	0.11	0.66	0.38	<0.01	100.09
4059	60	Leics	91.56	0.20	3.22	1.76	0.03	0.24	0.27	0.63	0.42	<0.01	98.37
4060	70	BGS	87.91	0.08	1.58	0.99	0.03	0.20	0.04	0.48	0.21	<0.01	100.01
4061	80	Leics	91.38	0.26	3.66	2.13	0.03	0.31	0.11	0.20	0.37	<0.01	98.46
4062	90	BGS	88.88	0.10	1.97	1.32	0.03	0.16	0.07	0.41	0.20	<0.01	99.44
4063	100	Leics	91.79	0.20	2.90	1.61	0.02	0.20	0.26	0.44	0.36	<0.01	97.81
4064	110	BGS	86.18	0.13	3.27	2.00	0.08	1.42	0.31	0.87	0.54	<0.01	104.38
4065	120	Leics	62.97	0.17	2.56	1.69	0.02	0.31	0.08	0.09	0.27	<0.01	68.19
4066	130	BGS	84.31	0.26	4.54	3.16	0.07	0.35	0.05	0.76	0.40	<0.01	100.76
4067	140	Leics	84.65	0.39	5.87	4.08	0.06	0.45	0.36	0.38	0.63	0.01	96.93
4069	160	Leics	63.29	0.87	13.79	10.36	0.21	0.48	1.04	1.92	2.05	0.07	94.18
4070	170	BGS	82.64	0.25	4.78	2.85	0.05	0.33	0.08	0.92	0.51	<0.01	100.54
4071	180	Leics	60.96	0.44	6.43	4.65	0.05	0.47	0.12	0.15	0.52	0.02	73.81
4073	200	Leics	82.67	0.56	8.27	4.97	0.07	0.61	0.17	0.31	0.70	0.03	98.36
4074	210	BGS	79.38	0.01	<0.01	0.33	0.30	0.59	0.31	1.38	1.09	<0.01	101.15
4075	220	Leics	66.12	0.24	3.27	2.15	0.02	0.28	0.10	0.10	0.32	<0.01	72.61
4076	230	BGS	88.03	0.07	1.54	0.97	0.05	0.44	0.18	0.61	0.35	<0.01	101.26
4077	240	Leics	71.27	0.33	4.72	3.16	0.04	0.33	0.09	0.10	0.39	0.01	80.45
4078	250	BGS	87.99	0.05	1.24	0.87	0.04	0.16	0.09	0.43	0.26	<0.01	99.58
4079	260	Leics	87.34	0.42	5.67	3.74	0.05	0.41	0.30	0.30	0.62	0.02	98.89
4080	270	BGS	88.09	0.09	1.41	0.87	0.06	0.16	0.12	0.57	0.32	<0.01	100.38
4081	280	Leics	87.44	0.34	5.14	3.23	0.04	0.39	0.11	0.30	0.55	0.01	97.56

Sample	Height	Lab	SiO_2	TiO_2	Al_2O_3	Fe_2O_3	MnO	MgO	CaO	Na_2O	K_2O	P_2O_5	Total
4082	290	BGS	88.06	0.12	2.23	1.71	0.04	0.16	0.09	0.54	0.26	<0.01	100.28
4083	300	Leics	81.32	0.53	7.71	5.53	0.05	0.67	0.12	0.23	0.63	0.03	96.83
4084	310	BGS	84.46	0.16	3.14	2.30	0.06	0.43	0.08	0.75	0.39	<0.01	100.60
4085	320	Leics	76.80	0.55	8.84	6.67	0.06	0.70	0.12	0.19	0.55	0.04	94.51
4087	340	Leics	85.12	0.43	6.26	4.32	0.05	0.53	0.12	0.35	0.69	0.02	97.90
4088	350	BGS	87.13	0.16	2.96	1.83	0.03	0.23	0.09	0.54	0.29	<0.01	99.75
4089	360	Leics	85.65	0.43	6.03	4.31	0.05	0.50	0.11	0.19	0.54	0.03	97.84
4090	370	BGS	88.08	0.11	1.85	1.82	0.05	0.17	0.03	0.50	0.23	<0.01	99.74
4091	380	Leics	85.08	0.47	6.40	4.16	0.05	0.50	0.27	0.45	0.70	0.02	98.09
4092	390	BGS	87.78	0.11	1.65	1.09	0.05	0.20	0.03	0.66	0.38	<0.01	100.44
4093	400	Leics	86.36	0.39	5.53	3.96	0.03	0.38	0.10	0.22	0.50	0.01	97.50
4094	410	BGS	88.24	0.08	1.43	1.15	0.03	0.28	0.23	0.55	0.25	<0.01	100.14
4095	420	Leics	89.04	0.31	4.09	2.75	0.03	0.27	0.10	0.33	0.54	<0.01	97.49
4096	430	BGS	79.74	0.07	1.28	1.02	0.03	0.10	0.02	0.38	0.17	<0.01	99.30
4097	440	Leics	89.52	0.30	4.14	2.38	0.02	0.27	0.09	0.21	0.42	<0.01	97.37
4098	450	BGS	88.90	0.08	1.46	1.03	0.06	0.11	0.04	0.55	0.29	<0.01	99.82
4099	460	Leics	70.51	0.62	8.02	7.25	0.06	0.60	0.42	0.28	0.72	0.09	88.57
4100	470	BGS	76.40	0.09	1.53	1.29	0.08	0.32	0.24	0.78	0.44	<0.01	98.85
4101	480	Leics	85.66	0.44	6.04	3.67	0.03	0.37	0.11	0.34	0.69	0.02	97.37
4102	490	BGS	85.65	0.13	2.51	1.60	0.04	0.22	0.31	0.76	0.36	<0.01	99.64
4103	500	Leics	75.41	0.70	10.46	6.19	0.06	0.71	0.17	0.74	1.12	0.03	95.62
4104	510	BGS	74.01	0.57	9.84	5.98	0.07	0.66	0.12	1.28	0.77	0.03	100.11
4105	520	Leics	77.75	0.72	10.10	6.36	0.04	0.64	0.13	0.27	0.72	0.03	96.77
4108	540	Leics	76.95	0.71	10.43	6.56	0.05	0.60	0.14	0.90	1.20	0.03	97.62
4109	550	BGS	86.18	0.09	2.18	1.28	0.07	0.66	0.16	0.43	0.37	<0.01	100.17

Sample	Height	Lab	SiO_2	TiO_2	Al_2O_3	Fe_2O_3	MnO	MgO	CaO	Na_2O	K_2O	P_2O_5	Total
4110	560	Leics	68.25	0.84	12.47	7.05	0.05	0.75	0.13	0.35	0.90	0.03	90.85
4112	580	Leics	74.98	0.82	12.88	6.56	0.05	0.85	0.31	0.35	0.76	0.03	97.59
4114	600	Leics	71.22	0.77	11.17	6.88	0.04	0.74	0.11	0.32	0.75	0.03	92.04
4115	610	BGS	77.59	0.43	7.16	4.77	0.06	0.59	0.08	1.12	0.64	<0.01	99.75
4116	620	Leics	66.85	0.95	12.93	8.63	0.06	1.13	0.13	0.21	0.87	0.03	91.79
4117	630	BGS	70.57	0.72	10.68	7.51	0.07	0.94	0.05	1.65	0.92	<0.01	100.65
4118	640	Leics	79.74	0.67	8.96	5.30	0.04	0.72	0.13	0.39	0.78	0.02	96.79
4121	660	Leics	74.18	0.62	8.91	6.14	0.04	0.69	0.09	0.25	0.66	0.03	91.64
4123	680	Leics	64.23	0.90	11.76	7.84	0.06	0.92	0.21	1.26	1.00	0.04	88.26
4125	700	Leics	69.93	0.79	12.93	7.41	0.05	1.02	0.21	0.32	0.81	0.03	93.54
4127	720	Leics	70.53	0.85	13.77	7.41	0.05	0.96	0.13	1.12	0.75	0.03	95.61
4129	740	Leics	67.99	1.15	15.40	9.80	0.08	1.04	0.26	1.56	1.14	0.04	98.46
4131	760	Leics	70.69	0.92	12.07	7.36	0.06	0.87	0.17	1.46	1.15	0.03	94.79
4133	780	Leics	60.39	1.41	17.34	10.21	0.09	1.32	0.30	1.97	2.17	0.04	95.25
4134	790	Leics	61.54	1.19	16.02	11.29	0.22	0.85	0.32	2.65	2.69	0.07	96.86
TUFF	N/A	Leics	64.63	0.71	13.59	10.20	0.49	0.72	0.99	4.64	2.70	0.08	98.77
TUFF 2	N/A	BGS	58.97	1.51	17.16	7.16	0.52	0.64	1.03	4.72	4.77	0.01	96.59
CLAY	N/A	SEM	58.08	1.95	24.62	8.28	-	1.81	1.36	0.74	0.85	1.16	100
BFC	N/A	Leics	91.91	0.07	1.38	0.39	0.01	0.24	0.33	0.14	0.07	0.00	100.57

Table 5.1 Compiled XRF results for major oxide compositions of Barsemoi diatomite samples from sequence RE26. Data are quoted in weight percentages. Samples in red (# 4074 and #4099) were removed from exploratory analysis of the data as a result of issues encountered during XRF analysis. A t-test performed on XRF analyses of the BFC standard at each laboratory showed there was no difference between the two institutions at the 5% significance level (t = 0.00578; 5% level = 2.1199 – the t value would have to exceed this for the two samples to be statistically different).

data set as a result of problems identified during XRF analysis (sample #4074: low sample weight; sample #4099: laboratory analysis error).

In general, samples further up the section contain greater proportions of elemental oxides, broadly indicating higher levels of contamination than those further down. Sample #4069 (160 cm) was taken from the green tuff layer within the lower third of the section, and subjected to the same cleaning procedure as the other diatomite samples. However, due to similarities in the size, density and silica content of tephra and diatoms, it was not possible to purely isolate one or the other component using cleaning methods alone. Diatom samples with the highest proportion of SiO_2 are considered to be the least contaminated or purest samples and generally occur within the lower half of the sequence.

5.2.4 Modelling of oxygen isotope signal

Using the relative proportions of elemental oxides measured using XRF geochemistry, estimated levels of tephra and clay contamination remaining within the samples were calculated through the progressive development of a series of contamination models. Analysis of the sediment stratigraphy and SEM imagery indicated the presence of two types of contaminant in the form of clay particles and fragments of air-fall tephra reworked within the sequence from two ash layers. The following section aims to outline the steps taken to develop and test the most accurate way to model isotope data from contaminated samples. All the models follow the basic approach of Brewer et al. (2008), which has since been developed by Swann and Leng (2009) and Mackay et al. (2011), and are based around mass-balance calculations used to quantify relative contamination levels:

$$\%\,\text{contamination} = \left[\frac{\text{Sample}_C - \text{Clean}_C}{\text{Modern}_C}\right] \times 100 \qquad \textit{(Equation 22)}$$

where sample_c is the percentage value of elemental oxide or trace metal within the sample, clean_c is the value of that particular oxide or trace metal within the least contaminated sample and contaminant_c is the oxide abundance within the end-member contaminant. This equation is used not only in the mass-balance calculations to define isotope corrections, but also to establish the scaled proportions of each elemental oxide present within a sample relative to both pure and contaminated end-members. The characteristics of the models are summarised in table 5.2. Isotope corrections were performed using equations 20 and 21 given in chapter 4.5.2.3.

Model	Outlier	Ordination			Model Components			End-Members				Outcome / Comments
								Contaminant 1		Contaminant 2		
		PCA	λ_1	λ_2	Total or Purity	Contaminant 1 (Tephra)	Contaminant 2 (Clay)	Sample	$\delta^{18}O$ value	Sample	$\delta^{18}O$ value	
Al_2O_3 Content	4099	No	n/a	n/a	Not calculated	n/a	Al_2O_3	n/a	n/a	4134	16.180‰	At this point sample 4134 was believed to be clay
Tephra-based Corrective Model	4099	No	n/a	n/a	Not calculated	Fe_2O_3, Na_2O_3, K_2O, Y, Zr	n/a	4134	n/a	n/a	n/a	The tephra components here were taken from Brewer et al. (2008) and do not reflect the specific geochemistry of the Baringo tephra component
Tephra-based Corrective Model v.2	4099	No	n/a	n/a	Not calculated	CaO, Na_2O, K_2O, Y, Sr	n/a	Average of 4134 & TUFF	n/a	n/a	n/a	Whilst the tephra components are reflective of the Baringo tephras, the model does not encompass any secondary clay component.
Clay & Tephra Components	4074 4099	No	n/a	n/a	Not calculated	CaO, Na_2O, K_2O, Y, Sr	MgO, Cr, V	Average of 4134 & TUFF	16.432 ‰	Modern (Tarits et al. 2006)	16.432‰	No attempt made to combine contamination components as there is some overlap in contamination as shown by relative enrichment in Al_2O_3 in both clay and tephra samples.
Multivariate Analysis-based Model	4074 4099	Yes	0.705	0.146	Not calculated	CaO, Na_2O, K_2O, MnO	MgO, Fe_2O_3, Al_2O_3, TiO_2	TUFF	16.432 ‰	Modern (Tarits et al. 2006)	12.697‰	Clay $\delta^{18}O$ value estimated by regression from available data. No attempt made to combine contamination components as there is some overlap in contamination as shown by relative enrichment in Al_2O_3 in both clay and tephra samples
SiO_2 Purity Model	4074 4099	Yes	0.705	0.146	SiO_2 scale	CaO, Na_2O, K_2O, MnO	MgO, Fe_2O_3, Al_2O_3, TiO_2	'TUFF 2'	10.000 ‰	CLAY	14.048‰	Contaminant 2 $\delta^{18}O$ value estimated by regression from available data. Corrected values vary wildly, SiO2 does not work when used to estimate total contamination or purity
Weighted-averages Model	4074 4099	Yes	0.705	0.146	Weighted average of elemental oxides using PCA ax1 scores	CaO, Na_2O, K_2O	MgO, Al_2O_3, TiO_2	'TUFF 2'	10.000 ‰	CLAY	14.605‰	Contaminant 2 $\delta^{18}O$ value estimated by regression from available data. Works well but is not as good at correcting more extreme low values than averages model
3 End-member Averages Model	4074 4099	Yes	0.705	0.146	Average proportion of all elemental oxides	CaO, Na_2O, K_2O	MgO, Al_2O_3, TiO_2	'TUFF 2'	10.000 ‰	CLAY	14.605‰	Values of PCA axis 1 highly correlated (r^2 = 0.92) with estimated percentages of contaminant 2 (clay)

Table 5.2 Summary of development of models to correct values of $\delta^{18}O_{diatom}$ for the effects of contamination remaining after cleaning.

It should be noted that the development and testing of each model stage took place over several months and that the models were refined as more data from isotope and XRF analyses became available. Figures 5.7 **A** and **B** were constructed from a minimal set of coupled XRF - $\delta^{18}O$ measurements following the initial round of XRF analysis whilst figures 5.7 **C** – **G** show the results of models developed using the complete data set.

5.2.4.1 Al_2O_3 content model

Brewer et al. (2008) were the first to describe the use of XRF analysis to quantify the geochemical differences between samples in order to assess contamination levels and their effect on the $\delta^{18}O_{diatom}$ signal. By analysing a deglacial diatom isotope record from Lake Baikal (Morley et al., 2005), Brewer et al. (2008) used the relative abundance of aluminium oxide (Al_2O_3) as an indicator of clay contamination.

Initial examination of SEM imagery of bulk diatomite samples from RE26 suggests that, despite the presence of two distinctive tephra horizons, the principle contaminant within the samples is clay. On this basis, and as an experimental test of the Brewer method, initial corrections of the first sets of pilot data were calculated by employing Al_2O_3 as an indicator of clay content. However, detailed examination of the XRF data suggested that the character of contamination in the RE26 sequence is more complex, and Al_2O_3 would not be adequate as an indicator oxide. Whilst this approach may be sufficient for less complicated records (e.g. Mackay et al., 2011), the resulting corrections to $\delta^{18}O_{diatom}$ values (figure 5.7, **A**) were found to have the effect of reversing negative excursions in the record and were thus judged to be a poor representation of the true signal.

5.2.4.2 Tephra-based corrective models

In addition to the Al_2O_3-based corrections made to the Lake Baikal $\delta^{18}O_{diatom}$ record, Brewer et al. (2008) also examined a record from Lake Tilo in Ethiopia (Lamb et al., 2005, 2007). The Lake Tilo samples were contaminated by small rhombic-shaped carbonate grains and volcanic ash shards (Fig. 5.5, images **H**, **I**). In order to resolve the character of the contamination within this record, Brewer et al. (2008) adopted a dual approach using mass-balance geochemistry to estimate contaminant levels within each sample.

Due to the known presence of tephra within the RE26 sequence, and in order to test the approach used by Brewer et al. (2008), a model using the relative abundance of a series of

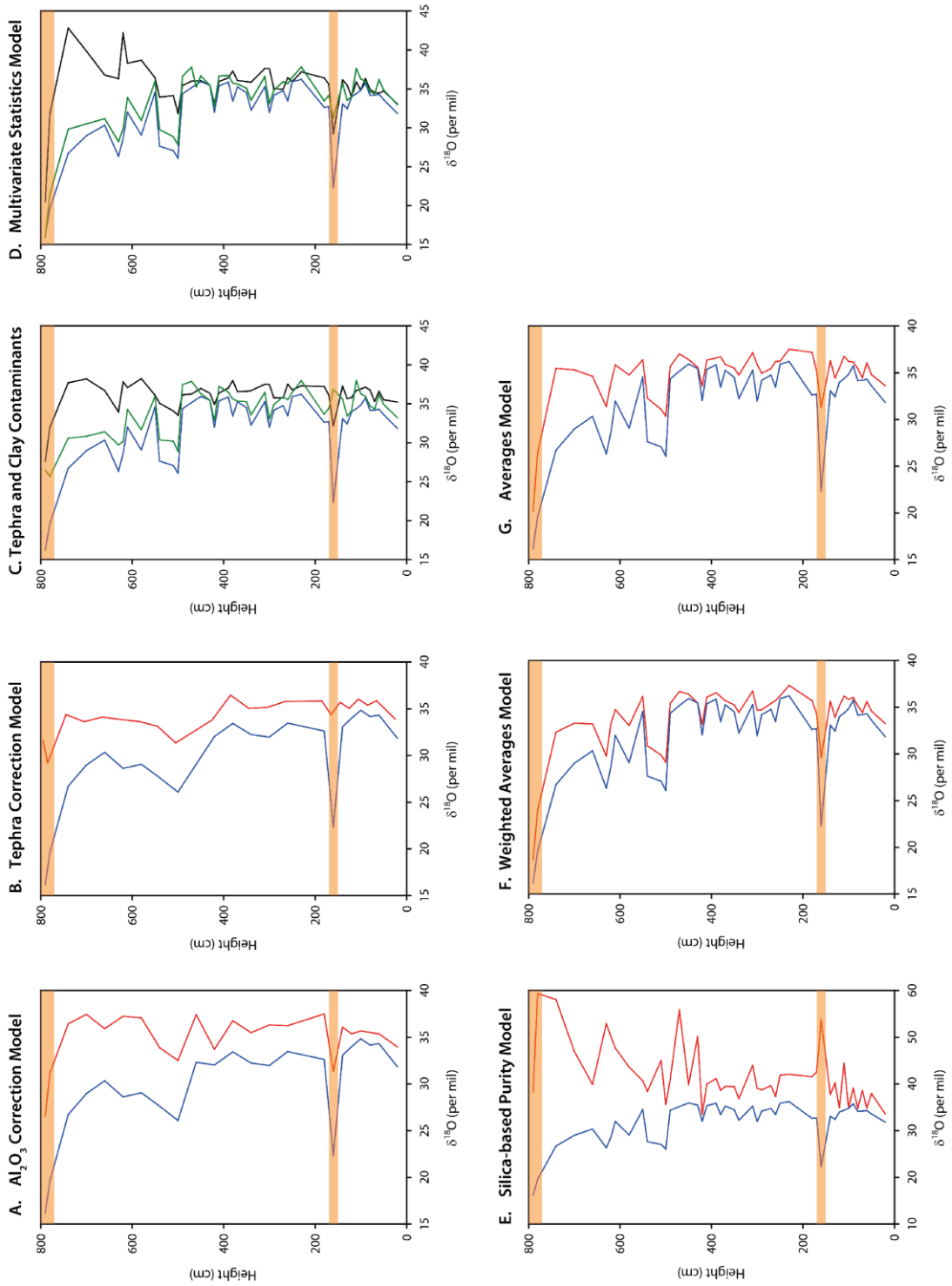

Figure 5.7 Corrected isotope records resulting from the development of models described in sub-sections in chapter 5.2.4. In all graphs, raw uncorrected $\delta^{18}O_{diatom}$ values are shown in blue. In graphs **A**-**B** and **E**-**G** inclusive, corrected values of $\delta^{18}O_{diatom}$ are shown in red whilst in graphs **C** and **D**, where corrections were made separately for clay and tephra, these are displayed separately, depicted by the black and green lines, respectively. Positions of known tephras within the section are marked by orange bars.

elemental oxides (Fe_2O_3, Na_2O_3, K_2O) and trace metals (Y, Zr) was tested to estimate tephra contamination. In an initial model the indicator metals used were those suggested by Brewer et al. (2008) for the Lake Tilo samples. However, due to the diverse nature of tephra geochemistry and differences in the geochemical signatures of different volcanic sources, the corrections described above were subsequently adapted in order to better reflect the geochemistry of the tephra layers present within the Barsemoi sequence. In contrast to the suite of elemental oxides used by Brewer et al. (2008), this updated model was developed using the relative abundances of CaO, Na_2O, K_2O, Y and Sr. The resulting isotopic corrections (figure 5.7, **B**) for both of these models are not sufficient to accurately account for the variation observed within the XRF and $\delta^{18}O_{diatom}$ datasets, and it is evident that further assessment is required in order to accurately characterise and assess contamination levels.

5.2.4.3 Model for the separation of tephra and clay components

Analysis of additional XRF data made available following further analyses revealed two distinct contaminant components present with the Baringo diatomite samples. Due to the limited amount of data previously available, this was not clearly evident in previous attempts to develop contamination models. For the models described hereafter, in addition to the tephra contaminant described above (calculated using the relative abundances of CaO, Na_2O, K_2O, Y and Sr), contamination levels were also estimated based on the perceived influence of clay within the samples (figure 5.7, **C**). By examining the specific geochemistry of samples which are highly contaminated but enriched in different elemental oxides to the tephra end-member, clay proportions were initially estimated using mass-balance equations based on the relative abundances of MgO, Cr and V. However further quantification and analysis of an end-member sample for clay is necessary to ensure that clay contamination is accounted for as accurately as possible. As an initial investigation to isolate the contaminant proportions of clay and tephra within the samples, no attempt was made at this stage to combine estimates for the two components and quantify the total amount of contamination present within each of the samples.

5.2.4.4 The use of multivariate statistics to identify contamination components

Previous models revealed the highly complex nature of the contamination present within the diatomite samples and that more detailed statistical analyses would be required in order to explore variation within the geochemical dataset. Statistical analysis of the whole-sample geochemical dataset produced by XRF spectrometry was conducted using indirect

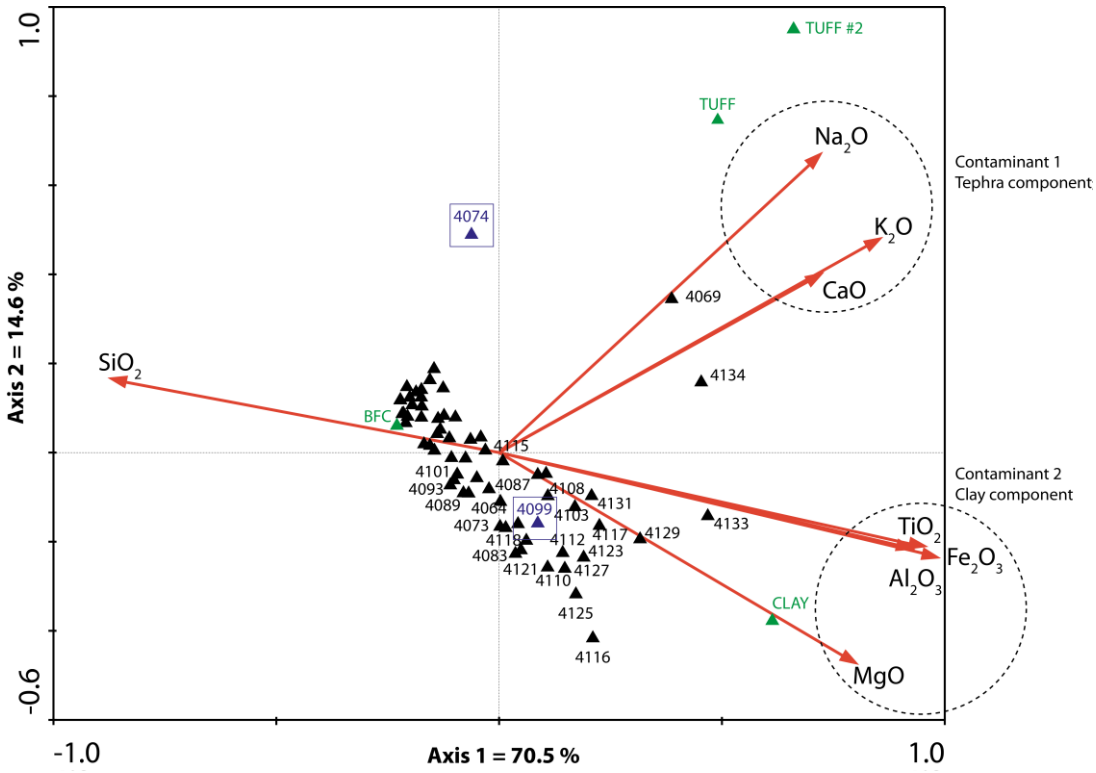

Figure 5.8 Ordination biplot showing results of PCA performed on XRF data set (displayed in table 5.1) in order to explore variation within the geochemical compositions of remnant contamination. End-member samples of tephra (TUFF and TUFF #2), clay and diatomite (BFC) are shown in green. Relative positions of samples identified as outliers, #4074 (analytical error in Leicester) and #4099(low sample weight, results unreliable) are highlighted in blue, however these were not included in the analysis. Results show that contamination is strongly influenced by variation along PC axis 1, representing enrichment in clay (as shown by enrichment in TiO_2, Fe_2O_3, Al_2O_3 and MgO) with a smaller element controlled by the presence of tephra (enriched in Na_2O, K_2O and CaO).

ordination techniques. Analyses were conducted using Canoco ver. 4.5 for Windows, and ordination biplots were produced using CanoDraw (ter Braak & Smĭlauer 2002).

Principal Components Analysis (PCA) was used to explore variation in the chemical composition of the purified samples and thus to establish relationships between different elemental components. PCA linear analysis was focussed on inter-species correlations and species data were centred and standardised in order to calculate a correlation matrix for the data. PCA indicated that 85.1% of the variance within the data can be explained by axes 1 and 2 which represent the environmental gradients of the measured elemental oxides (eigenvalues (λ): $\lambda_1 = 0.705$; $\lambda_2 = 0.146$). Results from the PCA are plotted in the ordination biplot shown in figure 5.8 and in the attribute plots displayed by oxide in figures 5.9 and 5.10. Figure 5.8 shows the distribution of the cleaned diatomite samples with respect to their concentrations of the various elemental oxides and shows that the oxides 'cluster' in two different theoretical groups indicating that contamination within the samples consists of two

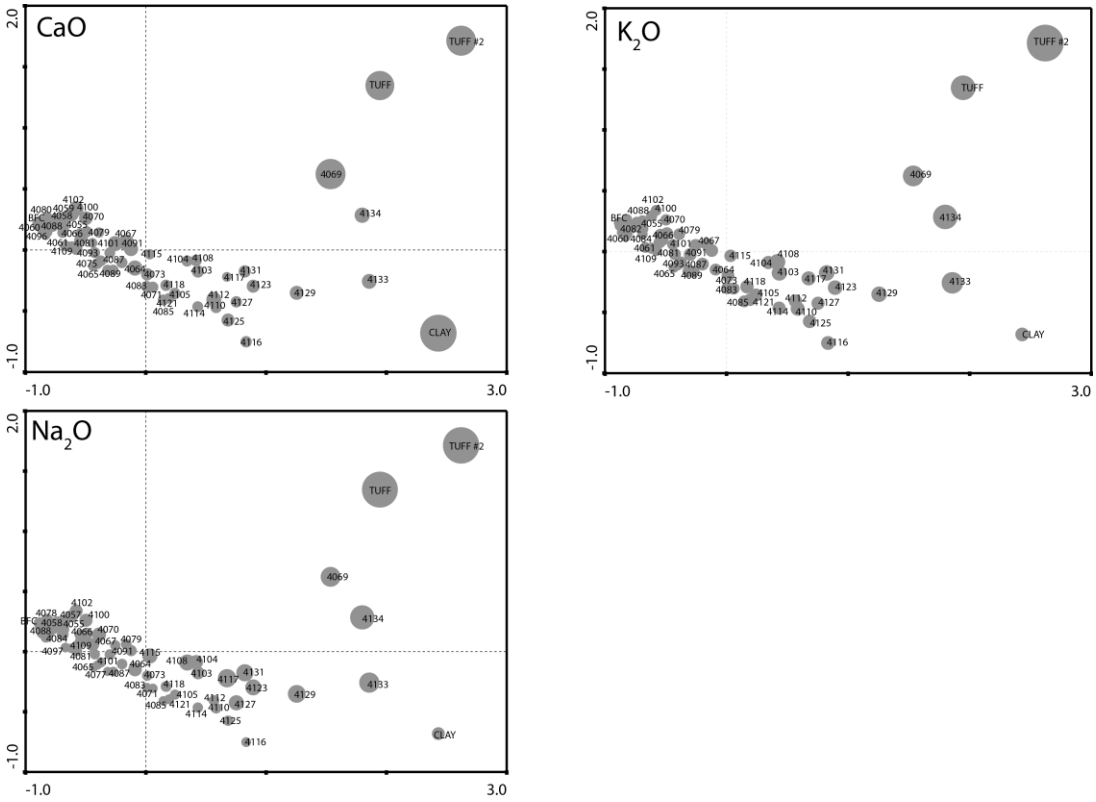

Figure 5.9 Attribute plots for elemental oxides found to be 'indicators' of tephra contamination. The position of each circle is determined by the results of the PCA in figure 5.8. The size of the circle marks the relative abundance of the particular elemental oxide within that sample – the larger the circle, the greater the concentration.

different components. Figure 5.8 also includes the relative position of samples #4074 and #4099 (already identified as outliers) with respect to the whole data set. Whilst the position of sample #4099 within the broad geochemical distribution of the entire data set, the results were deemed to be unreliable due to a low sample weight. The results suggest that contamination within the samples arises from two principal sources. The positions in the ordination biplot of the end-member #TUFF and #TUFF2 samples and the tephra-rich samples #4069 and #4134 indicate that levels of tephra contamination can be defined by the relative proportions of CaO, MnO, Na_2O and K_2O within a sample. The results of the PCA also suggest that clay contamination within the samples comes from a different source and is controlled by the relative proportions of MgO, Fe_2O_3, Al_2O_3 and TiO_2.

At this stage, no geochemical or isotope measurements were available for analysis of a clay end-member and therefore representative values of modern clays from Lake Baringo were used in place of XRF data in order to approximate the geochemical composition of clay within the sequence (Tarits et al., 2006). By assuming that a linear relationship exists between the proportion of clay (determined from the relative proportions of MgO, Fe_2O_3,

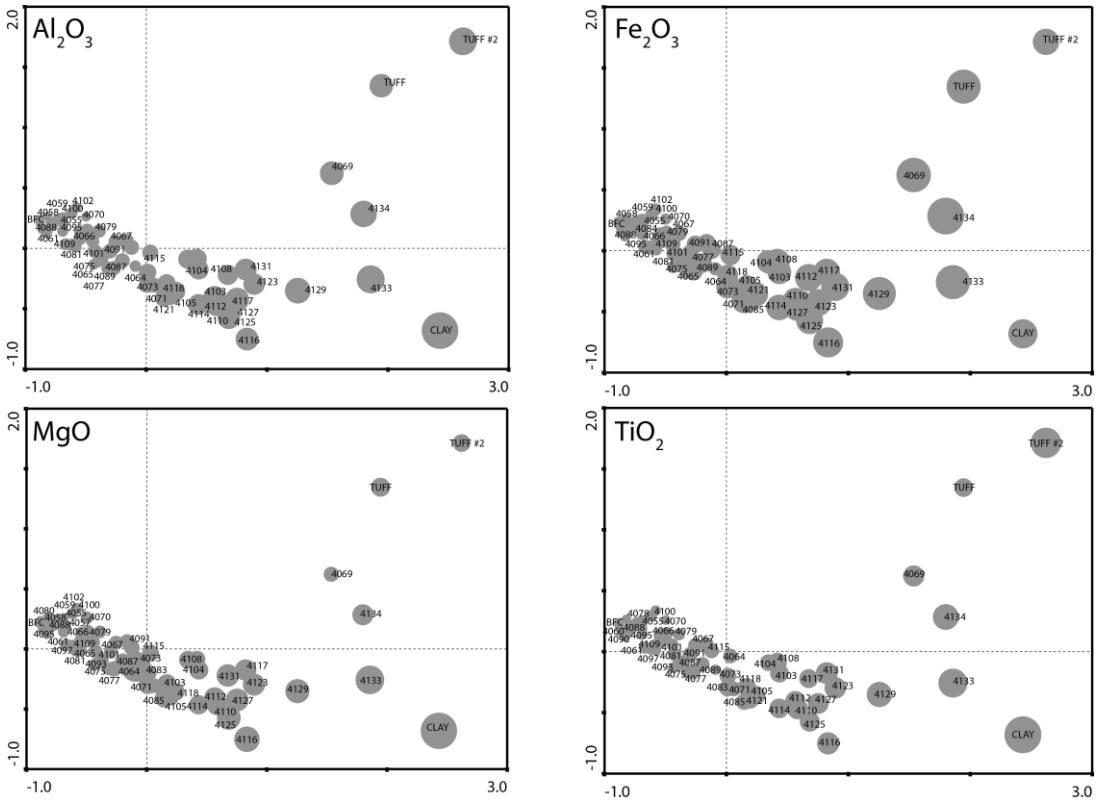

Figure 5.10 Attribute plots for elemental oxides found to indicate relative enrichment in clay. Sizes and positions of circles are determined by the results of the PCA (figure 5.8) and the relative concentration of the elemental oxide within the sample.

Al_2O_3 and TiO_2) and uncorrected $\delta^{18}O$ values ($r^2 = 0.82$), it is possible to estimate a value for $\delta^{18}O_{clay}$ from the associated regression equation. This generates a value for the oxygen isotope composition of clay ($\delta^{18}O_{clay}$) of 12.697 ‰, which is similar to other published $\delta^{18}O$values for end-member contaminants ($\delta^{18}O_{silt}$ = 11.7 ‰, Morley et al., 2005; $\delta^{18}O_{tephra}$ = 11.6‰, Lamb et al., 2007; $\delta^{18}O_{tephra}$ = 10.0 ‰, this study). Corrections to $\delta^{18}O_{diatom}$ values (figure 5.6, **D**) were applied based on the separate calculation of levels of tephra and clay within samples. However as per the previous contamination model, no attempt was made at this stage to combine the two contamination components or to approximate the total amount of contamination present within the samples, but merely to more accurately determine the geochemical characteristics of the different components.

5.2.4.5 Three end-member models

One of the main issues encountered in previous attempts to develop a model to assess and correct for contamination levels has surrounded the combination of estimates for the clay and tephra components and to accurately account for any potential geochemical overlap. In order to correct the $\delta^{18}O_{diatom}$ signal for the presence two contaminants, a three end-member

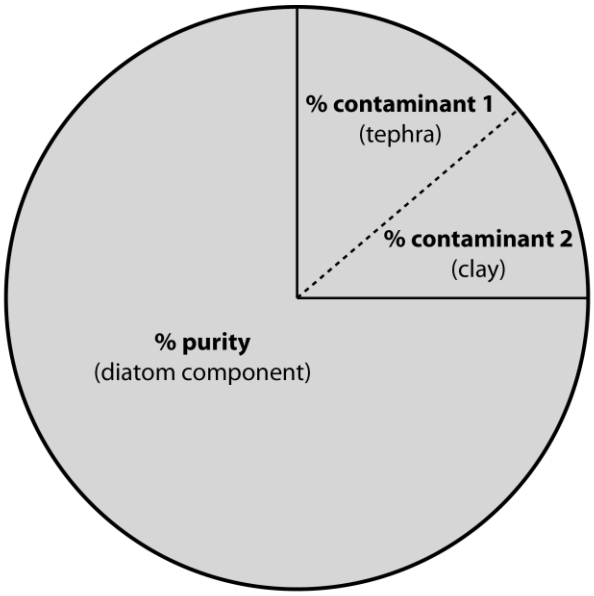

$$\delta^{18}O_{modelled} = \frac{\delta^{18}O_{sample} - \left[(\%\ \text{contaminant 1}/100 \times \delta^{18}O_{contaminant\ 1}) + (\%\ \text{contaminant 2}/100 \times \delta^{18}O_{contaminant\ 2})\right]}{\%\ \text{purity}/100}$$

Figure 5.11 Conceptual model for three end-member contamination models constructed to explore variance in contamination by clay and tephra with a pure biogenic silica (diatom) end-member. Different modelling approaches are discussed in chapter 5.2.4.5.

model was adopted. A theoretical representation of this model is shown in figure 5.11. For simplicity, the three end-members are described as 'contaminant 1' (tephra), 'contaminant 2' (clay) and 'purity' (diatoms). The model requires that the 'purity' or total contamination ('contaminant 1' and 'contaminant 2', minus any overlap) proportion of the sample be calculated in order to accurately establish the quantities of the two components.

5.2.4.5.1 SiO_2 purity-based model

Previous efforts to accurately model contamination levels have done a reasonable job of estimating individual levels of clay and tephra, however it is clear from the geochemical composition of the samples and end-members, that there is some degree of overlap between the two components such that the proportions of particular oxides such as Al_2O_3 and Fe_2O_3 increase regardless of the type of contamination present (figure 5.10).

In order to estimate the total amount of contamination, the relative abundance of SiO_2 was scaled, ranging from pure diatomite (~ 93% SiO_2) to tephra (~ 58% SiO_2). Using this gradational scale a percentage value was calculated as an indicator of 'purity' and, from this,

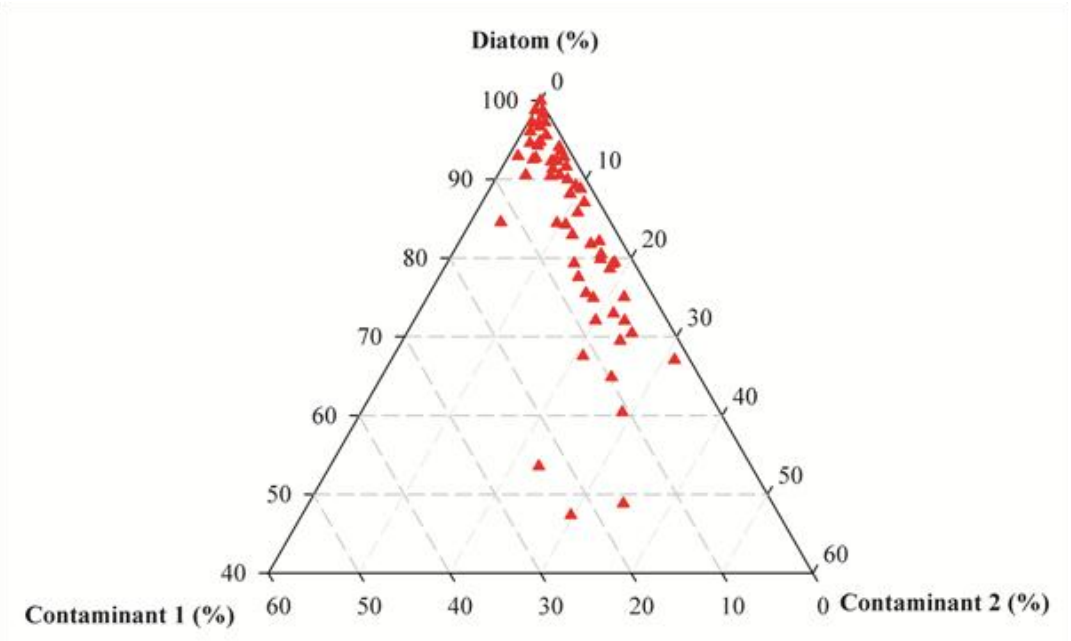

Figure 5.12 Ternary plot showing modelled distribution of diatom material with respect to the calculated amounts of two different contamination components. X (Contaminant 1) and Z (Contaminant 2) axes range from 0 to 60 % whilst Y axis (Diatom silica) is shown from 40 to 100%. Values computed using final three end-member averages model.

'total contamination' is assumed to represent the remaining proportion of sample material. Tephra contamination was determined by relative enrichment in CaO, Na_2O and K_2O whilst clay contamination is defined by enrichment in Al_2O_3, Fe_2O_3, TiO_2 and MgO. Manganese oxides were excluded from the tephra calculations at this stage due to the measurement of two different oxides (MnO and Mn_3O_4) during XRF analysis. In addition to the difficulties of combining these oxides, there was very little variation in Mn levels suggesting that it has a minimal effect on contamination levels.

As previously described, the $\delta^{18}O_{clay}$ end-member value was estimated using a regression equation based on the assumption that a linear relationship exists between $\delta^{18}O$ value and the proportion of clay. This was re-calculated for the newly estimated clay levels and gave a $\delta^{18}O_{clay}$ value of 14.605 ‰. As a first attempt to combine the effects of clay and tephra contamination on the $\delta^{18}O_{diatom}$ signal, the modelled results (figure 5.7, **E**) indicate an extreme degree of variation with some corrected values as high as 60 ‰ and imply that this model is flawed and is not an effective way to correct for contamination levels. If the actual $\delta^{18}O_{diatom}$ values did vary in the fashion suggested by this reconstruction then it would imply a highly saline and evaporative lake system. Such a shift in conditions would also be evident through changes in the diatom assemblage.

5.2.4.5.2 Weighted averages model

The weighted averages model involves the estimation of 'total contamination' fraction by taking a weighted average of the proportion of each indicator elemental oxide (CaO, Na_2O, K_2O for tephra; Al_2O_3, TiO_2, MgO for clay) used as being representative of a contaminant. At this stage, Fe_2O_3 was removed as an indicator oxide for clay as it was found to introduce a bias in the calculation of clay contamination, resulting in the consistent over-estimation of clay proportions. The derived mean value is representative of the proportion of the sample which consists of non-diatom material. Compared to previous attempts, the model (figure 5.7, **F**) works well and produces realistic modelled isotope values. However, the model does not perform well in relatively uncontaminated samples, and consistently underestimates the amount of contamination, as indicated by the variation displayed in the results of the PCA.

5.2.4.5.3 Three end-member averages model

The three end-member averages model differs slightly from the weighted averages model such that rather than use the weighted averages of elemental oxides to estimate total contamination, this model uses only the average proportion of the relevant elemental oxides to ascertain total contamination levels.

Modelled distribution of the three components is shown in figure 5.12 and resulting isotope corrections are displayed in figure 5.7, graph **G**. In contrast to the results of the weighted averages model (figure 5.7, **F**), it does not underestimate the contamination levels in purer samples. The modelled contaminant levels were cross-checked with the PCA axis scores (figure 5.13) where PCA axis 1 and axis 2 scores correspond to 'contaminant 2' (clay) and to 'contaminant 1' (tephra) respectively. The high correlation ($r^2 = 0.92$) between the PCA axis 1 scores and estimated proportions of clay suggests that the model does a good job of estimating contamination levels. Correlation between the PCA axis 2 scores and tephra proportions is not as good, ($r^2 = 0.39$ for samples with positive PCA scores) however in samples where tephra is deemed to be an important component (>5 %), the model does a better job of measuring contamination.

The application of the three end-member averages model to the $\delta^{18}O_{diatom}$ record has the effect of increasing the $\delta^{18}O_{diatom}$ values by an average of 2.49 ‰ (σ = 1.94 ‰; n = 42, values from tephra layers and outliers are excluded). The two samples identified as outliers (#4074 and #4099) were not used in any of the isotope corrections. The resulting modelled isotope curve (figure 5.7, **G**) is less noisy than the original $\delta^{18}O_{diatom}$ data and exhibits a

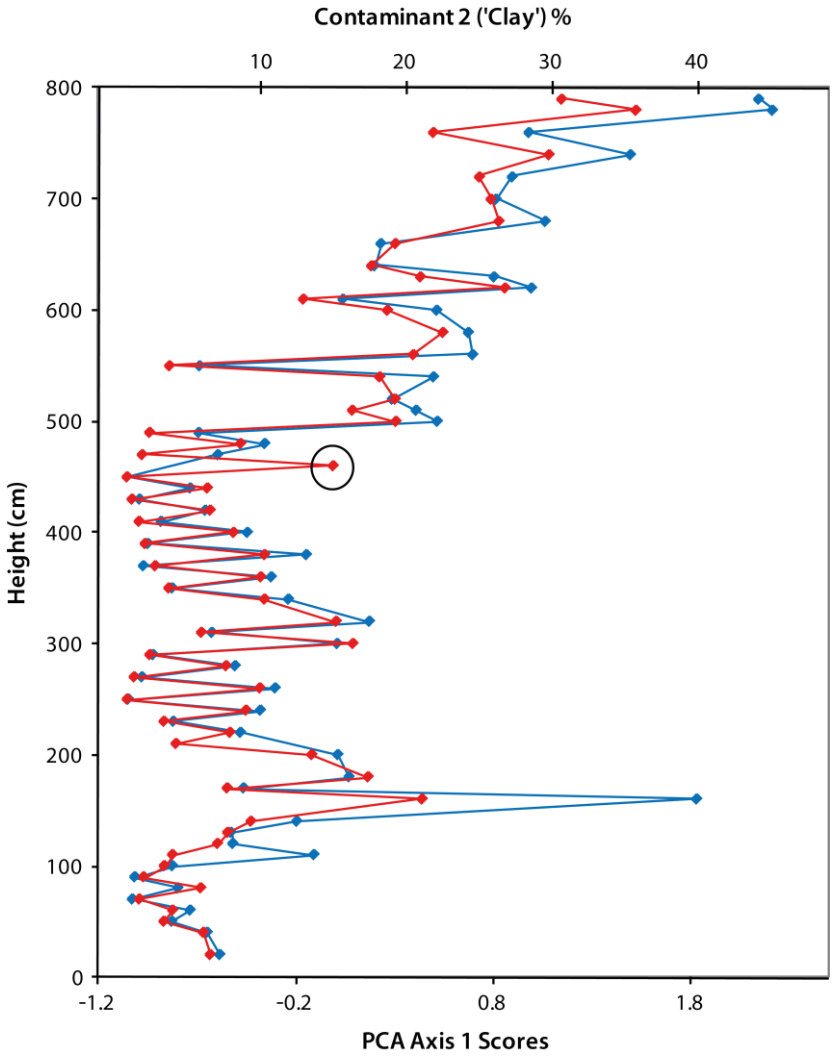

Figure 5.13 Graph comparing modelled amounts of clay (red line) against PCA axis 1 scores (blue line). The two parameters are highly correlated (r^2 = 0.92) showing that the model does a good job of estimating clay percentages within the contaminated samples.

distinct cyclical pattern with regular negative excursions of up to 5 ‰ that occur throughout the sequence.

5.3 Evaluation of $\delta^{18}O$ changes recorded in the Barsemoi diatomite sequence

Raw oxygen isotope data was corrected for the effect of clay and tephra contamination using the three end-member model described in section 5.2.4.5.3, as this was found to to consistently approximate accurate estimates for clay contamination. Figure 5.14 shows the modelled $\delta^{18}O$ data ($\delta^{18}O_{modelled}$) plotted against calculated values of total contamination (comprised of both clay and tephra components) and changes in the proportion of *Stephanodiscus* species present in sequence RE26. By applying the chronology of Deino et

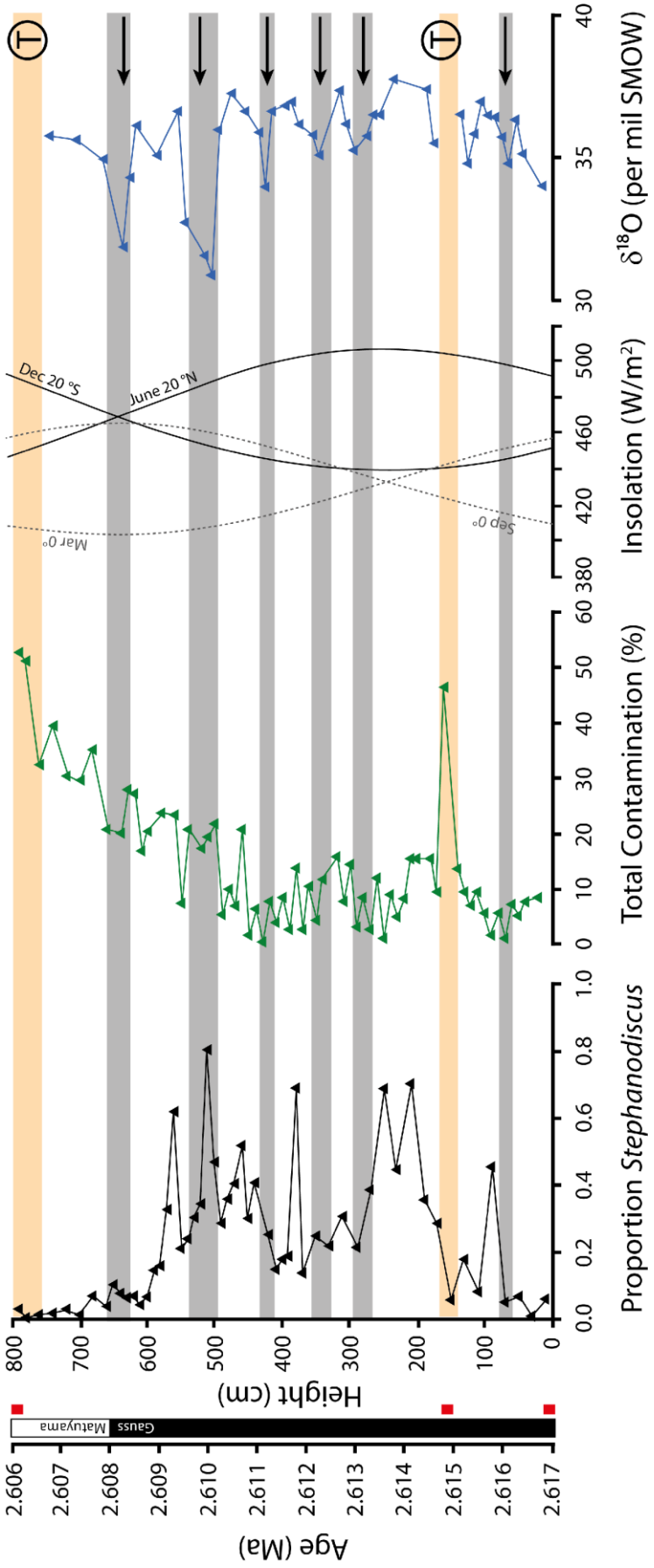

Figure 5.14 Compilation of results from high-resolution analysis of Barsemoi diatomite unit #4, sequence RE26. Diatom counts were performed by Dr. R. Edgar, Harvard University. The small proportions of diatom taxa other than *Aulacoseira* or *Stephanodiscus* (< 3%) mean that the changes presented above can be regarded as a proportional representation of *Aulacoseira* versus *Stephanodiscus*. Total contamination values are derived from the calculated abundance of clay and tephra contamination remaining within the purified samples. Summer insolation values shown for 20 °N and 20 °S and changes in March and September equatorial insolation (Laskar et al., 2004). Corrected $\delta^{18}O_{modelled}$ values are shown in blue. Positions of known tephra layers within the sequence are given by orange bars (T). Grey bars and black arrows illustrate millennial-scale wet-dry cycles inferred from corrected $\delta^{18}O_{diatom}$ values. Red squares highlight positions of $^{40}Ar/^{39}Ar$ dating (Deino et al., 2006).

al. (2006) to the diatomite #4 unit (described in chapter 3.5.2.), it is possible to approximate dates for the sequence. Based on three calibrated $^{40}Ar/^{39}Ar$ ages taken below, within and above diatomite #4, Deino et al. (2006) estimated a uniform sedimentation rate of 16 cm/kyr.

Fine scale laminae (on the order of a few hundred microns) are visible within the diatomites. These are particularly evident during the early stages of the cleaning process when layers are observed to peel away from one another when samples are submerged in liquid. Kingston et al. (2007) observe an apparent segregation within some samples between *Aulacoseira* and *Stephanodiscus* species and also note the presence of microlaminae within the Barsemoi diatomites. They attribute this as evidence for multi-annual cycling within the lake. Similar laminae have also been observed in the preliminary analyses of some diatomites from the Suguta Valley. SEM analysis of the Rupa diatomites from Suguta shows distinct seasonal couplets of diatom and clay layers (A. Junginger, pers. comm.). Such fine scale laminae are often a characteristic feature of diatomite deposits (e.g. McKenzie et al., 1980; O'Brien et al., 2002; Vilaclara et al., 2010). The presence of laminations within diatomite unit #4 is in no way quantifiable as an independent approximation of chronological control, however it does provide some indication of consistent palaeoenvironmental conditions and suggests that there was little variation in sedimentation rate throughout the sequence thus supporting the estimation of a uniform sedimentation rate by Deino et al. (2006).

By plotting the chronology of Deino et al. (2006) against the corrected $\delta^{18}O_{modelled}$ signal, it is possible to estimate a timescale for the cyclicity present within the $\delta^{18}O_{modelled}$ record. On the basis of these dates, diatomite #4 spans the period between 2.606 and 2.617 Ma. The cycles observed within the record occur on average every 1,380 years, marked by a total of six negative excursions in the $\delta^{18}O_{modelled}$ record. The negative excursions are of up to 5 ‰ in amplitude and are of relatively short duration. Following each excursion, $\delta^{18}O_{diatom}$ values recover towards a baseline value of 36 - 37 ‰ which is line with $\delta^{18}O_{diatom}$ reconstructions from other large African lakes characterised by highly evaporative conditions (e.g. Rietti-Shati et al., 1998; Barker et al., 2001; Street-Perrott et al., 2008).

As described in chapter 2.4.2, the isotopic composition of lakewater is influenced by the oxygen isotope composition of precipitation which in turn is controlled by temperature, seasonality and air-mass source region. In $\delta^{18}O_{diatom}$ records from tropical regions where there is little variation in seasonality or temperatures, changes in air-mass source region and

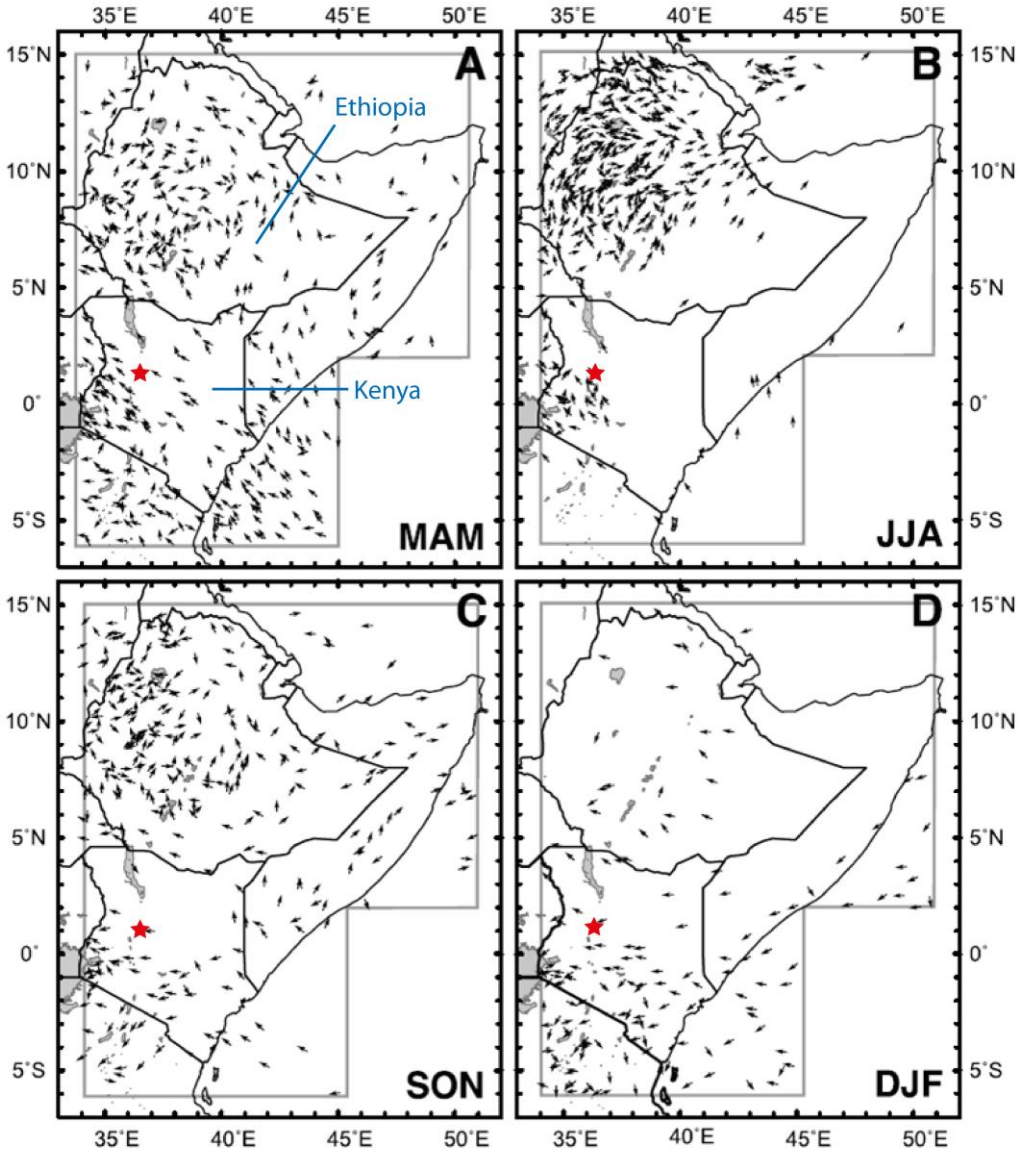

Figure 5.15 NCEP-derived 850hPa wind angle for mesoscale convective system events between 1998 and 2000, grouped by season. Red star marks the location of Lake Baringo in the Central Kenyan Rift. From Levin et al. (2009).

the relative balance between evaporation and precipitation become more important for determining changes in $\delta^{18}O_{lakewater}$, and therefore changes in $\delta^{18}O_{diatom}$ and $\delta^{18}O_{modelled}$. Negative excursions of up to 5 ‰ in the Barsemoi $\delta^{18}O_{modelled}$ record show that $\delta^{18}O_{lakewater}$ values underwent periods of markedly fresher values on average, every 1,380 years. These excursions are likely to have resulted from either a prolonged change in air-mass source region or from a relative increase in the dominance of precipitation over evaporation.

As outlined in chapter 3.3.2.2, studies of the modern isotopic composition of precipitation (Levin et al., 2009, 2010; Beck, 2010; Williams, 2010) show that rainfall in Kenya during both rainy seasons is associated with easterly and south-easterly winds derived from an

Indian Ocean source (figure 5.15). Levin et al. (2009) demonstrate that the difference between the $\delta^{18}O$ values of water from Kenya and Ethiopia is a function of differences in moisture sources. Ethiopia is subject to isotopically heavier transpired continental precipitation, ultimately derived from an Atlantic Ocean source, transported by the African monsoon during the months of June, July and August (figure 5.15). The influence of the African monsoon is generally restricted to the more northerly regions of East Africa in connection with the position of the Congo Air Boundary (CAB) (chapter 3.3.1.2; Nicholson, 1996; Kiage and Liu, 2006). In addition to the position of the CAB, moist westerly air is also prevented from reaching the central and eastern portions of Kenya due to blocking by the highlands of the western branch of the Great Rift Valley (Slingo et al., 2005), thus making it unlikely that rainfall associated with the African monsoon played a significant role in the past climate of the Baringo-Bogoria basin.

In order to invoke a shift in moisture source as a mechanism to explain the observed negative excursions in $\delta^{18}O_{modelled}$, an increased input of more isotopically negative precipitation is required. The modern distribution of precipitation over Kenya (see figure 3.6) and the nature of the changes in $\delta^{18}O_{modelled}$ suggest that this is unlikely since this would imply a relative increase in the input from the Indian Ocean, and require that a significant proportion of rainfall reaching the Tugen Hills came from the African monsoon in comparison to a reduced contribution from the Indian Ocean monsoonal system. Such a scenario would necessitate a major reorganisation of atmospheric circulation over equatorial Africa and thus seems improbable.

Allowing for minimal variations in seasonality, temperature and changes in moisture source, fluctuations in the relative balance between input (precipitation) and output (evaporation) seem to be the most likely mechanism for determining changes in $\delta^{18}O_{modelled}$. Heavier (more positive) values are therefore indicative of a relative increase in evaporation, or greater aridity, while lighter (more negative) $\delta^{18}O_{modelled}$ values reflect a relative increase in precipitation, likely linked to a strengthening in monsoonal circulation.

A comparison to the changes in diatom assemblage (figure 5.14) described in section 5.1.2 shows that, during periods when $\delta^{18}O_{modelled}$ values are markedly more negative and imply a freshening of palaeo-lake Baringo, the assemblage is dominated (usually >80 %, with the exception of ~ 2.610 Ma) by *Aulacoseira* species which, as outlined previously, tend to dominate when silica supply to the epilimnion is enhanced. Such an increase in nutrient supply would occur during periods of increased vertical mixing of the water column

(Kilham et al., 1986), driven by wind fetch and intensity and are consistent with the inference from the $\delta^{18}O_{modelled}$ values that the negative excursions denote periods of increased SW summer monsoonal circulation generating more rainfall in the East African Rift Valley.

5.4 Evolution of palaeo-lake Baringo

The high-resolution analysis of one of the Barsemoi diatomite units (diatomite #4) permits the detailed reconstruction of one of the five lake phases represented by the diatomite sequence. Whilst the previous sections have discussed the millennial-scale climate perturbations recorded within the $\delta^{18}O_{diatom}$ record, it is also important to contextualise the character of lake evolution as a whole. Previous analysis of variations in diatom assemblage (Kingston et al., 2007) suggests that there is a significant amount of variability occurring both within and between the diatom units (figure 4.1) with the highest proportions of *Stephanodiscus* species occurring in diatomite units #2 and #3 (median values of 0.69 and 0.57, respectively) whilst the two units bracketing the sequence (units #1 and #5) are characterised by far lower proportions of *Stephanodiscus* (medians of 0.11 and 0.07, respectively). Kingston et al. (2007) suggest that this is indicative of a longer-term cycling trend between 2.58 and 2.7 Ma, resulting from the eccentricity modulation of precessionally-controlled insolation shifts. However, without further detailed research into the remaining four Barsemoi diatomites, it is difficult to evaluate the extent to which the short-term climate variability observed within unit #4 is representative of all five lake phases.

Figure 5.16 shows the relative timings of the five Barsemoi diatomite units, superimposed on the LR04 global benthic stack (Lisiecki and Raymo, 2005) which highlights changes in high latitude glacial cycles during the Plio-Pleistocene and demonstrates that the timing and nature of the Baringo lake phases is not consistent with the obliquity-driven pacing of high latitude glaciations. Instead, as demonstrated by the dating of the five diatomite units, East African climate during this time was clearly linked to precession-driven forcing of low-latitude monsoonal circulation (Deino et al., 2006; Kingston et al., 2007). The chronology of Deino et al. (2006) suggests that the duration of the deep lake phases recorded by the Barsemoi diatomites were approximately 6 kyr, 6 kyr, 11 kyr, 11 kyr and 7 kyr (units 1 – 5, respectively). These timings correspond closely to half- and quarter- precessional cycles and are possibly representative of the presence of precessional harmonics in the amplitude of seasonal insolation. Such precessional harmonics have been previously shown to play an

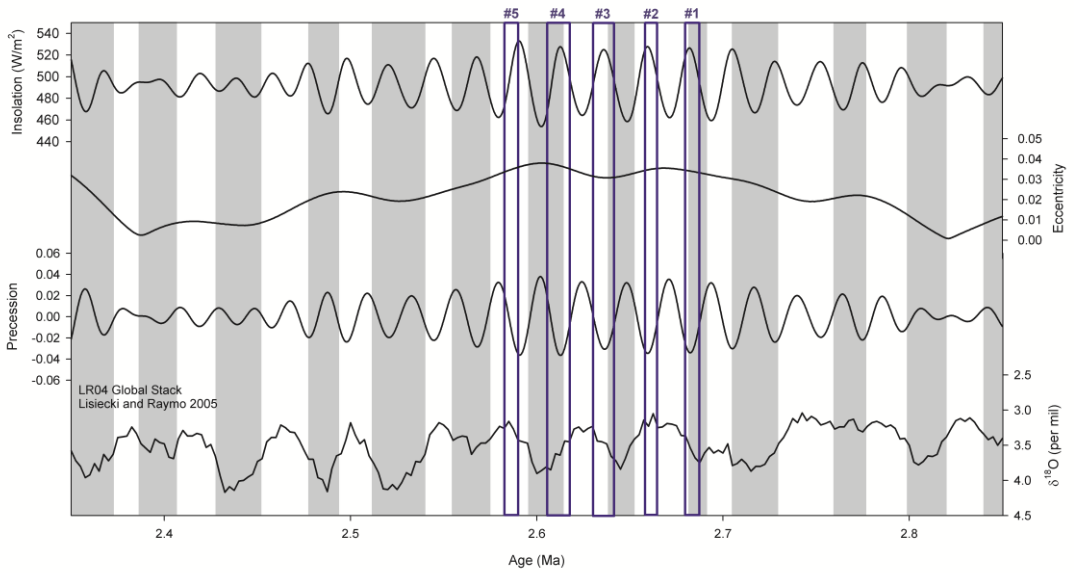

Figure 5.16 Long-term climatic setting of the five Barsemoi diatomite units juxtaposed against summer insolation (June 30 °N), eccentricity and precession and the global benthic $\delta^{18}O$ LR04 stack (Lisiecki and Raymo, 2005). Grey bars mark glacial periods and white bars are interglacials, according to the timings of Lisiecki and Raymo (2005). The five diatomite units coincide with precessional-modulated insolation maxima, but bear little relationship to high-latitude glacial stages.

important role in the modulation of the global climate signal (e.g. Berger et al., 2006, and references therein; Sun and Huang, 2006; Weber et al., 2010).

Verschuren et al. (2009) observe similar linkages in a 25 kyr record of moisture history from Lake Challa on the slopes of Mount Kilimanjaro. At a latitude of 3°19' S, Lake Challa experiences bimodal seasonal rainfall distribution with precipitation, from an Indian Ocean source, controlled by the NE and SE monsoons, analogous to that at observed at Lake Baringo and elsewhere within the Central Kenya Rift. By measuring the seismic reflection stratigraphy and the branched and isoprenoid tetraether (BIT) index of soil bacterial versus aquatic archaeal membrane lipids extracted from lake sediments, Verschuren et al. (2009) reconstruct the monsoonal history of equatorial East Africa over the last glacial cycle. They find low-latitude orbital forcing to be the primary control on regional climate over the last 25 kyr and suggest that high-latitude influences only challenged this dominant control during the Younger Dryas and Heinrich events. Alternate enhancement of the intensity of either the NE or SE monsoons means that the Lake Challa record exhibits a 'double-frequency' dynamic rainfall pattern with peaks in precipitation (at ~ 22.5, 11.5 and 1.5 kyr BP) occurring with a half-precessional periodicity of ~ 11,500-years (Verschuren et al., 2009). Berger et al. (2006) suggest that half- and quarter- precessional cycles of ~11.5 and ~5.5 kyr respectively are more important than previously considered for driving equatorial and intertropical climate variability.

The timings of the five diatomite units coincide with maxima in tropical insolation (June 20 °N) (figure 5.16). Based on modelling and proxy observations (e.g. Prell and Kutzbach, 1992; Vuille et al., 2005; Fleitmann et al., 2007; Wang et al., 2008b) which show a strong link between increases in insolation, Indian Ocean sea surface temperatures and SE monsoon strength, this was likely accompanied by a concurrent strengthening of monsoonal circulation in the Indian Ocean. However the precise nature of the causes for the formation and disappearance of such an extensive lake system remain unclear. It seems likely that some threshold effects exist which permit the rapid growth and persistence of deep freshwater lakes within the axial portion of the rift under certain conditions of minimum insolation which would reduce the impact of evaporation whilst maintaining sufficient precipitation levels to permit lake expansion.

Verschuren et al. (2009) note in their examination of a 25-kyr record of moisture balance from Lake Challa, that rainfall in equatorial East Africa is increased when the winter-summer inter-hemispheric insolation gradient is large or summer insolation reaches a maximum in either the northern or southern hemisphere (at 20 °N or 20 °S). The resulting intensification in either of the two monsoons, leading to high rainfall and wetter conditions, is recorded in the BIT index from Lake Challa. Deino et al. (2006) and Kingston et al. (2007) also note the importance of the correlation between maximum lake extent in palaeo-lake Baringo and summer insolation maxima at 30 °N. Examination of tropical and equatorial insolation levels in the context of the results from diatomite unit #4 (figure 5.14) show that lake development coincided with increasing summer insolation at 20 °N and a likely intensification of the SE summer monsoon. This early phase of the lake cycle, coincident with peak summer insolation (from 2.617 until 2.610 Ma), appears to be marked by a period of relative stability with total contamination values of less than 15%, punctuated by millennial-scale wet-dry cycles. After 2.610 Ma, summer insolation at 20 °N starts to decrease, total contamination levels increase (largely due to increased catchment influx of clay – see figure 5.13) and the nature of the wet-dry cycles become more extreme and climate more variable, marked by negative excursions in $\delta^{18}O_{diatom}$ of up to 5 ‰.

Variations in local equatorial insolation during March and September may have played a significant role in controlling regional drought. Verschuren et al. (2009) suggest that rainfall is reduced in equatorial East Africa when the inter-hemispheric insolation gradient is modest and neither the NE or SE monsoon is intensified. A coincident minimum in March or September equatorial insolation could result in the failure of the preceding rainy season,

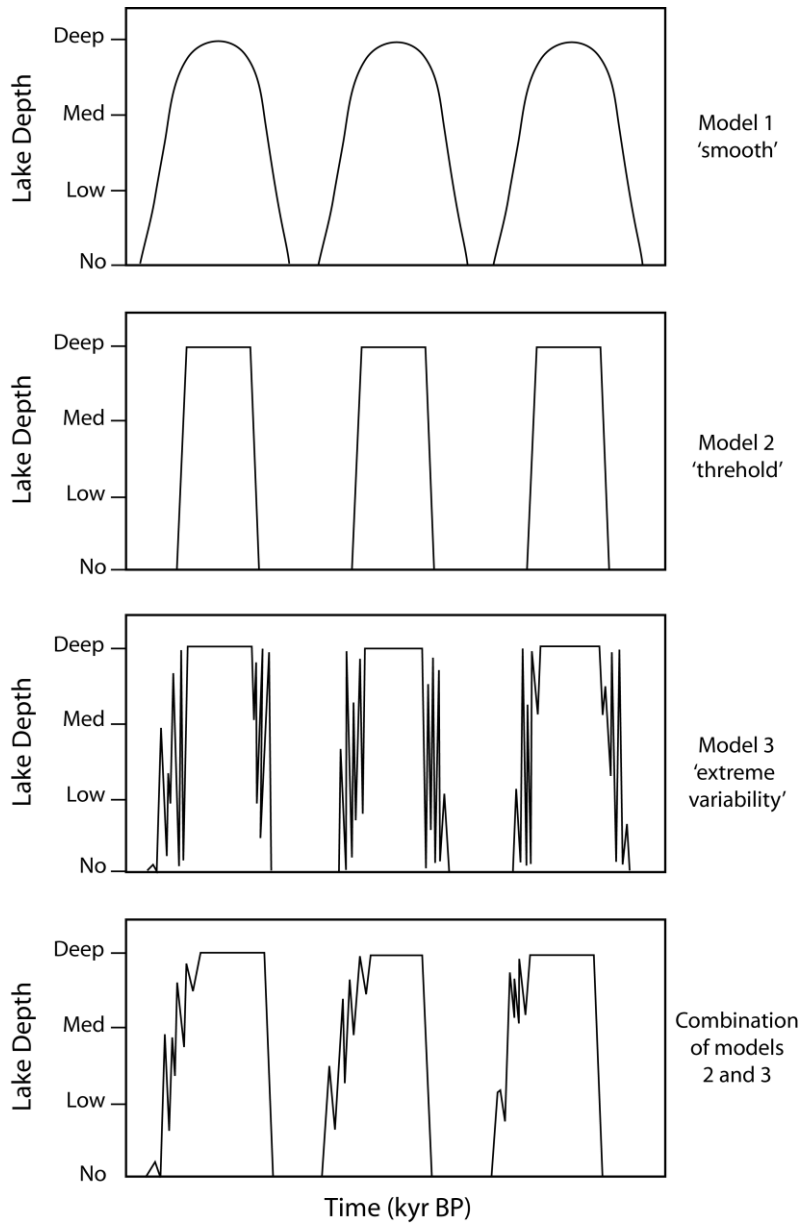

Figure 5.17 Conceptual models showing theoretical changes in the development of East African rift valley lakes during the Plio-Pleistocene., after Maslin and Christensen (2007) and Maslin and Trauth (2009). Model 1 shows 'smooth' and relatively gradual transitions between high and low lake stands; Model 2 illustrates a theoretical 'threshold' scenario whereby there are rapid transitions between wet and dry conditions. Model 3 suggests that there are two stable states (deep lakes and no lakes) and that the transition between these two states is characterised by 'extreme variability' or fluctuations between the wet and dry conditions. The lowermost model represents the scenario which best characterises the lake development suggested by the stratigraphic and isotopic analysis of diatomite unit #4 whereby the lake 'appears' very rapidly and a more gradual 'disappearance' of the lake is marked by wet-dry cycles which show a corresponding increase in amplitude. Modified from Maslin and Trauth (2009).

leading to greater incidences of drought (Verschuren et al., 2009). Concurrent with decreasing summer insolation values, local insolation during March reaches minimum values between 2.609 and 2.606 Ma (figure 5.14). A possible increase in the number of

incidences of drought in line with an overall weakening in the intensity of the SE summer monsoon would have had profound consequences for the lake-system which, given its high evaporative potential, would likely have responded rapidly to large-scale shifts in the precipitation-evaporation balance. An increase in summer insolation at 20 °S after 2.610 Ma, and corresponding intensification in the strength of the winter monsoon is unlikely to have been sufficient to account for the overall trend towards a lowering of lake levels. As suggested for the factors which lead to the development and growth of the lake system, it is likely that there were also intrinsic (e.g. geomorphological changes in the lake basin) or extrinsic (e.g. monsoonal circulation changes) threshold effects which influenced the disappearance of palaeo-lake Baringo.

As outlined above, the role played by tropical and equatorial insolation in modulating rift-lake development and disappearance appears to have controlled the long-term evolution of palaeo-lake Baringo and dominated the character of climate variability within the Rift Valley. However the influence of high-latitude climate in the Northern Hemisphere, through 'D-O like' oscillations originating in the North Atlantic, also seems to have been an important control in the pacing of millennial-scale wet-dry cycles observed within the $\delta^{18}O_{modelled}$ record.

Maslin and co-workers (Maslin and Christensen, 2007; Maslin and Trauth, 2009) present a series of three hypothetical models of lake response to orbital forcing which they discuss in terms of possible implications for evolutionary theory (figure 5.17). Whilst it is not possible to properly evaluate the proposed models on the basis of high-resolution analysis from only one diatomite unit, the findings from Barsemoi unit #4 appear to support a fourth scenario whereby lake growth and development bears close resemblance to the 'threshold' model but the lake disappearance phase is more similar to that of the 'extreme climate variability' model (figure 5.17). However, further analysis of the remaining Barsemoi diatomite units is required in order to properly test this hypothesis.

5.5 Millennial-scale cyclicity in the Barsemoi diatomite sequence

Once corrected for the effects of contamination, the results of oxygen isotope analyses conducted on Barsemoi diatomite #4 reveal a series of sub-Milankovitch scale oscillations which occur with a mean frequency of 1,380 ± 600 years (figure 5.14). This cyclicity is marked by negative excursions in the oxygen isotope signal of up to 5‰ which indicate the presence of a persistent millennial-scale climate oscillation manifested as periods of relative

wetness or relative aridity. Fluctuations between the different modes are abrupt, marking rapid changes in the hydrological balance of the lake system. Other rift valley lakes, such as palaeo-lake Suguta, have been shown to respond extremely rapidly to changes in tropical monsoonal circulation driven by insolation forcing. Trauth et al. (2010) describe such rift valley lakes as 'amplifier lakes' whereby high catchment precipitation levels are offset by the high evaporation rates in the lake area. Such lake systems are able to rapidly respond to precessionally-forced climate shifts linked to the intensity of the tropical monsoons, particularly in equatorial regions where the climate is characterised by bimodal rainfall distribution linked to the northward and southward passages of the ITCZ. In the Suguta Valley, the dating of palaeo-shorelines from the Holocene suggests that abrupt drops in lake level of between 30 to 100 m occurred within 50 to 100 years during the African Humid Period (AHP) and that at the termination of the AHP the lake dried out completely (equivalent to a 250 m drop in lake level) over a period of 1,600 years (Junginger et al., 2010). Coupled with the high evaporative potential of the modern Lake Baringo (>2600 mm/yr; see chapter 3.2), it is possible to envisage how large rift valley lake systems, such as palaeo-lake Suguta or palaeo-lake Baringo were able to respond so rapidly to shorter-term climate fluctuations.

The periodicity of the cycles in the Barsemoi diatomite $\delta^{18}O$ record is similar to that of Dansgaard-Oeschger (D-O) oscillations, which constitute a dominant mode of abrupt climate change evident in many palaeoclimate records from the late Pleistocene, particularly in and around the North Atlantic region (Bond et al., 1999). The large-scale temperature variations associated with D-O events are regarded as a consequence of changes in the state of thermohaline circulation in the North Atlantic, possibly triggered by the periodic input of freshwater in the high northern latitudes. The effects of D-O events are not restricted to the high latitudes, and are also evident in tropical and subtropical climate patterns through monsoon-related changes in upwelling, ocean ventilation, aeolian dust and productivity archives (Alley et al., 1999; Sirocko et al., 1999).

The timing of diatomite #4 between 2.617 – 2.606 Ma demonstrates that a large freshwater lake occupied the Baringo-Bogoria basin during the early part of the glacial stage MIS 104 (2.614 – 2.595 Ma; Lisiecki and Raymo, 2005). The existence of a large lake basin in the East African Rift Valley at this time is in contrast to the typical arid conditions experienced in Africa during high latitude glaciations. An analysis of pollen from ODP Site 658 from Cap Blanc off the coast of West Africa indicates that MIS 104 was marked by high percentages of vegetative taxa such as *Ephedra*, Asteraceae Tubuliflorae, Caryophyllaceae

and Chenopodiaceae-Amaranthaceae, which are characteristic of drier conditions and suggest that Northwest Africa experienced aridity during this time (Leroy and Dupont, 1997). Leroy and Dupont (1997) suggest that a shift towards obliquity-driven climate forcing occurred after or around ~ 2.6 Ma and that after this point regular vegetation shifts occur in line with glacial-interglacial transitions. Palynological analyses from South West Africa (ODP Site 1082) support these findings and suggest that Late Pliocene-Early Pleistocene cold stages (MIS G4, 104, 100, 96, 92 and 88) were marked by periodic increases in semi-desert and desert pollen taxa superimposed on a longer-term trend of aridification and desertification and an increase in climate variability after 2.7 Ma (Dupont et al., 2005; Dupont 2006). Evidence from the North Atlantic (Kleiven et al., 2002; Thierens et al., 2011) suggests that there was substantial ice sheet expansion in the high northern latitudes during MIS 104. An increase in ice-rafting debris present in sediments from the Porcupine Seabight off the South West coast of Ireland documents the repeated presence of a British-Irish ice sheet since 2.6 Ma (Thierens et al., 2011). This suggests that the ice-margins during the early Pleistocene glacial were much further south than previously thought.

5.5.1 The manifestation of millennial-scale cyclicity in African palaeoclimate records

In order to understand the manifestation of millennial-scale climate variability in equatorial regions, it is necessary to examine climate records that document D-O events during the last 50 ka due to the paucity of Pliocene-aged climate records which exhibit millennial-scale variability in the low latitudes (see Chapter 1.5). There is widespread evidence that climate forcing in the D-O bandwidth affected both hemispheres, however the origin and mechanisms responsible for global teleconnections are poorly understood. Whilst many records, particularly from Europe and Northern Asia, suggest that D-O events are the result of a meteorological response to episodic decreases in North Atlantic sea surface temperatures, palaeoclimate records from some other regions seem to be more closely associated with climate variability in the Southern Hemisphere. For example, Leuschner and Sirocko (2000) suggest that D-O scale humid periods recorded in sediment cores from the Arabian Sea may be correlated with temperature maxima in the Antarctic Vostok ice core implying that the low frequency, sub-Milankovitch forcing of the Indian Ocean monsoon is associated with the Southern Hemisphere. However, other studies have found that a close coupling exists between the Arabian Sea and the North Atlantic. Records from elsewhere in the Arabian Sea show that changes are linked to abrupt temperature changes in Greenland

and that there is a strong expression of D-O cyclicity within low-latitude climate variability indicating that atmospheric moisture and other greenhouse gases may play an important role in propagating the effects of millennial-scale climate change in the North Atlantic to other parts of the globe (von Rad et al., 1995; Sirocko et al., 1996; Schulz et al., 1998; Schulte and Müller, 2001).

The majority of palaeoclimate records from equatorial Africa which document 1-2 kyr cyclicity, like that evident in the Baringo $\delta^{18}O$ record, indicate that during glacial stadials, African climate is largely typified by enhanced aridity (e.g. Stager et al., 1997, 2002; Johnson et al., 2002, 2004, 2010; Holmgren et al., 2003; Barker et al., 2007; Brown et al., 2007; Burnett et al., in press). Analysis of $\delta^{18}O_{diatom}$ data from Lake Malawi (10-15°S, 34.5°E) reveal multi-centennial to millennial-scale wet-dry intervals, which occur approximately every 2.3 kyr throughout the last 25 ka such that arid periods in Lake Malawi can be correlated to cold episodes documented in the GISP2 Greenland ice core record (Barker et al., 2007). Analysis of diatom productivity (Johnson et al., 2004) and Zr/Ti and Si/Ti records (Brown et al., 2007) from the same lake also demonstrate that episodes of relative aridity at Lake Malawi occur during Greenland stadials and are consistent with southward shifts in the mean position of the ITCZ and associated changes in meridional temperature gradients. Stager et al. (1997, 2002) have shown by analysis of the diatom record from Lake Victoria that, during cool interstadials and Heinrich events, the lake experienced periods of enhanced aridity and episodes of dessication. This pattern has also been observed in other locations throughout the African continent. Evidence for rapid climate oscillations has been found in Cameroon margin sediments where Fe/Ca ratios are used as a proxy for terrestrial versus marine sediment fluxes linked to West African monsoon variability and document abrupt changes in precipitation over West and Central Africa over the last 52 ka (Adegbie et al., 2003). Faunal sea surface temperature records from ODP Site 658 on the West African margin also document abrupt millennial-scale cooling events during the Holocene (deMenocal et al., 2000). Street-Perrott and Perrott (1990) link periods of prolonged drought in the Sahel to episodes of decreased temperature and salinity in the North Atlantic resulting from a glacial shutdown in the formation of North Atlantic deep water (NADW). By reconstructing aeolian and fluvial sedimentation patterns off the coast of Senegal over the last 57 ka, Mulitza et al. (2008) also find that the abrupt onset of aridity in the Western Sahel was linked to cold sea surface temperatures in the North Atlantic, associated with cold Heinrich Stadials.

However, not all palaeoclimate proxy records support the interpretation that glacial stadials are marked by arid conditions in Africa. A pollen record from Lake Masoko in southern Tanzania suggests that, whilst the Last Glacial Maximum was characterised by dry conditions, tree cover was most developed during the Younger Dryas and that wetter conditions prevailed during this time in response to a southward shift in the African rainfall belt (Garcin et al., 2006). Additionally, analysis of a 5,400-yr record geochemical record from Lake Edward finds a non-linear correlation with Northern Hemisphere climate change, such that both warm and cold extremes of the North Atlantic's 1,500-yr cycle are marked by periods of drought in equatorial Africa (Russell and Johnson, 2005).

Older records from the Mid-Late Pleistocene also indicate that glacial stadials were marked by enhanced aridification in Africa, resulting from cooler Atlantic Ocean sea surface temperatures (e.g. deMenocal 1995, 2004; Schefuss et al., 2003; Dupont et al., 2005; Dupont 2006; Scholz et al., 2007; Burnett et al., in press; Stone et al., in press). A long-term record of C_4 plant abundance derived from compound-specific carbon isotope variations in sediments from ODP Site 1077 in the Southeast Atlantic demonstrates that large-scale changes in African vegetation patterns between 1.2 – 0.45 Ma are closely linked to changes in tropical sea surface temperatures and the strength of the African monsoon (Schefuss et al., 2003). Scholz et al. (2007) describe arid episodes between 135 and 75 ka when lake level indicators such as ostracod abundance and total organic carbon (TOC) content suggest that water volume in Lake Malawi was reduced by at least 95%, far more arid than the conditions of the LGM. Similar analysis of a 90,000-yr record from Lake Tanganyika (Burnett et al., in press) shows that lake levels prior to ~90 ka were highly variable and that extreme arid conditions led to a decrease in lake level in excess of 400 m (lake levels during the LGM fell by 250-300 m). This preceded a period of more stable lake levels after ~88 ka, linked to a reduction in precession-driven insolation forcing (Burnett et al., in press).

By analysing continuous long-term records from Lake Malawi, Lake Tanganyika and Lake Bosumtwi, Scholz et al. (2007) suggest that a high-eccentricity interval between ~145-70 ka was responsible for generating high precession-scale variability in East African lake levels during this time. The precessionally-forced nature and timing of the Barsemoi diatomite sequence between 2.55 and 2.68 Ma also coincides with a period of high eccentricity values (figure 5.16). In addition to this, an earlier diatomite preserved within the Chemeron Formation can be correlated to the previous eccentricity maxima at ~ 3.05 Ma (Kingston et al., 2007). These findings from the Baringo basin support the hypothesis of Scholz et al.

(2007) and provide further evidence for the importance of eccentricity maxima in driving periods of precessional climate variability in East Africa.

5.5.2 Mechanisms for millennial-scale cyclicity

Millennial-scale climate variations are too short and occur too frequently to be explained by orbital forcing. It is therefore necessary to search for an alternative explanation for these 'sub-Milankovitch' events. Late Pleistocene D-O cycles follow a ~ 1,470 ± 532 yr periodicity and are particularly pronounced during glacial stages, when they are closely coupled with Heinrich events i.e. phases of surging of the Laurentide ice sheet through the Hudson Strait (Bond et al., 1993, 1999; Alley et al., 1999).

Modelling experiments (e.g. Paillard and Labeyrie, 1994; Sakai and Peltier, 1997; Ganopolski and Rahmstorf, 2001) and palaeoceanographic proxy data studies (e.g. Bond and Lotti, 1995; van Kreveld et al., 2000) suggest that D-O oscillation is an oceanic process, triggered by the release of meltwater pulses that result in switches in the thermohaline circulation mode of the North Atlantic. Episodic cooling and warming associated with the D-O oscillation would have had a widespread impact on regions such as Europe and the tropics which experience a strong atmospheric response to changes in the North Atlantic (Alley et al., 1999; Clark et al., 1999). However, the precise forcing mechanism responsible for the origin and persistence of D-O cycles through time is not clearly understood. Bond et al. (1999) suggest that the recurrence of D-O events is the result of amplification and modulation of a pervasive underlying 1-2 kyr climate cycle rather than being the result of ice sheet instability as proposed by Broecker (1994). Alley et al. (1999) also support the idea that the D-O oscillation is a persistent oceanic process amplified during times of intermediate ice sheet growth which is centred on the North Atlantic and propagated globally by atmospheric and oceanic feedbacks.

Other suggestions invoke internally-forced oscillations of the ocean-atmosphere system (Sakai and Peltier, 1997; Maslin et al., 2001; Schulz et al., 2002) or an ongoing cyclical process induced by external solar forcing (Hoyt and Schatten, 1993; van Geel et al., 1999; Bond et al., 2001). Synchronous variations in the production rate of cosmogenic nuclides (^{10}Be and ^{14}C) and stacked records of marine ice drift are suggestive of an underlying 1,500-year cycle in solar irradiance, at least during the Holocene, implying that the Earth's climate system is highly sensitive to even weak perturbations in insolation (Bond et al., 2001). Sirocko et al. (1999) suggest that a low-latitude equivalent to D-O cycles, related to changes

in monsoon intensity and ventilation of Pacific intermediate waters, is more likely to be linked to the El Niño Southern Oscillation and associated changes in the position of the subtropical/subpolar jet stream. Despite the lack of a clear understanding of the mechanism responsible for D-O events, it is clear from palaeoclimate records that millennial-scale cyclicity on the order of ~ 1-2 kyr persisted throughout much of the Pleistocene.

Bartoli et al. (2006) compare records of millennial-scale climate variability both prior to and after the iNHG (placed at 2.82 – 2.95 Ma). The authors hypothesised that if D-O oscillations are triggered by Northern Hemisphere ice sheet instabilities, then they should not be present in records older than the iNHG. However, if D-O events are driven by solar cyclicities, such as those present during the Holocene (Bond et al., 2001; Sarnthein et al., 2003), then the cycles should be present prior to the iNHG. Their findings suggest that synglacial cycles with periodicities similar to D-O oscillations only occurred after MIS G14 (ca. 2.88 Ma) implying a causal link to ice sheet instability in the high northern latitudes. The presence of substantial ice sheets in the Northern Hemisphere during MIS 104 and evidence for ice-rafting during this stage (Kleiven et al., 2002; Thierens et al., 2011) suggests that, similar to Late Pleistocene D-O cycles, millennial-scale cooling episodes linked to meltwater pulsing in the North Atlantic provide a feasible explanation for the cyclicity observed within the Barsemoi Diatomites. Whilst this points to a North Atlantic origin for the millennial-scale 'D-O' signal during the Late Pliocene, further research on the nature of sub-orbital cyclicities operating on older timescales is required before it is possible to ascertain the precise driving forces behind them.

5.5.2.1 Teleconnection mechanisms between the North Atlantic and Indian Oceans

Modern day precipitation in Kenya is derived from an Indian Ocean moisture source (see chapter 3.3.2.2, Nicholson 1996; Levin et al., 2009, 2010; Williams 2010). If these findings are applied to the Late Pliocene, then it is necessary to find a mechanism which might explain the propagation of abrupt climate change in the North Atlantic region to the low-latitudes, particularly to the Indian Ocean monsoonal system. Alley et al. (1999) postulate that millennial-scale changes in North Atlantic oceanic circulation are transmitted to the tropical monsoonal regions through the oceans and the atmosphere. This signal is further amplified and modified by various feedback mechanisms which propagate the changes throughout the Northern and Southern Hemispheres. Given the rapidity of the global response to D-O oscillations in the Late Quaternary (e.g. Schulz et al., 1998), transmission of this signal via atmospheric forcing is arguably more likely.

The synchroneity of events between the North Atlantic and the Indian Ocean and Asian monsoonal systems has led to the suggestion that the two regions are linked via a direct atmospheric mechanism such as the strength of the Westerly storm track across Eurasia (Porter & An, 1995; An & Porter, 1997; Schulz et al., 1998; Gupta et al., 2003). The zonal Westerlies are caused by an eastward deflection of northward flowing air which develops as a result of the inter-hemispheric temperature gradient generated by more intense heating of the equatorial regions than occurs at the poles. Modelling studies have demonstrated the importance of the Westerlies and the Tibetan Plateau in modulating atmospheric circulation between the Asian continent and the North Atlantic (e.g. Kutzbach et al., 1989, 1993; Ruddiman & Kutzbach, 1989; Guo et al., 1996; Ding and Wang, 2005; Li et al., 2008; Bothe et al., 2010; Zhu et al., 2011).

During glacial stadials, cool North Atlantic temperatures and disruption to thermohaline circulation lead to increased westerly flow of cold air over Eurasia. The stronger Westerlies cause an intensification of the NE winter monsoon over the Indian Ocean and weaken the strength of the Tibet low. This leads to a reduction in the inter-hemispheric pressure gradient and a relative weakening in the strength of the SW summer monsoon and a reduction in moisture transport over East Africa (Fang et al., 1999). During interstadials, the above scenario is reversed and the SW summer monsoon is intensified leading to increased rainfall over East Africa and India, and a corresponding weakening of the NE winter monsoon (Overpeck et al., 1996).

The Westerlies provide a feasible atmospheric mechanism for the transmission of millennial-scale changes from the North Atlantic Ocean to the Indian Ocean. However, given the paucity of evidence documenting millennial-scale climatic cycles during the Pliocene, it is not possible to be certain of the exact nature of the mechanisms driving these changes and a great deal more evidence is required in order to better understand the manifestation and nature of these short-term climate oscillations on older timescales.

5.5.3 Millennial-scale cyclicity during the Pliocene

As outlined in chapter 1.5, scientific understanding of sub-orbital climate variability during the Late Pliocene, around the time of the iNHG, has thus far been limited by a paucity of palaeoclimate archives which offer the potential to investigate environmental change at high-resolution (records summarised in table 5.3). With the notable exception of the older sediments (~ 4.3-6.8 Ma) from the Ptolemais Basin, NW Greece (Steenbrink et al., 2003;

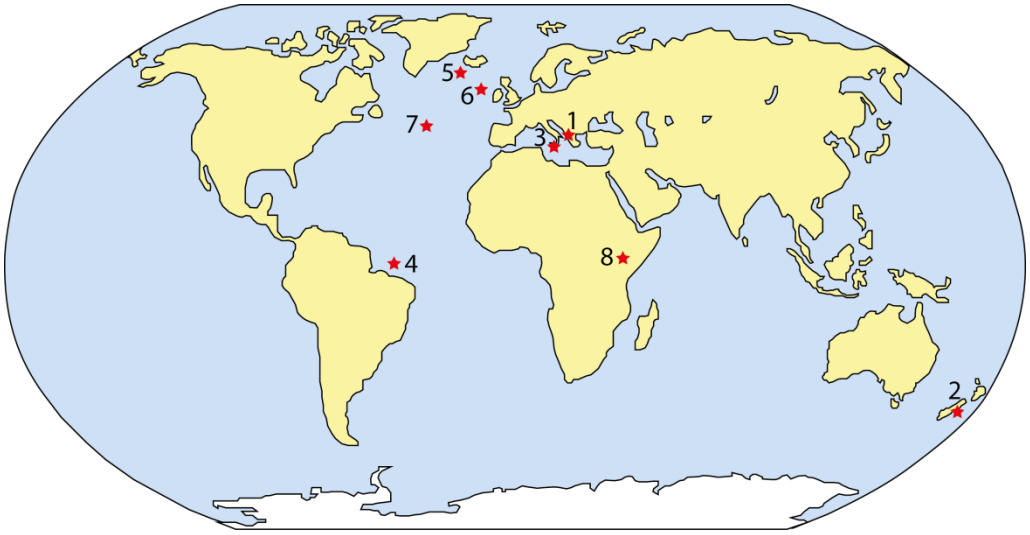

No.	Location	Proxy	Study Interval	Climatic Bandwidth	Reference
1.	Ptolemais Basin, Greece	i). Colour reflectance	~ 4.35–4.23 Ma	~11, ~5.5, ~2 kyr	Steenbrink et al. (2003)
		ii). Pollen	~ 4.33-4.31 Ma	~10, ~2.5, ~1.5 kyr	Kloosterboer-van Hoeve et al. (2006)
		iii).	~ 6.85-6.57 Ma ~ 6.46-5.98 Ma	~ 1.5-8 kyr	Weber et al. (2010)
2.	ODP Site 1119, SW Pacific Ocean, E of New Zealand	Gamma ray signal	3.9 – 0 Ma	~ 1-2 kyr	Carter and Gammon (2004)
3.	Monte San Nicola, Sicily	Foraminiferal oxygen isotopes (benthic and planktonic)	~ 2.56-2.50 Ma	~ 3–5 kyr	Becker et al. (2005, 2006)
4.	ODP Site 925, Ceara Rise, W equatorial Atlantic Ocean	Foraminiferal oxygen isotopes (planktonic)	4.24 – 4.13 Ma	~ 8-4 kyr	Niemitz and Billups (2005)
5.	ODP Site 984, Reykjanes Ridge	Magnetic susceptibility, foraminiferal oxygen isotopes (planktonic)	~ 3.1-2.5 Ma	500±100, 900±100 yr (prior to 2.9 Ma) 1470, 2900, 4400 yr (after 2.9 Ma)	Bartoli et al. (2006)
	ODP Site 983, Gardar Drift	Foraminiferal oxygen isotopes (benthic), IRD counts	1.93-1.75 Ma	~ 2-5 kyr	McIntyre et al. (2001)
6.	ODP Site 981, North Atlantic Ocean	Foraminiferal oxygen isotopes (benthic and planktonic), IRD counts	i). ~ 3.3-3.1 Ma	~ 1-2 kyr	Draut et al. (2003)
			ii). 2.48-2.56 Ma	~ 1.5-2 kyr	Becker et al. (2006)
7.	IODP U1313, North Atlantic Ocean	Foraminiferal oxygen isotopes (planktonic)	~ 2.6-2.4 Ma	~ 1.8-6.2 kyr	Bolton et al. (2010)
8.	Baringo-Bogoria Basin	Diatom oxygen isotopes	2.606–2.617 Ma	~ 1.4 kyr	This Study

Table 5.3 Summary and map of Pliocene-aged records of millennial-scale climate oscillations

Kloosterboer-van Hoeve et al., 2006; Weber et al., 2010), those studies which do document evidence for millennial-scale cycling during the Pliocene are restricted to the marine realm and are largely concentrated in the North Atlantic Ocean. The $\delta^{18}O_{diatom}$ analysis of the Barsemoi diatomites offers a rare opportunity to understand the manifestation of millennial-scale cycles in a terrestrial and equatorial framework during the Late Pliocene. From this record it is evident the Earth's climate has oscillated on millennial timescales since at least the Late Pliocene and that periods of extreme climate variability operate on both longer (precessional) and shorter (millennial) frequencies.

In the context of the records discussed in chapter 1.5 and summarised in table 5.3, the most prominent sub-orbital periodicity is between 1 and 2 kyr in duration (e.g. Draut et al., 2003; Carter and Gammon, 2004; Bartoli et al., 2006; Becker et al., 2006; Bolton et al., 2010). This closely parallels the timing of the Late Pleistocene D-O cycles and is in line with the pacing of the cyclicity observed within diatomite unit #4. The results from the Barsemoi Diatomites not only support previous findings of evidence for the existence of millennial-scale climate cycles in the Late Pliocene but also provide evidence that the effects of these oscillations were propagated beyond the North Atlantic region. The abrupt nature of the fluctuations between relatively wet and dry conditions at Lake Baringo is also similar to the lake responses to D-O oscillations reported from other parts of East Africa (see section 5.4.1 and references therein) where 'amplifier lakes' have been shown to respond rapidly to moderate and extreme shifts in climate (Trauth et al., 2010). Given the variation observed within the sediments of the Chemeron Formation, it is likely that the palaeo-lake Baringo was just such an 'amplifier' lake and that rapid changes in lake morphology in response to climate would have had a significant impact on the surrounding biosphere.

Due to a lack of high-resolution data spanning MIS104 and uncertainty associated with the dating of the diatomite sequence, it is not possible at this stage to correlate the cycles observed at Baringo with any of the North Atlantic records in order to further investigate potential causal mechanisms. Additionally the relatively short duration of the unit #4 record (11 kyr) and number of cycles (n=6) preclude the long-term investigation of such cycles over multiple glacial stages. Similar high-resolution analyses of the remaining diatomite units, including additional high-resolution measurements of sedimentary properties using gamma-ray logging techniques, would permit the further assessment of lower-order climatic cycling during both high-latitude glacial (units #1 and #4) and interglacial (units #2, #3 and #5) (figure 5.16).

5.6 Summary

The work presented here demonstrates the importance of adopting quantitative geochemical analysis techniques, such as XRF, to assess the geochemical signature of contamination remaining within purified samples of diatom silica. Multivariate statistical analysis of the geochemical spectra from the analysed samples confirmed the presence of two different contaminants, clay and tephra, within Barsemoi diatomite unit #4. The development of a three end-member model based on elemental oxide abundance data has enabled the determination of the levels of contamination within the samples and the subsequent application of an isotopic correction to the raw $\delta^{18}O_{diatom}$ values in order to more accurately model the nature of climate-driven changes in $\delta^{18}O_{modelled}$.

Changes in $\delta^{18}O_{modelled}$ values record fluctuations in the isotopic composition of palaeo-lake Baringo. Variations in $\delta^{18}O_{modelled}$ reflect changes in the relative balance between precipitation and evaporation at palaeo-lake Baringo and indicate that the humid period between 2.617 and 2.606 Ma was punctuated by wet-dry cycles that lasted approximately 1,400 years. Periods of more negative $\delta^{18}O_{modelled}$ values coincide with a relative dominance (>70 %) in the abundance of *Aulacoseira* species and imply a freshening of palaeo-lake Baringo through a relative increase in precipitation levels via strengthening of the SE summer monsoon. This is supported by changes in diatom assemblage which, based on correlations with the contemporary habitat and hydrological preferences of the *Aulacoseira* and *Stephanodiscus* genera, indicate that *Aulacoseira* dominate during periods when Si supply to the epilimnion is enhanced, such as during times of greater wind-induced vertical mixing in the water column, as might be expected with intensified monsoonal circulation.

The timescale and nature of these cycles is similar in nature to the Dansgaard-Oeschger cycles widely documented in palaeoclimate archives from the Late Quaternary. D-O events are linked to meltwater pulses in the North Atlantic during glacial stadials which drive changes in thermohaline circulation and result in abrupt changes in sea surface temperatures. Equatorial palaeoclimate records largely show that, during Late Quaternary D-O events, climate in East Africa was typified by periodic arid episodes which correspond to decreases in Atlantic Ocean sea surface temperature. Whilst the mechanism responsible for the propagation of the effects of D-O events to other parts of the globe remain unclear, it is evident (c.f. Leuschner & Sirocko, 2000) that they can affect all parts of East Africa and the Indian Ocean. It is thus plausible that during the glacial cycles of the Late Pliocene

following the iNHG, similar sub-Milankovitch cyclicity existed within global climate patterns.

Evaluation of the longer-term evolution of palaeo-lake Baringo suggests that the rhythmic growth and disappearance of the lake was closely linked to tropical summer insolation at 20-30 °N The demise of the lake represented by diatomite unit #4 seems to have been linked to falling summer insolation levels, coupled with a coincident minima in local equatorial insolation during March, which could have lead to increased incidences of drought due to the failure of the summer rainy season (‘long rains’).

Chapter 6: The Arabian Sea

6.1 Introduction

Much of the early scientific understanding of palaeoclimate changes on glacial-interglacial timescales was focussed on climate archives from the high-latitude regions, particularly in the Northern Hemisphere. Until relatively recently the influence of the tropics and low-latitudes on global climate was poorly understood and considered to be largely passive, however a number of studies have now demonstrated that these regions play an important role in modulating and propagating the effects of climate change throughout both the northern and southern hemispheres (e.g. Prell and Kutzbach, 1992; deMenocal 1995, 2004; Schulz et al., 1998; Wang et al., 2008b; Schott et al., 2009). The interactions between the tropical Indian Ocean and the atmosphere are important for shaping regional and global climate patterns, and the close proximity of the Arabian Sea to the arid and semi-arid areas of eastern and northern Africa, the Arabian Peninsula and the Indian sub-continent make it an ideal location to investigate changes in low-latitude climate.

As described in chapter 3.3, climate in the region is dominated by the intensity of the Asian and Indian Ocean monsoons. The Indian Ocean monsoon has a significant impact on the dynamics of low-latitude climate across a broad geographical area. The seasonal reversal of atmospheric circulation and precipitation distribution that gives rise to the monsoon generates major rainy periods in East Africa. Differential land-ocean heating results in the formation of a low pressure cell over the Tibetan Plateau and a high pressure cell over the Indian Ocean. Coupled with latent heating of the troposphere, this drives the formation of the monsoon which enables regional cyclonic circulation to prevail during boreal summer. This drives the seasonal upwelling of cold, nutrient-rich waters along the margin of the Arabian sub-continent and transports dust into the Arabian Sea (figure 6.1), adding a terrigenous component to the sediment record. The orographic effects of the Tibetan Plateau interact with regional anticyclonic circulation to reduce coastal upwelling in the Arabian Sea during boreal winter (Hastenrath, 1985).

Evidence of past changes in the dynamics of the Indian Ocean monsoon is derived from sedimentary archives of upwelling intensity and of dust and pollen input into the Arabian Sea. Previous studies have attempted to address fluctuations in the aeolian dust flux linked to continental aridity in Arabia and East Africa (Clemens et al., 1991; deMenocal et al.,

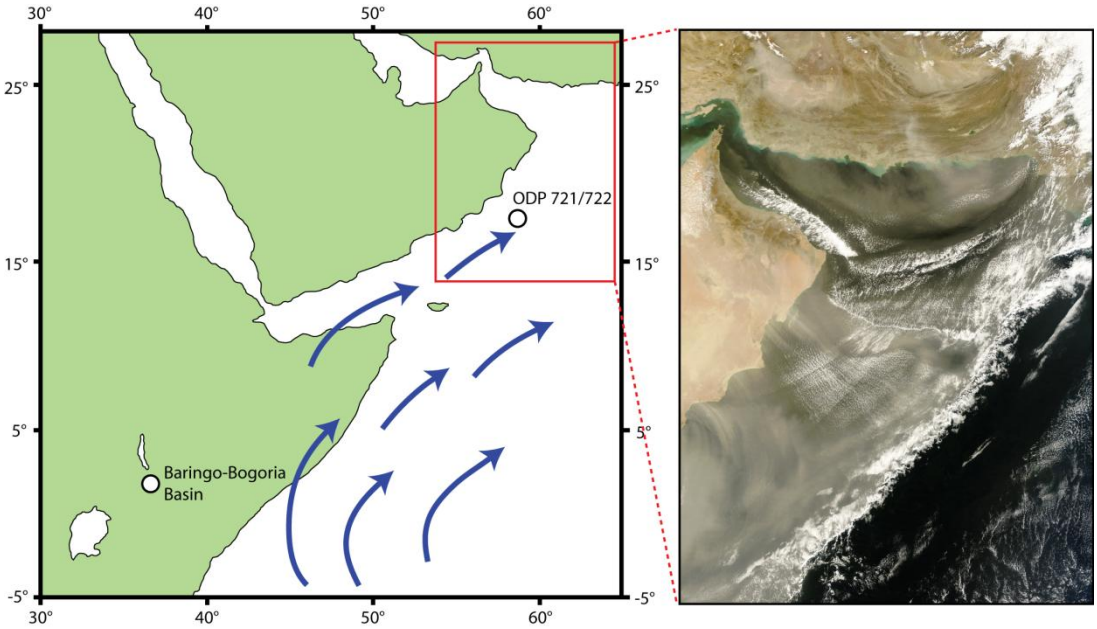

Figure 6.1 Map illustrating relative positions of the Baringo-Bogoria basin and ODP Sites 721 and 722 in the Arabian. Blue arrows mark dominant wind directions during Indian Ocean summer monsoon which generates 'long rains' in the East African Rift Valley and largely controls dust supply to the Arabian Sea. MODIS Satellite image shows offshore transport of aeolian dust to the Arabian Sea. Image courtesy of NASA (http://visibleearth.nasa.gov/).

1991; deMenocal 1995, 2004; Clemens and Prell, 2003) and analysis of variations in major and minor element geochemistry has also shown that the dust flux into the Arabian Sea from the surrounding deserts is controlled by the intensity of Indian Ocean monsoonal circulation (Shimmield and Mowbray, 1991; Sirocko et al., 2000). In order to assess the wider context of changes in tropical monsoonal circulation during the Late Pliocene and Early Pleistocene, with respect to the precessionally-forced cycling of palaeo-lake Baringo, the following three chapters detail the high-resolution analysis of ocean cores from Ocean Drilling Program (ODP) Sites 721 and 722, drilled on the Owen Ridge in the Arabian Sea.

6.2 The Owen Ridge – ODP Sites 721 and 722

The Owen Ridge is an asymmetric northeast-trending ridge situated approximately 300 km from the coast of Oman (figure 6.2). It lies obliquely parallel to the passive Arabian Margin and is bounded by the Indus Fan to the east and by the Owen Basin to the west. The ridge originates at 15° 30' N, 59° 50' E at the point where the Owen Fracture Zone is intersected by the Sharbithat Ridge, and extends to approximately 20 °N, 61 °E where it merges with the Murray Ridge (Leg 117 Shipboard Scientific Party, 1989). The crest of the ridge lies at water depths of between 1900 m and 2100 m below sea level, and rises 1200-1600 m above the Owen Basin and more than 2000 m above the surface of the Indus Fan (figure 6.3).

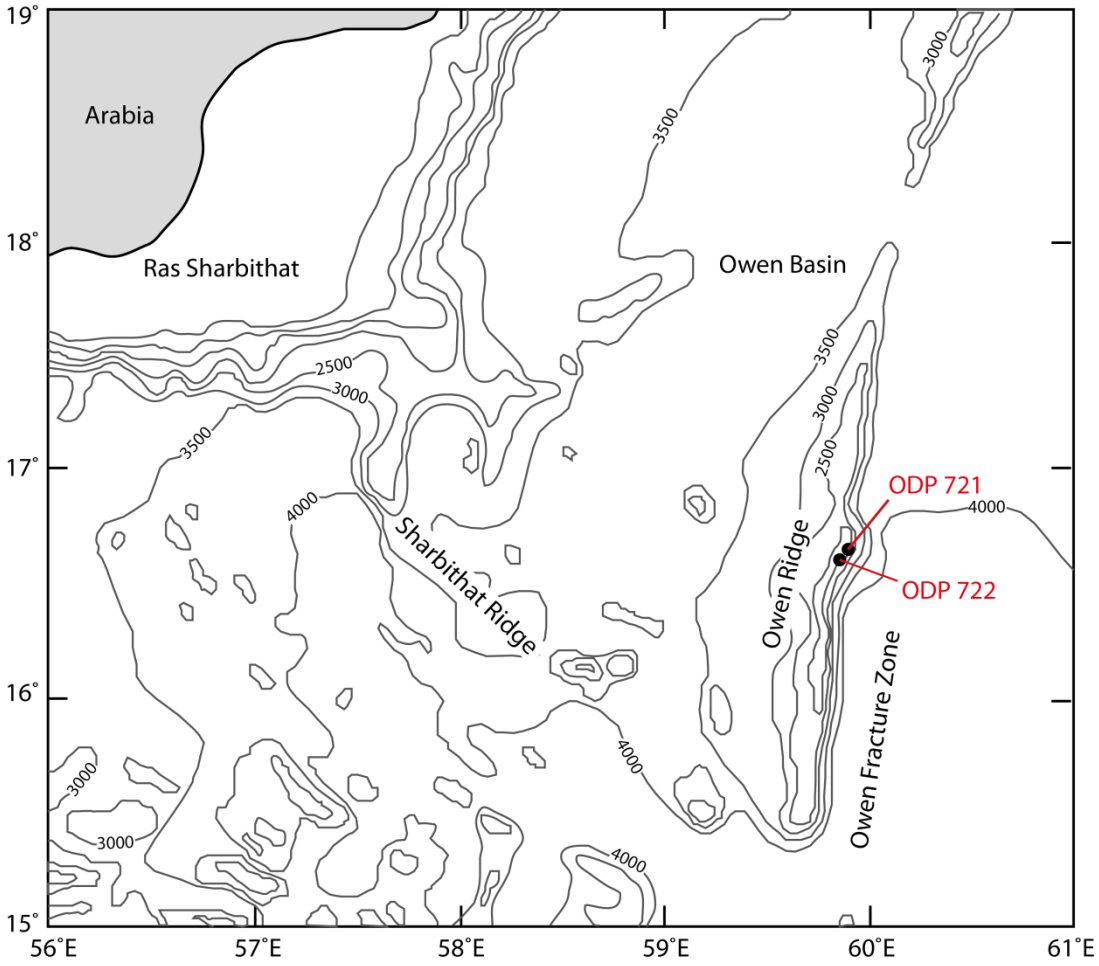

Figure 6.2 Regional bathymetric setting of the Owen Ridge within the Arabian Sea. Positions of ODP drill Sites 721 and 722 are marked. Redrawn and modified from Leg 117 Shipboard Scientific Party (1989).

The structure is capped by deposits of thick, subhorizontal pelagic sediments with a rich terrigenous mineral component resulting from the high concentrations of mineral aerosols transported over the Arabian Sea. The steeply-dipping (~ 15°) eastern escarpment of the ridge is bounded by the Owen Fracture Zone, a transform fault which runs along the eastern boundary of the Arabian tectonic plate, separating it from the Indo-Australian and African plates (Matthews, 1966). The western flank of the ridge dips more gently (~ 4°) and merges with the Owen Basin (figure 6.3). It is characterised by a complex network of eastward-trending valleys containing slump deposits of displaced sediment. The origin of the Owen Ridge and the underlying bedrock is linked to both the separation of India and Madagascar and to the seafloor spreading that began in the middle Cenozoic. The Owen Fracture Zone is believed to have been the major transform dividing the spreading centres to the north and south of the Arabian Margin.

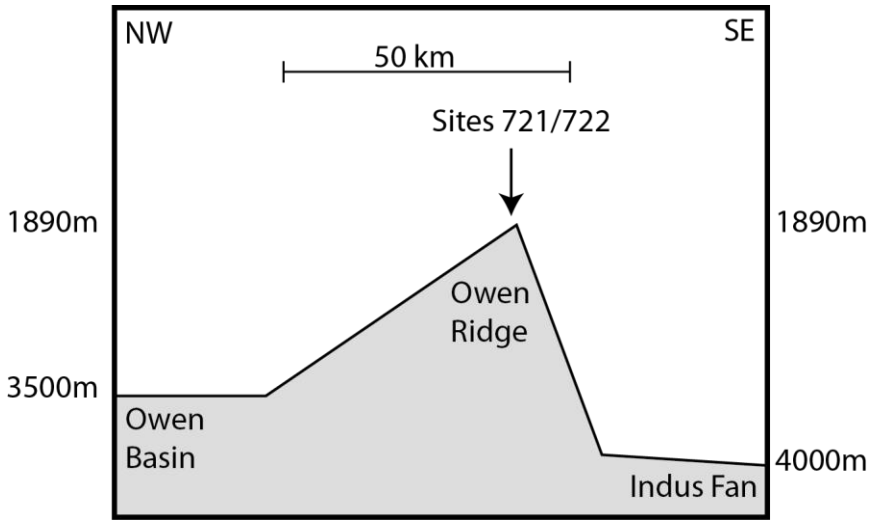

Figure 6.3 Schematic profile of Owen Ridge, perpendicular to the ridge axis showing the relative elevation of ODP Sites 721 and 722 compared to the surrounding ocean basin. The elevated site location ensures fluvial input to ODP Sites 721 and 722 is minimal. Illustration not to scale. Redrawn from Clemens and Prell (1991).

Current scientific understanding of the uplift history of the Owen Ridge is based partly on drilling results from Deep Sea Drilling Program (DSDP) Site 224 (Whitmarsh et al., 1974) and partly on seismic data from the ODP Leg 117 (Leg 117 Shipboard Scientific Party, 1989). The basal trachybasalt and hyaloclastic breccia basement rocks underlying the Owen Ridge are Triassic-Jurassic in age and are overlain by late Palaeocene tuffaceous clays and Eocene lamprophyric igneous rocks. Overlying turbidite beds that grade into pelagic sediments were deposited in the Upper Oligocene and Lower Miocene. These sediments have since been tilted westward and uplifted along the Owen Fracture Zone as a result of compression caused by changes in the spreading direction associated with tectonic activity related to the ongoing collision between the Indian and Eurasian plates and the opening of the Gulf of Aden (Whitmarsh, 1979). This led to uplift of the Owen Ridge, the rate of which was likely to have been relatively rapid during the late Miocene and to have decreased significantly during the Pliocene (Hermelin, 1990). Since the late Neogene, the ridge crest has acted as a platform for the accumulation of pelagic, carbonate-rich sediments.

ODP Sites 721 (16°40.636'N, 59°51.879'E; water depth 1,945 m) and 722 (16°37.312'N, 59°47.755'E; water depth 2,028 m) are located near the crest of the Owen Ridge (figure 6.2). They were drilled in 1987 as part of ODP Leg 117 to the western Arabian Sea and Oman Margin. The sites are located approximately 9.5 km apart. Due to their close proximity and as a result of significant hiatuses (up to 1.9 m) in the cores, sediment from Sites 721 and 722 are combined to create a composite depth model (Murray and Prell, 1991, 1992). All the

sites on the ridge crest are shallower than the regional carbonate lysocline which lies at a water depth of 3,300 m (Cullen and Prell, 1984) meaning that palaeoenvironmental interpretations based on carbonate organisms such as foraminifera should not be biased by major dissolution changes. Pelagic carbonates account for 50 – 80 % of the sediments and are diluted by a lithogenic mineral component delivered via aeolian transport to the ridge (Leg 117 Shipboard Scientific Party, 1989). The elevated position of the Owen Ridge, relative to the surrounding ocean floor, ensures that fluvial transport of terrigenous material is minimal. Previous work on sediments from the Owen Ridge has demonstrated that the lithogenic component is composed of sediments of aeolian origin (Clemens and Prell, 1991) and that 80 % of the flux of aeolian minerals to the Arabian Sea floor occurs during the southwest monsoon months of June –September (Nair et al., 1989; deMenocal et al., 1991). Mineralogical studies suggest that the Arabian and Somali peninsulas and the Iran-Pakistan region are all important source areas for the aeolian dust component that is transported into the Arabian Sea (Kolla et al. 1981) and that spatially, the highest aerosol concentrations are found over the Gulf of Oman and off the Omani coast, specifically in the area of the Owen Ridge (Pease et al. 1998). Examination of the record of aeolian transport and deposition on the Owen Ridge provides a palaeoclimatic insight into the relative strengths of the summer (SW) and winter (NE) monsoons in Northeast Africa and Arabia over the past few million years.

6.3 Modern Climatic Setting

As detailed in chapter 3.3, much of the climatic variability experienced in low-latitude regions is governed by monsoonal circulation, particularly in Central Africa, India, China, Japan and Southeast Asia which are all impacted by the Asian monsoons. Monsoons develop as a function of a significant land-ocean temperature difference as the heat capacity of land is smaller than that of the ocean. Warming of large continental landmasses generates convective heating of the atmosphere above creating an overlying low pressure cell. Meanwhile, air over nearby oceans is denser, more humid and under higher pressure, creating an upper level pressure gradient between the two systems. In order to maintain atmospheric balance, there is a constant air flow from high pressure areas into low pressure areas in the form of monsoonal winds. The cycle is completed by the upper level atmosphere flow of air from the top of the low pressure cell to high pressure areas. A seasonal reversal of these atmospheric circulation patterns occurs during the winter months when land surfaces cool quickly in response to cooler weather conditions. The phenomenon of monsoonal circulation is particularly pronounced in areas surrounding the Tibetan

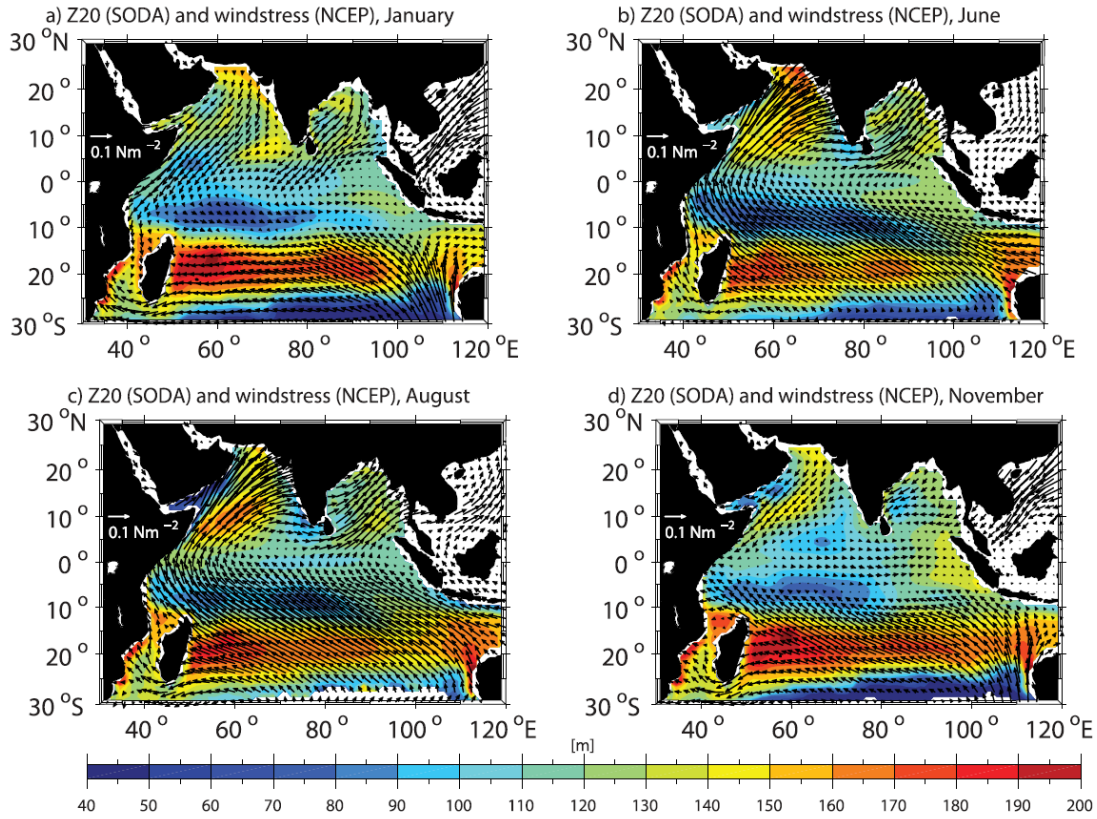

Figure 6.4 Monsoon wind stress fields for a) January, b) June, c) August and d) November. Climatology (vectors) data from National Centre for Environmental Prediction (NCEP) for 1990-1998. Colours show relative depths of 20 °C isotherm from Simple Ocean Data Assimilation (SODA). From Schott et al. (2009).

Plateau, producing the East Asian monsoon and the Indian Ocean monsoon. Meteorological observations demonstrate a common southern hemisphere Indian Ocean moisture source for both the Indian Ocean and East Asian summer monsoons (Wajsowicz and Schopf, 2001; Ding et al., 2004; Ding and Chan, 2005; Liu and Tang, 2005; Park et al., 2007)

6.3.1 Indian Ocean monsoonal circulation

The climatic setting of the Arabian Sea is characterised by the seasonal variability of the monsoonal circulation system in the Indian Ocean. The monsoon is predominantly wind-driven but is also modified by heat and freshwater fluxes (figure 6.4) (Schott and McCreary, 2001). Sensible heating of the Asian landmass coupled with latent heating within the troposphere over Asia results in a differential land-ocean temperature gradient during the boreal spring and summer months and causes a strong atmospheric low pressure cell to develop over the Tibetan Plateau, relative to a higher pressure area over the southern subtropical Indian Ocean. Latent heat is transported across the equator in low-level

monsoon flow and released as precipitation when the moisture-laden clouds reach the Himalayan foothills, which enhances the strength of the Tibetan low cell and the northeast-southwest pressure gradient established by differential sensible heating (Cadet and Diehl, 1984; Hastenrath and Greischar, 1993). As such, the latent heat source is believed to have been a critical factor in driving palaeomonsoon variability (Clemens and Prell, 2003). The annual development of the summer monsoon is delayed by the northward migration of the high-level subtropical jet stream (Hastenrath, 1985). As summer progresses the jet stream moves northward to higher latitudes and must eventually pass the substantial obstacle posed by the Himalayan Mountains. Once it has done so, it reforms over Central Asia and a cyclonic summer monsoon cell forms over the Indian Ocean (Hastenrath, 1985). Cyclonic circulation associated with the low pressure cell over the Tibetan Plateau generates strong southwesterly winds over the Arabian Sea during boreal summer forming the Indian Ocean summer (SW) monsoon. The strength of the monsoonal circulation controls the wind fields and the amount of precipitation delivered to many areas of Southern Asia. The intensity of the monsoon has been linked to the orographic effects of the Himalayan Mountains and the Tibetan Plateau which act to enhance the convergence of convective moisture and latent heat. The summer monsoon in the Arabian Sea typically lasts from June until mid-September and the associated southwesterly winds (figure 6.4) drive strong upwelling systems in coastal and open-ocean areas of the Arabian Sea (see section 6.4). This consequently impacts upon a range of oceanographic variables such as sea surface temperature (SST), nutrient content, productivity and mixed layer depth (Dickey et al., 1998). In addition, the strong winds (in excess of 10 ms^{-1}) and close proximity of numerous arid regions lead to the delivery of a large flux of dust from the Somali and Arabian Peninsulas into the Arabian Sea during the summer monsoon season (figure 6.1) (Sirocko and Sarnthein, 1989; Clemens, 1998; Clemens and Prell, 1991, 2003). The area to the north of the Persian Gulf is also particularly associated with dust transport to the Arabian Sea when local 'Shamal' winds blow from Iraq and Kuwait, generating intense dust storms between May and July (Clemens, 1998). The annual dust flux from these winds alone is estimated to be 105 x 10^6 metric tons (Sirocko and Sarnthein, 1989).

During the winter season (December until February), the pattern of atmospheric circulation is reversed (figure 6.4) and the land cools relative to the surrounding oceans, generating a broad high-pressure cell over the Tibetan Plateau. The interaction of the resulting anticyclonic circulation with the orographic effects of the Tibetan Plateau and the regional Hadley circulation produces cold, dry, intense northeasterly trade winds over Southern Asia and the Northern Indian Ocean between October and April (Hastenrath, 1985). These

northeasterly winds are considerably weaker (~ 5 ms^{-1}) than the summer southwesterly monsoon winds and are associated with less moisture transport. The NE winter monsoon winds blow from the strong high-pressure cell over the Tibetan Plateau to the region of low pressure associated with the southern-most extent of the Intertropical Convergence Zone (ITCZ) at approximately 12 °S. At this time, dust deposition and coastal upwelling are reduced in the Arabian Sea (Clemens, 1998).

The Indian Ocean monsoons have profound and far-reaching effects across Africa and Southern Asia. Concurrent with the northward migration of the Intertropical Convergence Zone, the summer monsoonal winds are concentrated into a high-speed jet stream (the Findlater Jet) which flows out from the East African Highlands towards the Arabian Sea and is concomitant with the arrival of moist air and the 'long rains' season to areas of Central East Africa between April and June (Bruce et al., 1994) (see chapter 3.3).

6.3.2 The aeolian dust flux

The presence of mineral or soil aerosols in the atmosphere is recognised as an active component of the global climate system and is important for mediating physical and biogeochemical exchanges between the atmosphere, land and ocean. This is best exhibited in the discovery that the amount of dust trapped within polar ice varies by more than an order of magnitude on glacial-interglacial timescales (Petit et al., 1990, 1999). Thus, dust could have been a critical factor in past climate changes and in addition, may contribute to climate changes in the future (Harrison et al., 2001). Dust is normally composed of a mixture of biogenic matter, such as diatoms, and minerals including quartz, clay minerals, calcite, gypsum and iron oxides occurring either as individual mineral grains or mixed aggregates, the chemical and optical properties of which are indicative of source area.

Mineral dust aerosols are entrained into the atmosphere by wind activity over areas of sparse vegetation cover such as North Africa and the Arabian Peninsula (figure 6.1). The largest natural sources of mineral aerosols are in the arid and semi-arid environments of the tropics and subtropics, principally the Sahara-Sahel region of Northern Africa and the Gobi-Taklamakan desert in Central Asia. It is estimated that approximately 30% of the total continental landmass, covering an area of 50 x 10^6 km^2, is a potential source for dust entrainment (Sokolik and Toon, 1996). After deposition on the ocean surface, the downward vertical flux of lithogenic particles is controlled by the production, sinking, scavenging and deposition of biogenic matter (Nair, 2006).

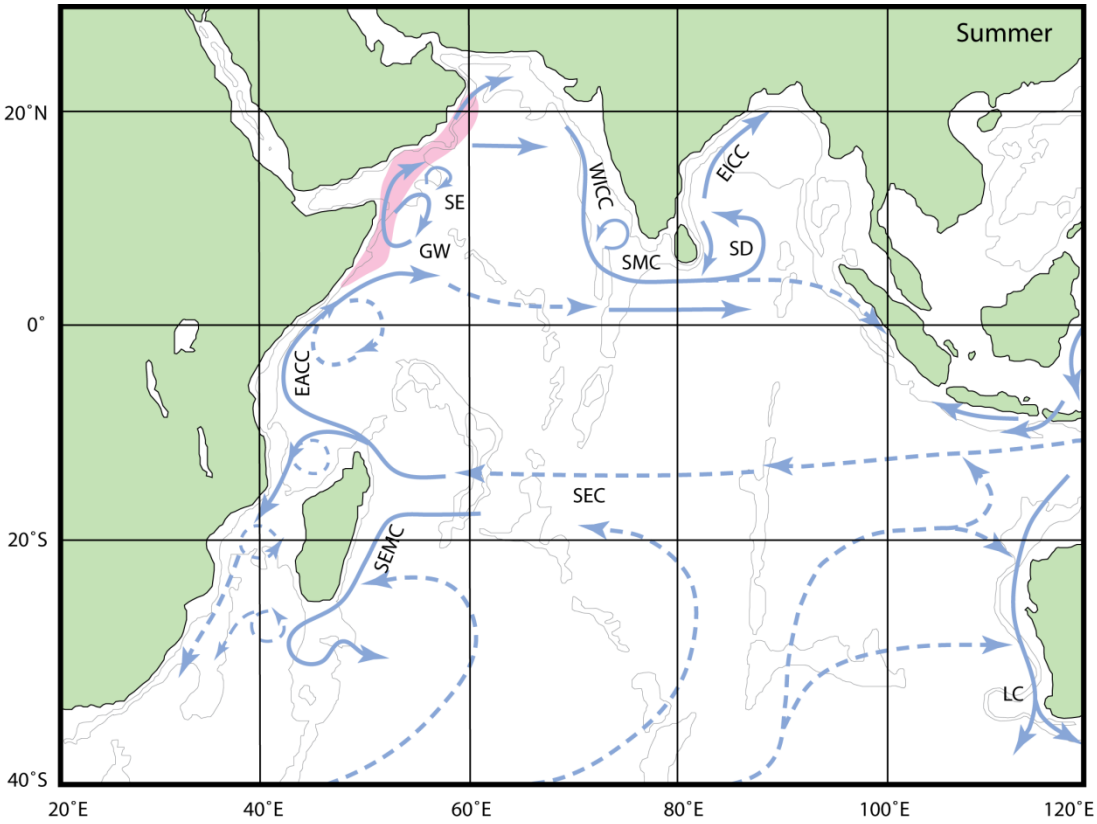

Figure 6.5 Schematic representation of surface water circulation in the Indian Ocean during the summer (SW) monsoon season between July and August. Currents indicated by blue arrows are the South Equatorial Current (SEC), the Southeast Madagascar Current (SEMC), the East African Coastal Current (EACC), Leeuwin Current (LC), West and East India Coastal Currents (WICC and EICC), Southwest Monsoon Current (SMC) and the Socotra Eddy (SE) and Great Whirl (GW). Upwelling areas along the Arabian Margin and Somali coast are shown in pink. Redrawn from Schott and McCreary (2001).

Strong southwesterly winds over Arabia and Northeast Africa during the SW summer monsoon result in the entrainment and transport of large quantities of dust into the northwest Arabian Sea (Sirocko and Sarnthein, 1989). Sediment trap data has demonstrated that 80% of the lithogenic flux of dust to the seafloor occurs during the peak summer monsoon months of June, July and August, implying an instantaneous transfer of the atmospheric dust signal to the sediment record (Nair et al., 1989). Satellite imagery and geochemical analyses of aerosol particles indicates that dust deposited in the Arabian Sea originates from arid regions in Arabia, the Persian Gulf and the Somali Peninsula (Sirocko and Sarnthein, 1989; Clemens, 1998). Lithogenic mineral grains entrained into the Arabian Sea by aeolian transport are carried in winds at heights of 1-2 km within the troposphere and can be transported for thousands of kilometres before deposition. Whilst the Indus River in Northwest India is the dominant sediment source for terrigenous material transported into the northern and eastern Indian Ocean basins, there is no significant input of fluvial material to the northwestern

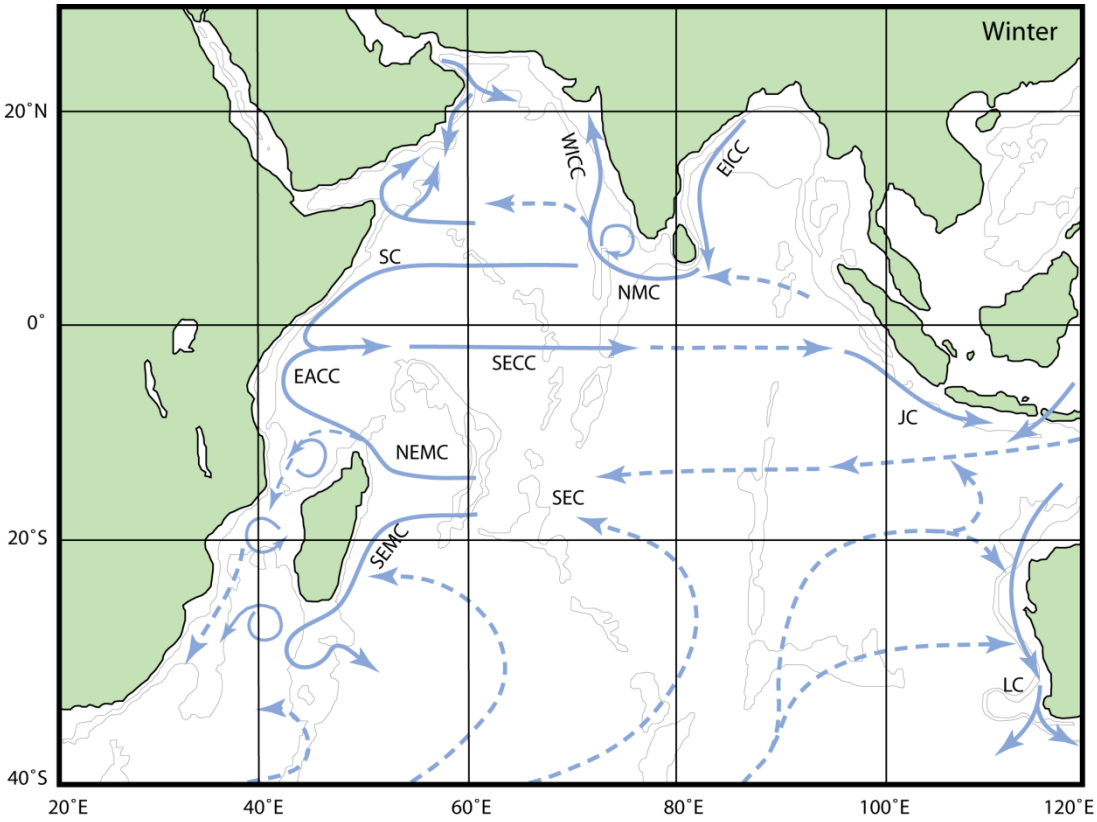

Figure 6.6 Schematic representation of surface currents in the Indian Ocean during the winter monsoon season (December to February). Current acronyms as for figure 6.5 with the addition of the Northeast Madagascar Current (NEMC), the South Equatorial Countercurrent (SECC), South Java Current (JC), Somali Current (SC) and Northeast Monsoon Current (NMC). Redrawn from Schott and McCreary (2001).

Arabian Sea due to the barrier effectively imposed by the Owen Ridge (Clemens and Prell, 1990). Core studies suggest that lithogenic material deposited in the northwest Arabian Sea, including on the Owen Ridge, is dominantly aeolian in origin and that it is transported almost exclusively during the summer monsoon season (deMenocal et al., 1991; Clemens et al., 1991; Clemens and Prell, 2003). The strong winds generated by seasonal monsoon circulation, coupled with the close proximity to arid source regions makes the Arabian Sea an ideal location to assess past changes in the aeolian transport of lithogenic material.

6.4 Oceanographic Setting

6.4.1 Indian Ocean circulation

Circulation in the Indian Ocean is characterised by two oceanic gyres generating asymmetric circulation patterns about the equator. In the northern hemisphere, circular

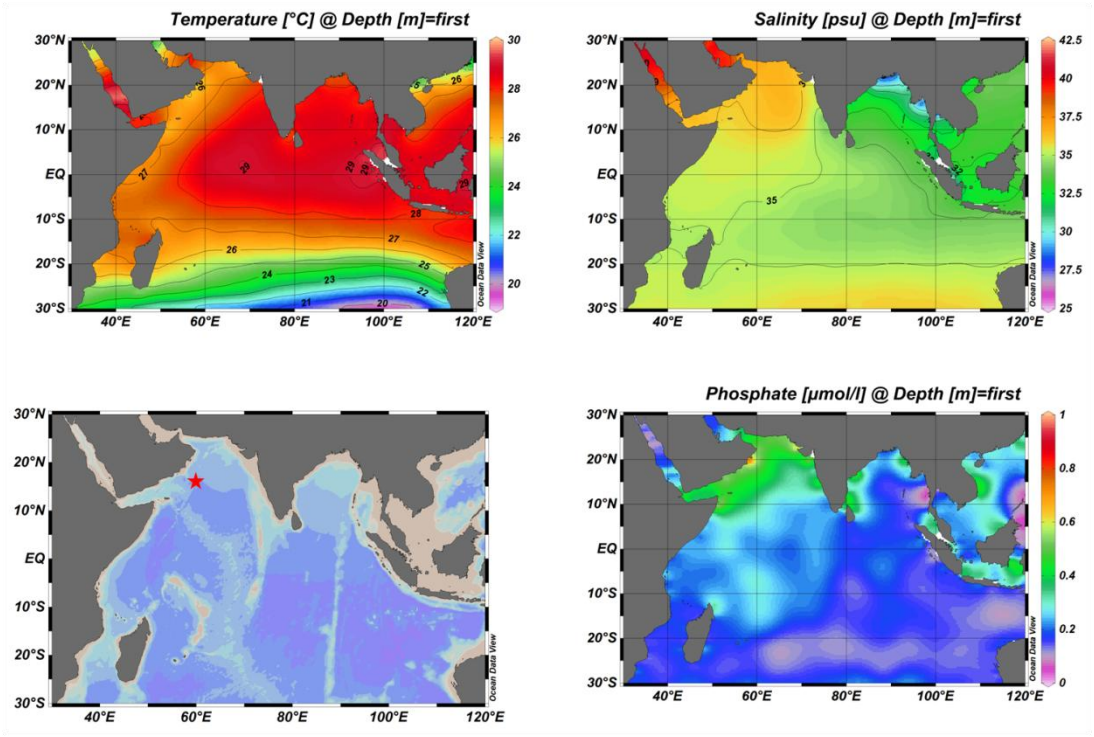

Figure 6.7 Variations in surface water parameters of the tropical and northern Indian Ocean. Figures show variations in sea surface temperature and salinity and nutrient (phosphate) concentration. The Arabian Sea is characterised by higher salinities and more nutrient-rich waters, upwelled along the Arabian margin as a result of the strong winds associated with the Indian Ocean summer (SW) monsoon. Position of red star in lower left bathymetric map marks the location of ODP Sites 721 and 722 on the Owen Ridge. Data from Ocean Data View v.4.3 (Schlitzer, 2010).

clockwise flowing currents are dominant whereas in the southern hemisphere, currents are reversed and a more substantial subtropical gyre is influenced by influx from the Southern Ocean (figures 6.5 and 6.6). During the winter monsoon season in the northern hemisphere, currents are reversed as high pressure over Central Asia from cool, descending air generates northeasterly winds and anticlockwise surface water currents. Three fundamental types of water mass can be distinguished in the Indian Ocean: firstly, those that are generated within the Indian Ocean by subduction; secondly those which are the product of the mixing of other existing water masses and finally; those which enter the Indian Ocean from elsewhere, namely via the flow of Pacific waters into the Indian Ocean via the Indonesian throughflow (Schott and McCreary, 2001; Shankar et al., 2002). In the northern Arabian Sea, high salinity Arabian Sea Water (figure 6.7) is formed during the NE winter monsoon and is subducted underneath the mixed surface layer waters into the upper thermocline (Schott and Fischer, 2000).

Oceanic surface current flow in the Southern Hemisphere section of the Indian Ocean is similar to that in the other major oceans. Zonal influx of the South Equatorial Current (SEC)

is driven by southeast trade winds across the Indian Ocean. East of Madagascar at approximately 17°S, the SEC splits into northward and southward flowing branches. The northward flowing branch, the Northeast Madagascar Current, joins the East African Coastal Current (EACC) which flows along the coastal regions of Tanzania and Kenya. During the summer monsoon season (figure 6.5) the SEC and the EACC supply the northward flowing Somali Current which crosses the equator and eventually turns eastwards and flows back towards the southern tip of the Indian subcontinent. Also at this time, the West Indian Coastal Current (WICC) flows southwards parallel to the Indian coast joining the Southwest Monsoon Current. This partially supplies the East Indian Coastal Current (EICC) which flows northwards into the Bay of Bengal and bifurcates.

During the winter monsoon season, the Somali Current flows south and converges with the EACC at 2-4°S. This combined current then merges with the South Equatorial Countercurrent (SECC), an eastward-flowing boundary current which flows across the entire width of the Indian Ocean and eventually becomes the South Java Current which flows southeastwards along the southern edge of the Indonesian archipelago (figure 6.6). Surface water currents in the area around India are reversed at this time; the EICC flows southwards out of the Bay of Bengal to supply the westward-flowing Northeast Monsoon Current (NMC) which supplies the northward transport of the WICC. For a comprehensive and detailed review of Indian Ocean oceanography, see Schott and McCreary (2001), Shankar et al. (2002) and Schott et al. (2009).

6.4.2 Interannual variability

There are two dominant modes of interannual variability which impact the Indian Ocean: the El Niño Southern Oscillation (ENSO) and the Indian Ocean Dipole. These are discussed in the following sections.

6.4.2.1 El Niño Southern Oscillation

The influence of the Indian Ocean on climate variability in tropical countries, through the seasonal development of the monsoons, has only recently become more fully understood, following the widespread impact of the 1997-1998 El Niño event which resulted in widespread drought in Indonesia and large-scale flooding in East African countries such as Kenya, Ethiopia and Somalia. The effects of El Niño were further exacerbated by unusual conditions in the Indian Ocean which caused the usual westerlies to switch to easterlies

between July and November (see section 6.4.2.2) (Schott et al., 2009). The El Niño Southern Oscillation induces an interannual SST anomaly in the Indian Ocean characterised by basin-wide warming which peaks during boreal spring and influences precipitation events in the surrounding regions (Saji and Yamagata, 2003). During El Niño events, atmospheric convection over the tropical Indian Ocean is suppressed resulting in an increase in the amount of solar radiation received at the ocean surface, due to reduced albedo effects, and contributes to SST warming.

6.4.2.2 Indian Ocean Dipole

A second type of interannual temperature anomaly is related to the oscillatory mode of coupled ocean-atmosphere variability known as the Indian Ocean Dipole (IOD) (Saji et al., 1999). The IOD is characterised by strong reversed zonal SST gradients in the equatorial Indian Ocean which has a distinctive dipole-like structure (Abram et al., 2007, 2008). During positive IOD events, the direction of surface winds in the equatorial regions are reversed from westerlies to easterlies and SSTs become warm in the west and cool in the east i.e. reversed relative to normal (Saji and Yamagata, 2003). IOD events develop in June and peak in October causing the formation of a rainfall anomaly over the tropics with increased precipitation in the west as a result of convergence associated with the easterly winds. This reversal of dominant wind patterns also has a profound impact upon sea level and thermocline dynamics, resulting in heightened sea levels in the central and western Indian Ocean during positive IOD events.

Climate-ocean model simulations suggest that IOD events can be initiated by El Niño events which cause a decrease in thermocline depth in the eastern Indian Ocean, associated with the area of the Indonesian throughflow (Fischer et al., 2005; Behera et al., 2006). Whilst there is a close coupling between IOD and ENSO events, the interactions between the two modes of interannual variability remain unclear. Not all ENSO events are accompanied by a positive IOD phase and climate simulations have also suggested that IOD events originate from Indian Ocean region internal processes such as intensified Hadley cell circulation of the Asian and Australasian monsoonal systems which promotes the upwelling of cooler water in the eastern Indian Ocean (Fischer et al., 2005; Behara et al., 2006). Recent and Holocene-aged climate records from the geochemical analysis of corals in the Mentawai Islands, west of Sumatra (Abram et al., 2007, 2008) support this latter hypothesis and suggest that the recent intensification of IOD events is coupled with the development of positive IOD-monsoon feedback effects (Abram et al.,2008). This has particularly important

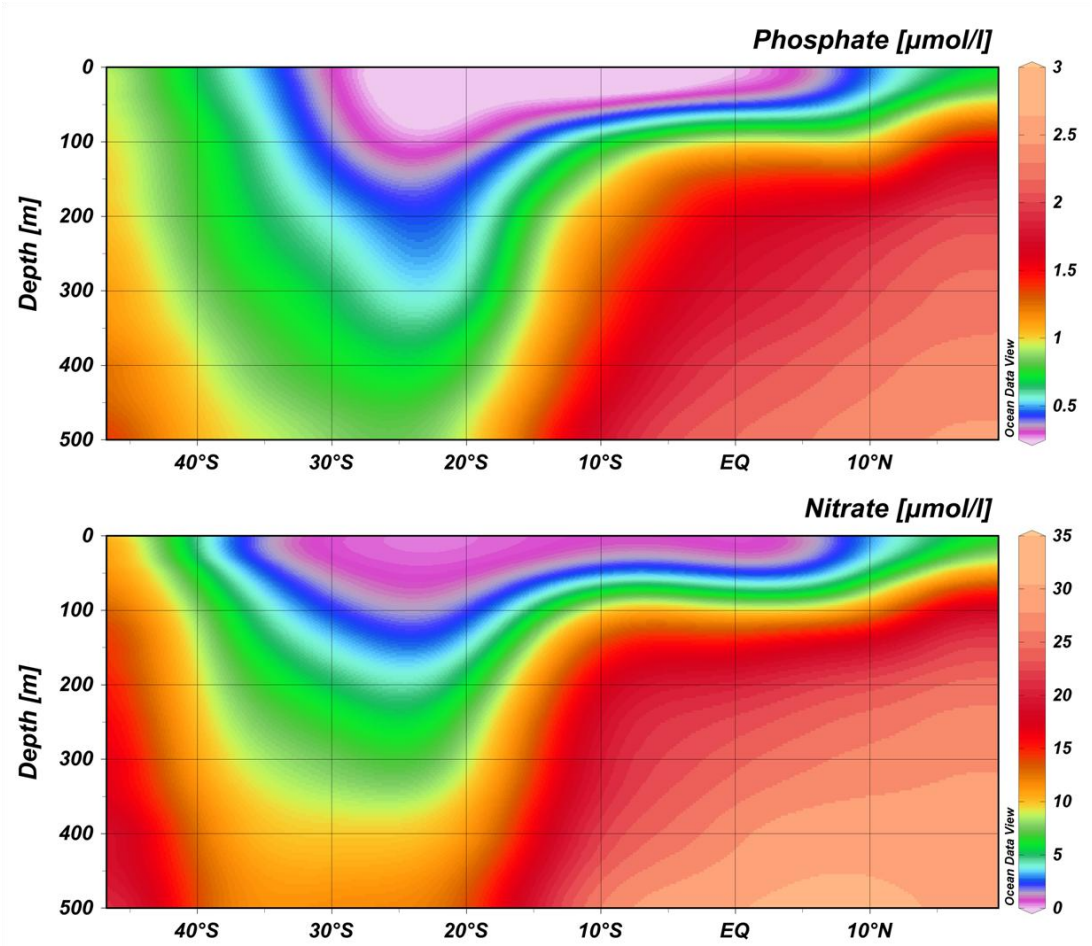

Figure 6.8 Upper water profiles of nutrient (phosphate and nitrate) concentration sin the Indian Ocean. Profiles extend from boundary between the central Indian Ocean and the Southern Ocean (~ 45 °S) to the Oman Margin (~ 20 °N). Structure of the water column illustrates upwelling of deep, nutrient-rich water in the Arabian Sea, driven by the SW summer monsoon. Data from Ocean Data View v. 4.3 (Schlitzer, 2010).

implications for climate variability in the Indian Ocean region in view of future climate change.

6.4.3 Arabian Sea circulation

The seasonal northward and southward excursions of the ITCZ across the Indian Ocean induce reversals in wind stress and ocean surface currents associated with monsoonal circulation. The impacts of these reversals are particularly pronounced in the Arabian Sea where the effects of Ekman pumping and wind stress forcing associated with the Findlater Jet produce a series of eddy currents and lead to the upwelling of cold, nutrient-rich waters into the nutrient-depleted euphotic zone along the Arabian Margin (figure 6.8) (Bruce et al., 1994; Emeis et al., 1995). The Indian subcontinent divides the North Indian Ocean into two tropical ocean basins and plays an important role in altering the direction and magnitude of

surface wind patterns and ocean currents in the Arabian Sea (figure 6.4), which is characterised by mixed-layer deepening and warming at a depth of 100m.

In contrast to the Bay of Bengal, the Arabian Sea has high salinity (35-37 psu) due to an excess of evaporation over precipitation (figure 6.7). The monsoonal reversals in wind stresses and surface currents act to maintain the freshwater and salt balance between the Arabian Sea and the Bay of Bengal (Vinayachandran and Kurian, 2008). During the summer monsoon season, the Somali Current crosses the equator and turns offshore at a latitude of approximately 4°N generating an upwelling zone to the northwest, off the Somalian coast. To the north of this, two gyres are formed, the 'Great Whirl' and the 'Socotra Eddy', which circulate in the Arabian Sea (figure 6.5) (Schott and McCreary, 2001). The intense upwelling generated by the SW summer monsoon results in extremely high primary productivity levels off the coasts of Oman and Somalia (Brock et al., 1992; Schulte and Müller, 2001). The northeastward drift of nutrient-rich surface waters, driven by SW monsoon winds, also generates high primary productivity in the NE Arabian Sea (Schulz et al., 1996, 1998; Andruleit et al., 2000).

During the NE winter monsoon, the Somali Current is a southward-flowing near-surface current which supplies the SECC (figure 6.6). The Somali Current has branched inflow from the Arabian Sea to the east and has a northward undercurrent beneath the cross-equatorial southward flow. Inflow to the Arabian Sea originates from the westward-flowing NMC off the southern tips of India and Sri Lanka and supplies the northward transport of waters in the WICC. However the mode in which the waters inflowing from the WICC and the Somali Current interact within the Arabian Sea remains poorly understood (Levitus, 1988; Schott and McCreary, 2001). In contrast to the summer monsoon, the NE winter monsoon does not cause upwelling in the Arabian Sea. However, cooling of surface waters drives convective mixing which results in continued nutrient supply to the Arabian Sea throughout the winter months helping to maintain high primary productivity levels (Madhupratap et al., 1996).

The southeastern part of the Arabian Sea is known as the Arabian Sea Mini Warm Pool (ASMWP) and exhibits high SST values during February – May (28 °C or greater) which is believed to be important for the onset and advance of the summer monsoon in the Arabian Sea and along the west coast of India. The formation of the ASMWP is due to the orographic effects of the Western Ghat mountains which block the flow of cold northeasterly winds over the southeastern Arabian Sea (Vinayachandran and Kurian, 2008).

During the southwest summer monsoon, lateral variations in wind stress to either side of the Findlater Jet drive Ekman pumping which leads to the open ocean upwelling and shallow mixed-layers to the north of the windstress maximum and downwelling and deeper mixed-layers to the south (Bauer et al., 1991; Lee et al., 2000). By analysing modern observational data, Lee et al. (2000) suggest that the mechanisms driving the response to surface forcing vary with season and location. During the northeast winter monsoon, strong mid-basin latent heat loss drives convective overturning and produces net surface cooling and deep mid-basin mixed-layers which deepen dramatically with distance offshore. During the summer monsoon, wind-driven mixing produces deep mixed-layers and causes the entrainment of cooler fresh water to the surface layers. This, in conjunction with coastal upwelling and the offshore advection of upwelled waters results in the cooling and freshening of northern Arabian Sea surface waters during boreal summer (Lee et al., 2000).

In contrast to other prominent upwelling systems located within eastern boundary currents, the coastal upwelling system offshore from the Arabian Peninsula lies within a western boundary current and exhibits strong seasonal variability as a result of the regional influence of the Indian Ocean monsoon (Hermelin, 1992). The semi-enclosed nature of the Arabian Sea between East Africa, India and the Arabian Peninsula together with strong seasonal upwelling, high rates of productivity and the relative stability of the intermediate water masses result in low oxygen concentrations between water depths of <200 m and ~1,100 m, known as the oxygen minimum zone (OMZ). The OMZ is defined by oxygen concentrations of <0.5 ml/l, with the most severe depletion occurring in the Owen Basin (Hermelin and Shimmield, 1990; Schulte et al., 1999). The stable mid-level OMZ is maintained by various factors including high levels of oxygen consumption driven both by the decay of organic matter and high primary productivity during the monsoon, and the supply of low-oxygen intermediate waters from across the equator to the south. Geochemical proxy records (C_{35}/C_{31}-*n*-alkane ratio) from the northeastern Arabian Sea show that the intensity of the OMZ has varied considerably through time and that, during times of reduced ocean circulation such as the Younger Dryas or Heinrich events, it has disappeared completely (Schulte et al., 1999).

6.5 Summary

In order to assess the wider context of changes in tropical monsoonal circulation during the Plio-Pleistocene against the results from the Baringo-Bogoria basin (Chapter 5), sediments from the Arabian Sea were analysed. The elevated position of ODP Sites 721 and 722,

relative to the surrounding ocean floor, ensures that delivery of lithogenic material is solely through aeolian transport. As discussed above, regional climate and oceanic circulation in the Arabian Sea are closely linked to the seasonal reversals in atmospheric circulation and formation of the Indian Ocean summer and winter monsoons. This drives the seasonal upwelling of cool, nutrient-rich waters along the Arabian Margin and controls the delivery of aeolian dust to the Owen Ridge.

Chapter 7: Arabian Sea Project Methodologies

7.1 Introduction

The following chapter describes the sampling and laboratory methods used to investigate palaeoclimatic changes recorded in oceanic sediment cores from Ocean Drilling Program (ODP) Sites 721 and 722 drilled on the Owen Ridge in the Arabian Sea, spanning a ~ 600,000-year period between 2.3 and 2.9 million years ago.

7.2 Core Sampling

Cores from ODP Sites 721 and 722 were sampled at approximately 10 cm intervals over sections of cores spanning a total of 14 metres. Discrete sediment samples of 20 cm^3 in volume were obtained from the working halves of the core sections held at the Integrated Ocean Drilling Program (IODP) Core Repository in Kochi, Japan. Due to prior extensive sampling of the sediment cores, sampling intervals were readjusted at the discretion of the repository staff. Wherever possible, gaps of approximately 10 cm were left between the sampling intervals, as per the planned sampling strategy. The sediment samples were split for inorganic and organic analyses. In addition, 13 archive core halves from ODP sites 721 and 722 (figure 7.1) corresponding to the intervals for discrete sampling were sent from the Kochi IODP Core Repository to UCL for analysis using an Avaatech XRF core scanner, described in section 7.5.

The samples chosen for analysis were selected on the basis of the outcomes of initial investigations conducted during and immediately following ODP Leg 117 (Clemens and Prell, 1990, 1991; Clemens et al., 1991; deMenocal et al., 1991; Murray and Prell, 1991, 1992; Shimmield and Mowbray, 1991; deMenocal, 1995). The age-depth model described by Murray and Prell (1991) and used by a number of authors in subsequent studies of the ODP 721/722 cores was detuned and reconstructed according to a revision of the date for the Gauss/Matuyama boundary from 2.470 Ma to 2.608 Ma (Lisiecki and Raymo, 2005). The revised version of the age-depth model was then used to initially select a sediment interval for detailed sampling between approximate ages of 2.4 and 2.9 Ma corresponding to composite depths of 83.00 metres below sea floor (mbsf) and 97.50 mbsf, respectively. A revised chronology based on foraminiferal oxygen isotope stratigraphy and palaeomagnetic data was then later constructed for this study (see chapter 8.2).

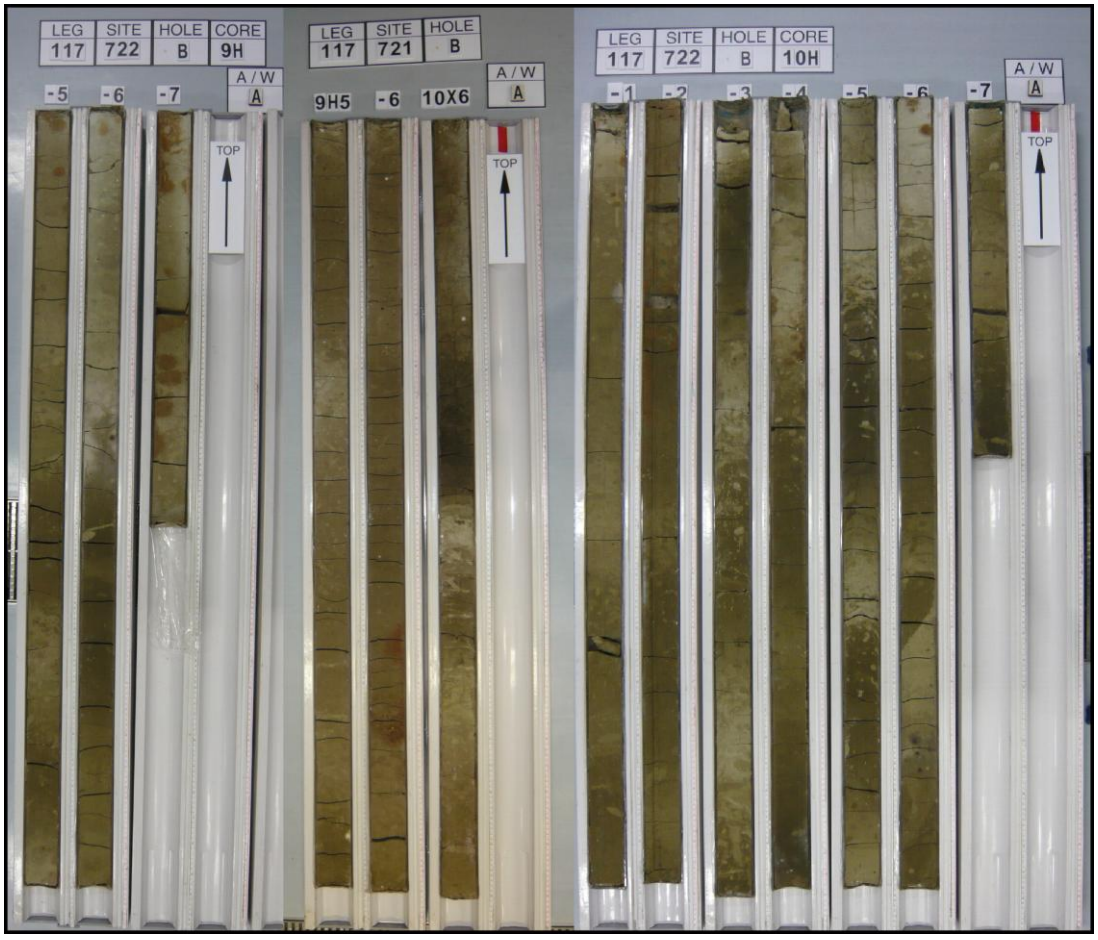

Figure 7.1 Photographic compilation of archive core halves from ODP Sites 721 and 722 from between composite depths of 84 mbsf and 98 mbsf. Archive core material was shipped from the IODP Core Repository in Kochi, Japan to UCL for XRF analysis. Each core section is 1.5 m in length and was cleaned and smoothed prior to measurement. Positions of significant gaps in cores were noted and adjustments made to resulting data wherever necessary.

7.3 Foraminiferal Stable Isotopes

Calcareous marine organisms such as foraminifera, coccolithophores, ostracods and molluscs precipitate their calcium carbonate shells from the marine oxygen and carbon pools available in the oceans. The isotopic composition of the shells is reflective of the isotopic balance of seawater at the time of calcite precipitation. As outlined in sections 2.4.3.2 and 2.5.2, there are a number of factors which influence the isotope ratios of oxygen and carbon.

Whilst the analysis of isotope ratio data from foraminifera can provide a wealth of information about changes in parameters such as productivity, ocean circulation, sea surface temperature, global ice volume and upwelling regimes, there are some intrinsic limitations

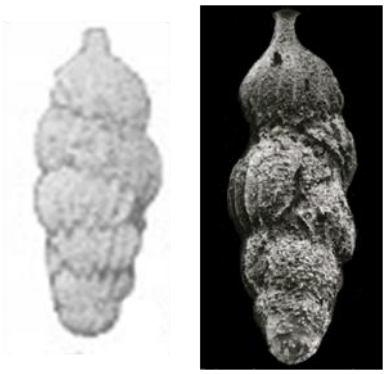

Figure 7.2 Illustration and SEM image of benthic foraminfer *Uvigerina peregrina* var. *dirupta*. From Foraminiferal Taxonomy Atlas (http://ead.univ-angers.fr/~geologie/atlas/

which must be considered when analysing foraminiferal populations. One such caveat is the effect caused by bioturbation at the sediment surface which can result in a smoothing of sharp transitions resulting from rapid palaeo-environmental shifts (Ravelo and Hillaire-Marcel, 2007). Sediment mixing and differences in the flux rate of shells to the sea floor are additional issues which may complicate the analysis of foraminiferal calcite. An additional consideration concerns the size-dependence of isotopic composition in foraminiferal shells. This is particularly important when analysing planktonic foraminifera which are mobile in the water column, meaning that juvenile specimens may exhibit a markedly different isotopic composition to mature foraminifera. In order to minimise this effect, isotopic analyses are usually performed on shells from a specific size range. In this study, specimens of the benthic foraminifera *Uvigerina peregrina* var. *dirupta* (figure 7.2) were selected from the 250-350 µm size fraction. Whilst this helps to eliminate within-species size-related variability, it may also result in a palaeoecological reconstruction that is biased towards optimum growth conditions (Berger et al., 1981).

7.3.1 Sample preparation and analysis

Oxygen and carbon stable isotope analyses were performed on foraminiferal calcite preserved within sediments from ODP Sites 721 and 722. Once aliquots of sediment had been removed from the bulk sample for organic analysis, the remaining sample was used for analysis of benthic foraminiferal tests. Samples were first freeze-dried in order to partially disaggregate the sediment before washing over a 125 µm sieve with distilled water. Both size fractions (<125 µm and >125 µm) were air-dried at 40 °C and decanted into separate vials. The >125 µm size fraction was subsequently dry-sieved using 150 µm, 180 µm, 250 µm and 350 µm stainless steel mesh sieves to isolate different size fractions prior to microscope analysis. Following this, up to 30 individual specimens of the infaunal benthic species *Uvigerina peregrina* (mostly var. *dirupta*) were then picked from the 250-350 µm fraction under 40x magnification using a Leica S6E optical microscope. Remaining sample material has been retained for future analysis.

Samples were analysed at the NERC Isotope Geosciences Laboratory (NIGL) in Keyworth, UK. Measurements were performed on between 2 and 6 individuals of *Uvigerina peregrina* var. *dirupta*. Samples were homogenised and aliquots were reacted at 90 °C in a VG Iso-Carb common acid bath system attached to an Optima mass spectrometer. $\delta^{18}O$ and $\delta^{13}C$ measurements are expressed relative to the V-PDB scale by reference to an internal laboratory working standing (KCM), calibrated against the NBS-19 standard. Analytical reproducibility was assessed by repeat measurements of the KCM standard which resulted in figures of 0.05‰ for $\delta^{18}O$ and 0.03‰ for $\delta^{13}C$.

7.4 Bulk Organics

The flux of total organic carbon (TOC) to the seafloor and thus the percentage of TOC recorded in marine sediments is thought to broadly approximate the degree of transfer of organic material produced in the oceanic euphotic zone to deep sea sediments. As outlined in chapter 2.5.3, values of $\delta^{13}C_{org}$ reflect a combination of land- and marine-sourced organic matter and related processes such as primary ocean productivity, surface water CO_2 and the input of terrigenous material to the site.

7.4.1 Sample preparation

Bulk $\delta^{13}C_{org}$, TOC and carbon/nitrogen (C/N) ratios were analysed on organic material within discrete samples of decarbonated sediment sampled from ODP Sites 721 and 722. Carbonates were removed by reacting approximately 2 g of wet bulk sediment with 100 ml of 5 % HCl in a beaker. Samples were placed in a fume cupboard and left for 24 hours. In order to ensure that all residual HCl was removed from the samples, they were rinsed in deionised water and centrifuged at 1200 rpm for 4 minutes, before the supernatant liquid was carefully decanted off. The samples were rinsed again with deionised water and the cleaning steps were repeated a further three times. These acid reaction steps were then repeated after it was found that 100 ml was not sufficient to completely remove all carbonate content from the samples. Finally, samples were dried at 40 °C and ground to a fine powder using a pestle and mortar.

Laboratory analysis of the prepared samples was conducted at NIGL, Keyworth. Between 20-30 mg of powder from each sample was weighed on a micro-balance into tin foil capsules. The capsules were immediately pressed and sealed in order to remove air pockets from within the sample. Measurements of total carbon, total nitrogen and $\delta^{13}C_{org}$ were

performed using a Carlo-Erba 1500 elemental analyser coupled online to a VG Triple Trap and Optima dual-inlet mass spectrometer. Carbon isotope values were then converted to the V-PDB scale by cross-calibration to the NBS-19 and NBS-22 standards. The standards were also used to monitor machine reproducibility and within-run precision.

7.5 X-Ray Fluorescence Elemental Analysis

7.5.1 Background information

The development of X-ray fluorescence (XRF) logging techniques has allowed the generation of continuous, high-resolution stratigraphic records from marine and lacustrine split sediment cores. XRF core scanners track down-core changes in the chemical composition of minor, major and trace elements and work through the interaction of x-rays with the surface of a split sediment core. XRF core scanner measurements are therefore non-destructive, consumable costs are relatively low and sample preparation is minimised in comparison to the XRF analysis of discrete samples. Under the influence of incoming x-ray radiation, electrons are excited to a higher energy state, in turn causing the displacement of other electrons to lower energy states to fill the resulting vacancies (figure 7.3). The surplus electromagnetic energy emitted by the displaced electrons has a wavelength(s) and frequency that are characteristic of a specific element. The characteristic electromagnetic spectra follow Moseley's Law, an empirical law that relates the electromagnetic frequency to the atomic number of an element (Moseley, 1914). The measurement of these wavelengths allows the characterisation and proportion of elemental intensities within the analysed sample to be semi-quantitatively assessed in counts per second (cps). The incident x-ray beam only interacts with small sample volumes and so the emitted x-rays only contain information from a thin surficial layer on the sediment core surface. The response depths of the different elements within the sample depend on the wavelength of the fluorescent radiation so that for lighter elements such as Al and Si, this depth is a few μm whereas for heavier elements such as Fe the depth rises to a few hundred μm (figure 7.3) (Jansen et al., 1998). The relatively shallow penetration of x-rays below the sediment surface means that continuous XRF data may exhibit a pronounced degree of scatter as the analysis are sensitive to small morphological variations in the core surface. Data scatter may also result from variations in sediment porosity, density, water content and grain size (Boning et al., 2007).

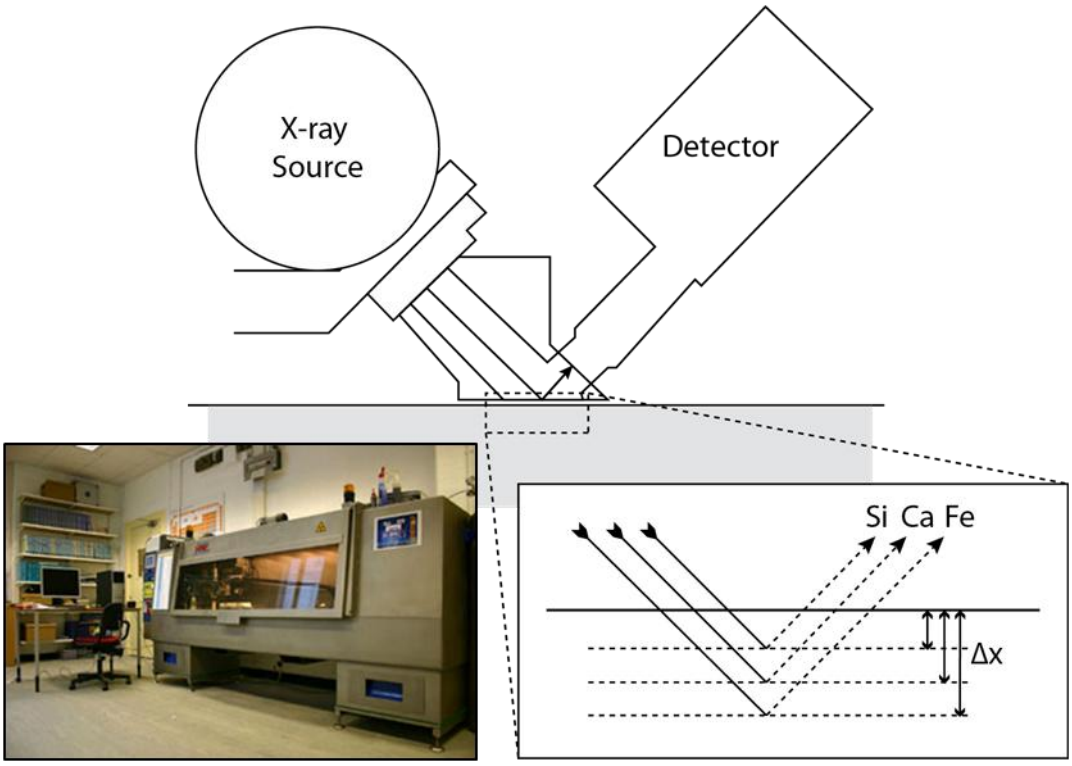

Figure 7.3 Schematic illustration of excitation geometry at the sediment surface - analyser interface in XRF core scanner analysis. The critical depth (Δx) of elements Si, Ca and Fe (not to scale) is linked to the amounts of fluorescence energies emitted by different elements. Inset image show the Avaatech XRF core scanner within the Department of Earth Sciences, University College London. Modified from Tjallingii (2007).

The major advantage of scanning XRF over conventional geochemical analytical techniques is that measurements are non-destructive and can be taken at high spatial resolution and obtained directly from the sediment surface, thus negating the need for lengthy sample preparation. The advantages of scanning XRF suggest that this technique has great potential as a tool for palaeoenvironmental research if the results are properly converted into elemental concentrations by means of an appropriately tested calibration model (Weltje and Tjallingii, 2008). In addition to providing a useful device for examining palaeoenvironmental data, XRF core scanners also offer a means of initial (shipboard) correlation between sediment cores as well as other applications such as stratigraphic interpretations including the tuning of sediment sequences to astronomical forcing (Pälike et al., 2001), aeolian dust fluxes (Jahn et al., 2003), diagenetic processes (Funk et al., 2004) and the recognition of sedimentological events such as turbidites (Richter et al., 2006).

7.5.2 Core preparation and measurement

Analysis of archive core halves was conducted on an Avaatech XRF core scanner housed in the Department of Earth Sciences, University College London (figure 7.3). A detailed technical description of the use of the Avaatech core scanner is given in Richter et al. (2006). The Avaatech core scanner is equipped with a Rhodium X-ray source and thermoelectrically-cooled Peltier spectrometer detector, a 125 μm Beryllium window and has an operating voltage range of 7-50 kV capable of detecting elements from Aluminium to Uranium. The system used a helium-flushed prism in order to minimise radiation scattering between the incoming X-ray beams and outgoing XRF radiation. The analytical precision of the XRF core scanner varies with element intensity that is linked to element concentration, lithology and the physical properties (e.g. grain size, porosity) of the sample material, as well as with changes in hardware settings (Röhl and Abrams, 2000; Westerhold, 2003).

Before scanning XRF analysis can be conducted, samples must be homogenous, dry and have a smooth, flat surface. Split sediment cores, especially older material, are susceptible to cracking as a result of drying out or gas expansion and as such require preparation prior to analysis. The cores were wetted with distilled water and carefully cleaned and smoothed using a flat, rounded steel plate to remove surface irregularities. The surface was then covered with Ultralene^{TM} X-ray transmission foil which was pressed over the smoothed core face using a roller and a brush to remove any remove any trapped air and ensure total contact between the sediment surface and transmission foil. Whilst XRF analyses are not temperature dependent, the cores were warmed to room temperature prior to analysis in order to avoid condensation of water droplets on the underside of the Ultralene^{TM} foil which may interfere with the XRF measurements.

Each core section was scanned three times for 45 seconds per measurement at operating voltages of 10 kV with no filter (for Al, Si, P, S, Cl, K, Ca, Ti, Mn, Fe, Cu, Zn), 30 kV with a Pd-thick filter (for Br, Rb, Sr, Zr) and 50 kV with a Cu filter (for Ba, Pb, U) to measure an extensive suite of elemental intensities. Measurements were made at a resolution of 2 mm with a corresponding slit size of 2 mm and at an electrical current setting of 1.0 mA. Cores were carefully measured prior to analysis to avoid cracks and interruptions in the sediment surface. Despite this, data from the ends of core sections were found to exhibit a large degree of scatter where the sediment surface becomes more disrupted. In these instances, values were removed from the dataset.

7.5.3 Calibration of XRF data

Calibration of raw XRF counts was performed using the WinAxil XRF conversion software and WinBatch software from Canberra. The software uses an iterative least-squares fitting model with a Gaussian function in order to approximate the characteristic fluorescence lines. This enabled raw spectral data to be processed using predefined models to calculate elemental intensities, which are calculated as the peak areas of the processed model. Models were checked prior to calibration where model performance was tested using chi-squared (χ^2) statistical testing to indicate goodness-of-fit where values of $\chi^2 = 1$ indicated a perfect fit and values greater than $\chi^2 = 3$ were rejected.

7.6 Core Chronology

As briefly outlined in section 7.2, the original age-depth model described by Murray and Prell (1991) was detuned and reconstructed using a revised age for the Gauss/Matuyama boundary of 2.608 Ma. The original age-depth model for these sites was developed using magnetic and nannofossil datums in addition to an oxygen isotope stratigraphy constructed by Clemens and Prell (1991) for the period dating back to 1.0 Ma. On the basis of revisions to the dates of palaeomagnetic reversal boundaries, this age-depth model was corrected and locations for core sampling were selected for the period spanning 2.3 to 2.9 Ma. As part of this study, a new chronology for ODP 721/722 was constructed using foraminiferal oxygen isotope stratigraphy, combined with palaeomagnetic data. The oxygen isotope values of specimens of the benthic foraminifera *Uvigerina peregrina* var. *dirupta* were analysed and correlated with the LR04 stack (Lisiecki and Raymo, 2005).

7.6.1 Composite depth model

Whilst core recovery for Hole 722B was largely excellent (Shipboard Scientific Party, 1989), detailed analysis of magnetic susceptibility records, sampled at 5 cm intervals, revealed hiatuses of up to 1.9 m across core breaks. To ensure complete analysis of the core records, Murray and Prell (1991) developed a composite depth model for ODP sites 721/722 by splicing short sections from Holes 721B and 722A with the record for Hole 722B (figure 7.4). Correlation between the different core records was achieved using visible marker layers in addition to characteristics in the magnetic susceptibility records. Within the sections corresponding to the period between 2.3 and 2.9 Ma, this composite record is composed of sediments from Holes 722B and 721B. Following analysis of archive core

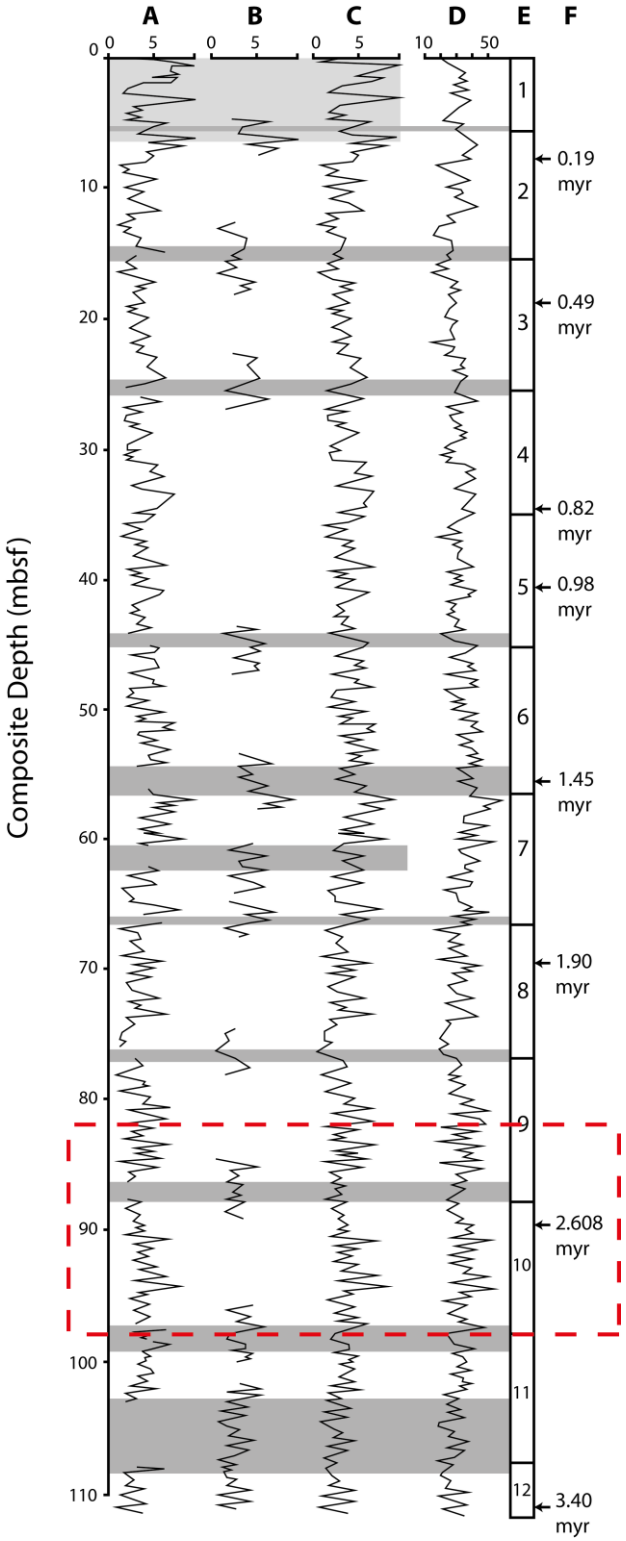

Figure 7.4 Spliced composite depth model for ODP Sites 722 and 721. Hole 722B magnetic susceptibility record shown versus composite depth (**A**) for Cores 1H to12X (**E**). Dark grey shaded bars denote gaps in magnetic susceptibility data at core breaks or in disturbed areas which were spliced with magnetic susceptibility data from Holes 722A and 721B (**B**). Graph (**C**) shows the composite magnetic splice for ODP Site 722. Non-carbonate concentrations for Hole 722B (**D**) were used in places to estimate values for data gaps. Palaeomagnetic and biostratigraphic datums are shown in (**F**), where the age for the Gauss/Matuyama reversal has been revised from 2.47 Ma to 2.608 Ma. Area outlined in red highlights sections investigated in this study. Redrawn from Murray and Prell (1992).

From sample	To sample	Original Depth (mbsf)		Composite Depth (mbsf)	
		From	To	From	To
722B-1H-1, 1 cm	lH-4,19 cm	0.01	5.19	0.01	5.19
722A-1H-3, 80 cm	1H-3, 130 cm	3.80	4.30	5.20	5.70
722B-2H-1, 21 cm	2H-7, 9 cm	5.71	14.59	5.71	14.59
722A-2H-3, 90 cm	2H-4, 34 cm	13.70	14.64	14.60	15.54
722B-3H-1, 45 cm	3H-7, 54 cm	15.45	24.64	15.55	24.74
721B-3H-4, 25 cm	3H-4, 130 cm	23.85	24.90	24.75	25.80
722B-4H-1, 86 cm	5H-7, 59 cm	25.56	43.89	25.81	44.14
721B-5H-3, 30 cm	5H-3, 120 cm	41.80	42.70	44.15	45.05
722B-6H-1, 6 cm	6H-7, 34 cm	43.96	53.24	45.06	54.34
721B-6H-3, 40 cm	6H-4, 105 cm	51.50	53.65	54.35	56.45
722B-7H-l,26cm	7H-3, 150 cm	53.46	57.65	56.46	60.70
721B-H-l, 75 cm	7H-2, 60 cm	58.15	59.50	60.85	62.20
722B-7H-5, 1 cm	7H-7, 70 cm	59.25	62.90	62.21	65.90
721B-7H-4, 146 cm	7H-5, 54 cm	63.36	63.94	65.91	66.49
722B-8H-1, 5 cm	8H-7, 64 cm	62.95	72.54	66.50	76.09
721B-8H-4, 130 cm	8H-5, 55 cm	72.70	73.45	76.10	76.85
722B-9H-1, 11 cm	9H-7, 79 cm	72.61	82.29	76.86	86.54
721B-9H-5, 80 cm	9H-6, 45 cm	83.20	84.35	86.55	87.70
722B-10H-1, 11 cm	10H-7, 69 cm	82.81	92.39	87.71	97.29
721B-10X 6, 20 cm	10X-6, 110 cm	94.20	94.60	97.30	97.70
722A-10X-3, 90 cm	10X-4, 90 cm	90.40	91.90	97.75	99.25
722B-11X-2, 31 cm	11X-4, 119 cm	93.71	97.59	99.26	103.14
721B-11X-4, 70 cm	11X-6, 20 cm	100.80	103.30	103.15	105.65
722A-11X-3, 40 cm	11X-4, 145 cm	99.60	102.15	105.70	108.25
722B-12X-l, 96cm	12X-3, 105 cm	102.46	105.55	108.26	111.35

Table 7.1 Details of composite depth model defined by composite magnetic susceptibility splice shown in figure 7.5. The model is composed mainly of core material from Hole 722B with gaps filled by material from Holes 722A and 721B. From Murray and Prell (1992).

sections and discrete samples, original depth information for all material was converted to composite depth below seafloor using the composite depth model outlined by Murray and Prell (1991), which is outlined in table 7.1. Despite the change in age, the position of the Gauss/Matuyama palaeomagnetic polarity reversal within the sediment cores, at a composite depth of 89.40 metres below sea floor (m.b.s.f) within Hole 722B, was assumed to be correct and is used as a tie-point with which to constrain the oxygen isotope stratigraphy to the LR04 benthic stack.

7.6.2 Orbital dating

In the absence of an independent age-control mechanism for palaeoceanographic data from the Arabian Sea, such as tephrochronology or sapropel records, the most widely-used method for establishing a reliable chronology is to astronomically tune individual oxygen isotope stratigraphies to a standard chronology. To date, the most comprehensive data set available for the period investigated here is the LR04 stack, compiled by Lisiecki and Raymo (2005). The LR04 stack comprises a total of 57 component oxygen isotope records derived from benthic foraminiferal calcite (usually from *Uvigerina peregrina* or *Cibicidoides wuellerstorfi*) from a number of sites which are globally distributed in terms of latitude, longitude and depth in the Atlantic, Pacific and Indian Oceans. Appropriate isotopic corrections were applied for species offsets based on the findings of Shackleton and Hall (1984). The 57 records were aligned using an automated graphical correlation technique to create a global fit for records dating back to 5.3 Ma. In contrast to previously used records such as SPECMAP, the LR04 stack is used to develop a conservatively tuned $\delta^{18}O$ timescale in order to minimise deviations in globally averaged sedimentation rates by aligning the benthic stack with a simple model of ice volume (Lisiecki and Raymo, 2005).

In order to correlate the benthic oxygen isotope record from this study in the Arabian Sea with the LR04 stack, a simple comparison was made between the two isotope curves. The position of the Gauss/Matuyama (G/M) boundary at a composite depth of 89.40 m.b.s.f was used as a tie-point to initially correlate the Site 721/722 record to the LR04 stack at an age of 2.608 Ma. Following this, correlation was performed by eye based on strong similarities between the characteristic features of the two records. Following the correlation of the Site 721/722 oxygen isotope record with the LR04 stack, the timings of the record were extended from what was originally approximated, based on revisions made to the original age-depth model. This is further discussed in Chapter 8.2 and a comparison of the different age models for ODP Site 721/722 is discussed in Chapter 8.2.4.

7.7 Data Analysis

In order to explore variation within the XRF data set generated from the high-resolution scanning measurements of cores from ODP Site 721/722, a set of time-series analyses and statistical models were developed using a number of different methods. Time-series analysis aims to investigate the temporal behaviour of one or several variables which can be random,

clustered, cyclic or chaotic through time. These are briefly summarised in the following sections.

7.7.1 Generalised linear and additive modelling

Generalised linear models (GLMs) are distribution-driven models with a linear predictor where the distribution of the independent response variable can be defined as belonging to a particular exponential family such as Gaussian, Poisson, binomial, geometric or gamma. GLMs therefore require an *a priori* statistical model to define the distribution of the response variable (Yee and Mitchell, 1991). Sometimes GLMs do not have sufficient flexibility to adequately model the true regression surface; this is particularly true in the natural world when analysing environmental variables.

Generalised additive models (GAMs) are a non-parametric extension of GLMs in which the sum of regression coefficients and explanatory variables in a linear regression is replaced by the sum of smoothed functions of the explanatory variables i.e. where a linear predictor is replaced by a smooth predictor (Simpson and Anderson, 2009). The models are data-driven where the complexity of the smoothing function is characterised by the number of degrees of freedom and the resulting fitted values are not determined from an *a priori* model, as is the case with GLMs (Yee and Mitchell, 1991). This makes GAMs a particularly useful tool for the exploration of data as they are able to deal with non-linear data structures.

The mixed-effects model (GAMM) is one which contains both fixed and random effects. Fixed effects are the standard representation of variables in a linear model whereas random effects arise from additional sources of variability within the data caused by grouping structures (Simpson and Anderson, 2009). The GAMM used here is more complex and takes significantly longer (approximately 5 days) to run, but generates a more statistically accurate trendline and includes a function to explore autocorrelation structure between the data.

The different types of models were tested to determine the best way to explore trends within the XRF elemental ratios such as Ti/Al, which is commonly adopted as a proxy for terrigenous content. The models were run using either the raw or log-transformed data. Models were run using the software R (v. 2.12.1, 2010). A gamma GLM was found to be the best way to analyse the data and plots were generated. The gamma GLM uses the same

systematic fit as a normal linear model but with an additional random part which has a gamma distribution. The model was fitted with an adaptive smoother which allows for periods where there is limited structure within the data and adapts for periods where there is evidence of more rapid change. 99% confidence intervals and derivatives were plotted for each variable.

7.7.2 Spectral analysis

The adoption of GLMs and GAMs allows the examination of changes and trends in the XRF data sets from ODP Site 721/722. However, in order to understand the more detailed complexities of periodicities present within the data, it is necessary to use auto-spectral and cross-spectral analysis. Auto-spectral analysis aims to describe variation within a single variable through time as a function of frequency or wavelength using methods such as the Blackman-Tukey method which is popular in palaeoclimate studies and uses a complex Fourier transform of an autocorrelation sequence (Trauth, 2010). One drawback of the Blackman-Tukey method (and other spectral analysis techniques such as the Welch method) is that it requires data to be evenly spaced in time. This can be problematic in the Earth Sciences where material is typically sampled at constant depth intervals which are unevenly spaced in time. This requires the addition of an extra step which involves the interpolation of the data to account for the uneven spacing. Interpolation is commonly performed using either linear of cubic-spline interpolation, although both can introduce artefacts into the data set. An alternative method for performing spectral analysis on unevenly-spaced data is the Lomb-Scargle power spectrum algorithm (Lomb, 1976; Scargle, 1982). The advantage of this technique over other methods is that it does not require data to be first interpolated at evenly-spaced time intervals, thus eliminating the introduction of further uncertainty to the data. A more detailed review and discussion of the method can be found in Schulz and Strattegger (1998).

Another method of examining time-series data and identifying changes in dominant cyclicities through time is through the use of wavelet analysis. Wavelet analysis is an increasingly used technique to explore variation within palaeoclimate data by analysing local variations in time-frequency space using the wavelet transform. This enables both the analysis of the dominant modes of variability within the data and the determination of how these modes change through time (Torrence and Compo, 1998). In contrast to the Fourier transform, the wavelet transform uses base functions or wavelets which are small packets of waves defined by a specific frequency. The translation and dilation of wavelets in the time-

frequency domain is performed using a mother wavelet $\psi(t)$. The most popular mother wavelet in Earth Sciences is the Morlet wavelet. For a more detailed explanation of wavelet analysis and its use as a tool for palaeoclimate analysis, see Torrence and Compo (1998), and Trauth (2010).

A number of different techniques for spectral analysis were performed on the Ti/Al data set from ODP Site 721/722. The Lomb-Scargle method was found to be the best technique for spectral analysis. Wavelet analysis was also performed and the resulting model plotted alongside variations in Ti/Al through time. A low-pass filter of 800 years was applied prior to analysis in order to eliminate some of the high-frequency noise within the data set without compromising the resulting power spectra. All analyses and plotting of data were performed using MATLAB version 7.10.0 (R2010a) for Windows.

7.8 Summary

Sediments from ODP Sites 721 and 722 were sampled for analysis of Plio-Pleistocene changes in parameters related to monsoon intensity. Discrete samples, taken every 10 cm, were analysed for bulk organic and inorganic isotope composition from benthic foraminifera. These were used to construct a revised oxygen isotope chronology for ODP 721/722, tied to the LR04 global benthic stack (Lisiecki and Raymo, 2005). Core halves were scanned at high-resolution (2 mm) for changes in elemental composition using an XRF scanner. Data sets were then analysed using a range of time-series analysis techniques to explore variation and trends within the data.

Chapter 8: A 600-kyr Record of Dust Transport to the Arabian Sea

8.1 Outline

The following chapter describes the assessment of long-term variations in the flux of aeolian dust to Ocean Drilling Program (ODP) Sites 721 and 722, situated on the Owen Ridge in the Arabian Sea. In order to address differences in the published age models for the Site and so that variations in dust flux may be accurately assessed and compared to the timings of wet phases in the East African Rift Valley, a new chronology was constructed for the period between ~2.9 Ma and ~2.3 Ma. This is then applied to the results from high-resolution (2 mm) XRF scanning of core sediments from ODP 721/722 which, through the analysis of the abundance of lithogenic elements, permits the reconstruction of changes in aeolian delivery of terrigenous material. The transport of dust to the Arabian Sea is closely linked to changes in source area climate which are controlled by the strength of Indian Ocean monsoonal circulation. Changes in the relative abundance of lithogenic elements such as titanium thus reflect the strength of the monsoon system. In order to critically assess Plio-Pleistocene changes in aeolian dust transport, the record is later compared to other tropical dust records from around Africa, reflecting changes in the relative strengths of the different monsoon systems.

8.2 Revised Chronology for ODP Site 721/722

Pre-existing age-models for ODP 721/722 relied on a combination of oxygen isotope stratigraphy (Clemens and Prell, 1991; Clemens et al., 1996), biostratigraphic datums and magnetic polarity reversal data (Murray and Prell 1991). The initial chronology developed for Site 721/722 was based on a combination of $\delta^{18}O$ data for the period between 0 – 1 million years ago (Ma) (Clemens and Prell, 1991), nannofossil datums, foraminiferal biostratigraphic first and last appearance datums and palaeomagnetic reversal stratigraphy established from shipboard data (Murray and Prell, 1991, 1992). The later age-depth model of Clemens et al. (1996) was constructed from the astronomical tuning of lithogenic flux data between 0 – 3 Ma. Lithogenic flux records were used in place of oxygen isotope stratigraphy in this instance as the data had double the resolution of the available $\delta^{18}O$

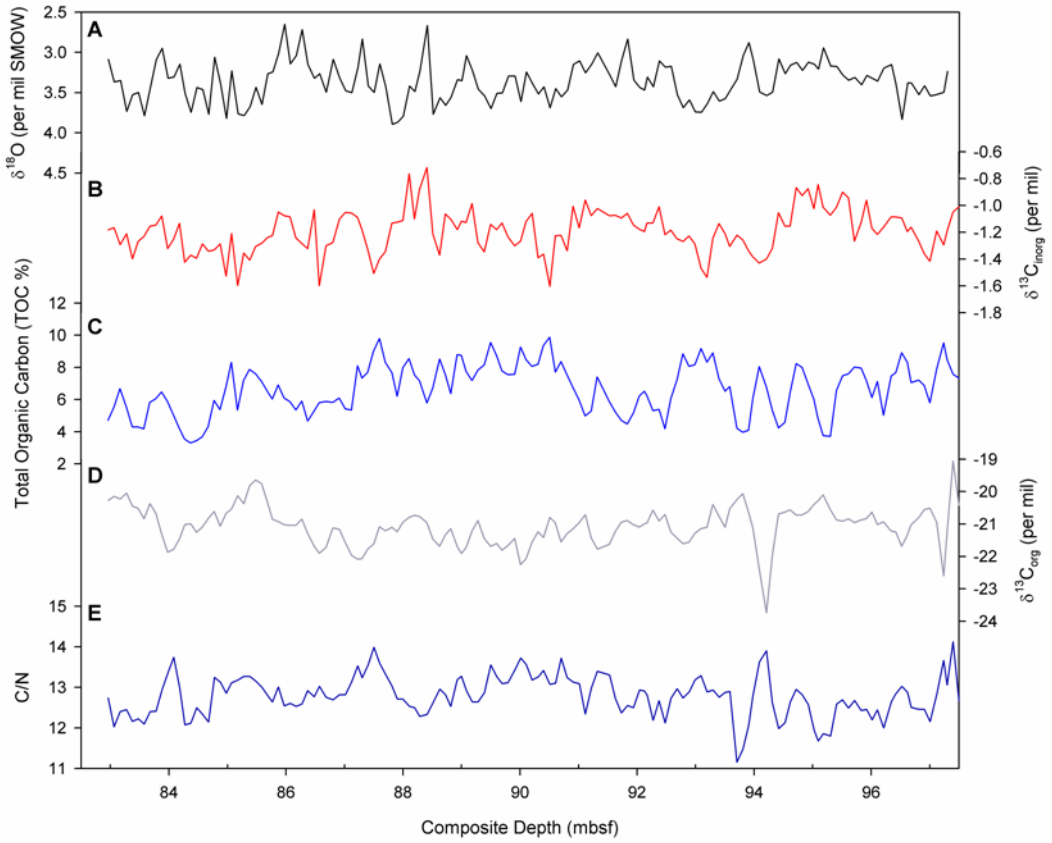

Figure 8.1 Raw data from the analysed core sections of ODP Sites 721 and 722, plotted against composite depth (in metres below sea floor). Oxygen isotope ($\delta^{18}O$) (Graph **A**) and carbon isotope data ($\delta^{13}C_{inorg}$) (Graph **B**) from benthic foraminifera are broadly correlated with one another. Parameters measured on bulk sediment include total organic carbon content (Graph **C**), organic carbon isotope data ($\delta^{13}C_{org}$) (Graph **D**) and C/N ratios (Graph **E**). $\delta^{13}C_{org}$ values reflect the input of marine versus terrestrially-derived organic matter to the site where more negative values indicate terrestrial input and less negative values reflect marine-sourced material (Levanthal, 2004).

measurements and were found to contain a well-resolved precessional signal. Clemens et al. (1996) used the results of cross-spectral analysis of their $\delta^{18}O$ and lithogenic flux data to establish phase differences between the two whilst assuming that global ice volume remained constant (at Late Pleistocene values) through time. This assumption and the use of lithogenic flux data to establish an age-depth model for Site 721/722 may explain the large discrepancy evident between the different age models (see later discussion in section 8.2.4). As a result of the relatively low resolution of the original age models during the Late Pliocene and the revision in the age of the Gauss/Matuyama palaeomagnetic reversal boundary from 2.47 to 2.608 Ma (Lisiecki and Raymo, 2005), it was necessary to construct a new chronology for the period between ~ 2.3 and ~ 2.9 million years ago (see discussion in chapter 7.2). The revised chronology is based on the oxygen isotope analysis of the benthic foraminifera *Uvigerina peregrina* var. *dirupta*, picked at 10 cm intervals from core sections from ODP Sites 721 and 722.

8.2.1 Benthic foraminiferal isotopes

Oxygen isotope ($\delta^{18}O$) values, plotted against composite depth, are displayed in figure 8.1. $\delta^{18}O$ values of individual data points range from 2.5 to 4 ‰ throughout the ~ 14 m section analysed whilst carbon isotope ($\delta^{13}C$) values vary between -1.6 and -0.7 ‰ throughout the section. Repeat measurements of the internal laboratory standard (KCM) found that analytical precision was 0.05‰ for $\delta^{18}O$ and 0.03‰ for $\delta^{13}C$ during the period of analysis. The $\delta^{13}C$ record (figure 8.1) is well correlated with the main features of the $\delta^{18}O$ record and shows an average glacial-interglacial change in $\delta^{13}C$ of 0.5 ‰, which is consistent with other observations of mean ocean changes (Draut et al., 2003). The $\delta^{18}O$ record displays a characteristic saw-tooth pattern analogous to the typical benthic $\delta^{18}O$ signal from the Late Pliocene as demonstrated by the LR04 global stack (Lisiecki and Raymo, 2005). These features permit the application of the LR04 chronology to the studied section at ODP Site 721/722 by correlation of the two $\delta^{18}O$ data sets.

8.2.2 Correlation to the LR04 global benthic stack

In order to establish the most accurate degree of chronological control for this study, benthic $\delta^{18}O$ data was aligned with the LR04 stack, which is comprised of 57 globally distributed oxygen isotope records from benthic foraminiferal calcite. A comparison of the Site 721/722 isotope record with the LR04 benthic stack is shown in figure 8.2, including points of correlation between the two records. The position of the Gauss/Matuyama (G/M) boundary at a composite depth of 89.4 metres below sea floor (mbsf) (Murray and Prell, 1991) provides an initial age-control tie point at 2.608 Ma and alignment of the $\delta^{18}O$ data with the LR04 stack was then conducted on the basis of visual correlation (figure 8.2). Based on similiarities between the characteristic peaks and troughs of each data set, a number of age tie-points were applied to the Site 721/722 data set based on dates calculated from the LR04 stack. By assuming a linear sedimentation rate between each of these points, an age-scale was calculated for the entire section. The new chronology generates dates for the core section analysed at Site 721/722 spanning 2.295 to 2.863 Ma.

Whilst the position of the Gauss/Matuyama palaeomagnetic reversal provides an independent point of control between the ODP 721/722 $\delta^{18}O$ and LR04 records, there remains a degree of uncertainty as to the alignment of the other visually established tie-points, and any subsequent re-positioning of values can significantly affect the resulting age-depth scale. A number of different tie-points were trialled, however the model presented

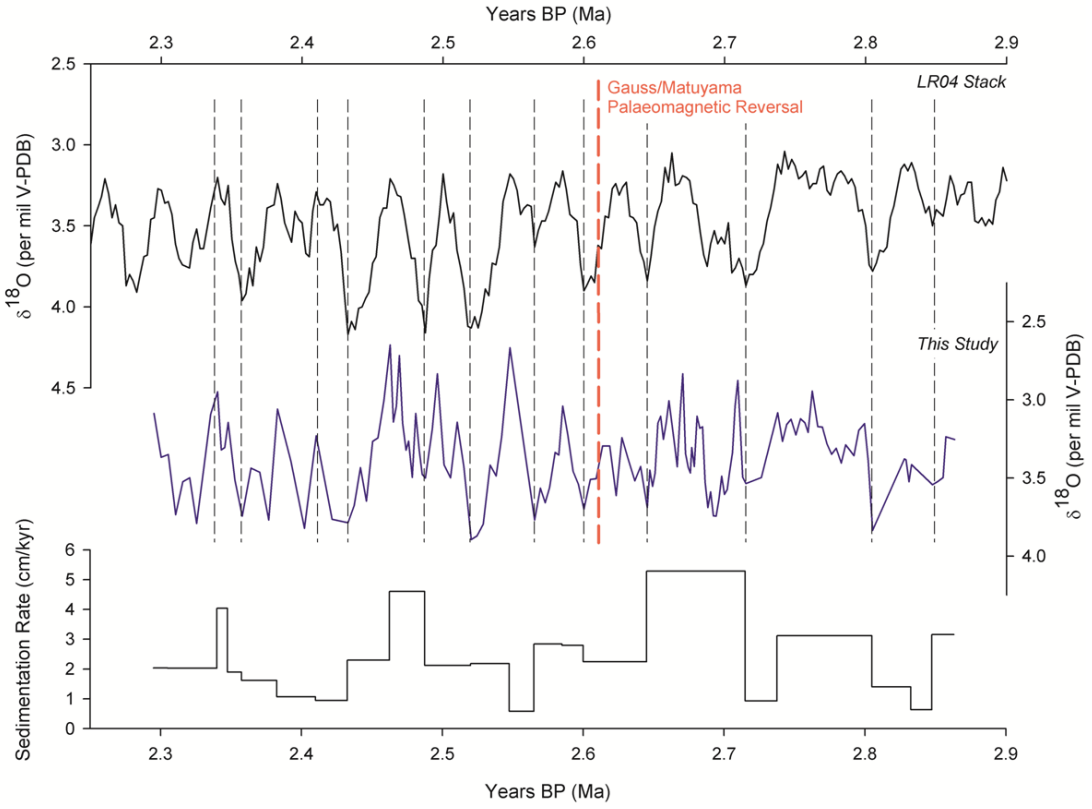

Figure 8.2 Alignment of the $\delta^{18}O$ data from ODP Sites 721 and 722 against the global benthic LR04 oxygen isotope stratigraphy (Lisiecki and Raymo, 2005). The position of the Gauss/Matuyama palaeomagnetic reversal boundary (89.40 mbsf and 2.608 Ma) is used as an independent tie point for the two records (dashed red line). Significant peaks and troughs were then aligned by visual correlation (dashed grey lines) and the resulting chronology constructed from this calibration. The resultant changes in sedimentation rates based on the age-depth model constructed here are also shown.

in figure 8.2 is deemed to be the best fit, and most representative of the timescale defined by global changes in the benthic $\delta^{18}O$ signal.

8.2.3 Sedimentation rates

Using the tie-points resulting from the correlation of the ODP 721/722 $\delta^{18}O$ record with the LR04 stack, average sedimentation rates were calculated for the period represented by the core section using linear regression equations generated for different sections of the age-depth model. The resulting sedimentation rates vary between 0.5 and 5 cm/kyr, with an average of 2.3 cm/kyr. Changes in sedimentation rate are displayed in figure 8.2. Sedimentation rates are generally higher during interglacial periods, however the relatively low resolution of the Site 721/722 $\delta^{18}O$ data in comparison to the LR04 stack means that it is not possible to detect changes in sedimentation rate at each glacial-interglacial transition. The sedimentation rates calculated here are in line with those previously estimated for

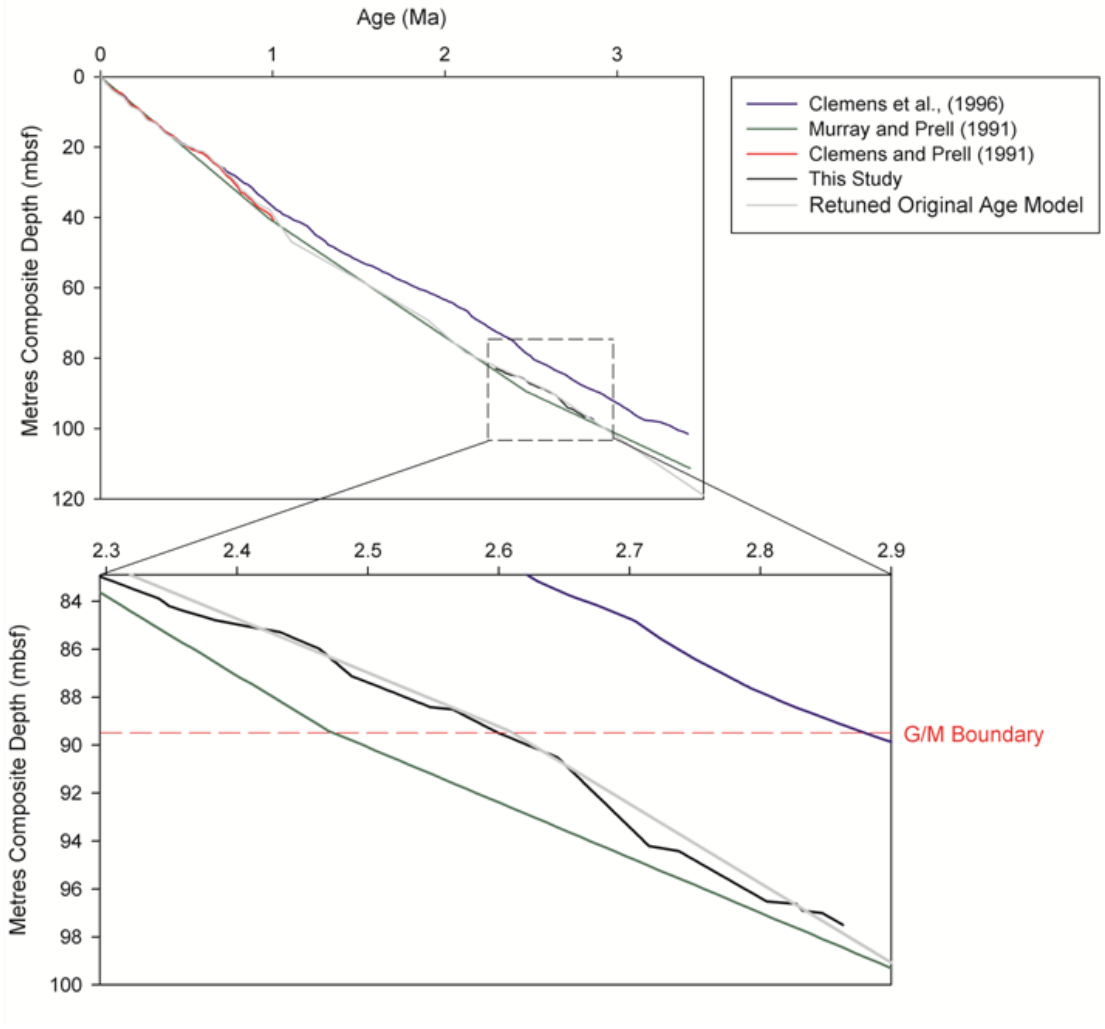

Figure 8.3 A comparison of the published age-depth models for ODP Site 721/722 on the Owen Ridge by Clemens and Prell (1991), Murray and Prell (1991) and Clemens et al. (1996). The principal difference between the models arises from the position of the Gauss/Matuyama (G/M) palaeomagnetic boundary (red dashed line). Descriptions of the proxies used for the construction of each chronology are detailed in the text.

Pliocene-aged sediments from ODP Site 722 (1.8 to 4.2 cm/kyr) and ODP Site 721 (3.0 to 4.1 cm/kyr) (Leg 117 Shipboard Scientific Party, 1989).

Due to previous intensive sampling of the core material, it was not possible to obtain samples at a higher resolution for much of the analysed interval. The application of the revised age-depth model to the geochemical data leads to some degree of stretching and compression of the XRF elemental counts, which were analysed at a resolution of every 2 mm, and results in a time-series containing unevenly spaced data where the chronological resolution can vary by up to a factor of 10.

8.2.4 Comparison to other age models

The revision of the Late Pliocene to Early Pleistocene chronology results in marked differences to the earlier age-depth models developed for ODP Site 721/722. A comparison of these models is displayed in figure 8.3. Figure 8.3 shows that the discrepancy between the Murray and Prell (1991) model and that of this study arises largely because of the revision in the age of the G/M palaeomagnetic reversal and that if it were not for this, the two models would be very similar in general form albeit with improved resolution. There is a much more substantial discrepancy between the age-depth model of Clemens et al. (1996) and that produced here. Clemens et al. (1996) do not include the palaeomagnetic reversal stratigraphy data used here and by Murray and Prell (1991) in the development of their age-depth model which relies on the astronomical tuning of lithogenic flux data to orbital obliquity and precession. This means that in places the difference between the three different age models is as great as 400 kyr. The pace of development in the accuracy, availability and dating of palaeoclimatic archives now mean that age-scales are quickly re-defined and are being constantly updated, which can cause potential discrepancies to arise between the dating of records. Figure 8.4 shows a comparison of the Clemens et al. (1996) ages for the composite depth section of ODP 721/722 studied here with the $\delta^{18}O$-based chronology developed above through correlation to the LR04 stack. This demonstrates the large difference between the suggested time spans of the two age-depth models and demonstrates the importance of utilising independent age control tie-points such as palaeomagnetic datums to constrain the chronostratigraphy.

8.2.5 Summary

The construction of a revised chronology for the ~ 2.3 – ~ 2.9 Ma section of ODP 721/722 has resulted in a correction to the original age-depth model for this site compiled from Clemens and Prell (1991) and Murray and Prell (1991), which principally arises from the adjustment made to the age of the G/M boundary. This difference has implications for other studies of Site 721/722 that have subsequently adopted the chronology of Clemens et al. (1996) (e.g. deMenocal, 1995, 2004; Cleaveland and Herbert, 2007; Herbert et al., 2010). For the purposes of this study, the age model developed and described above is adopted for the interpretation of the $\delta^{18}O$ and XRF elemental intensity data. Since the time period covered by this study is of limited duration and does not span the entire core record, the revised $\delta^{18}O$ chronology would ideally need to be expanded at higher resolution to ensure that the chronology can be easily applied and adopted in future studies.

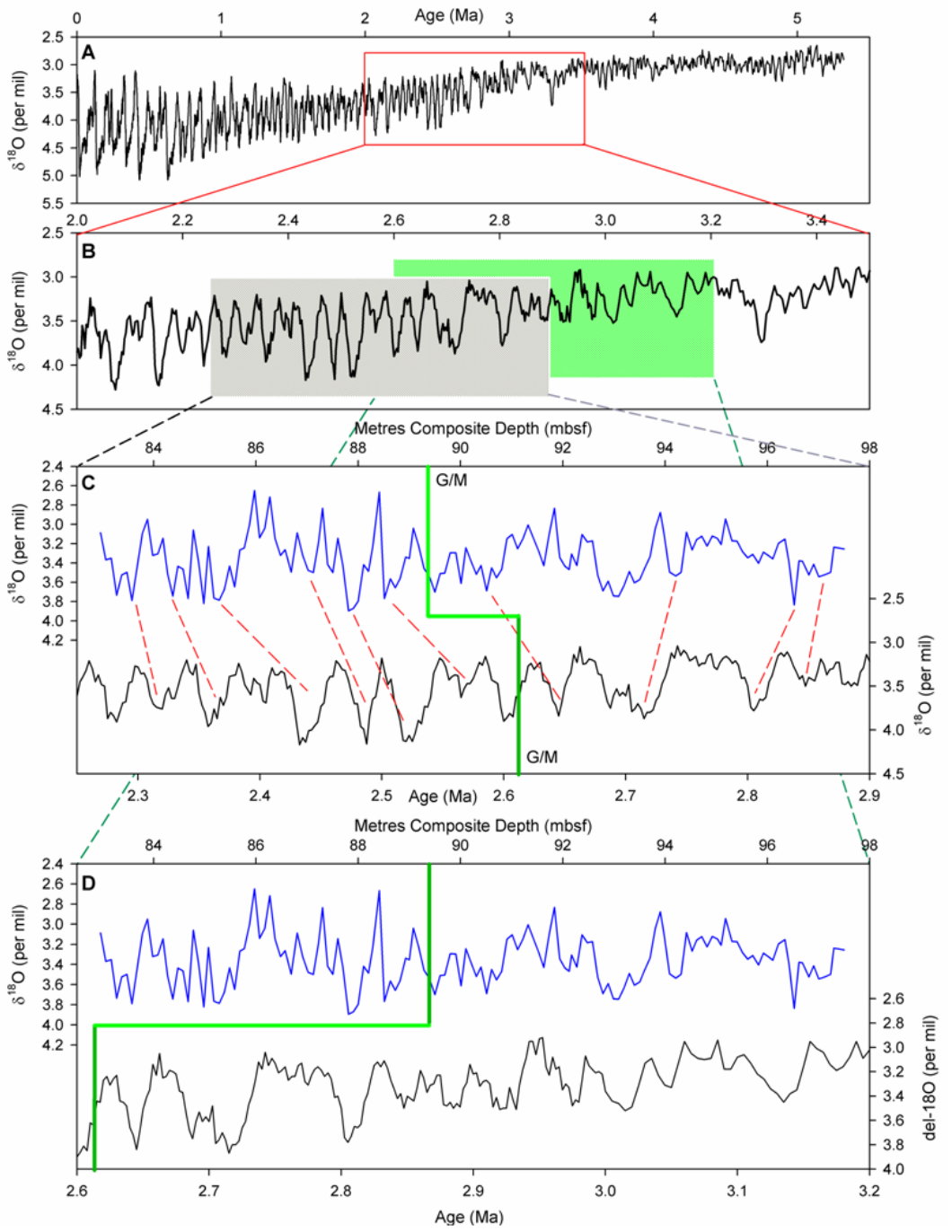

Figure 8.4 Detailed comparison of the timing of the age-depth model of Clemens et al. (1996) with the oxygen isotope stratigraphy developed in this study. According to the age-depth model of Clemens et al. (1996) the core sections analysed in this study correspond to the period between ~3.2 and ~2.6 Ma. Panel **A** shows the full global benthic LR04 stack for the last 5 million years, developed by Lisiecki and Raymo (2005). This is then expanded in Panel **B** for the period between 3.5 and 2.0 Ma. In Panel **B**, the grey box refers to the timespan of the record suggested by this study whilst the green box outlines the timeframe of the record according to the chronology of Clemens et al. (1996). Panel **C** shows the alignment of the benthic $\delta^{18}O$ data (blue line) from ODP 721/722 to the LR04 stack (black line) developed in this study, using the position of the Gauss/Matuyama (G/M) boundary as a point of independent age control (green line). Visual correlation markers are shown by the dashed red lines. Panel **D** shows the alignment of the ODP 721/722 $\delta^{18}O$ data (blue line) against the age and depth described by Clemens et al. (1996) with the relevant portion of the LR04 stack data (black line). The theoretical alignment of the G/M boundary is again shown to mark the offset between the two models.

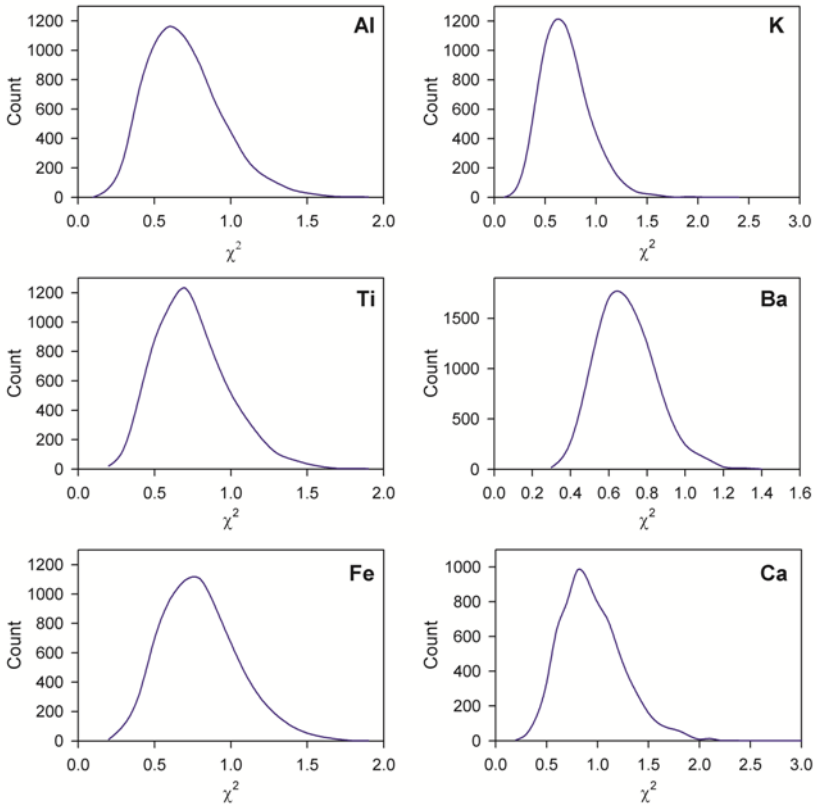

Figure 8.5 Results of the modelling of XRF data showing the Gaussian χ^2 distributions of the fluorescence spectra data for Al, K, Ti, Ba, Fe and Ca. Data are calibrated to a standard of known composition and processing models are pre-defined for each element. Values of χ^2 greater than 3 are rejected.

8.3 Elemental Indicators of Terrigenous Dust Flux

In order to reconstruct low-latitude changes in the variability of the Indian Ocean monsoonal system during the Late Pliocene, core material from ODP Site 721/722 was analysed at high-resolution (2 mm) using an XRF core scanner as described in chapter 7.5. Changes in the elemental ratios of terrigenous minerals such as titanium and iron can then be used as a record of variations in the monsoon-driven flux of lithogenic material to the Arabian Sea.

8.3.1 Calibration and normalisation of XRF data

The accuracy of the calibration of raw XRF counts into elemental intensity data is given by a measure of goodness-of-fit (χ^2) between the outgoing electromagnetic spectrum generated during analysis using the XRF core scanner and pre-determined processing models defined by calibration to a known standard. Values of greater than χ^2=3 are rejected. Figure 8.5 shows the Gaussian χ^2 distributions for Si, Al, Ca, Fe, K, Ti and Ba indicating a good fit of the fluorescence spectra to the processed models. Detailed studies conducted alongside this

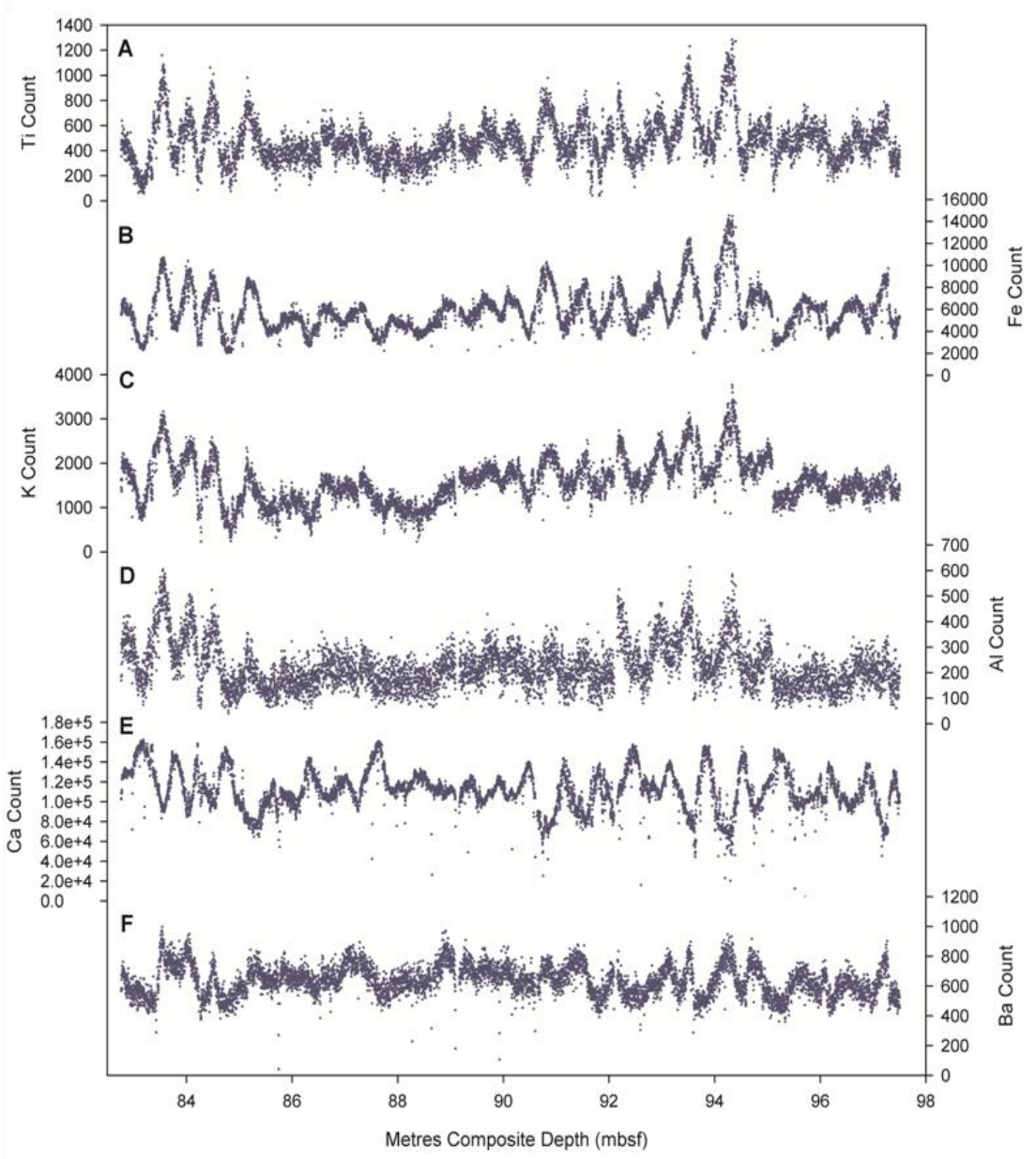

Figure 8.6 Raw count data from analysis using AVAATECH x-ray fluorescence core scanner showing concentrations of different elements including titanium (graph **A**), iron (graph **B**), potassium (graph **C**), aluminium (graph **D**), calcium (graph **E**) and barium (graph **F**). Elemental counts are plotted against the composite depth scale detailed in table 7.1. In particular, titanium, iron and potassium are thought to be indicative of changes in the aeolian flux of terrigenous dust. Changes in barium are believed to reflect changes in the strength of oceanic upwelling and primary productivity in the Arabian Sea.

one using the same core scanner investigated the analytical precision and reliability of measurements of different light elements analysed during five duplicate scans of the same material. The findings indicate that reproducibility is good for Al, Si, K, Ca, Ti, Fe, Sr and Zr (Scotchman, pers. comm.). Raw elemental count data is displayed in figure 8.6. Prior to

further analysis, XRF data was examined for variations occurring across core breaks and at notable gaps in the sediment section (e.g. figure 8.7). Any data affected in this way was removed from the time-series and excluded from further analysis in order to avoid introducing artificial features into the data-set.

Conventional XRF measurements performed on discrete samples were conducted after loss on ignition has been measured, and thus any organic matter is accounted for and the analysis reflects only the composition of lithogenic material. As the X-ray fluorescence signal emitted from the core surface is a function of sediment composition, large variations in lighter elements (e.g. C, O, N) outside the detection limits of the core scanner may cause a dilution effect of the heavier elements which results in the signal mirroring organic matter and/or carbonate content (Calvert, 1983; Löwemark et al., 2010).

Figure 8.1 includes data showing variations in total organic carbon (TOC) and carbon/nitrogen (C/N) ratios to illustrate changes in the flux of marine and terrestrial organic matter to Site 721/722 on the Owen Ridge. Variations in the carbon isotope composition of bulk organic matter ($\delta^{13}C_{org}$) are also shown (figure 8.1). As described in chapter 2.5.3, concentrations of TOC and $\delta^{13}C_{org}$ values reflect the source and depositional environment of organic matter; marine-derived $\delta^{13}C_{org}$ is typically enriched in ^{13}C relative to terrestrial organic carbon and $\delta^{13}C_{org}$ range from -18 to -22 ‰ (Druffel et al., 1992). Values of $\delta^{13}C_{org}$ for terrestrially-sourced C_3 organic matter typically range from -24 to -30 ‰ (Opsahl and Zepp, 2001) and therefore $\delta^{13}C_{org}$ values reflect a combination of ocean productivity, surface water CO_2 concentrations and the input of terrestrial matter to the ocean. Generally, $\delta^{13}C_{org}$ values vary between -19 and -22 ‰, indicating that organic matter is largely marine sourced. However, at a composite depth of approximately 94.40 mbsf, $\delta^{13}C_{org}$ drops to -24 ‰, implying that there was a significant influx of terrestrially-derived C_3 organic material at this time. This decrease is accompanied by high C/N values and a minor peak in TOC.

In order to remove the effect of differential dilution of the lithogenic components by the aluminosilicate fraction and by calcium carbonate, elemental data from the lithogenic component of the sediment must be first normalised against a conservative element to allow for changes in lithogenic input to be accurately quantified. Aluminium was chosen as a normalisation parameter to estimate 'background' elemental concentrations as it is stable, abundant and relatively unaffected by diagenetic and biological changes (Calvert et al., 2001; Calvert and Pedersen, 2007; Löwemark et al., 2010). As Al forms a major structural

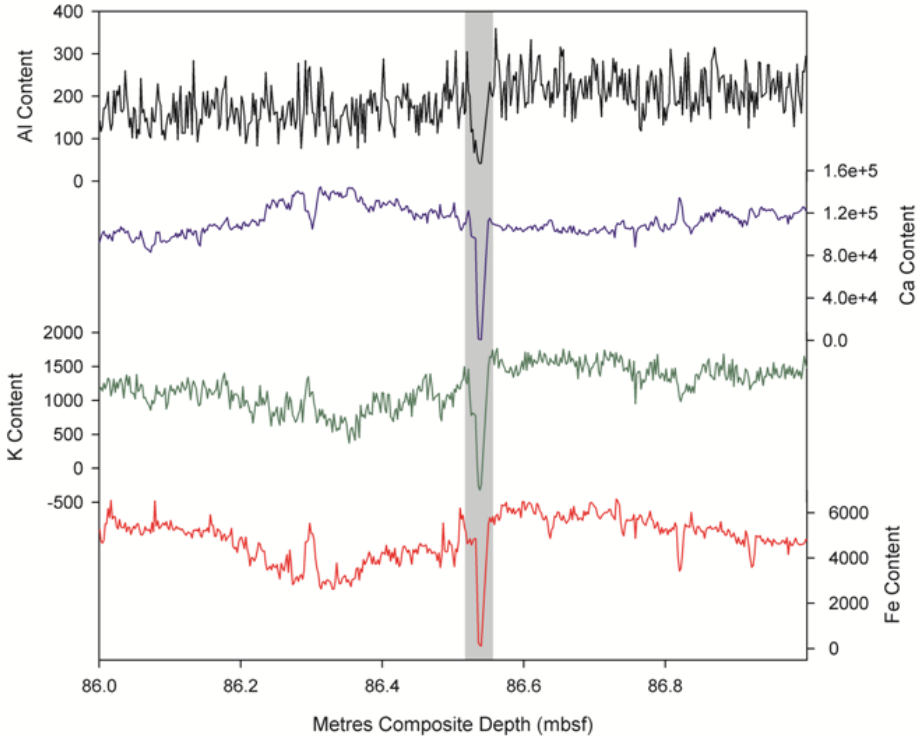

Figure 8.7 Raw elemental XRF count data illustrating a notable hiatus due to a break in the core material (depicted by grey shaded bar). Significant gaps were noted prior to analysis and data was subsequently removed from the time-series in order to avoid introducing skew to the data.

component of all silicate minerals, the normalisation of elements to Al allows changes in the lithogenic fraction through time to be assessed. Al-normalisation is increasingly adopted in the analysis of scanning XRF data (e.g. Funk et al., 2004; Brumsack, 2006; Löwemark et al., 2010), and therefore all data presented here were normalised to Al prior to interpretation or further analysis.

8.3.2 The interpretation of geochemical trends as records of aeolian dust flux

There are three basic assumptions, which must be considered in the interpretation of dust records (Rea, 1994):

1. The amount of dust generated is directly related to climatic conditions in the dust source area, which drive relative aridity or control the amount of soil deflation through the expansion of vegetation cover.
2. Changes in grain size are reflective of the energy of the transporting agent (i.e. wind) such that stronger winds are capable of carrying material of a larger size.

3. The quantity of dust transported to distal locations is not necessarily related to the average speed of the zonal tropospheric winds which are responsible for dust transport.

The factors influencing the degree of source area weathering, soil deflation, aeolian transport and the incorporation of dust into the oceanic sediment record are complex and can vary extensively from one region to the next. For example, soil deflation potential depends on the physical characteristics of the soil (such as moisture content, cohesion and particle roughness) and the extent of vegetative cover, both of which are strongly dependent on local climate (Rea, 1994).

Dust transported to the Arabian Sea is derived from three different source regions; the inner deserts and coastal regions of the Arabian Peninsula, the horn of Africa and from the northern tip of the Persian Gulf near Iraq and Kuwait (Sirocko and Sarnthein, 1989; Clemens, 1998). Dust transport occurs mainly during boreal summer when the SW monsoon develops in the Arabian Sea. Local low-level 'Shamal' winds across Mesopotamia generate seasonally strong dust storms between late May and early July which transport dust along the axis of the Persian Gulf. The modern dust flux during this time of the year is estimated to be 1.05×10^8 tonnes (Clemens, 1998). During the NE winter monsoon, cool, dry surface winds blow from the Indian sub-continent at considerably reduced speeds. During this time, dust transport to the Arabian Sea is minimal.

In order to examine variations in the aeolian input of terrigenous material to the Arabian Sea, elemental concentrations derived from scanning XRF using lithogenic elements such as iron, potassium and titanium are used. There is general agreement that marine sediment records of the ratio of titanium to aluminium (Ti/Al) and other lithogenic proxies reflect the input of continentally-derived dust to the oceans. At ODP Site 721/722, this is deemed to be by aeolian transport due to the elevated position of the Owen Ridge within the Arabian Sea. However the signal imprint of the mechanisms controlling the transport of aeolian dust remain unclear and hence there remains some debate over the degree to which aeolian dust flux or lithogenic input (from both aeolian and fluvial transport) reflects continental aridity and to what extent it is influenced by wind strength and monsoonal circulation. It follows that during periods of stronger monsoonal circulation, wind speeds are intensified thus resulting in an increase in dust transport. However, this is tempered by an increase in precipitation during stronger monsoons, which allow the stabilisation of surface sediments against deflation by enabling vegetation growth (Prospero et al., 2002).

Shimmield (1992) and others (Reichart et al., 1997; Calvert and Pedersen, 2007) argue that Ti/Al, in particular, reflects grain size, since titanuium is known to be concentrated in heavy minerals (e.g. ilmenite, rutile, titanomagnetite and augite) in the coarser size fraction (Schmitz, 1987). Reichart et al. (1997) found that downcore changes in Ti/Al over the last 225 kyr are positively correlated with fluctuations in global ice volume and suggest that this reflects increased glacial wind speed. Shimmield and Mowbray (1991) find that, in addition to wind speed, the availability of dust in the source area and wind trajectory is also of importance in controlling the aeolian dust flux.

However, Rea (1994) argues that wind intensities vary over shorter time-scales than the 100-kyr eccentricity periodicity which dominates the forcing of Late Pleistocene glacial cycles. By conducting cross-spectral analyses of dust flux data and aeolian grain size, he shows that the two proxies do not respond to the same orbital forcing parameters and that grain size data typically displays dominant forcing at precessional, obliquity and ~ 30-kyr frequencies. He concludes that the generalisation that winds are uniformly stronger during glacial periods is not valid and that aeolian dust flux is not related to wind intensity, rather that the level of dust transport is directly related to the climate of the source region. The relationship is more complex than sometimes suggested and is not as simplistic as stronger winds or drier conditions coinciding with glacial stages (Wang, 2009).

8.3.3 XRF elemental ratios

8.3.3.1 Changes in Ti/Al

Ti/Al ratios range between 0.25 and 6.61, with a median value of 2.11 ($1\sigma = 0.84$). The conversion of the data from composite depth to an age scale generates a ~ 600 kyr time-series that contains a number of interesting features (figure 8.8). As an artefact of fitting the data to the age model, the variations in sedimentation rates result in significant bunching and stretching of the evenly spaced measurements. The data exhibits a large degree of variation, particularly towards the higher range of values as a result of the data being expressed as ratios. In a number of places the record is punctuated by abrupt, short-lived negative excursions of approximately 10 kyr in duration. There is no overall trend in the data set, although there is a decrease in mean Ti/Al values between 2.4 (average Ti/Al =3.15, $1\sigma = 0.87$) and 2.3 Ma (average Ti/Al = 1.03, $1\sigma = 0.34$). Parts of the record are characterised by greater variability than others. For example, the period between 2.8 and

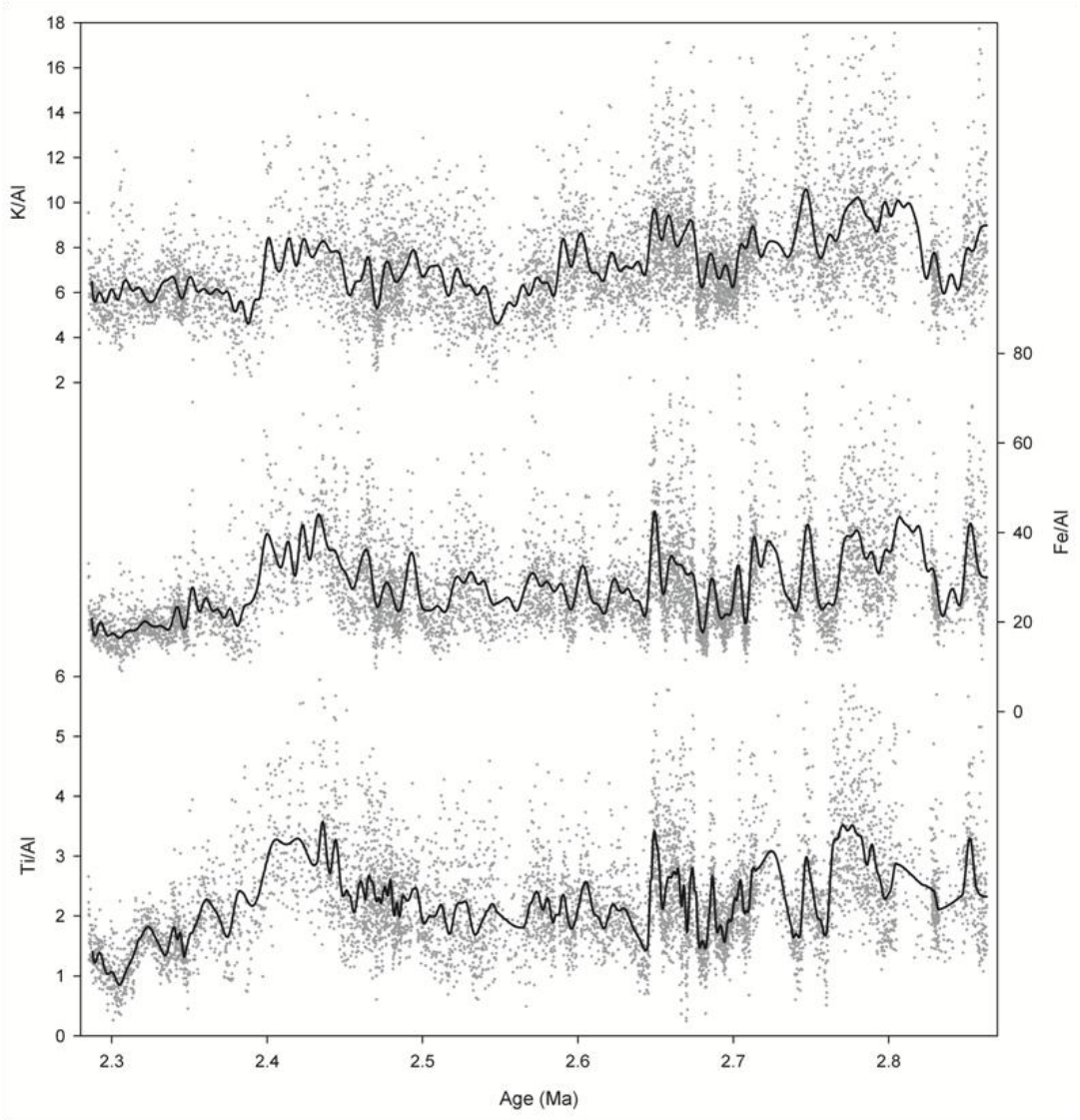

Figure 8.8 Time-series data from scanning XRF analysis of sediment from ODP Site 721/722 detailing elemental ratios linked to the influx of terrigenous material, K/Al, Fe/Al and Ti/Al. Grey dots indicate raw data measurements with a loess smoother applied to illustrate main changes, shown by the black lines.

2.65 Ma is characterised by significant fluctuations in the data with a large degree of variation, whereas the period between 2.65 and 2.5 Ma is relatively stable in comparison and characterised by a smaller range in Ti/Al. The significance of the trend and rates of change are further investigated in section 8.4.1.

The concentration of titanium is related to heavy mineral input from terrigenous material and Ti/Al has been used by a number of authors as a proxy for aeolian dust flux (e.g. Rea 1994; Calvert et al., 1996; Wehausen and Brumsack 2002; Haug et al., 2003; Leuschner et al., 2004). The Ti/Al ratio has also been applied as an indicator of grain size, and therefore also wind intensity, due to the concentration of titanium in the coarser size fraction (e.g.

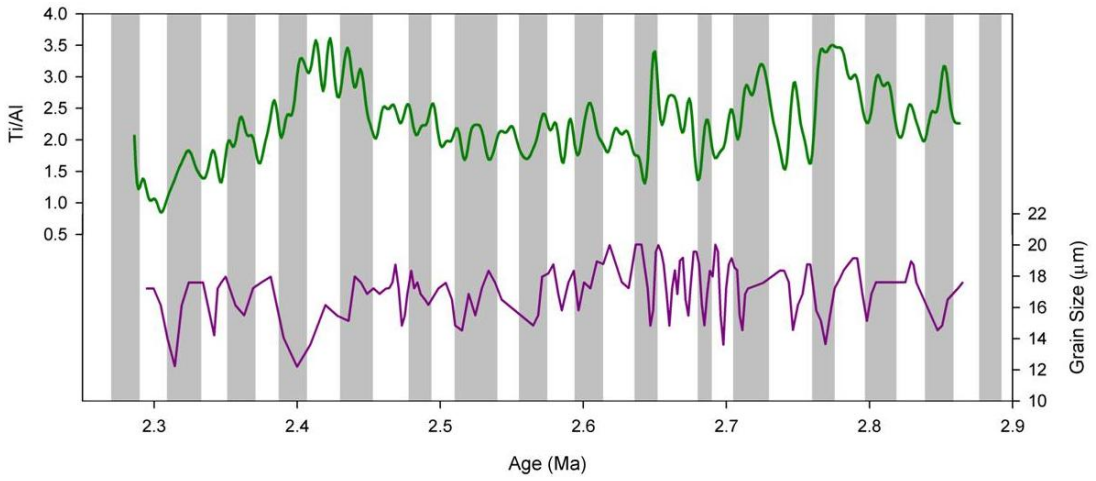

Figure 8.9 Graphs illustrating changes in Ti/Al and corresponding changes in grain size from ODP Site 721/722. Ti/Al data (green line) has been filtered using a lowpass 800-year filter to eliminate excess noise. Grain size data (purple line) from Clemens et al. (1996) has been re-calibrated to the chronology developed for this study in order to directly compare changes during glacial (grey vertical bars) and interglacial (white vertical bars) periods.

Boyle 1983; Shimmield 1992; Reichart et al., 1997; Ziegler et al., 2010). Bulk Ti content has also been used as a lithogenic proxy in areas such as the equatorial Pacific where the total biogenic flux is small and almost all Al is contained with lithogenic aluminosilicates, thus obviating the use of Al-normalisation (Murray and Leinen, 1993; Zabel et al., 1999; Yarincik et al., 2000; Mora and Martinez, 2005). However, this is not applicable in the Arabian Sea where the need to account for organic content is more important as shown by the fluctuations in total organic carbon (TOC) displayed in figure 8.1.

In order to address the relationship between Ti/Al and grain size and to assess the extent to which Ti/Al should be used as a proxy for wind speed, grain size (μm) data measured on cores from ODP Site 722 (Clemens et al., 1996) is plotted against the Ti/Al ratios measured here (figure 8.9). The chronology for the grain size data has been converted from the original age model to that developed as part of this study using the composite depth model described by Murray and Prell (1991, 1992). Grain size measurements are taken to be a direct measure of wind intensity (Clemens et al., 1996) where larger values are associated with stronger wind velocities and thus the increased transport capacity of the winds. If Ti/Al is representative of wind speed, one would expect these two records to mirror one another. However, whilst there are a few occasions where they are in phase, there is otherwise a distinct anti-correlation between the two data sets. Figure 8.9 shows that in general, glacial periods are marked by an increase in Ti/Al and a concomitant decrease in grain size implying that wind speed and Ti/Al are inversely correlated. This supports the assertion by

Rea (1994) that the generalisation that winds are uniformly stronger during glacial episodes is not valid and that glacial periods are generally characterised by arid conditions whilst stronger insolation during interglacial episodes results in an increase in convective precipitation and a strengthening of monsoonal circulation. As a consequence of the seemingly anti-phase relationship between Ti/Al and grain size, Ti/Al is here interpreted to reflect variations in climate, namely relative aridity in the source area.

8.3.3.2 Changes in K/Al

Ratios of potassium to aluminium (K/Al) range from 2 to 18 with a median value of 7.04 ($1\sigma = 2.20$). As with the changes described for Ti/Al, the application of a chronology to this data set has resulted in bunching and stretching of the data at certain points due to changes in sedimentation rate generated from the age-depth model. The resulting K/Al data is highly variable and exhibits a large degree of random noise (figure 8.8). A low-pass bandwidth filter of 800 years was applied to the data in order to eliminate some of this noise and assess 'real' changes within the K/Al data. The filtered data illustrates that there is a very gradual overall decrease in K/Al values between ~ 2.9 and ~ 2.3 Ma. This is punctuated by episodes of high variability e.g. between 2.76 and 2.81 Ma. There are a number of similarities between the time-series for Ti/Al and K/Al. Filtered data for both records demonstrate that the significant features in the Ti/Al data, such as a prominent peak between 2.40 and 2.45 Ma and another between 2.64 and 2.68 Ma, are also reflected to a lesser degree in the K/Al data. The filtered data demonstrates that K/Al varies in a stepwise fashion through time characterised by abrupt shifts to higher values at 2.82 Ma, 2.75 Ma and 2.68 Ma, and rapid decreases at 2.73 Ma, 2.64 Ma and 2.40 Ma.

K/Al is normally adopted as a proxy for fluvial dynamics and is taken to represent the relative compositional balance between the influx of smectitic clays (low K/Al) and illites (high K/Al). Smectites are found in hydromorphic soils and therefore represent wetter climatic conditions whereas illites are generally formed during sediment diagenesis and are often incorporated into the detrital sediment component (Hofmann et al., 2003, 2008). However the elevated positions of ODP 721 and ODP 722 on the Owen Ridge ensure that there is no significant fluvial input to the sites and in such cases, K/Al has also been used as an indicator for continental humidity (De Jonge et al., 2010). The broad similarity between the Ti/Al and K/Al implies that continental humidity does exert some control over the flux of potassium-rich minerals to the Owen Ridge and that it is more likely to represent changes

in the compositional assemblage of clay material delivered to ODP Sites 721/722, primarily through aeolian transport.

8.3.3.3 Changes in Fe/Al

Throughout the 600-kyr record, ratios of iron to aluminium (Fe/Al) range between 10 and 70, with a median value of 26 ($1\sigma = 10$). Changes in Fe/Al (figure 8.8) are highly correlated with changes in Ti/Al and, to a lesser degree, with changes in K/Al. All three time-series display prominent stepped peaks between 2.40 – 2.45 Ma and 2.64 – 2.68 Ma. Whilst there are only broad similarities between the Ti/Al and K/Al data, the Fe/Al time-series exhibits trends that correlate with each record individually. For example, a period of relatively stable values between 2.29 and 2.38 Ma is observed in both the K/Al and Fe/Al records, but not in the Ti/Al time-series.

Fe/Al ratios have been used as proxies for different processes in a variety of depositional settings. Spofforth et al. (2008) use Fe/Al ratios as a proxy for anoxia intensity in a study of sediments from the Arctic Ocean, while Bertrand et al. (2010) find Fe/Al to be indicative of the proximity of the sampling location to the main points of fluvial inflow within fjords in Chile. Contrastingly, Jilbert et al. (2010) find that both K/Al and Fe/Al records from the Eastern Mediterranean are closely coupled to Sahelian aridity. They find that dust sources in North Africa activate or deactivate in response to variations in the distribution of precipitation which in turn is linked to SST variability in the Mediterranean Sea. The diverse variety of ways in which Fe/Al ratios are adopted to investigate environmental change means that there is no consensus over the mechanisms controlling iron flux to the oceans on a global scale and that Fe delivery is more closely related to local, region-specific processes. At ODP 721/722, the close correlation of Fe/Al ratios the Ti/Al and K/Al records suggests that Fe/Al in the Arabian Sea is likely linked to aeolian dust input and, more specifically, to climate conditions in the dust source areas.

8.3.4 Summary

The similarities between the Ti/Al, K/Al and Fe/Al records suggest that all records are broadly indicative of variations in aeolian dust flux, related to changes in source area climate conditions. K/Al ratios reflect changes in the compositional clay assemblage of the lithogenic material and are thus correlated to Ti/Al values through modulation by regional climate processes whereas Fe/Al ratios are closely correlated to both the Ti/Al and K/Al

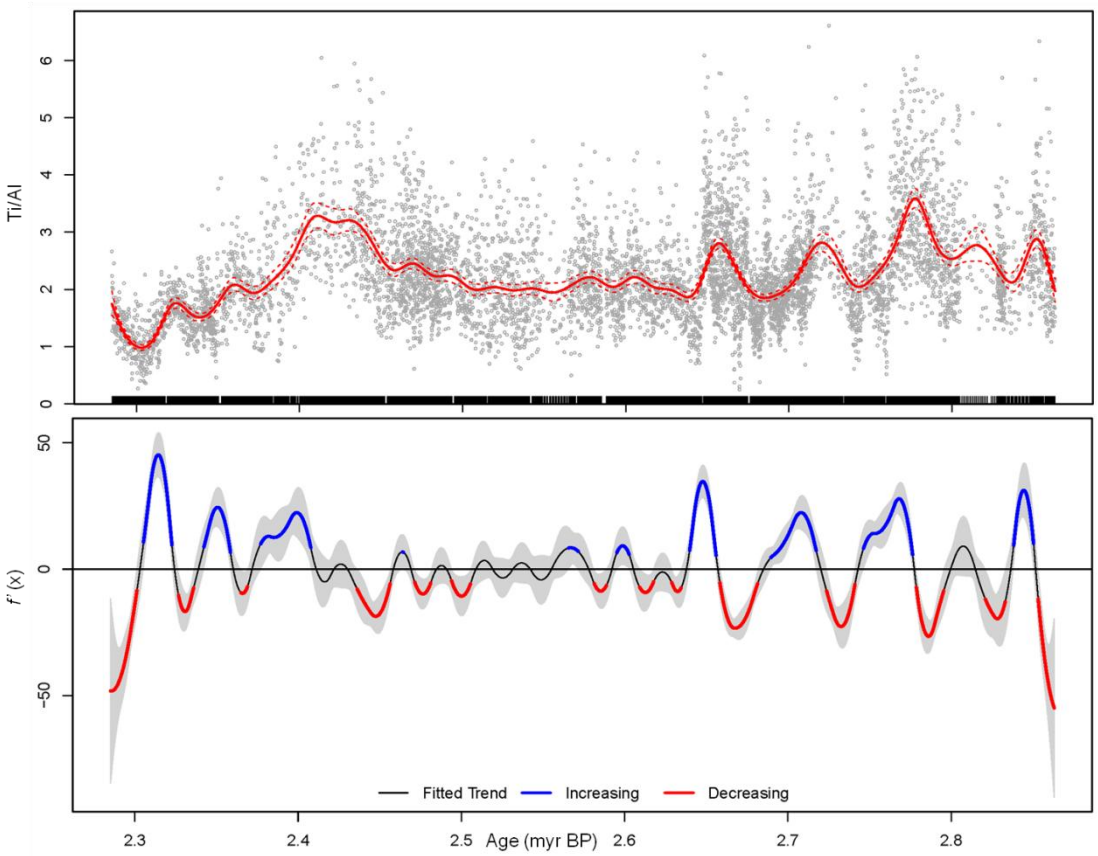

Figure 8.10 Upper graph illustrates raw Ti/Al data (grey dots) and the fitted trend (red line) for the time-series determined using a generalised linear model where the adaptive smoother component is defined by gamma distribution (see text). 99% confidence intervals for the fitted trend are shown by the dashed red lines. Lower graph shows the first derivatives of the fitted trend which are a function of how the degree of change in the trend varies through time. Areas where the trend is significantly increasing or decreasing are shown in blue and red, respectively.

records and appear to reflect variations in the delivery of Fe-rich terrigenous dust to the Arabian Sea. As a result of the similarity between these records, the wider and more established use of Ti/Al as a dust proxy and the more comprehensive understanding of the mechanisms controlling the flux of titanium to the oceans, Ti/Al will be further used to investigate monsoonal circulation variability during the Plio-Pleistocene as a proxy for the aeolian dust flux, controlled by climatic fluctuations in dust source areas.

8.4 Time-Series Analysis of Ti/Al data

As outlined in chapter 7.7, a variety of time-series analyses were conducted on the Ti/Al data generated from ODP Site 721/722 in order to examine the main trends and periodicities present within the record and to assess variations in the intensity of Indian Ocean monsoonal circulation during the Plio-Pleistocene. The results of the different techniques adopted are discussed in detail in the following sections.

8.4.1 Generalised additive models (GAM)

Time-series analyses using generalised linear models (GLM) and generalised additive models (GAM) were used in order to explore the main trends in the XRF data generated from the high-resolution scanning of the ODP Site 721/722 sediment cores. It was found that the most suitable way of applying a model to fit the data in order to best explain the variance was by using a GLM with an adaptive smoother where the response variable was defined as having a gamma distribution (a flexible, continuous probability distribution defined by two parameters, θ and k). The fitting of the gamma GLM, with 99% confidence levels outlined (figure 8.10), permits the identification of significant periods of change and trends within the record. The adaptive smoother allows for the trend to be smooth where there is not much structure within the data and for it to have greater variance during periods of significant change, thus permitting greater flexibility within the fitted trend without the need for a more complex model (Simpson, 2008.). Figure 8.10 shows the fitted trend in the Ti/Al data set. Periods of significant change, determined from the first derivatives of the fitted trend (figure 8.10) are also shown. The derivatives are a measure of how a function changes as its input changes and are an effective way of displaying the rate of change of a fitted function through time.

The model shows that the trend from ~ 2.9 Ma until 2.65 Ma was characterised by episodes of significant and rapid change in Ti/Al ratios. This was followed, from 2.65 Ma until shortly before 2.5 Ma, by a period of relative stability when there is no evident increase or decrease in the fitted trend. After 2.5 Ma, the model demonstrates an overall increasing trend in the Ti/Al data, which appears to start gradually and increase with time. After approximately 2.4 Ma until the end of the time-series, the fitted model shows an overall decreasing stepped trend in the data towards a minimum at around 2.3 Ma (figure 8.10).

Using the first derivatives of the trend fitted to the Ti/Al data, it is possible to further interpret areas of larger variance. Figure 8.10 shows changes in the rate of change of the fitted function with time, and shows that the trend can be broadly divided into three zones. Zones are defined on the basis of a combination of wavelet analysis and GLM modelling and thus may appear slightly different to the trends shown in figure 8.10. The first zone, between ~ 2.9 Ma and ~ 2.6 Ma, is marked by large-scale fluctuations in the first derivatives of the fitted trend indicating highly significant changes in both the positive and negative rates of change of the fitted trend. Contrastingly, the second zone between ~ 2.6 Ma and ~ 2.5 Ma is different in character and marked by a period of relative stability where there is little variation in the trend. The third zone, from approximately 2.5 Ma until ~ 2.3 Ma bears

a greater similarity to the first and is characterised by an overall decreasing trend in the Ti/Al data as shown by the greater tendency towards positive derivative values in figure 8.10.

Whilst the model is of relatively low resolution (n = 1,000), the fitted trend does a good job of explaining the variance within the data and highlights a number of points where the variance, which might otherwise have been regarded as noise, is statistically significant and indicative of important periods of change. In order to analyse changes at a higher resolution, the complexity of the model would have to be greatly increased, thus increasing the computing time and power required to process each of the GAMs or GLMs tested. The size of the data set analysed (n=6,891) and the amount of spurious noise associated with the data obscure shorter-term significant changes in the signal and it is therefore necessary to adopt other techniques to further explore the Ti/Al data.

8.4.2 Spectral analysis

In addition to the fitted trends described above which look at variance within the data set as a whole, spectral analysis techniques were used to explore cyclicities present within the data. Results of the spectral analysis, using the Lomb-Scargle method and wavelet analysis (described in chapter 7.7) of the Ti/Al data, are discussed below. The construction of the $\delta^{18}O$-based chronology presented here means that it is difficult to accurately assess the associated dating errors and therefore it is important to note that due to these inherent uncertainties in the age model, all cyclicities are referred to as approximate in duration.

8.4.2.1 Lomb-Scargle spectral analysis

In order to evaluate the nature of the dominant periodicities present within the Ti/Al record, spectral analysis was conducted using the Lomb-Scargle Fourier Transform method (Lomb, 1976; Scargle, 1982). Unlike other techniques for spectral analysis, the Lomb-Scargle method does not require data to be evenly spaced in time, something which is rarely the case when dealing with palaeoclimate data where material is typically sampled at linearly-spaced depth intervals. Most other forms of spectral analysis require data to be interpolated onto an evenly-spaced age scale prior to analysis, which can introduce artefacts to the data in both the time and frequency domains (Trauth, 2010). In order to eliminate some of the noise contained within the Ti/Al dataset, a low-pass 800-year filter was applied to the data prior to spectral analysis. A comparison of the raw and filtered data is shown in figure 8.11a. The resulting Lomb-Scargle power spectrum is displayed in figure 8.11b.

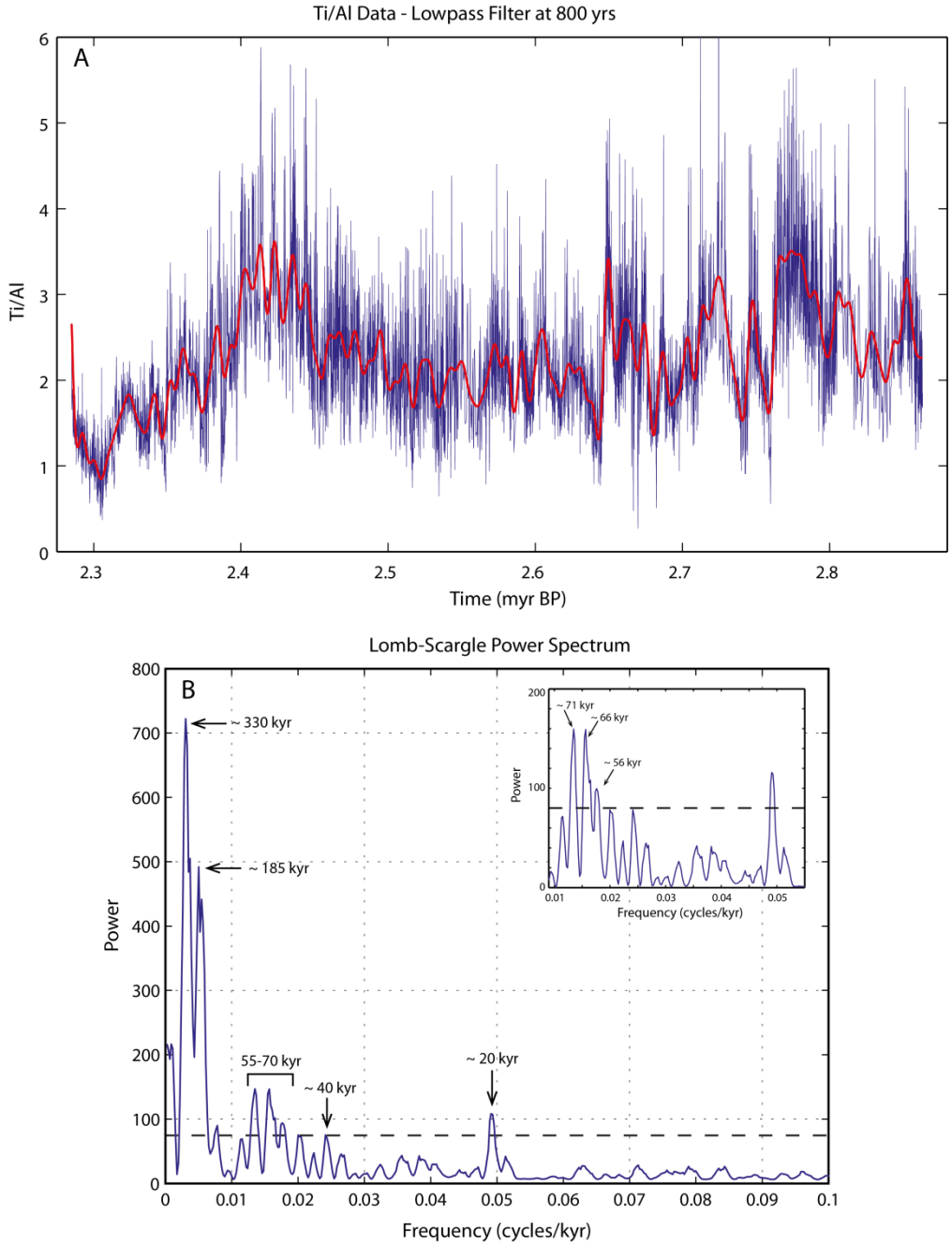

Figure 8.11 Graph **A** shows raw Ti/Al data (in blue). A lowpass filter at 800 years was applied to the data (in red) in order to perform spectral analysis and better compare the ODP 721/722 record with data from other sites. Graph **B** shows the resulting power spectrum when Lomb-Scargle spectral analysis was performed on the filtered Ti/Al data. Inset focuses on the spectral peak representing periodicities between 55 and 70 kyr. Dashed lines indicate 95% confidence levels

A number of features of the power spectrum are immediately apparent. There is a dominant double spectral peak at frequencies corresponding to approximately 330 kyr (f = 0.003) and 200 kyr (f = 0.005). Given that the total time span of the ODP 721/722 dust record is approximately 577 kyr, this suggests that the spectral analysis is detecting cycles which

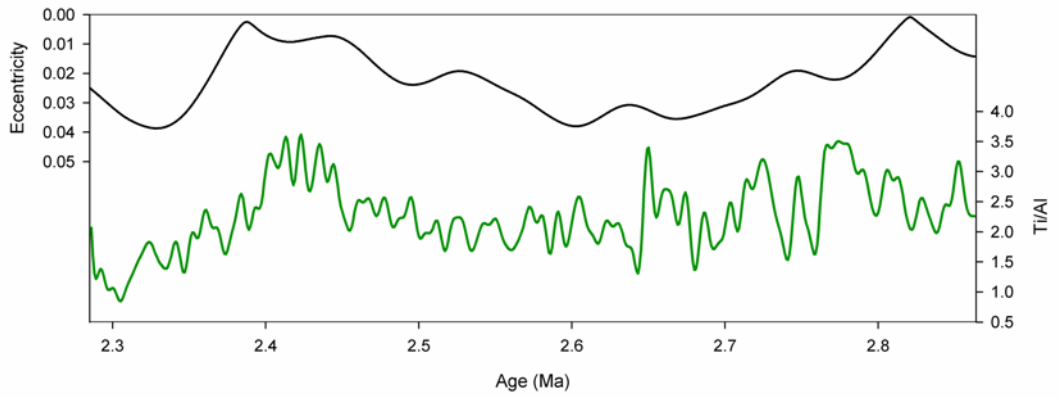

Figure 8.12 Graph illustrating the strong relationship between eccentricity and changes in Ti/Al. Filtered Ti/Al data is plotted against calculated eccentricity values (Laskar et al., 2004) for the period studied. Note that the eccentricity axis is reversed.

cannot be fully explored or tested due to the comparatively short duration of the time-series.

Through visual inspection of the Ti/Al record it is evident that there is a prominent long-term 400 kyr cycle within the record which is related to the long phase of eccentricity (figure 8.12). The expression of this in the Ti/Al record is less than 400 kyr, with one full cycle occurring between 2.77 Ma and 2.42 Ma (350 kyr) that approximately correlates with the peak observed in the Lomb-Scargle spectral analysis. This correlation to eccentricity could explain the persistent ~ 330 kyr cycle observed in the results of other methods such as evolutionary or Welch's power spectral analyses (see appendix).

At higher frequencies, the results of the spectral analysis are more reliable. Figure 8.11b shows significant spectral peaks at frequencies of ~ 0.014, ~ 0.015 and ~ 0.049 which correspond to periodicities of ~ 71, ~ 66 and ~ 20 kyr, respectively. There is also a minor peak at a frequency of ~ 0.024 which corresponds to a periodicity of ~41 kyr. Spectral peaks at ~ 40 and ~ 20 kyr correspond to the orbital cyclicities of obliquity and precession and demonstrate the relative importance of orbital forcing in driving low-latitude monsoonal circulation in the Indian Ocean. In addition to these, there is also a complex double spectral peak at ~ 71 and ~ 66 kyr with a side peak at ~56 kyr (see figure 8.11b). This is discussed in greater detail in section 8.4.2.3.

8.4.2.2 Wavelet analysis

In order to explore changes in cyclicity through time, wavelet analysis was also conducted on the filtered Ti/Al time-series. In contrast to Lomb-Scargle analysis, wavelet analysis

requires that data are evenly spaced in the time domain and data were linearly interpolated at 100-yr intervals prior to analysis (mean spacing on an uneven time axis = 83.5 years). Wavelet analysis uses base functions or wavelets consisting of small packets of waves defined within certain frequencies that are translated into changes in the time-frequency domain using a mother wavelet, in this case the Morlet wavelet which is commonly used in palaeoclimate studies (Torrence and Compo, 1998; Trauth 2010).

The wavelet power spectrum for the Ti/Al data is displayed in figure 8.13. The spectrum shows high-resolution changes in both the time and frequency axes and demonstrates that the periodicities detected by Lomb-Scargle analysis are not necessarily present throughout the entire time series. Figure 8.13 shows significant periodicities at frequencies of ~ 0.01, ~0.015, ~ 0.025 and ~ 0.05 kyr^{-1} corresponding to cycles of approximately 95, 70, 40 and 20 kyr in length, respectively. The wavelet power spectrum shows that there is a relatively weak ~ 40 kyr (obliquity) cycle and stronger ~ 20 kyr (precession) cycle which are probably present through the entire time series whereas a strong ~ 95 kyr cycle appears after approximately 2.45 Ma. Similarly there is a strong signal within the 60-70 kyr frequency band which is present until approximately 2.6 Ma but not after this time.

8.4.2.3 The 60-70 kyr cycle

The pervasive 60-70 kyr cycle present within the early part of the Ti/Al record is observed within the results of both Lomb-Scargle (figure 8.11b) and wavelet analysis (figure 8.13). Periodicities of this duration are not in line with the expected orbital cycles associated with eccentricity (413 kyr, 95 kyr), obliquity (41 kyr) and precession (23 kyr, 19 kyr) which are more often observed within palaeoclimate time-series. Despite this there are occasional reports of a 60-70 ka cycle within some other palaeoclimate records (e.g. Hooghiemstra et al., 1993; Muller and MacDonald, 2000; Dawson et al., 2004; Tian et al., 2006; Phedorin and Goldberg, 2008). Hooghiemstra et al. (1993) find that long-term spectral analysis of part of the Funza I pollen record from Colombia (30 – 1450 Ka) exhibits a notable 60-70 kyr cycle in addition to the more classical precessional and obliquity periodicities. However, this cycle is not present in all elements of the data, which are classified by vegetation group, and is only prominent in the analysis of the 'subparamo', 'marsh' and older part of the "arboreal pollen excluding *Alnus*" elements. The authors do not assign any special significance to this oscillation and suggest that it, and other cycles of ~ 10, ~ 13 and ~ 15 kyr are the result of a non-linear response of the climate system.

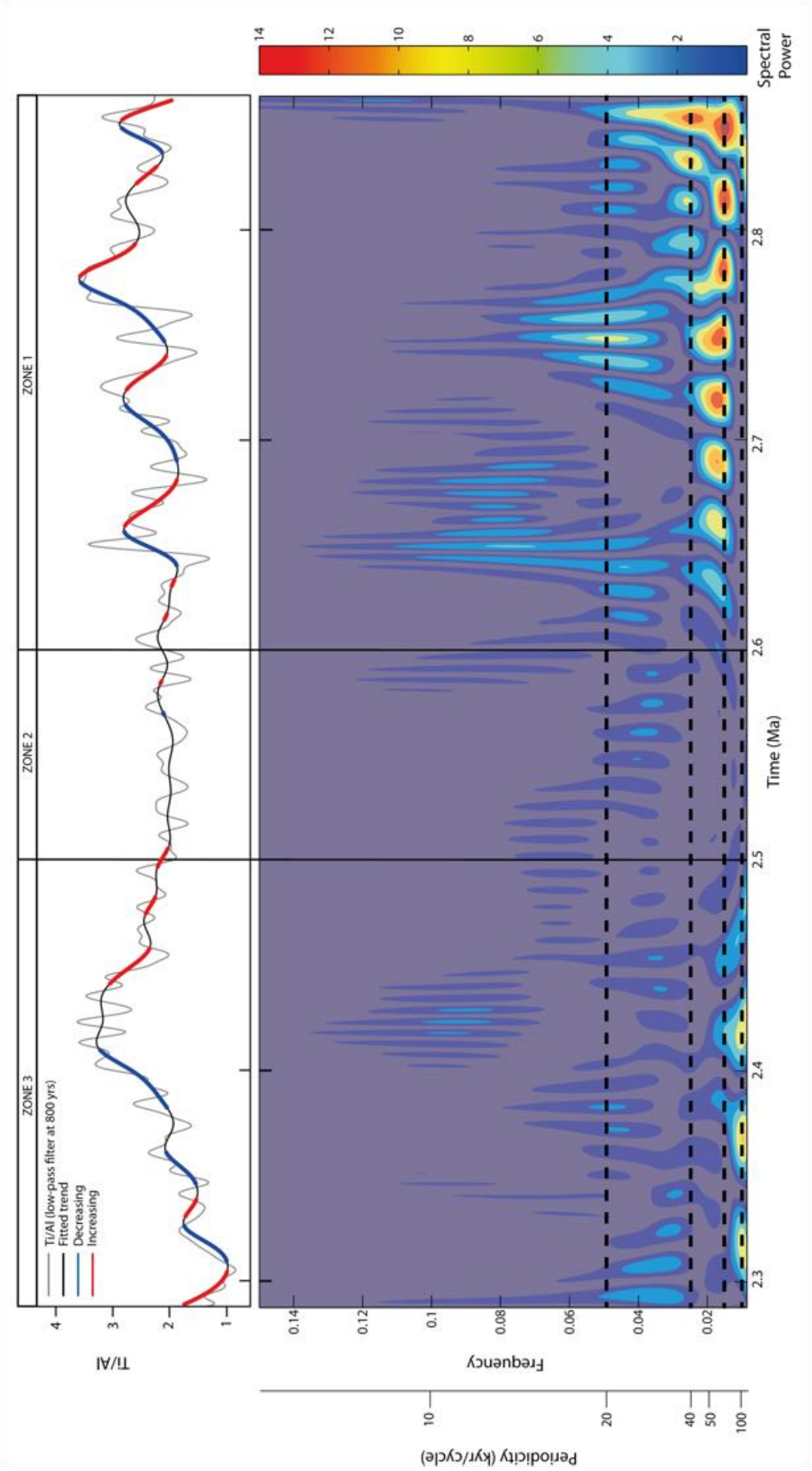

Figure 8.13 Upper panel shows filtered Ti/Al data with fitted trend superimposed over the data. Periods of significant increase or decrease in the fitted trend are shown in red and blue, respectively. The lower panel shows the wavelet power spectrum for the filtered Ti/Al data. Frequencies and the equivalent periodicities are shown on the left and the prominent cycles are marked by dashed black lines. The timings of Zones 1-3 is depicted in both diagrams and shows the division of the record based on changes in variability and trend.

Muller and MacDonald (2000) examine a number of published palaeoclimate records and assess the degree to which the spectral analysis of these data is affected by astronomical tuning to orbital timescales, thus introducing the potential for circular reasoning and making it difficult to validate different tuning methods. They find that when examined in detail, the ~ 100 kyr eccentricity spectral peak of the Low Latitude Stack (LLS) (Bassinot et al., 1994) is composed of a main peak at 95 kyr with side peaks at 121 kyr and 72 kyr, whilst analysis of another record from ODP Site 664 (Raymo et al., 1997) shows that a sub-peak periodicity at 66 kyr is only present in the data set after the application of a time scale tuned to eccentricity, obliquity and precession. Muller and MacDonald (2000) demonstrate that improper tuning creates significant bias within the resulting power spectra towards the expected orbital frequencies. They circumvent the problems of overtuning by adopting linear sedimentation rates calculated from estimated ages at the beginning and end of the sequences. However this also carries limitations as it has been shown (e.g. Droxler and Schlager, 1985; Francois et al., 1993; Emeis et al., 1995) that there are often significant variations in sedimentation rates during glacial-interglacial cycles. Such variations in sedimentation rates, and thus the corresponding differences in the age-depth models could also generate uncertainties within the resultant power spectra. Muller and MacDonald (2000) recommend wherever possible to work with unturned or minimally tuned data in order to more accurately assess the role of orbitally-driven insolation in driving past climate change.

Phedorin and Goldberg (2008) also note the presence of a residual 70 kyr cycle in the spectral analysis of a continental palaeoclimate record from Lake Baikal (Goldberg et al., 2000) and suggest that the existence of spectral peaks in the 60-70 kyr frequency band represents a nonlinearity which arises either through errors in the astronomical tuning of the age model used or is inherent in the natural climate response through feedback mechanisms or threshold effects. Dawson et al. (2004) also report a strong ~70 kyr cycle in the spectral analysis of elemental silicon concentrations from Lake Baikal between 1.43 and 0.70 Ma. The strong ~ 70 kyr cycle occurs in conjunction with a weaker 42 kyr cycle during a transitional period in the record compared to a strong 100 kyr cycle after 0.7 Ma and moderate 465 kyr and 155 kyr cycles prior to 1.43 Ma. Dawson et al. (2004) attribute this to the findings of Muller and MacDonald (1997) who suggest that the period between 1.5 and 1.0 Ma is not clearly defined relative to the dominance of the ~100 kyr eccentricity or ~ 41 kyr obliquity cycles.

In a Late Pliocene sea surface temperature record from the South China Sea, Tian et al. (2006) find that there are strong variations at the non-orbital periodicities of 58-kyr and 31-kyr with only weak variations at the primary orbital phases of precession, obliquity and eccentricity. Phase analysis of an Arabian Sea summer monsoon stack constructed from 5 independent dust proxies from the Owen Ridge over the last 350,000 years (Clemens and Prell, 2003) found that while much of the total variance of the monsoon stack is explained by obliquity (26%) and precessional (18%) forcing, a further 22% of the variance is distributed at periodicities of 66 kyr and 16 kyr. The authors suggest that these non-orbital peaks maybe be explained by heterodynes (the result of combining different oscillating waveforms) of precession and obliquity. From their analysis, Clemens and Prell (2003) also infer that the dominance of variance in the obliquity bandwidth over that of precession indicates that the strength, onset and duration of the summer monsoon in the Arabian Sea are sensitive to internal forcing mechanisms or additional factors such as a Southern Hemisphere latent heat source (for further discussion, see chapter 1.6.3 and Clemens and Prell, 2003). In the case of the ODP 721/722 Ti/Al data examined here, it is evident that there is significant forcing in the orbital precessional (~ 20 kyr) and, to a lesser extent, obliquity (~ 41 kyr) spectral bands. As discussed above, the ~ 60-70 kyr periodicity cannot be easily explained by astronomical oscillations and could possibly arise from:

- Errors, such as overtuning, in the astronomical tuning of age models linked to orbitally-forced insolation changes (for further details, see Muller and MacDonald, 2000) or;
- Natural nonlinearity inherent in the orbital climate response which may arise through feedback or threshold effects.

The age-scale in this project was determined by correlation to the LR04 global benthic $\delta^{18}O$ stack (Lisiecki and Raymo, 2005) which was constructed using a conservative timing strategy whereby the stacked $\delta^{18}O$ data was tuned to a simple ice model. Because tuning is minimised in the construction of the LR04 stack, it suggests that the presence of the 60-70 kyr periodicity may be more likely to have resulted from a nonlinear climate response of the Arabian Sea and dust source regions to orbital forcing. However, as shown in figure 8.13, the 60-70 kyr cycle is not present throughout the entire period spanned by the Ti/Al data and would appear to only be of importance prior to approximately 2.6 million years ago.

Spectral analysis of the LR04 benthic stack for the same time period (between ~ 2.9 and ~ 2.3 Ma) generates significant peaks at the expected orbital frequencies of ~ 0.01 (~ 100 kyr),

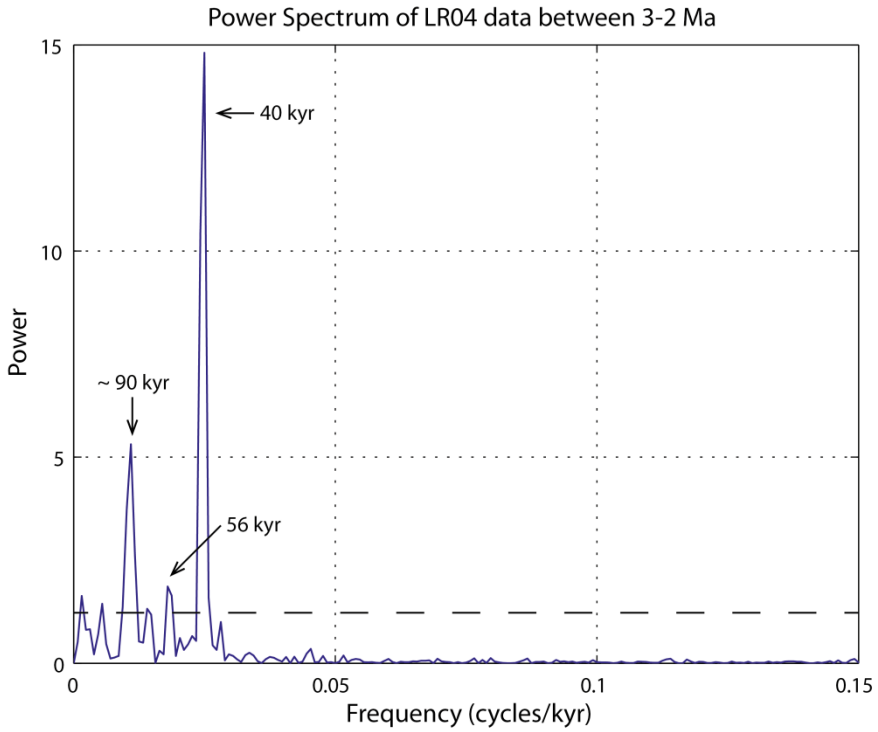

Figure 8.14 Power spectrum from spectral analysis conducted on the LR04 global benthic stack (Lisiecki and Raymo, 2005) between 3.0 Ma and 2.0 Ma. There is a dominant spectral peak corresponding to the ~ 40-kyr obliquity cycle and a significant peak at the ~90-kyr short cycle of eccentricity. There is also a more minor peak at approximately 56-kyr which corresponds with the results from the spectral analysis of the Ti/Al data from ODP Site 721/722. Dashed line indicates 95% confidence level.

~ 0.025 (~ 40 kyr) and ~ 0.043 (~ 23 kyr) (figure 8.14). However it also generates some variance at periodicities of ~ 56 and ~ 70 kyr, possibly explaining some of the presence of the dominant 60-70 kyr cycle observed in the Ti/Al record.

The transition in the record at approximately 2.6 Ma coincides with the newly redefined start of the Quaternary period (Gibbard et al., 2010) which is marked by fundamental cooling and changes in the Earth's climate which occurred between 2.8 and 2.4 Ma (Head et al., 2008). As described in chapter 1.4, the Pliocene – Pleistocene transition is marked by the intensification of Northern Hemisphere glaciation (iNHG) between approximately 2.7 Ma and 2.5 Ma. This transition in global climate is thought to be linked to the closure of oceanic seaways or gradual tectonic uplift (see chapter 1.4.3) (Mudelsee and Raymo, 2005) and occurs in conjunction with an increase in the amplitude of orbital obliquity cycles (Berger and Loutre, 1991). A shift in climate at this time is also noted in North Atlantic records of ice-rafted debris (Kleiven et al., 2002; Bartoli et al., 2005), in the onset of water column stratification in the Southern Ocean (Sigman et al., 2004) and in the North Pacific (Haug et al., 2005), in the widespread expansion of loess and palaeosol sequences in China (Ding et

al., 2005) and in records of climate variability from East Africa (e.g. Trauth et al., 2005, 2007; Kingston et al., 2007).

8.4.3 Summary

The resulting trend fitted to the data by a gamma GLM does a good job of explaining much of the variance within the Ti/Al data set. The results of this model are largely supported by the results of wavelet analysis (figure 8.13), and the two analyses suggest that the Late Pliocene Ti/Al record from ODP 721/722 can be broadly subdivided into three zones, which are defined as follows:

- **Zone 1 (prior to ~ 2.6 Ma)**
  Fluctuations in Ti/Al are highly variable and undergo rapid and substantial changes associated with a ~ 60-70 kyr cyclicity. There is also a strong ~ 20 kyr precessional cycle present throughout this time. The presence of the ~ 60-70 kyr periodicity during this time is possibly the result of nonlinearity in the climatic response to orbital forcing or the result of errors in the astronomical tuning of the age model. The marked transition in the record between zones 1 and 2 at approximately 2.6 Ma is coincident with the start of the Quaternary period and a widespread cooling transition in global climate.

- **Zone 2 (~ 2.6 Ma to ~ 2.5 Ma)**
  The trend in Ti/Al is relatively stable with no significant overall change in values or variance. A ~ 25 kyr cycle persists throughout, likely related to precession, yet somewhat weaker than in zone 1.

- **Zone 3 (~ 2.5 Ma to ~ 2.3 Ma)**
  The early part of zone 3, prior to ~ 2.43 Ma is characterised by an increasing trend in Ti/Al. For the latter part of the record, there is a marked overall stepwise decrease in the trend in Ti/Al. After approximately 2.45 Ma, the record is characterised by a prominent ~ 95 ka eccentricity periodicity and a persistent ~ 20 kyr precessional cycle.

The time-span of the record studied here is not sufficient to permit analysis at greater bandwidths such as the 400-kyr eccentricity cycle. However as described in section 8.3.3.1, there is a very clear anti-phase correlation between long-term changes in Ti/Al with eccentricity. Periods of low eccentricity values occur between 2.38 and 2.45 Ma and

between 2.80 and 2.84 Ma (figure 8.12) and correlate with episodes of high Ti/Al flux. The record clearly shows that, over long timescales, the influence of eccentricity is an important driving mechanism for the control of climatic variability.

8.5 Low-latitude Monsoonal Variability during the Pliocene

As outlined above (section 8.3), changes in Ti/Al ratios are assumed here to reflect variations in the flux of aeolian dust to the Owen Ridge in the Arabian Sea, which is largely driven by changes in the climate of the dust source regions. Higher Ti/Al ratios reflect an increase in the amount of titanium, and therefore dust, being delivered to the Owen Ridge as a result of aridification and soil deflation. The record of dust flux to the Arabian Sea exhibits precessional ~ 20-kyr and ~ 70-kyr periodicities and is also strongly modulated by the 400-kyr eccentricity cycle with highs in Ti/Al coincident with eccentricity minima.

There are a number of previously published records from the Arabian Sea region which explore changes in different variables, including dust-related parameters, throughout the Pleistocene and occasionally as far back as the Pliocene (e.g. deMenocal et al., 1991; Clemens and Prell, 1991, 2003; Krissek and Clemens, 1992; Shimmield, 1992; deMenocal, 1995, 2004; Emeis et al., 1995; Clemens et al., 1996, 2008; Reichart et al., 1997; Honjo et al., 1999; Prins et al., 2000; Sirocko et al., 2000; Preusser et al., 2002; Leuschner et al., 2004; Cleaveland and Herbert, 2007; Thamban et al., 2007; Herbert et al., 2010). A number of these studies analyse data from ODP Sites 721 and 722 which, as a virtue of its elevated position on the Owen Ridge, is not influenced by fluvial sediment input from the surrounding continents and which has a long sediment recovery that extends back to the Miocene (~ 7 Ma).

8.5.1 Sea surface temperatures

A record of Uk37' alkenone-based sea surface temperature (SST) change developed for ODP sites 721 and 722 (Herbert et al., 2010) spans the last 3.4 million years and shows that, during the Late Pliocene, SST values varied between 25.7 and 28.0 °C, largely in accordance with glacial-interglacial cycles. Glacial periods are marked by an average decrease in temperature of approximately 0.7 °C, with the notable exception of a marked decrease in temperature of 1.5 °C at a composite depth of 85.19 mbsf (figure 8.15). In general, negative excursions in SST occur in line with an increase in Ti/Al values marking an increase in the input of terrigenous material to ODP 721/722 and therefore an increase in

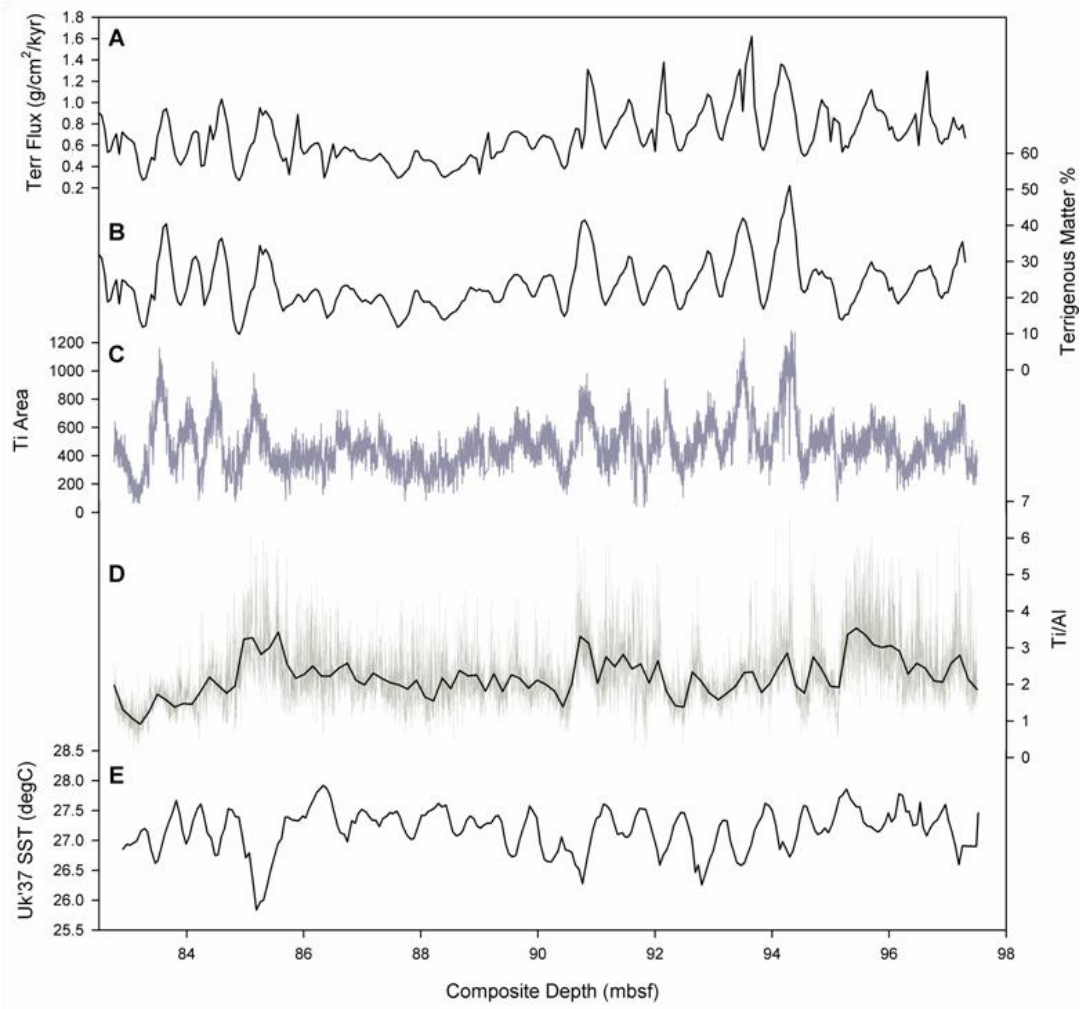

Figure 8.15 Various dust-related proxies have been investigated using sediments from ODP Sites 721 and 722 including a terrigenous dust flux parameter (graph **A**) and the relative proportion of terrigenous matter within the core sediment (graph **B)** from deMenocal (1995, 2004). These are plotted against the high-resolution raw Ti count data (graph **C**) and normalised Ti/Al values (graph **D**) from this project and the alkenone Uk37' sea-surface temperature record (graph **E**) of Herbert et al. (2010). The records shown are plotted against composite depth where records **A** and **B** have been adjusted to the composite depth model of Murray and Prell (1992) – see section 8.5.2.1.

source area aridity around the Arabian Sea region, linked to the intensity of the SW summer monsoon.

The record was initially calibrated to the age model of Clemens et al. (1996), which, as described in section 8.2.4, is based on the orbital tuning of lithogenic flux data based on a prominent precessional periodicity. When compared to the updated chronology based on benthic foraminiferal $\delta^{18}O$ values developed as part of this study, there is a difference of up to 330 kyr between the time span of the different age models. In order to directly compare the SST record with other data from ODP 721/722, the data is plotted against composite depth (figure 8.15) and was subsequently aligned to the age-depth model developed for this

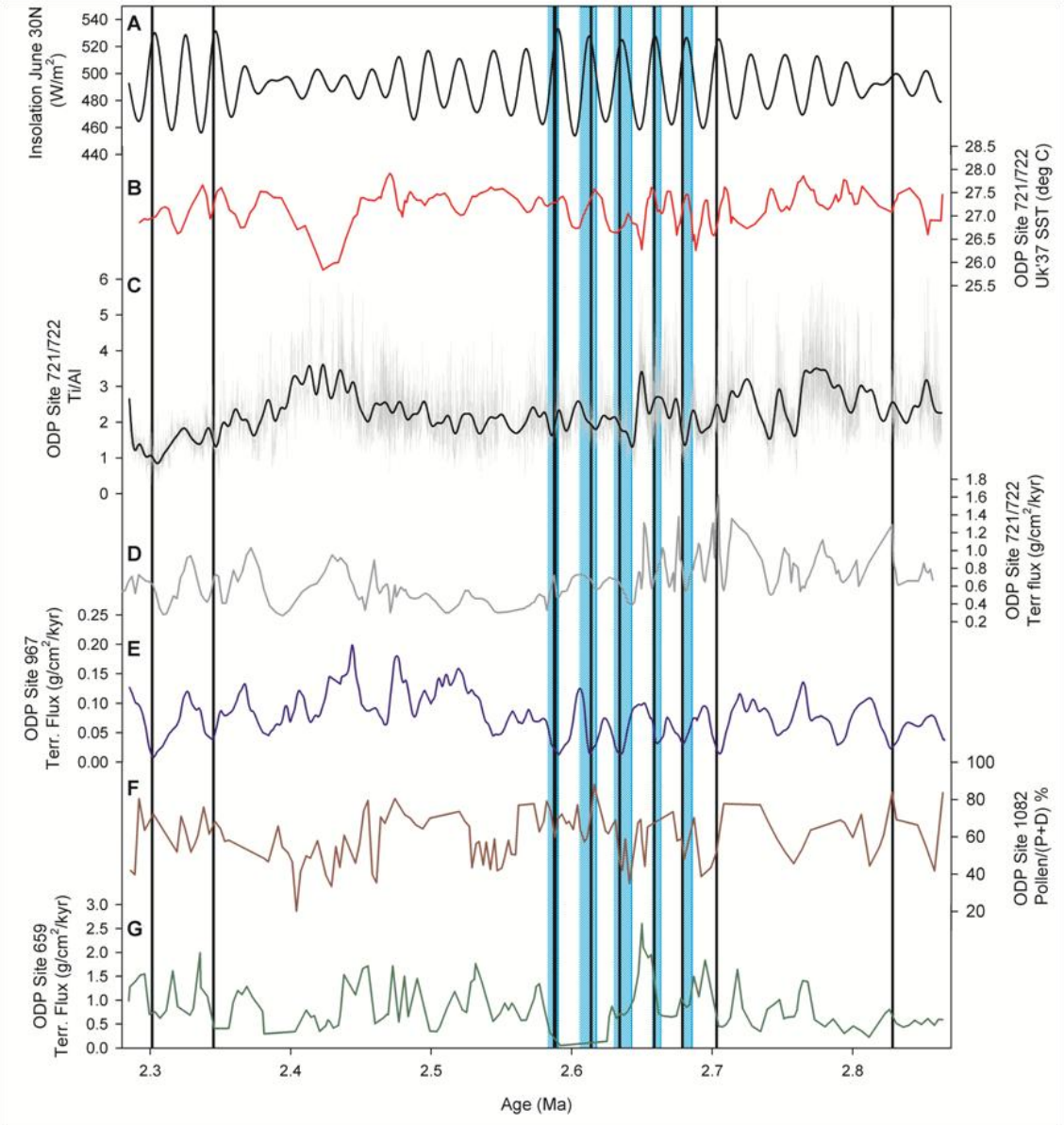

Figure 8.16 Plio-Pleistocene dust flux changes at ODP Site 721/722 as derived from variations in the Ti/Al ratio compared to other records of aeolian dust transport from around Africa. Graph **A** shows the calculated changes in summer (June) insolation at 30 °N for the studied period (Laskar et al., 2004) against changes in sea-surface temperature (Graph **B**) (Herbert et al., 2010) and Ti/Al changes (Graph **C**; raw data = grey, filtered data = black line). The low-resolution terrigenous flux data from ODP 721/722 (deMenocal 1995, 2004) is shown in Graph **D**. Data for graphs **B** and **D** have been adjusted to the chronology developed for this study in order to make direct comparisons. These are compared to records from the Eastern Mediterranean Sea (Graph **E**; Larrasoaña et al., 2003), Southwest Africa (Graph **F**; Dupont et al., 2005, where P+D is the sum of pollen and dinoflagellate cysts) and West Africa (Graph **G**; Tiedemann et al., 1994). The timings of the Barsemoi diatomites deposited in the Barino-Bogoria Basin in the East African Rift Valley (blue vertical bars; Deino et al., 2006) and periods of sapropel formation in the Mediterranean Basin (grey vertical bars; Kroon et al., 1998; Lourens et al., 2004).

study so that wider comparisons can be made to assess regional differences in monsoon strength. The application of the revised chronology to the SST data results in a shift of the marked cold period (at a composite depth of 85.19 mbsf) dated at 2.71 Ma (according to the

age defined by Clemens et al., 1996) to a revised age of 2.42 Ma which is coincident with Marine Isotope Stage (MIS) 96, the last of three strong glacial periods during the early Pleistocene (MIS 100, MIS 98, MIS 96).

Comparison to other data from ODP 721/722 demonstrates that SST and grain size (wind speed) vary coherently in line with glacial and interglacial cycles with glacial periods being characterised by lower temperatures and generally lower wind speeds. This can be explained by a general reduction in the strength of monsoonal circulation during glacial periods that is linked to lower sea surface temperatures and would cause reduced wind speeds. However as discussed in chapter 1.6.3, the linkages between monsoonal circulation and glacial-interglacial cycles are not straightforward and source area aridity is believed to be more important for the interpretation of dust flux records.

It is widely recognised that enhanced sea surface temperatures in the Indian Ocean have a marked impact on the strength of the Indian Ocean and Asian monsoonal systems through the generation of greater levels of convective precipitation (Saji et al., 1999; Webster et al.,1999; Annamalai et al., 2005; Abram et al., 2008). Temperature fluctuations in the Indian Ocean may also be affected by either El Niño Southern Oscillation (ENSO) cycles (Saji and Yamagata, 2003) or the Indian Ocean Dipole (IOD) (Abram et al., 2007, 2008) which form dominant modes of interannual variability that can have a drastic effect on climatic extremes and ocean-atmosphere circulation in the region (see chapter 6.4.2). Climate modelling studies (e.g. Annamalai et al., 2005; Vuille et al., 2005) have demonstrated a close linkage between enhanced precipitation in East Africa and the coupled ocean-atmosphere system in the Indian Ocean (i.e. IOD) at times when the eastern Indian Ocean is cool and the western Indian Ocean is anomalously warm such that there is a strong basin-wide E-W SST gradient. Given the established relationship between SST and rainfall levels it follows that during the extreme wet episodes in East Africa characterised by extensive lake development in the Baringo-Bogoria basin, SSTs in the Arabian Sea are elevated. Figure 8.16 shows that the timing of diatomite units #1-5 coincides with an average increase in temperature at Site 721/722 of 1 °C. This correlation provides further support for the hypothesised strengthening in monsoon circulation which resulted in the rapid, precessionally-paced development of palaeo-lake Baringo. This is further discussed in section 8.5.4.

8.5.2 Tropical records of aeolian dust supply

A number of studies of variations in past monsoonal circulation have employed various dust proxies as indicators of relative changes in the amount of aeolian transport to the tropical oceans (e.g. Tiedemann et al., 1994; deMenocal, 1995, 2004; Clemens et al., 1996; Larrasoaña et al., 2003; Dupont et al., 2005, 2006; Ziegler et al., 2010). The following section aims to compare the ODP 721/722 dust flux data to some other Plio-Pleistocene dust records from sites around the African continent (figure 8.17), including other records from the Arabian Sea.

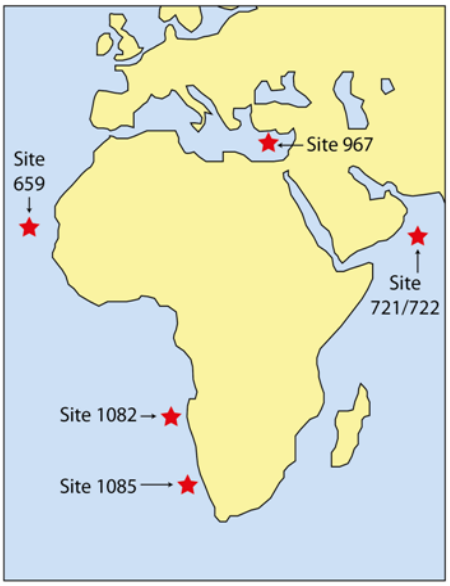

Figure 8.17 Map showing the locations of dust records from around the African continent discussed in the main text.

8.5.2.1 Arabian Sea

In order to directly compare Plio-Pleistocene variations in the different dust flux parameters measured on sediments from ODP Sites 721 and 722 between ~ 2.9 and ~ 2.3 Ma, data is compared on a composite depth scale to avoid complications caused by the adoption of different age models. However even this approach is not straightforward. Studies by deMenocal (1995) and Clemens et al. (1996) analyse both the percentage of lithogenic matter with the sediment record and a measurement of terrigenous dust flux ($g/cm^2/kyr$). Theoretically, on a composite depth scale, the same proxy measurements from the two studies should vary in parallel with one another. However, as displayed in figure 8.18, there is a notable offset between the two data sets. Closer examination of the data reveals that this is an artefact of the composite depth models used which result in a difference of approximately 40 cm between the two records. Clemens et al. (1996) adopt the composite depth model used in this study and first described by Murray and Prell (1991, 1992) whilst deMenocal (1995) uses a different model. Therefore in order to make direct comparisons between the two records and to compare this data to the high-resolution Ti/Al record, it is necessary to subtract a 40 cm lag from the composite depth scale given by deMenocal (1995). This adjustment means that changes in the lithogenic component and terrigenous flux calculated from Clemens et al. (1996) and deMenocal (1995) more closely reflect the actual core position from which measurements were made. Figure 8.18 shows that once this

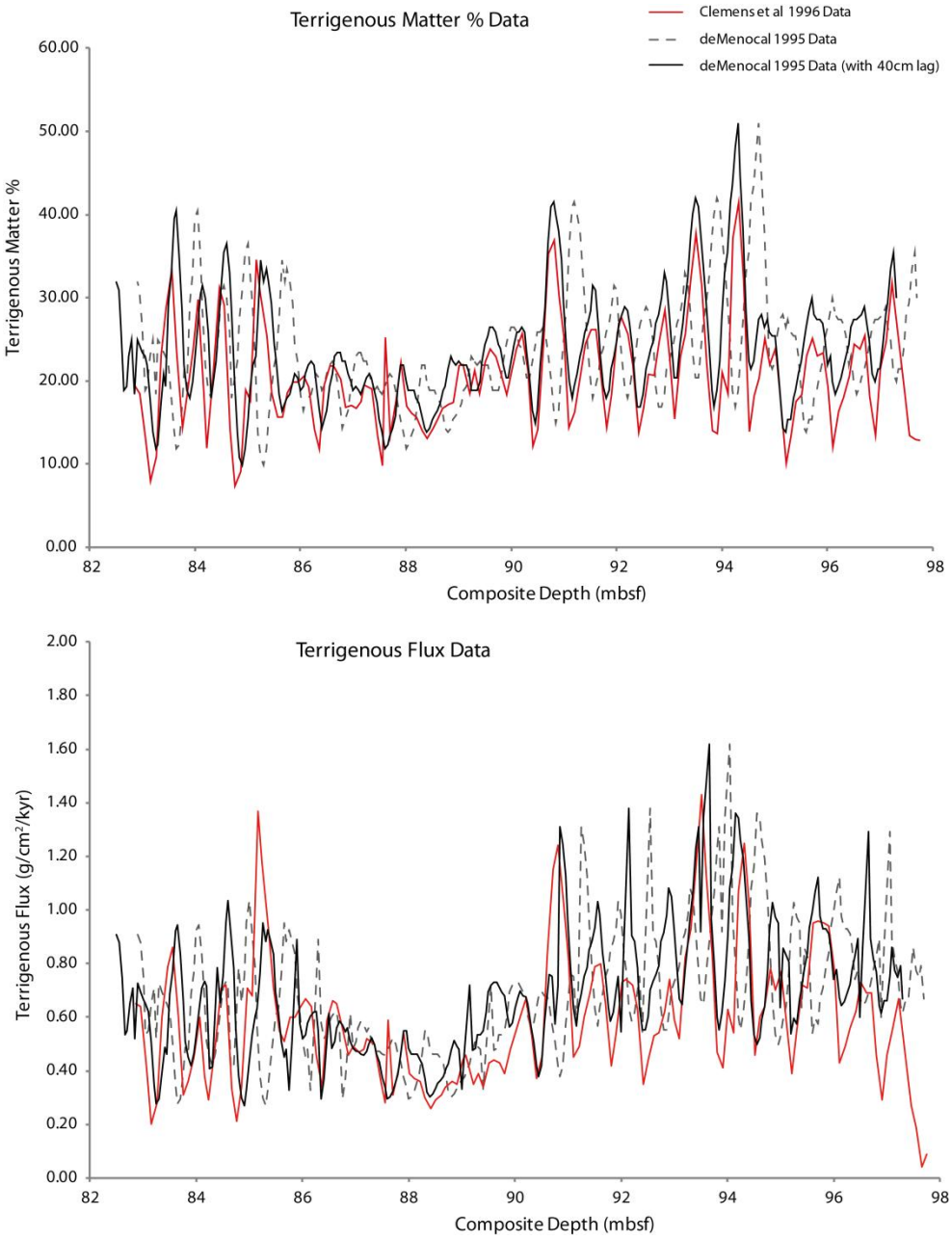

Figure 8.18 A comparison of the different terrigenous matter and dust flux data previously published for ODP Site 721/722 (deMenocal, 1995; Clemens et al., 1996). The two records use the same proxies which ought to reflect the same changes, however there is a notable offset between the records of deMenocal (1995) (dashed grey line) and Clemens et al. (1996) (red line). This is the result of the use of a different composite depth model by deMenocal (1995). In order to correct for this offset, it is necessary to apply a 40 cm lag to the deMenocal (1995) record (black line).

correction is applied, variations in terrigenous dust flux and lithogenic matter are largely synchronous. The record from deMenocal (1995) is of higher resolution (measurements every 5 cm) than that of Clemens et al. (1996) (every 10 cm) and is therefore used for further comparison. Figure 8.15 compares the terrigenous dust records from ODP Site

721/722 (deMenocal, 1995) with the higher resolution Ti/Al data and changes in sea surface temperature (Herbert et al., 2010) on a composite depth scale (adjusted as described above). As is evident from figure 8.15, the different dust parameters all display similar variations. In particular, changes in the lithogenic component (figure 8.15, graph B) mirror fluctuations in Ti content (figure 8.15, graph C). In particular both Ti content and dust flux values exhibit a notable peak at a composite depth of approximately 94.40 mbsf. This also coincides with a marked in decrease in $\delta^{13}C_{org}$ (section 8.3.1, figure 8.1) suggesting an increase in land-sourced organic matter. This is not surprising since Ti is known to be of terrigenous origin (see section 8.3.2). There is less similarity between the deMenocal (1995) dust records and variations in Ti/Al once Ti content has been normalised to aluminium. As discussed in section 8.3.1, normalisation to Al is necessary in order to account for the effect of differential dilution of the lithogenic component by the aluminosilicate and calcium carbonate fractions. However the process of normalisation to Al introduces an additional component of random noise to the data and has the effect of suppressing the amplitude of some of the variations in Ti content. In spite of this, the main features of the various dust parameters are similar, namely that the record is marked by periods of high variability (between ~ 83 to 86 m and ~ 90 to 95 m composite depth) and a prolonged episode of relative stability between 86 m and 90 m. These correspond to the zones outlined previously, based on the results of wavelength analysis and additive modelling (section 8.4.3). The similarity between the lower resolution dust records from deMenocal (1995) and the broader-scale features of the high-resolution Ti and Ti/Al data sets confirms that Ti/Al is an appropriate proxy for dust variability during the Plio-Pleistocene.

deMenocal (1995, 2004) used the results of discrete and evolutive spectral analyses of the Site 721/722 lithogenic component data to suggest that major shifts in hominin evolution were mediated by shifts towards more arid and variable conditions during the major Plio-Pleistocene transitions in global climate at ~ 2.8 (±0.2) Ma, ~ 1.7 (±0.1) Ma and ~ 1.0 (±0.2) Ma (discussed in chapter 1.5.4). According to the results of these analyses, there was a marked transition towards more arid conditions at 2.8 Ma, associated with the intensification of Northern Hemisphere glaciation (iNHG). deMenocal (1995) suggests that before 2.8 Ma, low-latitude monsoonal circulation was modulated by precessionally-driven changes in insolation and finds that after 2.8 Ma, there is a marked reduction in the amplitude of precessional cycles, replaced by a more dominant obliquity cycle until 1.0 Ma. During the period between 1.0 and 0 Ma there was an increase in 100-kyr variance in aeolian concentration related to the short eccentricity cycle.

In order to evaluate these findings in the context of the updated high-resolution Ti/Al record developed as part of this study, it is first necessary to review the chronology used. deMenocal (1995) uses an age-depth model similar to that of Clemens et al. (1996) (section 8.2.4) and states that a composite depth of 87.70 mbsf is equivalent to 2.8 Ma. With the necessary correction for the difference in composite depth models, this is equivalent to a composite depth (this study) of 87.30 mbsf. Based on the revised $\delta^{18}O$ chronology described above, this depth correlates with a date of 2.496 Ma. This corresponds with the results of wavelet analysis on the Ti/Al data that suggest a transition at ~ 2.5 Ma towards a period of increased variability (figure 8.13). Visual inspection of the compiled dust records displayed in figure 8.15 does not support the notion of a marked transition at this point and whilst there is evidence for an increase in variability after a composite depth of approximately 86 mbsf, there is no overall increase in dust transport which would support a shift towards more arid conditions. Similarly, the Ti/Al and Ti records also do not support deMenocal's findings for a dominant obliquity signal after 2.8 Ma (2.496 Ma, according to the new chronology), and spectral analysis of the Ti/Al data identifies only a minor peak in variance at the ~ 41-kyr periodicity.

The complete ODP 721/722 dust record of deMenocal (1995) was re-assessed by Trauth et al. (2009) in a bid to assess apparent inconsistencies between marine and terrestrial records of African climate change. Trauth et al. (2009) used a variety of statistical methods to investigate trends and events in three dust flux records from ODP Site 659 (West Africa), ODP Site 967 (Mediterranean Sea) and ODP Site 721/722 during the last 5 million years. Their results also found no evidence for a gradual increase in African aridity after the iNHG or for a transition at 2.8 Ma. Instead they found that the ODP Site 721/722 record is overprinted by dust transport mechanism effects and that the most significant changes in the record occur between 3.35 Ma and 3.15 Ma (equivalent in adjusted composite depth to 96.85 mbsf and 100.15 mbsf, respectively), marking the onset and termination of a period of significantly reduced dust transport. There is also evidence for additional minor transitions in the record at 3.95 Ma, 3.70 Ma, 2.25 Ma, 2.05 Ma, 1.05 Ma, 0.90 Ma and 0.40 Ma (according to the timescale of deMenocal, 1995). However analysis within the ~ 20-kyr precessional frequency band reveals a number of periods of high variability between 3.2 – 2.9 Ma, 2.7 – 2.55 Ma, 2.4 – 2.05 Ma and 1.1 – 0.85 Ma. Of these, the periods between 3.2 – 2.9 Ma and 2.7 – 2.55 Ma correspond to the episodes of higher amplitude below 90 mbsf composite depth and above 85 mbsf composite depth described above (figure 8.15). This agrees with the findings of the wavelet analysis conducted on the Ti/Al data set (figure 8.13). Breakfit regression conducted on the dust record by Trauth et al. (2009) suggests that

there is a significant breakpoint in the trend of the dust data at 1.86 ± 0.44 Ma, coincident with the episode of extreme climate variability between 1.9 and 1.7 Ma (Trauth et al., 2005). At this point the records from ODP Sites 967, 659 and 721/722 all show a marked increase in the amplitude of fluctuations in dust transport and an increase in the trend towards more arid conditions (Trauth et al., 2009).

In summary, the results of this high-resolution study are not completely in agreement with the interpretations of deMenocal (1995, 2004) and do not support a trend towards increasing aridity throughout the Plio-Pleistocene. There is however a transition towards increased variability at approximately 2.5 Ma, which corresponds to ~ 2.8 Ma (according to the timescale of deMenocal, 1995) once differences between composite depth models and chronologies are accounted for. A critical re-assessment of the Site 721/722 dust data by Trauth et al. (2009) also does not support the original findings by deMenocal (1995, 2004) but identifies 'packets' of precessionally-forced variability which correspond to those observed in the Ti/Al record.

8.5.2.2 Atlantic Ocean

A continuous pollen record from ODP Site 1082 in the southeast Atlantic Ocean (figure 8.17) documents changes in vegetation in southwest Africa throughout the Plio-Pleistocene, between 3.5 and 1.7 Ma (Dupont et al., 2005). Site 1082 is located towards the northern tip of the Benguela upwelling system offshore from the Kalahari Basin and Namib Desert. Sediments at the Site provide a well-preserved archive of terrestrial pollen delivered to the southeast Atlantic Ocean via predominantly south-westerly Southern Hemisphere trade winds that entrain terrestrial material from southern Africa and deposit it into the Benguela system (Shi and Dupont, 1997; Dupont and Wyputta, 2007). Dupont et al. (2005) describe a declining trend in grass pollen percentages during the late Pliocene, which culminated in a minimum during Marine Isotope Stage (MIS) 100 at 2.53 Ma. During glacial stages, an increase in semi-desert pollen and decrease in grass pollen are indicative of more arid conditions, whilst during interglacial periods pollen fluctuations imply an expansion in the savannah biome in warmer climates (Dupont et al., 2005). Results from ODP 1082 for the period between ~ 2.9 and ~ 2.3 Ma are displayed in figure 8.16. Changes in the total influx of pollen, expressed as a percentage of total pollen relative to dinoflagellate cysts (P/(P+D)), reflect important shifts in the terrestrial climate variability of Southern Africa. After 2.7 Ma, changes in the pollen record imply increased climate variability through an enhancement in the latitudinal vegetational shifts between glacial and interglacial stages.

Dupont et al. (2005) suggest that this was caused by an increase in the E-W thermal gradient in the Atlantic Ocean and a strengthening in the trade winds linked to enhanced Hadley circulation. The authors also document a marked and rapid desiccation event in Namibia at approximately 2.2 Ma when pollen influx rates dropped to much lower levels, accompanied by a disproportional decline in Cyperaceae pollen (e.g. sedges, rushes) indicating a disappearance of perennial fluvial discharge to the Site due to the typical presence of such vegetation in rivers, marshes and lacustrine environments.

The highly variable changes in the SW African climate during the Plio-Pleistocene implied by the pollen record of Dupont et al. (2005) are in contrast to the findings of Maslin et al. (submitted) who suggest that the long-term moisture history of SW Africa over the last 3.5 million years was relatively stable. Maslin et al. (submitted) examine the *n*-alkane $\delta^{13}C$ record from ODP Site 1085 (figure 8.17) situated further south within the Benguela Current system off the coast of South Africa. The record from Site 1085 shows very little variation in *n*-alkane $\delta^{13}C$ values suggesting that there was little change in the proportions of C_3 and C_4 plants over the last 3.5 million years.

In addition to the record from Site 1082, a further Pliocene-aged, high-resolution dust flux archive is available from ODP Site 659 in the eastern sub-tropical Atlantic Ocean (figure 8.17) (Tiedemann et al., 1994). Site 659 is located atop the Cape Verde Plateau off the coast of northwest Africa and is situated in the trajectory of the African Easterly Jet (AEJ) (see chapter 3.3.1.2) thus making it an ideal location to monitor fluctuations in continental aridity in the southern Sahara and Sahel regions of North Africa. Precipitation in these areas is primarily controlled by the interaction of northward incursions of the West African monsoon with squall lines located between 10-15 °N, which affects the entrainment of dust into the AEJ. Tiedemann et al. (1994) analysed dust transport to Site 659 for the last 5 million years and, through the study of benthic foraminiferal oxygen isotope data, constructed an astronomically calibrated timescale for the Pliocene, prior to 2.85 Ma. Age control for the last 2.85 million years is based on the timescale of Shackleton et al. (1990). The previously described record from ODP Site 1082 is also aligned to the standard benthic isotope stratigraphy of Site 659 thus making the two records comparable without encountering limitations with dating inconsistencies. The dust flux record at Site 659 reveals that strong aridity cycles dominated Saharan-Sahelian climate during the last 5 Ma. Evolutionary spectral analysis of the dust flux data illustrates that between 4.5 and 3.0 Ma, the climatic evolution of the region was dominated by the influence of precession and was linked to the strength of low-latitude monsoonal forcing. Between 5.0 – 4.5 Ma and from

3.0 to 1.5 Ma, dominant precessional (19-kyr and 23-kyr cycles) and obliquity (41-kyr cycle) periodicities suggest that a combined low-latitude and high-latitude climate forcing controlled dust transport in the Sahara-Sahelian region. Tiedemann et al. (1994) also observe a long-term increase in dust flux rates between 2.8 and 2.0 Ma, which they link to the ongoing intensification of glaciation in the Northern Hemisphere, and a further increase between 1.6 and 1.4 Ma, related to the amplification of Pleistocene ice age cycles.

For the period between ~ 2.9 and ~ 2.3 Ma that corresponds to the Ti/Al record from Site 721/722 in the Arabian Sea (figure 8.16), data from Site 659 and Site 1082 can be used to compare changes in aridity from West Africa with records from the Indian Ocean and Mediterranean regions. Since the Site 1082 record was aligned to the astronomical timescale of Tiedemann et al. (1994), it is possible to compare the records without needing to consider any possible adjustments to the chronologies. Figure 8.16 shows that changes in SW African climate (ODP Site 1082) during this time were highly variable and marked by large fluctuations in the total amount of pollen transported to the Site. Variations in pollen content range from a maximum of 88% (at ~ 2.61 Ma) to a minimum of 20% (at ~ 2.40 Ma). During this time there is no overall trend towards higher or lower values however the enhanced resolution of the record after 2.7 Ma reveals increased variability between wet and arid periods. Changes in the terrigenous dust flux record from Site 659 also display a high degree of variability between ~ 2.9 and ~ 2.3 Ma with marked peaks in dust transport at ~ 2.72 Ma, ~ 2.69 Ma, ~ 2.65 Ma, ~ 2.53 Ma, ~ 2.45 Ma and ~ 2.33 Ma. The variable resolution of both dust records means that it is difficult to precisely correlate some features of the data however it is evident that the two West African records (figure 8.16) do contain some similarities but there are also some clear differences between the Northern (Site 659) and Southern (Site 1082) Hemisphere Sites (figure 8.17). After approximately 2.55 Ma the two records are broadly coherent however prior to this time, there are some differences between the two Sites, such as at ~ 2.69 Ma when low pollen levels suggest that SW Africa was relatively wet while a peak in terrigenous flux at Site 659 implies that the southern Sahara-Sahel region was dry.

The relatively low-resolution of certain parts of the ODP 659 (Tiedemann et al., 1994) and ODP 1082 (Dupont et al., 2005) records makes it hard to precisely analyse the precessional-scale variability associated with the timing of the Barsemoi Diatomites and the deposition of sapropel layers in the Mediterranean Basin. Sapropels are layers of dark-coloured organic-rich matter characterised by higher $\delta^{15}N$ and lower $\delta^{13}C$ values that are formed during periods of reduced oxygen availability in the bottom waters of the Mediterranean Sea

(Meyers and Arnaboldia, 2008). Figure 8.16 shows the alignment of the dust records with the rhythmic expansion of palaeo-lake Baringo. During the lake phase represented by diatomite unit #1, dust transport to both Site 659 and Site 1082 is relatively low suggesting that precipitation in both W and SW Africa was increased at this time leading to enhanced vegetative cover and decreased soil deflation. Terrigenous dust flux levels to Site 659 during the period coincident with diatomite unit # 2 imply that conditions in West Africa were similar and characterised by enhanced rainfall in the Sahara-Sahelian region. The low-resolution of the Site 1082 record means that it is not possible to identify any significant climatic shift during this time. Figure 8.16 shows that during the period coincident with Barsemoi unit #3, both W and SW Africa experienced episodes of increased precipitation leading to reduced dust and pollen transport to the East Atlantic Ocean. A hiatus in the data from Site 659 between 2.625 and 2.592 Ma means that it is not possible to correlate this record to the timings of diatomites #4 and #5 however the pollen record from Site 1082 documents moderate decreases during this time. During the lake phases represented by diatomite units #4 and #5, total pollen content was approximately 60% implying that pollen transport, and therefore also aeolian flux, were slightly reduced. However this is in stark contrast to the significant decreases in aeolian dust flux observed in the Ti/Al record from the Arabian Sea and elsewhere in the Mediterranean Basin (see section 8.5.2.3).

Additional correlations can be made between the West and Southwest African records from ODP 659 and ODP 1082 with the timings of sapropel formation in the Mediterranean Basin (Kroon et al., 1998; Lourens et al., 2004). Sapropel layers S62 – S66 coincide with the deposition of the Barsemoi diatomite units in East Africa (discussed further in section 8.5.4) and conditions at Sites 659 and 1082 are as outlined above. During the period between 2.9 and 2.3 Ma, there are a further 4 sapropel layers (figure 8.16) at ~ 2.30 Ma (S60), ~ 2.34 Ma (S61), ~ 2.70 Ma (S67) and ~ 2.83 Ma (S68) (Kroon et al., 1998). All four periods are marked by episodes of low dust transport to the Mediterranean Sea (Larrasoaña et al., 2003) and to the Arabian Sea. The timing of sapropel layers S60, S61, S67 and S68 is also coincident with dust flux minima at ODP Site 659 indicating that the Saharan-Sahelian region was relatively wet during these times. However there is a marked difference in the pollen record from Site 1082 (Dupont et al., 2005) where these periods are generally characterised by increases in total pollen content implying that SW Africa experienced relatively arid conditions whilst North Africa, and specifically the Nile catchment region, underwent brief periods of enhanced precipitation from a strengthening of the African monsoon.

8.5.2.3 Mediterranean Sea

Larrasoaña et al. (2003) present a high-resolution three million year record of aeolian dust supply to the eastern Mediterranean Basin (figure 8.17). They analysed the haematite content of sediments from ODP Site 967 on the Eratosthenes Seamount as a proxy for variations in the export of dust from the Sahara Desert. Orbital precession exerts a fundamental control on the aeolian transport of dust from the Sahara to the Mediterranean Sea through variations in low-latitude monsoonal circulation. This is particularly evident in the timing and deposition in the Mediterranean Basin of organic-rich sapropel layers during precession minima (low dust flux, strong monsoon intensity) and marl layers during precession maxima (high dust flux, weak monsoon intensity) linked to oscillations in the strength of the African monsoon (Kroon et al., 1998; Wehausen and Brumsack, 2000; Lourens et al., 2004). During periods of increased monsoonal circulation, it is hypothesised that there was significant northward penetration of the African monsoon front beyond the central Saharan watershed, coincident with enhanced flooding within the Nile catchment that lead to increased drainage along the North African coast (Rohling et al., 2002). This would have resulted in an expansion in vegetation cover and lower levels of soil erosion leading to decreased dust production during periods of intensified African monsoon circulation. Larrasoaña et al. (2003) find that aeolian haematite within sediments from ODP Site 967 is derived from the eastern Algerian, Libyan and western Egyptian lowlands situated to the north of the central Saharan watershed where warm, dry conditions favour the formation of haematite from the secondary alteration of goethite-rich iron crusts during arid phases. The dust source area can be confined to the northern areas of the Saharan region since dust produced in the more southerly areas is exported westwards towards the Atlantic Ocean by the African easterly jet. The authors therefore use their record as a proxy for African monsoon strength during the Plio-Pleistocene.

Visual comparison of the ODP Site 967 and Site 721/722 records (figure 8.16) reveals that changes in aeolian dust export to the Mediterranean and Arabian Seas are largely synchronous during the period between 2.9 and 2.3 Ma. Periods of low dust production that correlate with wet phases in East Africa suggests that both the African and Indian Ocean monsoons were strengthened during these times reinforcing the dominant precessional control exerted on both tropical monsoon systems. Dust flux minima in the Site 967 record also coincide with organic-rich sapropel layers. There is a greater degree of similarity between records from the Arabian and Mediterranean Seas, than compared to records from West and Southwest Africa, however the lower resolution of this data somewhat hampers the correlation of certain features of the records.

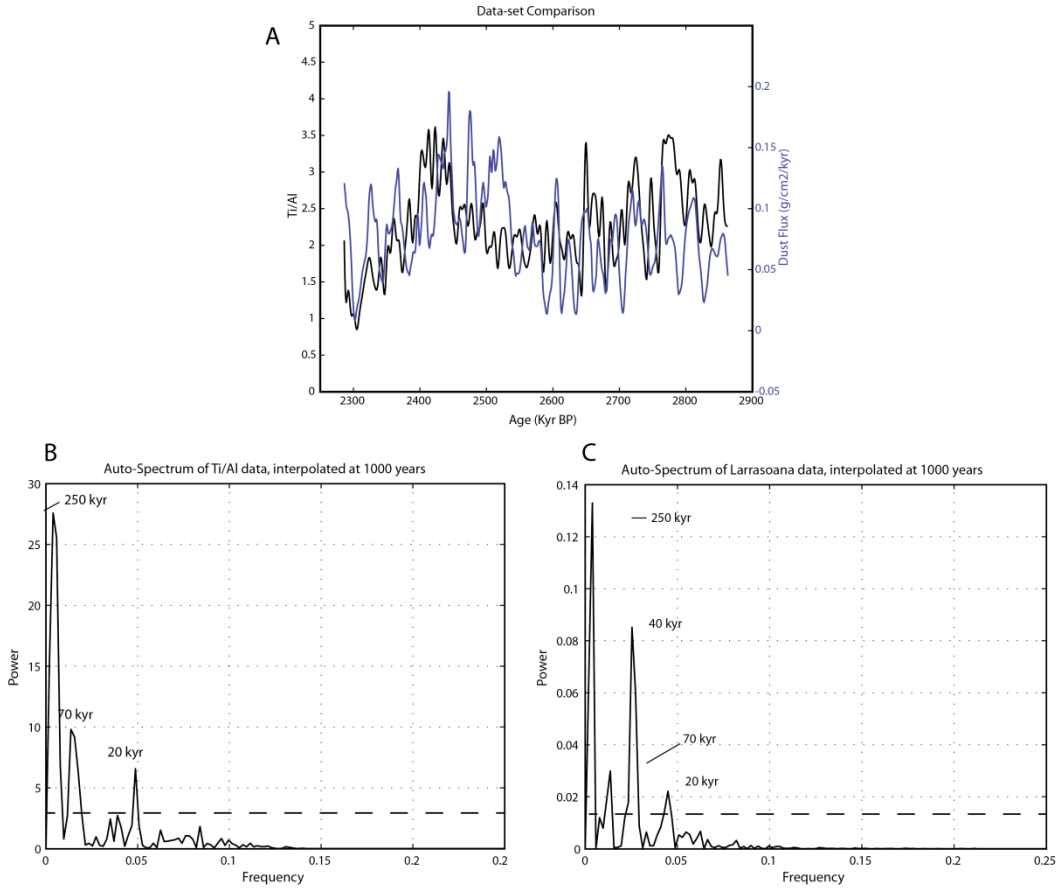

Figure 8.19 Analysis of dust records from Site 721/722 (using filtered Ti/Al data) and Site 967 (Larrasoaña et al., 2003). Both records have been linearly interpolated to 1,000 years in order to better compare trends and cycles within the two data sets. Graph **A** shows the ODP 721/722 (black line) and ODP 967 (blue line) data superimposed on one another. Graph **B** shows the power spectrum for the Ti/Al data (once interpolated to 1,000 years) whilst graph **C** shows the power spectrum for the ODP 967 dust flux data (Larrasoaña et al., 2003). There is a significant peak in the ODP 967 spectrum at a frequency corresponding to a ~40-kyr obliquity cycle, which is notably absent in the Ti/Al record.

Larrasoaña et al. (2003) observe that over the entire three million year record, almost 50% of the total variance in dust export is explained by the orbital components of precession (18 – 25 kyr frequency band), obliquity (39 – 43 kyr frequency band) and eccentricity (90 – 130 kyr and 394 – 414 kyr periodicities). Between 2 and 3 million years ago, approximately 10% of the variance is explained by precession whilst obliquity accounts for almost 15%.

During this time, the short eccentricity cycles of 96 and 126 kyr explain only 4% of the total variance while the longer eccentricity cycle of 413 kyr accounts for almost 20% of the fluctuations in dust production (Larrasoaña et al., 2003). During the late Pleistocene (1.0 - 0 Ma), precession and the longer eccentricity components become less important while between 1 and 2 million years ago obliquity accounted for more than 22% of the variance whilst the shorter eccentricity cycle explains more than 12% of the changes in the dust record. On precessional timescales, Larrasoaña et al. (2003) find that the variations in dust

flux to Site 967 (dust sourced from the northern Sahara) are in phase with changes in the dust record from ODP Site 659 (dust sourced from the southern Sahara) in the equatorial Atlantic Ocean (Tiedemann et al., 1994). They suggest that the significant obliquity component of the Site 967 record is an expression of a high-latitude mechanism driven through changes in the meridional temperature gradient in the Southern Hemisphere, which would affect the intensity and northward penetration of the African monsoon. They also suggest a possible additional threshold mechanism whereby obliquity-controlled variations in the position of the tropical solar zenith (the furthest latitudes at which the sun is directly overhead) affect the transport of dust to the eastern Mediterranean (Larrasoaña et al., 2003).

In order to directly compare the records from ODP Sites 967 and 721/722 for the period between ~ 2.9 and ~ 2.3 million years ago, power spectral analysis was performed on both data sets. A low-pass filter at 800 years was applied to both the Ti/Al record and ODP 967 terrigenous flux data. Both records were subsequently linearly interpolated to 1,000 years in order to compare real trends within the data. Interpolated data and results of spectral analysis of the records are displayed in figure 8.19. The power spectra of the ODP Site 967 data indicates a strong obliquity ~ 40-kyr periodicity and a more minor ~ 20-kyr precessional cycle. Contrastingly, the Site 721/722 Ti/Al data displays no discernible peak in the obliquity band but has a significant ~ 20-kyr precessional component. Both data sets exhibit pronounced variance at a periodicity of ~ 70 kyr, in line with the ~ 60-70 kyr cycle discussed in section 8.4.2.3. In addition to these cycles there is what appears to be a highly marked peak in both records, which represents a periodicity of ~ 250 kyr. This peak appears to be an artefact of examining only a truncated portion of the record and likely results from the detrending of data in order to eliminate linear trends from spectral analysis (M. Trauth, pers. comm.).

8.5.3 Orbital changes in insolation

Low-latitude insolation and thus tropical monsoonal circulation are dominated by the ~23-kyr precessional period which exerts a fundamental control over the African, Indian Ocean and Asian monsoon systems. As discussed in chapter 1.7.2, there has previously been considerable focus and debate (e.g. Clemens and Prell, 2003, 2007; Ruddiman, 2006) on the links between precessionally-driven changes in insolation and monsoonal circulation. This has been more widely studied in Late Pleistocene climate records that cover up to the last 350 kyr. Within these records and available reconstructions of Pliocene monsoonal

circulation, the precise linkages between high-latitude insolation, glacial-interglacial cycles and their influence on the tropical monsoons are not clearly understood.

The importance of the influence of the long 400-kyr eccentricity cycle on precessionally-forced variations in Northern Hemisphere summer insolation is evident in both the ODP 721/722 Ti/Al and ODP Site 967 dust records. Visual inspection of both data sets reveals broad intervals of high and low dust transport during eccentricity minima and maxima, respectively. Larrasoaña et al. (2003) suggest that this reflects the impact of eccentricity upon precession, causing relative changes in the northward penetration of the African monsoon and affecting the production of dust in the northern Sahara. This relationship is also evident in the timings of clusters of sapropel layers in the Mediterranean Sea (Kroon et al., 1998; Lourens et al., 2004). However, this is in contrast to the findings of Trauth et al. (2009) who note that, over the last 5 million years, high dust fluxes in the ODP 721/722 (deMenocal, 1995) and ODP 659 (Tiedemann et al., 1994) records correspond to 400-kyr eccentricity maxima. The marked difference between this correlation and the clear expression of the 400-kyr eccentricity period in the Ti/Al record is potentially the result of the dating of the previous ODP 721/722 age-depth models which had been aligned to the old date of 2.470 Ma for the Gauss/Matuyama magnetic reversal (see section 8.2.4). Trauth et al. (2009) suggest that the observed differences in the eccentricity response of the dust records of the Arabian and Mediterranean Seas imply that the dust flux records were overprinted by a transport mechanism effect linked to monsoon dynamics, which are also affected by transport effects linked with glacial-interglacial cycles (deMenocal, 2004). Through modulation of precession, eccentricity minima lead to low-amplitude insolation peaks, weakened monsoonal circulation and elevated dust transport as a result of source area aridity. This is manifested in East Africa as long-term periods characterised by low lake levels and pervasive arid conditions (Trauth et al., 2005, 2007). By contrast, eccentricity maxima result in high-amplitude variations in insolation which generates episodes of extreme climate variability. This is clearly evident in the ODP 721/722 Ti/Al dust record from the Arabian Sea (figure 8.12) and in the correlation of record with the timing of the variable lake phases in the East African Rift Valley represented by the Barsemoi Diatomites. The amplification of the precessionally-driven insolation cycles during eccentricity maxima induces highly variable changes in monsoon circulation which creates the periods of extreme variability documented in East Africa palaeoclimate records (see discussion in chapter 1.7.2). This reinforces the theory that the long 400-kyr eccentricity cycle exerts a major control over tropical monsoon circulation and the African hydrological cycle (e.g.

Gasse, 2000, Trauth et al., 2003, 2009; Berger et al., 2006; Kingston et al., 2007; deMenocal, 2011).

Spectral analysis of the dust flux record from Site 967 in the Eastern Mediterranean Sea (Larrasoaña et al., 2003) also reveals significant variation at the ~ 41-kyr obliquity period. This strong obliquity-related signal is largely absent from the Ti/Al record from ODP 721/722 in the Arabian Sea. Variations in orbital obliquity affect the meridional temperature gradient which in turn controls the pole-ward transport of moisture, factors which both influence ice sheet development. For example, as obliquity decreases, high latitude temperatures become cooler thus increasing the latitudinal temperature gradient and enhancing the delivery of moisture to the high latitudes which promotes ice sheet growth (Raymo and Nisancioglu, 2003). As previously described, Larrasoaña et al. (2003) suggest both high-latitude and low-latitude mechanisms which could be responsible for the expression of obliquity within their dust record. For the period between 2.9 and 2.3 Ma, this signal is particularly prominent in the ODP 967 record (figure 8.19). Larrasoaña et al. (2003) relate dust flux minima with periods of high obliquity and infer that this would have increased the Southern Hemisphere latitudinal temperature gradients during austral winter, thus enhancing the intensity and northward penetration of the African monsoon. In their analysis of the obliquity component of a stacked summer monsoon record from the Arabian Sea spanning the last 350 kyr, Clemens and Prell (2003, 2007) also invoke a Southern Hemispheric influence on the strength of the Indian Ocean summer monsoon through latent heat transfer derived from evaporation over the southern sector of the Indian Ocean. This has also been tested using coupled ocean-atmosphere climate models which demonstrate that whilst both Northern and Southern Hemispheric insolation forcing can affect the strength of the Indian Ocean monsoon, only Southern Hemisphere changes can remotely force a response in the other hemisphere (Liu et al., 2006). This is linked to the asymmetrical distribution of landmasses and oceans and means that the effect of high insolation during boreal summer is restricted to the heating of the Northern Hemisphere continents whilst high insolation during austral summer heats the Southern Hemisphere oceans where the thermal storage effect of the oceans ensures the heat is retained and transferred northwards. However, if a Southern Hemisphere mechanism were responsible for the expression of the ~ 41-kyr obliquity period on tropical monsoonal circulation between ~ 2.9 and ~2.3 Ma, one would expect there to be a more dominant obliquity cycle in the Arabian Sea record. The absence of a prominent spectral peak at ~ 41-kyr suggests that this is only a minor factor in the forcing of the Indian Ocean monsoon during the Late Pliocene - Early Pleistocene period investigated here.

It is clear that the relationship between monsoonal circulation, glacial-interglacial cycles and the expression of monsoon strength in dust records is one of considerable complexity. While there is clear evidence for the direct orbital pacing of glacial cycles (at the ~41-kyr obliquity and ~100-kyr eccentricity periods) and monsoon system variation (at the ~23-kyr precessional period, strongly modulated by the 400-kyr eccentricity cycle), there is also an evident non-linear response in the dust flux record.

8.5.4 Correlation to the Barsemoi Diatomites

The compiled data from ODP Sites 721/722 (figure 8.20) have been re-calibrated to the revised age-depth model developed here which has been aligned with the LR04 global benthic stack (Lisiecki and Raymo, 2005). The $^{40}Ar/^{39}Ar$ ages established for each of the Barsemoi Diatomites (see chapter 3.5.2) have been adjusted to the Astronomical Polarity Time Scale (APTS) on the basis of an independent calibration to the Gauss/Matuyama palaeomagnetic transition (Deino et al., 2006). The APTS-adjusted age for the Gauss/Matuyama boundary calculated within the Barsemoi Diatomite sequence is 2.610 ± 0.003 Ma, which is in agreement with the age suggested by Lisiecki and Raymo (2005) of 2.608 Ma. Since the $\delta^{18}O$ chronology for Site 721/722 was correlated to the LR04 stack, it is possible to compare (within error) the timings of the Barsemoi diatomites and associated periods of lake formation with changes in the dust flux to the Arabian Sea.

Through the alignment of the ODP 721/722 Ti/Al dust record and the timing of the Barsemoi diatomites, figure 8.20 shows that periods when the East African Rift Valley is characterised by the development of large freshwater lake systems are also marked by decreases in the flux of dust to the Arabian Sea. These dust flux minima are indicative of a reduction in dust delivery due to increased wetness and enhanced vegetative cover in the dust source regions resulting from a strengthening of monsoonal circulation. Kingston et al. (2007) identified that the occurrence of the Barsemoi diatomites is coincident with precessionally-driven maxima in insolation (21 June, 30°N) and a 400-kyr eccentricity maximum. This pattern is clearly reflected in the aeolian dust flux record from the Arabian Sea and shows that periods of lake development in the Rift Valley are closely coupled with a reduction in dust transport to Site 721/722. Both processes are driven by strengthened monsoonal circulation.

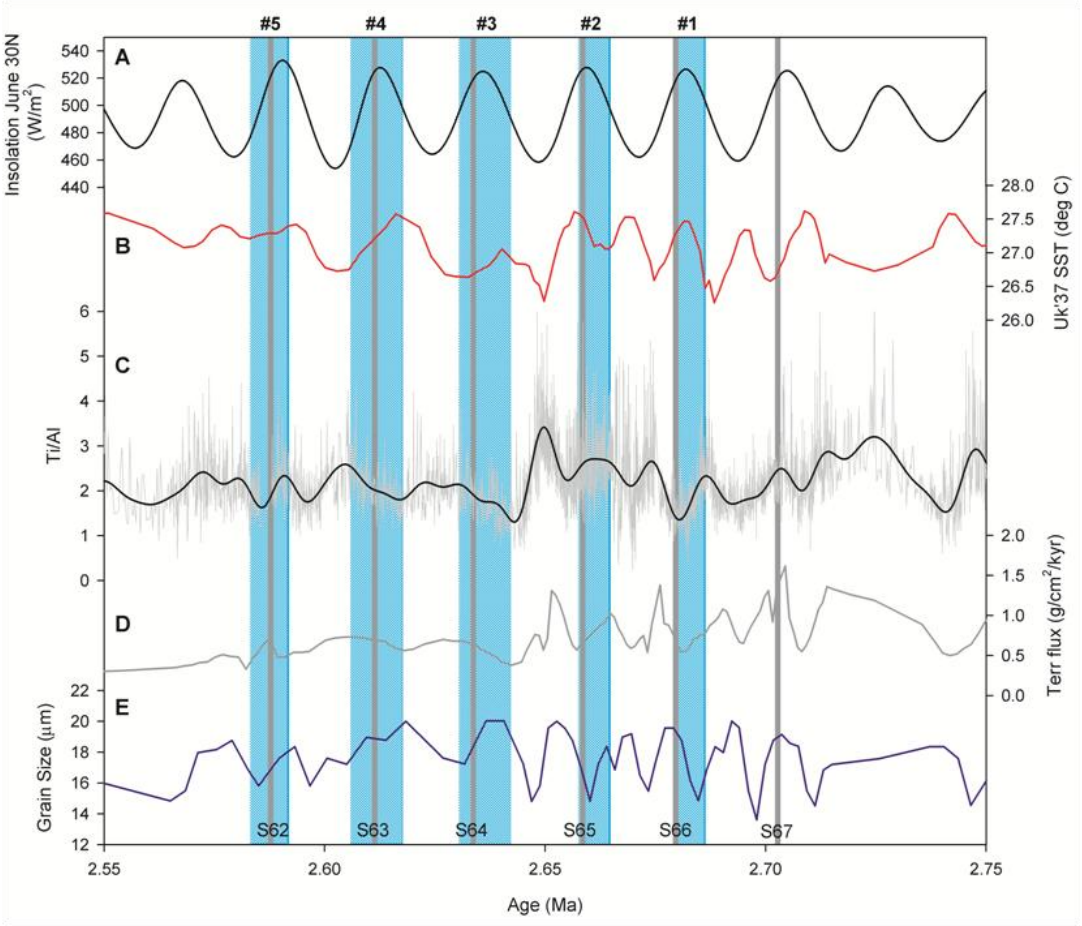

Figure 8.20 Plio-Pleistocene climate changes at ODP Site 721/722 on the Owen Ridge between 2.75 and 2.55 Ma, coincident with extreme climate variations in East Africa. Parameters shown include summer insolation at 30 °N (Graph **A**, Laskar et al., 2004), Arabian Sea surface temperature (Graph **B**, Herbert et al., 2010), raw (grey line) and filtered (black line) changes in Ti/Al (Graph **C**, this study), an estimate of terrigenous flux (Graph **D**, deMenocal, 1995) and changes in grain size (Graph **E**, Clemens et al., 1996) which are thought to be indicative of variations in wind speed. The relative timings of the Barsemoi diatomites, indicating periods of deep freshwater lake formation in the East African Rift Valley are shown by blue vertical bars, while the timing of sapropel layers in the Mediterranean Basin are shown by grey vertical bars (Kroon et al., 1998). This period coincides with a 400-kyr eccentricity maximum which amplifies the precessional forcing of insolation cycles, ultimately resulting in a prolonged episode of extreme climate variability in tropical Africa.

All five diatomite units occur during maxima in summer insolation (at 30 °N). Figure 8.20 shows that diatomite unit #1 dated between 2.680 Ma and 2.686 (APTS-adjusted ages) coincides with higher sea surface temperatures (SSTs) (Herbert et al., 2010) and a decrease in dust transport to the Arabian Sea, indicated by lower Ti/Al values and supported by decreases in grain size (Clemens et al., 1996) and terrigenous dust flux (deMenocal, 1995). The latter stages of diatomite #1 also coincide with the formation of sapropel layer S66 in the Mediterranean Sea.

Diatomite unit #2 was deposited during a period characterised by increasing SSTs. During this time, terrigenous flux and grain size values both decrease whilst Ti/Al ratios show highly variable fluctuations that, on average, are elevated compared to Ti/Al levels during other periods of diatomite deposition. The timing of sapropel S65 in the Mediterranean Sea coincides with the end of the deposition of diatomite #2, when SSTs have reached a maximum and dust transport is at a minimum implying that the strength of the African monsoon was intensified.

Diatomite unit #3 follows a significant, sharp decrease in Ti/Al values (figure 8.20) implying a sudden, marked decline in the degree of dust transport to ODP Site 721/722. Preceding this decrease, during the period between the deposition of diatomite units #2 and #3, SSTs in the Arabian Sea reached a minimum of 26.2 °C while Ti/Al, grain size and terrigenous dust flux all reach maximum values. This coincides with Marine Isotope Stage (MIS) G2, a glacial stage characterised by high levels of dust export around Africa implying that conditions were extremely arid during this time. The conditions in the Arabian Sea during the deposition of diatomite #3 were marked by a minor peak and subsequent decrease in SST, low Ti/Al values and relatively high grain size values, which are suggestive of an increase in the intensity of the Indian Ocean SW summer monsoon. As with units #1 and #2, diatomite unit #3 also coincides with the formation of sapropel layers (S64) in the Mediterranean Basin (figure 8.20).

The timing of diatomite unit #4 and associated wet phase in the East African Rift Valley is coincident with a peak and subsequent decrease in SSTs in the Arabian Sea which follow decreasing summer insolation at 30 °N (figure 8.20). During this wet phase, Ti/Al values at ODP Site 721/722 are low and then steadily increase throughout the period of diatomite deposition indicating a trend towards towards more arid conditions in dust source areas and weakening in the strength of the summer monsoon towards the end of the lake phase. At this time the resolution of the terrigenous dust record is not sufficient to resolve detailed changes however there is a steady decrease in grain size (Clemens et al., 1996) throughout this time implying decreasing wind speeds, which would be expected with weakening monsoonal circulation. The timing of sapropel S63 at 2.611 Ma also coincides with this wet phase in East Africa (Kroon et al., 1998).

During the deposition of diatomite #5, SSTs in the Arabian Sea were relatively high while Ti/Al, terrigenous flux and grain size values were decreasing. These changes all coincide with decreasing summer insolation. A minor core hiatus at this depth at ODP Site 721/722

means that the Ti/Al record for this time is not continuous. As with the other diatomite units the timing of unit #5 coincides with the deposition of sapropel S62 in the Mediterranean Sea.

Chemical analyses reveal that sapropels are marked by low $CaCO_3$ and Ti/Al concentrations with increases in Ba/Al, indicating increased primary productivity (Wehausen and Brumsack, 2000). The formation of these layers typically coincides with precession minima when tropical monsoonal circulation is intensified. During such periods, monsoonal circulation is increased and discharge from the Nile River is enhanced, leading to increased density stratification in the Mediterranean Basin. Fluctuations in Nile River outflow are particularly sensitive to the intensity of the African monsoon since the catchment area of the river lies within the African monsoon zone (Rohling and Hilgen, 1991). It has been suggested that the timings of sapropel formation in the eastern Mediterranean Sea, and therefore also maximum African monsoon strength, lag maximum Northern Hemisphere (65 °N) summer insolation by approximately 3,000 years (Hilgen et al., 1993). The parallel timing of the Barsemoi Diatomites and associated lake phases in the Central Kenya Rift in East Africa with the formation of sapropels in the Mediterranean Sea implies that during these wet phases, the Indian Ocean and African monsoons were largely in phase with each other and thus with summer insolation at 30 °N (Kingston et al., 2007).

In summary, the timing of the Barsemoi Diatomites in the Baringo-Bogoria Basin correlates with periodic reductions in dust flux to the Owen Ridge, marked by low Ti/Al values. Low Ti/Al ratios are indicative of periods when dust transport was minimised suggesting that climate in the dust source regions was wetter, thus decreasing levels of soil deflation. The aeolian transport of terrigenous dust to the Arabian Sea occurs primarily during boreal summer, coincident with the Indian Ocean SW summer monsoon (Clemens, 1998). The decreased dust flux, coupled with increased sea surface temperatures in the Arabian Sea, supports a hypothesised strengthening of the Indian Ocean monsoonal circulation, but particularly the summer monsoon phase, which generates the long rains in East Africa. Over prolonged periods, driven by precessionally-forced insolation maxima, the intensified monsoon circulation causes the build up of lakes in the Rift Valley.

8.6 Summary

This project has aimed to develop a long-term oceanic record for the period between ~ 2.9 and ~ 2.3 Ma in order to contextualise regional climatic changes in tropical East Africa.

This has been undertaken through the high-resolution analysis of sediment from the Arabian Sea so that changes in aeolian dust flux, linked to the strength of monsoonal circulation within the Indian Ocean can be investigated. In order to properly assess these changes it was necessary to revise the chronology for ODP Sites 721 and 722 due to significant differences between the previously published age models (Murray and Prell, 1991; Clemens et al., 1996). This has implications for the dating of a number of other studies which use records from ODP Site 721/722. This difference principally arises from the timing and position of the Gauss/Matuyama palaeomagnetic reversal. The development of the Clemens et al. (1996) age-model was based on the orbital tuning of lithogenic dust flux data which was found to contain a dominant precessional periodicity. However the results of this study show that there is likely to be an inherent non-linear component within the climatic response to orbital forcing in the Arabian Sea dust record which has implications for the assignment of a chronology based on dust flux data.

Ti/Al was selected as an indicator of the input of terrigenous material to the Arabian Sea via aeolian transport. Dust delivery occurs primarily during the SW summer monsoon and climate in source areas is controlled by monsoonal circulation thus relative changes in Ti/Al are an indication of changes in monsoon strength. Once aligned to the new $\delta^{18}O$-based chronology, a number of time-series analysis techniques were used to investigate trends and cycles within the Ti/Al data. The fitting of a gamma GLM and wavelet analysis suggest that the 600,000-year record can be sub-divided into three zones: Zone 1) Prior to ~ 2.6 Ma, highly variable fluctuations in Ti/Al are associated with a 60-70 kyr cyclicity and exhibit strong ~ 20-kyr precessional forcing; Zone 2) ~ 2.6 to ~ 2.5 Ma, no significant change in Ti/Al values which during a period of relative stability; Zone 3) ~ 2.5 to ~ 2.3 Ma, variable changes in dust flux with an overall stepwise decrease in Ti/Al. Spectral analysis of the Ti/Al data reveals a prominent ~ 330-kyr cycle, which is assumed to be linked to the long 400-kyr eccentricity cycle however, as the duration of the record is less than 600 kyr, this should be interpreted with caution. However, visual inspection of the record reveals clear variation at the long eccentricity period with broad periods of high dust transport coincident with eccentricity minima. There is also a significant spectral peak at the precessional periodicity of ~ 20-kyr and a minor peak at ~ 40-kyr, corresponding to obliquity forcing. A double peak at 60-70 kyr is likely to indicate an inherent non-linear response within the climate system.

The dust records from ODP Site 721/722 are highly correlated with a dust record from ODP Site 967 in the Mediterranean Basin (Larrasoaña et al., 2003), suggesting that the African

and Indian Ocean monsoons were in phase with each other. There is also some similarity with Plio-Pleistocene dust records from West and Southwest Africa (Tiedemann et al., 1994; Dupont et al., 2005). The timings of sapropel formation in the Mediterranean Sea and diatomite deposition in the Baringo-Bogoria Basin coincide with dust flux minima indicating that intensified monsoon circulation, in response to increased summer insolation, was the mechanism responsible for the development of extensive freshwater lakes in the East African Rift Valley. The long-term trends in aeolian dust transport to the Arabian Sea between ~ 2.9 and ~ 2.3 Ma do not support the previously hypothesised (deMenocal, 1995) marked increase in aridity following the intensification of Northern Hemisphere glaciation between 2.7 – 2.5 Ma but rather suggest that there were climatic episodes (as defined by Zones 1-3 above) characterised by increased variability or relative stability.

Chapter 9: Project Synthesis

9.1 Summary of Research

The climate history of Eastern Africa is characterised by a number of periods of extreme climatic variability when large lakes occupied the East African Rift Valley. The precession-modulated, rhythmic appearance and disappearance of an extensive freshwater palaeo-lake system in the Baringo-Bogoria basin between 2.7 and 2.55 million years ago (Ma) is one such period. The analysis of one of the five Barsemoi Diatomite units exposed within the Tugen Hills reveals that this humid phase was punctuated by millennial-scale, wet-dry cycles. Increases in the abundance of taxa dominant during periods of wind-induced mixing of the water column, and a decrease in the reconstructed oxygen isotope composition of diatom silica ($\delta^{18}O_{modelled}$), indicate that approximately every 1,400 years there was a freshening of palaeo-lake Baringo through a relative increase in monsoonal precipitation. These oscillations are similar in character and duration to the Dansgaard-Oeschger (D-O) events which are prominent in many Late Pleistocene climate records, and are thought to be linked to ice sheet instability and melt water pulses in the North Atlantic Ocean. An additional outcome of this research has been the development of a robust method to accurately characterise and correct for any contamination remaining within purified samples of diatomite. This ensures that measurements of the oxygen isotope composition of diatom silica can be used to provide an accurate assessment of past changes in climate.

Core material from Ocean Drilling Program (ODP) Sites 721 and 722, situated on top of the Owen Ridge in the Arabian Sea, was analysed at high-resolution using scanning XRF in order to compile a detailed record of variations in the flux of terrigenous matter during the Late Pliocene and Early Pleistocene (between ~2.9 and ~2.3 Ma). Due to its relationship to the heavy mineral input of lithogenic material, Ti/Al was identified as a reliable indicator of changes in the aeolian dust flux to the Owen Ridge, which is reflective of the climate of the dust source regions. Climate in these areas is dominated by the circulation of the Indian Ocean SW summer and NE winter monsoons. Since dust transport to the Arabian Sea occurs primarily during the Indian Ocean summer monsoon season, variations in Ti/Al are indirectly reflective of changes in the relative strength of the monsoon system. Time-series analysis of the Ti/Al dust record reveals that prior to approximately 2.6 Ma there were high-amplitude fluctuations in the Ti/Al content of the ODP 721/722 sediments. These high-amplitude changes are indicative of a highly variable climate regime and are coincident with

an extended period of extreme climatic variability in the East African Rift Valley, marked by the characteristic development of deep lakes which respond rapidly to precessionally-forced climate shifts (Trauth et al., 2010). During this period, the Ti/Al record exhibits a distinctly non-linear climatic response evident in the prominent non-orbital periodicity of 60-70 kyr. This is probably the result of the imprint of dust transport mechanisms, such as soil deflation, vegetation changes or local wind speed variations, on the Ti/Al signal. After ~2.6 Ma, the following 100 kyr until 2.5 Ma were characterised by comparatively stable conditions. During this time, persistently high sea surface temperatures and a reduction in the dust flux to the Arabian Sea indicate that Indian Ocean monsoonal circulation remained moderately strong. After 2.5 Ma there is a further increase in variability and a stepwise strengthening of monsoonal circulation after 2.4 Ma reflected in decreasing Ti/Al values.

The strength of the monsoon system is directly forced by variations in low-latitude summer insolation. From the results presented here and the emerging evidence for the dramatic appearance and disappearance of large lakes in the East African Rift Valley (e.g. Trauth et al., 2005, 2007, 2010), it is apparent that it is the amplitude of the oscillations in insolation which induce the variable conditions that characterise these periods. These variations respond directly to fluctuations in orbital precession but are strongly modulated by maxima in the 400-kyr cycle of eccentricity which enhances the amplitude of the insolation cycle and ultimately generates the extreme climate variability response in East Africa. This implies that there is some form of climatic threshold in operation for the development of 'amplifier' lake systems, whereby the climate response is not as dramatic during relatively stable periods, despite other indications that monsoonal circulation remained relatively strong.

9.1.1 Tropical climate fluctuations: A comparison to Barsemoi Diatomite #4

Detailed analysis of unit #4 of the Barsemoi Diatomites reveals that the lake phase was punctuated by wet-dry cycles that lasted, on average, ~ 1,400 years. Each brief wet period was characterised by a relative decrease in $\delta^{18}O_{diatom}$ of up to 5 ‰ and a predominance of *Aulacoseira* species. *Aulacoseira* dominates when the supply of Si to the epilimnion is enhanced such as when strong winds induce greater vertical mixing of the water column. Both these factors imply a freshening of the lake system due to increased precipitation, probably as a result of intensified monsoonal circulation. Due to the errors associated with the $^{40}Ar/^{39}Ar$ dating of the intercalated tephra layers (± 5 kyr), it is not possible to accurately relate the cycles observed in unit #4 to variations in dust record from the Arabian Sea..

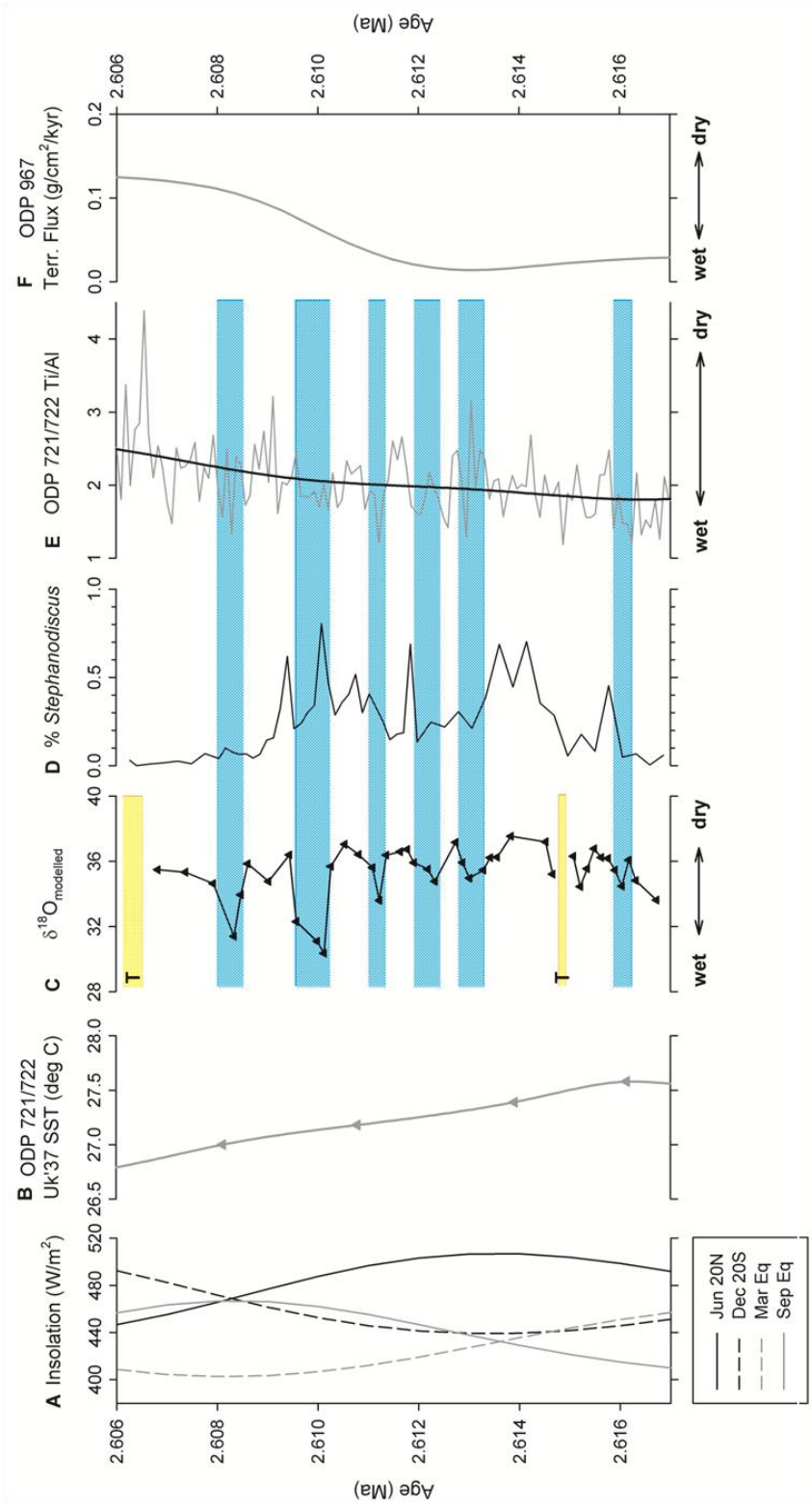

Figure 9.1 A comparison of millennial-scale changes in palaeo-lake Baringo during the deposition of diatomite unit #4 with changes in extra-regional climate and monsoonal circulation, including variations seasonal tropical and equatorial insolation (Graph **A**, Laskar et al., 2004) and changes in Arabian Sea surface temperature (Graph **B**, Herbert et al., 2010). Millennial-scale fluctuations in palaeo-lake Baringo are evident in the reconstructed changes in modelled oxygen isotope composition of diatom silica (Graph **C**), supported by a relative decline in the proportion of *Stephanodiscus* taxa (Graph **D**), indicating that the assemblage was dominated by the production of *Aulacoseira* species. Also shown are changes in the Ti/Al content of sediments from ODP Site 721/722 in the Arabian Sea (Graph **E**) and the change in terrigenous flux to ODP Site 967 in the eastern Mediterranean (Graph **F**, Larrasoaña et al., 2003) which both show an overall increase in aridity towards the end of the lake phase, supporting the gradual drying of the Rift Valley. Blue horizontal bars outline wet periods at palaeo-lake Baringo whilst yellow bars (**T**) mark positions of known tephras within the Barsemoi sequence.

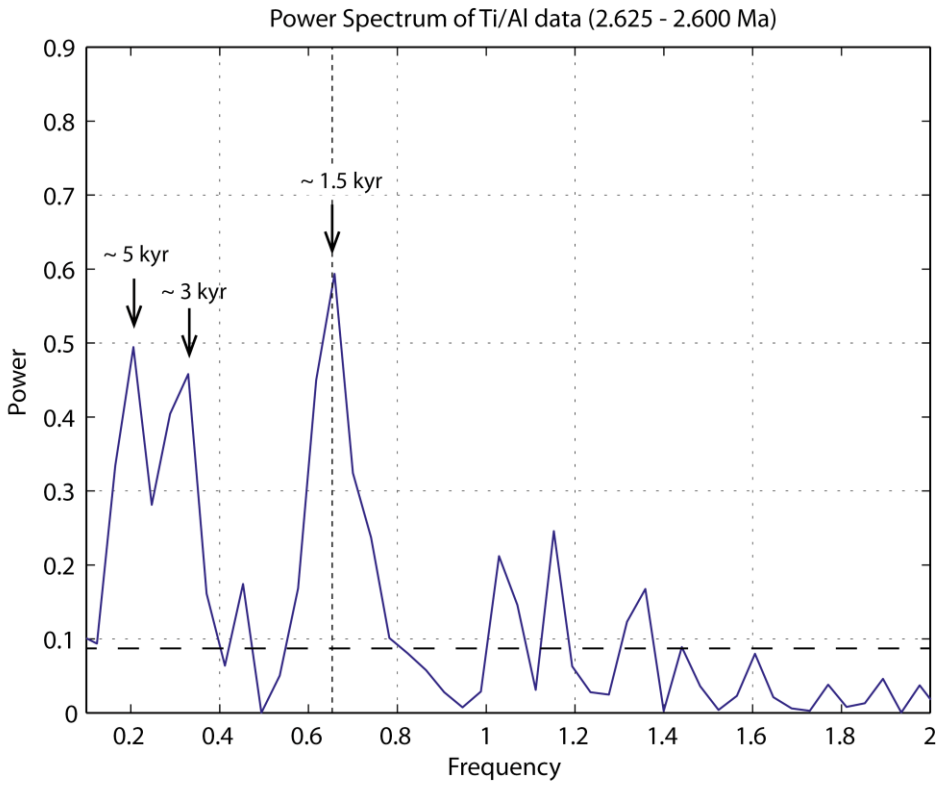

Figure 9.2 Power spectrum of Ti/Al data dated between 2.625 and 2.600 Ma. The spectral analysis reveals a prominent peak at a frequency corresponding to ~1.5 kyr which is in line with the millennial-scale wet-dry cycles observed within the analysis of Barsemoi Diatomite unit #4. Dashed line marks 95% confidence level

However in spite of these limitations, it is possible to make broad correlations between the two data sets.

During the period of lake occupation in the Baringo-Bogoria basin represented by diatomite unit #4, there was a gradual decrease in sea surface temperatures in the Arabian Sea, in line with decreasing summer insolation at 20 °N (figure 9.1, graphs **A** and **B**). During this time there is also an overall increase in Ti/Al (figure 9.1, graph **E**) indicating an increase in dust transport and implying increasing aridity in the dust source regions as a result of weakening monsoonal circulation. This is also coincident with a gradual increase in the flux of dust to ODP Site 967 in the Mediterranean Sea (figure 9.1, graph **F**). Once aligned to the timings of the millennial-scale cycles evident within the modelled diatomite $\delta^{18}O$ record (figure 9.1, graph **C**), it is apparent that the wet episodes coincide with moderate lows in the Ti/Al record. Spectral analysis of the Ti/Al data between 2.6 Ma and 2.625 Ma, spanning the glacial Marine Isotope Stage (MIS) 104 which coincides with the deposition of diatomite unit #4, reveals that there is a prominent spectral peak which corresponds to a periodicity of ~ 1.5 kyr (figure 9.2). There are also two additional, slightly less prominent peaks at frequencies corresponding to ~5 kyr and ~3 kyr cycles. In spite of the errors associated with

the dating of these sediments, the evidence of a prominent spectral peak at ~1.5 kyr within the Arabian Sea dust record is strongly supportive of the evidence for millennial-scale cyclicity within the Barsemoi Diatomite record. As previously discussed (see chapter 5.4), this periodicity is consistent with that of the Late Pleistocene D-O events. In tropical Africa, these events are manifested as wet-dry cycles that produce parallel fluctuations in lake levels caused by relative changes in rainfall, similar to the changes observed in palaeo-lake Baringo during the Late Pliocene. However, due to the inherent dating errors associated with analysing sediments of this age at high resolution, any connection between the two data sets should be considered a tentative one.

9.1.2 The impact of high-latitude changes upon tropical climate

As described in chapter 1.6.1, there is widespread evidence from palaeovegetation records across Africa for a shift towards cooler, more arid climate conditions since the Late Miocene, accompanied by a progressive expansion of more xeric taxa and C_4 biomes (e.g. Kingston et al., 1994; Cerling et al., 1997; Griffin, 1999; Wolde Gabriel et al., 2001; Ségalen et al., 2007). It has been suggested that this drying trend was marked by documented increases in aeolian dust transport off East and West Africa after 2.8 (±0.2) Ma, 1.7 (±0.1) Ma and 1.0 (±0.2) Ma (deMenocal, 1995, 2004). The first of these stepwise shifts in variability has been linked to the intensification of glacial cycles in the Northern Hemisphere (iNHG) as a result of the invigoration of glacial trade winds and/or a southward migration of the intertropical convergence zone (ITCZ) (deMenocal, 2004). General circulation models have also been used to explore the nature of African climate sensitivity to glacial boundary conditions and have demonstrated a shift towards cooler, more arid conditions during glacial stages (e.g. Clemens et al., 1991; deMenocal and Rind, 1993; Clark et al., 1999). From the dust record presented here, there is no evidence of an overall increase in the relative aridity of the dust source areas between ~2.9 and ~2.3 Ma, or of a marked stepwise increase in wind-borne dust transport at 2.8 Ma. It is likely that the time span of this record is not sufficiently long enough to fully capture the gradual increase in dust transport observed elsewhere throughout the Pliocene and Pleistocene. However as described above, there are packets of high variability evident in the dust record which are particularly associated with extreme wet-dry episodes in East Africa and with high amplitude fluctuations in insolation. On the basis of this study, it would appear that there is not an abrupt, short-term response in low-latitude climate in response to the iNHG, but rather that the build up of ice in the Northern Hemisphere is accompanied by a gradual shift towards drier conditions. Superimposed on this trend are periods of increased variability

which are not linked to high-latitude climate forcing, but rather to orbitally-forced changes in tropical insolation.

9.1.3 Linking African palaeoclimate changes with early human evolution

Despite intensive study, the relationship between climate and key periods of hominin evolution is not clearly understood and various different hypotheses have been proposed to attempt to explain the causal linkages between the two. These historically began with the classical *savanna hypothesis* (Dart, 1925, 1953; Bartholomew and Birdsell, 1953; Robinson, 1954) which links increasing aridity in tropical Africa over the last 5 million years to the adaptive shift of hominids from forested landscapes to more open, grassland habitats. The savanna hypothesis is an attractive concept, widely supported by regional and global climatic trends, and whilst it has now been largely disproved, it has influenced the development of other theories such as the *turnover pulse hypothesis* (TPH). Originally proposed by Elisabeth Vrba (Vrba, 1985b, 1993), the TPH specifically links a rapid increase in speciation in micromammal and bovid taxa at approximately 2.5 Ma to the iNHG. The turnover pulse hypothesis states that the onset of drier conditions in Africa, coincident with the iNHG meant that forest bovid species had to evolve and adapt to an open savanna environment resulting in faunal turnover. Recent evidence, which suggests that the iNHG was a gradual build up of ice rather than an abrupt event (e.g. Maslin et al., 1995; Haug and Tiedemann, 1998; Bartoli et al., 2005) and that inter-hemispheric teleconnections are more complex processes than originally assumed, has challenged this hypothesis and it is now thought that the development of Walker circulation between 1.9 and 1.7 Ma had a greater impact on African climate than the iNHG (Ravelo et al., 2004).

Theories of hominin evolution have evolved as our understanding of climate and faunal changes in Africa has improved. The *variability selection hypothesis* (Potts, 1996, 1998b) suggests that, rather than abrupt shifts in climate, orbitally-forced changes in insolation and complex, intrinsic feedback mechanisms result in periods of environmental instability that drive the emergence of new hominin and mammalian species. This theory has subsequently been modified based on the emerging palaeoclimate evidence from the East African Rift Valley concerning the phased appearance and disappearance of large freshwater lake systems. The *pulsed climate variability hypothesis* (Maslin and Trauth, 2009) is based on the evidence for extreme wet-dry periods of variable climate conditions which punctuated the long-term drying trend of the Plio-Pleistocene (see chapter 1.6.4). It is thought that these

alternating conditions would have had a profound effect on environmental habitats and may have provided a catalyst for driving key speciation and dispersal events.

In view of these competing theories, the current consensus is that human evolution was a dynamic and complex process that occurred within a shifting environmental framework that was characterised by a trend towards more arid conditions and more open, grassland habitats (Kingston, 2007). The results presented here are supportive of those hypotheses which are based on periods of variability (*variability selection hypothesis* and *pulsed climate variability hypothesis*) rather than those which invoke an abrupt aridification of Africa (*turnover pulse hypothesis*). The evidence from the Barsemoi Diatomites and from the longer-term Arabian Sea dust record suggests that low-latitude climate during the Plio-Pleistocene (between ~2.9 and ~2.3 Ma) was characterised by periods of highly variable climate when the strength of the Indian Ocean monsoon oscillated rapidly in response to precessionally-forced changes in summer insolation. These episodes of extreme variability were separated by periods of relative climatic stability. This indicates that the rapid and abrupt changes in habitat, from a dry rift setting to lake-occupied basins may have influenced the evolution and migration of early humans.

9.1.4 Summary of findings

The aims of the research presented in this thesis (outlined in Chapter 1.2) were largely concerned with understanding the linkages between orbital forcing and monsoonal circulation in driving extreme climate variability in East Africa by analysing diatomite units in the Baringo-Bogoria basin and long-term changes in the aeolian dust flux record from the Arabian Sea.

The main findings of this project are as follows:

1. Samples of Pliocene-aged diatomite cannot be sufficiently cleaned to remove all contaminant material and it is necessary to conduct further geochemical analyses to establish the character and extent of other material present within each sample.
2. Detailed XRF analysis and subsequent multivariate statistical analysis can be used to develop a three end-member contamination model which corrects oxygen isotope data for the effects of contaminant material, which exhibit much lower $\delta^{18}O$ values.
3. Oxygen isotope analysis of one of the five Barsemoi diatomite units reveals that the humid lake phase was punctuated by millennial-scale (~1,400-yr) cycles of relative

increases in precipitation, similar in nature to the Dansgaard-Oeschger events of the Late Quaternary.

4. Time-series analysis of a high-resolution record of changes in Ti/Al from ODP Sites 721 and 722 reveals that there are periods of high variability in source area climate prior to 2.6 Ma and after 2.5 Ma and that changes throughout the ~600,000 year record are highly correlated with the 400-kyr eccentricity cycle.
5. Spectral analysis of the Ti/Al record during glacial stage MIS 104, coincident with the deposition of diatomite unit #4, reveals a prominent ~ 1,500-yr periodicity, supporting the findings of millennial-scale cyclicity within the East African diatomite record.

All of the points outlined above represent new and major contributions to the field of low-latitude Palaeoclimatology. Both the oxygen isotope analysis of diatomite material and the development of a three end-member contamination model have not previously been attempted and are an important step forward in the use of isotope records from biogenic silica as a proxy for past climate change. In addition to this, very few records (see Chapter 1.5) have found evidence for millennial-scale climate change during the Pliocene, due largely to the scarcity of adequate archives. Almost all of those that do exist are from marine settings where sediments generally offer the best opportunity for studying long-term climate variability at high resolution. The results presented here mark a significant advancement in the understanding of sub-orbital-scale climate changes prior to the Late Pleistocene.

The findings of this research largely satisfy the original aims of the project. The development of a new model for correcting oxygen isotope records from biogenic silica for the effects of contamination demonstrates that even in complex systems where there is more than one type of contaminant material present, it is possible to correct for this and that such records are thus a reliable proxy for palaeoclimate change. Through the detailed investigation of one of the Barsemoi diatomite units and sediments from ODP Sites 721/722 in the Arabian Sea, it has been possible to correlate terrestrial and oceanic records which both show marked periods of climate variability between 2.7 and 2.6 Ma.

9.2 Directions for Future Research

Based on the results of the research described above, there are several avenues for further research which can be identified:

1) *The need to test the proposed lake cycle evolution in the East African Rift Valley and the occurrence and mechanism for millennial-scale climate variability during glacial and interglacial cycles:* The initial aims of this Ph.D. encompassed the high-resolution analysis of more than one of the Barsemoi Diatomite units in order to assess intra-diatomite variability and compare the relative evolution of the hydrological cycle during a wet phase. Due to the work necessary to assess the amount and geochemical characterisation of contamination remaining within these samples, it was not possible to conduct all of this work. However, the results of this study demonstrate that changes in the oxygen isotope composition of diatom silica ($\delta^{18}O_{diatom}$) can be reliably employed to assess climate variability, provided that thorough geochemical analysis is undertaken alongside isotope analysis. The analysis of the remaining Barsemoi diatomites will allow the precise evolutionary nature of the lake cycles to be better assessed and to test the hypothesis and conceptual model proposed in chapter 5.5 concerning the rapid onset and more gradual, stepwise decline of each lake phase. In addition, high-resolution studies of other diatomite units would enable an assessment of the millennial-scale changes observed in unit #4, and provide a test of whether these cycles are restricted to lake phases that occur during glacial cycles or if they also occur during interglacial periods, such as the Bond events observed during the Holocene. For example, the deposition of diatomite units #2 and #5 is coincident with interglacial stages (refer to figure 5.15). Silicon isotope analysis of diatomite samples can also be used to reconstruct productivity variations in relation to the hypothesised change in the strength of monsoonal circulation.

2) *The investigation of palaeoclimate archives from other periods of extreme climate variability in the East African Rift Valley:* The time span of the sedimentary Chemeron Formation (5.3 – 1.6 Ma) permits an assessment of the climate history of the East African Rift Valley. In addition to the Barsemoi Diatomites investigated here, there are a number of other diatomite packages exposed within the Chemeron Formation and underlying Lukeino Formation that have recently been identified within the scope of the ongoing work in the Tugen Hills. Preliminary stratigraphic analysis and $^{40}Ar/^{39}Ar$ dating of intercalated tephra layers within these sequences places them at ~ 3.9 Ma, ~4.9 - 4.8 Ma and at ~5.8 - 5.7 Ma (Deino et al., 2010). Each set of diatomites is unique in terms of the number of cycles, thickness, preservations and the nature of the non-lacustrine sediments. In a similar manner to the Barsemoi Diatomites, these diatomite deposits record the rhythmic cycling of freshwater lake systems and provide an opportunity to conduct detailed investigations of earlier wet phases in the climatic history of East

Africa. The newly discovered diatomite package at ~3.9 Ma corresponds to a deep lake interval at Bodo in Ethiopia whilst the diatomites dated at ~4.9-4.8 Ma may be linked to deposits from palaeo-lake Turasha further south in the Central Kenya Rift, dated between 4.7-4.5 Ma (Trauth et al., 2005, 2007). With the exception of the oldest units, all diatomite packages are clearly aligned with eccentricity maxima and precessionally driven high-amplitude oscillations in insolation, similar to the period studied for this thesis. There are also some largely unstudied, younger diatomite exposures within the Suguta Valley to the North of Lake Baringo. Initial examination and dating of these units suggests that these were deposited approximately 800 kyr ago (A. Deino, pers. comm.), coincident with the end of the Mid-Pleistocene Revolution when evidence from elsewhere in the Rift Valley suggests that East Africa was characterised by extreme climate variability (see chapter 1.6.4; figure 1.4). These deposits offer a further opportunity to explore the nature of climate variability during a major transitional period in global climate.

3) *The need to comprehensively test the proposed method for quantifying contamination within diatom silica:* The understanding of the effect of contamination upon the $\delta^{18}O$ composition of diatom silica and the development of reliable techniques to correct for this effect are still in their infancy. The use of XRF and multivariate statistics to quantify contaminants developed as part of this research is one of a variety of methods currently being explored to assess contamination in purified diatom samples in both single and multiple contaminant systems. There is a clear need for more robust testing of these techniques within different settings and where different types of contamination such as tephra, clay, calcite and other secondary mineral precipitates may be present. Factors such as sediment type, consolidation, depositional environment and age should also be considered since more recent lacustrine sediments which have been well preserved are likely to be easier to clean using traditional chemical and physical techniques than older, sub-aerial exposures that are highly compacted and may have been subject to secondary alteration. Such alteration effects are evident in some of the older diatomite packages described above where leaching of iron oxides has resulted in the individual diatomite layers acquiring a red-pink staining. There is also evidence for ‘baking’ of some parts of the units by intruded igneous deposits or overlying lava flows.

4) *Testing transitional changes within the Arabian Sea dust flux record in order to better understand the nature of any long-term transitions in the data such as the hypothesised increase in African aridity after the intensification of Northern Hemisphere glaciation*

(iNHG): Further statistical testing of the Ti/Al dust record is planned using multiple breakfit regression techniques currently being developed by Nadine Schütz and Martin Trauth at Universität Potsdam. Previous analysis of the lower resolution dust records from ODP Site 721/722 (deMenocal, 1995) by Trauth et al. (2009) suggests that there is no significant increase in aridity that occurs in response to the iNHG. The ongoing work by Nadine Schütz aims to establish whether any change or 'break' points exist within the Ti/Al record which can provide a useful insight into the long-term dynamics of Plio-Pleistocene monsoonal circulation. There is also scope for further statistical analysis of the Arabian Sea dust records which includes more detailed analysis of shorter portions of the record as opposed to the long-term data series analysed here.

5) *The need to assess the response of oceanic circulation in the Arabian Sea to variations in monsoonal circulation during the Late Pliocene and Early Pleistocene:* The suite of elemental data measured during the XRF scanning of core material from ODP Sites 721 and 722 is only partially analysed here to assess changes in the aeolian transport of terrigenous dust to the Owen Ridge. An additional outcome of this research is the ongoing analysis of changes in Arabian Sea palaeoceanographic parameters between ~2.9 and ~~2.3 Ma. These include changes in oceanic upwelling (as indicated by changes in Ba/Al) and palaeoproductivity (inferred from a range of geochemical proxies including $\delta^{13}C_{org}$ values and C/N ratios) in response to the variations in monsoonal circulation inferred from the changes in dust flux. Increased monsoon strength and therefore also intensified monsoonal winds offshore from the Arabian Peninsula would theoretically lead to an increase in the upwelling of cool, nutrient-rich waters from greater depths and generating an increase in marine productivity.

Chapter 10: References

Abell, P.I. (1982). Paleoclimates at Lake Turkana, Kenya, from oxygen isotope ratios of gastropod shells. *Nature*, **297**, 321-323.

Abram, N.J., Gagan, M.K., Cole, J.E., Hantoro, W.S. & Mudelsee, M. (2008). Recent intensification of tropical climate variability in the Indian Ocean. *Nature Geoscience*, **1**, 849-853.

Abram, N.J., Gagan, M.K., Liu, Z.Y., Hantoro, W.S., McCulloch, M.T. & Suwargadi, B.W. (2007). Seasonal characteristics of the Indian Ocean Dipole during the Holocene epoch. *Nature*, **445**, 299-302.

Adegbie, A.T., Schneider, R.R., Röhl, U. & Wefer, G. (2003). Glacial millennial-scale fluctuations in central African precipitation recorded in terrigenous sediment supply and freshwater signals offshore Cameroon. *Palaeogeography, Palaeoclimatology, Palaeoecology*, **197**, 323-333.

Alexandre, A., Basile-Doelsch, I., Sonzogni, C., Sylvestre, F., Parron, C., Meunier, J.-D. & Colin, F. (2006). Oxygen isotope analyses of fine silica grains using laser-extraction technique: Comparison with oxygen isotope data obtained from ion microprobe analyses and application to quartzite and silcrete cement investigation. *Geochimica et Cosmochimica Acta*, **70**, 2827-2835.

Alley, R.B., Clark, P.U. Keigwin, L.D. & Webb, R.S. (1999). Making sense of millennial scale climate change. In: Clark, P.U., Webb, R.S. & Keigwin, L.D. (Eds.), *Mechanisms of Global Climate Change at Millennial Time Scales*. Geophysical Monograph Vol. 112, American Geophysical Union, Washington, pp. 385-394.

An, Z.S. (2000). The history and variability of the East Asian paleomonsoon climate. *Quaternary Science Reviews*, **19**, 171-187.

An, Z.S. & Porter, S.C. (1997). Millennial-scale climatic oscillations during the last interglaciation in central China. *Geology*, **25**, 603-606.

Andruleit, H.A., von Rad, U., Bruns, A. & Ittekkot, V. (2000). Coccolithophore fluxes from sediment traps in the northeastern Arabian Sea off Pakistan. *Marine Micropaleontology*, **38**, 285-308.

Annamalai, H., Ping, L. & Shang-Ping, X. (2005). Southwest Indian Ocean SST variability: Its local effect and remote influence on Asian monsoons. *Journal of Climate*, **18**, 4150-4167.

Ashley, G.M. & Hay, R.L. (2002). Sedimentation patterns in a Plio-Pleistocene volcaniclastic rift-platform basin, Olduvai Gorge, Tanzania. In: Renaut, R.W., Ashley, G.M. (Eds.), *Sedimentation in Continental Rifts*. SEPM Special Publication, **73**, pp.107-122.

Baker, B.H., Mitchell, J.G. & Williams, L.A.J. (1988). Stratigraphy, geochronology and volcano-tectonic evolution of the Kedong-Naivasha-Kinangop region, Gregory Rift Valley, Kenya. *Journal of the Geological Society (London)*, **145**, 107-116.

Balling, R.C. Jr. (2005). Interactions of desertification and climate in Africa. In: Low, P.S. (Ed.) *Climate Change and Africa*. Cambridge University Press, Cambridge, pp. 41-49.

Ballot, A., Pflugmacher, S., Wiegand, C., Kotut, K. & Krienitz, L. (2003). Cyanobacteria toxins in Lake Baringo. *Limnologica*, **33**, 2-9.

Barker, P.A., Street-Perrott, F.A., Leng, M.J., Greenwood, P.B., Swain, D.L., Perrott, R.A., Telford, R.J. & Ficken, J.K. (2001). A 14,000-year Oxygen isotope record from diatom silica in two alpine lakes on Mt. Kenya. *Science*, **292**, 2307-2310.

Barker, P.A., Leng, M.J., Gasse, F. & Huang, Y. (2007). Century-to-millenial scale climatic variability in Lake Malawi revealed by isotope records. *Earth and Planetary Science Letters*, **261**, 93-103.

Barker, S., Cacho, I., Benway, H. & Tachikawa, K. (2005). Planktonic foraminifera Mg/Ca as a proxy for oceanic temperatures: a methodological overview and data compilation for the Last Glacial Maximum. *Quaternary Science Reviews*, **24**, 821-834.

Barry, R.G. & Chorley, R.J. (Eds.) (1995). *Atmosphere, Weather and Climate.* Routledge, London and New York, 6th Edition.

Bartholomew, G.A. & Birdsell, J.B. (1953). Ecology and the protohominids. *American Anthropology*, **55**, 481–498

Bartoli, G., Sarnthein, M., Weinelt, M., Erlenkeuser, H., Garbe-Schonberg, D. & Lea, D.W. (2005). Final closure of Panama and the onset of northern hemisphere glaciation. *Earth and Planetary Science Letters*, **237**, 33-44.

Bartoli, G., Sarnthein, M. & Wienelt, M. (2006). Late Pliocene millennial-scale climate variability in the northern North Atlantic prior to and after the onset of Northern Hemisphere glaciation. *Paleoceanography*, **21**, doi:10.1029/2005PA001185.

Bassinot, F. C., Labeyrie, L., Vincent, E., Quidelleur, X., Shackleton, N.J. & Lancelot, Y. (1994). The astronomical theory of climate and the age of the Brunhes-Matuyama magnetic reversal. *Earth and Planetary Science Letters*, **126**, 91-108.

Battarbee, R.W., Juggins, S., Gasse, F., Anderson, N.J., Bennion, H., Cameron, N.G., Ryves, D.B., Pailles, C., Chalie, F. & Telford, R. (2001). European Diatom Database (EDDI). An information system for palaeoenvironmental reconstruction. *ECRC Research Report*, **No. 81**, University College London, 94pp.

Bauer, S., Hitchcock, G.L. & Olson, D.B. (1991). Influence of monsoonally-forced ekman dynamics upon filaments along the Oman coast. *Deep-Sea Research*, **38**, 531-553.

Beck, C.C. (2010). Tracking precipitation sources using $\delta^{18}O$ isotopes, North Basin, Lake Turkana, Kenya. *Geological Society of America Meeting 2010*, Abstract Program, **42**, p.622.

Becker, J., Lourens, L.J., Hilgen, F.J., van der Laan, E., Kouwenhoven, T.J. & Reichart, G-J. (2005). Late Pliocene climate variability on Milankovitch to millennial time scales: A high-resolution study of MIS100 from the Mediterranean. *Palaeogeography, Palaeoclimatology, Palaeoecology*, **228**, 338-360.

Becker, J., Lourens, L.J. & Raymo, M.E. (2006). High-frequency climate linkages between the North Atlantic and the Mediterranean during marine oxygen isotope stage 100 (MIS 100).

Paleoceanography, **21**, PA3002, doi:10.1029/2005PA001168.

Beer, J. & van Geel, B. (2008). Holocene climate change and the evidence for solar and other forcing. In: Battarbee, R.W. & Binney, H.A., (Eds.), *Natural Climate variability and Global Warming: A Holocene Perspective.* Wiley-Blackwell, Chichester, UK, pp. 138—162.

Behera, S.K., Luo, J.J., Masson, S., Rao, S., et al. (2006). A CGCM study on the interactions between the IOD and ENSO. *Journal of Climate*, **19**, 1688-1705.

Bemis, B.E., Spero, H., Bijma, J. & Lea, D.W. (1998). Re-evaluation of the oxygen isotopic composition of planktonic foraminifera: experimental results and revised Palaeotemperature equations. *Paleoceanography*, **13**, 150-160.

Bender, M., Sowers, T. & Labeyrie, L. (1994). The Dole effect and its variation during the last 130,000 years as measured in the Vostok ice core. *Global Biogeochemical Cycles*, **8**, 363—376.

Berger, A. & Loutre, M.F. (1991). Insolation values for the climate of the last 10 million years. *Quaternary Science Reviews*, **10**, 29-317.

Berger, A., Loutre, M.F. & Melice, J.L. (2006). Equatorial insolation: from precession harmonics to eccentricity frequencies. *Climate of the Past*, **2**, 131–136.

Berger, W.H., Be, A.W.H. & Vincent, E. (Eds.) (1981). Oxygen and carbon isotopes in foraminifera. *Palaeogeography, Palaeoclimatology, Palaeoecology*, **33**, 1-277.

Bergner, A.G.N. & Trauth, M.H. (2004). Comparison of the hydrological and hydrochemical evolution of Lake Naivasha (Kenya) during three highstands between 175 and 60 kyr BP. *Palaeogeography, Palaeoclimatology, Palaeoecology*, **215**, 17-36.

Bergner, A.G.N., Trauth, M.H. & Bookhagen, B. (2003). Magnitude of precipitation/evaporation changes in the Naivasha Basin (Kenya) during the last 150 kyrs. *Global and Planetary Change*, **36**, 117-136.

Bergner, A.G.N., Strecker, M.R., Trauth, M.H., Deino, A., Gasse, F., Blisniuk, P. & Dühnforth, M. (2009). Tectonic and climatic control on evolution of rift lakes in the Central Kenya Rift, East Africa. *Quaternary Science Reviews*, **28**, 2804-2816.

Bertrand, S., Hughen, K. & Sepúlveda, J. (2010). Sedimentary geochemistry of the Chilean fjords: Spatial variability and potential to reconstruct Holocene climate and environmental change. Proceedings of the XRF core scanning workshop 2010. Royal NIOZ, The Netherlands.

Bigg, G.R. (Ed.) (1996). *The Oceans and Climate*. Cambridge University Press, Cambridge.

Billups, K., Ravelo, A.C., Zachos, J.C. & Norris, R.D. (1999). Link between oceanic heat transport, thermohaline circulation, and the Intertropical Convergence Zone in the early Pliocene, Atlantic. *Geology*, **27**, 319– 322.

Binz, P. (1987). Oxygen-isotope analysis on recent and fossil diatoms from Lake Walen and Lake Zurich (Switzerland) and its application on palaeoclimatic studies. PhD Thesis, Swiss Federal Institute of Technology, Zurich, 165pp.

Bishop, W.W. & Chapman, G.R. (1970). Early Pliocene Sediments and Fossils from the Northern Kenya Rift Valley. *Nature*, **226**, 914-918.

Black, E., Slingo, J. & Sperber, K.R. (2003). An observational study of the relationship between excessively strong short rains in coastal East Africa and Indian Ocean SST. *Monthly Weather Review*, **131**, 74-94.

Bobe, R. & Behrensmeyer, A.K. (2004). The expansion of grassland ecosystems in Africa in relation to mammalian evolution and the origin of the genus *Homo*. *Palaeogeography, Palaeoclimatology, Palaeoecology*, **207**, 399-420.

Bolton, C.T., Wilson, P.A., Bailey, I., Friedrich, O., Beer, C.J., Becker, J., Baranwal, S. & Schiebel, R. (2010). Millennial-scale climate variability in the subpolar North Atlantic Ocean during the late Pliocene. *Paleoceanography*, **25**, doi:10.1029/2010PA001951.

Bond, G.C. & Lotti, R. (1995). Iceberg discharges into the North Atlantic on millennial time scales during the last glaciation. *Science*, **267**, 1005-1010.

Bond, G.C., Broecker, W., Johnsen, S., McManus, J., Labeyrie, L., Jouzel, J. & Bonani, G. (1993). Correlations between climate records from North Atlantic sediments and Greenland ice. *Nature*, **365**, 143-147.

Bond, G.C., Showers, W., Elliot, M., Evans, M., Lotti, R., Hajdas, I., Bonani, G. & Johnson, S. (1999). The North Atlantic's 1-2 kyr Climate Rhythm: Relation to Heinrich Events, Dansgaard/Oeschger Cycles and the Little Ice Age. In: Clark, P.U., Webb, R.S., Keigwin, L.D. (Eds.), *Mechanisms of Global Climate Change at Millennial Time Scales*. Geophysical Monograph 112, AGU, Washington, D.C., pp. 35-58.

Bond, G.C., Kromer, B., Beer, J., Muscheler, R., Evans, M.N., Showers, W., Hoffmann, S., Lotti-Bond, R., Hajdas, I. & Bonani, G. (2001). Persistent solar influence on North Atlantic climate during the Holocene. *Science*, **294**, 2130-2136.

Boning, P., Bard, E. & Rose, J. (2007). Towards direct, micron-scale XRF elemental maps and quantitative profiles of wet marine sediments. *Geochemistry, Geophysics, Geosystems*, **8**, doi:10.1029/2006GC001480.

Bonnefille, R. (1983). Evidence for and drier climate in the Ethiopian Uplands towards 2.5Ma. *Nature*, **303**, 487-491.

Bonnefille, R. (1995). A Reassessment of the Plio-Pleistocene Pollen Record of East Africa. In: E.S. Vrba, G.H. Denton, T.C. Partridge & L.H. Burckle (eds.), *Paleoclimate and Evolution with emphasis on Human origins*, Yale University Press. pp. 299-310.

Bonnefille, R., Vincens, A. & Buchet, G. (1983). Palynology, stratigraphy and palaeoenvironment of a Pliocene hominid site (2.9-3.3 Ma) at Hadar, Ethiopia. *Palaeoclimatology, Palaeogeography, Palaeoecology*, **60**, 249-281.

Bonnefille, R., Potts, R., Charlie, F., Jolly, D. & Peyron, O. (2004). High-resolution vegetation and climate change associated with Pliocene Australopithecus afarensis. *Proceedings of the National Academy of Sciences of America*, **101**, 12,125-12,129.

Boos, W.R. & Kuang, Z. (2010). Dominant control of the South Asian monsoon by orographic insulation versus plateau heating. *Nature*, **463**, 218-222.

Bootsma, H.A. (1993). Spatio-temporal variation of phytoplankton biomass in Lake Malawi, Central Africa. *Verhandlungen Internationale Vereinigung für Limnologie*, **25**, 882-886.

Bothe, O., Fraedrich, K. & Zhu, X. (2010). The large-scale circulations and summer drought and wetness on the Tibetan Plateau. *International Journal of Climatology*, **30**, 844-855.

Boyle, E. A. (1983). Chemical accumulation variations under the Peru current during the past 130,000 years. *Journal of Geophysical Research*, **88(C12)**, 7667–7680, doi:10.1029/JC088iC12p07667.

Bradbury, J.P. & Krebs, W.N. (1982). Neogene and Quaternary lacustrine diatoms of the western Snake River Basin Idaho – Oregon, USA. *Acta Geologica Academiae Scientiarum*, **25**, 97-122.

Brandriss, M.E., O'Neil, J.R., Edlund, M.B. & Stoermer, E.F. (1998). Oxygen isotope fractionation between diatomaceous silica and water. *Geochimica et Cosmochimica Acta*, **62**, 1119-1125.

Brewer, T.S., Leng, M.J., Mackay. A.W., Lamb, A.L., Tyler, J.J. & Marsh, N.G. (2008). Unravelling contamination signals in biogenic silica oxygen isotope composition: The role of major and trace element geochemistry. Journal of *Quaternary Science*, **23**, 321-330.

Brierley, C.M. & Fedorov, A.V. (2010). Relative importance of meridional and zonal sea surface temperature gradients for the onset of the ice ages and Pliocene-Pleistocene climate evolution. *Paleoceanography*, **25**, PA2214, doi:10.1029/2009PA001809.

Broccoli, A.J., Dahl, K.A. & Stouffer, R.J. (2006). Response of the ITCZ to Northern Hemisphere cooling. *Geophysical Research Letters*, **33**, L01702, doi:10.1029/2005GL024546, 2006.

Brock, J.C., McClain, C.R., Anderson, D.M., Prell, W.L. & Hay, W.W. (1992). Southwest monsoon circulation and environments of recent planktonic foraminifera. *Paleoceanography*, **7**, 799-813.

Broecker, W.S. (1994). Massive ice-berg discharges as triggers for global climate change. *Nature*, **372**, 421-424.

Broecker, W.S. & Denton, G.H. (1989). The role of ocean-atmosphere reorganisation in glacial cycles. *Geochimica et Cosmochimica Acta*, **53**, 2465-2501.

Brook, E.J., Sowers, T. & Orchado, J. (1996). Rapid variations of atmospheric methane concentrations during the past 110,000 years. *Science*, **273**, 1087―1091.

Brown, E.T., Johnson, T.C., Scholz, C.A., Cohen, A.S. & King, J.W. (2007). Abrupt change in tropical African climate linked to the bipolar seesaw over the past 55,000 years. *Geophysical Research Letters*, **34**, doi: 10.1029/2008GL031240.

Brown, F.H. (1994). Development of Pliocene and Pleistocene chronology of the Turkana Basin, East Africa, and its relation to other sites. In: Corrucini, R.S. & Ciochon, R.L. (Eds.) *Integrative Paths to the Past*. Prentice-Hall, New Jersey, pp. 285-312.

Brown, F.H. (1995). The Potential of the Turkana Basin for Paleoclimatic Reconstruction in East Africa. In: E.S. Vrba, G.H. Denton, T.C. Partridge & L.H. Burckle (eds.), *Paleoclimate and Evolution with emphasis on Human origins*, Yale University Press. pp. 319-330.

Brown, F.H. & Feibel, C.S. (1991). In: *Koobi Fora Research Project Volume 3* (Harris, J.M., Ed.). Oxford, Clarendon, pp. 1-30.

Bruce, J.G., Johnson, D.R. & Kindle, J.C. (1994). Evidence for eddy formation in the eastern Arabian Sea during the northeast monsoon. *Journal of Geophysical Research*, **99**, 7651-7664.

Brumsack, H.-J. (2006). The trace metal content of recent organic carbon-rich sediments: implications for Cretaceous black shale formation. *Palaeogeography, Palaeoclimatology, Palaeoecology*, **232 (2–4)**, 344–361.

Buckle, C. (1996). *Weather and Climate in Africa*. Harlow, Longman. 312pp.

Budyko, M. and lzrael, Y.A. (Eds.). (1987). *Anthropogenic Climate Changes*. L. Gidrometeoizdat, Leningrad, 404 pp.

Burnett, A.P., Soreghan, M.J., Scholz, C.A. & Brown, E.T. (in press). Tropical East African climate change and its relation to global climate: A record from Lake Tanganyika, tropical East Africa, over the past 90+ kyr. *Palaeogeography, Palaeoclimatology, Palaeoecology*, doi:10.1016/j.palaeo.2010.02.011.

Burns, S. & Maslin, M.A. (1999). Composition and circulation of bottom water in the western Atlantic Ocean during the last glacial, based on pore-water analyses from the Amazon Fan. *Geology*, **27**, 1011-1014.

Cadet, D.L. & Diehl, B.C. (1984). Interannual variability of surface fields over the Indian Ocean during recent decades. *Monthly Weather Review*, **112**, 1921-1935.

Calvert, S.E. (1983). Geochemistry of Pleistocene sapropels and associated sediments from the eastern Mediterranean. *Oceanologica Acta*, **6**, 255–267.

Calvert, S.E., Pedersen, T.F. & Karlin, R.E. (2001). Geochemical and isotopic evidence for post-glacial palaeoceanographic changes in Saanich Inlet, British Columbia. *Marine Geology*, **174**, 287 – 305, doi:10.1016/S0025-3227(00)00156-0.

Calvert, S.E. & Pedersen, T.F. (2007). Elemental proxies for palaeoclimatic and palaeoceanographic variability in marine sediments: Interpretation and application. In: C. Hillaire-Marcel & De Vernal, A. (Eds.). *Proxies in Late Cenozoic Paleoceanography*. Elsevier, Amsterdam, pp.567-644.

Calvert, S.E., Bustin, R.M. & Ingall, E.D. (1996). Influence of water column anoxia and sediment supply on the burial and preservation of organic carbon in marine shales. *Geochimica et Cosmochimica Acta*, **60**, 1577–1593.

Cane, M.A. & Molnar, P. (2001). Closing of the Indonesian seaway as a precursor to east African aridification around 3-4 million years ago. *Nature*, **411**, 157-162.

Carter, R.M. & Gammon, P. (2004). New Zealand maritime glaciation: Millennial-scale southern climate change since 3.9 Ma. *Science*, **304**, 1659-1662.

Cerling, T.E. (1992). Development of grasslands, savannahs in East Africa during the Neogene. *Palaeogeography, Palaeoclimatology, Palaeoecology*, **97**, 241-247.

Cerling, T.E. & Hay, R.L. (1988). An isotopic study of paleosol carbonates from Olduvai Gorge. *Quaternary Research*, **25**, 63-78.

Cerling, T.E., Harris, J.M., MacFadden, B.J., Leakey, M.J., Quade, J., Eisenmann, V. &

Ehrlinger, J.R. (1997). Global vegetation change through the Miocene/Pliocene boundary. *Nature*, **389**, 153-158.

Chao, W.C. (2000). Multiple quasi-equilibria of the ITCZ and the origin of monsoon onset. *Journal of Atmospheric Science*, **57**, 641—651.

Chao, W.C. & Chen, B.D. (2001). The origin of monsoon. *Journal of Atmospheric Science*, **58**, 349-3507.

Chapligin, B., Meyer, H., Friedrichsen, H., Marent, A., Sohns, E. & Hubberten, H.-W. (2010a). A high-performance, safer and semi-automated approach for the $\delta^{18}O$ analysis of diatom silica and new methods for removing exchangeable oxygen. *Rapid Communications in Mass Spectrometry*, **24**, 2655-2664.

Chapligin, B., Alexandre, A., Dodd, J., Ijiri, A., Leng, M., Lücke, A., Shemesh, A., Webb, E., Abelmann, A., Longstaffe, F., Meyer, H., Moschen, R., Okazaki, Y., Sharp, Z., Sloane, H. J., Sonzogni, C., Swann, G., Sylvestre, F., Tyler, J. (2010b). Preliminary results from the on-going inter-laboratory comparison of the oxygen isotope composition of biogenic silica. Isotopes in Biogenic Silica (IBiS) Meeting 2010, Swansea, Wales (UK), February 8-9, 2010.

Chapman, G.R. (1971). *The Geological Evolution of the Northern Kamasia Hills, Baringo District, Kenya*. Ph.D. Thesis, University of London.

Chapman, G.R. & Brook, M. (1978). Chronostratigraphy of the Baringo Basin, Kenya. In: W.W. Bishop (Ed.), *Geological Background to Fossil Man*, The Geological Society, London. pp. 207-223.

Chapman, G.R., Lippard, S.J. & Martyn, J.E. (1978). The stratigraphy and structure of the Kamasia Range, Kenya Rift Valley. *Journal of the Geological Society of London*, **135**, 265-281.

Chappell, J. & Shackleton, N.J. (1986). Oxygen isotopes and sea level. *Nature*, **324**, 137-140.

Charney, J.G. (1971). Geostrophic turbulence. *Journal of the Atmospheric Sciences*, **28**, 1087-1095.

Chivas, A.R., De Dekker, P., Cali, J.A., Chapman, A., Kiss, E. & Shelly, J.M.G. (1993). Coupled stable isotope and trace element measurements of lacustrine carbonates as palaeoclimatic indicators. In: P.K. Swart, K.C. Lohmann, J.A. McKenzie & S. Savin (Eds.) *Climate change in continental isotopic records*. Geophysical Monograph 78, 113-122 pp.

Clark, I.D. & Fritz, P. (1997). Environment Isotopes in Hydrogeology, Lewis Publishers, Boca Raton, 328 pp.

Clark, P.U., Alley, R. & Pollard, D. (1999). Climatology - Northern hemisphere ice-sheet influences on global change. *Science*, **286**, 1104-1111.

Clark, P.U., Alley, R.B. & Pollard, D. (1999). Northern Hemisphere ice-sheet influences on global climate change. *Science*, **286**, 1104-1111.

Clayton, R.N. & Mayeda, T.K. (1963). The use of bromine pentafluoride in the extraction of oxygen from oxide and silicates for isotopic analysis. *Geochimica et Cosmochimica Acta*, **27**, 43–52.

Clayton, R.N., O'Neil, J.R. & Mayeda, T.K. (1972). Oxygen isotope exchange between quartz

and water. *Journal of Geophysical Research*, **77**, 3057-3067.

Clayton, R.N., Goldsmith, J.R., Karel, T.K., Mayeda, T.K. & Newton, R.C. (1975). Limits on the effect of pressure on isotopic fractionation. *Geochimica et Cosmochimica Acta*, **39**, 1197-2001.

Cleaveland, L.C. & Herbert, T.D. (2007). Coherent obliquity band and heterogeneous precession band responses in early Pleistocene tropical sea surface temperatures. *Paleoceanography*, **22**, PA2216.

Clemens, S.C. (1998). Dust response to seasonal atmospheric forcing: Proxy evaluation and calibration. *Paleoceanography*, **13**, 471-490.

Clemens, S.C. & Prell, W.L. (1990). Late Pleistocene variability of Arabian Sea summer monsoon winds and continental aridity: eolian records from the lithogenic component of deep-sea sediments. Paleoceanography, 5, 109-145.

Clemens, S.C. & Prell, W.L. (1991). One million year record of summer monsoon winds and continental aridity from the Owen Ridge (Site 722), Northwest Arabian Sea. *Proceedings of the Ocean Drilling Program, Scientific Results*, **Vol 117**, 365-388.

Clemens, S.C. & Prell, W.L. (2003). A 350,000-year summer-monsoon multiproxy stack from the Owen Ridge, Northern Arabian Sea. *Marine Geology*, **201**, 35―51.

Clemens, S.C. & Prell, W.L. (2007). The timing of orbital-scale Indian monsoon changes. *Quaternary Science Reviews*, **26**, 275―278.

Clemens, S.C. & Tiedemann, R. (1997). Eccentricity forcing of Pliocene-Early Pleistocene climate revealed in a marine oxygen-isotope record. *Nature*, **385**, 801-804.

Clemens, S.C, Prell, W., Murray, D., Shimmield, G. & Weedon, G. (1991). Forcing mechanisms of the Indian Ocean monsoon. Nature, 353, 720-725.

Clemens, S.C., Murray, D.W. & Prell, W.L. (1996). Nonstationary phase of the Plio-Pleistocene Asian monsoon. *Science*, **274**, 943-948.

Clemens, S.C., Prell, W.L., Sun, Y., Liu, Z. & Chen, G. (2008). Southern hemisphere forcing of Pliocene d-18O and the evolution of Indo-Asian monsoons. *Paleoceanography*, **23**, PA4210, doi:10.1029/2008PA001638.

Clement, A.C., Hall, A. & Broccoli, A.J. (2004). The importance of precessional signals in the tropical climate. *Climate Dynamics*, **22**, 327-341.

Coates, A. G., Jackson, J.B.C., Collins, L.S., Cronin, T.M., Dowsett, H.J., Bybell, L.M., Jung, P. & Obando, J.A. (1992). Closure of the Isthmus of Panama: The near-shore marine record of Costa Rica and western Panama. *Geological Society of America Bulletin*, **104**, 814–828.

Cole, J.E., Rind, D., Webb, R.S., Jouzel, J. & Healy, R. (1999). Climatic controls on interannual variability of precipitation delta O-18: simulated influence of temperature, precipitation amount and vapour source region. *Journal of Geophysical Research – Atmospheres*, **104**, 14223-14235.

Collins, L.S., Coates, A.G., Berggren, W.A., Aubry, M-P., & Zhang, J. (1996). The late Miocene Panama Isthmian Strait. *Geology*, **24**, 687–690.

Copeland, P., Harrison, T.M., Kidd, W.S.F., Ronghua, X. & Yuquan, Z. (1987). Rapid early

Miocene acceleration of uplift of the Gagdese Belt, Xizang (southern Tibet), and its bearing on accommodation mechanisms of the India-Asia collision. *Earth and Planetary Science Letters*, **86**, 240-252.

Coplen, T.B. (1996). New guidelines for the reporting of stable hydrogen, carbon and oxygen isotope ratio data. *Geochimica et Cosmochimica Acta*, **60**, 3359.

Craig, H. (1961). Isotopic variations in meteoric waters. *Science*, **133**, 1702-1703.

Craig, H. (1965). The measurement of oxygen isotope paleotemperatures. In: T. Tongiori (Ed.) *Stable Isotopes in Oceanographic Studies and Paleotemperature*s.

Craig, H. & Gordon, L.I. (1965). Isotope oceanography: deuterium and oxygen 18 variations in the oceans and the marine atmosphere. *Symposium on Marine Geochemistry*, University of Rhode Island, Occasional Publications **3**, 277-374.

Crespin, J., Alexandre, A., Sylvestre, F., Sonzogni, C., Paillès C. & Garreta, V. (2008). IR Laser extraction technique applied to oxygen isotope analysis of small biogenic silica samples. *Analytical Chemistry*, **80**, 2372-2378.

Crespin, J., Sylvestre, F., Alexandre, A., Sonzogni, C., Paillès, C. & Perga, M.-E. (2010). Re-examination of the temperature-dependent relationship between $\delta^{18}O_{diatoms}$ and $\delta^{18}O_{lakewater}$ and implications for palaeoclimate inferences. *Journal of Paleolimnology*, **44**, 547-557.

Criss, R.E. (1999). *Principles of stable isotope distribution*. Oxford University Press, New York, 254pp.

Cronin, T.M., Whatley, R.C., Wood, A., Tsukagoshi, A., lkeya, N., Brouwers, E.M. & Briggs, W.M. (1993). Microfaunal evidence for elevated mid-Pliocene temperatures in the Arctic Ocean. *Paleoceanography*, **8**, 161-173.

Crowley, T.J. (1996). Pliocene climates: the nature of the problem. *Marine Micropaleontology*, **27**, 3-12.

Cullen, J. & Prell, W. L. (1984). Planktonic foraminifera of the Northern Indian Ocean: distribution and preservation in surface sediments. *Marine Micropaleontology*, **9**, 1-5.

Curry, R.P. (1966). Glaciation about 3,000,000 years ago in the Sierra Nevada. *Science*, **154**, 770-771.

Dansgaard, W. (1964) Stable isotopes in precipitation. *Tellus*, **16**, 436-468.

Darling, W.G. & Talbot, J.C. (2003). The O and H stable isotopic composition of fresh waters in the British Isles 1. Rainfall. *Hydrology and Earth System Sciences*, **7**, 163-181.

Darling, W.G., Bath, A.H., Gibson, J.J. & Rozanski, K. (2005). Isotopes in Water. In: M.J. Leng (Ed.) *Isotopes in Palaeoenvironmental Research*, Springer, Dordrecht, pp. 1-66.

Dart, R. (1925). Australopithecus africanus: the man-ape of south Africa. *Nature*, **115**, 195-199.

Dart, R. (1953). The predatory transition from ape to man. *International Review of Anthropology and Linguistics*, **1**, 201-218.

Dawson, R., Wei, R., Tao, S., Ito, Y., Yamanaka, K. & Haraguchi, H. (2004). Analysis of silicon concentration periodicity for the past 2.4 Ma in sediments from Lake Baikal site BDP 96-2. *Climate Research*, **26**, 193-197.

De Heinzelin, J., Clark, J.D., White, T.D., Hart, W.K., Renne, P.R., Wolde Gabriel, G., Beyene,

Y. & Vrba, E. (1999). Environment and behaviour of 2.5 million year old Bouri hominids. *Science*, **284**, 625-629.

De Jonge, C., Stadnitskaia, A., De Mol, L., Blamart, D., Henriet, J-P., Sinninghe Damsté, J.S. & Van Rooij, D. (2010). A multi-proxy approach to assess oceanographic variability in the Southern Gulf of Cadiz during the last glacial cycle. Proceedings of the XRF core scanning workshop 2010, Royal NIOZ, The Netherlands.

De La Rocha, C.L., Brzezinski, M.A., DeNiro, M.J. & Shemesh, A. (1998). Silicon-isotope composition of diatoms as an indicator of past oceanic change. *Nature*, **395**, 680-683.

De Conto, R.M. & Pollard, D. (2003). Rapid Cenozoic glaciation of Antarctica induced by declining atmospheric CO_2. *Nature*, **421**, 245-249.

Degens, T.E. & Epstein, S. (1962). Relation between 18O/16O ratios in coexisting carbonates, cherts and diatomites. *American Association of Petroleum Geologists Bulletin*, **46**, 534– 542.

Deino, A.L., & Potts, R. (1990). Single-crystal 40Ar/39Ar dating of the Olorgesailie Formation, southern Kenya Rift. *Journal of Geophysical Research B, Solid Earth Planets*, **95**, 8453–8470.

Deino, A.L., Kingston, J.D., Glen, J.M., Edgar, R.K. & Hill, A. (2006). Precessional forcing of lacustrine sedimentation in the late Cenozoic Chemeron Basin, Central Kenya Rift, and the calibration of the Gauss/Matuyama boundary. *Earth and Planetary Science Letters*, **247**, 41-60.

Deino, A.L., Kingston, J.D., Wilson, K.E. & Hill, A. (2010). Global Climate Change and Sedimentation Patterns in the Neogene Baringo Basin, Central Kenya Rift. *EOS Transactions AGU*, Fall Meeting Supplement 2010, abstract GC51C-0761

Deino, A.L., Trauth, M.H., Bergner, A.G. & Potts, R. (2004). 40Ar/39Ar age calibration of the lacustrine sediments at Kariandusi, Central Kenya Rift. *EOS Transactions AGU*, Fall Meeting 2004 Supplement, abstract U21A-0703.

deMenocal, P.B. (1995). Plio-Pleistocene African climate. *Science*, **270**, 53-59.

deMenocal, P.B. (2004). African climate change and faunal evolution during the Plio-Pleistocene. *Earth and Planetary Science Letters*, **220**, 3-40.

deMenocal, P.B. (2011). Climate and Human Evolution. *Science*, **331**, 540-542.

deMenocal, P.B. & Bloemendal, J. (1995). Plio-Pleistocene Climatic Variability in Subtropical Africa and the Paleoenvironment of Hominid Evolution: A Combined Data-Model Approach. In: E.S. Vrba, G.H. Denton, T.C. Partridge & L.H. Burckle (Eds.), *Paleoclimate and Evolution With Emphasis on Human Origins*, Yale University Press. pp. 262-288.

deMenocal, P.B. & Rind, D. (1993). Sensitivity of Asian and African climate variations in seasonal insolation, glacial ice cover, sea-surface temperature and Asian orography. *Journal of Geophysical* Research, 98, 7265-7287.

deMenocal, P.B. & Rind, D. (1996). Sensitivity of Subtropical African and Asian Climate to Prescribed Boundary Condition Changes: Model Implications for the Plio-Pleistocene Evolution of Low-Latitude Climate. In: T.C. Johnson & E.O. Odada (Eds.) *The Limnology,*

Climatology and Paleoclimatology of the East African Lakes, Gordon & Breach, Amsterdam. pp. 57-77.

deMenocal, P., Bloemendal, J. & King, J. (1991) A rock-magnetic record of monsoonal dust deposition to the Arabian Sea: evidence for a shift in the mode of deposition at 2.4 Ma. In: W.L. Prell et al. (Eds.), *Proceedings of the Ocean Drilling Program, Scientific Results*, **Vol 117**, 389–407.

deMenocal, P.B., Ortiz, J., Guilderson, T., Adkins, J., Sarnthein, M., Baker, L. & Yarusinsky, M. (2000). Abrupt onset and termination of the African Humid Period: rapid climate responses to gradual insolation forcing. *Quaternary Science Reviews*, **19**, 347-361.

Denison, S.M., Maslin, M.A., Boot, C., Pancost, R.D. & Ettwein, V.J. (2005). Precession-forced changes in South West African vegetation during Marine Isotope Stages 101-100 (~2.56-2.51Ma). *Palaeogeography, Palaeoclimatology, Palaeoecology*, **220**, 375-386.

Dickey, T., Marra, J., Sigurdson, D.E., Weller, R.A., Kinkade, C.S., Zedler, S.E., Wiggert, J.D. & Langdon, C. (1998). Seasonal variability of bio-optical and physical properties in the Arabian Sea: October 1991 - October 1995. *Deep-Sea Research II*, **45**, 2001-2025.

Ding, Q. & Wang, B. (2005). Circumglobal teleconnection in the Northern Hemisphere summer. *Journal of Climate*, **18**, 3483-3505.

Ding, Y. & Chan, J.C.L. (2005). The East Asian summer monsoon: an overview. *Meterorological and Atmospheric Physics*, **89**, 117-142.

Ding, Y., Li, C. & Liu, Y. (2004). Overview of the South China Sea Monsoon Experiment,*Advances in Atmospheric Sciences*, **21**, 343-360.

Dodd, J.P. & Sharp, Z.D. (2010). A laser fluorination method for oxygen isotope analysis of biogenic silica and a new oxygen isotope calibration of modern diatoms in freshwater environments. *Geochimica et Cosmochimica Acta*, **74**, 1381-1390.

Dodonov, A.E. & Zhou, L.P. (2008). Loess deposition in Asia: its initiation and development before and during the Quaternary. *Episodes*, **31,** 222–225.

Dowsett, H.J. & Cronin, T.M. (1989). High eustatic sea level during the middle Pliocene: evidence from the southeastern U.S. Atlantic coastal plain. *Geology*, **18**, 435– 438.

Dowsett, H.J., Cronin, T.M., Poore, R.Z., Thompson, R.S., Whatley, R.C. & Wood, A.M. (1992). Micropaleontological evidence for increased meridional heat transport in the North Atlantic Ocean during the Pliocene. *Science*, **258**, 1133-1135.

Dowsett, H.J., Barron, J. & Poore, R.Z. (1996). Middle Pliocene sea surface temperatures: A global reconstruction. *Marine Micropaleontology*, **27**, 13-25.

Dowsett, H.J., Barron, J.A, Poore, R.Z., Thompson, R.S., Cronin, T.M., Ishman, S.E. & Willard, D.A. (1999). *Middle Pliocene Paleoenvironmental Reconstruction: PRISM2*.Q U.S.Geological Survey Open File Report 99-535, 236 pp. http://pubs.usgs.gov/openfile/of99-535/.

Draut, A.E., Raymo, M.E., McManus, J.F. & Oppo, D.W. (2003). Climate stability during the Pliocene warm period. *Paleoceanography*, **18**, doi: 10.1029/2003PA000889.

Driscoll, N.W. & Haug, G.H. (1998). A short circuit in thermohaline circulation: A cause for

northern hemisphere glaciation? *Science*, **282**, 436-438.

Droxler, A.W. & Schlager, W. (1985). Glacial versus interglacial sedimentation rates and turbidite frequency in the Bahamas. *Geology*, **13**, 99-802.

Druffel, E.R.M., Williams, P.M., Bauer, J.E & Ertel, J.R. (1992). Cycling of dissolved and particulate organic matter in the open ocean. *Journal of Geophysical Research (Oceans)*, **97**, 15639-15659.

Duplessy, J.C., Lalou, C. & Vinot, A.C. (1970). Different isotopic fractionation in benthic foraminifera and paleotemperatures revised. *Science*, **213**, 1247-1250.

Duplessy, J-C., Shackleton, N.J., Fairbanks, R.J., Labeyrie, L.D., Oppo, D. & Kallel, N. (1988). Deepwater source variation during the last climatic cycle and their impact on the global deepwater circulation. *Paleoceanography*, **3**, 343-360.

Duplessy, J-C., Labeyrie, L., Juillet-Leclerc, A., Maitre, F., Duprat, J. & Sarnthein, M. (1991). Surface salinity reconstruction of the North Atlantic Ocean during the Last Glacial Maximum. *Oceanologica Acta*, **14**, 311-324.

Duplessy, J-C., Labeyrie, L., Arnold, M., Paterne, M., Duprat, J. & van Weering, T. (1992). Changes in surface water salinity of the North Atlantic Ocean during the last deglaciation. *Nature*, **358**, 485-488.

Duplessy, J-C., Labeyrie, L. & Waelbroeck, C. (2002). Constraints on the ocean oxygen isotopic enrichment between the Last Glacial Maximum and the Holocene. *Quaternary Science Reviews*, **21**, 315-330.

Dupont, L.M. (2006). Late Pliocene vegetation and climate in Namibia (southern Africa) derived from palynology of ODP Site 1082. *Geochemistry, Geophysics, Geosystems*, **7**, doi:10.1029/2005GC001208.

Dupont, L.M. & Wyputta, U. (2003). Reconstructing pathways of aeolian pollen transport to the marine sediments along the coastline of SW Africa. *Quaternary Science Reviews*, **22**, 157-174.

Dupont, L.M., Donner, B., Vidal., L., Pérez, E.M. & Wefer, G. (2005). Linking desert evolution and coastal upwelling: Pliocene climate change in Namibia. *Geology*, **33**, 461-464.

Duque-Caro, H. (1990). Neogene stratigraphy, paleoceanography and paleobiogeography in northwest South America and the evolution of the Panama Seaway. *Palaeogeography, Palaeoclimatology, Palaeoecology*, **77**, 203-234.

Edlund, M.B. (2006). Persistent low diatom plankton diversity within the otherwise highly diverse Lake Baikal ecosystem. *Nova Hedwigia Beiheft*, **130**, 339-356.

Emeis, K.-C., Anderson, D.M., Doose, H., Kroon, D. & Shulz-Bull, D. (1995). Sea-surface temperatures and the history of monsoon upwelling in the northwest Arabian Sea during the last 500,000 years. *Quaternary Research*, **43**, 355-361.

Emiliani, C. (1955). Pleistocene temperatures. *Journal of Geology*, **63**, 538-578.

Emiliani, C. (1966). Paleotemperature analysis of Caribbean cores P6304-8 and P6304-9 and a generalized temperature curve for the past 425,000 years. *Journal of Geology*, **74**, 109-126.

Emiliani, C. (1971). The amplitude of Pleistocene climatic cycles at low latitudes and the

isotopic composition of glacial ice. In: K.K. Turehian (Ed.), *The late Cenozoic glacial ages*. Yale University, New Haven, Connecticut, 183-197 pp.

Epstein, S. & Taylor, H.P. (1971). O^{18}/O^{16}, Si^{30}/Si^{28}, D/H and C^{13}/C^{12} ratios in lunar samples. *Proceedings of the Second Lunar Conference*, **2**, 1421-1441.

Epstein, S., Buchsbaum, R., Lowenstam, H. & Urey, H.C. (1951). Carbonate-water isotopic temperature scale. *Journal of Geology*, **62**, 417-426.

Fairbanks, R.G. (1989). A 17,000-year glacio-eustatic sea level record: Influence of glacial melting rates on the Younger Dryas event and deep-ocean circulation. *Nature*, **342**, 637.

Fairhead, J.D. (1986). Geophysical controls on sedimentation in the African Rift System. In: L.E. Frostick, Renaut, R.W., Reid, I. & Tiercelin, J.J. (Eds.) *Sedimentation in the African Rifts*. Geological Society of London Special Publication **25**, pp. 19–27.

Fang, X-M., Ono, Y., Fukusawa, H., Bao-Tian, P., Li, J-J., Dong-Hong, G., Oi, K., Tsukamoto, S., Toril, M. & Mishima, T. (1999). Asian summer monsoon stability during the past 60,000 years: magnetic susceptibility and pedogenic evidence from the western Chinese Loess Plateau. *Earth and Planetary Science Letters*, **168**, 219-232.

Fedorov, A.V., Dekens, P.S., McCarthy, M., Ravelo, A.C., deMenocal, P.B., Barreiro, M., Pacanowski, R.C. & Philander, S.G. (2006). The Pliocene Paradox (Mechanisms for a permanent El Nino). *Science*, **312**, 1485-1489.

Fischer, A.S., Terray,P., Guilyardi, E., Gualdi, S. & Delecluse, P. (2005). Two independent triggers for the Indian Ocean Dipole/Zonal Mode in a coupled GCM. *Journal of Climate*, **18**, 3428-3449.

Fleitmann, D., Burns, S.J., Mangini, A., Mudelsee, M., Kramers, J., Villa, I., Neff, U., Al-Subbary, A.A., Buettner, A., Hippler, D. & Matter, A. (2007). Holocene ITCZ and Indian Ocean monsoon dynamics recorded in stalagmites from Oman and Yemen (Socotra). *Quaternary Science Reviews*, **26**, 170-188.

Francois, R., Bacon, M.P., Altabet, M.A. & Labeyrie, L.D. (1993). Glacial/interglacial changes in sediment rain rate in the SW Indian sector of subantarctic waters as recorded by ^{230}Th, ^{231}Pa and $\delta^{15}N$. *Paleoceanography*, **8**, 611-629.

Fröhlich, K., Kralik, M., Papesch, W., Rank, D., Scheifinger, H. & Stichler, W. (2008). Deuterium excess in precipitation of Alpine regions – moisture recycling. *Isotopes in Environmental and Health Sciences*, **44**, 61-70.

Funk, J.A., von Dobeneck, T. & Reitz, A. (2004). Integrated Rock Magnetic and Geochemical Quantification of Redoxomorphic Iron Mineral Diagenesis in Late Quaternary Sediments from the Equatorial Atlantic. In: Wefer, G., Mulitza, S. & Ratmeyer, V. (Eds.), *The South Atlantic in the Late Quaternary: Reconstruction of Material Budgets and Current Systems*, Springer-Verlag, pp 237-260.

Gadgil, S. (2003). The Indian monsoon and its variability. *Annual Review of Earth and Planetary Sciences*, **31**, 429-46.

Ganopolski, A. & Rahmstorf, S. (2001). Rapid changes of glacial climate simulated in a coupled climate model. *Nature*, **409**, 442-445.

Garcin, Y., Vincens, A., Williamson, D., Guiot, J. & Buchet, G. (2006). Wet phases in tropical southern Africa during the last glacial period. *Geophysical Research Letters*, **33**, doi:10.1029/2005GL025531.

Garcin, Y., Junginger, A., Melnick, D., Olago, D.O. & Strecker, M.R. (2009). Late Pleistocene-Holocene rise and collapse of Lake Suguta. *Quaternary Science Reviews*, **28**, 911-925.

Garlick, G.D. (1974). The stable isotopes of oxygen, carbon, hydrogen in the marine environment. In: G.D. Goldberg (ed.) *The Sea*. John Wiley & Sons, New York, pp. 393-425.

Gasse, F. (1980). Les diatomées lacustres plio-pléistocénes du Gadeb (Éthiopie): systématique, paléoécologie, biostratigraphie. *Revue Algolgique. Mémoire hors-série* no. 3. 62pp.

Gasse, F. (1990). Tectonic and climatic controls on lake distribution and environments in Afar from Miocene to present. In: Katz, B.J. (Ed.), *Lacustrine Basin Exploration, Case Studies and Modern Analogs*. AAPG Mem. **50**, 1-34.

Gasse, F. (2000). Hydrological changes in the African tropics since the Last Glacial Maximum. *Quaternary Science Reviews*, **19**, 189-211.

Gasse, F. (2006). Climate and hydrological changes in tropical Africa during the past million years. *Comptes Rendus Palevol*, **5**, 35-43.

Gasse, F., Talling, D.F. & Kilham, P. (1983). Diatom assemblages in East Africa: classification, distribution and ecology. *Re´vue d'Hydrobiologie Tropicale*, **16**, 3-34.

Gasse, F., Barker, P. & Johnson, T.C. (2002). A 24,000 yr diatom record from the northern basin of Lake Malawi. In: Odada, E., Olago, D.O. (Eds.), *The East African Great Lakes: Limnology, Paleolimnology and Biodiversity*. Kluwer, Dordrecht, Netherlands, pp. 393-414.

Gat, J.R. (2000). Atmospheric water balance – the isotopic perspective. *Hydrological Processes*, **14**, 1357-1369.

Gibbard, P.L., Head, M.J., Walker, M.J.C. & The Subcommission on Quaternary Stratigraphy. (2010). Formal ratification of the Quaternary System/Period and the Pleistocene Series/Epoch with a base at 2.58 Ma. *Journal of Quaternary Science*, **25**, 96-102.

Giddings, J.C. (1985). A system based on split-flow lateral-transport thin (SPLITT) separation cells for rapid and continuous particle fractionation. *Separation Science and Technology*, **20**, 749– 768.

Gilbert, C.C., Goble, E.D. & Hill, A. (2010). Miocene Cercopithecoidea from the Tugen Hills, Kenya. *Journal of Human Evolution*, **59**, 465-483.

Gillespie, R., Street-Perrot, F.A. & Switsur, R. (1983). Post-glacial arid episodes in Ethiopia have implications for climate prediction. *Nature*, **306**, 680-683.

Goddard, L. & Graham, N.E. (1999). Importance of the Indian Ocean for simulating rainfall anomalies over eastern and southern Africa. *Journal of Geophysical Research*, **104** D16, 19,099-19,116.

Goldberg, E.L., Phedorin, M.A., Grachev, M.A., Bobrov, V.A., Dolbnya, I.P., Khlystov, O.M., Levina, O.V. & Ziborova, G.A. (2000). Geochemical signals of orbital forcing in the records of palaeoclimates found in the sediments of Lake Baikal. *Nuclear Instruments and Methods in Physics Research*, **A448 (1-2)**, 384-393.

Gordon, W.A. (1975). Distribution by latitude of Phanerozoic evaporate deposit. *Journal of Geology*, **83**, 671-684.

Griffin, D.L. (1999). The late Miocene climate of northeastern Africa: unravelling the signals in the sedimentary succession. *Journal of the Geological Society of London*, **156**, 817-826.

Grine, F.E. (1986). Ecological causality and the pattern of Plio-Pleistocene hominid evolution in Africa. *South African Jounal of Science*, **82**, 87-89.

Grossman, E.L. (1987). Stable isotopes in modern benthic foraminifera: A study of vital effects. *Journal of Foraminiferal Research*, **17**, 48-61.

Grove, A.T. (1986). Geomorphology of the African Rift System. *Geological Society of London Special Publications*, **25**, 9-16.

Guo, Z., Liu, T., Guiot, J., Wu, N., Lü, H., Han, J., Liu, J. & Gu, Z. (1996). High frequency pulses of East Asian monsoon climate in the last two glaciations: link with the North Atlantic. *Climate Dynamics*, **12**, 701-709.

Gupta, A.K., Anderson, D.M. & Overpeck, J.T. (2003). Abrupt changes in the Asian southwest monsoon during the Holocene and their links to the North Atlantic Ocean. *Nature*, **421**, 354–357.

Haberyan, K.A. & Hecky, R.E. (1987). The late Pleistocene and Holocene stratigraphy and paleolimnology of Lakes Kivu and Tanganyika. *Palaeogeography, Palaeoclimatology, Palaeoecology*, **61**, 169-197.

Haimson, M. & Knauth, L.P. (1983). Stepwise fluorination — a useful approach for the isotopic analysis of hydrous minerals. *Geochimica et Cosmochimica Acta*, **47**, 1589– 1595.

Harrison, S.P., Kohfeld, K.E., Roelandt, C. & Claquin, T. (2001). The role of dust in climate changes today, at the last glacial miximum and in the future. *Earth Science Reviews*, **54**, 43-80.

Harrison, T.M., Copeland, P., Kidd, W.S.F. & Yin, A. (1992). Raising Tibet. *Science*, **255**, 663-670.

Harvey, T.J. (1976). The paleolimnology of Lake Mobutu Sese Seko, Uganda-Zaire: The last 28,000 years. Ph.D. thesis, Duke University, 104pp.

Hastenrath, S. (1985). *Climate and the Circulation of the Tropics*. Boston (D.Reidel).

Hastenrath, S. (1991). *Climate dynamics of the tropics*. Kluwer Academic Publishers, 486 pp.

Hastenrath, S. (1995). Recent advances in tropical climate prediction. *Journal of Climate*, **8**, 1519-1532.

Hastenrath, S. & Greischar, L. (1993). The monsoonal heat budget of the hydrosphere-atmosphere system in the Indian Ocean sector. *Journal of Geophysical Research*, **98**, 6869-6881.

Haug, G.H. & Tiedemann, R. (1998). Effect of the formation of the Isthmus of Panama on Atlantic Ocean thermohaline circulation. *Nature*, **393**, 673-676.

Haug, G.H., Sigman, D. M., Tiedemann, R., Pedersen, T.F.& Sarnthein, M. (1999). Onset of permanent stratification in the subarctic Pacific Ocean. *Nature*, **401**, 779-782.

Haug, G.H., Tiedemann, R., Zahn, R. & Ravelo, A.C. (2001). Role of Panama uplift on oceanic

freshwater balance. *Geology*, **29**, 207-210.

Haug, G.H., Günther, D., Peterson, L.C., Sigman, D.M., Hughen, K.A. & Aeschlimann, B. (2003). Climate and the collapse of Maya civilization. *Science*, **299**, 1731–1735.

Haug, G.H., Ganopolski, A., Sigman, D.M., Rosell-Mele, A., Swann, G.E.A., Tiedemann, R., Jaccard, S.L., Bollmann, J., Maslin, M.A., Leng, M.J. & Eglinton, G. (2005). North Pacific seasonality and the glaciation of North America 2.7 million years ago. *Nature*, **433**, 821-825.

Hays, P.D. & Grossman, E.L. (1991). Oxygen isotopes in meteoric calcite cements as indicators of continental palaeoclimate. *Geology*, **19**, 441-444.

Haywood, A.M., Sellwood, B.W. & Valdes, P.J. (2000b). Regional warming: Pliocene (3Ma) paleoclimate of Europe and the Mediterranean. *Geology*, **28**, 1063-1066.

Haywood, A.M., Valdes, P.J. & Sellwood, B.W. (2000a). Global scale palaeoclimate reconstruction of the middle Pliocene climate using the UKMO GCM: initial results. *Global and Planetary Change*, **25**, 239-256.

Haywood, A.M., Dekens, P., Ravelo, A.C. & Williams, M. (2005). Warmer tropics during the mid-Pliocene? Evidence from alkenone paleothermometry and a fully coupled ocean-atmosphere GCM. *Geochemistry, Geophysics, Geosystems*, **6**, Q03010.

Haywood, A.M., Valdes, P.J. & Peck, V.L. (2007). A permanent El Niño-like state during the Pliocene. *Paleoceanography*, **22**, PA1213, doi:10.1029/2006/PA001323.

Head, M.J., Gibbard, P.L. & Salvador, A. (2008). The Quaternary: its character and definition. *Episodes*, **31**, 234-238.

Henderson, A.C.G., Holmes, J.A. & Leng, M.J. (2010). Late Holocene isotope hydrology of Lake Qinghai, NE Tibetan Plateau: effective moisture variability and atmospheric circulation changes. *Quaternary Science Reviews*, **29**, 2215-2223.

Herbert, T.D., Cleaveland Peterson, L., Lawrence, K.T. & Liu, Z. (2010). Tropical Ocean Temperatures. *Science*, **328**, 1530-1534.

Hermelin, J.O.R. (1990) Benthic foraminifera and the evolution of the Owen Ridge (northwestern Indian Ocean). In: *Geology of the Oceans*, E.S.F. Consortium for Ocean Drilling, Milano, 49.

Hermelin, J.O.R. (1992). Variations in the benthic foraminiferal fauna of the Arabian Sea: a response to changes in upwelling intensity? In: C.P. Summerhayes, W.L. Prell & K.C. Emeis (Eds.) *Upwelling Systems: Evolution since the Early Miocene*, Geological Society Special Publication No 64, pp. 151-166.

Hermelin, J.O.R. & Shimmield, G.B. (1990). The importance of the oxygen minimum zone and sediment geochemistry on the distribution of recent benthic foraminifera from the NW Indian Ocean. *Marine Geology*, **91**, 1-29.

Hernandez, A., Bao, R., Giralt, S., Barker, P.A., Leng, M.J., Sloane, H.J. & Saoz, A. (2011). Biogeochemical processes controlling oxygen and carbon isotopes of diatom silica in Late Glacial to Holocene lacustrine rhythymites. *Palaeogeography, Palaeoclimatology, Palaeoecology*, **299**, 413-425.

Hilgen, F.J., Lourens, L.J., Berger, A. & Loutre, M.F. (1993). Evaluation of the astronomically

calibrated time scale for the Late Pliocene and earliest Pleistocene. *Paleoceanography*, **8**, 549-565.

Hill, A. (1995). Faunal and Environmental Change in the Neogene of East Africa: Evidence from the Tugen Hills sequence, Baringo district, Kenya. In: E.S. Vrba, G.H. Denton, T.C. Partridge & L.H. Burckle (eds.), *Paleoclimate and Evolution with emphasis on Human origins*, Yale University Press. pp. 178-193.

Hill, A. (1999). The Baringo Basin, Kenya: from Bill Bishop to BPRP. In: Andrews, P. & Banham, P. (eds.) *Late Cenozoic Environments and Hominid Evolution: a tribute to Bill Bishop*. Geological Society, London, pp. 85-97.

Hill, A., Drake, R., Tauxe, L., Monaghan, M., Barry, J.C., Behrensmeyer, A.K., Curtis, G. & Jacobs, B.F. (1985). Neogene palaeontology and geochronology of the Baringo Basin, Kenya. *Journal of Human Evolution*, **14**, 759-773.

Hill, A., Curtis, G. & Drake, R. (1986). Sedimentary stratigraphy of the Tugen Hills, Baringo, Kenya. In: L.E. Frostick et al. (eds.), *Sedimentation in the African Rifts*, Geological Society Special Publication No. 25, pp. 285-295.

Hoefs, J. (2009). *Stable Isotope Geochemistry*, (6th Ed.). Springer-Verlag, Berlin Heidelberg, 288pp.

Hofmann, P., Wagner, T. & Beckmann, B. (2003). Millennial- to centennial-scale record of African climate variability and organic carbon accumulation in the Coniacian-Santonian eastern tropical Atlantic (Ocean Drilling Program Site 959, off Ivory Coast and Ghana). *Geology*, **31**, 135-138.

Hofmann, P., Stüsser, I., Wagner, T., Schouten, S. & Sinninghe Damsté, J.S. (2008). Climate-ocean coupling off North-West Africa during the Lower Albian: The Oceanic Anoxic Event 1b. *Palaeogeography, Palaeoclimatology, Palaeoecology*, **262**, 157-165.

Holmes, J.A. & Chivas, R.A. (2002). Ostracod shell chemistry – overview. In: J.A. Holmes & R.A. Chivas (Eds.) *The Ostracoda: applications in Quaternary Research*, AGU Geophysical Monograph 11, American Geophysical Union, Washington DC, 185-204 pp.

Holmgren, K., Lee-Thorp, J.A., Cooper, G.R.J., Lundblad, K., Partridge, T.C., Scott, L., Sithaldeen, R., Talma, A.S. & Tyson, P.D. (2003). Persistent millennial-scale climatic variability over the past 25,000 years in Southern Africa. *Quaternary Science Reviews*, **22**, 2311-2326.

Honjo, S., Dymond, J., Prell, W. & Ittekot, V.U. (1999). Monsoon-controlled export fluxes to the interior of the Arabian Sea. *Deep Sea Research II*, **46**, 1859-1902.

Hooghiemstra, H., Melice, J.L., Berger, A. & Shackleton, N.J. (1993). Frequency spectra and palaeoclimatic variability of the high-resolution 30-1450 ka Funza I pollen record (Eastern Cordillera, Colombia). *Quaternary Science Reviews*, **12**, 141-156.

Hopley, P.J., Marshall, J.D., Weedon, G.P., Latham, A.G., Herries, A.I.R. & Kuykendall, K.L. (2007). Orbital-forcing and the spread of C4 grasses in the late Neogene: stable isotope evidence from South African speleothems. *Journal of Human Evolution*, **53**, 620-634.

Hoyt, D.V. & Schatten, K.H. (1993). A discussion of plausible solar irradiance variations, 1700-

1992. *Journal of Geophysical Research*, **98**, 18895-18906.

Hu, F.S. & Shemesh, A. (2003). A biogenic-silica $\delta^{18}O$ record of climatic change during the last glacial–interglacial transition in southwestern Alaska. *Quaternary Research*, **59**, 379– 385.

Hughen, K., Eglinton, T.E., Xu, L. & Makou, M. (2004). Abrupt tropical vegetation response to rapid climate changes. *Science*, **304**, 1955-1959.

Hurd, D.C., Wenkam, C., Pankratz, H.S. & Fugate, J. (1979). Variable porosity in siliceous skeletons: Determination and importance. *Science*, **203**, 1340-1343.

Hutchinson, G.E. (1961). The pardox of the plankton. *American Naturalist*, **93**, 13-145.

IAEA (2000). Stable isotope processes in the water cycle. International Atomic Energy Agency, Vienna. www.iaea.or.at/programmes/ripc/ih/volumes/ vol_two/cht_ii_03.pdf

IAEA/WMO (2006). Global Network of Isotopes in Precipitation. The GNIP Database. Accessible at http://www.iaea.org/water

Imbrie, J., Hays, J.D., Martinson, D.G., McIntyre, A., Mix, A.C., Morley, J.J., Pisias, N.G., Prell, W.L. & Shackleton N.J. (1984). The orbital theory of Pleistocene climate: support from a revised chronology of the marine δ18O record. In: Berger A., Imbrie J., Hays J., Kugla G. & Satzmann, B. (Eds.), *Milankovitch and climate*. Reidel Publishing Company, Dordrecht, pp. 269–305.

Imbrie, J., Boyle, E., Clemens, S., Duffy, A., Howard, W., Kukla, G., Kutzbach, J., Martinson, D., McIntyre, A., Mix, A., Molfino, B., Morley, J., Peterson, L., Pisias, N., Prell, W., Raymo, M., Shackleton, N.J. & Toggweiler, J. (1992). On the structure and origin of major glaciation cycles. 1. Linear responses to Milankovitch forcing. *Paleoceanography*, **7**, 701-738.

Imbrie, J., Berger, A., Boyle, E.A., Clemens, S.C., Duffy, A., Howard, W., Kukla, G., Kutzbach, J., Martinson, D.G., McIntyre, A., Mix, A.C., Molfino, B., Morley, J.J., Peterson, L.C., Pisias, N.G., Prell, W.G., Raymo, M.E., Shackleton, N.J. & Toggweiler, J.R. (1993). On the structure and origin of major glaciation cycles. 2. The 100,000 year cycle. *Paleoceanography*, **8**, 699-735.

Jahn, B., Donner, B., Muller, P.J., Rohl, U., Schneider, R.R. & Wefer, G. (2003). Pleistocene variations in dust input and marine productivity in the northern Benguela current: evidence of evolution of global glacial-interglacial cycles. *Palaeogeography, Palaeoclimatology, Palaeoecology*, **193**, 515-533.

Jansen, J.H.F., Van der Gaast, S.J., Koster,B. & Vaars, A.J. (1998). CORTEX, a shipboard XRF-scanner for element analyses in split sediment cores. *Quaternary Research*, **151**, 143-153.

Jilbert, T., Reichart, G-J., Aeschlimann, B., Günther, D., Boer, W. & de Lange, G. (2010). Climate-controlled multidecadal variability in North African dust transport to the Mediterranean. *Geology*, **38**, 19-22.

Jochum, M., Fox-Kemper, B., Molnar, P.H. & Shields, C. (2009). Differences in the Indonesian seaway in a coupled climate model and their relevance to Pliocene climate and El Nino. *Paleoceanography*, **24**, PA1212, doi:10.1029/2008PA001678.

Johnson, T.C., Brown, E.T., McManus, J., Barry, S., Barker, P. & Gasse, F. (2002). A high-

resolution palaeoclimate record spanning the past 25,000 years in southern East Africa. *Science*, **296**, 113-132.

Johnson, T.C., Brown, E.T. & McManus, J. (2004). Diatom productivity in Northern Lake Malawi during the past 25,000 years: Implications for the position of the Intertropical Convergence Zone at millennial and shorter time scales. In: Battarbee, R.W., Gasse, F., Stickley, C. (Eds.), *Past Climate Variability through Europe and Africa*, Developments in Paleoenvironmental Research, Volume 6, Springer, Dordrecht, The Netherlands, pp. 93-116.

Johnson, T.C., Brown, E.T. & Shi, J. (2010). Biogenic silica deposition in Lake Malawi, East Africa over the past 150,000 years. *Palaeogeography, Palaeoclimatology, Palaeoecology*, doi:10.1016/j.palaeo.2010.01.024.

Jones, V.J., Leng, M.J., Solovieva, N., Sloane, H.J. & Tarasov, P. (2004). Holocene climate of the Kola Peninsula: evidence from the oxygen isotope record of diatom silica. *Quaternary Science Reviews*, **23**, 833-839.

Juillet, A. (1980a). *Analyse isotopique de la silice des diatomees lacustres et marines: fractionnement des isotopes de l'oxygene en fonction de la temperature*. The`se de troisie`me cycle, Universite´ Paris–Sud XI.

Juillet, A. (1980b). Structure de la silice bioge´nique: nouvelles donne´es apportees par l'analyse isotopique de l'oxyge`ne. *CR Academy of Science, Paris*, **290**, 1237– 1239.

Juillet-Leclerc, A. (1986). Cleaning process for diatomaceous samples. In: Ricard, M. (Ed.) *Proceedings of the 8th Diatom Symposium*. Koeltz Scientific Books, Koenigstein, pp. 733–736.

Juillet-Leclerc, A. & Labeyrie, L. (1987). Temperature dependence of the oxygen isotopic fractionation between diatom silica and water. *Earth and Planetary Science Letters*, **84**, 69-74.

Junginger, A., Olago, D.O. & Trauth, M.H. (2010). The palaeo-lake Suguta and its importance for understanding lake level fluctuations in the East African Rift System. *EOS Transactions AGU*, Fall Meeting Supplement 2010, abstract GC51C-0765.

Keigwin, L.D. (1982). Isotope paleoceanography of the Caribbean and east Pacific: role of Panama uplift in late Neogene time. *Science*, **217**, 350-353.

Kennett, J.P. & Hodell, D.A. (1993). Evidence for relative climate stability of Antarctica during the early Pliocene: a marine perspective. *Geografiska Annaler*, **75A**, 205– 220.

Kiage, L.M. & Liu, K-B. (2006). Late Quaternary palaeoenvironmental changes in East Africa: a review of multiproxy evidence from palynology, lake sediments and associated records. *Progress in Physical Geography*, **30**, 633-658.

Kilham, P. (1971). A hypothesis concerning silica and the freshwater planktonic diatoms. *Limnology & Oceanography*, **16**, 10-18.

Kilham, P. (1990). Ecology of Melosira species in the Great Lakes of Africa. In: Tilzer, M.M., Serruya, C. (Eds.), *Large Lakes: Ecological Structure and Function*. Springer-Verlag, Berlin, pp. 414-427.

Kilham, P., Kilham, S.S. & Hecky, R.E. (1986). Hypothesised resource relationships among

African planktonic diatoms. *Limnology & Oceanography*, **31**, 1169-1181.

Kim, S-T. & O'Neil, J.R. (1997). Equilibrium and nonequilibrium oxygen isotope effects in synthetic carbonates. *Geochimica et Cosmochimica Acta*, **61**, 3461-3475.

Kim, S.J. & Crowley, T.J. (2000). Increased Pliocene North Atlantic deep water: Cause or consequence of Pliocene warming? *Paleoceanography*, **15**, 451-455.

Kingston, J.D. (2007). Shifting adaptive landscapes: Progress and challenges in reconstructing early hominid environments. *American Journal of Physical Anthropology*, *Supplement: Yearbook of Physical Anthropology*, **134**, Issue Supplement 45, 20–58.

Kingston, J.D., Marino, B.D. & Hill, A. (1994). Isotopic evidence for Neogene hominid paleoenvironments in the Kenya Rift Valley. *Science*, **264**, 955-959.

Kingston, J.D., Jacobs, B.F., Hill, A. & Deino, A.L. (2002). Stratigraphy, age and environments of the late Miocene Mpesida Beds, Tugen Hills, Kenya. *Journal of Human Evolution*, **42**, 95-116.

Kingston, J.D., Deino, A.L., Edgar, R.K. & Hill, A. (2007). Astronomically forced climate change in the Kenyan Rift Valley 2.7-2.55 Ma: implications for the evolution of early hominin ecosystems. *Journal of Human Evolution*, **53**, 487-503.

Kleiven, H.F., Jansen, E., Fronval, T. & Smith, T.M. (2002). Intensification of Northern Hemisphere glaciations in the circum Atlantic region (3.5-2.4 Ma) – ice-rafted detritus evidence. *Palaeogeography, Palaeocliimatology, Palaeoecology*, **184**, 213-223.

Klocker, A., Prange, M. & Schulz, M. (2005). Testing the influence of the Central American Seaway on orbitally forced Northern Hemisphere glaciation. *Geophysical Research Letters*, **32**, L03703, doi:10.1029/2004/GL021564.

Kloosterboer-van Hoeve, M.L., Steenbrink, J., Visscher, H. & Brinkhuis, H. (2006). Millennial-scale climatic cycles in the Early Pliocene pollen record of Ptolemais, northern Greece. *Palaeogeography, Palaeoclimatology, Palaeoecology*, **229**, 321-334.

Knauth, L.P. (1973). *Oxygen and hydrogen isotope ratios in cherts and related rocks*. PhD thesis, California Institute of Technology.

Knies, J., Matthiessen, J., Vogt, C., Laberg, J. S., Hjelstuen, B.O., Smelror, M., Larsen, E., Andreassen, K., Eidvin, T. & Vorren, T.O. (2009). The Plio-Pleistocene glaciation of the Barents Sea-Svalbard region: a new model based on revised chronostratigraphy. *Quaternary Science Reviews*, **28**, 812-829.

Kolla, V., Kostecki, J. A., Robinson, F. & Biscaye, P. E. (1981). Distribution and origins of clay minerals and quartz in surface sediments of the Arabian Sea. *Journal of Sedimentary Petrology*, **61**, 563-569.

Krijgsman, W., Hilgen, F.J., Raffi, I., Sierro, F.J. & Wilson, D.S. (1999). Chronology, causes and progression of the Messinian salinity crisis. *Nature*, **400**, 652-655.

Krissek, L.A. & Clemens, S.C. (1992). Evidence for aridity-driven dust flux to the northwest Arabian Sea and for decoupling of the dust and upwelling systems. In: Summerhayes, C.P., Prell, W.L. & Emeis, K.C. (Eds.), *Upwelling Systems: Evolution Since the Early Miocene*. Geological Society Special Publication No **64**, pp. 359-378.

Kroon, D., Alexander, I., Little, M., Lourens, L.J., Matthewson, A., Robertson, A.H.F. & Sakamoto, T. (1998). Oxygen isotope and sapropel stratigraphy in the Eastern Mediterranean during the last 3.2 million years. In: Robertson, A.H.F., Emeis, K.-C., Richter, C., Camerlenghi, A. (Eds.), *Proceedings of the Ocean Drilling Program, Scientific Results*, **160**, Ocean Drilling Program, College Station, Texas, pp. 181-190.

Kroopnick, P.M. (1985). The distribution of ^{13}C of ΣCO_2 in the world oceans. *Deep-Sea Research*, **32**, 57-84.

Kutzbach, J.E. (1981). Monsoon climate of the early Holocene: climate experiment with the Earth's orbital parameters for 9000 years ago. *Science*, **214**, 59-61.

Kutzbach, J.E. & Otto-Bliesner, B.L. (1982). The sensitivity of the African-Asian monsoonal climate to orbital parameter changes for 9000 years BP in a low-resolution general circulation model. *Journal of the Atmospheric Sciences*, **39**, 1177-1188.

Kutzbach, J.E. & Street-Perrott, F.A. (1985). Milankovitch forcing of fluctuations in the level of tropical lakes from 18 to 0 kyr BP. *Nature*, **317**, 130-134.

Kutzbach, J.E. & Gallimore, R.G. (1989). Pangaean climates: megamonsoons of the megacontinent. *Journal of Geophysical Research*, **9**, 3341-3357.

Kutzbach, J.E., Gueter, P.J., Ruddiman, W.F. & Prell, W.L. (1989). Sensitivity of climate to late Cenozoic uplift in southern Asia and the American West: numerical experiments. *Journal of Geophysical Research*, **94**, 18393-18407.

Kutzback, J.E., Prell, W.L. & Ruddiman, W.F. (1993). Sensitivity of Eurasian Climate to Surface Uplift of the Tibetan Plateau. *The Journal of Geology*, **101**, 177-190.

Kutzbach, J.E., Liu, X.D., Liu Z.Y. & Chen, C. (2007). Simulation of the evolutionary response of global summer monsoons to orbital forcing over the past 280,000 years. *Climate Dynamics*, **30**, doi:10.1007/s00382-007-0308-z

Labeyrie, L.D. (1972). Composition isotopique de l'oxyge`ne de la silice bioge´nique. *CR Academy of Science, Paris*, **274**, 1605–1608.

Labeyrie, L.D. (1974). New approach to surface seawater palaeotemperatures using $^{18}O/^{16}O$ ratios in silica of diatom frustules. *Nature*, **248**, 40-42.

Labeyrie, L.D. (1979). *La composition isotopique de l'oxygene de la silice des valves de diatomees. Mise au point d'une nouvelle methode de palaeo-climatologie.* Diss. Universitie de Paris XI (in French).

Labeyrie, L.D. & Juillet, A. (1982). Oxygen isotopic exchangeability of diatom valve silica; interpretation and consequences for paleoclimatic studies. *Geochimica et Cosmochimica Acta*, **46**, 967–975.

Lamb, A.L., Leng, M.J., Lamb, H.F. & Umer, M. (2000). A 9000-year oxygen and carbon isotope record of hydrological change in a small Ethiopian crater lake. *The Holocene*, **10**, 167-177.

Lamb, A.L., Leng, M.J., Lamb, H.F., Telford, R.J. & Mohammed, M.U. (2004). Holocene

climate and vegetation change in the Main Ethiopian Rift Valley, inferred from the composition (C/N and $\delta^{13}C$) of lacustrine organic matter. *Quaternary Science Reviews*, **23**, 881-891.

Lamb, A.L., Leng, M.J., Sloane, H.J. & Telford, R.J. (2005). A comparison of the palaeoclimate signals from diatom oxygen isotope ratios and carbonate oxygen isotope ratios from a low latitude crater lake. *Palaeogeography, Palaeoclimatology, Palaeoecology*, **223**, 290-302.

Lamb, A.L., Brewer, T.S., Leng, M.J., Sloane, H.J. & Lamb, H.F. (2007). A geochemical method for removing the effect of tephra on lake diatom oxygen isotope records. *Journal of Paleolimnology*, **37**, 499-516.

Larrasoaña, J.C., Roberts, A.P., Rohling, E.J., Winklhofer, M. & Wehausen, R. (2003). Three million years of monsoon variability over the northern Sahara. *Climate Dynamics*, **21**, 689-698.

Laskar, J., Robutel, P., Joutel, F., Gastineau, M., Correia, A.C.M. & Levram, B. (2004). A long term numerical solution for the insolation quantities of the Earth. *Astronomy & Astrophysics*, **428**, 261-285.

Lawrence, K.T., Liu, Z. & Herbert, T.D. (2006). Evolution of the Eastern Tropical Pacific through Plio-Pleistocene Glaciation. *Science*, **312**, 79-83.

Leakey, M.G., Feibel, C.S., McDougall, I. & Walker, A. (1995). New four-million-year-old hominid species from Kanapoi and Allia Bay, Kenya. *Nature*, **376**, 565-571.

Leakey, M.G., Feibel, C.S., McDougall, I., Ward, C. & Walker, A. (1998). New specimens and confirmation of an early age for Australopithecus anamensis. *Nature*, **393**, 62-66.

Lear, C. H., Rosenthal, Y. & Wright, J.D. (2003). The closing of a seaway: ocean water masses and global climate change. *Earth and Planetary Science Letters*, **210**, 425-436.

Lee, C.M., Jones, B.H., Brink, K.H. & Fischer, A.S. (2000). The upper-ocean response to monsoonal forcing in the Arabian Sea: seasonal and spatial variability. *Deep-Sea Research II*, **47**, 1177-1226.

Lee-Thorpe, J., Sponheimer, M. & Luyt, J. (2007). Tracking changing environments using stable carbon isotopes in fossil tooth enamel: an example from the South African hominin sites. *Journal of Human Evolution*, **53**, 595-601.

Leg 117 Shipboard Scientific Party (1989). Background and summary of drilling results – Owen Ridge. In: Prell, W.L., Niitsuma, N. et al., *Proceedings of the Ocean Drilling Program, Initial. Reports.*, **117**: College Station, TX (Ocean Drilling Program), pp. 35-42. doi:10.2973/odp.proc.ir.117.105.1989.

Lehman, J.T., Muggide, R. & Lehman, D.A. (1998). Lake Victoria plankton ecology: mixing depth and climate-depth control of lake condition. In: Lehman, J.T. (Ed.), *Environmental Change and Reponse in East African Lakes*. Kluwer, Dordrecht, pp. 99-116.

Leng, M.J. (Ed.) (2005) *Isotopes in Palaeoenvironmental Research*, Springer, Dordrecht, The Netherlands, 307 pp.

Leng, M.J. & Marshall, J.D. (2004). Palaeoclimate interpretation of stable isotope data from lake sediment archives. *Quaternary Science Reviews*, **23**, 811-831.

Leng, M.J. & Barker, P.A. (2006). A review of the oxygen isotope composition of lacustrine diatom silica for palaeoclimate reconstruction. *Earth Science Reviews*, **75**, 5-27.

Leng, M.J. & Sloane, H.J. (2008). Combined oxygen and silicon isotope analysis of biogenic silica. *Journal of Quaternary Science*, **23**, 313-319.

Leng, M.J. & Swann, G.E.A. (2010). Stable isotopes from diatom silica. In: Smol, J.P. & Stoermer, E.F. (Eds.), *The Diatoms: applications for the environmental and Earth Sciences*. Cambridge University Press, pp. 575-589.

Leng, M.J., Barker, P., Greenwood, P., Roberts, N. & Reed, J.M. (2001). Oxygen isotope analysis of diatom silica and authigenic calcite from Lake Pinarbasi, Turkey. *Journal of Paleolimnology*, **25**, 343–349.

Leng, M.J., Lamb, A.L., Heaton, T.H.E., Marshall, J.D., Wolfe, B.B., Jones, M.D., Holmes, J.A. & Arrowsmith, C. (2005). Isotopes in Lake Sediments. In: M.J. Leng (Ed.) *Isotopes in Palaeoenvironmental Research*, Springer, Dordrecht, The Netherlands, 148-184 pp.

Lepre, C.J., Quinn, R.L., Joordens, J.C.A., Swisher, C.C. & Feibel, C.S. (2007). Plio-Pleistocene facies environments from the KBS member, Koobi Fora Formation: Implications for climate controls on the development of lake-margin hominin habitats in the northwest Turkana Basin (northwest Kenya). *Journal of Human Evolution*, **53**, 504-514.

Leroy, S.A.G. & Dupont, L.M. (1997). Marine palynology of the ODP Site 658 (NW Africa) and its contribution to the stratigraphy of Late Pliocene. *GEOBIOS*, **30**, 351-359.

Leuschner, D.C. & Sirocko, F. (2000). The low-latitude monsoon climate during Dansgaard-Oeschger cycles and Heinrich events. *Quaternary Science Reviews*, **19**, 243-254.

Leuschner, D.C., Sirocko, F., Schettler, G. & Garbe-Schönberg, D. (2004). Geochemical implications for changing dust supply by the Indian Monsoon system to the Arabian Sea during the last glacial cycle. In: W. Smykatz-Kloss & P. Felix-Henningsen (Eds.), *Paleoecology of Quaternary Drylands*. Springer, Berlin. pp. 119-135.

Leventhal, J.S. (2004). Isotopic chemistry of organic carbon in sediments from Leg 184. In: Prell, W.L., Wang, P., Blum, P., Rea, D.K. & Clemens, S.C. (Eds.), *Proceedings of the Ocean Drilling Program, Scientific Results*, **Vol 184**, pp.1-13.

Levin, N.E., Quade, J., Simpson, S.W., Semaw, S. & Rogers, M. (2004). Isotopic evidence for Plio-Pleistocene environmental change at Gona, Ethiopia. *Earth and Planetary Science Letters*, **219**, 93-110.

Levin, N. E., Zipser, E. J. & Cerling, T. E. (2009). Isotopic composition of waters from Ethiopia and Kenya: Insights into moisture sources for eastern Africa. *Journal of Geophysical Research*, **114**, D23306, doi:10.1029/2009JD012166.

Levin, N.E., Cerling, T.E., Brown, F.H., Quade, J., Harris, J.M. (2010). Isotopic ratios of rainfall in eastern Africa: insights into reconstructing past climate from terrestrial archives. *EOS Transactions AGU*, Fall Meeting Supplement 2010, abstract GC51C-0763.

Levitus, S. (1988). Ekman volume fluxes for the world ocean and individual ocean basins. *Journal of Physical Oceanography*, **18**, 271–279.

Lewin, J.C. (1961). The dissolution of silica from diatom walls. *Geochimica et*

CosmochimicaActa, **21**, 182–198.

Li, J., Yu, R. & Zhou, T. (2008). Teleconnection between NAO and climate downstream of the Tibetan Plateau. *Journal of Climate*, **21**, 4680-4690.

Lisiecki, L.E. & Raymo, M.E. (2005). A Pliocene-Pleistocene stack of 57 globally distributed benthic $\delta^{18}O$ records. *Paleoceanography*, **20**, PA1003, doi:10.1029/2004PA001071.

Lisiecki, L.E. & Raymo, M.E. (2005). A Pliocene-Pleistocene stack of 57 globally distributed benthic $\delta^{18}O$ records. *Paleoceanography*, **20**, PA1003, doi:10.1029/2004PA001071.

Lisiecki, L.E. & Raymo, M.E. (2007). Plio-Pleistocene Climate evolution: trends and transitions in glacial cycle dynamics. *Quaternary Science Reviews*, **26**, 56-69.

Liu, T., & Tang, W. (2005). Estimating moisture transport over oceans using space-based observations. *Journal of Geophysical Research*, **110**.

Liu, X., Liu, Z., Kutzbach, J.E., Clemens, S.C. & Prell, W.L. (2006). Hemispheric insolation forcing of the Indian Ocean and Asian monsoon: Local versus remote impacts. *Journal of Climate*, **19**, 6195-6208.

Lohmann, G.P. (2006). A model for variation in the chemistry of planktonic foraminifera due to secondary calcification and selective dissolution. *Paleoceanography*, **10**, 445-458.

Lomb, N. R. (1976). Least squares frequency analysis of unequally spaced data. *Astrophysics and Space Science*, **39**, 447–462, doi:10.1007/BF00648343.

Lourens, L., Hilgen, F., Shackleton, N.J., Laskar, J. & Wilson, D. (2004). The Neogene period. In: Gradstein, F., Ogg, J.G., Smith, G. (Eds.) *A Geologic Time Scale*. Cambridge University Press, Cambridge, pp. 409-440.

Lourens, L.J., Antonarakou, A., Hilgen, F., Van Hoof, A.A.M., Vergnaud-Grazzini, C. & Zachariasse, W.J. (1996). Evaluation of the Plio-Pleistocene astronomical timescale. *Paleoceanography*, **11**, 391-413.

Löwemark, L., Chen, H.-F., Yang, T.-N., Kylander, M., Yu, E.-F., Hsu, Y.-W., Lee, T.-Q., Song, S.-R. & Jarvis, S. (2010). Normalizing XRF-scanner data: A cautionary note on the interpretation of high-resolution records from organic-rich lakes. *Journal of Asian Earth Sciences*, **40**, 1250-1256. doi:10.1016/j.jseaes.2010.06.002.

Lücke, A., Moschen, R. & Schleser, G.H. (2005). High temperature carbon reduction of silica: a novel approach for oxygen isotope analysis of biogenic opal. *Geochimica et Cosmochimica Acta*, **69**, 1423–1433.

Lunt, D.J., Valdes, P.J., Haywood, A. & Rutt, I.C. (2008). Closure of the Panama Seaway during the Pliocene: implications for climate and Northern Hemisphere glaciation. *Climate Dynamics*, **30**, 1-18.

Mackay, A.W., Swann, G.E.A., Brewer, T.S., Leng, M.J., Morley, D.W., Piotrowska, N., Rioual, P. & White, D. (2011). A reassessment of late glacial-Holocene diatom oxygen isotope record from Lake Baikal using a geochemical mass-balance approach. *Journal of Quaternary Science*, **26**, 627-634.

Mackensen, A., Schumacher, S., Radke, J. & Schmidt, D.N. (2000). Microhabitat preferences

and stable carbon isotopes of endobenthic foraminifera: clue to quantitative reconstruction of oceanic new production?, *Marine Micropaleontolgy*, **40**, 233–258.

Madhupratap, M., Kumar, S.P., Bhattathiri, P.M.A., Kumar, M.D., Raghukumar, S., Nair, K.K.C. & Ramaiah, N. (1996). Mechanism of the biological response to the winter cooling in the northeastern Arabian Sea. *Nature*, **384**, 549–552.

Marlow, L.R., Lange, C.B., Wefer, G. & Rosell-Mele, A. (2000). Upwelling intensification as a part of the Pliocene-Pleistocene climate transition. *Science*, **290**, 2288-2291.

Marshall, L. G. (1988). Land mammals and the Great American Interchange. *American Science*, **76**, 380–388.

Martyn, J.E. (1969). *The geological history of the country between Lake Baringo and the Kerio River, Baringo District, Kenya*. Ph.D. Thesis, University of London.

Maslin, M.A. & Ridgwell, A.J. (2005). Mid-Pleistocene revolution and the 'eccentricity myth'. *Special Publication of the Geological Society of London*, **247**, 19-34.

Maslin, M.A. & Swann, G.E.A. (2005). Isotopes in marine sediments. In: Leng, M.J. (Ed.) *Isotopes in Palaeoenvironmental Research*. Springer, Dordrecht, The Netherlands, pp. 227-290.

Maslin, M.A. & Christensen, B. (2007). Tectonics, orbital forcing, global climate change, and human evolution in Africa: introduction to the African palaeoclimate special volume. *Journal of Human Evolution*, **53**, 443-464.

Maslin, M.A. & Trauth, M.H. (2009). Chapter 13: Plio-Pleistocene East African Pulsed Climate Variability and its influence on early human evolution In: F.E. Grine, R.E. Leakey, J.G. Fleagle (Eds.), *The First Humans - Origins of the Genus Homo*), pp.151- 158.

Maslin, M.A., Haug, G.H., Sarntheim, M., Tiedemann, R., Erlenkeuser, H. and Stax, R. (1995a). Northwest Pacific Site 882: the initiation of Northern Hemisphere Glaciation. In: Rea, D.K., Basov, I.A., Scholl, D.W. and Allan, J.F. (Eds.) *Proceedings of the Ocean Drilling Program, Scientific. Results*, **145**, pp. 315–329.

Maslin, M.A., Shackleton, N.J. & Pflaumann, U. (1995b). Temperature, salinity and density changes in the Northeast Atlantic during the last 45,000 years: Heinrich events, deep water formation and climatic rebounds. *Paleoceanography*, **10**, 527-544.

Maslin, M.A., Li, X.S., Loutre, M-F. & Berger, A. (1998). The contribution of orbital forcing to the progressive intensification of northern hemisphere glaciation. *Quaternary Science Reviews*, **17**, 411-426.

Maslin, M.A., Seidov, D. & Lowe, J.J. (2001). Synthesis of the nature and causes of rapid climate transitions during the Quaternary. In: Seidov, D., Haupt, B.J., Maslin, M.A. (Eds.), *The Oceans and Rapid Climate Change: Past, Present and Future*. Geophysical Monograph Series, Volume 126, AGU, Washington, D.C., pp. 9-52.

Maslin, M.A., Pancost, R.D., Wilson, K.E., Lewis, J. & Trauth, M.H. (submitted). Three and a half million year history of moisture availability of South West Africa. *Submitted to Palaeogeography, Palaeoclimatology, Palaeoecology*.

Matheney, R.K. & Knauth, L.P. (1989). Oxygen-isotope fractionation between marine biogenic

silica and seawater. *Geochimica et Cosmochimica Acta*, **53**, 3207-3214.

Matthews, D.H. (1966). The Owen fracture zone and the northern end of the Carlsberg Ridge. *Philosophical Transactions of the Royal Society of London, Series A*, **259**, 172-186.

McBrearty, S. (1999). The Archaeology of the Kapthurin Formation. In: Andrews, P. & Banham, P. (Eds.) *Late Cenozoic Environments and Hominid Evolution: a tribute to Bill Bishop*. Geological Society, London, pp. 143-156.

McBrearty, S. & Jablonski, N.G. (2005). First Fossil Chimpanzee. *Nature*, **431**, 105-108.

McBrearty, S., Bishop, L. C. & Kingston, J. D. (1996). Variability in traces of middle Pleistocene hominid behavior in the Kapthurin Formation, Baringo, Kenya. *Journal of Human Evolution*, **30**, 563–580.

McCall, G.J.H., Baker, B.H. & Walsh, J. (1967). Late Tertiary and Quaternary sediments of the Kenya Rift Valley. In: Bishop,W.W., Clark, J.D. (Eds.), *Background to Evolution in Africa*. Chicago University, Chicago, pp. 191-220.

McCrea, J.M. (1950). On the isotopic chemistry of carbonates and a palaeotemperature scale. *The Journal of Chemical Physics*, **18**, 849-857.

McDougall, I. & Wensink, H. (1966). Paleomagnetism and geochronology of the Pliocene-Pleistocene lavas in Iceland. *Earth and Planetary Science Letters*, **1**, 232-236.

McDougall, I. & Watkins, R.T. (1988). Potassium-argon ages of volcanic rocks from northeast of Lake Turkana, northern Kenya. *Geol. Mag*. **125**, 15-23.

McKenzie, J.A., Jenkyns, H.C. & Bennet, G.C. (1980). Stable isotope study of the cyclic diatomite-claystones from the Tripoli formation, Sicily: A prelude to the Messinian salinity crisis. *Palaeogeography, Palaeoclimatology, Palaeoecology*, **29**, 125-141.

Merlivat, L. & Jouzel, J. (1979). Global climatic interpretation of the deuterium-oxygen 18 relationship for precipitation. *Journal of Geophysical Research*, **84**, 5029-5033.

Meyers, P.A. & Arnaboldia, M. (2008). Paleoceanographic implications of nitrogen and organic carbon isotopic excursions in mid-Pleistocene Basins, Mediterranean Sea. *Palaeogeography, Palaeoclimatology, Palaeoecology*, **266**, 112.

Mikkelsen, N., Labeyrie, L. & Berger, W.H. (1978). Silica oxygen isotopes in diatoms: a 20,000 yr record in deep sea sediments. *Nature*, **271**, 536– 538.

Milankovitch, M.M. (1949). Kanon der Erdbestrahlung und seine Anwendung auf das Eiszeitenproblem. *Roy. Serbian Sci., Spec. Pub*. **132**, Section Mathematical Nat. Sci. 33, Belgrade, 633pp. (Canon of Insolation and the Ice Age Problem, English translation by Israel Program for Scientific Translation and published for the U.S. Department of Commerce and the National Science Foundation, Washington, D.C., 1969).

Mix, A.C. & Ruddiman, W.F. (1984) Oxygen-isotope analyses and Pleistocene ice volumes. *Quaternary Research*, **21**, 1-20.

Molnar, P. & England, P. (1990). Late cenozoic uplift of mountain ranges and global climate change: chicken or egg? *Nature*, **346**, 29-34.

Molnar, P. & Cane, M.A. (2002). El Nino's tropical climate and teleconnections as a blueprint for pre-Ice Age climates. *Paleoceanography*, **17**, 10.1029/2001PA000663.

Molnar, P., England, P. & Martinod, J. (1993). Mantle dynamics, uplift of the Tibetan plateau, and the Indian monsoon. *Rev. Geophys*. **31**, pp. 357–396.

Mopper K. & Garlick G.D. (1971). Oxygen isotope fractionation between biogenic silica and ocean water. *Geochimica et Cosmochimica Acta,* **35**, 1185–1187.

Mora, G. & Martinez, J.I. (2005). Sedimentary metal ratios in the Colombia basin as indicators for water balance changes in northern South America during the past 400,000 years. *Paleoceanography*, **20**, PA4013.

Morgan, M.E., Kingston, J.D. & Marino, B.D. (1994). Carbon isotopic evidence for the emergence of C4 plants in the Neogene from Pakistan and Kenya. *Nature*, **367**, 162-165.

Morley, C.K., Westcott, W.A., Stone, D.M., Harper, R.M., Wigger, S.T. & Karanja, F.M. (1992). Tectonic evolution of the northern Kenya Rift. *Journal of the Geological Society*, **149**, 333-348.

Morley, D.W., Leng, M.J., Mackay, A.W., Sloane, H.J., Rioual, P. & Batterbee, R.W. (2004). Cleaning of lake sediment samples for diatom oxygen isotope analysis. *Journal of Palaeolimnology*, **31**, 391–401.

Morley, D.W., Leng, M.J., Mackay, A.W. & Sloane, H.J. (2005). Late glacial and Holocene atmospheric circulation change in the Lake Baikal region documented by oxygen isotopes from diatom. *Global and Planetary Change*, **46**, 221– 233.

Moschen, R., Lücke, A. & Schleser, G.H. (2005). Sensitivity of biogenic silica oxygen isotopes to changes in surface water temperature and palaeoclimatology. *Geophysical Research Letters*, **32**, L07708, doi:10.1029/2004GL022167, 2005.

Moseley, H.G.J. (1914). The high-frequency spectra of the elements. II, *Philosophy Magazine*, **27**, 703-714.

Mudelsee, M. & Raymo, M.E. (2005). Slow dynamics of the Northern Hemisphere glaciation. *Paleoceanography*, **20**, PA4022, doi:10.1029/2005PA001153.

Mulitza, S., Durkoop, A., Hale. W., Wefer, G. & Niebler, H.S. (1997). Planktonic foraminifera as recorders of past surface water stratification. *Geology*, **25**, 335-338.

Mulitza, S., Prange, M., Stuut, J-B., Zabel, M., von Dobeneck, T., Itambi, A.C., Nizou, J., Schulz, M. & Wefer, G. (2008). Sahel megadroughts triggered by glacial slowdowns of Atlantic meridional overturning. *Paleoceanography*, **23**, PA4206, doi:10.1029/2008PA00163.

Muller, R.A. & MacDonald, G.J. (1997). Glacial cycles and astronomical forcing. *Science*, **277**, 215-218.

Muller, R.A. & MacDonald, G.J. (2000). *Ice ages and astronomical causes: Data, spectral analysis, and mechanisms*. Springer Praxis, Berlin. 318pp.

Munsterman, D. & Kerstholt, S. (1996). Sodium polytungstate, a new non-toxic alternative to bromoform in heavy liquid separation. *Review of Palaeobotany and Palynology*, **91**, 417–422.

Murdock, T.Q., Weaver, A.J. & Fanning, A.F. (1997). Paleoclimatic response of the closing of

the Isthmus of Panama in a coupled ocean-atmosphere model. *Geophysical Research Letters*, **24**, 253-256.

Murray, D.W. & Prell, W.L. (1991). Pliocene to Pleistocene variations in calcium carbonate, organic carbon and opal on the Owen Ridge, Northern Arabian Sea. *Proceedings of the Ocean Drilling Program, Scientific Results*, **117**, 343-363.

Murray, D.W. & Prell, W.L. (1992). Late Pliocene and Pleistocene climatic oscillations and monsoon upwelling recorded in sediments from the Owen Ridge, northwestern Arabian Sea. In: Summerhayes, C.P., Prell, W.L. & Emeis, K.C. (Eds.), Upwelling Systems: Evolution Since the Early Miocene.Geological Society Special Publication No 64, pp. 301-321.

Murray, R.W. & Leinen, M. (1993). Chemical transport to the seafloor of the equatorial Pacific Ocean across a latitudinal transect at 135°: Tracking sedimentary, major, trace and rare earth element fluxes at the Equator and the Intertropical Convergence zone. *Geochimica et Cosmochimica Acta*, **57**, 4141-4163.

Nair, T.M.B. (2006). Monsoon control on trace metal fluxes in the deep Arabian Sea. *Journal of Earth System Science*, **115**, 461-472.

Nair, R.R., Ittekot, V., Manganini, S.J., Ramaswamy, V., Haake, B., Degens, E.T., Desai, B.N. & Honjo, S. (1989). Increased particle flux to the deep ocean related to monsoons. *Nature*, **338**, 749-751.

Namwamba, F. L. (1993). *Tephrostratigraphy of the Chemeron Formation, Baringo Basin, Kenya*. M.Sc. Dissertation, University of Utah.

Nicholson, S.E. (1986). The spatial coherence of African rainfall anomalies: Interhemispheric teleconnections. *Journal of Climate and Applied Meteorology*, **25**, 1365-1381.

Nicholson, S.E. (1993). An overview of African rainfall fluctuations of the last decade. *Journal of Climatology*, **6**, 1463-1466.

Nicholson, S.E. (1996). A review of climate dynamics and climate variability in eastern Africa. In: Johnson, T.C. & Odada, E.O. (Eds.), *The Limnology, Climatology and Paleoclimatology of the East African Lakes*. Gordon and Breach, Amsterdam, pp. 25-56.

Nicholson, S.E. (2000). The nature of rainfall variability over Africa on time scales of decades to millenia. *Global and Planetary Change*, **26**, 137-158.

Nicholson, S.E. (2001). Climatic and environmental change in Africa during the last two centuries. *Climate Research*, **17**, 123-144.

Nicholson, S.E. & Flohn, H. (1980). African evironmental and climatic changes and the general atmospheric circulation in the late Pleistocene and the Holocene. *Climatic Change*, **2**, 313-348.

Nicholson, S.E. & Kim, J. (1997). The relationship of El Nino-Southern Oscillation to African rainfall. *International Journal of Climatology*, **17**, 117-135.

Nicholson, S.E. & Selato, J.C. (2000). The influence of La Nina on African rainfall. *International Journal of Climatology*, **20**, 1761-1776.

Niebler, H-S., Hubberten, H-W. & Gersonde, R. (1999). Oxygen isotope values of planktonic

foraminifera: a tool for the reconstruction of surface water stratification. In: G. Fischer & G.Wefer (Eds.) *Use of proxies in Paleoceanography*, Springer-Verlag, Berlin, 165-189 pp.

Niedermeyer, E.M., Schefuβ, E., Sessions, A.L., Mulitza, S., Mollenhauer, G., Schulz, M. & Wefer, G. (2010). Orbital- and millennial-scale changes in the hydrologic cycle and vegetation in the western African Sahel: Insights from individual plant wax δD and $\delta^{13}C$. *Quaternary Science Reviews*, **29**, 2996-3005.

Niemitz, M.D. & Billups, K. (2005). Millennial-scale variability in western tropical Atlantic surface ocean hydrography during the early Pliocene. *Marine Micropaleontology*, **54**, 155-166.

O'Brien, N.R., Meyer, H.W., Reilly, K., Ross, A.M. & Maguire, S. (2002). Microbial taphonomic processes in the fossilization of insects and plants in the late Eocene Florissant Formation, Colorado. *Rocky Mountain Geology*, **37**, 1-11.

O'Neil, J., Clayton, R. & Mayeda, T. (1969). Oxygen isotope fractionation in divalent metal carbonates. *Journal of Chemical Physics*, **51**, 5547-5558.

Obasi, G.O.P. (2005). The impacts of ENSO in Africa. In: Low, P.S. (Ed.). *Climate Change and Africa*. Cambridge University Press, Cambridge, pp. 218-230.

Odada, E.O., Olago, D.O., Bugenyi, F., Kulindwa, K., Karimumuryango, J., West, K., Ntiba, M., Wandiga, S., Aloo-Obudho, P. & Achola, P. (2003). Environmental Assessment of the East African Rift Valley Lakes. *Aquatic Science*, **65**, 254-271.

Odada, E.O., Onyando, J.O. & Obudho, P.A. (2006). Lake Baringo: Addressing threatened biodiversity and livelihoods. *Lakes and Reservoirs: Research and Management*, **11**, 287-299.

Olaka, L.A., Odada, E.O., Trauth, M.H. & Olago, D.O. (2010). The sensitivity of East African rift lakes to climate fluctuations. *Journal of Paleolimnology*, **44**, 629-644.

Opsahl, S.P. & Zepp, R.G. (2001). Photochemically induced alteration of stable carbon isotope ratios in terrigenous dissolved organic carbon. *Geophysical Research Letters*, **28**, 2417-2420.

Ortiz, J.D., Wheeler, P.A., Mix, A.C. & Key, R.M. (2000). Anthropogenic CO_2 invasion into the northeast Pacific based on concurrent ^{13}CDIC and nutrient profiles from the California Current. *Global Biogeochemical Cycles*, **14**, 917-929.

Overpeck, J.T., Anderson, D.M., Trumbore, S. & Prell, W.L. (1996). The southwest Indian monsoon over the last 18,000 years. *Climate Dynamics*, **12**, 213-225.

Owen, R.B. (2002). Sedimentological characteristics and origins of diatomaceous deposits the East African Rift System. *SEPM Special Publication*, **73**, 233-246.

Owen, R.B., Barthelme, J.W., Renaut, R.W. & Vincens, A. (1982). Paleolimnology and archaeology of Holocene deposits north-east of Lake Turkana, Kenya. *Nature*, **298**, 523-529.

Pagani, M., Freeman, K.H. & Arthur, M.A. (1999). Late Miocene atmospheric CO_2 concentrations and the expansion of C4 grasses. *Science*, **285**, 876-879.

Paillard, D. & Labeyrie, L. (1994). Role of the thermohaline circulation in the abrupt warming after Heinrich events. *Nature*, **372**, 162-164.

Park, S.C., Sohn, B.J. & Wang, B. (2007). Satellite assessment of divergent water vapour transport from NCEP, ERA40, and JRA25 reanalyses over the Asian summer monsoon region. *Journal of the Meteorological Society of Japan*, **85**, 615-632.

Parrish, J.T. (1993). Climate of the supercontinent Pangaea. *Journal of Geology*, **101**, 213-233.

Pease, P.P., Tchakerian, V.P. & Tindale, N.W. (1998). Aerosols over the Arabian Sea: geochemistry and source areas for aeolian desert dust. *Journal of Arid Environments*, **39**, 477-496.

Peixoto, J.P. & Oort, A.H. (1983). The atmospheric branch of the hydrological cycle and climate. In: E. Street-Perrot et al. (Eds.) *Variations in the Global Water Budget*, D. Reidel, pp. 5-65.

Petit, J.R., Mounier, L., Jouzel, J., Korotkevich, Y.S., Kotlyakov, V.I. & Lorius, C. (1990). Paleoclimatological and chronological implications of the Vostok core dust record. *Nature*, **343**, 56–58.

Petit, J.R., Jouzel, J., Raynaud, D., Barkov, N.I., Barnola, J.M., Basile, I., Bender, M., Chappellaz, J., Davis, M., Delaygue, G., Delmotte, M., Kotlyakov, V.M., Legrand, M., Lipenkov, V.Y., Lorius, C., Pepin, L., Ritz, C., Saltzman, E. & Stievenard, M. (1999). Climate and atmospheric history of the past 420,000 years from the Vostok ice core, Antarctica. *Nature*, **399**, 429–436.

Phedorin, M.A. & Goldberg, E.L. (2008). Early response of continental Asia to Pleistocene climate cycles (*retuned orbital chronologies for Baikal, marine, and ice core records). Russian Geology and Geophysics*, **49**, 40-45.

Philander, S.G.H. & Fedorov, A.V. (2003). Role of tropics in changing the response to Milankovitch forcing some three million years ago. *Paleoceanography*, **18**, 1045.

Philander, S.G.H., Gu, D., Halpern, D., Lambert, G., Lau, N-C., Li, T. & Pacanowski, R.C. (1996). Why the ITCZ is mostly north of the equator. *Journal of Climate*, **9**, 2958-2972.

Pokras, E.M. & Mix, A.C. (1987). Earth's precession cycle and Quaternary climate change in tropical Africa. *Nature*, **326**, 486-487.

Polissar, P.J., Abbott, M.B., Shemesh, A., Wolfe, A.P. & Bradley, R.S. (2006). Holocene hydrologic balance of tropical South America from oxygen isotopes of lake sediment opal, Venezuelan Andes. *Earth and Planetary Science Letters*, **242**, 375-389.

Porter, S.C. & An, Z. (1995). Correlation between climate events in the North Atlantic and China during the last glaciation. *Nature*, **375**, 305-308.

Potts, R. (1996). Evolution and climate variability. *Science*, **273**, 922–923.

Potts, R. (1998a). Environmental hypotheses of human evolution. *Yearbook of Physical Anthropology*, **41**, 93-136.

Potts, R. (1998b). Variability selection in hominid evolution. *Evolutionary Anthropology*, **7**, 81–96.

Prange, M. & Schulz, M. (2004). A coastal upwelling seesaw in the Atlantic Ocean as a result of the closure of the Central American Seaway. *Geophysical Research Letters*, **31**, L17207.

Prell, W.L. & Van Campo, W. (1986). Coherent response of Arabian Sea upwelling and pollen transport to the late Quaternary monsoonal winds. *Nature*, **323**,

Prell, W.L. & Kutzbach, J.E. (1987). Monsoon variability over the past 150,000 years. *Journal of Geophysical Research*, **92**, 8411-8425.

Prell, W.L. & Kutzbach, J.E. (1992). Sensitivity of the Indian Ocean Monsoon to forcing parameters and implications for its evolution. *Nature*, **360**, 447-652.

Preusser, F., Radies, D. & Matter, A. (2002). A 160,000-Year record of dune development and atmospheric circulation in Southern Arabia. *Science*, **296**, 2018-2020.

Prins, M.A., Postma, G. & Weltje, G.J. (2000). Controls on terrigenous sediment supply to the Arabian Sea during the late Quaternary: the Makran continental slope. *Marine Geology*, **169**, 351-371.

Prospero, J.M., Ginoux, P., Torres, O., Nicholson, S.E. & Gill, T.E. (2002). Environmental characterization of global sources of atmospheric soil dust identified with the Nimbus-7 Total Ozone Mapping Spectrometer (TOMS) absorbing aerosol product. *Reviews of Geophysics*, **40**, 1002. doi:10.1029/2000RG000092.

Pälike, H., Shackleton, N.J. & Röhl, U. (2001). Astronomical forcing on late Eocene marine sediments. *Earth and Planetary Science Letters*, **193**, 589-602.

Qiang, X.K., Li, Z.X., Powell, C.McA. & Zheng, H.B. (2001). Magnetostratigraphic record of the Late Miocene onset of East Asian monsoon, and Pliocene uplift of northern Tibet. *Earth and Planetary Science Letters*, **187**, 83-93.

Quade, J. & Cerling, T.E. (1995). Expansion of C4 grasses in the late Miocene of Northern Pakistan: evidence from stable isotopes in palaeosols. *Palaeogeography, Palaeoclimatology, Palaeoecology*, **115**, 91-116.

Quay, P., Sonnerup, R., Westby, T., Stutsman, J. & McNichol, A. (2003). Changes in the $^{13}C/^{12}C$ of dissolved inorganic carbon in the ocean as a tracer of anthropogenic CO2 uptake. *Global Biogeochemical Cycles*, **17**, 1004, doi:10.1029/2001GB001817.

Raubitschek, S., Lücke, A. & Schleser, G.H. (1999). Sedimentation patterns of diatoms in Lake Holzmaar – on the transfer of climate signals to biogenic silica oxygen isotope proxies. *Journal of Paleolimnology*, **21**, 437-448.

Ravelo, A.C. & Fairbanks, R.G. (1995). Carbon isotopic fractionation in multiple species of planktonic-foraminifera from core-tops in the tropical Atlantic. *Journal of Foraminiferal Research*, **25**, 53-74.

Ravelo, A.C. & Andreasen, D.H. (2000). Enhanced circulation during a warm period. *Geophysical Research Letters*, **27**, 1001-1004.

Ravelo, A.C. & Wara, M.W. (2004). The role of the tropical oceans on global climate during a warm period and a major climate transition. *Oceanography*, **17**, 22-31.

Ravelo, A.C. & Hillaire-Marcel, C. (2007). The use of oxygen and carbon isotopes of foraminifera in Paleoceanography. In: C. Hillaire-Marcel & De Vernal, A. (Eds.). *Proxies in Late Cenozoic Paleoceanography*. Elsevier, Amsterdam, pp. 735-764.

Ravelo, A.C., Andreasen, D.H., Lyle, M., Lyle, A.O. & Wara, M.W. (2004). Regional climate shifts caused by gradual global cooling in the Pliocene epoch. *Nature*, **429**, 263-267.

Ravelo, A.C., Dekens, P.S. & McCarthy, M. (2006). Evidence for El Niño-like conditions during

the Pliocene. *GSA Today*, **16(3)**, doi: 10.1130/1052-5173(2006)016<4:EFENLC >2.0.CO;2.

Raymo, M.E. (1994). The Initiation of Northern Hemisphere Glaciation. *Annual Review of Earth & Planetary Sciences*, **22**, 353-383.

Raymo, M.E. (1998). Glacial Puzzles. *Science*, **281**, 1467-1468.

Raymo, M.E. and Ruddiman, W.F., (1992). Tectonic forcing of late Cenozoic climate. *Nature*, **359**, 117–122.

Raymo, M.E. & Nisancioglu, K. (2003). The 41 kyr world: Milankovitch's other unsolved mystery. *Paleoceanography*, **18**, doi:10.1029/2002PA000791.

Raymo, M.E., Ruddiman, W.F. & Froelich, P.N. (1988). Influence of late Cenozoic mountain building on ocean geochemical cycles. *Geology*, **16**, 649-653.

Raymo, M.E., Grant, B., Horowitz, M. & Rau, G.H. (1996). Mid-Pliocene warmth: stronger greenhouse and stronger conveyor. *Marine Micropalaeontology*, **27**, 313-326.

Raymo, M.E., Oppo, D.W. & Curry, W. (1997). The mid-Pleistocene climate transition: A deep sea carbon isotopic perspective. *Paleoceanography*, **12**, 546-559.

Raymo, M.E., Lisiecki, L.E. & Nisancioglu, K.H. (2006). Plio-Pleistocene Ice Volume, Antarctic Climate and the Global $\delta^{18}O$ Record. *Science*, **313**, 492-495.

Rea, D.K. (1994). The Paleoclimatic record provided by eolian deposition in the deep sea: The geologic history of wind. *Review of Geophysics*, **32**, 159-195.

Reading, H.G. (1986). African Rift Tectonics and Sedimentation, an introduction. In: L.E. Frostick et al. (Eds.) *Sedimentation in the African Rifts*, Geological Society Special Publication No. **25**, pp.- 3-7.

Reed, K.E. (1997). Early hominid evolution and ecological change through the African Plio-Pleistocene. *Journal of Human Evolution*, **32**, 289-322.

Reichart, G.-J., den Dulk, M., Visser, H. J., van der Weijden, C.H. & Zachariasse, W. J. (1997). A 225 kyr record of dust supply, paleoproductivity and the oxygen minimum zone from the Murray Ridge (northern Arabian Sea). *Palaeogeography, Palaeoclimatology, Palaeoecology*, **134**, 149–169.

Reichart, G.J., Lourens, L.J. & Zachariasse, W.J. (1998). Temporal variability in the northern Arabian Sea Oxygen Minimum Zone (OMZ) during the last 225,000 years. *Paleoceanography*, **13**, 607-621.

Renaut, R.W. & Owen, R.B. (1980). Late Quaternary fluvio-lacustrine sedimentation and lake levels in the Baringo basin, northern Kenya, Rift Valley. *Recherches Géologiques en Afrique*, **5**, 130–133.

Renaut, R.W., Ego, J., Tiercelin, J.-J., Le Turdu, C. & Owen, R.B. (1999). Saline, alkaline palaeolakes of the Tugen Hills–Kerio Valley region, Kenya Rift Valley. In: Andrews, P., Banham, P. (Eds.), *Late Cenozoic Environments and Hominid Evolution: A Tribute to Bill Bishop*. Geological Society Publishing House, Bath, 41–58.

Renaut, R.W., Tiercelin, J.-J. & Owen, R.B. (2000). Lake Baringo, Kenya Rift Valley, and its

Pleistocene Precursors. In: Gierlowski-Kordesch, E.H., Kelts, K.R. (Eds.), *Lake Basins through Space and Time*. AAPG Studies in Geology Series, no. 46. American Association of Petroleum Geologists, Tulsa, 561–568.

Revel, M., Sinko, J.A., Grousset, F.E. & Biscaye, P.E. (1996). Sr and Nd isotopes as tracers of North Atlantic lithic particles: Paleoclimatic implications. *Paleoceanography*, **11**, 95-113.

Richter, T.O., Van der Gaast, S.J., Koster, B., Vaars, A., Gieles, R., De Stigter, H.C., De Haas, H. & Van Weering, T.C.E. (2006). The Avaatech XRF Core Scanner: technical description and applications to NE Atlantic sediments. In: R.G. Rothwell (Ed.) *New Techniques in Sediment Core Analysis*. Geological Society, London, 39-50.

Rickaby, R.E.M., Elderfield, H., Roberts, N., Hendry, K.H., Hillenbrand, C-D. & Mackensen, A. (2008). A more alkaline Glacial Southern Ocean? Evidence from an 800 kyr record of foraminiferal trace metals in the Weddell Sea. *Geophysical Research Abstracts*, **vol. 10**, EGU2008-A-11673.

Rietti-Shatti, M., Shemesh, A. & Karlen, W. (1998). A 3000-year climate record from biogenic silica oxygen isotopes in an equatorial high-altitude lake. *Science*, **281**, 980-982.

Rings, A., Lücke, A. & Schleser, G.H. (2004). A new method for the quantitative separation of diatom frustules from lake sediments. *Limnology and Oceanography: Methods*, **2**, 25– 34.

Rioual, P., Andrieu-Ponel, V., Rietti-Shatti, M., Battarbee, R.W., de Beaulieu, J-L., Checkladi, R., Reille, M., Svobodova, H. & Shemesh, A. (2001). High-resolution record of climate stability in France during the last Interglacial period. *Nature*, **413**, 293-296.

Robinson, J.T. (1954). Prehominid dentition and hominid evolution. *Evolution*, **8**, 324–334.

Rohling, E.J. (2000). Paleosalinity: confidence limits and future applications. *Marine Geology*, **163**, 1-11.

Rohling, E.J. (2007). Oxygen isotope composition of seawater. In: Elias, S.A. (Ed.) *Encyclopedia of Quaternary Science* (vol. 3), Elsevier, pp. 1748-1756.

Rohling, E.J. & Hilgen, F.J. (1991). The eastern Mediterranean climate at times of sapropel formation: a review. *Geologie en Mijnbouw*, **70**, 253-264.

Rohling, E.J. & Bigg, G.R. (1998). Paleosalinity and $\delta^{18}O$: a critical assessment. *Journal of Geophysical Research*, **103**, 1307-1318.

Rohling, E.J. & Cooke, S. (2003). Stable oxygen and carbon isotopes in foraminiferal carbonate shells. *Modern Foraminifera*, 2003, part III, pp. 239-258, doi:10.1007/0-306-48104-9_14.

Rohling, E.J., Cane, T.R., Cooke, S., Sprovieri, M., Bouloubassi, I., Emeis, K.-C., Schiebel, R., Kroon, D., Jorissen, F.J., Lorre, A. & Kemp, A.E.S. (2002). African monsoon variability during the previous interglacial maximum. *Earth and Planetary Science Letters*, **202**, 61-75.

Rosqvist, G.C., Jonsson, C., Yam, R., Karlen, W. & Shemesh, A. (2004). Diatom oxygen isotopes in pro-glacial lake sediments from northern Sweden: a 5000 year record of atmospheric circulation. *Quaternary Science Reviews*, **23**, 851-859.

Rossignol-Stick, M. (1983). Africa monsoon, an immediate isotope response to orbital insolation. *Nature*, **303**, 46-49.

Round, F.E., Crawford, R.M. & Mann, D.G. (1990). The Diatoms: Biology and Morphology of

the Genera. Cambridge University Press, Cambridge, 747 pp.

Rozanski, K., Araguas-Araguas, L. & Gonfiantini, R. (1993). Isotopic patterns in modern global precipitation. In: P.K. Swart, K.C. Lohmann, J. McKenzie & S. Savin (Eds.) *Climate Change in Continental Isotopic Records*. Geophysical Monograph No. 78, American Geophysical Union, Washington DC, pp. 1-36.

Ruddiman, W.F. (2006). What is the timing of orbital-scale monsoon changes? *Quaternary Science Reviews*, **25**, 657-658.

Ruddiman, W.F. & McIntyre, A. (1981). Oceanic mechanisms for amplification of the 23,000-year ice volume cycle. *Science*, **212**, 617-627.

Ruddiman, W.F. & Janecek, T. (1989). Pliocene-Pleistocene biogenic and terrigenous fluxes at equatorial Atlantic Sites 662, 663, and 664. In: W.F. Ruddiman, M. Sarnthein et al. (Eds.), *Proceedings of the Ocean Drilling Program, Scientific Results*, **108**, 211-240.

Ruddiman, W.F. & Kutzbach, J.E. (1989). Forcing of late Cenozoic Northern Hemisphere climate by plateau uplift in Southern Asia and the American West. *Journal of Geophysical Research*, **94**, 18409-18427.

Ruddiman, W.F. & Kutzbach, J.E. (1990). Late Cenozoic plateau uplift and climate change. *Transactions of the Royal Society of Edinburgh: Earth Sciences*, **81**, 301-314.

Ruddiman, W.F. & Raymo, M.E. (2003). A methane-based time scale for Vostok ice: climatic implications. *Quaternary Science Reviews*, **21**, 141-155.

Ruddiman, W. F., Raymo, M.E., Lamb, H.H. & Andrews, J.T. (1988). Northern hemisphere climate regimes during the past 3Ma: Possible tectonic connections. *Philosophical Transactions of the Royal Society of London (Series B)*, **318**, 411-430.

Ruggieri, E., Herbert, T., Lawrence, K.T. & Lawrence, C.E. (2009). Change point method for detecting regime shifts in palaeoclimatic time series: Application to d-18O time series of the Plio-Pleistocene. *Paleoceanography*, **24**, PA1204, doi:10.1029/2007PA001568, 2009.

Ruhlemann, C., Mulitza, S., Muller, P.J., Wefer, G. & Zahn, R. (1999). Tropical Atlantic warming during conveyor shut down. *Nature*, **402**, 511-514.

Russell, J.M. & Johnson, T.C. (2005). Late Holocene climate change in the North Atlantic and equatorial Africa: Millennial-scale ITCZ migration. *Geophysical Research Letters*, **32**, L17705, doi:10.1029/2005GL023295.

Saji, N.H. & Yamagata, T. (2003). Possible impacts of Indian Ocean Dipole mode events on global climate. *Climate Research*, **25**, 151-169.

Saji, N.H., Goswami, B.N., Vinayachandran, P.N. & Yamagata, T. (1999). A dipole mode in the tropical Indian Ocean. *Nature*, **401**, 360-363.

Sakai, K. & Peltier, W.R. (1997). Dansgaard-Oeschger oscillations in a coupled atmospheric ocean climate model. *Journal of Climatology*, **10**, 949-970.

Saltzman, B. & Verbitsky, M.Y. (1993). Multiple instabilities and modes of glacial rhythmicity in the Plio-Pleistocene: a general theory of late Cenozoic climate change. *Climate Dynamics*, **9**, 1-15.

Sarnthein, M.K., Winn, K., Duplessy, J-C. & Fontugne, M.R. (1988). Global variations of

surface ocean productivity in low and mid-latitudes: Influence on CO_2. *Paleoceanography*, **3**, 361-399.

Sarnthein, M., Winn, K., Jung, S.J.A., Duplessy, J-C., Labeyrie, L., Erlenkreuser, H. & Ganssen, G.M. (1994). Changes in East Atlantic deepwater circulation over the last 30,000 years: eight time slice reconstructions. *Paleoceanography*, **10**, 1063-1094.

Sarnthein, M., van Kreveld, S., Erlenkeuser, H., Grootes, P.M., Kucera, M., Pflaumann, U. & Schulz, M. (2003). Centennial-to-millennial scale periodicities of Holocene climate and sediment injections off the western Barents shelf, 75_N, *Boreas*, **32**, 447– 461.

Scargle, J. D. (1982). Studies in astronomical time-series analysis 2. Statistical aspects of spectral analysis of unevenly spaced data. *Journal of Astrophysics*, **263**, 835–853, doi:10.1086/160554.

Schefuss, E., Schouten, S., Jansen, J.H.F. & Sinnighe Damste, J.S. (2003). African vegetation controlled by tropical sea surface temperatures in the mid-Pleistocene period. *Nature*, **422**, 418-421.

Schefuβ, E., Schouten, S. & Schneider, R.R. (2005). Central African hydrologic changes during the past 20,000 years. *Nature*, **437**, 1003-1006.

Schiff, C.J., Kauffman, D.S., Wolfe, A.P., Dodd, J. & Sharp, Z. (2009). Late Holocene storm-trajectory changes inferred from the oxygen isotope composition of lake diatoms, south Alaska. *Journal of Paleolimnology*, **41**, 189-208.

Schleser, G.H., Lücke, A., Moschen, R. & Rings, A. (2001). Separation of diatoms from sediment and oxygen isotope extraction from their siliceous valves — a new approach. *Terra Nostra, 2001/3. Schriften der Alfred-Wegener-Stiftung* (6th Workshop of the European Lake Drilling Programme, Potsdam.), pp. 187– 191.

Schlitzer, R. (2010). Ocean Data View, http://odv.awi.de, 2010.

Schmidt, M., Botz, R., Stoffers, P., Anders, T. & Bohrmann, G. (1997). Oxygen isotopes in marine diatoms: A comparative study of analytical techniques and new results on the isotope composition of recent marine diatoms. *Geochimica et Cosmochimica Acta*, **61**, 2275-2280.

Schmidt, M., Botz, R., Rickert, D., Bohrmann, G., Hall, S.R. & Mann, S. (2001). Oxygen isotopes of marine diatoms and relations to opal-A maturation. *Geochimica et Cosmochimica Acta*, **65**, 201-211.

Schmidt, M.W., Spero, H.J. & Lea, D.W. (2004). Links between salinity variation in the Caribbean and North Atlantic thermohaline circulation. *Nature*, **428**, 160-163.

Schmittner, A., Sarnthein, M., Kinkel, H., Bartoli, G., Bickert, T., Crucifix, M., Crudeli, D., Groeneveld, J., Kosters, F., Mikolajewicz, U., Millo, C., Reijmer, J., Schafer, P., Schmidt, D., h, S., Tiedemann, R., Weinelt, M. & Zuvela, M. (2004). Global Impact of the Panamanian Seaway Closure. *EOS*, **85**, p.526.

Schmitz, B (1987). The TiO2/Al2O3 ratio in the Cenozoic Bengal abyssal fan sediments and its use as a palaeostream energy indicator. *Marine Geology*, **76**, 195-206.

Schneider, B. & Schmittner, A. (2006). Simulating the impact of the Panamanian seaway closure

on ocean circulation, marine productivity and nutrient cycling. *Earth and Planetary Science Letters*, **246**, 367-380.

Schneider, R., Muller, P.J. & Wefer, G. (1994). Late Quaternary paleoproductivity changes off the Congo deduced from stable isotopes of planktonic foraminifera. *Palaeogeography, Palaeoclimatology, Palaeoecology*, **110**, 255-274.

Scholtz, C.A., Johnson, T.C., Cohen, A.S., King, J.W., Peck, J.A., Overpeck, J.T., Talbot, M.R., Brown, E.T., Kalindekafe, L., Amoako, P.Y.O., Lyons, R.P., Shanahan, T.M., Castañeda, I.S., Heil, C.W., Forman, S.L., McHargue, L.R., Beuning, K.R., Gomez, J. & Pierson, J. (2007). East African megadroughts between 135 and 75 thousand years ago and bearing on early-modern human origins. *Proceedings of the National Academy of Sciences of the United States of America*, **104**, 16416-16421.

Scholz, C.A., Cohen, A.S., Johnson, T.C., King, J., Talbot, M.R. & Brown, E.T. (2011). Scientific drilling in the Great Rift Valley: The 2005 Lake Malawi Scientific Drilling Project – An overview of the past 145,000 years of climate variability in Southern Hemisphere East Africa. *Palaeogeography, Palaeoclimatology, Palaeoecology*, 303, 3-19, doi:10.1016/j.palaeo.2010.10.030.

Schott, F., & Fischer, J. (2000). Winter monsoon circulation of the northern Arabian Sea and Somali Current. *Journal of Geophysical Research*, **105**, 6359–6376.

Schott, F.A. & McCreary Jr, J.P. (2001). The monsoon circulation of the Indian Ocean. *Progress in Oceanography*, **51**, 1-123.

Schott, F.A., Xie, S.-P. & McCreary Jr, J.P. (2009). Indian Ocean circulation and climate variability. *Reviews of Geophysics*, **47**, RG1002, doi:10.1029/2007RG000245.

Schrag, D.P., Hampt, G. & Murray, D.W. (1996). Pore fluid constraints on the temperature and oxygen isotope composition of the glacial ocean. *Science*, **272**, 1930-1932.

Schrag, D.P., Adkins, J.F., McIntyre, K., Alexander, J.L., Hodell, D.A., Charles, C.D. & McManus, J.F. (2002). The oxygen isotope composition of seawater during the Last Glacial Maximum. *Quaternary Science Reviews*, **21**, 331-342.

Schulte, S. & Müller, P.J. (2001). Variations of sea surface temperature and primary productivity during Heinrich and Dansgaard-Oeschger events in the northeastern Arabian Sea. *Geo-Marine Letters*, **21**, 168-175.

Schulte, S., Rostek, F., Bard, E., Rullkötter, J. & Marchal, O. (1999). Variations of oxygen-minimum and primary productivity recorded in sediments of the Arabian Sea. *Earth and Planetary Science Letters*, **173**, 205-221.

Schulz, H., von Rad, U. & von Stackelberg, U. (1996). Laminated sediments from the oxygen minimum zone of the northeastern Arabian Sea. In: Kemp, A.E.S. (Ed.) *Paleoclimatology and Paleoceanography from Laminated Sediments.* Geological Society of London Special Publication, **116**, 185-207.

Schulz, H., von Rad, U. & Erlenkeuser, H. (1998). Correlation between Arabian Sea and Greenland climate oscillations of the past 110,000 years. *Nature*, **393**, 54-57.

Schulz, M. & Strattegger, K. (1998). SPECTRUM: Spectral analysis of unevenly spaced

palaeoclimatic time series. *Computers & Geosciences*, **23**, 929-945.

Schulz, M., Paul, A. & Timmermann, A. (2002). Relaxation oscillators in concert: A framework for climate change at millennial timescales during the Late Pleistocene. *Geophysical Research Letters*, **29**, 2193, doi:10.1029/2002GL016144.

Ségalen, L., Lee-Thorp, J.A. & Cerling, T. (2007). Timing of C4 grass expansion across sub-Saharan Africa. *Journal of Human Evolution*, **53**, 549-559.

Seki, O., Foster, G.L., Schmidt, D.N., Mackensen, A., Kawamura, K. & Pancost, R.D. (2010). Alkenone and boron-based Pliocene pCO_2 records. *Earth and Planetary Science Letters*, **292**, 201-211.

Sepulchre, P., Ramstein, G., Fluteau, F., Schuster, M., Tiercelin, J-J. & Brunet, M. (2006). Tectonic Uplift and Eastern Africa Aridification. *Science*, **313**, 1419-1423.

Shackleton, N.J. (1967). Oxygen isotope analyses and Pleistocene temperatures re-assessed. *Nature*, **215**, 15-17.

Shackleton, N.J. (1974). Attainment of isotopic equilibrium between ocean water and the benthic foraminifera Genus Uvigerina: isotope changes in the ocean during the last glacial. In: *Les methods quantitatives d'étude des variations due climat au cours du Pleistocene, 219.* Colloques Internationaux de Central National de la Recherce Scientifique CNRS, Paris, 203-209 pp.

Shackleton, N.J. (1987). Oxygen isotopes, ice volume and sea-level. *Quaternary Science Reviews*, **6**, 183-190.

Shackleton, N.J. (2000). The 100,000 year ice age cycle identified and found to lag temperature, carbon dioxide and orbital eccentricity. *Science*, **289**, 1897-1902.

Shackleton, N.J. & Opdyke, N.D. (1977). Oxygen isotope and paleomagnetic evidence for early northern hemisphere glaciation. *Nature*, **270**, 216-219.

Shackleton, N.J. & Hall, M.A. (1984). Oxygen and carbon isotope stratigraphy of DSDP Hole 552A: Plio-Pleistocene glacial history. Initial Rep. Deep Sea Drill. Project, 81, 599-609.

Shackleton, N.J., Backman, J., Zimmerman, H., Kent, D.V., Hall, M.A., Roberts, D.G. et al. (1984). Oxygen isotope calibration of the onset of ice-rafting and history of glaciation in the North Atlantic region. *Nature*, **307**, 620-623.

Shackleton, N.J., Berger, A. & Peltier, W.R. (1990). An alternative astronomical calibration of the lower Pleistocene time based on ODP Site 677. *Transactions of the Royal Society of Edinburgh: Earth Sciences*, **81**, 251-261.

Shankar, D., Vinayachandran, P.N. & Unnikrishnan, A.S. (2002). The monsoon currents in the north Indian Ocean. *Progress in Oceanography*, **52**, 63-120.

Sharp, Z. (2007). *Principles of Stable Isotope Geochemistry*, Pearson Prentice Hall, New Jersey, 344pp.

Shemesh, A. (1992). Silica-carbonate isotopic temperature calibration. *Science*, **258**, 1163.

Shemesh, A., Mortlock, R.A., Smith, R.J. & Froelich, P.N. (1988). Determination of Ge/Si in marine siliceous microfossils: separation, cleaning and dissolution of diatoms and radiolaria. *Marine Chemistry*, **25**, 305– 323.

Shemesh, A., Charles, C.D. & Fairbanks, R.G. (1992). Oxygen Isotopes in biogenic silica: Global changes in ocean temperature and isotopic composition. *Science*, **256**, 1434-1436.

Shemesh, A., Burckle, L.H. & Hays, J.D. (1994). Meltwater input into the Southern Ocean during the last glacial maximum. *Science*, **266**, 1542-1544.

Shemesh, A., Burckle, L.H. & Hays, J.D. (1995). Late Pleistocene oxygen isotope records of biogenic silica from the Atlantic sector of the Southern Ocean. *Paleoceanography*, **10**, 179–196.

Shemesh, A., Rosqvist, G.C., Rietti-Shatti, M., Rubensdotter, L., Bigler, C., Yam, R. & Karlen, W. (2001a). Holocene climatic change in Swedish Lapland inferred from an oxygen-isotope record of lacustrine biogenic silica. *The Holocene*, **11**, 447-454.

Shemesh, A., Rietti-Shatti, M., Rioual, P., Batterbee, R.W., de Beaulieu, J-L., Reillie, M., Andrieu, V. & Svobodova, H. (2001b). A oxygen isotope record of lacustrine opal from a European Maar indicates climatic stability during the last Interglacial. *Geophysical Research Letters*, **28**, 2305-2308.

Shi, N. & Dupont, L.M. (1997). Vegetation and climatic history of south-west Africa: A marine palynological record of the last 300,000 years. *Vegetation History and Archaeobotany*, **6**, 117-131.

Shimmield, G.B. (1992). Can sediment geochemistry record changes in coastal upwelling palaeoproductivity? Evidence from northwest Africa and the Arabian Sea. In: Summerhayes, C.P., Prell, W.L. & Emeis, K.C. (Eds.), *Upwelling Systems: Evolution Since the Early Miocene.* Geological Society Special Publication No 64, pp. 29-46.

Shimmield, G.B. & Mowbray, S.R. (1991). The inorganic geochemical record of the northwest Arabian Sea: a history of productivity variation over the last 400 k.y. from Sites 722 and 724. In: Prell, W.L., Niitsuma, N., et al., *Proceedings of the Ocean Drilling Program, Scientific Results*, **Vol 117**, College Station, TX (Ocean Drilling Program), 409–429. doi:10.2973/odp.proc.sr.117.170.

Shipboard Scientific Party (1989). Site 722. In: Prell, W.L., Niitsuma, N., et al., *Proceedings of the Ocean Drilling Program, Initial Reports*, **117**, pp. 255-317, doi:10.2973/odp.proc.ir.117.107.1989

Siegenthaler, U. & Oeschger, H. (1980). Correlation of ^{18}O in precipitation with temperature and altitude. *Nature*, **285**, 314-331.

Sigman, D.M., Jaccard, S.L. & Haug, G.H. (2004). Polar ocean stratification in a cold climate. *Nature*, **428**, 59–63.

Simpson, G.L. (2008). Numerical analysis of biological and environmental data. Environmental Change Research Centre, University College London, London.

Simpson, G.L. & Anderson, N.J. (2009). Deciphering the effect of climate change and separating the influence of confounding factors in sediment core records using additive models. *Limnology and Oceanography*, **54**, 2529-2541.

Sirocko, F. & Sarnthein, M. (1989). Wind-borne deposits in the north-west Indian Ocean: record

of Holocene sediments versus modern satellite data. In: Leinen, M. & Sarnthein, M. (Eds.), *Paleoclimatology and Paleometeorology – Modern and Past Patterns of Global Atmospheric Transport.* NATO ASI Ser., 282: 401-433.

Sirocko, F., Garbe-Schönberg, D., McIntyre, A. & Molfino, B. (1996). Teleconnections between the subtropical monsoons and high-latitude climates during the last deglaciation. *Science*, **272**, 526-529.

Sirocko, F., Leuschner, D., Staubwasser, M., Maley, J. & Heusser, L. (1999). High-frequency oscillations of the last 70,000 years in the tropical/subtropical and polar climates. In: Clark, P.U., Webb, R.S., Keigwin, L.D. (Eds.), *Mechanisms of Global Climate Change at Millennial Time Scales*. Geophysical Monograph 112, AGU, Washington, D.C., pp. 113-126.

Sirocko, F., Garbe-Schonberg, D. & Devey, C. (2000). Processes controlling trace element geochemistry of Arabian Sea sediments during the last 25,000 years. *Global and Planetary Change*, **26**, 217-303.

Slingo, J., Spencer, H., Hoskins, B., Berrisford, P. & Black, E. (2005). The meteorology of the Western Indian Ocean, and the influence of the East African Highlands. *Philosophical Transactions of the Royal Society A*, **363**, 25– 42, doi:10.1098/rsta.2004.1473.

Sokolik, I.N. & Toon, O.W. (1996). Direct radiative forcing by anthropogenic airborne mineral aerosols. *Nature*, **381**, 681-683.

Spero, H.J. & Lea, D.W. (1993). Intraspecific stable isotope variability in the planktonic foraminifera *Globigerinoides sacculifer*: results from laboratory experiments. *Marine Micropaleontology*, **22**, 221-234.

Spero, H.J., Bijma, J., Lea, D.W. & Bemis, B.E. (1997). Effect of seawater carbonate concentration on foraminiferal carbon and oxygen isotopes. *Nature*, **390**, 497-500.

Spofforth, D.J.A., Pälike, H. & Green, D. (2008). Paleogene record of elemental concentrations in sediments from the Arctic Ocean obtained by XRF analyses. *Paleoceanography*, **23**, PA1S09, doi:10.1029/2007PA001489.

Srinivasan, M.S. & Sinha, D.K. (1998). Early Pliocene closing of the Indonesian Seaway: evidence from north-east Indian Ocean and Tropical Pacific deep sea cores. *Journal of Asian Earth Sciences*, **16**, 29-44.

Stager. J.C., Cumming, B. & Meeker, L.D. (1997). An 11,400-year, high-resolution diatom record from Lake Victoria, East Africa. *Quaternary Research*, **47**, 81-89.

Stager, J.C., Mayewski, P.A. & Meeker, L.D. (2002). Cooling cycles, Heinrich Event 1 and the dessication of Lake Victoria. *Palaeogeography, Palaeoclimatology, Palaeoecology*, **183**, 169-178.

Steenbrink, J., Kloosterboer-van Hoeve, M.L. & Hilgen, F.J. (2003). Millennial-scale climate variations recorded in Early Pliocene colour reflectance time series from the lacustrine Ptolemais Basin (NW Greece). *Global and Planetary Change*, **36**, 47-75.

Stein, R. (1991). Accumulation of organic carbon in marine sediments: Results from the Deep

Sea Drilling Program/Ocean Drilling Program (DSDP/ODP). *Lecture Notes from the Earth Sciences*, **vol. 34.**

Steph, S., Tiedemann, R., Prange, M., Groeneveld, J., Nurnberg, D., Reuning, L., Schulz, M. & Haug, G.H. (2006). Changes in the Caribbean surface hydrography during the Pliocene shoaling of the Central American seaway. *Paleoceanography*, **21**, PA4221.

Stone, J.R., Westover, K.S. & Cohen, A.S. (in press). Late Pleistocene palaeohydrology and diatom paleoecology of the central basin of Lake Malawi, Africa. *Palaeogeography, Palaeoclimatology, Palaeoecology*, doi:10.1016/j.palaeo.2010.01.012.

Street, F.A. (1980). The relative importance of climate and local hydrogeological factors in influencing lake-level fluctuations. *Palaeoecology of Africa*, **12**, 137-158.

Street-Perrott, F.A. & Perrott, A. (1990). Abrupt climate fluctuations in the tropics: the influence of Atlantic Ocean circulation. *Nature*, **343**, 607-612.

Street-Perrott, F.A., Barker, P.A., Leng, M.J., Sloane, H.J., Wooller, M.J., Ficken, K.J. & Swain, D.L. (2008). Towards an understanding of late Quaternary variations in the continental biogeochemical cycle of silicon: multi-isotope and sediment-flux data for Lake Rutundu, Mt Kenya, East Africa, since 38 ka BP. *Journal of Quaternary Science*, **23**, 375-387.

Sun, J. & Huang, X. (2006). Half-precession cycles recorded in Chinese loess: response to low-latitude insolation forcing during the last interglaciation. *Quaternary Science Reviews*, **25**, 1965-1972.

Sun, Y.B., Clemens, S.C., An, Z. S. & Yu, Z.W. (2006a). Astronomical timescale and palaeoclimatic implication of stacked 3.6-Ma monsoon records from the Chinese Loess Plateau. *Quaternary Science Reviews*, **25**, 33-48.

Sun, Y.B., Chen, J., Clemens, S.C., Liu, Q.-S., Ji, F.-J. & Tada, R. (2006b). East Asian monsoon variability over the last seven glacial cycles recorded by a loess sequence from the northwestern Chinese Loess Plateau. *Geochemistry, Geophysics, Geosystems*, **7**, Q12Q02, doi:10.1029/2006GC001287.

Swann, G.E.A. & Leng, M.J. (2009). A review of diatom $\delta^{18}O$ in palaeoceanography. *Quaternary Science Reviews*, **28**, 384-398.

Swann, G.E.A. & Patwardhan, S.V. (2011). Application of Fourier Transform Infrared Spectroscopy (FTIR) for assessing biogenic silica sample purity in geochemical analyses and palaeoenvironmental research. *Climate of the Past*, **7**, 65-74.

Swann, G.E.A., Maslin, M.A., Leng, M.J., Sloane, H.J. & Haug, G.H. (2006). Diatom $\delta^{18}O$ evidence for the development of the modern halocline system in the subarctic northwest Pacific at the onset of major Northern Hemisphere glaciation. *Paleoceanography*, **21**, PA1009, doi:10.1029/2005PA001147.

Swann, G.E.A., Leng, M.J., Sloane, H.J., Maslin, M.A. & Onodera, J. (2007). Diatom oxygen isotopes: evidence of a species effect in the sediment record. *Geochemistry, Geophysics, Geosystems* **8**, Q06012, doi:10.1029/2006GC 001535.

Swann, G.E.A., Leng, M.J., Sloane, H.J. & Maslin, M.A. (2008). Isotope offsets in marine diatom $\delta^{18}O$ over the last 200 ka. *Journal of Quaternary Science*, **23**, 389–400.

Swann, G.E.A., Leng, M.J., Juschus, O., Melles, M., Brigham-Grette, J. & Sloane, H.J. (2010). A combined oxygen and silicon diatom isotope record of Late Quaternary change in Lake El-gygytgyn, North East Siberia. *Quaternary Science Reviews*, **29**, 774-789.

Talling, J.F. (1986). The seasonality of phytoplankton in African lakes. *Hydrobiologia*, **138,** 139-160.

Tarits, C., Renaut, R.W., Tiercelin, J.-J., Le Hérissé, A., Cotton, J. & Cabon, J.-Y. (2006). Geochemical evidence of hydrothermal recharge in Lake Baringo, central Kenya Rift Valley. *Hydrological Processes*, **20**, 2027-2055.

Taylor, H.P. & Epstein, S. (1962). Relationships between $^{18}O/^{16}O$ ratios in coexisting minerals of igneous and metamorphic rocks, part I, Principles and experimental results. *Bulletin of the Geological Society of America*, **73**, 461-480.

Ter Braak, C.J.F. & Šmilauer, P. (2002) *CANOCO Reference Manual and Canodraw for Windows User's Guide: Software for Canonical Community Ordination (Version 4.5)*. Microcomputer Power, Ithaca, NY, USA.

Thamban, M., Kawahata, H. & Rao, V.P. (2007). Indian summer monsoon variability during the Holocene as recorded in sediments of the Arabian Sea: Timing and implications. *Journal of Oceanography*, **63**, 1009-1020.

Thierens, M., Pirlet, H., Colin, C., Latruwe, K., Vanhaecke, F., Lee, J.R., Stuut, J.-B., Titschack, J., Huvenne, V.A.I., Dorschel, B., Wheeler, A.J. & Henriet, J.-P. (2011). Ice-rafting from the British-Irish ice sheet since the earliest Pleistocene (2.6 million years ago): Implications for long-term mid-latitudinal ice-sheet growth in the North Atlantic region. *Quaternary Science Reviews*, doi:10.1016/j.quascirev.2010.12.020.

Thorliefson, J.T. (1984). *A modified stepwise fluorination procedure for the oxygen isotopic analysis of hydrous silica*. MS thesis, Arizona State University.

Thorliefson, J.T. & Knauth, L.P. (1984). An improved stepwise fluorination procedure for the oxygen isotopic analysis of hydrous silica. *Geological Society of America Abstracts Progress*, **16**, 675.

Tian, J., Pak, D.K., Wang, P., Lea, D., Cheng, X. & Zhao, Q. (2006). Late Pliocene monsoon linkage in the tropical South China Sea. *Earth and Planetary Science Letters*, **252**, 72-81.

Tiedemann, R., Sarnthein, M. & Shackleton, N.J. (1994). Astronomic time scale for the Pliocene Atlantic δ18O and dust flux records of Ocean Drilling Program Site 659. *Paleoceanography*, **9**, 619-638.

Tierney, J.E., Russell, J.M., Huang, Y., Sinninghe Damsté, J.S., Hopmans, E.C. & Cohen, A.S. (2008). Northern hemisphere controls on tropical southeast African climate during the past 60,000 years. *Science*, **322**, 252-255.

Tjallingii, R. (2007). Application and quality of X-Ray Fluorescence core scanning in reconstructing Late Pleistocene NW African continental margin sedimentation patterns and palaeoclimate variations. Ph.D. Thesis, Universität Bremen, Germany.

Torrence, C. & Compo, G.P. (1998). A practical guide to wavelet analysis. *Bulletin of the American Meteorological Society*, **79**, 61-78.

Torrence, C. & Torrence, G.P. (1998). A practical guide to wavelet analysis. *Bulletin of the American Meteorological Society*, **79**, 61-78.

Trauth, M.H. (2010). *MATLAB® Recipes for Earth Sciences*, Third Edition. Springer-Verlag, Berlin. 336pp.

Trauth, M.H., Deino, A.L., Bergner, A.G.N. & Strecker, M.R. (2003). East African climate change and orbital forcing during the last 175 kyr BP. *Earth and Planetary Science Letters*, **206**, 297-313.

Trauth, M.H., Maslin, M.A., Deino. A.L. & Strecker, M.R. (2005). Late Cenozoic Moisture History of East Africa. *Science*, **309**, 2051-2053.

Trauth, M.H., Maslin, M.A., Deino, A.L., Strecker, M.R., Bergner, A.G.N. & Dühnforth, M. (2007). High- and low-latitude forcing of Plio-Pleistocene East African climate and human evolution. *Journal of Human Evolution*, **53**, 475-486.

Trauth, M. H., Larrasoana, J.C. & Mudelsee, M. (2009). Trends, rhythms and events in Plio-Pleistocene African climate. *Quaternary Science Reviews*, **28**, 399-411.

Trauth, M.H., Maslin, M.A., Deino, A.L., Junginger, A., Lesoloyia, M., Odada, E.O., Olago, D.O., Olaka, L.A., Strecker, M.R. Tiedemann, R. (2010). Human evolution in a variable environment: the amplifier lakes of Eastern Africa. *Quaternary Science Reviews*, **29**, 2981-2988.

Tuenter, E., Weber, S.L., Hilgen, F.J., Lourens, L.J. & Ganopolski, A. (2005). Simulation of climate phase lags in response to precession and obliquity forcing and the role of vegetation. *Climate Dynamics*, **24**, 279-295.

Tyler, J.J., Leng, M.J., Sloane, H.J., Sachse, D. & Gleixner, G. (2008). Oxygen isotope ratios of sedimentary biogenic silica reflect the European transcontinental climate gradient. *Journal of Quaternary Science*, **23**, 341–350.

Tyson, P.D. & Partridge, T.C. (2000). Evolution of Cenozoic climates. In: Partridge, T.C, Maul, R.R. (Eds.), *The Cenozoic of Southern Africa*. Oxford University Press, New York, pp. 371-387.

Tyson, P.D. & Preston-White, R.A. (2000). *The Weather and Climate of Southern Africa*, Oxford University Press, New York, pp. 371-387.

Urey, H.C. (1947). The thermodynamic properties of isotopic substances. *Journal of the Chemical Society*, **152**, 190-219.

Urey, H.C. (1948). Oxygen isotopes in nature and in the laboratory. *Science*, **108**, 489-496.

Urey, H.C., Epstein, S., McKinney, C. & McCrea, J. (1948). Method for measurement of paleotemperatures. *Bulletin of the Geological Society of America – New York Meeting (abstract)*, **59**, 1359-1360.

Urey, H.C., Epstein, S. & McKinney, C. (1951). Measurement of paleotemperatures and temperatures of the Upper Cretaceous of England, Denmark and the southeastern United States. *Geological Society of America Bulletin*, **62**, 399-416.

Van Bennekom, A.J. & van der Gaast, S.J. (1976). Possible clay structures in frustules of living diatoms. *Geochimica et Cosmochimica Acta*, **40**, 1 –6.

Van der Burgh, J., Visscher, H., Dilcher, D.L. & Kürschner, W.M. (1993). Paleoatmospheric signatures in Neogene fossil leaves. *Science*, **260**, 788-790.

Van Geel, B., Raspopüov, O.M., Renssen, H., van der Plicht, J., Dergachev, V.A. & Meijer, H.A.J. (1999). The role of solar forcing upon climate change. *Quaternary Science Reviews*, **18**, 331-338.

Van Kreveld, S., Sarnthein, M., Erlenkeuser, H., Grootes, P., Jung, S., Nadeau, M.J., Pflaumann, U. & Voelker, A. (2000). Potential links between surging ice sheets, circulation changes, and the Dansgaard-Oeschger cycles in the Irminger Sea, 60-18 kyr. *Paleoceanography*, **15**, 425-442.

Verschuren, D., Sinninghe Damsté, J.S., Moernaut, J., Kristen, I., Blaauw, M., Fagot, M., Haug, G.H. & CHALLACEA Project Members. (2009). Half-precessional dynamics of monsoon rainfall near the East African equator. *Nature*, **462**, 637-641.

Vilaclara, G., Martinez-Mekler, G., Cuna, E. & Ugalde, E. (2010). Diatom-inferred palaeoenvironmental changes of a Pliocene lake disturbed by volcanic activity. *Journal of Paleolimnology*, **44**, 203-215.

Vinayachandran, P.N. & Kurian, J. (2008). Modelling Indian Ocean Circulation: Bay of Bengal Fresh Plume and Arabian Sea Mini Warm Pool. *Proceedings of the 12th Asian Congress of Fluid Mechanics*, Daejeon, Korea.

Von Grafenstein, U., Erlenrkeuser, H. & Trimborn, P. (1999). Oxygen and carbon isotopes in modern freshwater ostracod valves: Assessing vital offsets and autecological effects of interest for palaeoclimate studies. *Palaeogeography Palaeoclimatology Palaeoecology*, **148**, 133–152.

Von Rad, U., Schulz, H. & SONNE 90 Scientific Party (1995). Sampling the oxygen minimum zone off Pakistan: glacial-interglacial variations of anoxia and productivity (preliminary results, SONNE 90 cruise). *Marine Geology*, **125**, 7-19.

Vrba, E.S. (1985a). Environment and evolution: alternative causes of the temporal distribution of evolutionary events. *South African Journal of Science*, **81**, 229–236.

Vrba, E.S. (1985b). Ecological and adaptive changes associated with early hominid evolution. In: Delson, E., (Ed.). *Ancestors: the hard evidence*. New York: Alan R. Liss, p 63–71.

Vrba, E.S. (1993). Turnover-pulses, the Red Queen, and related topics. *American Journal of Science*, **293**, 418–452.

Vuille, M., Werner, M., Bradley, R.S., Chan, R.Y. & Keimig, F. (2005). Stable isotopes in East African precipitation record Indian Ocean zonal mode. *Geophysical Research Letters*, **32**, L21705, doi:10.1029/2005GL023876.

Waelbroeck, C., Labeyrie, L., Michel, E., Duplessy, J.C., McManus, J.F., Lambeck, K., Balbon, E. & Labracherie, M. (2002). Sea level and deep water temperature changes derived from benthic foraminifera isotope records. *Quaternary Science Reviews*, **21**, 295-305.

Waelbroeck, C., Mulitza, S., Spero, H.J., Dokken, T., Kiefer, T. & Cortijo, E. (2005). A global compilation of late Holocene planktonic foraminiferal $\delta^{18}O$: relationship between surface water temperature and $\delta^{18}O$. *Quaternary Science Reviews*, **24**, 853-868.

Wajsowicz, R. C. & Schopf, P. S. (2001). Oceanic influences on the seasonal cycle in evaporation over the Indian Ocean. *Journal of Climate*, **14**, 1199-1266.

Waliser, D.E. & Somerville, R.C.J. (1994). Preferred latitudes of the Intertropical Convergence Zone. *Journal of the Atmospheric Sciences*, **51**, 1619-1639.

Wang, C-H. & Yeh, H-W. (1985). Oxygen isotope composition of DSDP Site 480 diatoms: Implications and applications. *Geochimica et Cosmochimica Acta*, **49**, 1469-1478.

Wang, P.X. (2009). Global monsoon in a geological perspective. *Chinese Scientific Bulletin*, **54**, 1113-1136.

Wang, Y.J., Cheng, H., Edwards, R.L., An, Z.S., Wu., J.Y., Shen, C.C. & Dorale, J.A. (2001). A high-resolution absolutely dated late Pleistocene monsoon record from Hulu Cave, China. *Science*, **294**, 2345-2348.

Wang, Y.J., Cheng, H., Edwards, R.L., He, Y., Kong, X., An, Z.S., Wu, J.Y., Kelly, M.J., Dykoski, C.A. & Li, X. (2005). The Holocene Asian monsoon: Links to solar changes and North Atlantic climate. *Science*, **308**, 854-857.

Wang, Y.J., Cheng, H., Edwards, R.L., Kong, X., Xiaohua, S., Chen, S., Wu, J.Y., Jiang, X., Wang, X. & Zhisheng, A. (2008a). Millennial- and orbital-scale changes in the East Asian monsoon over the past 224,000 years. *Nature*, **451**, 1090-1093.

Wang, Y.J., Cheng, H., Edwards, R.L., He, Y.Q., Kong, X.G., An, Z., Wu, J.Y., Kelly, M.J., Dykoski, C.A. & Li, X.D. (2008b). The Holocene Asian Monsoon: Links to Solar Changes and North Atlantic Climate. *Science*, **308**, 854-857.

Wara, M.W., Ravelo, A.C. & Delaney, M.L. (2005). Permanent El Nino-like conditions during the Pliocene Warm Period. *Science*, **309**, 758-761.

Watanabe, T., Suzuki, A., Minobe, S., Kawashima, T., Kameo, K., Minoshima, K., Aguilar, Y.M., Wani, R., Kawahata, H., Sowa, K., Nagai, T. & Kase, T. (2011). Permanent El Niño during the Pliocene warm period not supported by coral evidence. *Nature*, **471**, 209-211.

Webb, S.D. (1997). The great American faunal interchange. In Coates, A.G., ed., *Central America: A natural and cultural history*: New Haven, Connecticut, Yale University Press, pp. 97–122.

Weber, M.E., Tougiannidis, N., Kleineder, M., Bertram, N., Ricken, W., Rolf, C., Reinsch, T. & Antoniadis, P. (2010). Lacustrine sediments document millennial-scale climate variability in northern Greece prior to the onset of the northern hemisphere glaciation. *Palaeogeography, Palaeoclimatology, Palaeoecology*, **291**, 360-370.

Webster, P.J. (1981). Monsoon. *Scientific American*, **1981**, 70-80.

Webster, P.J., Moore, A.M., Loschnigg, J.P. & Leben, R.R. (1999). Coupled ocean-atmosphere dynamics in the Indian Ocean during 1997-98. *Nature*, **401**, 356-360.

Wefer, G. & Berger, W.H. (1991). Isotope palaeontology: growth and composition of extant calcareous species. *Marine Geology*, **100**, 207-248.

Wefer, G., Berger, W.H., Bijma, J. & Fischer, G. (1999). Clues to Ocean History: A brief overview of proxies. In: G. Fischer & G. Wefer (Eds.) *Uses of proxies in Paleoceanography: Examples from the South Atlantic.* Springer-Verlag, Berlin, pp. 1-68.

Wehausen, R. & Brumsack, H.-J. (2000). Chemical cycles in Pliocene sapropel-bearing and sapropel-barren eastern Mediterranean sediments. *Palaeogeography, Palaeoclimatology, Palaeoecology*, **158**, 325-352.

Wehausen, R. & Brumsack, H.-J. (2002). Astronomical forcing of the East Asian monsoon mirrored by the composition of Pliocene South China Sea sediments. *Earth and Planetary Science Letters*, **201**, 621-636.

Weltje, G.J. & Tjallingii, R. (2008). Calibration of XRF core scanners for quantitative geochemical logging of sediment cores: Theory and application. *Earth and Planetary Science Letters*, **274**, 423-438.

Wesselman, H.B. (1985). Fossil micromammals as indicators of climatic change about 2.4 myr ago in the Omo Valley, Ethiopia. *South African Journal of Science*, **81**, 260-261.

Wesselman, H.B. (1995). Of Mice and Almost-Men: Regional Paleoecology and Human Evolution in the Turkana Basin. In E.S. Vrba, G.H. Denton, T.C. Partridge & L.H. Burckle (eds.), *Paleoclimate and Evolution with emphasis on Human origins*, Yale University Press. pp. 356-368.

Whitmarsh, R.B. (1979). The Owen Basin off the South-east margin of Arabia and the evolution of the Owen Fracture Zone. *Geophysical Journal of the Royal Astronomical Society*, **58**, 441-470.

Whitmarsh, R. B., Weser, O. E., Ross, D. A., et al., (1974). *Initial Reports Deep Sea Drilling Program*, **23**, Washington (U.S. Govt. Printing Office).

Williams, D.F., Bé, A.W.H. & Fairbanks, R.G. (1979). Seasonal oxygen isotopic variations in living planktonic foraminifera off Bermuda. *Science*, **206**, 447-449.

Williams, L.A.J. & Chapman, G.R. (1986). Relationships between major structures, salic volcanism and sedimentation in the Kenya Rift from the equator northwards to Lake Turkana. In: L.E. Frostick et al. (Eds.) *Sedimentation in African Rifts*, Geological Society Special Publication No. **25**, pp. 59-74.

Williams, M.A.J., Williams, F.M., Gasse, F., Curtis, G.H. & Adamson, D.A. (1979). Pliocene-Pleistocene environments at Gadeb prehistoric site, Ethiopia. *Nature*, **282**, 29-33.

Williams, P. (2010). Diagnosing the causes of decadal-scale precipitation variability in northeastern sub-Saharan Africa. *EOS Transactions AGU*, Fall Meeting Supplement 2010, abstract GC51C-0768.

Wolde Gabriel, G., White, T.D., Suwa, G., Renne, P.R., de Heinzelin, J., Hart, W.K. & Heiken, G. (1994). Ecological and temporal placement of early Pliocene hominids at Aramis, Ethiopia. *Nature*, **371**, 330-333.

Wolde Gabriel, G., Haile-Selassie, Y., Renne, P.R., Hart, W.K., Ambrose, S.H., Asfaw, B., Heiken, G. & White, T. (2001). Geology and Paleontology of the Late Miocene Middle Awash Valley, Afar Rift, Ethiopia. *Nature*, **412**, 175-182.

Wolfe, B.B., Edwards, T.W.D., Aravena, R., Forman, S.L., Warner, B.G., Velichko, A.A. &

MacDonald, G.M. (2000). Holocene palaeohydrology and paleoclimate at treeline, north-central Russia, inferred from oxygen isotope records in lake sediment cellulose. *Quaternary Research*, **53**, 319–329.

Wolfe, B.B., Edwards, T.W.D., Jiang, H.B., MacDonald, G.M., Gervais, B.R. & Snyder, J.A. (2003). Effect of varying oceanicity on early to mid-Holocene palaeohydrology, Kola Peninsula, Russia: isotopic evidence from treeline lakes. *The Holocene*, **13**, 153–160.

Wood, B. (1999). Plio-Pleistocene hominins from the Baringo Region, Kenya. In: Andrews, P. & Banham, P. (Eds.) *Late Cenozoic Environments and Hominid Evolution: a tribute to Bill Bishop*. Geological Society, London, pp. 113-122.

Wright, J.D. & Miller, K.G. (1996). Control of North Atlantic Deep Water circulation by the Greenland–Scotland Ridge. *Paleoceanography*, **11**, 157–170.

Xia, J., Engstrom, D.R. & Ito, E. (1997). Geochemistry of ostracode calcite: 1. An experimental determination of oxygen isotope fractionation. *Geochimica et Cosmochimica Acta*, **61**, 377–382.

Yarincik, K.M., Murray, R.W. & Peterson, L.C. (2000). Climatically sensitive eolian and hemipelagic deposition in the Cariaco Basin, Venezuela, over the past 578,000 years: Results from Al/Ti and K/Al. *Paleoceanography*, **15**, 210-228.

Zabel, M., Bickert, T., Dittert, L. & Haese, R.R. (1999). Significance of the sedimentary Al:Ti ratio as an indicator for variations in the circulation patterns of the equatorial North Atlantic. *Paleoceanography*, **14**, 789-799.

Zachos, J., Pagini, M., Sloan, L., Thomas, E. & Billups, K. (2001). Trends, Rhythms and Aberrations in Global Climate 65Ma to Present. *Science*, **292**, 686-693.

Zahn, R., Winn, K. & Sarnthein, M.K. (1986). Benthic foraminiferal ^{13}C and accumulation rates of organic carbon: *Uvigerina peregrina* group and *Cibicidoides wuellerstorfi*. *Paleoceanography*, **1**, 27-42.

Zeebe, R.E. (1999). An explanation of the effect of seawater carbonate concentration on foraminiferal oxygen isotopes. *Geochimica et Cosmochimica Acta*, **63**, 2001-2007.

Zeebe, R.E. (2005). Reply to the comment by P.Deines on "An explanation of the effect of seawater carbonate concentration on foraminiferal isotopes", by R.E. Zeebe (1999). *Geochimica et Cosmochimica Acta*, **69**, 789-790.

Zhu, X., Bothe, O. & Fraedrich, K. (2011). Summer atmospheric bridging between Europe and East Asia: Influences on drought and wetness on the Tibetan Plateau. *Quaternary International*, doi: 10.1 016/j.quaint.2010.06.015.

Ziegler, M., Tuenter, E. & Lourens, L.J. (2010a). The precession phase of the boreal summer monsoon as viewed from the eastern Mediterranean (ODP Site 968). *Quaternary Science Reviews*, **29**, 1481-1490.

Ziegler, M., Lourens, L.J., Tuenter, E. & Reichart, G.-J. (2010b). High Arabian Sea productivity conditions during MIS13 - odd monsoon event or intensified overturning circulation at the end of the Mid-Pleistocene transition. *Climate of the Past*, **6**, 63-76.